Development and Mechanistic Investigations of Chemical Transformations Involving Single Electron Processes

Inaugural-Dissertation
to obtain the academic degree
Doctor rerum naturalium (Dr. rer. nat.)

Submitted to the Department of Biology, Chemistry, Pharmacy
of Freie Universität Berlin

by
Amiera Madani

June 2023

This work was performed between April 2019 and November 2022 under the direction of Prof. Dr. Dr. h. c. Peter H. Seeberger in the Department of Biomolecular Systems, at the Max Planck Institute of Colloids and Interfaces.

1st reviewer: Prof. Dr. Dr. h. c. Peter H. Seeberger
2nd reviewer: Prof. Dr. Siegfried Eigler

Date of oral defense: 28.08.2023

Acknowledgements

I want to thank Prof. Dr. Dr. h. c Peter Seeberger for giving me the opportunity to conduct my doctoral studies in the Bimolecular Systems Department at the Max Planck Institute of Colloids and Interfaces. I am thankful to Prof. Dr. Siegfried Eigler for kindly agreeing to review this thesis. I would like to thank my supervisor Dr. Bartholomäus Pieber for his scientific guidance throughout the years, his time and effort, dedication and his tireless motivation.

Many thanks to Eva Settels, Olaf Niemeyer and Dorothee Böhme for technical and organizational support.

To my family, my strength. My biggest acknowledgements go to you, for your unlimited and unconditional love and support. My brother Faris, for being the most positive person I´ve ever met and my mother, for being stronger than she knows. I want to thank my Dad for believing in me and teaching me how to stand up for myself and others. In this spirit, I would like to thank my chosen brother Jamal Malik, who was my mentor in my very first project and is still real-time monitoring my life. Thank you for being there, for being genuinely good and vegan. I want to thank Mark for his solid support and for sharing everything - your home, kitties and countless memories. I want to thank my first flatmate and dear friend Lisa for making our WG a warm home, for lazy Sunday mornings in the kitchen and untiringly listening to my practice talks. Many thanks go to my long-term friends and favorite women in STEM, Anna, Kim und Janina, for always inspiring me and sharing your experience. I want to thank my home-based friends Jurij and Felix K.-Preusch for always being there and up to no good. My Berlin-based friends Niki, Agata, Samu for making my time here a good one & Kimberly for being my swim-buddy. Special thanks go to Jessi, who is in my life since most of my life - cancer stands no chance with you! Thank you to my best friend Selina and her husband Micha for being family and always having my back. I always feel like home when Im with you.

I am thankful for all my colleagues of the BS Department, especially Sabrina, Paula and Jakob for the nice and motivating working environment, all the fruitful discussions and exchange of knowledge. I want to thank Eric for his great support, patience and sharing of knowledge in my last project.

Special thanks go to my current and former labmates of the CATs group, Cristian, Sebastian, Susanne, Lucia, Cosima, Sho, Haralds, Aleksander, Christos and Valerio. Thank you for creating such a great atmosphere in the lab and enduring my love for techno. Coffee with orange juice is great.

Difference is that raw and powerful connection from which our personal power is forged.

Audre Lorde

List of Publications

Madani A.; Pieber B. In Situ Reaction Monitoring in Photocatalytic Organic Synthesis. *ChemCatChem* **2023**, 15, e20220158.

Madani A.; Anghileri L.; Heydenreich M.; Möller H. M.; Pieber B. Benzylic Fluorination Induced by a Charge-Transfer Complex with a Solvent-Dependent Selectivity Switch. *Organic Letters* **2022**, 24, 29, 5376-5380.

Madani A.;[†] Sletten E. T.;[†] Cavedon C.; Seeberger P. H.; Pieber, B. Visible-light-mediated oxidative debenzylation of 3-*O*-benzyl-1,2:5,6-di-*O*-isopropylidene-α-D-glucofuranose. *Manuscript under Revision*.

[†] These Authors contributed equally.

Malik A. J.; **Madani, A.**; Seeberger, P. H.; Pieber, B. Evidence for Photocatalyst Involvement in Oxidative Additions of Nickel-Catalyzed Carboxylate *O*-Arylations. *Journal of the American Chemical Society* **2020**, 142, 11042-11049.

Cavedon, C.; **Madani, A**.; Seeberger, P. H.; Pieber, B. Semiheterogeneous Dual Nickel/Photocatalytic (Thio)etherification Using Carbon Nitrides. *Organic Letters* **2019**, *21*, 5331-5334.

Cavedon, C.; Sletten, E. T.; **Madani, A**.; Niemeyer, O.; Seeberger, P. H.; Pieber, B. Visible-Light-Mediated Oxidative Debenzylation Enables the Use of Benzyl Ethers as Temporary Protecting Groups. *Organic Letters* **2021**, *23*, 514-518.

Table of Contents

Statement of Authorship

I hereby certify that the herein presented dissertation was authored by myself and was completed using only the cited literature and sources. This thesis is submitted to the Department of Biology, Chemistry, Pharmacy of Freie Universität Berlin to obtain the academic degree Doctor rerum naturalium (Dr. rer. nat.) and has not been submitted for any other degree.

Selbstständigkeitserklärung

Hiermit versichere ich, dass ich die vorliegende Dissertation selbstständig und lediglich unter Benutzung der angegebenen Quellen und Hilfsmittel verfasst habe. Diese Arbeit wird beim Fachbereich Biologie, Chemie, Pharmazie der Freien Universität Berlin zur Erlangung des akademischen Grades Doctor rerum naturalium (Dr. rer. nat.) eingereicht und wurde für keinen anderen Abschluss eingereicht.

Berlin, den

Amiera Madani

Abstract

Radicals play a pivotal role in nature and are involved in many biochemical processes. However, until the late 20th century only minor attention was given to single electron processes in synthetic organic chemistry, due to the persistent notion of being difficult to control. With the development of new synthetic approaches to access such reactive open-shell intermediates in a practical fashion, radical chemistry has gained renewed interest. Photoredox catalysis (PRC) has emerged as the cornerstone in accessing these reactive open-shell intermediates under mild conditions. Key to the success of these strategies is the ability of chromophores to harvest visible light and reach long-lived excited states. Subsequently, the excited photocatalytic species can activate intermediates or reagents via single electron transfer (SET), energy transfer (ET), or hydrogen atom transfer (HAT) to yield radicals and enable chemical transformations. The mechanism of such photocatalytic systems often includes multiple catalytic species and reagents, which are actively involved in the catalytic cycle and render mechanistic investigations complicated. State-of-the-art methodologies to investigate photocatalytic systems mainly focus on the properties of the excited state species and consecutive quenching interaction with reagents, catalysts or intermediates. A more holistic picture of the overall process can be acquired via in situ monitoring techniques (Chapter 4).

The value of real-time monitoring for gaining mechanistic insights was demonstrated during the development of a photocatalytic benzyl ether cleavage (Chapter 9). Due to their high stability, benzyl ethers are commonly used protecting groups in carbohydrate and natural product syntheses, though commonly utilized harsh deprotection strategies with poor functional group tolerance render them typically unattractive for multistep organic synthesis. Upon visible light irradiation, 2,3-dichlor-5,6-dicyano-1,4-benzoquinone (DDQ) reaches a highly oxidizing, long-lived excited triplet state (DDQ*), capable of oxidative cleavage of benzyl ethers.

A combination of DDQ and *tert*-butyl nitrite (TBN) cleaved benzyl groups from monosaccharides under ambient atmosphere and visible light irradiation with high functional group tolerance. Real-time monitoring using LED-NMR spectroscopy gave insights in the crucial role of TBN and light. The scale-up of light promoted reactions is typically detrimental to the efficiency of photocatalytic reactions, due to poor light penetration. Careful optimization of the reaction conditions for photooxidative debenzylations was required to access a deprotection methodology applicable on the gram scale (Chapter 6).

The facile access to reactive open-shell intermediates enabled by photocatalysis has led to a myriad of new synthetic approaches, including photoredox catalyzed cross-coupling reactions. This is achieved using a combination of nickel and noble metal photocatalysts (PC). A more sustainable alternative to commonly used expensive and homogeneous iridium- and ruthenium polypyridyl complexes was found in graphitic carbon nitrides (gCN). The ability of CN-OA-m in combination with a nickel complex was showcased in an etherification and extended to the coupling of aryl iodides with thiols (Chapter 8). In situ IR-monitoring was applied for detailed kinetic analysis of the developed semi-heterogeneous system and the state-of-the-art photocatalyst tris(2-phenylpyridine)iridium(III) on a model *O*-arylation reaction. This indicated that different photocatalysts can result in different mechanistic scenarios, that result in the same product (Chapter 7).

Incorporating fluorine into organic scaffolds increases the compounds physicochemical properties, such as lipophilicity and metabolic stability, resulting in improved active pharmaceutical ingredients and agrochemicals. Hence, the development of new safe and simple fluorination methodologies is of interest. A divergent benzylic radical fluorination reaction, initiated via a charge transfer complex that does not require visible-light activation, selectively yielded either benzyl fluorides or α-fluorophenylacetic acids depending on the conditions (Chapter 5). Charge transfer complex mediated in situ generation of a highly reactive radical species enabled hydrogen atom transfer (HAT) as well as single electron transfer (SET), solely depending on the p*K*a of the phenylacetic acid starting material.

Zusammenfassung

Radikale spielen eine zentrale Rolle in der Natur und sind an einer Vielzahl biochemischer Prozesse beteiligt. Bis Ende des 20. Jahrhunderts wurden Einzelelektronenprozesse in der synthetischen organischen Chemie jedoch nur wenig Aufmerksamkeit zuteil, da sie lange Zeit als schwer kontrollierbar galten.

Die Entwicklung neuer Synthesestrategien für den praktischen Zugang zu reaktiven open-shell-Intermediaten hat das Interesse an er Radikalchemie wieder geweckt. Photoredoxkatalyse hat sich als Eckpfeiler für den Zugang zu diesen reaktiven Zwischenstufen unter milden Bedingungen herausgestellt. Der Schlüssel zum Erfolg dieser Strategien ist die Fähigkeit von Chromophoren, sichtbares Licht zu absorbieren und langlebige angeregte Zustände zu erreichen. Anschließend kann der angeregte Photokatalysator sowohl Zwischenstufen, als auch Reagenzien über Einzelelektronentransfer, Energietransfer oder Wasserstoffatomtransfer aktivieren, um Radikale zu bilden und chemische Umwandlungen zu ermöglichen. Der Mechanismus solcher photokatalytischer Systeme umfasst oft mehrere katalytische Spezies und Reagenzien, die aktiv am Katalysezyklus beteiligt sind und mechanistische Untersuchungen erschweren. Hochmoderne Methoden zur Untersuchung photokatalytischer Reaktionen beschäftigen sich hauptsächlich mit den Eigenschaften der Spezies im angeregten Zustand und auf die darauffolgende quenching-Wechselwirkung mit anderen Reagenzien, Katalysatoren oder Zwischenprodukten. Ein ganzheitlicheres Bild des Gesamtprozesses kann durch In-situ-Monitoring gewonnen werden (Kapitel 4).

Der Wert von In-situ-Monitoring zum Erlangen mechanistischer Einblicke wurde anhand einer entwickelten photokatalysierten Abspaltung von Benzylethern demonstriert (Kapitel 9). Aufgrund ihrer hohen Stabilität sind Benzylether häufig verwendete Schutzgruppen in Kohlenhydrat- und Naturstoffsynthese. Typische Entschützungsstrategien basieren jedoch auf harschen Reaktionsbedingungen und weisen eine geringe Toleranz gegenüber funktionellen Gruppen auf, was sie unattraktiv für mehrstufige organische Synthesen macht.

Die Bestrahlung von 2,3-Dichlor-5,6-dicyano-1,4-benzochinon (DDQ) mit sichtbarem Licht dieses in einen stark oxidierenden, langlebigen angeregten Triplett-Zustand (DDQ*) anregt, der zur oxidativen Abspaltung von Benzylether befähigt ist. Eine Kombination aus DDQ und *tert*-Butylnitrit (TBN) spaltete Benzylgruppen von Monosacchariden unter Umgebungsatmosphäre durch Bestrahlung mit sichtbarem Licht und mit hoher Toleranz gegenüber funktionellen Gruppen. Echtzeit-Monitoring mittels LED-NMR-Spektroskopie lieferte wichtige mechanistische Erkenntnisse, wie die entscheidende Rolle von Licht und TBN. Die Durchführung photochemischer Reaktionen in größeren Maßstäben ist aufgrund schlechter Lichtdurchdringung oft ineffizienter. Sorgfältige Optimierung der Reaktionsbedingungen der photooxidativen Debenzylierungen konnte jedoch eine Methode entwickelt werden, die im Grammmaßstab anwendbar ist (Kapitel 6).

Der durch Photokatalyse ermöglichte einfache Zugang zu reaktiven open-shell-Intermediaten hat zu einer Vielzahl neuer Syntheseansätze geführt, einschließlich photoredox-katalysierte Kreuzkupplungsreaktionen. Diese werden durch die Kombination von Nickel und Edelmetall-Photokatalysatoren (PC) ermöglicht. Eine nachhaltigere Alternative zu den üblicherweise verwendeten teuren und homogenen Iridium- und Ruthenium-Polypyridylkomplexen wurde in graphitischen Kohlenstoffnitriden (gCN) gefunden. Die Effizienz von CN-OA-m in Kombination mit einem Nickelkomplex wurde anhand einer Veretherung demonstriert und auf die Kupplung von Aryliodiden mit Thiolen erweitert (Kapitel 8). Eine detaillierte kinetische Analyse mittels In-Situ IR Monitoring des entwickelten semi-heterogenen Systems und des üblicherweise verwendeten Photokatalysators Tris(2-phenylpyridin)iridium(III) wurde an einer *O*-Arylierungsreaktion durchgeführt. Diese indizierte, dass die Verwendung unterschiedlicher Photokatalysatoren zu verschiedene mechanistische Szenarien, jedoch dem selben Produkt führen kann (Kapitel 7).

Der Einbau von Fluor in organische Grundgerüste verbessert die physikalisch-chemischen Eigenschaften der Verbindungen, wie Lipophilie und Stoffwechselstabilität, was zu optimierten pharmazeutischen Wirkstoffen und Agrochemikalien führt. Daher ist die Entwicklung neuer sicherer und einfacher Fluorierungsmethoden von großem Interesse.

Eine divergente benzylische radikalische Fluorierungsreaktion wurde entwickelt, die über einen charge-transfer-Komplex initiiert wird, welcher nicht durch sichtbares Licht aktiviert werden muss und je nach den Reaktionsbedingungen selektiv entweder Benzylfluoride oder α-Fluorphenylessigsäuren ergibt (Kapitel 5). In Abhängigkeit vom p*K*s Wert der Phenyessigsäuren findet entweder eine Wasserstoffatomtransfer (HAT) oder Einzelelektronentransfer (SET) vermittelter Mechanismus durch in situ geneierten radikalen statt.

Chapter 1

Introduction

This chapter provides the scientific concepts and notions necessary to understand the content of this thesis. Chapters 4 to 9 report the publications listed on page xi. For each publication, supporting information containing experimental details is found in the appendix. Copies of the NMR spectra of isolated compounds are excluded and available through the website of the respective journal.

1.1 Charge-Transfer Complex Mediated Initiation of Radical Reactions

Single electron transfer (SET) processes have a long history in organic synthesis that dates back to 1848, when Kolbe reported the electrochemical dimerization of carboxylic acids via radical intermediates.[1] Since then, numerous examples, such as the Borodin-Hunsdiecker and the Hoffmann-Löffler-Freytag reaction have followed.[2] However, harnessing reactive open-shell intermediates in a controlled fashion remains challenging.[3] Open-shell intermediates are common in nature due to their high reactivity that enables low energy barrier transformations. Electron transfer processes mediated by electron donor-acceptor (EDA) complexes are of interest since their discovery in 1952.[4] Recently, strategies exploiting EDA-complex-mediated generation of radical intermediates have emerged as a useful tool in synthetic organic chemistry. EDA complexes are ground-state aggregates of donor- (D) and acceptor (A) molecules, associated via dipole-dipole interactions (Figure 1.1 A).[5] Overlapping frontier orbitals (HOMO/LUMO) of donor and acceptor molecules lead to new molecule orbitals in the EDA entity, resulting in physical properties, different from those of the starting materials. The isolated acceptor and donor compounds may, for example not absorb light, while the resulting EDA complex does.

Upon excitation with a suitable wavelength, an intramolecular single electron transfer from the donor to the acceptor results reactive radical intermediates.

Often the electronic transition between ground-state (Ψ_{GS}) and excited-state (Ψ_{ES}) lies within the visible range of the electromagnetic spectrum, rendering EDA complexes useful synthetic tools in visible light photochemistry.[6] Complexes formed between excited donor (D*) and ground-state acceptor (A) molecules are called exciplexes (Figure 1.1 B). Reversible back electron transfer (BET) between the radical ion pair restores the starting donor-acceptor complex.

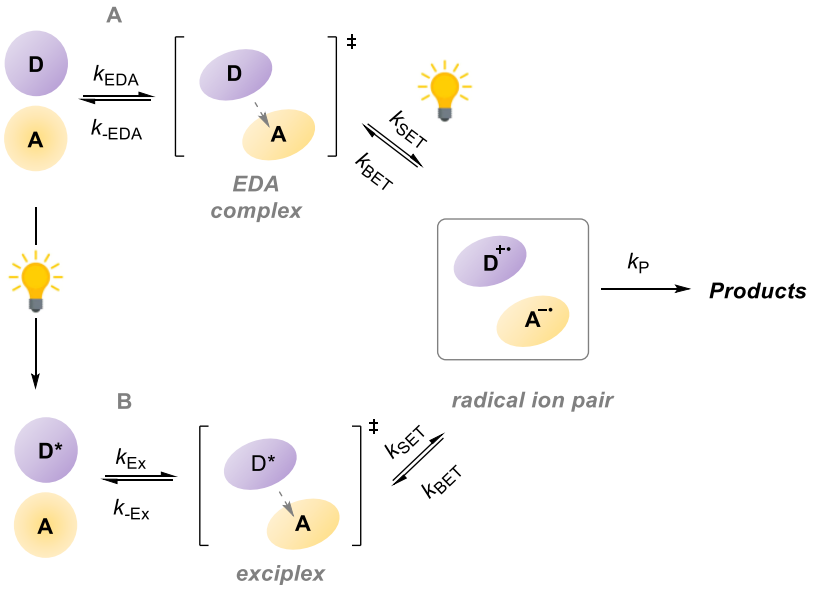

Figure 1.1 Schematic pathway of **A** the bimolecular EDA complex and **B** exciplex-mediated outer sphere electron transfer.[7]

In order to enhance the applicability of EDA complex activation in synthetic organic chemistry, strategies to circumvent unproductive back electron transfer had been developed (Figure 1.2). Cleavage of a suitable leaving group (LG) installed in the donor or acceptor moiety, can promote an irreversible fragmentation of the radical ion pair. If that process is rapid enough to outcompete the BET, synthetically useful reactive open-shell intermediates can be gained.

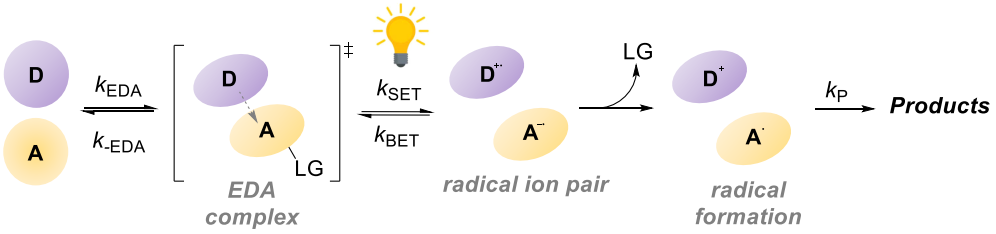

Figure 1.2 Schematic pathway of the photoinduced EDA complex activation, followed by the cleavage of an acceptor embedded leaving group (LG).

Many different types of interactions can drive the formation of these EDA complexes, such as anion-л, cation-л, lone-pair-л and л-л stacking.[6, 8] A common example of a π-stacking-driven formation is the EDA complex between the electron-poor 2,3-dichlor-5,6-dicyano-1,4-benzoquinone (DDQ) and electron rich *para*-methoxybenzene ether (PMB) that facilitates the single electron transfer (SET) and deprotonation events, resulting in C-O cleavage and liberation of a free alcohol (Figure 1.3).[9]

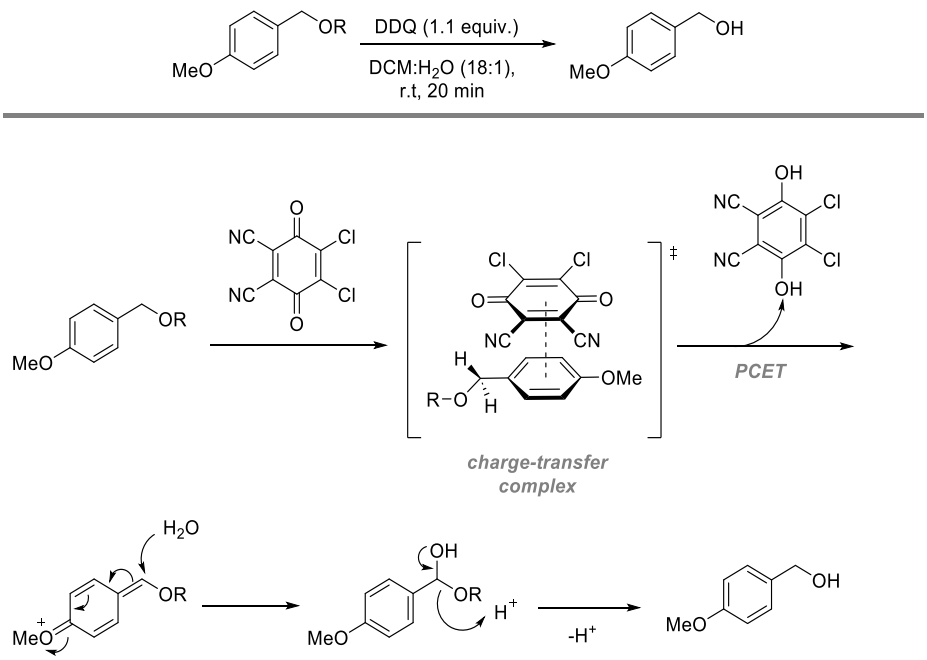

Figure 1.3 Oxidative C-O cleavage of *para*-methoxybenzyl ether via charge-transfer–complex-mediated.

Since the 1950s, the photophysical properties of EDA complexes had been studied intensively.

Recently their potential in synthetic organic chemistry has gained more attention. Seminal examples demonstrated the potential of EDA complexes in photochemistry to promote synthetically useful radical processes under mild conditions (Figure 1.4).[4]

For example, a thermally inaccessible arylation and alkylation of carbonyl compounds and imines was achieved via EDA complex formation of enamines and enolates with aryl -and perfluoralkyl iodides (A) (Figure 1.4 A).[10] Cleavage of the iodide moiety upon excitation fosters fragmentation of the radical ion pair, preventing synthetically unproductive back electron transfer.

The electron transfer substitution was further extended by Russell and co-workers, showcasing the ability of benzyl chlorides (A) to form an EDA aggregate with *N*-donors, such as sodium azide (Figure 1.4 B).[11] The group of Kornblum demonstrated the formation of a photoactive EDA complex of an electron-poor arene acceptor with an *N*-centered enamin donor moiety.[12] Further, electron-rich arenes (D) were found to form EDA complexes with tetranitromethane (A), ultimately leading to nitration of the aromatic system (Figure 1.4 C).[13] These examples rely on the cleavage of a leaving group, embedded in the acceptors scaffold, to prevent BET. In contrast, the group around Kochi developed a reaction proceeding via an EDA complex formed, between an organostannanes (D) and an electron-poor alkene (A), where both fragments are embedded in the final product (Figure 1.4 C).[14]

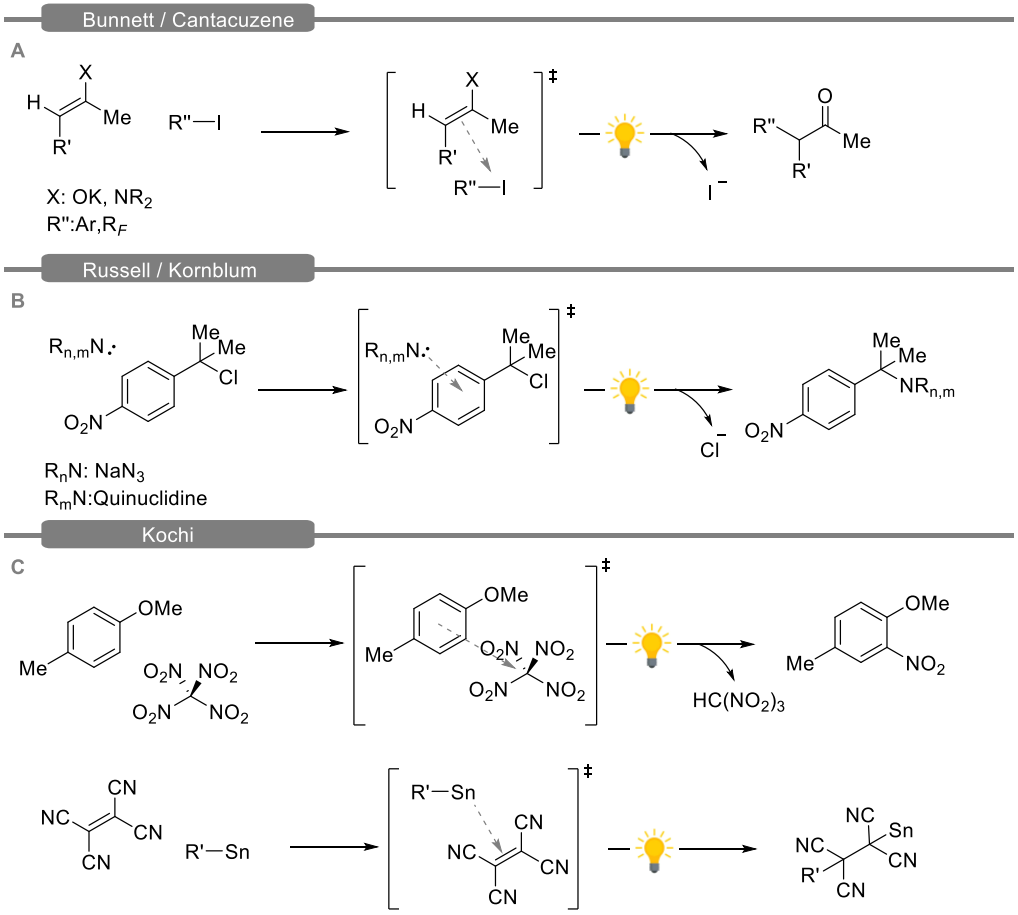

Figure 1.4 Seminal examples of photoinduced chemical transformations mediated via EDA complex between **A** aryl- and perfluoroalkyl iodides (R_F) acceptors with enamines and enolates (D) **B** *N*-centered donors with electron-poor benzyl chlorides (A) in nucleophilic substitution reactions **C** electron-rich arene donors with tetranitromethane (A) in a $S_{RN}1$ reaction and an organostannene (D) with an electron-deficient ethylene acceptor (A).

A charge-transfer complex was used to generate a reactive *N*-centered radical, that acts as hydrogen atom transfer (HAT) reagent to facilitate the direct C(sp^3)–H functionalization of unactivated aliphatic bonds. The direct fluorination reported by Tan uses a combination of Selectfluor™ and anthraquinone (AQN) under visible light irradiation.[15] The proposed mechanism suggested the initial formation of an exciplex between AQN and Selectfluor™ via C–F···aryl interactions (Figure 1.5). An outer-sphere electron transfer (OSET) from AQN* to Selectfluor™ yields the *N*-centered radical, $TEDA^{2+\bullet}$, which undergoes hydrogen atom transfer (HAT) with the aliphatic substrate to result the key radical intermediate. Subsequent fluorine transfer from Selectfluor™ results the alkyl fluoride and *N*-(chloromethyl)triethylenediamine ($TEDA^{2+\bullet}$) as a chain carrier species.

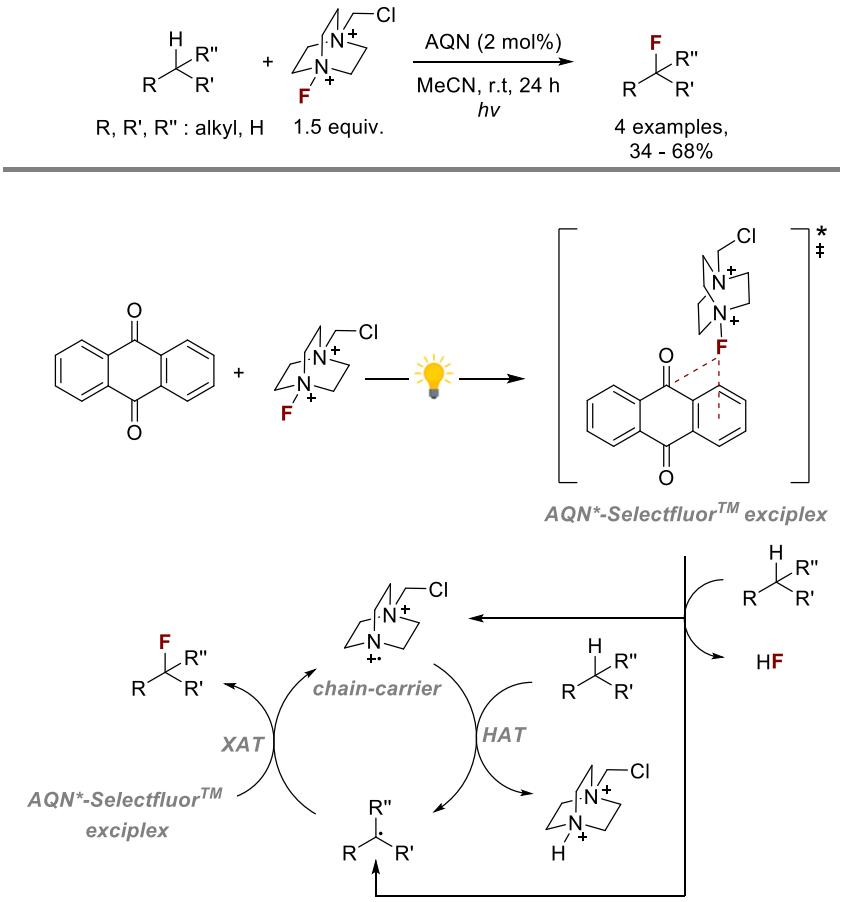

Figure 1.5 Reaction scheme and proposed mechanistic pathway of the direct C(sp^3)–H functionalization, mediated via an AQN*-Selectfluor™ exciplex.

1.2 Photocatalysis

Visible light is an inexhaustible, traceless source of energy and driving force of various biochemical processes.[16] Inspired by nature, synthetic photochemistry uses the energy delivered by light to promote chemical reactions.[17] Such transformations were traditionally UV-light-driven, since many organic molecules absorb in that region of the electromagnetic spectrum.[18] However, the direct excitation of reagents with such high energy light comes at the cost of selectivity, due to undesired side reactions.

Alternatively, chromophoric species can harvest visible light to access an excited state species.

The absorbed energy can then be transferred to another molecule to create a reactive intermediate to perform a variety of transformations.[19]

Upon irradiation with a suitable wavelength, light-absorbing molecules in the ground state (S_0) can be promoted to an excited state (S_1, S_2 or higher) of the same spin multiplicity (Figure 1.6).[20] Once the electron is excited, vibrational relaxation (10^{-14} - 10^{-11} s) redistributes vibrational energy into kinetic energy, leaving the excited electron in the lowest vibrational level of the singlet excited state.[21] The subsequent relaxation to the ground state (e.g $S_1 \rightarrow S_0$) can occur in a radiative or non-radiative fashion. Internal conversion from the ground level of S_1 to a high energetic vibrational level of the electronic ground state (S_0) can result in non-radiative deactivation via vibrational relaxation. Spin-allowed radiative transition (fluorescence, $S_1 \rightarrow S_0$) can occur readily ($\leq 10^{-10}$ to 10^{-7} s), limiting the lifetime of the excited state. However, another radiative relaxation path is available for molecules with a large spin-orbit coupling. The electron in the S_1 level can non-radiatively pass to an excited triplet state (T_1). This intersystem crossing (ISC) process is followed by phosphorescence, leading back to the ground state ($T_1 \rightarrow S_0$). Transitions between electronic states with different spin multiplicities are spin-forbidden, which results in extended excited state lifetimes ($\geq$ 100 ns) for molecules that have a large spin-orbit coupling.

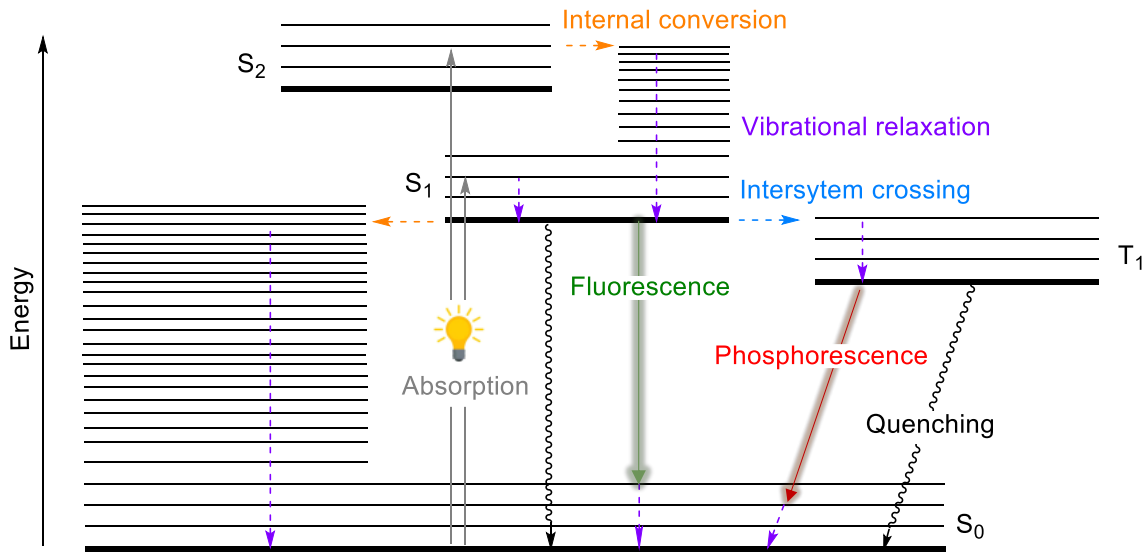

Figure 1.6 Perrin-Jablonski diagram, illustrating the electronic transitions.

Extended lifetimes are a fundamental feature in photocatalysis and allow the excited photocatalytic species to engage in bimolecular processes (quenching) (Figure 1.7).[22]

In the presence of a suitable acceptor molecule (A), such as a reagent or co-catalyst, the excited light absorbing molecule (PC*) can transfer energy to an otherwise inert ground state species, triggering a chemical transformation.

Upon absorption of light, the photocatalytic species (PC) enters an excited state PC*, via collision with an acceptor molecule (A), energy- or single electron transfer activates the acceptor molecule (A*), relaxing the PC back to the ground state (*vide supra*). The excitation of the acceptor (A) by PC* can proceed via different modes of activation. Amongst the most common pathways are energy transfer (EnT) catalysis and photoredox catalysis (PRC).

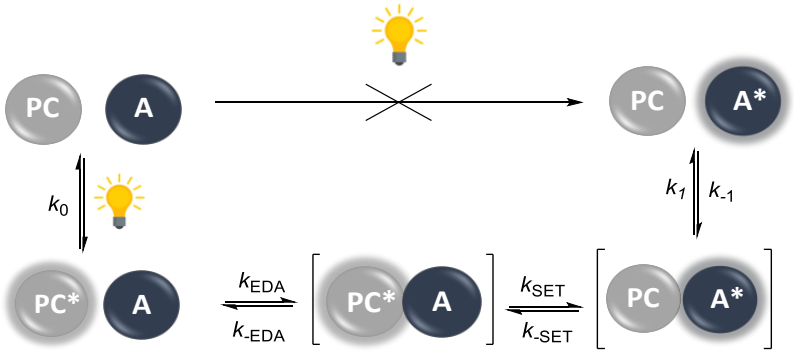

Figure 1.7 Schematic illustration of a bimolecular photochemical reaction proceeding via an electron donor acceptor (EDA) complex.

1.2.1 Accessing Open-Shell Intermediates via Photoredox Catalysis

In photoredox catalysis (PRC), the excited photocatalytic species is quenched by an acceptor molecule via single electron transfer (SET) events.[23, 24] Excitation of the photon-absorbing species and ISC results in a long-lived excited triplet state (T_1, *vide supra*), which is both more reducing and oxidizing then the ground state species. Consequently, quenching can proceed via donating or accepting a single electron, depending on the type of quencher and the redox potential of the excited state of the photocatalyst. Reductive quenching cycles proceed via a single electron oxidation of a donor molecule (D), resulting in a radical cationic species $D^{\bullet+}$ and the counterpart $PC^{\bullet-}$ (Figure 1.8). A subsequent single electron reduction by a suitable acceptor (A) species closes the catalytic cycle, restoring the ground state PC. In an oxidative quenching cycle, the events occur vice versa after excitation of the PC.

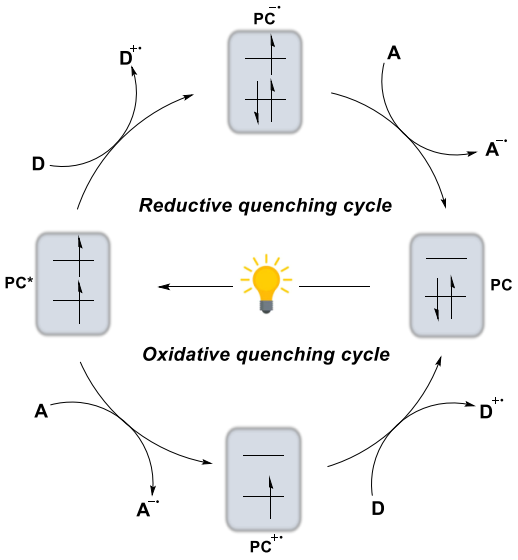

Figure 1.8 Schematic illustration of reductive and oxidative quenching cycles.

The Stephenson group utilized an oxidative quenching cycle for the photocatalyzed cleavage of *para*-methoxybenzyl (PMB) ether with an iridium complex ($Ir[dF(CF_3)ppy]_2(dtbbpy)PF_6$) in combination with a sacrificial oxidant ($BrCCl_3$).[25] The proposed mechanism is reported to proceed via an initial excitation of the Ir^{III} photocatalyst, followed by oxidative quenching with $BrCCl_3$ to afford Ir^{IV} alongside the trichloromethyl radical (Figure 1.9). The oxidation of the PMB ether moiety closes the photocatalytic cycle, yielding an arene radical cation. Subsequent hydrogen atom transfer (HAT) by the trichloromethyl radical results an oxocarbenium ion, which is hydrolyzed to produce the alcohol.

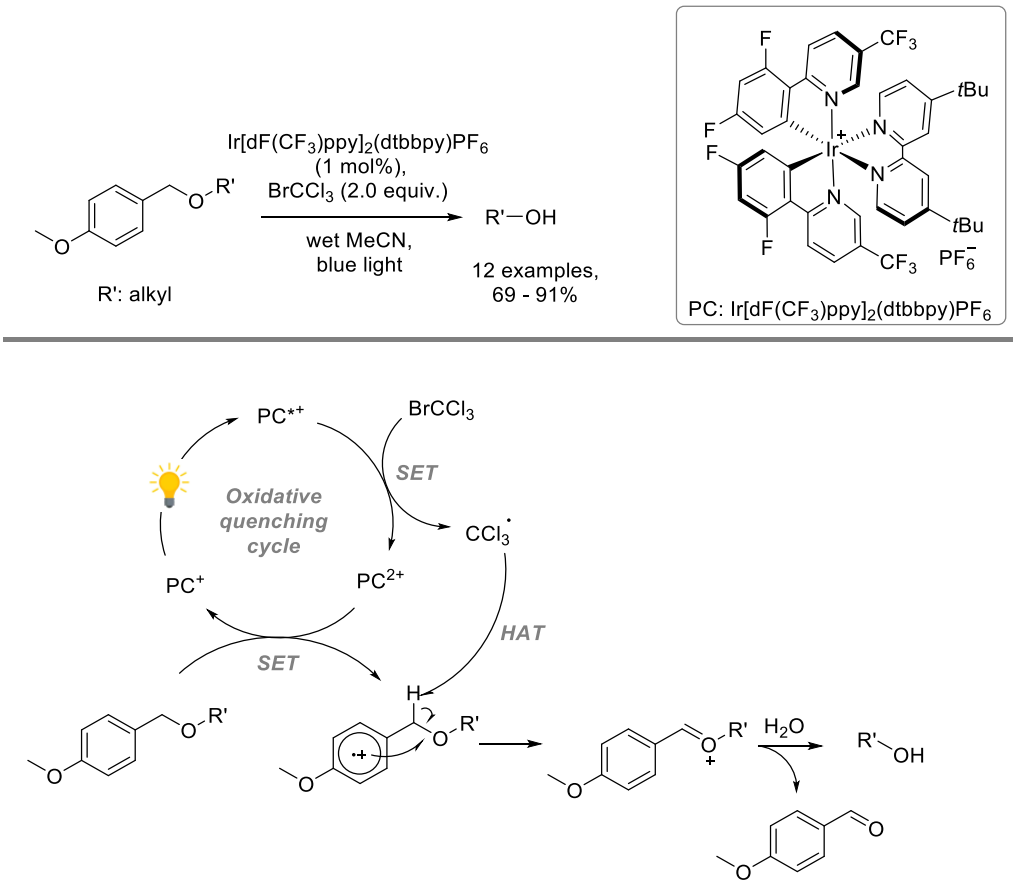

Figure 1.9 Reaction scheme and proposed mechanistic pathway of the iridium-complex-catalyzed photooxidative cleavage of PMB ether protective group.

Stephenson and colleagues also recently reported a photocatalyzed aza-Henry reaction, which proceeds via the corollary reductive quenching cycle.[26] The mechanistic proposal involves the initial reductive quenching of the excited photocatalytic species (Ir^{III}*) by the α–amine to afford the reducing agent Ir^{II} and the *N*-centered radical cationic species (Figure 1.10). The following reduction of either oxygen or nitromethane turns over the photocatalyst and closes the photocatalytic cycle. Hydrogen atom abstraction by the thereby generated oxygen located radical anionic intermediate yields the desired iminium ion. The subsequent addition of the nitronate affords the final product.

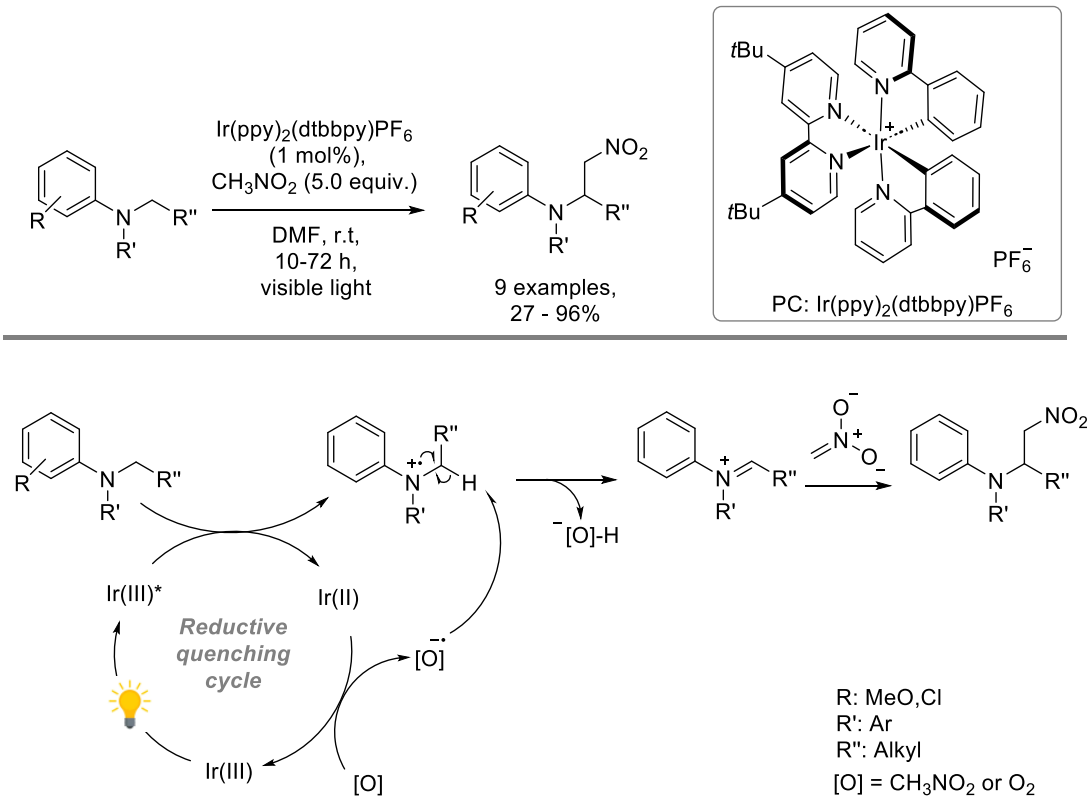

Figure 1.10 Reaction scheme and mechanistic proposal of the photocatalyzed α-amine functionalization.

Photocatalysis is a versatile tool for substrate activation, yielding reactive open-shell intermediates. Moreover, modern cross-coupling reactions rely on the merging of photoredox catalysis and traditional transition-metal catalysis. Such transformations commonly rely on initial SET by an excited photocatalyst to activate the pre-catalyst.

1.2.2 Photoredox-Enabled Activation of Co-Catalysts

Transition metal (TM) catalysis has a rich history in synthetic chemistry, enabling the making and breaking of carbon-heteroatom and carbon-carbon bonds to access valuable organic compounds.[27] Palladium-catalyzed cross-couplings are amongst the most prominent TM-catalyzed transformations.[28] However, the shift towards sustainability has led efforts that aim to replace this rare and expensive metal. The higher abundance and consequently lower price of nickel, in combination with its ability to achieve multiple oxidation states (particularly $Ni^{0/I/II/III}$) crucial for cross-coupling reactions, renders it a promising alternative.[29] Nevertheless, the usage of nickel in cross-coupling reactions holds challenges.

Thermal cross-coupling reactions with nickel proceed via a thermodynamically stable Ni^{II} intermediate, formed by the oxidative addition of an aryl halide to the in situ generated Ni^{0} species.[30] Reductive elimination demands the application of increased temperatures, strong bases or a dedicated ligand system. The merger of nickel and photocatalysis has opened up a new straightforward approach that was originally proposed to proceed through the destabilization of the Ni^{II} intermediate via energy- or single electron transfer, depending on the photocatalytic species and redox potentials.[31] Reduction of the Ni^{II} to Ni^{0} catalyst is followed by the oxidative addition of the aryl halide and ligand exchange with the nucleophile (Figure 1.11 A). Single electron transfer (SET) by the excited photocatalytic species (PC*) yields the Ni^{III} complex, which readily undergoes the reductive elimination, resulting the product. Reductive quenching of Ni^{I} to Ni^{0} closes both catalytic cycles. Recently, evidence for the photocatalysts involvement in the activation of the aryl halide was reported, suggesting an alternative mechanistic proposal (Figure 1.11 B).

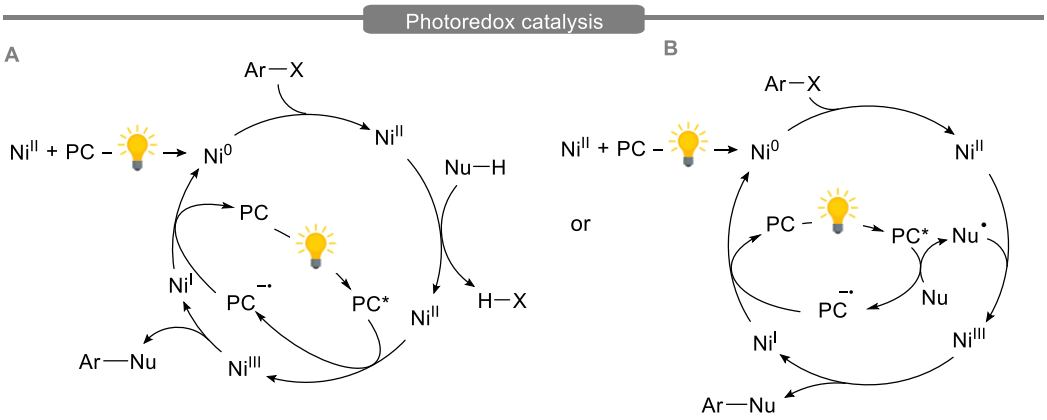

Figure 1.11 Representative mechanistic proposals for dual nickel- and photocatalyzed cross-coupling reactions, proceeding via **A** single electron reduction of the Ni^{II} pre-catalyst, followed by the oxidative addition of the aryl halide to the catalytic active Ni^{0} species. After ligand exchange with the coupling partner, single electron oxidation to Ni^{III} by the excited PC* triggers the reductive elimination, yielding the product and closing the catalytic cycle.[32] Alternatively, a mechanistic pathway **B** involving the photocatalysts involvement in the activation of the nucleophile via single electron oxidation was proposed. Upon the activation of the pre-catalyst resulting in Ni^{0}, oxidative addition of the aryl halide outturns a thermodynamically stable Ni^{II} intermediate. The addition of a nucleophile radical yields a Ni^{III} complex, capable of the product forming reductive elimination step.[33]

More recently, the mechanism and especially role of the photocatalyst in dual nickel- and photoredox catalyzed carbon-heteroatom (C-X) cross-coupling reactions has been reconsidered.

Upon initial reduction of the Ni^{II} pre-catalyst to an active Ni^{I} species, C-X cross-coupling reactions is likely to proceed via a Ni^{I}/Ni^{III} cycle (Figure 1.12).[34, 35]

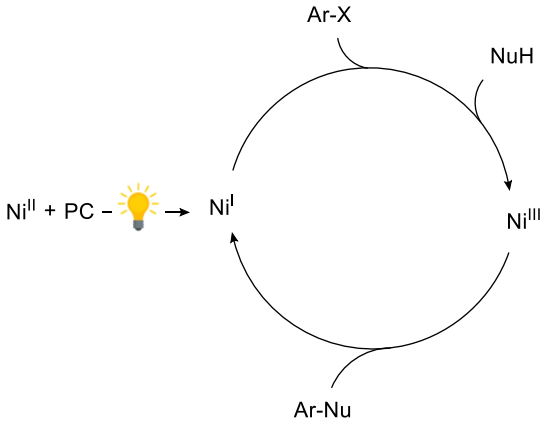

Figure 1.12 Revised mechanistic proposal of a dual nickel and photocatalyzed C-X cross-coupling reaction via Ni^{I}/Ni^{III} sequence.[35]

1.2.3 Photocatalyst

The success of a photoredox catalysis relies on its ability to harvest visible light and transform it into chemical energy. Organic dyes, heterogeneous semiconductors, and metal-polypyridyl complexes are the main classes of photocatalysts currently used.

Amongst the most popular photocatalysts are iridium- and ruthenium-polypyridyl complexes, due to their ability to generate long-lived excited states, capable of engaging in bimolecular EnT and SET. Upon absorption of visible light, a metal-to-ligand charge transfer (MLCT) occurs, promoting an electron from a metal-based ground state orbital (t_{2g}) to a ligand-centered π^* orbital (Figure 1.13).[24] The subsequent intersystem crossing (ISC) yields an excited triplet state with a relatively long lifetime ($\tau \sim 1000$ ns). The excitation of an electron consequently generates a vacancy in the metal-located t_{2g} orbital, rendering the excited photocatalytic species an oxidant and reductant at the same time. The redox properties of such complexes can be manipulated via ligand and metal modification. However, the use of these powerful photocatalysts is hampered due to the low abundance and high costs of ruthenium and iridium.

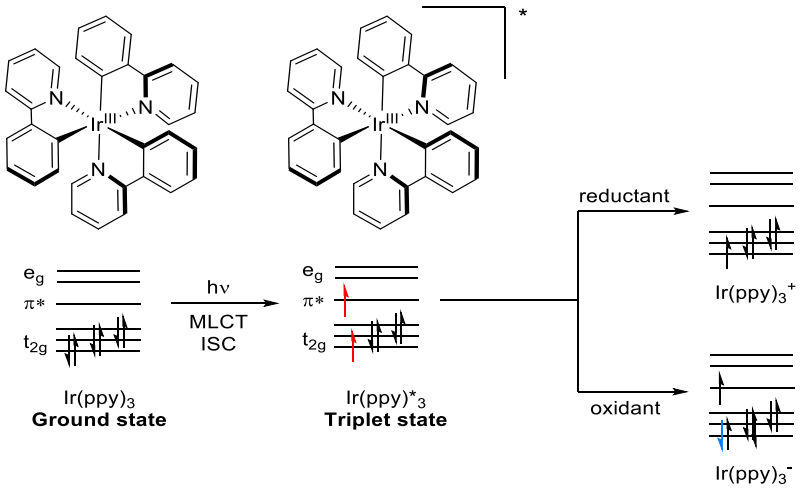

Figure 1.13 Visible light mediated excitation of the $Ir(ppy)_3$, followed by MLCT and ISC, resulting a long-lived exited triplet state ($\tau \sim 1900$ ns), capable of oxidative ($E^{III*/II} = -1.73$ V vs SCE) and reductive ($E^{IV/III*} = +0.31$ V vs SCE) quenching.

A more sustainable alternative to noble metal-based photocatalysts (*vide infra*) are semiconductors. The interaction of light with valence electrons of semiconductors possessing a suitable band gap results in an exited photocatalytic species (Figure 1.14).[36] The absorption of light promotes electrons from the valence band (VB) to the conduction band (CB), generating a redox-active electron-hole-pair. Electrons occupying the CB can participate in single electron transfer events, reducing suitable acceptors, while the simultaneously formed holes (h^+) in the VB act as oxidants. However, undesired recombination of the charge carriers often limits photocatalytic performance.

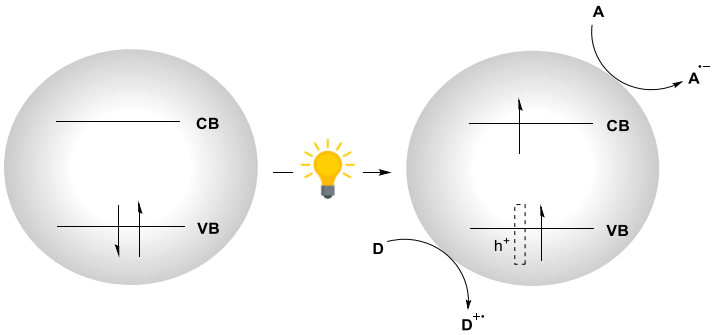

Figure 1.14 Schematic illustration of a semiconductor photocatalyst in the ground state and after light-induced charge separation.

Commonly used semiconducting materials are metal oxides, such as TiO_2 and ZnO. However, their large band gap (~ 3.2 eV) requires excitation with UV light, limiting their application in organic chemistry.

Other inorganic semiconductors such as cadmium sulfide (~ 2.50 eV) and cadmium selenide (~ 1.74 eV) readily undergo visible-light-induced charge separation. An attractive alternative is carbon nitrides, which are metal-free polymers prepared from simple and cheap bulk chemicals like urea and oxamide.[37] The porous material possesses a medium band gap (~ 2.7 eV) allowing for the absorption of visible-light. Another class of substances capable of absorbing light to promote chemical transformations are organic dyes. The structural variety ranges from acridinium-based photocatalysts, diaryl ketones, flavins and xanthenes to boron dipyrromethenes (BODIPY) (Figure 1.15).[38]

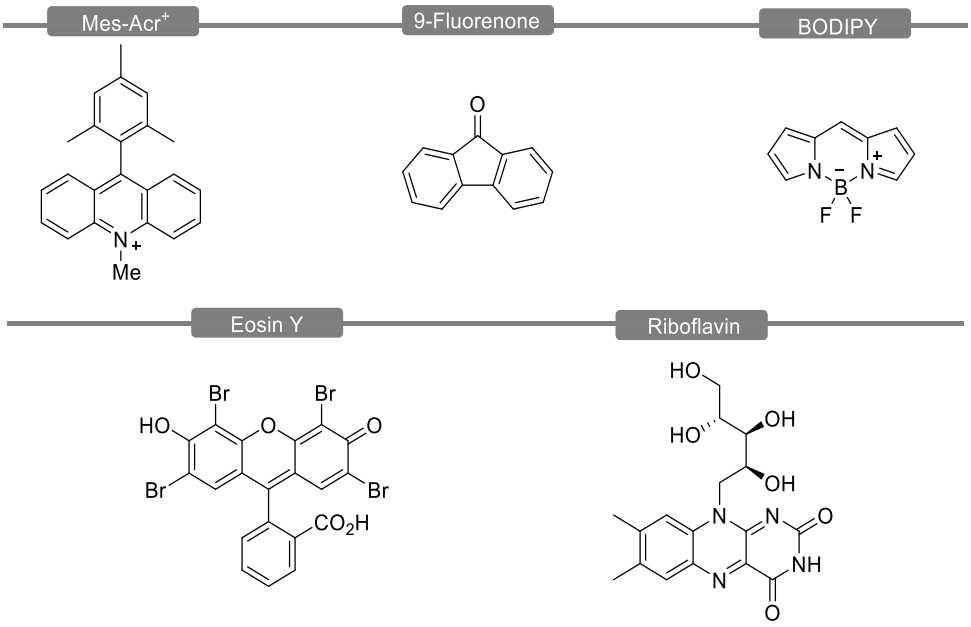

Figure 1.15 Selected examples of typical organic dyes used in photocatalytic transformations.

Organic dyes are well-studied and readily available compounds with easily tunable spectroscopical redox properties. Unfortunately, the applicability of these photocatalysts is limited due to short exited-state lifetimes.[39]

Upon excitation, the majority of organic dyes only reach excited single states (S_1) and relax via fluorescence ($\leq 10^{-10}$ to 10^{-7} s), a process occurring too fast to engage in bimolecular energy- or single electron transfer processes.

1.3 Visual Kinetic Analysis

Though much work has been accomplished (*vide supra*), the increasing interest in the development and optimization of new photochemical reactions has created a demand of understanding the underlying mechanisms and interdependencies of the reaction parameters. Most state-of-the-art techniques to investigate such transformations are based on steady-state experiments, focusing on the interaction between the excited photocatalyst and co-catalyst or substrate. Commonly, excited-state kinetics are investigated via luminescence quenching studies to understand the dynamics of photocatalytic process.

Such a process was utilized in the study of a dual nickel- and photocatalyzed C–S cross-coupling reaction of aryl iodides and thiols was developed and investigated by Johannes and colleagues in 2016 (Figure 1.16).[33] The proposed mechanistic pathway starts with the reductive quenching of the excited photocatalyst (Ir^{III}*) by the thiol, resulting a thiol radical cationic intermediate, which gets deprotonated by pyridine to yield the key radical species. Concomitantly, a single electron reduction of the Ni^{II} precatalyst by the Ir^{II} species delivers the active Ni^{I} halide. Trapping of the thiyl radical by the Ni^{I} halide results a Ni^{II} species. Subsequent reduction of Ni^{II} by Ir^{II} results a Ni^{I} sulfide intermediate and the ground state Ir^{III} complex, closing the photocatalytic cycle. Oxidative addition of the aryl halide to Ni^{I} yields a Ni^{III} complex. Subsequent reductive elimination yields the product and closes the catalytic cycle.

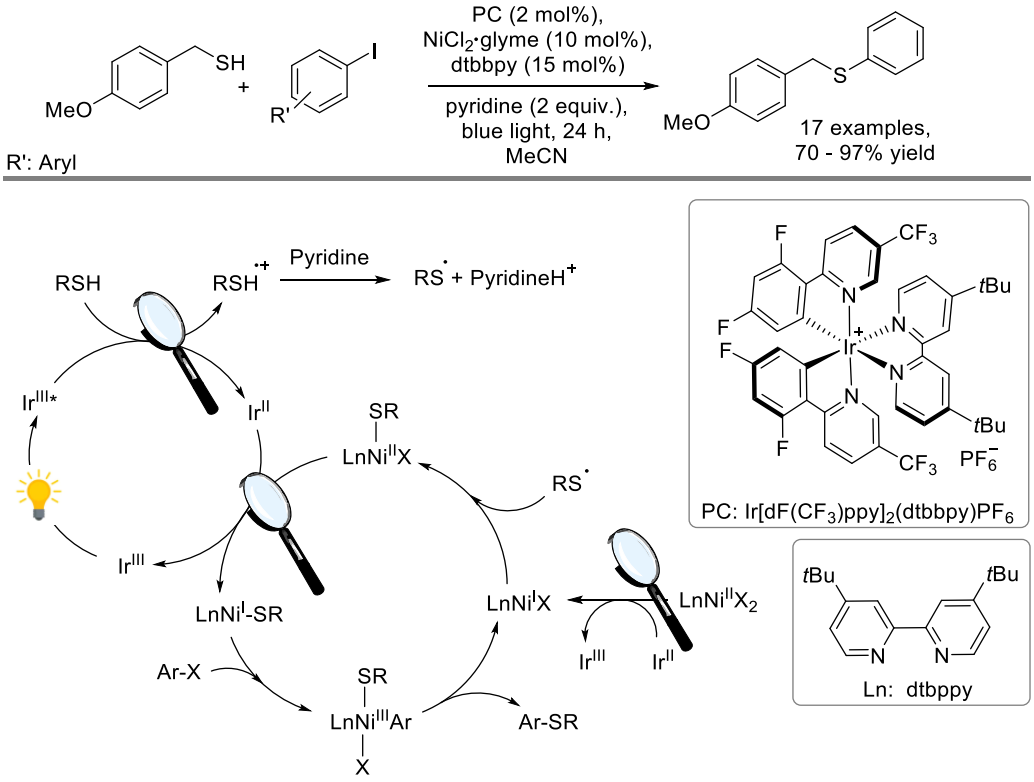

Figure 1.16 Mechanistic proposal of the photoredox mediated C-S cross-coupling.

The mechanistic proposal was rationalized based on Stern-Volmer analysis, confirming the quenching of the long-lived excited state (2.25 µs) Ir^{III}* by 4-methoxybenzyl thiol. Further, redox potentials obtained via cyclic voltammetry allowed the estimation of thermodynamical and kinetical favorability of the redox events involved. However, investigating isolated events of complex systems can have limited informative value, given that (thermal) follow-up events occur on a comparatively longer time scale.

Real-time monitoring of chemical transformations allows extraction of meaningful mechanistic information by continuously monitoring the concentration evolution of key reactive species. Following a reaction over its whole course allows for the detection and identification of transient species and offers a qualitative overview of the overall process. Real-time monitoring enabled kinetic analysis facilitates the visual interrogation of kinetic information via overlay experiments.[40] Historically, kinetic analysis has been used to identify concentration dependencies and differentiate between types of enzyme inhibition by interpreting the slope and intercepts of linearized plots (Figure 1.17).

A popular example is the double-reciprocal plot for the interpretation of reaction rates of enzymatic reactions, developed by Lineweaver and Burke in 1934.

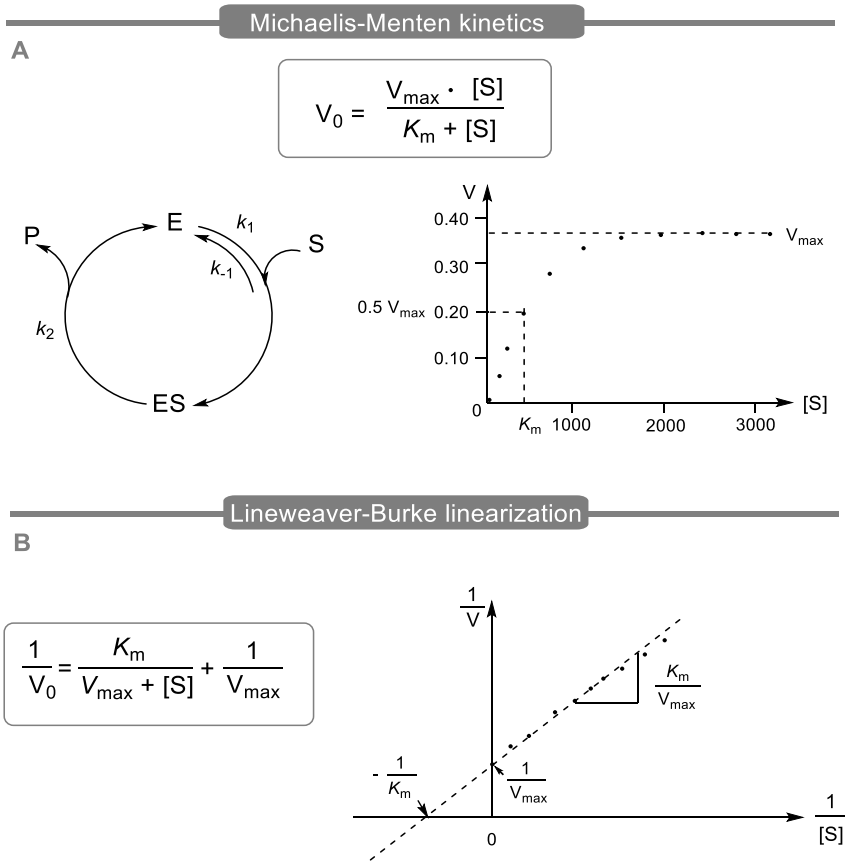

Figure 1.17 **A** Michaelis-Menten equation and diagram for enzyme kinetics and **B** Lineweaver-Burke linearization.

More traditional kinetic analysis methodologies are based on ex situ initial rate studies under pseudo-first order conditions, applying an excess of one or more reagents, relative to the reagent of interest.[41] Significant advances in reaction monitoring technology and computer analysis tools have led to the development of more accurate kinetic analysis techniques.

In 2005, Blackmond and co-workers formalized reaction progress kinetic analysis (RPKA) to interrogate kinetic information from entire reaction progress profiles obtained under synthetically relevant conditions.[42]

Based on the construction of graphical rate equations, overlay experiments facilitate two key reaction behaviors and parameters: a) the identification of catalyst deactivation or product inhibition; and b) the elucidation of catalyst and reagent orders.

To investigate the former, the rates of reactions are plotted with different starting points versus substrate concentration [A] (Figure 1.18 A). The reactions start at different initial concentrations, however the difference between the concentartion of the reagents is the same ("same excess" experiment), so that a certain point the reactions have the same concentration in starting material. Given the different product concentration and number of turnovers completed by the catalyst, a mismatched overlay of the curves indicates catalyst deactivation or product inhibition. The experiment designed to determine reagent orders compares the progress profiles of reactions with varying concentrations of the reagent of interest (B). The resulting progress profiles are plotted as rate/$[B]^{\beta}$ versus [A]. To elucidate the order of [B], the exponent β is altered until the progress profiles overlay, indicating the reagent's order (Figure 1.18 B).

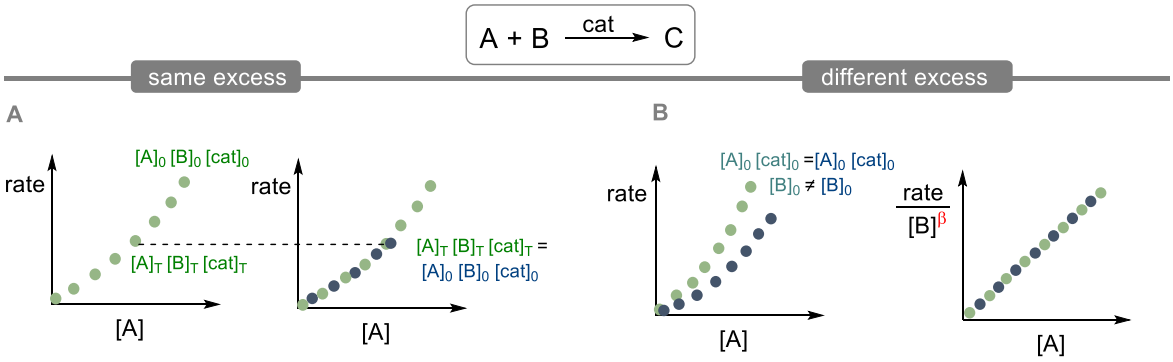

Figure 1.18 Reaction progress kinetic analysis of a catalyzed, bimolecular reaction of A and B. **A** Same excess plot to detect catalyst deactivation and **B** different excess plot for obtaining reagents orders.

However, reaction progress kinetic analysis uses reaction rates, which are mainly acquired via reaction calorimetry and incompatible with many reactions. Further, the raw data output of many analytical tools used for in situ monitoring (*vide infra*) display the reactions concentration, requiring conversion to rate.

To overcome these limitations, variable time normalization analysis (VTNA) was developed which uses concentration profiles, that are readily obtained by commonly used analysis techniques, such as FTIR, NMR, UV/Vis, HPLC and GC. The concept, introduced by Bures in 2016 visually determines reagent orders adjusting the time-axis.[43]

The same reaction behaviors and parameters that are observable with RPKA are obtainable with VTNA, only through different visual and mathematical manipulations.

The same excess experiment plots concentration profile of two reactions with different initial concentrations ($A_0 \neq A_0$) as concentration versus time (Figure 1.19 A). Time-shifting the curve of the lower-concentrated reaction resulting in overlay ($A_T = A_0$) signifies the absence of catalyst deactivation or product inhibition. As in RPKA, the reagent and catalyst orders are obtained carrying out excess-based experiments, varying the concentration of the reagent of interest (Figure 1.19 B). Substituting the time-axis by the time integral of the respective reagents' concentration taken to an arbitrary power α (Eq 1), normalizes the time between the data points. The value of α resulting an overlay of the concentration profiles represents the reagent order.

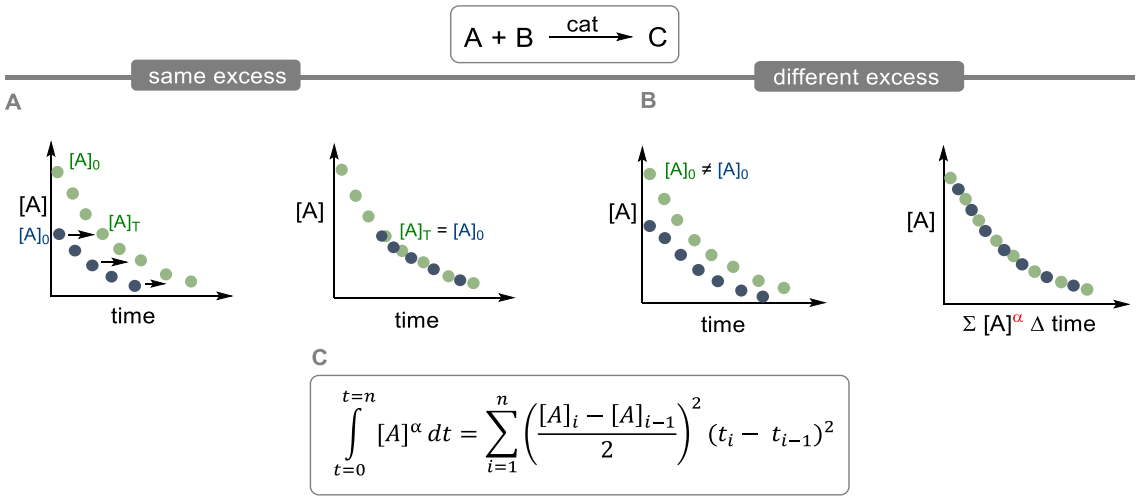

Figure 1.19 Variable time normalization analysis of a bimolecular reaction. **A** Same excess plot for the evaluation of the catalyst's robustness and **B** different excess diagram, plotting concentration versus normalized time, to determine reagents and catalysts order. **C** VTNA formula, normalizing the time-axis in reagent A to remove the kinetic effects.

1.4 Aim of this Thesis

The aim of my doctoral studies was the development and mechanistic investigation of organic transformations that proceed via reactive open-shell intermediates.

A particular interest was given to the development of a new and simple approach for benzylic radical fluorinations. I developed a divergent strategy for the direct benzylic C(sp^3)–H fluorination, as well as a decarboxylative fluorination of phenylacetic acids, using Selectfluor™ in combination with a *N*-heterocyclic additive. Key to the success was the charge-transfer complex mediated generation of $TEDA^{2+\bullet}$, a versatile transient species, capable of hydrogen atom transfer and single electron oxidation. Controlled by the pK_a of the substrate, this highly reactive intermediate triggers both reaction pathways with excellent selectivity. A mechanistic proposal was outlined, based on in- and ex situ mechanistic investigations.

Another major focus of my doctoral studies was dedicated to the development of photoredox cross-coupling reactions and the in situ monitoring-based investigation of the underlying mechanisms. A protocol for a photocatalyzed cross-coupling reaction of an aryl halide with a variety of thiols under visible light irradiation. A mixture of a homogeneous nickel catalyst in combination with a graphitic carbon nitride (CN-OA-m) was used as the catalytic cocktail. The organic polymer, readily prepared from bulk chemicals, offers a cheap and sustainable alternative to commonly used transition metal photocatalysts. However, dual nickel- and photocatalyzed systems often suffer from catalyst deactivation, limiting the efficacy of the reaction. In order to investigate the underlying mechanism of such transformations, an in situ IR based kinetic study of an *O*-arylation using the same catalytic system was conducted and compared to the state-of the art homogeneous congener. Kinetic information of both catalytic systems in different concentration regimes were extracted using in situ FTIR-enabled variable time normalization analysis (VTNA). Mechanistic scenarios, based on the determined rate laws, were proposed, revealing the photocatalyst's involvement in the activation of the aryl halide, prior the oxidative addition to the nickel catalyst.

The last part of my thesis evaluates the mechanism of the oxidative debenzylation of monosaccharides using a customized LED-based illumination NMR setup. A time-resolved ^{1}H NMR study of the blue light irradiated deprotection of acetyl 2,4,6-tri-*O*-acetyl-β-D-glucopyranose, using a combination of DDQ and *tert*-butyl nitrite (TBN) in aqueous media. Chopped illumination- and delayed addition experiments provided valuable mechanistic insights, ultimately supporting our mechanistic hypothesis.

Further, the previously described visible light mediated debenzylation protocol was applied on the gram scale, using 3-*O*-benzyl-1,2:5,6-di-*O*-isopropylidene-α-D-glucofuranose as a model substrate. Limitations arising from poor light penetration were overcome adjusting the experimental procedure.

1.5 References

(1) Zersetzung der Valeriansäure durch den elektrischen Strom. *Liebigs Ann. Chem.* **1848**, *64* (3), 339-341. DOI: https://doi.org/10.1002/jlac.18480640346.
(2) Borodine, A. Über Bromvaleriansäure und Brombuttersäure. *Liebigs Ann. Chem.* **1861**, *119* (1), 121-123. DOI: https://doi.org/10.1002/jlac.18611190113. Hunsdiecker, H.; Hunsdiecker, C. Über den Abbau der Salze aliphatischer Säuren durch Brom. *Ber. dtsch. chem. Ges. (A and B Series)* **1942**, *75* (3), 291-297. DOI: https://doi.org/10.1002/cber.19420750309. Johnson, R. G.; Ingham, R. K. The Degradation Of Carboxylic Acid Salts By Means Of Halogen - The Hunsdiecker Reaction. *Chem. Rev.* **1956**, *56* (2), 219-269. DOI: 10.1021/cr50008a002. Löffler, K. Über eine neue Bildungsweise N-alkylierter Pyrrolidine. *Ber. dtsch. chem. Ges.* **1910**, *43* (2), 2035-2048. DOI: https://doi.org/10.1002/cber.191004302146. Hofmann, A. W. Zur Kenntniss der Coniin-Gruppe. *Ber. dtsch. chem. Ges.* **1885**, *18* (1), 5-23. DOI: https://doi.org/10.1002/cber.18850180103. Wolff, M. E. Cyclization of N-Halogenated Amines (The Hofmann-Löffler Reaction). *Chem. Rev.* **1963**, *63* (1), 55-64. DOI: 10.1021/cr60221a004.
(3) Yan, M.; Lo, J. C.; Edwards, J. T.; Baran, P. S. Radicals: Reactive Intermediates with Translational Potential. *J. Am. Chem. Soc.* **2016**, *138* (39), 12692-12714. DOI: 10.1021/jacs.6b08856.
(4) Mulliken, R. S. Molecular Compounds and their Spectra. III. The Interaction of Electron Donors and Acceptors. *J. Phys. Chem.* **1952**, *56* (7), 801-822. DOI: 10.1021/j150499a001.
(5) Lima, C. G. S.; de M. Lima, T.; Duarte, M.; Jurberg, I. D.; Paixão, M. W. Organic Synthesis Enabled by Light-Irradiation of EDA Complexes: Theoretical Background and Synthetic Applications. *ACS Catal.* **2016**, *6* (3), 1389-1407. DOI: 10.1021/acscatal.5b02386.
(6) Crisenza, G. E. M.; Mazzarella, D.; Melchiorre, P. Synthetic Methods Driven by the Photoactivity of Electron Donor–Acceptor Complexes. *J. Am. Chem. Soc.* **2020**, *142* (12), 5461-5476. DOI: 10.1021/jacs.0c01416.
(7) Sumida, Y.; Ohmiya, H. Direct excitation strategy for radical generation in organic synthesis. *Chem. Soc. Rev.* **2021**, *50* (11), 6320-6332, 10.1039/D1CS00262G. DOI: 10.1039/D1CS00262G.

(8) Buglioni, L.; Mastandrea, M. M.; Frontera, A.; Pericàs, M. A. Anion–π Interactions in Light-Induced Reactions: Role in the Amidation of (Hetero)aromatic Systems with Activated N-Aryloxyamides. *Chem. Eur. J.* **2019**, *25* (50), 11785-11790. DOI: https://doi.org/10.1002/chem.201903055. Xiao, F.; Pignatello, J. J. π+–π Interactions between (Hetero)aromatic Amine Cations and the Graphitic Surfaces of Pyrogenic Carbonaceous Materials. *Environ. Sci. Technol.* **2015**, *49* (2), 906-914. DOI: 10.1021/es5043029.
(9) Horita, K.; Yoshioka, T.; Tanaka, T.; Oikawa, Y.; Yonemitsu, O. On the selectivity of deprotection of benzyl, mpm (4-methoxybenzyl) and dmpm (3,4-dimethoxybenzyl) protecting groups for hydroxy functions. *Tetrahedron* **1986**, *42* (11), 3021-3028. DOI: https://doi.org/10.1016/S0040-4020(01)90593-9.
(10) Bunnett, J. F. Aromatic substitution by the SRN1 mechanism. *Acc. Chem. Res.* **1978**, *11* (11), 413-420. DOI: 10.1021/ar50131a003. Cantacuzène, D.; Wakselman, C.; Dorme, R. Condensation of perfluoroalkyl iodides with unsaturated nitrogen compounds. *J. Chem. Soc., Perkin Transactions 1* **1977**, (12), 1365-1371. DOI: 10.1039/P19770001365.
(11) Russell, G. A.; Wang, K. Electron transfer processes. 53. Homolytic alkylation of enamines by electrophilic radicals. *J. Org. Chem.* **1991**, *56* (11), 3475-3479. DOI: 10.1021/jo00011a007.
(12) Wade, P. A.; Morrison, H. A.; Kornblum, N. Substitution reactions which proceed via radical anion intermediates. Part 30. Effect of light on electron transfer substitution at a saturated carbon atom. *J. Org. Chem.* **1987**, *52* (14), 3102-3107. DOI: 10.1021/jo00390a026.
(13) Sankararaman, S.; Haney, W. A.; Kochi, J. K. Annihilation of aromatic cation radicals by ion-pair and radical pair collapse. Unusual solvent and salt effects in the competition for aromatic substitution. *J. Am. Chem. Soc.* **1987**, *109* (25), 7824-7838. DOI: 10.1021/ja00259a035.
(14) Fukuzumi, S.; Mochida, K.; Kochi, J. K. A unified mechanism for thermal and photochemical activation of charge-transfer processes with organometals. Steric effects in the insertion of tetracyanoethylene. *J. Am. Chem. Soc.* **1979**, *101* (20), 5961-5972. DOI: 10.1021/ja00514a016.
(15) Kee, C. W.; Chin, K. F.; Wong, M. W.; Tan, C.-H. Selective fluorination of alkyl C–H bonds via photocatalysis. *Chem. Commun.* **2014**, *50* (60), 8211-8214, 10.1039/C4CC01848F. DOI: 10.1039/C4CC01848F.
(16) Nelson, N.; Ben-Shem, A. The complex architecture of oxygenic photosynthesis. *Nat. Rev. Molecular Cell Biology* **2004**, *5* (12), 971-982. DOI: 10.1038/nrm1525.
(17) Scholes, G. D.; Fleming, G. R.; Olaya-Castro, A.; van Grondelle, R. Lessons from nature about solar light harvesting. *Nat. Chem.* **2011**, *3* (10), 763-774. DOI: 10.1038/nchem.1145.
(18) Hoffmann, N. Photochemical Reactions as Key Steps in Organic Synthesis. *Chem. Rev.* **2008**, *108* (3), 1052-1103. DOI: 10.1021/cr0680336.
(19) Melchionna, M.; Fornasiero, P. Updates on the Roadmap for Photocatalysis. *ACS Catal.* **2020**, *10* (10), 5493-5501. DOI: 10.1021/acscatal.0c01204.
(20) Lichtman, J. W.; Conchello, J.-A. Fluorescence microscopy. *Nat. Methods* **2005**, *2* (12), 910-919. DOI: 10.1038/nmeth817.
(21) Kasha, M. Characterization of electronic transitions in complex molecules. *Discuss. Faraday Soc.* **1950**, *9* (0), 14-19, 10.1039/DF9500900014. DOI: 10.1039/DF9500900014.
(22) Arias-Rotondo, D. M.; McCusker, J. K. The photophysics of photoredox catalysis: a roadmap for catalyst design. *Chem. Soc. Rev.* **2016**, *45* (21), 5803-5820, 10.1039/C6CS00526H. DOI: 10.1039/C6CS00526H.
(23) Shaw, M. H.; Twilton, J.; MacMillan, D. W. C. Photoredox Catalysis in Organic Chemistry. *J. Org. Chem.* **2016**, *81* (16), 6898-6926. DOI: 10.1021/acs.joc.6b01449.

(24) Prier, C. K.; Rankic, D. A.; MacMillan, D. W. C. Visible Light Photoredox Catalysis with Transition Metal Complexes: Applications in Organic Synthesis. *Chem. Rev.* **2013**, *113* (7), 5322-5363. DOI: 10.1021/cr300503r.
(25) Tucker, J. W.; Narayanam, J. M. R.; Shah, P. S.; Stephenson, C. R. J. Oxidative photoredox catalysis: mild and selective deprotection of PMB ethers mediated by visible light. *Chem. Commun.* **2011**, *47* (17), 5040-5042, 10.1039/C1CC10827A. DOI: 10.1039/C1CC10827A.
(26) Condie, A. G.; González-Gómez, J. C.; Stephenson, C. R. J. Visible-Light Photoredox Catalysis: Aza-Henry Reactions via C−H Functionalization. *J. Am. Chem. Soc.* **2010**, *132* (5), 1464-1465. DOI: 10.1021/ja909145y.
(27) Jana, R.; Pathak, T. P.; Sigman, M. S. Advances in Transition Metal (Pd,Ni,Fe)-Catalyzed Cross-Coupling Reactions Using Alkyl-organometallics as Reaction Partners. *Chem. Rev.* **2011**, *111* (3), 1417-1492. DOI: 10.1021/cr100327p.
(28) Devendar, P.; Qu, R.-Y.; Kang, W.-M.; He, B.; Yang, G.-F. Palladium-Catalyzed Cross-Coupling Reactions: A Powerful Tool for the Synthesis of Agrochemicals. *J. Agric. Food Chem.* **2018**, *66* (34), 8914-8934. DOI: 10.1021/acs.jafc.8b03792.
(29) Ananikov, V. P. Nickel: The "Spirited Horse" of Transition Metal Catalysis. *ACS Catal.* **2015**, *5* (3), 1964-1971. DOI: 10.1021/acscatal.5b00072.
(30) Han, R.; Hillhouse, G. L. Carbon−Oxygen Reductive-Elimination from Nickel(II) Oxametallacycles and Factors That Control Formation of Ether, Aldehyde, Alcohol, or Ester Products. *J. Am. Chem. Soc.* **1997**, *119* (34), 8135-8136. DOI: 10.1021/ja9714999.
(31) Twilton, J.; Le, C.; Zhang, P.; Shaw, M. H.; Evans, R. W.; MacMillan, D. W. C. The merger of transition metal and photocatalysis. *Nat. Rev. Chem.* **2017**, *1*, 0052, Review Article. DOI: 10.1038/s41570-017-0052.
(32) Corcoran, E. B.; Pirnot, M. T.; Lin, S.; Dreher, S. D.; DiRocco, D. A.; Davies, I. W.; Buchwald, S. L.; MacMillan, D. W. Aryl amination using ligand-free Ni(II) salts and photoredox catalysis. *Science* **2016**, *353* (6296), 279-283. DOI: 10.1126/science.aag0209 From NLM.
(33) Oderinde, M. S.; Frenette, M.; Robbins, D. W.; Aquila, B.; Johannes, J. W. Photoredox Mediated Nickel Catalyzed Cross-Coupling of Thiols With Aryl and Heteroaryl Iodides via Thiyl Radicals. *J. Am. Chem. Soc.* **2016**, *138* (6), 1760-1763. DOI: 10.1021/jacs.5b11244.
(34) Na, H.; Mirica, L. M. Deciphering the mechanism of the Ni-photocatalyzed C–O cross-coupling reaction using a tridentate pyridinophane ligand. *Nat. Commun.* **2022**, *13* (1), 1313. DOI: 10.1038/s41467-022-28948-8. Ting, S. I.; Williams, W. L.; Doyle, A. G. Oxidative Addition of Aryl Halides to a Ni(I)-Bipyridine Complex. *J. Am. Chem. Soc.* **2022**, *144* (12), 5575-5582. DOI: 10.1021/jacs.2c00462. Qin, Y.; Sun, R.; Gianoulis, N. P.; Nocera, D. G. Photoredox Nickel-Catalyzed C–S Cross-Coupling: Mechanism, Kinetics, and Generalization. *J. Am. Chem. Soc.* **2021**, *143* (4), 2005-2015. DOI: 10.1021/jacs.0c11937. Till, N. A.; Tian, L.; Dong, Z.; Scholes, G. D.; MacMillan, D. W. C. Mechanistic Analysis of Metallaphotoredox C–N Coupling: Photocatalysis Initiates and Perpetuates Ni(I)/Ni(III) Coupling Activity. *J. Am. Chem. Soc.* **2020**, *142* (37), 15830-15841. DOI: 10.1021/jacs.0c05901. Sun, R.; Qin, Y.; Nocera, D. G. General Paradigm in Photoredox Nickel-Catalyzed Cross-Coupling Allows for Light-Free Access to Reactivity. *Angew. Chem. Int. Ed.* **2020**, *59* (24), 9527-9533. DOI: https://doi.org/10.1002/anie.201916398.
(35) Cavedon, C.; Gisbertz, S.; Reischauer, S.; Vogl, S.; Sperlich, E.; Burke, J. H.; Wallick, R. F.; Schrottke, S.; Hsu, W.-H.; Anghileri, L.; et al. Intraligand Charge Transfer Enables Visible-Light-Mediated Nickel-Catalyzed Cross-Coupling Reactions**. *Angew. Chem. Int. Ed.* **2022**, *61* (46), e202211433. DOI: https://doi.org/10.1002/anie.202211433.

(36) Gisbertz, S.; Pieber, B. Heterogeneous Photocatalysis in Organic Synthesis. *ChemPhotoChem* **2020**, *4* (7), 456-475. DOI: https://doi.org/10.1002/cptc.202000014.
(37) Riente, P.; Noël, T. Application of metal oxide semiconductors in light-driven organic transformations. *Catalysis Science & Technology* **2019**, *9* (19), 5186-5232, 10.1039/C9CY01170F. DOI: 10.1039/C9CY01170F. Wang, X.; Blechert, S.; Antonietti, M. Polymeric Graphitic Carbon Nitride for Heterogeneous Photocatalysis. *ACS Catal.* **2012**, *2* (8), 1596-1606. DOI: 10.1021/cs300240x.
(38) Nicewicz, D. A.; Nguyen, T. M. Recent Applications of Organic Dyes as Photoredox Catalysts in Organic Synthesis. *ACS Catalysis* **2014**, *4* (1), 355-360. DOI: 10.1021/cs400956a.
(39) Romero, N. A.; Nicewicz, D. A. Organic Photoredox Catalysis. *Chem. Rev.* **2016**, *116* (17), 10075-10166. DOI: 10.1021/acs.chemrev.6b00057.
(40) Nielsen, C. D. T.; Burés, J. Visual kinetic analysis. *Chem. Sci.* **2019**, *10* (2), 348-353, 10.1039/C8SC04698K. DOI: 10.1039/C8SC04698K.
(41) Casado, J.; Lopez-Quintela, M. A.; Lorenzo-Barral, F. M. The initial rate method in chemical kinetics: Evaluation and experimental illustration. *J. Chem. Educ.* **1986**, *63* (5), 450. DOI: 10.1021/ed063p450.
(42) Blackmond, D. G. Reaction Progress Kinetic Analysis: A Powerful Methodology for Mechanistic Studies of Complex Catalytic Reactions. *Angew. Chem. Int. Ed.* **2005**, *44* (28), 4302-4320. DOI: 10.1002/anie.200462544. Blackmond, D. G. Kinetic Profiling of Catalytic Organic Reactions as a Mechanistic Tool. *J. Am. Chem. Soc.* **2015**, *137* (34), 10852-10866. DOI: 10.1021/jacs.5b05841.
(43) Burés, J. Variable Time Normalization Analysis: General Graphical Elucidation of Reaction Orders from Concentration Profiles. *Angew. Chem. Int. Ed.* **2016**, *55* (52), 16084-16087. DOI: 10.1002/anie.201609757.

Chapter 2

Synopsis

Throughout my doctoral research I contributed to five research projects which are published or currently under revision and wrote one minireview. I was a major contributor to three of the projects and a minor contributor to two, all of which are listed below.

2.1 Major contributions

1. **Madani A**.; Anghileri L.; Heydenreich M.; Möller H. M.; Pieber B. Benzylic Fluorination Induced by a Charge-Transfer Complex with a Solvent-Dependent Selectivity Switch. *Org. Lett.* **2022**, 24, 5376-5380.

The prominence of organofluorine compounds amongst pharmaceutical and agrochemicals has led to a tremendous increase in interest in fluorination reactions.[1-3] Nucleophilic and electrophilic fluorination strategies are at the forefront; however, recent developments of non-hazardous radical fluorinating agents unlocked the development of new methodologies, harvesting the unparalleled reactivity of radical chemistry in a safe and selective fashion.[4] Using a charge-transfer complex between a bench-stable electrophilic fluorinating agent and 4-dimethylamino pyridine (DMAP), I developed a novel benzylic radical fluorination strategy for phenylacetic acids. The user-friendly protocol offers short reaction times (1-30 min) and a solvent controlled selectivity-switch. Polar aprotic solvents cleanly result in α-fluorophenylacetic acids, whereas in aqueous media the decarboxylative benzylic fluorination reaction, resulting in benzyl fluorides, is dominant. Mechanistic investigations suggest a single electron transfer (SET) mechanism for the decarboxylative fluorination, whereas the direct C(sp^3)–H fluorination to α-fluorophenylacetic acids is proposed to proceed via hydrogen atom transfer (HAT) pathway.

2. **Madani A.**;† Sletten E. T.;† Cavedon C.; Seeberger P. H.; Pieber, B. Visible-light-mediated oxidative debenzylation of 3-*O*-benzyl-1,2:5,6-di-*O*-isopropylidene-α-D-glucofuranose. *Org. Synth.* **2023**, 100, 271.

After our protocol for the photooxidative debenzylation (*Visible-Light-Mediated Oxidative Debenzylation Enables the Use of Benzyl Ethers as Temporary Protecting Groups, Chapter 9*) was well received by the community and found application in several multistep syntheses of complex biomolecules, the *Organic Syntheses* journal requested us to probe the upscaling of the methodology.[5-7] The work described in Chapter 6 presents my effort in applying our previously developed photooxidative debenzylation protocol on the gram scale (>2 g of product), while overcoming limitations arising from inefficient light penetration. Careful optimization and adjusting of reaction parameters, such as orientation and position of the light sources, glassware, reaction time and reagent quantities, ultimately resulted a reproducible protocol for the photooxidative benzyl ether cleavage on large-scale and opening the doors to new applications of the methodology.

3. Malik J. A.; **Madani, A**.; Seeberger, P. H.; Pieber, B. Evidence for Photocatalyst Involvement in Oxidative Additions of Nickel-Catalyzed Carboxylate *O*-Arylations. *J. Am. Chem. Soc*. **2020**, 142, 11042-11049.

The merger of nickel- with photoredox catalysis has led to a renaissance in radical chemistry and enabled the development of new cross-coupling reactions.[8] Unravelling the underlying mechanism of these transformations conveys valuable information, which can ultimately help with upscaling, reaction development and optimization. While state-of-the-art techniques to investigate such systems focus on steady-state measurements, such as quenching studies and DFT calculations, real-time monitoring offers to complete the picture.[9] Chapter 7 presents my efforts in the first in-depth kinetic analysis of dual photo- and nickel catalyzed cross-coupling reactions. Using in situ ATR-IR spectroscopy, we monitored a model esterification reaction, using two different photocatalytic systems: the state-of-the-art iridium-based photocatalyst $Ir(ppy)_3$, and a graphitic carbon nitride (CN-OA-m). In situ monitoring enabled visual kinetic analysis of both systems which resulted in rate laws indicative for different mechanistic proposals ultimately revealed a hitherto-undisclosed role of the photocatalyst in the oxidative addition.

The conclusions from this study have been influential on further kinetics studies in the field of nickel metallaphotoredox catalysis from established groups in academia, including recent in situ kinetics reports by Lloyd-Jones and Yoon, where their findings are discussed in detailed comparison to ours.[10, 11]

2.2 Minor contributions

4. Cavedon, C.; **Madani, A.**; Seeberger, P. H.; Pieber, B. Semiheterogeneous Dual Nickel/Photocatalytic (Thio)etherification Using Carbon Nitrides. *Org. Lett.* **2019**, 21, 5331-5334.

Inspired by nature, photocatalysis uses light, a sustainable and traceless "reagent", to trigger chemical transformations. Combining nickel-catalysis with visible-light photocatalysis has enabled the development of cross-coupling reactions, replacing palladium, rendering these transformations more sustainable. However, these methodologies are mainly based on homogeneous iridium- or ruthenium polypyridyl complexes as photocatalysts. Chapter 8 reports our research efforts to replace a state-of-the-art homogeneous photocatalyst ($Ir(ppy)_3$) with a heterogenous semi-conductor in a dual photo- and nickel catalyzed cross-coupling reaction. A semi-heterogenous protocol for C–O cross-coupling reaction was developed, and I extended the reaction's scope to include thioethers.

5. Cavedon, C.; Sletten, E. T.; **Madani, A.**; Niemeyer, O.; Seeberger, P. H.; Pieber, B. Visible- Light-Mediated Oxidative Debenzylation Enables the Use of Benzyl Ethers as Temporary Protecting Groups. *Org. Lett.* **2021**, 23, 514-518.

Selective installation and removal of protective groups (PG) for hydroxyl groups is of particular importance in carbohydrate chemistry.[12, 13] Benzyl ethers are easily installed and stable over most reaction conditions, however their removal requires harsh conditions limiting their applicability. Developing a mild strategy to remove benzyl ethers, we enabled their usage as temporary PG during oligosaccharide assembly and expanded their applicability in carbohydrate building block synthesis.

Using an LED-illuminated NMR spectroscopy setup, I monitored the reaction in real-time and gained mechanistic insights that later helped me to prepare the reaction for scale-up.

2.3 References

(1) Gillis, E. P.; Eastman, K. J.; Hill, M. D.; Donnelly, D. J.; Meanwell, N. A., Applications of fluorine in medicinal chemistry. *J. Med. Chem.* **2015,** *58*, 8315-8359.
(2) Meanwell, N. A., Fluorine and fluorinated motifs in the design and application of bioisosteres for drug design. *J. Med. Chem.* **2018,** *61*, 5822-5880.
(3) Fujiwara, T.; O'Hagan, D., Successful fluorine-containing herbicide agrochemicals. *J. Fluor. Chem.* **2014,** *167*, 16-29.
(4) Rueda-Becerril, M.; Chatalova Sazepin, C.; Leung, J. C. T.; Okbinoglu, T.; Kennepohl, P.; Paquin, J.-F.; Sammis, G. M., Fluorine Transfer to Alkyl Radicals. *J. Am. Chem. Soc.* **2012,** *134*, 4026-4029.
(5) Cavedon, C.; Sletten, E. T.; Madani, A.; Niemeyer, O.; Seeberger, P. H.; Pieber, B., Visible-Light-Mediated Oxidative Debenzylation Enables the Use of Benzyl Ethers as Temporary Protecting Groups. *Org. Lett.* **2021,** *23*, 514-518.
(6) Konrad, D. B.; Rühmann, K. P.; Ando, H.; Hetzler, B. E.; Strassner, N.; Houk, K. N.; Matsuura, B. S.; Trauner, D., A concise synthesis of tetrodotoxin. *Science* **2022,** *377*, 411-415.
(7) Nicolaou, K. C.; Pan, S.; Shelke, Y.; Rigol, S.; Bao, R.; Das, D.; Ye, Q., A unified strategy for the total syntheses of eribulin and a macrolactam analogue of halichondrin B. *Proc. Natl. Acad. Sci.* **2022,** *119*, e2208938119.
(8) Chan, A. Y.; Perry, I. B.; Bissonnette, N. B.; Buksh, B. F.; Edwards, G. A.; Frye, L. I.; Garry, O. L.; Lavagnino, M. N.; Li, B. X.; Liang, Y.; Mao, E.; Millet, A.; Oakley, J. V.; Reed, N. L.; Sakai, H. A.; Seath, C. P.; MacMillan, D. W. C., Metallaphotoredox: The Merger of Photoredox and Transition Metal Catalysis. *Chem. Rev.* **2022,** *122*, 1485-1542.
(9) Welin, E. R.; Le, C.; Arias-Rotondo, D. M.; McCusker, J. K.; MacMillan, D. W., Photosensitized, energy transfer-mediated organometallic catalysis through electronically excited nickel(II). *Science* **2017,** *355*, 380-385.
(10) Swords, W. B.; Chapman, S. J.; Hofstetter, H.; Dunn, A. L.; Yoon, T. P., Variable Temperature LED–NMR: Rapid Insights into a Photocatalytic Mechanism from Reaction Progress Kinetic Analysis. *J. Org. Chem.* **2022,** *87*, 11776-11782.
(11) Ben-Tal, Y.; Lloyd-Jones, G. C., Kinetics of a Ni/Ir-Photocatalyzed Coupling of ArBr with RBr: Intermediacy of ArNiII(L)Br and Rate/Selectivity Factors. *J. Am. Chem. Soc.* **2022,** *144*, 15372-15382.
(12) Pétursson, S., Protecting Groups in Carbohydrate Chemistry. *J. Chem. Educ.* **1997,** *74*, 1297.
(13) Wang, T.; Demchenko, A. V., Synthesis of carbohydrate building blocks via regioselective uniform protection/deprotection strategies. *Org. Biomol. Chem.* **2019,** *17*, 4934-4950.

Chapter 3

Summaries

3.1 In situ Reaction Monitoring in Photocatalytic Organic Synthesis (Chapter 4)

Throughout the past decade, photocatalysis has emerged as a fundamental process in synthetic organic chemistry, that provides facile access to reactive open-shell intermediates under mild conditions.[1] The further pursuit of photocatalytic reaction development and optimization demands an understanding of underlying reaction mechanisms and interdependencies of reaction conditions and parameters. Unfortunately, investigating complex catalytic systems, which include multiple reactive species remains a challenge. State-of-the-art techniques to investigate such transformations commonly rely on static experiments that characterize only interactions between excited state- and ground state species, while avoiding the reactive intermediates.[2] To complete the picture, in situ monitoring techniques have been established to track the reaction and allow the observation of key species and intermediates. This work highlights recent efforts in development and design of setups capable of real-time monitoring of photocatalytic reactions in synthetic organic chemistry and displays examples, emphasizing the importance of mechanistic investigations.

I collected state-of-the-art literature existing on that topic at that time (December 2022). Together with Dr. Bartholomäus Pieber, I organized the literature and outlined the mini review. I wrote the first draft of the manuscript, and Dr. Bartholomäus Pieber revised and corrected the manuscript.

3.2 Benzylic Fluorination Induced by a Charge-Transfer Complex with a Solvent-dependent Selectivity Switch (Chapter 5)

The improved physicochemical properties of fluorinated organic compounds influences the development of active pharmaceutical ingredients and agrochemicals, and hence creates a demand for efficient and selective fluorination reactions.[3-5] Nucleophilic and electrophilic fluorinations are at the forefront, but recent developments of non-hazardous and selective radical fluorinating agents have increased the utility of these strategies. Amino-based *N*–F fluorinating reagents had previously only been used as electrophilic fluorine sources, but recently their ability to transfer fluorine to carbon-centered radicals was discovered.[6]

We developed a divergent strategy for benzylic C(sp^3)–H radical fluorination reactions, triggered by an in situ formed charge-transfer complex between a pyridine derivative and Selectfluor™. Together with Dr. Bartholomäus Pieber, listed as corresponding author, I conceived the idea behind the project and investigated the feasibility. Carefully optimizing the reaction conditions, I found that the reaction's outcome can be controlled by the reaction media. In aqueous media, the decarboxylative benzylic fluorination was dominant, whereas polar aprotic solvents cleanly result in α-fluorophenylacetic acids. I investigated the scope and limitations of the direct C(sp^3)–H fluorination reaction. Lucia Anghileri optimized the decarboxylative benzylic fluorination reaction and investigated the scope and limitations of this transformation. Using in situ ATR-IR spectroscopy, I monitored the direct benzylic fluorination of 4-*tert*-butylphenylacetic acid, the highlight was the high reactivity of the charge-transfer complex, which instantaneously leads to product formation after the fluorinating agent is added to a stirring solution of the phenylacetic acid and 4-dimethylamino pyridine (DMAP) in acetonitrile. Absence of the substrate in the reaction mixture resulted in fast consumption of Selectfluor™, supporting our mechanistic proposal stating the in situ formation of a charge-transfer complex. Further, this experiment revealed that the order of reagent addition is essential for a successful reaction. Investigating the degradation products arising from mixing Selectfluor™ with the pyridine additive, Matthias Heydenreich and Heiko Moeller identified DMAP·HF adducts in a series of ^{1}H NMR studies, using Teflon inserts.

Further, I undertook competitive experiments between phenylacetic acids with different electronic properties, supporting a mechanism, which proceeds via hydrogen atom transfer (HAT) to result the carbon-centered radical intermediate, rather than the initiation via single electron transfer (SET). The enediolate was not observed treating phenylacetic acid with DMAP in MeCN-d_3, speaking against a polar reaction mechanism. Addition of a radical trap (TEMPO) to the reaction mixture resulted a complex reaction mixture and no product formation, indicating a radical reaction. Ultimately, a mechanism was proposed that proceeds via a HAT pathway in non-aquous solvent, whereas in aqueous media a SET pathway is dominant.

I wrote the first draft of the mansucript and supporting information. Lucia Anghileri contributed to the supporting information. Dr. Bartholomäus Pieber revised and corrected the manuscript.

3.3 Visible-Light-Mediated Oxidative Debenzylation of 3-*O*-Benzyl-1,2:5,6-di-*O*-isopropylidene-α-D-glucofuranose (Chapter 6)

Protecting groups play a pivotal role in multistep organic synthesis ensuring regio-, chemo- and stereoselectivity.[7] They are especially vital in carbohydrate synthesis, which relies on the temporal and permanent manipulation of multiple hydroxyl groups. A key feature of such entities is their stability under given reaction conditions and their orthogonal cleavage. Benzyl ethers provide a versatile means of protection for hydroxyl moieties, being that they are installed under neutral or basic conditions and stable to a wide range of reaction conditions. While their stability renders benzyl ethers ideal candidates to mask hydroxyl groups through multistep syntheses, their removal requires harsh conditions, such as a Birch reduction, catalytic hydrogenolysis, or oxidation with ozone, all of which suffer from low functional group tolerance. Using photoredox catalysis, we developed a mild strategy to cleave benzyl ether protective groups from carbohydrates in high chemoselectivity.[8]

After several well-known academic groups utilized our protocol in the synthesis of complex molecules, we were asked to scale-up our protocol to be published in *Organic Syntheses*.[9, 10] This journal specializes in reporting large-scale, reproducible procedures of different methodologies. In our original manuscript, we published two different protocols, one that was fully catalytic, using a combination of 2,3-dichlor-5,6-dicyano-1,4-benzoquinone (DDQ) as photocatalyst and *tert*-butyl nitrite (TBN) as terminal oxidant, and one which required a stoichiometric amount of DDQ. Dr. Eric T. Sletten, listed as co 1st author, probed the debenzylation of 3-*O*-benzyl-1,2:5,6-di-*O*-isopropylidene-α-D-glucofuranose on a 4 g scale, using the catalytic protocol and four Kessil™ lamps. After the revision, the journal requested the reaction was to be carried out in a pressure-rated flask, using only two lamps. I probed the deprotection on large-scale using two Kessil™ lamps and the pressure-rated flask, which resulted poor yields (≤ 30%) and reproducibility issues, using a catalytic protocol. As dictated by the Beer–Lambert's law, light penetration can be a critical issue, inhibiting large-scale applicability of photochemical transformations. Hence, I trialed different orientation of the lights to maximize the yield, with no significant improvement.

The mechanistic knowledge I previously gained through real-time monitoring of the transformation allowed me to identify the cocatalyst (TBN) to be responsible of inefficient product formation. Low photon flux and narrow headspace of the requested flask, limiting O_2 supply, hampered efficient NO_2 generation. Consequently, insufficient turnover of $DDQH_2$ resulted its precipitation along with incomplete reactions. Further, decomposition of the starting material was observed. I overcame these limitations using stoichiometric amounts of DDQ (1.2 equiv.), which resulted in good yields and in a reproducible fashion on a 11.4 mmol scale using two LED lamps.

I wrote the first draft of the manuscript and precisely documented it with pictures of every step of the procedure. Dr. Eric T. Sletten, Dr. Bartholomäus Pieber and Prof. Dr. Dr. h. c. Peter Seeberger revised and corrected the manuscript.

The manuscript is currently under revision, as an unaffiliated lab is confirming the reproducibility of our protocol.

3.4 Evidence for Photocatalyst Involvement in Oxidative Additions of Nickel-Catalyzed Carboxylate *O*-Arylations (Chapter 7)

The synthetic advances possible with nickel metallaphotoredox catalysis are easily apparent, presenting a potential alternative to palladium chemistry, which is likely unsustainable long-term. However, only little is understood about the underlying mechanisms of these transformations, and open questions remain. Until recently, common techniques to study the mechansim of dual nickel- and photocatalyzed reactions were limited to approaches such as Stern–Volmer quenching studies, transient absorption spectroscopy, and computational studies.[11] Such techniques can impart useful information but usually focus on potential interactions between the photocatalyst and metal catalyst under static conditions, outside of the reality of a dynamic catalytic process. In contrast, in situ monitoring allows the observation of reaction progress in real time and under synthetically relevant conditions. Recent development of graphical approaches, that are able to visually interrogate kinetic information from data-rich progress profiles, provide facile access to rate laws.[12, 13]

During the development of a nickel metallaphotoredox reaction which used a graphitic carbon nitride (CN-OA-m) as a heterogeneous photocatalyst, our group had previously developed a setup with which to observe a photocatalytic cross-coupling in real time using in situ ATR-IR spectroscopy.[14] However, in depth kinetic analysis of such systems requires meticulous experimental planning and consideration. Data obtained under typical synthetic conditions (referred to as native reaction conditions) offers information that may be useful to discovery-scale or academic chemists wishing to probe reactivity. However, such conditions may mask the intrinsic reactivity of the system, as it may be obscured by turnover-limiting processes occurring between the photocatalyst and nickel catalyst.

Given that we were the first to perform detailed kinetics studies on this class of reactions, we therefore sought to obtain four comprehensive data sets: 1) native reaction conditions, with CN-OA-m photocatalyst;

2) native reaction conditions, with a homogeneous iridium catalyst ($Ir(ppy)_3$), commonly used in the field 3) data obtained in a concentration regime where nickel catalyst is saturated with excited-state CN-OA-m photocatalyst ("intrinsic reactivity regime"); and 4) an analogous regime where the nickel catalyst is saturated with excited-state Ir photocatalyst.

I conducted half of the experiments to identify these "intrinsic reactivity regimes" for data sets 3 and 4, which required numerous initial-rate studies and extensive troubleshooting to ensure reproducibility. I ran the majority of experiments for data sets 2 and 4, which included: experiments to determine the nickel catalyst order, "same-excess" experiments to probe potential catalyst deactivation or product inhibition, "different-excess" experiments to determine reagent orders of the aryl halide substrate and its cross-coupling partner, and different-excess experiments to analyze the impact of the Brønsted base (*N-tert*-butylisopropylamine). I further investigated in influence of the CN-OA-m concentration on the reaction. During the revision process, we decided to standardize the metal catalyst concentrations across all data sets, so one of these data sets was collected multiple times to support the integrity of our data. I also conducted a minor portion of experiments for data sets 1 and 3, using an identical experimental approach.

We discovered that the iridium photocatalyst leads to significant amounts of dehalogenated substrate, which suggests some mechanistic commonalities between the graphitic carbon nitride- and iridium catalyzed systems. Further, catalyst deactivation was found when the iridium photocatalyst was used. Last, the data obtained for the iridium photocatalyst supported the hypothesis that reductive elimination is turnover-limiting.

Dr. Jamal A. Malik wrote the manuscript. I contributed to the supporting information. Dr. Bartholomäus Pieber and Prof. Dr. Dr. h. c. Peter H. Seeberger revised and corrected the manuscript.

3.5 Semi-Heterogeneous Dual Nickel/Photocatalytic (Thio)Etherification using Carbon Nitrides (Chapter 8)

Photocatalysis is a powerful synthetic tool, using photons as a traceless "reagent" to trigger chemical transformations. In particular, the merging of photoredox- with nickel catalysis has emerged as a valuable strategy, enabling carbon-heteroatom and carbon-carbon bond formations under mild conditions.[15] However, these transformations commonly rely on expensive homogeneous iridium- or ruthenium-polypyridyl complexes as photocatalyst.[11] Combining nickel catalysis with a semi-heterogeneous graphitic carbon nitride (gCN) photocatalyst, we showed that the noble metal complexes can be replaced and still able to successfully perform C–O and C–S cross-coupling. Graphitic carbon nitrides are heterogeneous semiconductors that can absorb light in the visible part of the spectrum.[16] We prepared the material used in this project (CN-OA-m) from oxamide and urea via calcination and characterized via UV/Vis spectroscopy.

Cristian Cavedon, listed as 1st author, investigated the feasibility of the C–O cross-coupling and optimized the reaction conditions. Investigation of the scope limitations showed that electron-poor aryl bromides were readily coupled with primary and secondary alcohols in good to excellent yields. Further, the applicability in API synthesis was showcased.

I extended the reaction scope, investigating the method's applicability to the coupling of thiols with an aryl halide. Primary, secondary, and tertiary thiols were successfully coupled with 4-iodobenzoate.

Cristian Cavedon wrote the first draft of the manuscript. I contributed to the supporting information and revised the manuscript. Dr. Bartholomäus Pieber and Prof. Dr. Dr. h. c. Peter H. Seeberger revised and corrected the manuscript.

3.6 Visible Light-Mediated Oxidative Debenzylation Enables the Use of Benzyl Ethers as Temporary Protecting Groups (Chapter 9)

Protective groups are commonly used to ensure chemo-, regio- and stereoselectivity throughout multistep organic synthesis. Especially the synthesis of complex oligosaccharides, which are densely functionalized, relies on orthogonal installation and cleavage strategies.[7, 17, 18] Highly stable benzyl ethers are amongst the most commonly used permanent protective groups for hydroxyl moieties.[18] Their stability, however, often limits their utility since harsh reductive/oxidative conditions are required for their removal.[19] Mild deprotection strategies for *para*-methoxybenzyl ethers (PMB) had been developed, using photoredoxcatalysis, however, scission of benzyl ethers requires a sufficiently stronger oxidant.[20]

This work addresses the limitation by developing a photocatalytic debenzylation protocol, which uses a combination of DDQ and a sacrificial oxidant *tert*-butyl nitrite (TBN) under green light irradiation.

Up to two benzyl ether moieties were able to be simultaneously removed from carbohydrates moieties, while other commonly used protective groups were tolerated, such as acetyl-, isopropylidene- or benzoyl groups.

Cristian Cavedon, listed as first author, optimized the reaction conditions and investigated the scope and limitations of the reaction. The reaction's applicability under flow conditions was investigated by Dr. Eric T. Sletten.

To gain mechanistic insights into the newly developed deprotection strategy I developed a LED-illumination setup suitable for in situ monitoring of photochemical transformations via NMR spectroscopy.[21] I designed and conducted experiments to investigate the interdependencies of reagents and the reaction's light-dependency. Analysis and interpretation of the obtained data ultimately helped me to support our mechanistic hypothesis.

Cristian Cavedon and Dr. Eric T. Sletten wrote the first draft of the manuscript. I contributed to the manuscript and the supporting information. Dr. Bartholomäus Pieber and Prof. Dr. Dr. h. c Peter H. Seeberger revised and corrected the manuscript.

3.7 References

(1) Marzo, L.; Pagire, S. K.; Reiser, O.; König, B. Visible-Light Photocatalysis: Does It Make a Difference in Organic Synthesis? *Angew. Chem. Int. Ed.* **2018**, *57* (32), 10034-10072. DOI: https://doi.org/10.1002/anie.201709766.
(2) Buzzetti, L.; Crisenza, G. E. M.; Melchiorre, P. Mechanistic Studies in Photocatalysis. *Angew. Chem. Int. Ed.* **2019**, *58* (12), 3730-3747. DOI: 10.1002/anie.201809984.
(3) Meanwell, N. A. Fluorine and Fluorinated Motifs in the Design and Application of Bioisosteres for Drug Design. *J. Med. Chem.* **2018**, *61* (14), 5822-5880. DOI: 10.1021/acs.jmedchem.7b01788.
(4) Gillis, E. P.; Eastman, K. J.; Hill, M. D.; Donnelly, D. J.; Meanwell, N. A. Applications of Fluorine in Medicinal Chemistry. *J. Med. Chem.* **2015**, *58* (21), 8315-8359. DOI: 10.1021/acs.jmedchem.5b00258.
(5) Fujiwara, T.; O'Hagan, D. Successful fluorine-containing herbicide agrochemicals. *J. Fluor. Chem.* **2014**, *167*, 16-29.
(6) Rueda-Becerril, M.; Chatalova Sazepin, C.; Leung, J. C. T.; Okbinoglu, T.; Kennepohl, P.; Paquin, J.-F.; Sammis, G. M. Fluorine Transfer to Alkyl Radicals. *J. Am. Chem. Soc.* **2012**, *134* (9), 4026-4029. DOI: 10.1021/ja211679v.
(7) Pétursson, S. Protecting Groups in Carbohydrate Chemistry. *J. Chem. Educ.* **1997**, *74* (11), 1297. DOI: 10.1021/ed074p1297.
(8) Cavedon, C.; Sletten, E. T.; Madani, A.; Niemeyer, O.; Seeberger, P. H.; Pieber, B. Visible-Light-Mediated Oxidative Debenzylation Enables the Use of Benzyl Ethers as Temporary Protecting Groups. *Org. Lett.* **2021**, *23* (2), 514-518. DOI: 10.1021/acs.orglett.0c04026.
(9) Konrad, D. B.; Rühmann, K. P.; Ando, H.; Hetzler, B. E.; Strassner, N.; Houk, K. N.; Matsuura, B. S.; Trauner, D. A concise synthesis of tetrodotoxin. *Science* **2022**, *377* (6604), 411-415. DOI: 10.1126/science.abn0571 From NLM.
(10) Nicolaou, K. C.; Pan, S.; Shelke, Y.; Rigol, S.; Bao, R.; Das, D.; Ye, Q. A unified strategy for the total syntheses of eribulin and a macrolactam analogue of halichondrin B. *Proc. Natl. Acad. Sci.* **2022**, *119* (32), e2208938119. DOI: doi:10.1073/pnas.2208938119.
(11) Welin, E. R.; Le, C.; Arias-Rotondo, D. M.; McCusker, J. K.; MacMillan, D. W. Photosensitized, energy transfer-mediated organometallic catalysis through electronically excited nickel(II). *Science* **2017**, *355* (6323), 380-385. DOI: 10.1126/science.aal2490 From NLM.
(12) Burés, J. Variable Time Normalization Analysis: General Graphical Elucidation of Reaction Orders from Concentration Profiles. *Angew. Chem. Int. Ed.* **2016**, *55* (52), 16084-16087. DOI: https://doi.org/10.1002/anie.201609757.
(13) Blackmond, D. G. Reaction Progress Kinetic Analysis: A Powerful Methodology for Mechanistic Studies of Complex Catalytic Reactions. *Angew. Chem. Int. Ed.* **2005**, *44* (28), 4302-4320. DOI: https://doi.org/10.1002/anie.200462544.
(14) Pieber, B.; Malik, J. A.; Cavedon, C.; Gisbertz, S.; Savateev, A.; Cruz, D.; Heil, T.; Zhang, G.; Seeberger, P. H. Semi-heterogeneous Dual Nickel/Photocatalysis using Carbon Nitrides: Esterification of Carboxylic Acids with Aryl Halides. *Angew. Chem. Int. Ed.* **2019**, *58* (28), 9575-9580. DOI: 10.1002/anie.201902785.
(15) Chan, A. Y.; Perry, I. B.; Bissonnette, N. B.; Buksh, B. F.; Edwards, G. A.; Frye, L. I.; Garry, O. L.; Lavagnino, M. N.; Li, B. X.; Liang, Y.; et al. Metallaphotoredox: The Merger of Photoredox and Transition Metal Catalysis. *Chem. Rev.* **2022**, *122* (2), 1485-1542. DOI: 10.1021/acs.chemrev.1c00383.

(16) Savateev, A.; Ghosh, I.; König, B.; Antonietti, M. Photoredox Catalytic Organic Transformations using Heterogeneous Carbon Nitrides. *Angew. Chem. Int. Ed.* **2018**, *57* (49), 15936-15947. DOI: https://doi.org/10.1002/anie.201802472.
(17) Wang, T.; Demchenko, A. V. Synthesis of carbohydrate building blocks via regioselective uniform protection/deprotection strategies. *Org. Biomol. Chem.* **2019**, *17* (20), 4934-4950, 10.1039/C9OB00573K. DOI: 10.1039/C9OB00573K.
(18) Guberman, M.; Seeberger, P. H. Automated Glycan Assembly: A Perspective. *J. Am. Chem. Soc.* **2019**, *141* (14), 5581-5592. DOI: 10.1021/jacs.9b00638.
(19) Crawford, C.; Oscarson, S. Optimized Conditions for the Palladium-Catalyzed Hydrogenolysis of Benzyl and Naphthylmethyl Ethers: Preventing Saturation of Aromatic Protecting Groups. *Eur. J. Org. Chem.* **2020**, *2020* (22), 3332-3337. DOI: https://doi.org/10.1002/ejoc.202000401.
(20) Tucker, J. W.; Narayanam, J. M. R.; Shah, P. S.; Stephenson, C. R. J. Oxidative photoredox catalysis: mild and selective deprotection of PMB ethers mediated by visible light. *Chem. Commun.* **2011**, *47* (17), 5040-5042, 10.1039/C1CC10827A. DOI: 10.1039/C1CC10827A.
(21) Feldmeier, C.; Bartling, H.; Riedle, E.; Gschwind, R. M. LED based NMR illumination device for mechanistic studies on photochemical reactions--versatile and simple, yet surprisingly powerful. *J Magn Reson* **2013**, *232*, 39-44. DOI: 10.1016/j.jmr.2013.04.011 From NLM.

Chapter 4

In situ Reaction Monitoring in Photocatalytic Organic Synthesis

Madani A.; Pieber B. In Situ Reaction Monitoring in Photocatalytic Organic Synthesis. *ChemCatChem* **2023**, 15, e20220158.

https://doi.org/10.1002/cctc.202201583

Check for updates

ChemCatChem

Review
doi.org/10.1002/cctc.202201583

Chemistry Europe
European Chemical Societies Publishing

www.chemcatchem.org

Special Collection

In situ Reaction Monitoring in Photocatalytic Organic Synthesis

Amiera Madani[a, b] and Bartholomäus Pieber*[a]

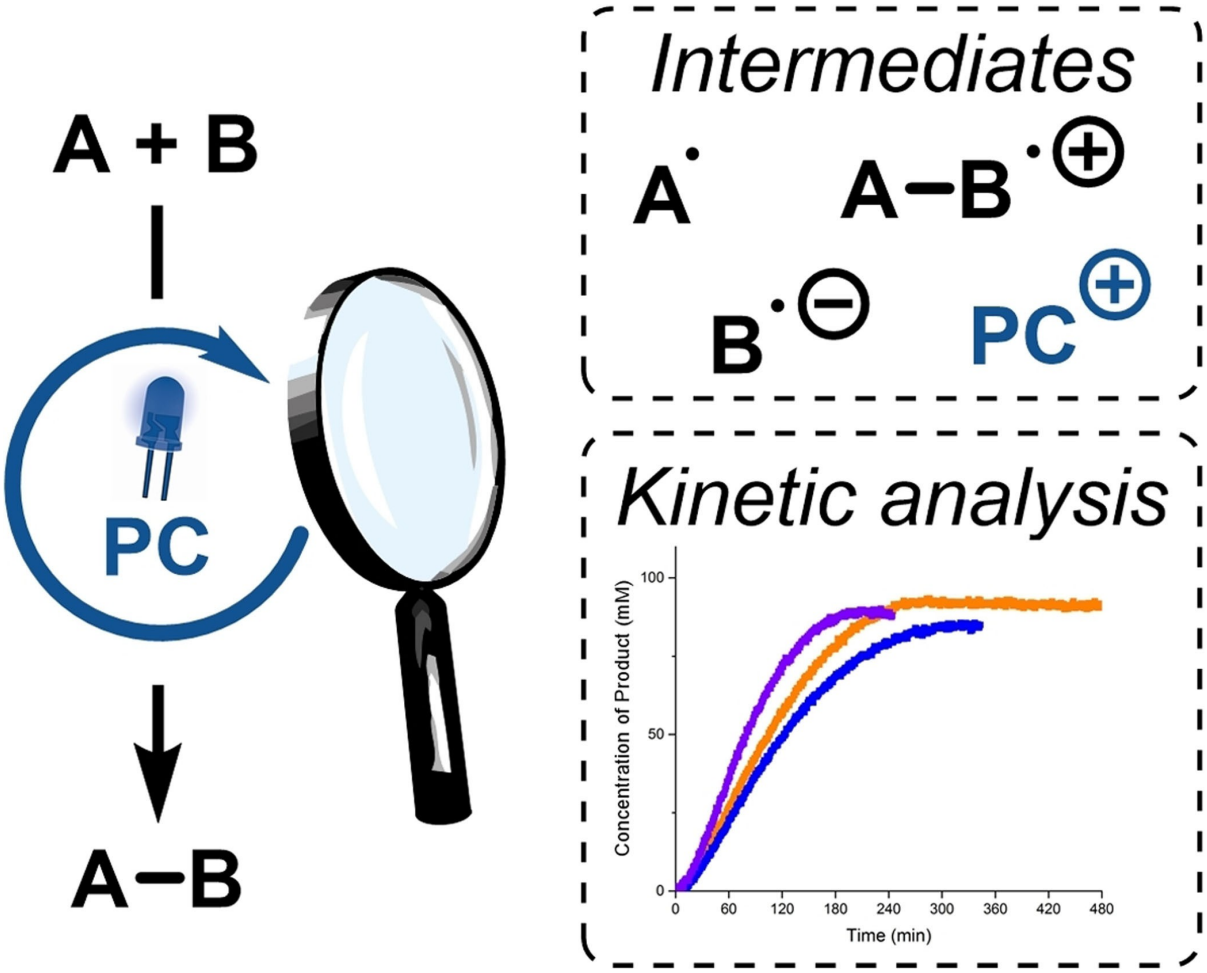

ChemCatChem
Review
doi.org/10.1002/cctc.202201583
Chemistry Europe
European Chemical Societies Publishing

Visible-light photocatalysis provides numerous useful methodologies for synthetic organic chemistry. However, the mechanisms of these reactions are often not fully understood. Common mechanistic experiments mainly aim to characterize excited state properties of photocatalysts and their interaction with other species. Recently, in situ reaction monitoring using dedicated techniques was shown to be well-suited for the identification of intermediates and to obtain kinetic insights, thereby providing more holistic pictures of the reactions of interest. This minireview surveys these technologies and discusses selected examples where reaction monitoring was used to elucidate the mechanism of photocatalytic reactions.

1. Introduction

Visible-light photocatalysis has become a cornerstone of modern organic synthesis.[1] Key to success is the ability of certain chromophores, including organometallic complexes,[2] organic dyes[3] and semiconducting materials[4] to reach long-lived excited states that can act as single electron oxidants/reductants (photoredox catalysis, PRC),[5] transfer energy to substrates or reagents (energy transfer catalysis, EnT),[6] or serve as hydrogen atom transfer catalysts (HAT).[7] These events provide straightforward access to reactive open-shell intermediates under mild conditions and resulted in the development of a myriad of new reaction methodologies.[1]

Unraveling the mechanisms of these transformations is challenging, because many state-of-the-art photocatalytic transformations include more than one catalytic species and several reagents that are necessary to complete catalytic cycles.[1] Further, certain photocatalysts can act as SET, HAT and EnT catalysts, undergo consecutive photoinduced electron transfer events,[8] or access different reactivity depending on the photon energy/intensity leading to complex mechanistic scenarios.[9] It is therefore not surprising that more than one mechanism can be used to plausibly explain the outcome of photocatalytic transformations. Indeed, proposed mechanisms are critically discussed,[10] and were revised after careful investigations.[11]

The vast majority of mechanistic studies of photocatalytic reactions rely on experiments that aim to characterize the excited state properties of photocatalysts and their interaction with substrates, reagents and co-catalysts under idealized conditions.[12] These include computational and electrochemical methods, static optical spectroscopy, quantum yield analysis, quenching experiments, (ultra)fast spectroscopy and the identification of radical intermediates using trapping agents and radical clock experiments, as well as electron paramagnetic resonance (EPR) spectroscopy.[12] These experiments undoubtedly provide essential insights that build the foundation for mechanistic proposals.

However, more holistic pictures of photocatalytic reactions are highly desirable and require the determination of rate laws and studies on (thermal) follow-up events that typically occur on a comparably longer time scale than the initial photocatalytic activation steps. As such, real-time monitoring of reactions is a complementary analysis method that allows obtaining quantitative reaction profiles and identifying relevant species in solution, including catalysts, substrates, reagents, intermediates, products, as well as side- and byproducts.[13] The obtained profiles can be further processed using, for example, reaction kinetic progress analysis (RKPA) or variable time normalization analysis (VTNA) to extract valuable kinetic information.[13] Further, reaction monitoring provides important data to design and operate large scale reactions in a safe, controllable and reproducible manner.[14]

Although common for thermal reactions, real-time reaction monitoring has been only sparingly applied in synthetic photocatalysis, which likely results from the (slightly) higher complexity of setups capable of such analysis. Moreover, kinetic data of photochemical reactions is somewhat difficult to reproduce due to the strong dependence on the exact photochemical setup.[15] The spectral output (wavelength distribution, photon equivalents, etc.) of the light source and other factors, such as the distance between the light source and the reaction vessel, the reaction vessel itself (i.e. material and thickness), or temperature effects can directly impact reaction profiles.[15]

This minireview surveys in situ reaction monitoring approaches for photocatalytic reactions. The first part aims to provide a general overview over techniques that are used by synthetic organic chemists to monitor reaction profiles and intermediates in real-time. The second part discusses selected examples from the scientific literature, where these monitoring techniques shed light on the mechanism of photocatalytic reactions.

2. Techniques for reaction monitoring in photocatalysis

An ideal technique for reaction monitoring of photocatalytic reactions should provide information of all relevant species within a reaction mixture under synthetically relevant conditions with high sensitivity and sufficient temporal resolution. In

[a] A. Madani, Dr. B. Pieber
Department of Biomolecular Systems
Max-Planck-Institute of Colloids and Interfaces
Am Mühlenberg 1
14476 Potsdam (Germany)
E-mail: bartholomaeus.pieber@mpikg.mpg.de
Homepage: Homepage: https://www.pieberlab.com
[b] A. Madani
Department of Chemistry and Biochemistry
Freie Universität Berlin
Arnimallee 22
14195 Berlin (Germany)

Special Collection This publication is part of a Special Collection on "Photocatalytic Synthesis". Please check the ChemCatChem homepage for more articles in the collection.

ChemCatChem
Review
doi.org/10.1002/cctc.202201583
Chemistry Europe
European Chemical Societies Publishing

practice, no technology that fulfills all requirements for the broad range of photocatalytic methods is available to date. The practitioner has to choose between different approaches on a case-by-case basis depending on the specific needs of the reaction of interest.

In addition to design criteria that are specific to light-mediated reactions (light source, vessel materials, etc.), other factors have to be taken into consideration. For example, many homogeneous solution-phase reactions can be carried out reliably in a nuclear magnetic resonance (NMR) spectrometer,[16] whereas heterogeneous (solid-liquid, gas-liquid, gas-liquid-solid) transformations typically require other techniques due to problems associated with mixing. Moreover, paramagnetic species complicate NMR measurements and data interpretation, specifically for quantitative analysis.[17]

In general, all nondestructive analytical methods, including NMR spectroscopy and vibrational spectroscopy (FTIR, Raman) are suitable for reaction monitoring. Depending on the technique, the reaction has to be carried out inside of the analytical instrument or by using a dedicated probe that can be inserted into a reaction vessel. Alternatively, destructive methods, such as mass spectrometry (MS), that continuously analyze small aliquots of the reaction mixture in an automated fashion, without significantly altering its chemical composition and scale, can be used.[18] However, quantification is limited and MS techniques are typically not used for monitoring the concentration of specific species over time. Nevertheless, MS analysis is ideally suited for the identification of (reactive) intermediates, which can be important for elucidating reaction mechanisms. As such, we have included relevant technologies and examples in this minireview.

2.1. NMR spectroscopy

NMR spectroscopy is a non-destructive and non-invasive technique that is routinely used in synthetic organic chemistry for the identification and quantification of products, substrates, reagents as well asintermediates .[19] A particular strength is the complementary structural information of dissolved molecules that can be gained by multi-nuclear detection (^{1}H, ^{13}C, ^{19}F, ^{31}P, ^{11}B, etc.) and two-dimensional NMR techniques (DOSY, NOESY, HSQC, HMBC, etc.). Reaction monitoring using in situ NMR measurements is also commonly applied to obtain kinetic insights.[13] Illuminating solutions inside NMR spectrometers mainly relies on setups that use waveguides to transport photons from the respective light source into the NMR vial.[20] The most common approach used for real-time monitoring of photocatalytic reactions is the fiber optic LED-NMR illumination setup that was developed by Gschwind and co-workers.[20c] Here, light from a high power LED is guided into the sample by an optical fiber. Uniform irradiation is achieved by roughening the fiber tip that is immersed into the reaction mixture through a coaxial insert (Figure 1, A). Fiber optic LED-NMR was also combined with optical spectroscopy to simultaneously acquire UV/Vis and NMR spectra.[21]

A related illumination setup uses the NMR tube itself as waveguide (Figure 1, B).[22] Here, the LED is positioned directly at the top of the NMR tube rather than outside of the spectrometer. Good sample illumination is achieved through abrasive etching of the exterior surface of NMR tubes in the sample area.

Although powerful, these waveguide-based setups use a single LED and therefore only provide relatively low light intensities. Roughening of the fiber tip as well as the abrasive etching of the NMR tube might cause reproducibility problems. Furthermore, these approaches do not enable the use of pressurized NMR tubes. A recently developed LED irradiation insert for NMR probes overcomes these problems (Figure 1, C).[23]

It is, however, important to note that reaction monitoring using NMR is limited to homogeneous reactions, because heterogeneous reaction mixtures require vigorous stirring to achieve reproducible and synthetically relevant results. Solid

Amiera Madani completed her undergraduate studies in chemistry at the University of Tübingen (Germany). In 2019 she joined the Max-Planck-Institute of Colloids and Interfaces in Potsdam (Germany) as a PhD student. Her research focuses on the development and mechanistic investigation of reactions involving reactive open-shell intermediates.

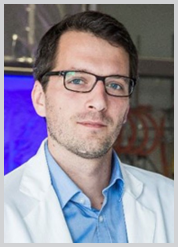

Bartholomäus (Bart) Pieber studied chemistry at the University of Graz (Austria), where he completed his PhD in the group of C. Oliver Kappe in 2015. Following his doctoral work, Bart moved to Peter Seeberger's lab in Potsdam (Germany). In 2018, he started his independent research career as a group leader at the Max Planck Institute of Colloids and Interfaces (Potsdam, Germany) and was appointed as a lecturer at the University of Potsdam. In 2022, he spent time as visiting scholar at the California Institute of Technology (Pasadena, USA, Host: Prof. Greg Fu). In summer 2023, his team will move to the Institute of Science and Technology Austria (ISTA), where he is joining faculty as an Assistant Professor (tenure track). The research of his team focuses on catalytic methods for organic synthesis using visible-light as energy source.

ChemCatChem
Review
doi.org/10.1002/cctc.202201583
Chemistry Europe
European Chemical Societies Publishing

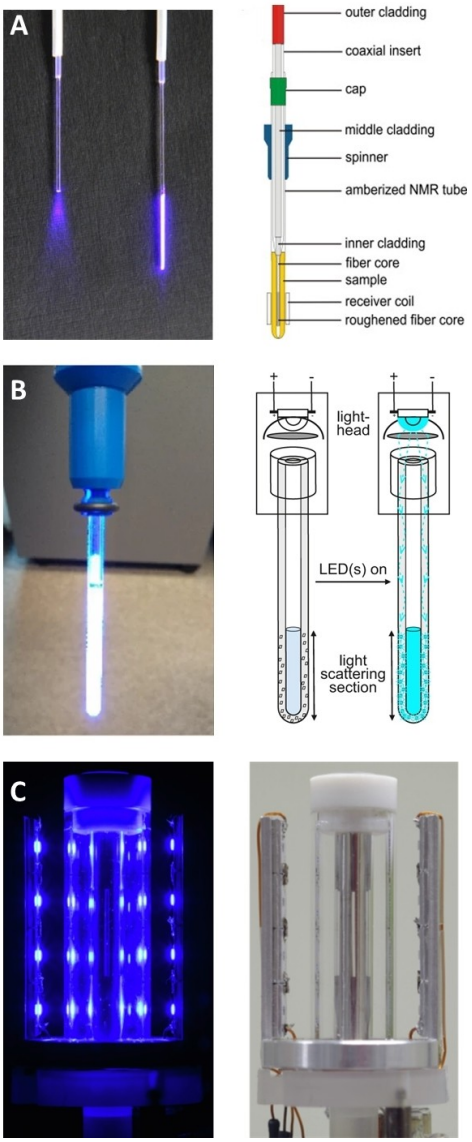

Figure 1. LED-NMR setups for in situ reaction monitoring of photochemical reactions. Irradiation is realized using a fiber optic (A) and the NMR tube itself as waveguide (B), or using a LED insert for NMR probes (C). Reproduced from ref. [20c], [22] and [23] with permission from Elsevier and Springer Nature.

catalysts or reagents settle without proper mixing, which has detrimental effects on the quality of the data obtained. In special cases, depositing heterogeneous photocatalysts on the inner wall of NMR tubes might be an option to address this limitation.[24]

2.2. Vibrational and optical spectroscopy

In contrast to NMR analysis, real-time vibrational and optical spectroscopy can be carried out using dedicated probes rather than immersing the reaction vessel into an analytical device.[25] These methods are not limited to homogeneous reactions and small scales. Fourier-transform infrared spectroscopy (FTIR) is among the most convenient and simultaneously broadly applicable methods for monitoring organic transformations.[26] It provides a molecular fingerprint of the chemical composition of compounds in solution and the change of signal intensity of a functional group of substrates or products can be related to their concentration. Attenuated total reflectance (ATR) is the most widely used technology for devices that enable static and time-correlated FTIR studies. In brief, this technique is based on multiple reflection of an IR beam within a crystal (i.e. silicon, or diamond) that is in contact with the sample. The interaction of the beam with the sample leads to detectable changes that can be processed to result in a typical infrared spectrum. ATR enabled the design of commercially available probes that can be directly dipped into a reaction vessel to continuously record FTIR spectra of (photocatalytic) transformations (Figure 2).[25a] The same technology is used for UV/Vis and fluorescence probes. However, the absorption and emission of photocatalysts dominates UV/Vis and fluorescence spectroscopy spectra, limiting the applicability of these techniques for reaction monitoring of photocatalytic reactions.[25e]

Raman spectroscopy allows to monitor gases, substances in solution and undissolved particles using fiber optic probes and is therefore broadly applicable in chemical analysis.[25b–d] Raman probes are either immersed into the reaction mixture (invasive), or placed outside of a transparent reaction vessel (non-invasive).[25f] In general, invasive probes, including the ATR-FTIR

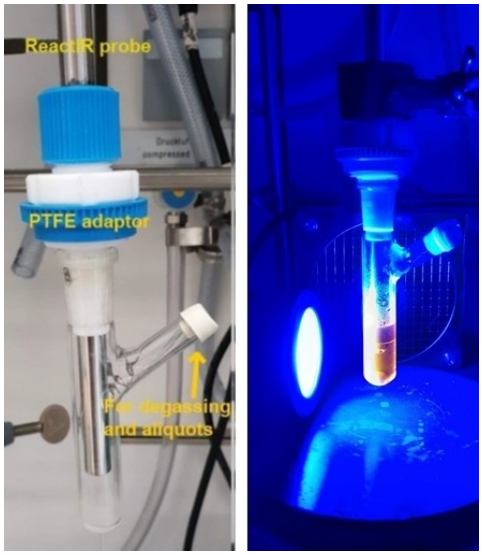

Figure 2. Setup for in situ reaction monitoring of photocatalytic reactions using an ATR-FTIR probe.

ChemCatChem
Review
doi.org/10.1002/cctc.202201583
Chemistry Europe
European Chemical Societies Publishing

and FTIR-UV/Vis devices described above, impact the irradiation characteristics (smaller path length, reflection phenomena, etc.). This can lead to different time-profiles compared to a reaction carried out without a probe. Thus, non-invasive Raman probes are advantageous, because reaction monitoring can be carried out using completely unaltered setups. Another advantage of Raman spectroscopy over other techniques is that signals do not typically interfere with water vibrational modes, allowing its use in aqueous reactions.[25f] However, for photocatalytic applications the light source and the fluorescence of a chromophore may interfere, resulting in a lowering of the signal-to-noise ratio, which limits its application in photochemistry.[25e]

2.3. Mass spectrometry

The high sensitivity of modern mass spectrometry instruments allows to detect species that are present in very low concentrations in reaction mixtures.[27] More importantly, MS allows to identify reactive intermediates that are otherwise only (indirectly) accessible using trapping and radical clock experiments.[12] This can result in mechanistic hints that are hard to obtain using other techniques. However, analyzing (photo)chemical reactions via mass spectrometry in a batch setup requires an interface that constantly delivers small aliquots of the reaction mixture to a mass spectrometer (ex situ). A prototype setup using a probe electrospray ionization mass spectrometer (PESI-MS) was recently developed for such purposes (Figure 3).[28] This technology is based on a stainless steel acupuncture needle that repeatedly transfers small aliquots of the reaction mixture directly to the ion source with an estimated time of 575 ms per sampling cycle. The reactor consists of a stirred reaction vessel with a sampling orifice and a light source. Importantly, the probe surface conditions were reported to play a key role in the signal consecutiveness in PESI-MS experiments. An untreated acupuncture needle gave inconsistent results, which was attributed to the attachment of photocatalyst particles (TiO_2) on the probe tip. Surface modification of the tip with TiO_2 eliminated these problems.

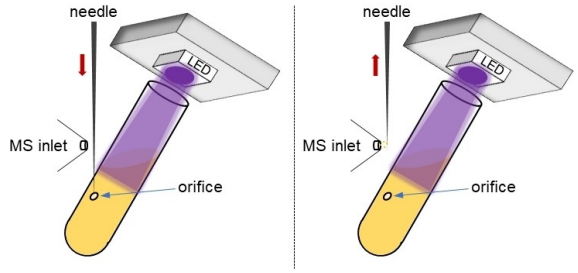

Figure 3. Monitoring photocatalytic reactions using PESI-MS.

2.4. Reaction monitoring using flow techniques

In continuous flow chemistry, non-destructive analytical methods that enable real-time analysis are directly integrated after a (photo)reactor unit via an analytical flow-through cell (termed in-line analysis). Common techniques include FTIR,[29] Raman,[30] UV/Vis,[31] or (benchtop) NMR spectroscopy[32] and are nowadays regularly applied due to their "plug-and-play" nature (Figure 4, A). Reaction monitoring at preparative scales using destructive analytical methods, such as mass spectrometry, requires setups that periodically sample aliquots or split the flow stream (termed on-line analysis) (Figure 4, B).[33] Analysis of flow chemical reactions using such process analytical techniques is fundamentally different to reaction monitoring in batch reactions for two reasons. First, batch reactions require monitoring techniques that analyze a chemical transformation directly in (or sample continuously from) the reaction vessel, whereas monitoring of flow reactions is spatially decoupled from the reactor unit.[34] Second, in batch the substrate concentration is uniformly distributed throughout the flask and decreases exponentially over time. In a flow reaction, the concentration of the starting material decreases along the reactor unit reaching a minimum at its end. Consequently, monitoring a flow reaction under steady state conditions gives continuous feedback of a reaction at a fixed reaction time, which is, for example, used to evaluate the stability of heterogeneous photocatalysts in packed-bed reactors.[35] Tracking the time course in flow, on the contrary, requires a multitude of experiments with varied flow rates under steady state conditions[36] and is therefore not discussed in this minireview.

More relevant approaches in the context of this minireview are flow techniques that directly feed a reaction mixture into a mass spectrometer and irradiate the catalytic cocktail either before, or only at the tip of an ESI-MS spray capillary (Figure 5).[37] This approach (termed "photoflow ESI-MS" throughout this minireview) allows to identify (short-lived) reactive intermediates that are generated during photochemical processes and can therefore give important mechanistic insights. For

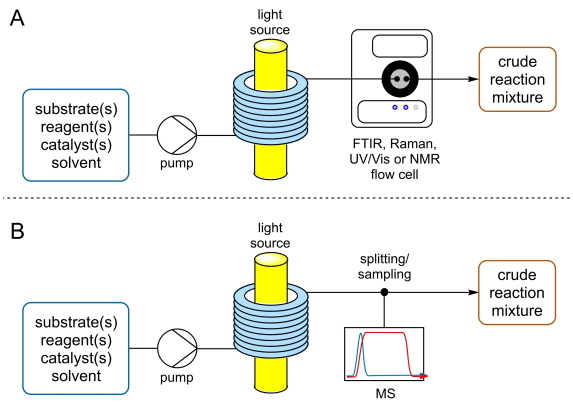

Figure 4. Reaction monitoring in flow photocatalysis. Nondestructive analytical tools are directly integrated in the flow path (A), whereas destructive methods require splitting or sampling techniques (B).

ChemCatChem
Review
doi.org/10.1002/cctc.202201583
Chemistry Europe
European Chemical Societies Publishing

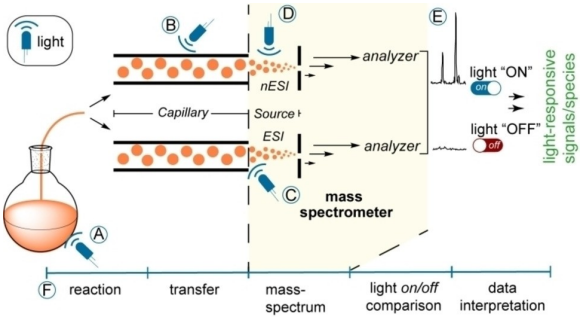

Figure 5. Monitoring (short-lived) intermediates in photocatalysis by directly feeding the reaction mixture into an ESI-MS device (photoflow ESI-MS). Irradiation can be carried out in the flask or syringe (A), in the capillary (B); on the tip of the capillary and plume at the needle tip (C), or on the tip of a nanospray-ESI (nESI) device (D). Reproduced from ref. [37e] with permission from John Wiley and Sons.

detailed discussions on these techniques, we refer to specialized, we refer to specialized reviews by the groups of Ananikov[37e] and Roithovà.[37d]

3. Mechanistic insights gained through reaction monitoring

3.1. Identification of intermediates

The flavin catalyzed photooxidation of 4-methoxybenzyl alcohol (MBA) was among the first photocatalytic reactions that was studied using a fiber optic LED-NMR setup (Figure 6, A).[38] Reaction monitoring under anaerobic conditions was carried out in combination with chemically induced dynamic nuclear polarization (CIDNP) experiments, which allow the detection of short-lived radical species.[39] These studies provided evidence that different mechanisms are operating depending on the reaction medium. A slow reaction that likely proceeds via a formal two-electron-transfer mechanism on the NMR timescale was observed in CD_3CN. The same reaction proceeded significantly faster in a CD_3CN:D_2O mixture. More importantly, line broadening of the NMR signals under aqueous conditions was indicative for a long-lived semiquinone radical species ($RFTA^{\cdot+}$, confirmed by UV/VIS spectroscopy), suggesting a single-electron transfer mechanism. The authors concluded that this results from the stabilization and separation of the radical counterions in presence of D_2O, whereas non-aqueous conditions lead to contact ion pairs that facilitate back electron transfer.

Another oxidative flavin catalyzed reaction was investigated using photoflow ESI-MS monitoring (Figure 6, B).[40] More specifically, the authors studied the aerobic oxidation of toluene derivatives using a chiral ethylene-bridged flavinium salt that leads to the corresponding benzyl alcohols and benzaldehydes. Various reaction times were simulated by irradiating the reaction mixture in a flow reactor before entering the mass

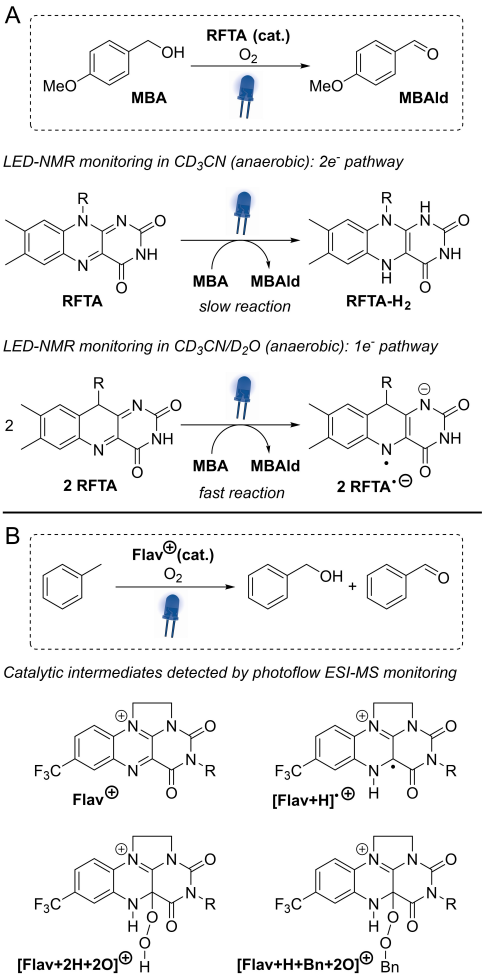

Figure 6. Reaction monitoring in flavin photocatalysis. LED-NMR studies revealed that the solvent impacts the reaction mechanism (A). Photoflow ESI-MS monitoring provided evidence for several catalytic intermediates (B).

spectrometer, or only at the tip of the spray capillary. Several short-lived species were identified that agree with postulated intermediates of a plausible catalytic cycle. In addition, a series of side-products, including arylated flavinium ions, were detected and attributed to result from undesired off-cycle events. It is worth noting that all detected intermediates were further confirmed by isotope labelling studies, as well as IR and UV/Vis spectroscopy.

Tetrahydroisoquinolines (THIQs) are amongst the most studied substrates that are activated through photoredox catalysis. These reactions are typically proposed to involve the initial formation of the corresponding radical cation via single electron oxidation that opens opportunities for several follow-up reactions.[41] A classic example is the photocatalyzed aza-Henry reaction of THIQs and $MeNO_2$ that was originally reported by the Stephenson laboratory.[42] The groups of König and Gschwind reported an extensive mechanistic study of this

ChemCatChem
Review
doi.org/10.1002/cctc.202201583
Chemistry Europe
European Chemical Societies Publishing

transformation that included reaction monitoring using a fiber optic LED-NMR setup under anaerobic conditions.[43] In addition to the substrate (**1**) and product (**2**), the authors were able to identify and monitor the formation and consumption of a dimeric species (**3**) and nitrone **4** (Figure 7). Further, iminium ion (**5**) as well as THIQ-OOH (**6**) that results from reaction with residual oxygen were identified in low concentrations during the initial phase of the reaction. Additional experiments under aerobic conditions were carried out by analyzing aliquots of a batch reaction via ex situ NMR. Here, a significantly faster reaction rate was observed and THIQ-OOH (**6**) was identified as main intermediate. Based on these observations, the authors carefully studied the formation and fate of these species. These investigations resulted in a complex mechanistic picture of the photocatalytic aza-Henry reaction that consists of several pathways that lead to the formation of the desired product. In brief, photocatalytic initiation generates the key radical cation that leads to the desired product under aerobic conditions via **5**, or a α-amino radical. The α-amino radical was also proposed to trigger formation of dimer **3** and nitrone **4** under anaerobic conditions via two different pathways. Both species are converted to the desired product. The authors also provided evidence for two productive background reactions that do not involve the photocatalyst.

Photoredox catalysis can be used to convert 1,2,3,4-tetrahydroquinoline into quinoline under aerobic conditions (Figure 8, A).[37c] This reaction was discovered using a photoflow ESI-MS approach as reaction screening tool that also identified a radical cation intermediate and the reduced photocatalyst ($Ru(bpy)_3^+$). Similar intermediates were detected during a photoflow ESI-MS study of the photocatalytic [3 + 2] annulation of N-cyclopropyl aniline and styrene (Figure 8, B).[44]

The groups of Ananikov and König developed a photoredox catalyzed Markovnikov-type thiol-yne reaction of terminal alkynes and thiophenol derivatives.[45] To support their mechanistic rationale, an alkyne with an ionizable sulfate group (**7**) was synthesized to study the formation of the desired product (**8**) and an undesired side product (**9**) via photoflow ESI-MS reaction monitoring (Figure 9, A). More recently, the same groups extended this photocatalytic method to an intermolecular thiol-yne-ene reaction.[46] The reaction was studied using alkyne **7**, 2-fluorothiophenol (**10**) and vinylsulfide **11** in presence of (tert-butyl)-N-(perfluorobiphenyl-4-yl)oxylamine (**12**) as radical trap with a high resolution photoflow ESI-UHRMS monitoring setup (Figure 9, B). In presence of green light, radical adduct **13** was detected, indicating that **14** is a reactive intermediate.

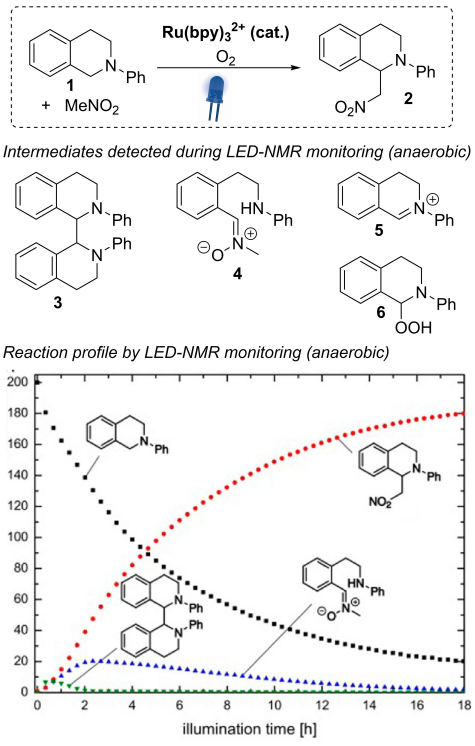

Figure 7. Monitoring of the photocatalytic aza-Henry reaction by LED-NMR identified several productive intermediates. Reproduced from ref. [43] with permission from the American Chemical Society.

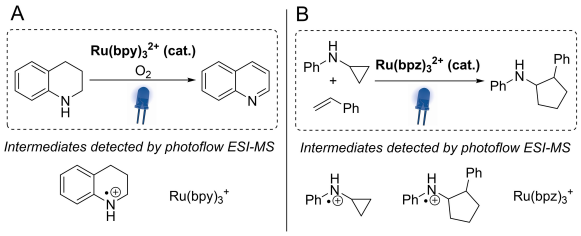

Figure 8. ESI-MS monitoring of photocatalytic reactions of amines identified radical cation intermediates and reduced photocatalyst species.

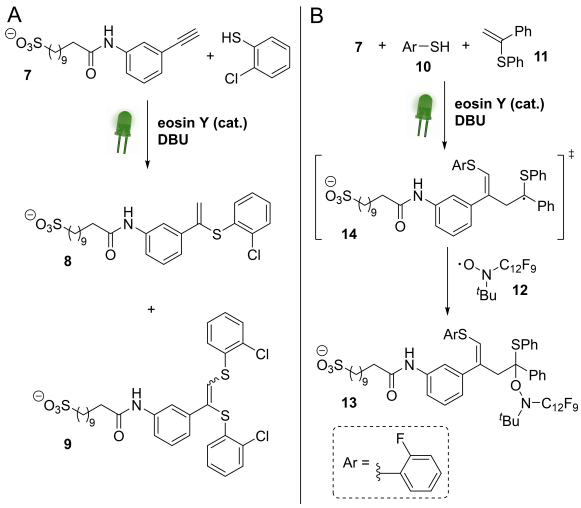

Figure 9. Photoflow ESI-(UHR)MS reaction monitoring of a photocatalytic thiol-yne (A) and a thiol-yne-ene reaction (B).

ChemCatChem
Review
doi.org/10.1002/cctc.202201583
Chemistry Europe
European Chemical Societies Publishing

Photoflow ESI-MS monitoring was also applied to identify intermediates in the photocatalytic Meerwein arylation of pyrazin-2-amine with 4-methoxybenzenediazonium tetrafluoroborate (Figure 10, A).[47] This study provided evidence that the reaction proceeds through the formation of radical cation **15.**

Schultz and coworkers used decatungstate photocatalysis for the oxygenation of amines in presence of hydrogen peroxide under acidic conditions.[48] Using LED-NMR and photoflow ESI-MS monitoring, **16** was identified as key intermediate when pyrrolidine was used as substrate (Figure 10, B). This observation suggested that oxygen might also serve as a suitable oxidant and the authors subsequently showed that an aerobic oxidation is indeed feasible.

Reaction monitoring further gave key insights in the photocatalytic C(sp^3)-F bond cleavage of trifluoromethylarenes to produce aryldifluoromethyl compounds using stoichiometric amounts of pinacolborane (HBpin) and 2,2,6,6-tetramethylpiperidine (TMP). (Figure 10, C).[49] Using a LED-NMR setup the authors tracked the reaction via ^{11}B-NMR and observed the formation of borenium cation **17**. Subsequent mechanistic experiments indicated that this Lewis acidic species, which is formed in situ from protonated TMP and HBpin, plays an important role in the key C–F bond abstraction.

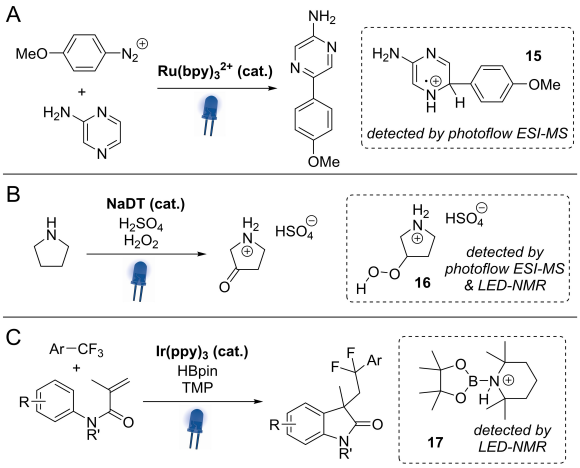

Figure 10. Intermediates identified through reaction monitoring of the photocatalytic Meerwein arylation (A) the photocatalytic oxygenation of amines (B), and the photocatalytic C(sp^3)-F bond cleavage of trifluoromethylarenes (C).

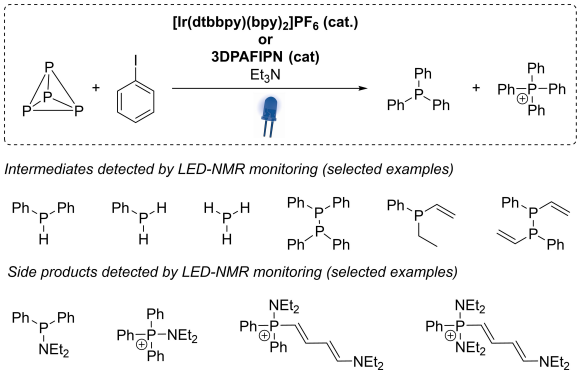

Figure 11. Intermediates and side products in the photocatalytic arylation of white phosphorous identified through reaction monitoring using LED-NMR.

In a collaborative effort, the groups of Gschwind and Wolf showed that [Ir(dtbbpy)(bpy)$_2$]PF$_6$ can trigger the reaction of white phosphorous (P_4) and aryl iodides to yield valuable triarylphosphines and tetraarylphosphonium salts in presence of blue light and triethylamine as sacrificial electron donor.[50] Time resolved ^{31}P-NMR analysis of the reaction between P_4 and iodobenzene using a LED-NMR setup was used to track the reaction. These experiments visualized the evolution and consumption of primary, secondary and tertiary monophosphine intermediates, and identified traces of Ph_4P_2, benzene and Et_2NH as minor side-products (Figure 11). A follow-up study using an organic photocatalyst (3DAFIPN) revealed numerous additional intermediates and side-products that are derived from a non-innocent behavior of Et_3N.[51] Of specific interest was the identification of PH_3, which prompted the authors to develop an alternative strategy that can directly convert this industrial P_1 precursor to several Ar_3P and Ar_4P^+ products using a similar photocatalytic protocol.

3.2. Kinetic analysis

Reaction monitoring enables detailed kinetic analysis to gain a holistic understanding of chemical reactions under native reaction conditions. In the case of photocatalytic reactions, care has to be taken, as kinetic studies may give data obfuscated by turnover-limiting processes derived from interaction between the excited photocatalyst and the respective quencher. In other words, the practitioner has to keep in mind that, depending on the conditions, the reaction of interest may be "photon-limited" or "photon-unlimited". Under photon-limited conditions, reaction rates depend on the absorption of photons and are typically zero-order in the photocatalyst. Photon-unlimited regimes refer to a situation where the quencher is constantly saturated with excited photocatalyst species. Under such conditions, the excited photocatalyst can be essentially treated as a reagent in high excess.

Yoon and colleagues studied the kinetics of an enantioselective intramolecular [2 + 2] cycloaddition that is catalyzed by a chiral iridium photocatalyst (Figure 12).[52] The authors initially monitored the concentration of substrate and product over time using an LED-NMR setup, which showed that the reaction is complete within less than three minutes. Initial rate studies by several LED-NMR experiments showed a first order dependency in photocatalyst concentration and light intensity (Figure 12) as well as zero-order in substrate. Consequently, the authors concluded that the model reaction operates in a photon-unlimited regime under these monitoring conditions.

More recently, the same group reported a detailed kinetic analysis of a related intermolecular [2 + 2] cycloaddition using the same chiral photocatalyst.[53] Visual kinetic analysis techni-

ChemCatChem
Review
doi.org/10.1002/cctc.202201583
Chemistry Europe
European Chemical Societies Publishing

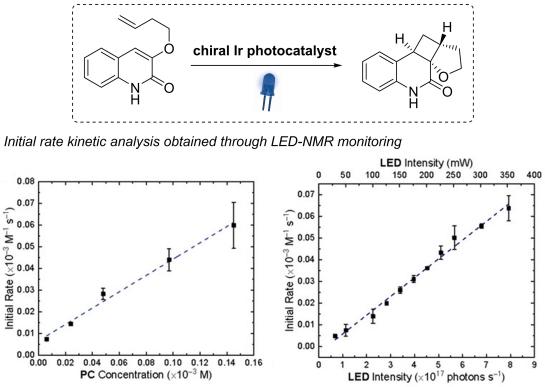

Figure 12. Initial rate kinetic analysis using LED-NMR of an enantioselective photocatalytic intramolecular [2 + 2] cycloaddition. Reproduced from ref. [52] with permission from John Wiley and Sons.

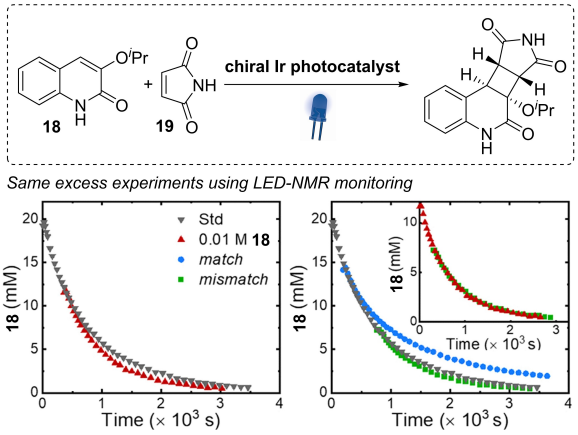

Figure 13. Same excess experiments of a photocatalytic intermolecular [2 + 2] cycloaddition. Left: Same excess comparison between standard condition and conditions that mimic 40% conversion. Right: Comparison of standard conditions to conditions approximating 30–50% conversion with the addition of the expected concentration of the product. Blue = matched Ir and product chirality; green = mismatched Ir and product chirality. Reproduced from ref. [53] with permission from the American Chemical Society.

ques using data obtained from LED-NMR monitoring experiments were used to extract kinetic information. A "same excess" experiment was carried out. Here, the initial concentration of starting materials for two reactions using LED-NMR monitoring was different, but chosen in a way that the experiments allow comparison of sections of the reaction profiles that have same concentration of reactants, but different concentration of product. These experiments mimic different turnovers of the catalyst to determine if the reaction suffers from product inhibition or catalyst deactivation. Non-overlaying reaction profiles are indicative for product inhibition or catalyst deactivation and require further experiments for clarification. The same excess experiment of the [2 + 2] cycloaddition of **18** and maleimide indeed showed that the profiles do not overlay (Figure 13, bottom left). The authors carried out additional experiments in presence of the enantioenriched product and the matched and mismatched chiral photocatalyst, which provided evidence that product inhibition by the major enantiomer is responsible for the outcome of the same excess experiment (Figure 13, bottom right).

Next, rate laws for the title reaction at different temperatures were constructed from reaction profiles using variable time normalization analysis (VTNA).[53] Therefore, multiple reaction profiles are collected by strategically changing the concentration of a single ingredient of the reaction mixture ("different excess" experiments). Normalizing the time between each pair of data points using the VTNA approach enables to determine the order in each parameter through a graphical overlay comparison. Therefore, the time-scale is substituted by the time integral of the reagent concentration, taken to an arbitrary power α [Eq. (1)]. The value for α that leads to an overlay of the graphs, is the order of the respective reagent.

$$\int_{t=0}^{t=n} [A]^{\alpha} dt = \sum_{i=1}^{n} \left(\frac{[A]_i - [A]_{i-1}}{2} \right)^{\alpha} (t_i - t_{i-1}) \quad (1)$$

Interestingly, VTNA of the cycloaddition resulted in different rate laws at different temperatures (Figure 14). Under both conditions the rate is first-order in light intensity and zero-order in photocatalyst concentration, which is indicative of a photon-limited regime. The dependency on the substrates, on the contrary, changes depending on the temperature. This suggests that the mechanism of asymmetric product formation varies as a function of temperature. The rate law obtained under cryogenic conditions agrees with a bimolecular energy transfer mechanism that was previously postulated based on DFT calculations,[54] whereas the rate law at room temperature is more indicative for an intramolecular energy transfer mechanism.

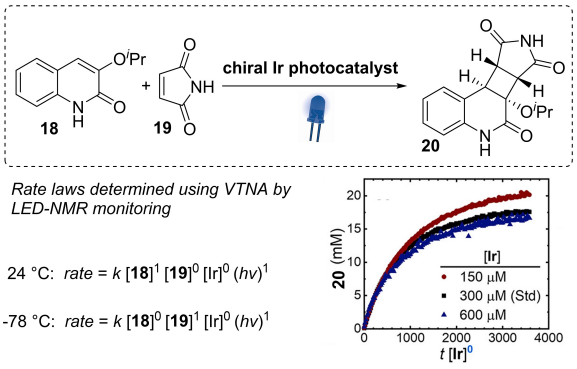

Figure 14. Rate laws of a photocatalytic intermolecular [2 + 2] cycloaddition determined at different temperatures using LED-NMR monitoring and VTNA. Bottom right: VTNA overlay for [Ir] at 24 °C. Reproduced from ref. [53] with permission from the American Chemical Society.

ChemCatChem
Review
doi.org/10.1002/cctc.202201583
Chemistry Europe
European Chemical Societies Publishing

VTNA was also applied to study the metallaphotocatalytic C–O arylation of methyl 4-iodobenzoate (**21**) with N-Boc-proline (**22**) using a nickel catalyst in combination with either $Ir(ppy)_3$ or a graphitic carbon nitride (CN-OA-m) as photocatalyst (Figure 15).[25a] Due to the heterogeneous nature of CN-OA-m, an ATR-FTIR probe was the reaction monitoring tool of choice for this comparative study. The reaction was studied with both photocatalysts under photon-limited and photon-unlimited conditions. The photon-unlimited regime was postulated to be of specific interest, because under such conditions the photocatalyst drops out of the rate law enabling a direct comparison of both methods. Interestingly, the authors found that the kinetics of the two catalytic systems are not identical. In case of the carbon nitride catalyst, a fractional order of aryl iodide **21** was determined, indicating that the photocatalyst activates **21** before it enters the nickel catalytic cycle. The authors further found that the iridium photocatalyst is less selective under photon-unlimited conditions and identified a significant amount of the corresponding protodehalogenation side product. Moreover, same excess experiments indicated catalyst deactivation, which was later shown to be likely resulting from the formation of nickel-black.[55]

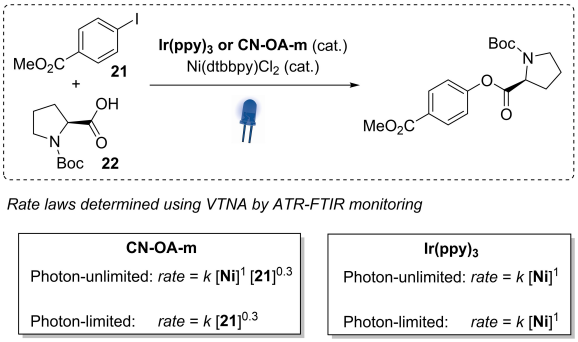

Figure 15. Rate laws of a metallaphotocatalytic C–O arylation obtained using ATR-FTIR monitoring and VTNA using two different photocatalysts under photon-limited and photon-unlimited reaction regimes.

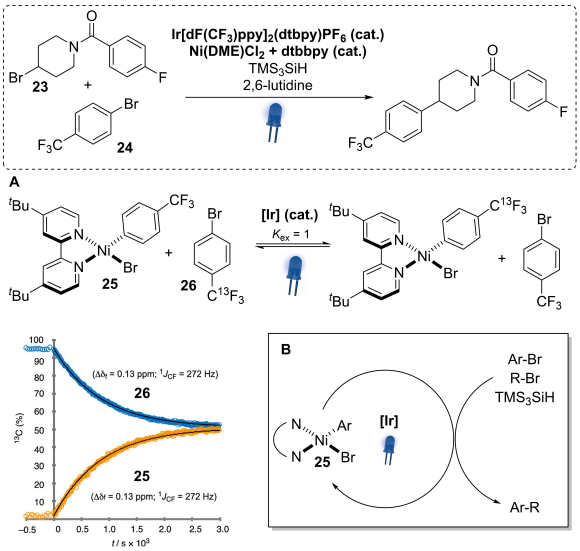

Figure 16. Metallaphotocatalytic cross-electrophile-coupling studied via LED-NMR reaction monitoring identified a photochemical exchange phenomenon (A). This provided evidence that intermediate **25** is responsible for product formation (B). Reproduced from ref. [56] with permission from the American Chemical Society.

A metallaphotocatalytic cross-electrophile-coupling of aryl bromide **23** and alkyl bromide **24** was investigated using online monitoring with a LED-NMR setup (Figure 16).[56] The initial reaction profile (^{19}F-NMR) showed not only the generation of the desired product, but also led to the identification of two minor side products arising from a coupling reaction of the aryl bromide with the solvent (Ar-solv) and protodehalogenation of **24** (Ar–H). More importantly, a transient Ni^{II} species (**25**) was identified. Isotope entrainment experiments using **25** in presence of **26**, the photocatalyst and light unveiled a hitherto unreported exchange phenomenon (Figure 16, A). Based on that finding, further investigations were carried out, which provided evidence for a mechanistic scenario in which product formation occurs directly through **25** (Figure 16, B).

With that finding in hand, the authors performed a detailed visual kinetic analysis that included alterations of all seven components of the catalytic cocktail (40 different sets of conditions). These investigations led to a series of important insights into this transformation under LED-NMR conditions. For example, the rate of the aryl bromide consumption was shown to be controlled by the concentration of the Ni catalyst, the photocatalyst, the photon flux and the aryl bromide (**23**). The rate of turnover approaches concentration independence (= saturation) in **23**. Excess of $(TMS)_3SiH$ and **24** are responsible for the high selectivity of this C–C coupling. Changes in catalyst loadings do not necessarily translate directly into changes in the rate of productive catalysis. Moreover, complex **25** and the photocatalyst compete for incident photons. With these data in hand, the authors constructed a minimal kinetic model for the title reaction (Figure 17, A). The flow diagram shows five discrete events that control the rate of product formation (fractionations f_1-f_5). A series of simulations using this model resulted in kinetic behavior that is reconciled with two plausible mechanisms, which only differ in the interaction between the photo- and the nickel catalyst (single electron transfer versus energy transfer) (Figure 17, B).

3.3. Miscellaneous

Reaction monitoring is not only a powerful tool to identify intermediates and gain kinetic information, but also allows to gain insights into other aspects of photocatalytic reactions. For example, a LED-NMR setup was used to visualize that tert-butyl nitrite (TBN) is key to realize the light-mediated cleavage of benzyl ether protective groups using 2,3-dichloro-5,6-dicyano-1,4-benzoquinone (DDQ) as photocatalyst (Figure 18, A).[57] In the absence of TBN, the reaction stopped after a single turnover of the photocatalyst. Delayed injection of excess TBN immedi-

ChemCatChem
Review
doi.org/10.1002/cctc.202201583
Chemistry Europe
European Chemical Societies Publishing

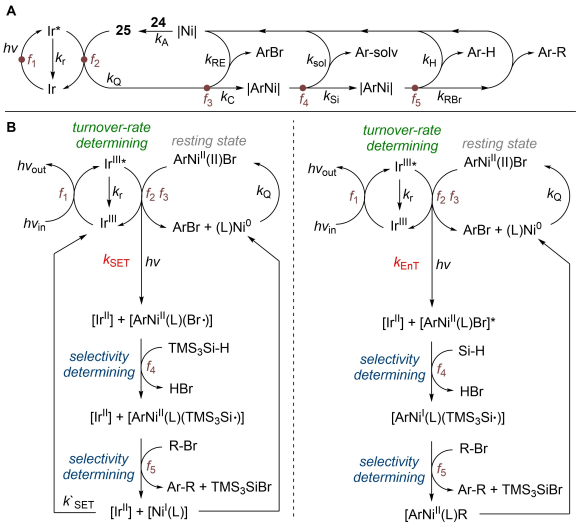

Figure 17. Minimal kinetic model for simulations of the metallaphotocatalytic cross-electrophile coupling (A). These simulations agree with two mechanistic proposals (B).

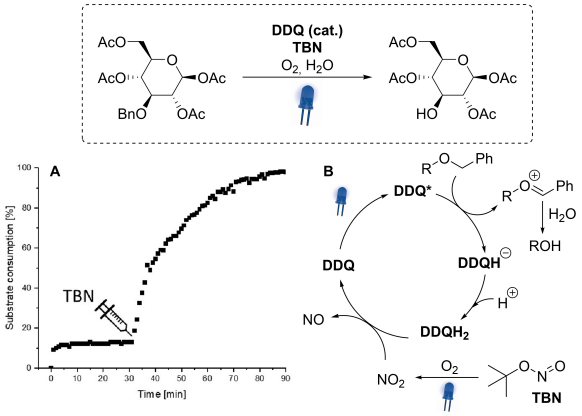

Figure 18. Reaction monitoring of a photocatalytic benzyl ether cleavage. Only one turnover of the photocatalyst is observed before addition of TBN (A), because TBN is required to close the catalytic cycle (B). Reproduced from ref. [57] with permission from the American Chemical Society.

ately started further product formation and the reaction proceeded until completion. This provides evidence that TBN photochemically releases NO, which is ultimately oxidized to NO_2 by dissolved O_2 (Figure 18, B). The potent gaseous oxidant converts 2,3-dichloro-5,6-dicyano-1,4-dihydroquinone ($DDQH_2$) to DDQ to close the catalytic cycle.

The authors further carried out a light on/off experiment using the LED-NMR setup that showed that no product is formed when the light source is switched off. Such experiments are carried out to study if chain processes are active or not. However, care has to be taken when conclusions are drawn from such experiments, because no product formation in the absence of light does not conclusively rule out radical chain involvement.[58]

Nevertheless, light on/off experiments can lead to important discoveries. An interesting example was reported by Lenherr, Ji and coworkers during their development of a cycloisomerization of alkynols using an iron pre-catalyst that is activated using visible-light (Figure 19).[59] In addition to qualitative observations that showed an induction period, initial rate studies to identify the photon-limited and unlimited regime, same-excess experiments that indicated catalyst deactivation and reaction progress kinetic analysis, the authors observed an unexpected behavior during light on/off experiments using a LED-NMR setup (Figure 19, A). When the light source was switched off, the reaction did not stop immediately, but the rate of product formation significantly decreased. Subsequently, experiments using a catalyst with ^{13}C-enriched CO ligands and LED-^{13}C-NMR monitoring were carried out to study if the light-mediated CO decomplexation that initiates catalysis is reversible. These monitoring experiments showed a decrease of dissolved ^{13}CO and a simultaneous increase of Fe-bound ^{13}CO upon switching off the light source (Figure 19, B). Constant illumination, on the contrary, results quickly in a steady state of both species that lasts until the substrate is fully consumed (Figure 19, C). This is indicative for an equilibrium between the catalytically inactive pre-catalyst **27** and the active Fe species **28** that can be externally controlled by light (Figure 19, D). It is important to note that the authors also found that removal of CO from the reaction mixture by sparging leads to catalyst deactivation, presumably due to the loss of another CO molecule from **27**. As

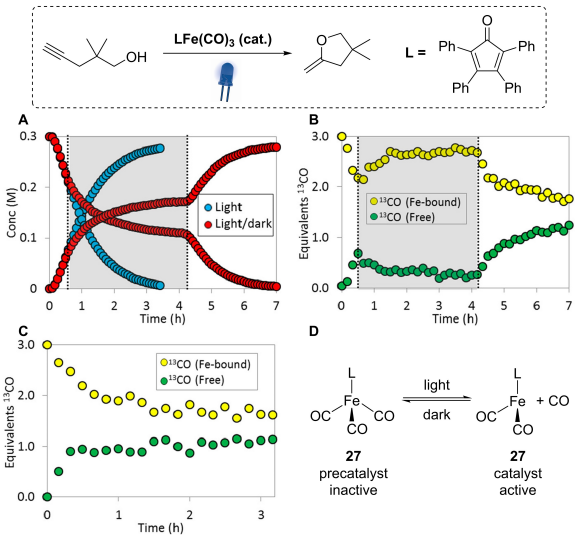

Figure 19. Reaction monitoring of a light induced cycloisomerization. The reaction proceeds quickly in presence of constant irradiation (blue) and does not stop when light is switched off (red) (A). LED-^{13}C-NMR shows light-mediated CO complexation in the dark (B) that does not occur upon constant irradiation (C) indicating that light mediated catalyst activation is reversible (D). Reproduced from ref. [59] with permission from the American Chemical Society.

ChemCatChem
Review
doi.org/10.1002/cctc.202201583
Chemistry Europe
European Chemical Societies Publishing

such, best results were obtained using constant irradiation and a closed system with minimal headspace.

4. Conclusion

Reaction monitoring is slowly evolving as a valuable technique to acquire a better understanding of photocatalytic reactions. As shown in this minireview, such approaches are powerful tools that allow identifying reactive intermediates and access detailed kinetic information when combined with visual kinetic analysis. In addition, other aspects of photocatalytic reactions can be easily visualized. Together with other experiments, reaction monitoring paves the way towards a detailed mechanistic understanding of complex photocatalytic reactions. However, the field is still in its infancy and such methods are only rarely used, especially when compared to the plethora of new photocatalytic methodologies that appear in the literature on a daily basis.

To choose a suitable method, the type of mechanistic information required and the nature of the photochemical reaction of interest needs to be considered. Photoflow ESI-MS approaches allow qualitative analysis of intermediates, including short lived open-shell species. LED-NMR setups can also be used to track intermediates and additionally offer the opportunity for kinetic analysis. The small scale of LED-NMR experiments is characterized by short photon-path lengths, which facilitates photochemical experiments. Similarly, these dimensions ensure efficient heat-transfer and are ideally suited for investigating temperature effects in photocatalytic reactions. However, in case of multiphasic reactions, such as heterogeneous photocatalysis and reactions involving solid or gaseous reagents, efficient mixing is required to enable reliable and reproducible kinetic analysis. In such cases, FTIR probes are the technology of choice. This technique allows to run photocatalytic reactions under synthetically relevant conditions and is generally applicable for obtaining kinetic data, but does only provide limited structural information of intermediates and side-products. These individual limitations can be potentially addressed through combining two (or more) monitoring techniques. The combination of vibrational and optical spectroscopy probes is technically most straightforward.[25e] Moreover, fiber optic LED-NMR was combined with optical spectroscopy to simultaneously acquire UV/Vis and NMR spectra to monitor and quantify paramagnetic and diamagnetic species simultaneously in a time-resolved manner.[21] Combining ESI-MS with other monitoring techniques in a single device was, to the best of our knowledge, not yet realized for photocatalytic reactions. We anticipate that future efforts will overcome technical hurdles associated with combining multiple monitoring techniques to streamline mechanistic analysis of light-mediated transformations.

Acknowledgements

We gratefully acknowledge the Max Planck Society for 5generous financial support. A.M. and B.P. acknowledge the Deutsche Forschungsgemeinschaft (DFG, German Research Foundation) under Germany's Excellence Strategy-EXC 2008/1 (UniSysCat) – 390540038 for financial support. B.P. thanks the Boehringer Ingelheim Foundation for funding through the Plus 3 Perspectives Programme. Open Access funding enabled and organized by Projekt DEAL.

Conflict of Interest

The authors declare no conflict of interest.

Keywords: photocatalysis · reaction monitoring · mechanistic studies · kinetic analysis · reactive intermediates

[1] L. Marzo, S. K. Pagire, O. Reiser, B. König, *Angew. Chem. Int. Ed.* **2018**, *57*, 10034–10072; *Angew. Chem.* **2018**, *130*, 10188–10228.
[2] D. M. Arias-Rotondo, J. K. McCusker, *Chem. Soc. Rev.* **2016**, *45*, 5803–5820.
[3] A. Vega-Penaloza, J. Mateos, X. Companyo, M. Escudero-Casao, L. Dell'Amico, *Angew. Chem. Int. Ed.* **2021**, *60*, 1082–1097; *Angew. Chem.* **2021**, *133*, 1096–1111.
[4] S. Gisbertz, B. Pieber, *ChemPhotoChem* **2020**, *4*, 456–475.
[5] M. H. Shaw, J. Twilton, D. W. MacMillan, *J. Org. Chem.* **2016**, *81*, 6898–6926.
[6] F. Strieth-Kalthoff, M. J. James, M. Teders, L. Pitzer, F. Glorius, *Chem. Soc. Rev.* **2018**, *47*, 7190–7202.
[7] L. Capaldo, D. Ravelli, *Eur. J. Org. Chem.* **2017**, *2017*, 2056–2071.
[8] F. Glaser, C. Kerzig, O. S. Wenger, *Angew. Chem. Int. Ed.* **2020**, *59*, 10266–10284; *Angew. Chem.* **2020**, *132*, 10350–10370.
[9] S. Reischauer, B. Pieber, *iScience* **2021**, *24*, 102209.
[10] a) I. Ghosh, R. S. Shaikh, B. Konig, *Angew. Chem. Int. Ed.* **2017**, *56*, 8544–8549; *Angew. Chem.* **2017**, *129*, 8664–8669; b) M. Marchini, G. Bergamini, P. G. Cozzi, P. Ceroni, V. Balzani, *Angew. Chem. Int. Ed.* **2017**, *56*, 12820–12821; *Angew. Chem.* **2017**, *129*, 12996–12997; c) I. Ghosh, J. I. Bardagi, B. Konig, *Angew. Chem. Int. Ed.* **2017**, *56*, 12822–12824; *Angew. Chem.* **2017**, *129*, 12998–13000.
[11] N. A. Till, L. Tian, Z. Dong, G. D. Scholes, D. W. C. MacMillan, *J. Am. Chem. Soc.* **2020**, *142*, 15830–15841.
[12] L. Buzzetti, G. E. M. Crisenza, P. Melchiorre, *Angew. Chem. Int. Ed.* **2019**, *58*, 3730–3747; *Angew. Chem.* **2019**, *131*, 3768–3786.
[13] a) C. D. T. Nielsen, J. Burés, *Chem. Sci.* **2019**, *10*, 348–353; b) J. Bures, *Angew. Chem. Int. Ed.* **2016**, *55*, 16084–16087; *Angew. Chem.* **2016**, *128*, 16318–16321; c) D. G. Blackmond, *J. Am. Chem. Soc.* **2015**, *137*, 10852–10866.
[14] M. Sezen-Edmonds, J. E. Tabora, B. M. Cohen, S. Zaretsky, E. M. Simmons, T. C. Sherwood, A. Ramirez, *Org. Process Res. Dev.* **2020**, *24*, 2128–2138.
[15] H. E. Bonfield, T. Knauber, F. Levesque, E. G. Moschetta, F. Susanne, L. J. Edwards, *Nat. Commun.* **2020**, *11*, 804.
[16] F. Susanne, D. S. Smith, A. Codina, *Org. Process Res. Dev.* **2012**, *16*, 61–64.
[17] A. J. Pell, G. Pintacuda, C. P. Grey, *Prog. Nucl. Magn. Reson. Spectrosc.* **2019**, *111*, 1–271.
[18] V. Termopoli, E. Torrisi, G. Famiglini, P. Palma, G. Zappia, A. Cappiello, G. W. Vandergrift, M. Zvekic, E. T. Krogh, C. G. Gill, *Anal. Chem.* **2019**, *91*, 11916–11922.
[19] E. E. Kwan, S. G. Huang, *Eur. J. Org. Chem.* **2008**, *2008*, 2671–2688.
[20] a) I. Kuprov, M. Goez, P. A. Abbott, P. J. Hore, *Rev. Sci. Instrum.* **2005**, *76*, 084103; b) T. Kühn, H. Schwalbe, *J. Am. Chem. Soc.* **2000**, *122*, 6169–6174; c) C. Feldmeier, H. Bartling, E. Riedle, R. M. Gschwind, *J. Magn. Reson.* **2013**, *232*, 39–44; d) Y. Ji, D. A. DiRocco, J. Kind, C. M. Thiele, R. M. Gschwind, M. Reibarkh, *ChemPhotoChem* **2019**, *3*, 984–992; e) P.

ChemCatChem
Review
doi.org/10.1002/cctc.202201583
Chemistry Europe
European Chemical Societies Publishing

Nitschke, N. Lokesh, R. M. Gschwind, *Prog. Nucl. Magn. Reson. Spectrosc.* **2019**, *114–115*, 86–134.
[21] L. K. G. Ackerman, J. I. Martinez Alvarado, A. G. Doyle, *J. Am. Chem. Soc.* **2018**, *140*, 14059–14063.
[22] J. E. Bramham, A. P. Golovanov, *Commun. Chem.* **2022**, *5*, 90.
[23] T. Paululat, M. Rabe, D. V. Berdnikova, *J. Magn. Reson.* **2021**, *327*, 106990.
[24] A. Mills, C. O'Rourke, *J. Org. Chem.* **2015**, *80*, 10342–10345.
[25] a) J. A. Malik, A. Madani, B. Pieber, P. H. Seeberger, *J. Am. Chem. Soc.* **2020**, *142*, 11042–11049; b) H. Pataki, I. Csontos, Z. K. Nagy, B. Vajna, M. Molnar, L. Katona, G. Marosi, *Org. Process Res. Dev.* **2013**, *17*, 493–499; c) W. Yang, A. S. Mondol, C. Stiebing, L. Marcu, J. Popp, I. W. Schie, *J. Biophotonics* **2019**, *12*, e201800447; d) I. Csontos, H. Pataki, A. Farkas, H. Bata, B. Vajna, Z. K. Nagy, G. Keglevich, G. J. Marosi, *Org. Process Res. Dev.* **2015**, *19*, 189–195; e) M. Rößler, P. U. Huth, M. A. Liauw, *React. Chem. Eng.* **2020**, *5*, 1992–2002; f) G. Amberchan, A. L. Allen, J. H. Golden, B. Singaram, J. Z. Zhang, *ACS Sustainable Chem. Eng.* **2021**, *9*, 6068–6078.
[26] J. M. Dreimann, E. Kohls, H. F. W. Warmeling, M. Stein, L. F. Guo, M. Garland, T. N. Dinh, A. J. Vorholt, *ACS Catal.* **2019**, *9*, 4308–4319.
[27] A. M. Tsedilin, A. N. Fakhrutdinov, D. B. Eremin, S. S. Zalesskiy, A. O. Chizhov, N. G. Kolotyrkina, V. P. Ananikov, *Mendeleev Commun.* **2015**, *25*, 454–456.
[28] Z. Han, X. Gu, S. Wang, L. Liu, Y. Wang, Z. Zhao, Z. Yu, *Analyst* **2020**, *145*, 3313–3319.
[29] C. F. Carter, H. Lange, S. V. Ley, I. R. Baxendale, B. Wittkamp, J. G. Goode, N. L. Gaunt, *Org. Process Res. Dev.* **2010**, *14*, 393–404.
[30] a) S. Schwolow, F. Braun, M. Rädle, N. Kockmann, T. Röder, *Org. Process Res. Dev.* **2015**, *19*, 1286–1292; b) T. A. Hamlin, N. E. Leadbeater, *Beilstein J. Org. Chem.* **2013**, *9*, 1843–1852.
[31] a) H. Lu, M. A. Schmidt, K. F. Jensen, *Lab Chip* **2001**, *1*, 22–28; b) J. Yue, F. H. Falke, J. C. Schouten, T. A. Nijhuis, *Lab Chip* **2013**, *13*, 4855–4863; c) F. Benito-Lopez, W. Verboom, M. Kakuta, J. G. E. Gardeniers, R. J. M. Egberink, E. R. Oosterbroek, A. van den Berg, D. N. Reinhoudt, *Chem. Commun.* **2005**, 2857–2859.
[32] a) M. V. Gomez, A. de la Hoz, *Beilstein J. Org. Chem.* **2017**, *13*, 285–300; b) P. Giraudeau, F.-X. Felpin, *React. Chem. Eng.* **2018**, *3*, 399–413.
[33] D. L. Browne, S. Wright, B. J. Deadman, S. Dunnage, I. R. Baxendale, R. M. Turner, S. V. Ley, *Rapid Commun. Mass Spectrom.* **2012**, *26*, 1999–2010.
[34] a) M. B. Plutschack, B. Pieber, K. Gilmore, P. H. Seeberger, *Chem. Rev.* **2017**, *117*, 11796–11893; b) M. Rodriguez-Zubiri, F.-X. Felpin, *Org. Process Res. Dev.* **2022**, *26*, 1766–1793; c) G. A. Price, D. Mallik, M. G. Organ, *J. Flow Chem.* **2017**, *7*, 82–86; d) C. N. Talicska, E. C. O'Connell, H. W. Ward, A. R. Diaz, M. A. Hardink, D. A. Foley, D. Connolly, K. P. Girard, T. Ljubicic, *React. Chem. Eng.* **2022**, *7*, 1419–1428.
[35] a) C. Cavedon, S. Gisbertz, S. Reischauer, S. Vogl, E. Sperlich, J. H. Burke, R. F. Wallick, S. Schrottke, W.-H. Hsu, L. Anghileri, Y. Pfeifer, N. Richter, C. Teutloff, H. Müller-Werkmeister, D. Cambié, P. H. Seeberger, J. Vura-Weis, R. M. van der Veen, A. Thomas, B. Pieber, *Angew. Chem. Int. Ed.* **2022**, *61*, e202211433; b) W.-H. Hsu, S. Reischauer, P. H. Seeberger, B. Pieber, D. Cambié, *Beilstein J. Org. Chem.* **2022**, *18*, 1123–1130.
[36] C. J. Taylor, J. A. Manson, G. Clemens, B. A. Taylor, T. W. Chamberlain, R. A. Bourne, *React. Chem. Eng.* **2022**, *7*, 1037–1046.
[37] a) W. Ding, K. A. Johnson, C. Kutal, I. J. Amster, *Anal. Chem.* **2003**, *75*, 4624–4630; b) W. Ding, K. A. Johnson, I. J. Amster, C. Kutal, *Inorg. Chem.* **2001**, *40*, 6865–6866; c) S. Chen, Q. Wan, A. K. Badu-Tawiah, *Angew. Chem. Int. Ed.* **2016**, *55*, 9345–9349; *Angew. Chem.* **2016**, *128*, 9491–9495; d) J. Zelenka, J. Roithová, *ChemBioChem* **2020**, *21*, 2232–2240; e) J. V. Burykina, V. P. Ananikov, *ChemPhotoChem* **2022**, *7, e202200175*.
[38] C. Feldmeier, H. Bartling, K. Magerl, R. M. Gschwind, *Angew. Chem. Int. Ed.* **2015**, *54*, 1347–1351; *Angew. Chem.* **2015**, *127*, 1363–1367.
[39] M. Goez, *Concepts Magn. Reson.* **1995**, *7*, 69–86.
[40] J. Zelenka, R. Cibulka, J. Roithová, *Angew. Chem. Int. Ed.* **2019**, *58*, 15412–15420; *Angew. Chem.* **2019**, *131*, 15558–15566.
[41] a) L. Shi, W. Xia, *Chem. Soc. Rev.* **2012**, *41*, 7687–7697; b) J. Hu, J. Wang, T. H. Nguyen, N. Zheng, *Beilstein J. Org. Chem.* **2013**, *9*, 1977–2001; c) J. W. Beatty, C. R. J. Stephenson, *Acc. Chem. Res.* **2015**, *48*, 1474–1484.
[42] A. G. Condie, J. C. González-Gómez, C. R. J. Stephenson, *J. Am. Chem. Soc.* **2010**, *132*, 1464–1465.
[43] H. Bartling, A. Eisenhofer, B. König, R. M. Gschwind, *J. Am. Chem. Soc.* **2016**, *138*, 11860–11871.
[44] Y. Cai, J. Wang, Y. Zhang, Z. Li, D. Hu, N. Zheng, H. Chen, *J. Am. Chem. Soc.* **2017**, *139*, 12259–12266.
[45] J. V. Burykina, N. S. Shlapakov, E. G. Gordeev, B. König, V. P. Ananikov, *Chem. Sci.* **2020**, *11*, 10061–10070.
[46] J. V. Burykina, A. D. Kobelev, N. S. Shlapakov, A. Y. Kostyukovich, A. N. Fakhrutdinov, B. König, V. P. Ananikov, *Angew. Chem. Int. Ed.* **2022**, *61*, e202116888.
[47] W. Ai, Q. Yang, Y. Gao, X. Liu, H. Liu, Y. Bai, *Anal. Chem.* **2020**, *92*, 11967–11972.
[48] D. M. Schultz, F. Lévesque, D. A. DiRocco, M. Reibarkh, Y. Ji, L. A. Joyce, J. F. Dropinski, H. Sheng, B. D. Sherry, I. W. Davies, *Angew. Chem. Int. Ed.* **2017**, *56*, 15274–15278; *Angew. Chem.* **2017**, *129*, 15476–15480.
[49] K. Chen, N. Berg, R. Gschwind, B. König, *J. Am. Chem. Soc.* **2017**, *139*, 18444–18447.
[50] U. Lennert, P. B. Arockiam, V. Streitferdt, D. J. Scott, C. Rödl, R. M. Gschwind, R. Wolf, *Nat. Catal.* **2019**, *2*, 1101–1106.
[51] R. Rothfelder, V. Streitferdt, U. Lennert, J. Cammarata, D. J. Scott, K. Zeitler, R. M. Gschwind, R. Wolf, *Angew. Chem. Int. Ed.* **2021**, *60*, 24650–24658; *Angew. Chem.* **2021**, *133*, 24855–24863.
[52] K. L. Skubi, W. B. Swords, H. Hofstetter, T. P. Yoon, *ChemPhotoChem* **2020**, *4*, 685–690.
[53] W. B. Swords, S. J. Chapman, H. Hofstetter, A. L. Dunn, T. P. Yoon, *J. Org. Chem.* **2022**, *87*, 11776–11782.
[54] J. Zheng, W. B. Swords, H. Jung, K. L. Skubi, J. B. Kidd, G. J. Meyer, M.-H. Baik, T. P. Yoon, *J. Am. Chem. Soc.* **2019**, *141*, 13625–13634.
[55] S. Gisbertz, S. Reischauer, B. Pieber, *Nat. Catal.* **2020**, *3*, 611–620.
[56] Y. Ben-Tal, G. C. Lloyd-Jones, *J. Am. Chem. Soc.* **2022**, *144*, 15372–15382.
[57] C. Cavedon, E. T. Sletten, A. Madani, O. Niemeyer, P. H. Seeberger, B. Pieber, *Org. Lett.* **2021**, *23*, 514–518.
[58] M. A. Cismesia, T. P. Yoon, *Chem. Sci.* **2015**, *6*, 5426–5434.
[59] D. Lehnherr, Y. Ji, A. J. Neel, R. D. Cohen, A. P. J. Brunskill, J. Yang, M. Reibarkh, *J. Am. Chem. Soc.* **2018**, *140*, 13843–13853.

Manuscript received: December 12, 2022
Revised manuscript received: February 23, 2023
Accepted manuscript online: February 27, 2023
Version of record online: March 24, 2023

Chapter 5

Benzylic Fluorination Induced by a Charge-Transfer Complex with a Solvent-Dependent Selectivity Switch

Madani, A.; Anghileri, L.; Heydenreich, M.; Möller, H. M.; Pieber, B.

Org. Lett. **2022**, *24*, 29, 5376-5380.

https://doi.org/10.1021/acs.orglett.2c02050

OL Organic Letters

pubs.acs.org/OrgLett Letter

Benzylic Fluorination Induced by a Charge-Transfer Complex with a Solvent-Dependent Selectivity Switch

Amiera Madani, Lucia Anghileri, Matthias Heydenreich, Heiko M. Möller, and Bartholomäus Pieber*

Cite This: *Org. Lett.* 2022, 24, 5376–5380 Read Online

ACCESS | Metrics & More | Article Recommendations | Supporting Information

ABSTRACT: We present a divergent strategy for the fluorination of phenylacetic acid derivatives that is induced by a charge-transfer complex between Selectfluor and 4-(dimethylamino)pyridine. A comprehensive investigation of the conditions revealed a critical role of the solvent on the reaction outcome. In the presence of water, decarboxylative fluorination through a single-electron oxidation is dominant. Non-aqueous conditions result in the clean formation of α-fluoro-α-arylcarboxylic acids.

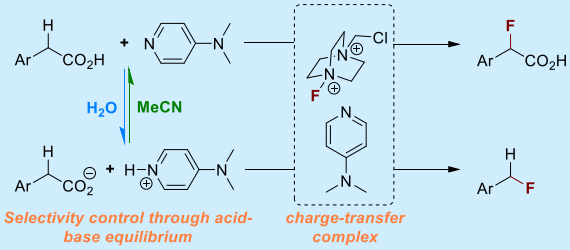

Fluorination increases the lipophilicity and metabolic stability of organic molecules, resulting in improved active pharmaceutical ingredients and agrochemicals.[1−4] Position emission tomography (PET) of ^{18}F-labeled radiopharmaceuticals is important for studying biochemical pathways and physiological processes.[5] Consequently, the development of efficient and selective protocols for constructing C−F bonds is desirable.[6] Nucleophilic fluorination and electrophilic fluorination dominate the field, but radical fluorinations recently gained significant momentum for two reasons.[6] First, the restriction to hazardous radical fluorine sources, such as XeF_2 and F_2, was overcome by the discovery that electrophilic N−F reagents transfer fluorine atoms to carbon-centered radicals.[7] Second, the increasing interest in synthetic radical chemistry resulted in attractive methods for generating C-centered radicals using dedicated catalysts and reagents.[8]

The formation of benzylic C(sp^3)−F bonds using 1-(chloromethyl)-4-fluoro-1,4-diazabicyclo[2.2.2]octane-1,4-diium ditetrafluoroborate (Selectfluor)[9] is among the most studied C−F bond formations that proceed via a radical mechanism.[6,7,10−13] These transformations are promising tools for modifying drug candidates for preventing undesired benzylic oxidation by cytochrome P450 oxidases.[14] Common strategies are decarboxylative fluorinations that use photocatalysts[15−18] or silver catalysts to induce single-electron-transfer (SET) oxidation[19−21] and the direct fluorination of benzylic C(sp^3)−H bonds using catalysts or reagents that enable hydrogen atom transfer (HAT) (Scheme 1A).[22−26] It must be noted that the α-fluorination of phenylacetic acids can also be carried out using Selectfluor via a silyl ketene acetal that is formed using a strong base[21,27,28] or with the aid of catalytic amounts of a strong Lewis acid and an organic base to generate an enediolate intermediate.[29]

A dedicated catalyst or reagent is regularly used to generate the key benzylic radical, which ultimately undergoes F atom transfer with Selectfluor to yield the desired product. Such benzylic fluorinations may also proceed through electron transfer or proton-coupled electron transfer rather than HAT.[30] Catalyst-free benzylic fluorination of aza-heterocycles

Scheme 1. Benzylic C(sp^3)−F Bond Formation Using Selectfluor through Radical Intermediates

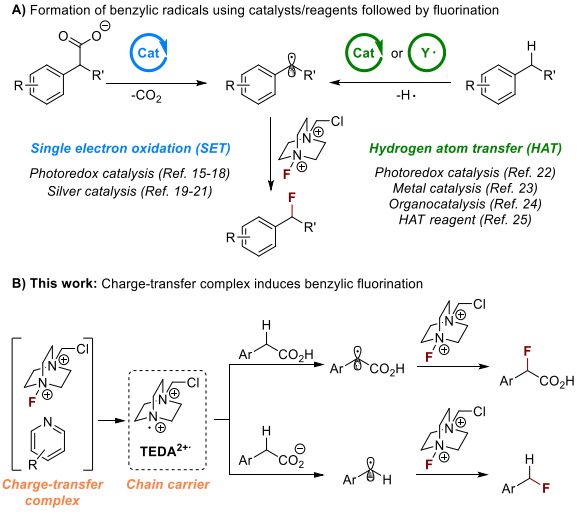

Received: June 16, 2022
Published: July 18, 2022

was reported to proceed through the formation of a charge-transfer (CT) complex between N-heterocyclic substrates and Selectfluor. This induces a stepwise electron/proton transfer or a concerted proton-coupled electron-transfer process.[31] Nitrogen−fluorine halogen bonding between Selectfluor and pyridine additives was proposed to facilitate silver-catalyzed radical fluorinations, but no product was observed in the absence of the metal catalyst.[32]

We envisioned that a CT complex between Selectfluor and an aromatic N-heterocyclic compound could generate the *N*-(chloromethyl)triethylenediamine radical dication (TEDA2$^{+\bullet}$), a potent single-electron oxidant and hydrogen atom-transfer reagent.[33] This would access an operationally simple and divergent strategy for the generation of benzylic carbon-centered radicals that could ultimately engage with Selectfluor to form C−F bonds. Here we present that this mechanistic blueprint can indeed be applied to achieve the direct fluorination of benzylic C(sp^3)−H bonds that likely proceeds via a HAT mechanism and the decarboxylative formation of benzylic C(sp^3)−F bonds through a SET process (Scheme 1B).

We started our investigations by studying whether a combination of Selectfluor and 4-(dimethylamino)pyridine (DMAP) triggers decarboxylative C−F bond formation or direct fluorination of benzylic C(sp^3)−H bonds. We chose 2-(4-fluorophenyl)acetic acid as model substrate that serves as an ideal probe for both scenarios (Scheme 2A). To our delight, we indeed observed a mixture of both fluorination products at room temperature with good selectivity toward the decarboxylative product in an acetonitrile/water mixture. Under non-aqueous conditions, α-fluorination occurred selectively.

After considerable experimentation (see the Supporting Information), we found that the decarboxylative fluorination works best in an acetone/water (1:1) mixture using 2 equiv of DMAP and an excess of Selectfluor (3 equiv) (Scheme 2B). Also, the addition of sodium fluoride (2 equiv) and an increased temperature (70 °C) were beneficial for converting a series of phenylacetic acid derivatives to the corresponding, volatile SET products (1−10) within 30 min in moderate to good NMR yields. Unreacted starting material was observed in many cases, and no major side product could be identified (see the Supporting Information).

A combination of 2 equiv of DMAP and 1.2 equiv of Selectfluor in acetonitrile produced the α-fluorination products (11−30) at room temperature in good to excellent NMR yields (Scheme 2B). Phenylacetic acid derivatives with electron-rich and electron-deficient substituents were cleanly converted to the respective α-fluoro-α-arylacetic acids. Small amounts of unreacted starting material were detected in all cases, which were difficult to separate by column chromatography and resulted in modest isolated yields in certain cases. A reaction time of 1 h was used for practical reasons, but detailed investigations revealed that the fluorination occurs in <5 min (Tables S14 and S15). Interestingly, the carboxylic acid functionality is crucial for α-fluorination. No reaction was observed using other functional groups, such as ketones, esters, amides, boronic acid esters, or boronates (see the Supporting Information).

We propose that a mixture of DMAP and Selectfluor spontaneously produces TEDA2$^{+\bullet}$, which acts as a chain carrier in a SET or HAT process (Scheme 3). The radical chain is efficient for the HAT route (1.2 equiv of Selectfluor under optimized conditions), whereas the SET pathway seems

Scheme 2. Initial Results and Scope of the Benzylic C(sp^3)−F Bond Formation Using Selectfluor and DMAP[a]

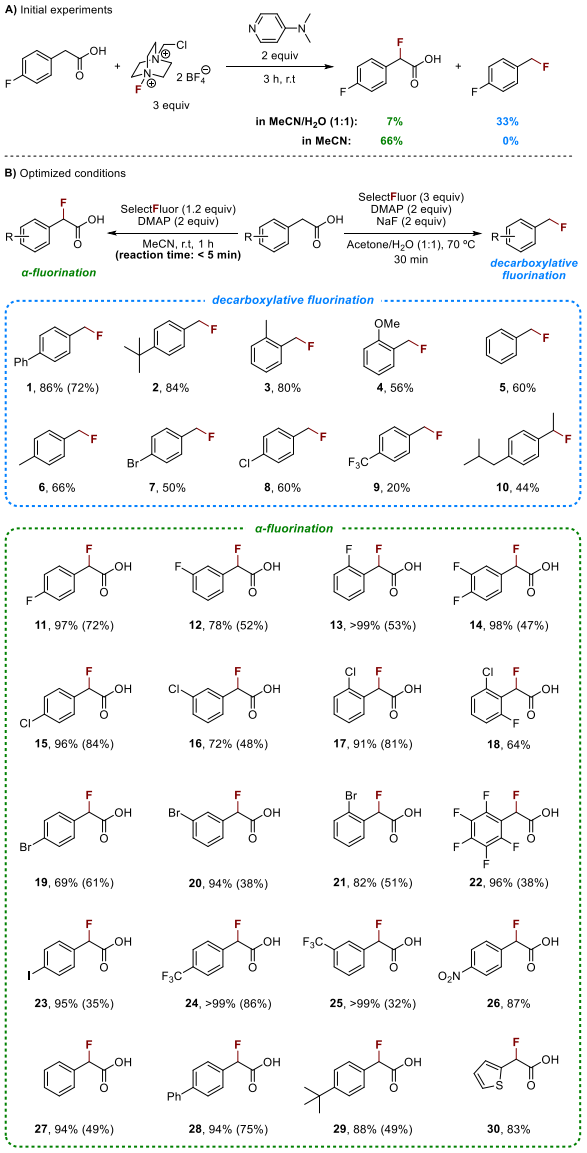

[a]Yields were determined by ^{1}H NMR using dimethyl maleate as the internal standard. Isolated yields are in parentheses.

to suffer from a significant amount of undesired termination events (3 equiv of Selectfluor under optimized conditions). The switch between the SET and HAT pathway is a consequence of different pK_a values of phenylacetic acids and DMAP under the applied conditions. The organic base deprotonates the carboxylic acid in an aqueous environment, enabling single-electron oxidation of the carboxylate by TEDA$^{2+\bullet}$. SET oxidation triggers decarboxylation to produce a C-centered radical that ultimately reacts with Selectfluor to yield the desired product and TEDA$^{2+\bullet}$. Phenylacetic acid derivatives have low acidity in aprotic polar solvents (pK_a of phenylacetic acid in $MeNO_2$ > 19).[34] The pK_a of the conjugated acid of pyridine derivatives in MeCN is lower.[35] As a result, the amount of carboxylate under these conditions is

https://doi.org/10.1021/acs.orglett.2c02050
Org. Lett. 2022, 24, 5376−5380

Scheme 3. Proposed Mechanism for the Formation of Benzylic C(sp^3)−F Bonds via the Activation of Selectfluor Using DMAP

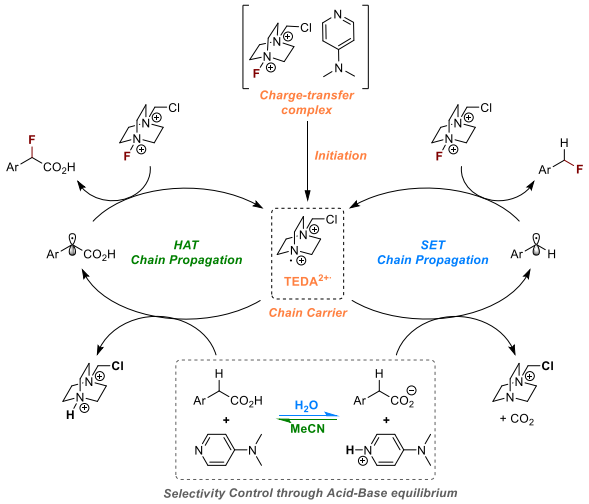

negligible. This reduces the likelihood of decarboxylative SET and HAT becoming the dominant pathway.

While there are no plausible alternatives to the SET mechanism, α-fluoro-α-arylacetic acid formation may occur through a more traditional "electrophilic" fluorination mechanism rather than HAT. Surprisingly, we also observed product formation using NFSI (*N*-fluorobenzenesulfonimide) instead of Selectfluor (Table S10), which was, to the best of our knowledge, never reported to produce a radical chain carrier. We therefore carried out a series of experiments to shed some light on the mechanism. An enediolate species was not observed upon treatment of phenylacetic acid with DMAP in MeCN-d_3 (Figure S3). This is in agreement with a study that shows that the formation of such species using organic bases requires strong Lewis acids as activators.[29] However, a radical clock experiment did not prove the formation of the proposed benzylic radical intermediate (Scheme S2). The addition of the radical scavenger TEMPO resulted in the consumption of the substrate, but no trace of the fluorination product was formed, indicative of a radical mechanism (Scheme S3). Competition experiments involving deuterium-labeled substrates indicate that C−H bond cleavage is the rate-determining step (Scheme S4). In addition, competitive experiments between phenylacetic acids with different substituents on the aromatic ring showed that electron-rich aromatic systems react slower (Scheme S5). These experiments suggest that the reaction does not proceed through a SET oxidation followed by deprotonation.

The simple preparation of α-fluoro-α-arylcarboxylic acids through our method is attractive compared to the most common approach for synthesizing such scaffolds that requires formation of a silyl ketene acetal using a strong base, followed by treatment with Selectfluor.[21,27,28] Our α-fluorination is not sensitive to air or moisture, works with bench-stable reagents, and produces the desired products in up to quantitative yields as determined by ^{19}F NMR (isolated yields range from 32% to 86%). This operational simplicity is promising for the synthesis of ^{18}F-labeled radiopharmaceuticals using [^{18}F]Selectfluor. In particular, the short reaction times are ideally suited for such applications, due to the short half-lives of ^{18}F-labeled radionuclides (110 min).[36] Monitoring the fluorination of 4-*tert*-butylphenylacetic acid using in situ FTIR spectroscopy showed that the reaction forms the desired product instantaneously once Selectfluor is added to a solution of DMAP and the substrate in MeCN (Figure 1A). Fast

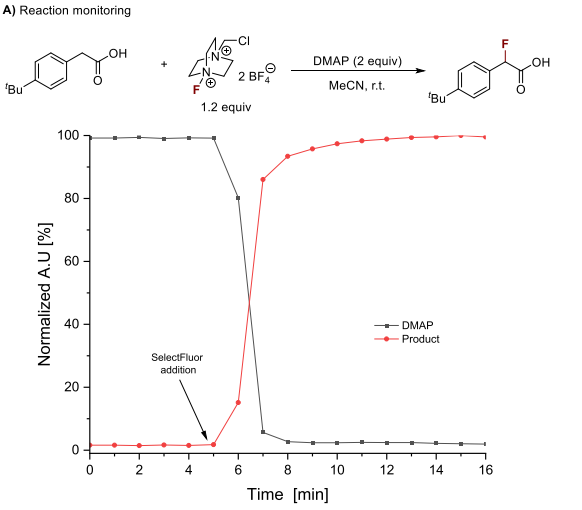

Entry	Compound added delayed[a]	Conversion [%][b]	Yield [%][c]
1	Substrate	n.d.	n.d.
2	SelectFluor	>98	>98
3	DMAP	88	88

Figure 1. Practical aspects of the HAT protocol. (A) Reaction monitoring using in situ FTIR spectroscopy. (B) Delayed addition experiments.

consumption of the fluorination reagent was also monitored in the absence of the substrate (Figure S6). This supports our mechanistic proposal that the fluorine source and the organic base form a reactive, labile species that leads to productive fluorination or, if no substrate is present in the reaction mixture, to degradation products. ^{1}H NMR experiments using Teflon inserts showed the formation of a DMAP·HF adduct upon mixing DMAP and Selectfluor along with several unidentified compounds that are likely N-fluorinated DMAP derivatives.[37] We carried out a series of "delayed addition" experiments to clarify if the order of reagent addition is crucial for successful fluorination (Figure 1B). When Selectfluor and DMAP were mixed in MeCN and the substrate was added after 30 min, no reaction was observed. Premixing the substrate with Selectfluor or DMAP is possible.

Finally, we sought to study if a strong electron-donating substituent on the pyridine base is crucial for reactivity. Exchanging DMAP with 4-aminopyridine or 4-methoxypyridine reduced the efficacy of this reaction (Table 1). Modest

https://doi.org/10.1021/acs.orglett.2c02050
Org. Lett. 2022, 24, 5376−5380

conversions were obtained with pyridine, emphasizing that a strong Lewis basicity is key for the generation of $TEDA^{2+\bullet}$.

Table 1. Influence of Lewis Basicity on N−F Bond Activation of Selectfluor[a]

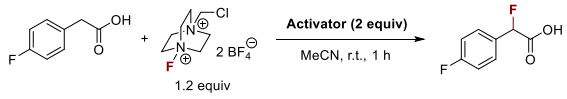

Entry	Activator	Conversion [%][b]	Yield [%][c]
1		97	97
2		82	82
3		66	66
4		9	9

[a]Reaction conditions: 4-fluorophenylacetlc acid (0.3 mmol), Selectfluor (0.36 mmol), DMAP (0.6 mmol), MeCN (1.5 mL), rt, 4 h. [b]Converaion of 4-fluorophenylacetic acid determined by ^{1}H NMR using dimethyl maleate as an internal standard. [c]NMR yield determined by ^{1}H NMR using dimethyl maleate as an internal standard.

In summary, we developed a new strategy for the formation of benzylic C(sp^3)−F bonds that is proposed to proceed via the formation of $TEDA^{2+\bullet}$ from Selectfluor and 4-(dimethylamino)pyridine. Controlling the pK_a of phenylacetic acid derivatives via the reaction media enables switching between reaction mechanisms that enables the selective formation of different products. Under aqueous conditions, a decarboxylative fluorination was observed, whereas non-aqueous conditions allow for direct fluorination of benzylic C(sp^3)−H bonds. This enables a facile and clean formation of α-fluoro-α-arylacetic acids within a few minutes at room temperature.

■ ASSOCIATED CONTENT

Supporting Information

The Supporting Information is available free of charge at https://pubs.acs.org/doi/10.1021/acs.orglett.2c02050.

Experimental procedures and characterization data (PDF)

■ AUTHOR INFORMATION

Corresponding Author

Bartholomäus Pieber − *Department of Biomolecular Systems, Max-Planck-Institute of Colloids and Interfaces, 14476 Potsdam, Germany;* orcid.org/0000-0001-8689-388X; Email: Bartholomaeus.Pieber@mpikg.mpg.de

Authors

Amiera Madani − *Department of Biomolecular Systems, Max-Planck-Institute of Colloids and Interfaces, 14476 Potsdam, Germany; Department of Chemistry and Biochemistry, Freie Universität Berlin, 14195 Berlin, Germany*

Lucia Anghileri − *Department of Biomolecular Systems, Max-Planck-Institute of Colloids and Interfaces, 14476 Potsdam, Germany; Department of Chemistry and Biochemistry, Freie Universität Berlin, 14195 Berlin, Germany*

Matthias Heydenreich − *Institute of Chemistry/Analytical Chemistry, University of Potsdam, 14476 Potsdam, Germany*

Heiko M. Möller − *Institute of Chemistry/Analytical Chemistry, University of Potsdam, 14476 Potsdam, Germany*

Complete contact information is available at: https://pubs.acs.org/10.1021/acs.orglett.2c02050

Funding

Open access funded by Max Planck Society.

Notes

A version of this research was previously posted to chemRxiv.[38] The authors declare no competing financial interest.

■ ACKNOWLEDGMENTS

The authors gratefully acknowledge the Max Planck Society for generous financial support. A.M. and B.P. acknowledge the Deutsche Forschungsgemeinschaft (DFG, German Research Foundation) under Germany's Excellence Strategy-EXC 2008/1 (UniSysCat)-390540038 for financial support. L.A. and B.P. acknowledge the DFG for financial support (PI 1635/2-19). B.P. acknowledges financial support by a Liebig Fellowship from the German Chemical Industry Fund [Fonds der Chemischen Industrie (FCI)]. The authors thank our colleague John J. Molloy (Max-Planck-Institute of Colloids and Interfaces) for fruitful scientific discussions.

■ REFERENCES

(1) Meanwell, N. A. Fluorine and Fluorinated Motifs in the Design and Application of Bioisosteres for Drug Design. *J. Med. Chem.* **2018**, *61*, 5822−5880.

(2) Gillis, E. P.; Eastman, K. J.; Hill, M. D.; Donnelly, D. J.; Meanwell, N. A. Applications of Fluorine in Medicinal Chemistry. *J. Med. Chem.* **2015**, *58*, 8315−8359.

(3) O'Hagan, D. Fluorine in health care: Organofluorine containing blockbuster drugs. *J. Fluorine Chem.* **2010**, *131*, 1071−1081.

(4) Fujiwara, T.; O'Hagan, D. Successful fluorine-containing herbicide agrochemicals. *J. Fluorine Chem.* **2014**, *167*, 16−29.

(5) Brooks, A. F.; Topczewski, J. J.; Ichiishi, N.; Sanford, M. S.; Scott, P. J. H. Late-stage [18F]fluorination: new solutions to old problems. *Chem. Sci.* **2014**, *5*, 4545−4553.

(6) Champagne, P. A.; Desroches, J.; Hamel, J.-D.; Vandamme, M.; Paquin, J.-F. Monofluorination of Organic Compounds: 10 Years of Innovation. *Chem. Rev.* **2015**, *115*, 9073−9174.

(7) Chatalova-Sazepin, C.; Hemelaere, R.; Paquin, J.-F.; Sammis, G. M. Recent Advances in Radical Fluorination. *Synthesis* **2015**, *47*, 2554−2569.

(8) Crespi, S.; Fagnoni, M. Generation of Alkyl Radicals: From the Tyranny of Tin to the Photon Democracy. *Chem. Rev.* **2020**, *120*, 9790−9833.

(9) Nyffeler, P. T.; Durón, S. G.; Burkart, M. D.; Vincent, S. P.; Wong, C. H. Selectfluor: mechanistic insight and applications. *Angew. Chem., Int. Ed.* **2005**, *44*, 192−212.

(10) Tarantino, G.; Hammond, C. Catalytic C(sp3)−F bond formation: recent achievements and pertaining challenges. *Green Chem.* **2020**, *22*, 5195−5209.

(11) Szpera, R.; Moseley, D. F. J.; Smith, L. B.; Sterling, A. J.; Gouverneur, V. The Fluorination of C−H Bonds: Developments and Perspectives. *Angew. Chem., Int. Ed.* **2019**, *58*, 14824−14848.

(12) Lantaño, B.; Postigo, A. Radical fluorination reactions by thermal and photoinduced methods. *Org. Biomol. Chem.* **2017**, *15*, 9954−9973.

(13) Xiao, P.; Pannecoucke, X.; Bouillon, J.-P.; Couve-Bonnaire, S. Wonderful fusion of organofluorine chemistry and decarboxylation strategy. *Chem. Soc. Rev.* **2021**, *50*, 6094−6151.
(14) Purser, S.; Moore, P. R.; Swallow, S.; Gouverneur, V. Fluorine in medicinal chemistry. *Chem. Soc. Rev.* **2008**, *37*, 320−330.
(15) Ventre, S.; Petronijevic, F. R.; MacMillan, D. W. C. Decarboxylative Fluorination of Aliphatic Carboxylic Acids via Photoredox Catalysis. *J. Am. Chem. Soc.* **2015**, *137*, 5654−5657.
(16) Wu, X.; Meng, C.; Yuan, X.; Jia, X.; Qian, X.; Ye, J. Transition-metal-free visible-light photoredox catalysis at room-temperature for decarboxylative fluorination of aliphatic carboxylic acids by organic dyes. *Chem. Commun.* **2015**, *51*, 11864−11867.
(17) Tarantino, G.; Hammond, C. Catalytic Formation of C(sp3)−F Bonds via Heterogeneous Photocatalysis. *ACS Catal.* **2018**, *8*, 10321−10330.
(18) Pieber, B.; Shalom, M.; Antonietti, M.; Seeberger, P. H.; Gilmore, K. Continuous Heterogeneous Photocatalysis in Serial Micro-Batch Reactors. *Angew. Chem., Int. Ed.* **2018**, *57*, 9976−9979.
(19) Nguyen, T. V.; Pham, V. T.; Nguyen, T. V. T.; Phan, N. T. S.; Truong, T. Decarboxylative fluorination of aliphatic carboxylic acids under heterogeneous delafossite $AgFeO_2$ nanoparticle catalysis: The utilization of bimetallic cooperativity. *J. Catal.* **2018**, *360*, 270−276.
(20) Wang, Z.; Guo, C.-Y.; Yang, C.; Chen, J.-P. Ag-Catalyzed Chemoselective Decarboxylative Mono- and gem-Difluorination of Malonic Acid Derivatives. *J. Am. Chem. Soc.* **2019**, *141*, 5617−5622.
(21) Mizuta, S.; Stenhagen, I. S. R.; O'Duill, M.; Wolstenhulme, J.; Kirjavainen, A. K.; Forsback, S. J.; Tredwell, M.; Sandford, G.; Moore, P. R.; Huiban, M.; Luthra, S. K.; Passchier, J.; Solin, O.; Gouverneur, V. Catalytic Decarboxylative Fluorination for the Synthesis of Tri- and Difluoromethyl Arenes. *Org. Lett.* **2013**, *15*, 2648−2651.
(22) Xia, J.-B.; Zhu, C.; Chen, C. Visible Light-Promoted Metal-Free C−H Activation: Diarylketone-Catalyzed Selective Benzylic Mono- and Difluorination. *J. Am. Chem. Soc.* **2013**, *135*, 17494−17500.
(23) Xu, P.; Guo, S.; Wang, L.; Tang, P. Silver-Catalyzed Oxidative Activation of Benzylic C-H Bonds for the Synthesis of Difluoromethylated Arenes. *Angew. Chem., Int. Ed.* **2014**, *53*, 5955−5958.
(24) Amaoka, Y.; Nagatomo, M.; Inoue, M. Metal-Free Fluorination of C(sp3)−H Bonds Using a Catalytic N-Oxyl Radical. *Org. Lett.* **2013**, *15*, 2160−2163.
(25) Hua, A. M.; Mai, D. N.; Martinez, R.; Baxter, R. D. Radical C−H Fluorination Using Unprotected Amino Acids as Radical Precursors. *Org. Lett.* **2017**, *19*, 2949−2952.
(26) Ma, J.-j.; Yi, W.-b.; Lu, G.-p.; Cai, C. Transition-metal-free C−H oxidative activation: persulfate-promoted selective benzylic mono- and difluorination. *Org. Biomol. Chem.* **2015**, *13*, 2890−2894.
(27) Zhang, F.; Song, J. Z. A novel general method for preparation of α-fluoro-α-arylcarboxylic acid. Direct fluorination of silyl ketene acetals with Selectfluor®. *Tetrahedron Lett.* **2006**, *47*, 7641−7644.
(28) Wang, H.; Liu, C.-F.; Song, Z.; Yuan, M.; Ho, Y. A.; Gutierrez, O.; Koh, M. J. Engaging α-Fluorocarboxylic Acids Directly in Decarboxylative C−C Bond Formation. *ACS Catal.* **2020**, *10*, 4451−4459.
(29) Hu, H.; Wang, C.; Wu, X.; Liu, Y.; Yue, G.; Su, G.; Feng, J. Boron-catalyzed α-C−H fluorination of aryl acetic acids. *Org. Chem. Front.* **2022**, *9*, 1315−1320.
(30) Bloom, S.; McCann, M.; Lectka, T. Photocatalyzed benzylic fluorination: shedding "light" on the involvement of electron transfer. *Org. Lett.* **2014**, *16*, 6338−6341.
(31) Danahy, K. E.; Cooper, J. C.; Van Humbeck, J. F. Benzylic Fluorination of Aza-Heterocycles Induced by Single-Electron Transfer to Selectfluor. *Angew. Chem., Int. Ed.* **2018**, *57*, 5134−5138.
(32) Hua, A. M.; Bidwell, S. L.; Baker, S. I.; Hratchian, H. P.; Baxter, R. D. Experimental and Theoretical Evidence for Nitrogen−Fluorine Halogen Bonding in Silver-Initiated Radical Fluorinations. *ACS Catal.* **2019**, *9*, 3322−3326.
(33) Aguilar Troyano, F. J.; Merkens, K.; Gómez-Suárez, A. Selectfluor® Radical Dication (TEDA2+.) − A Versatile Species in Modern Synthetic Organic Chemistry. *Asian J. Org. Chem.* **2020**, *9*, 992−1007.
(34) Subirats, X.; Porras, S. P.; Rosés, M.; Kenndler, E. Nitromethane as solvent in capillary electrophoresis. *J. Chrom A* **2005**, *1079*, 246−253.
(35) Tshepelevitsh, S.; Kütt, A.; Lõkov, M.; Kaljurand, I.; Saame, J.; Heering, A.; Plieger, P. G.; Vianello, R.; Leito, I. On the Basicity of Organic Bases in Different Media. *Eur. J. Org. Chem.* **2019**, *2019*, 6735−6748.
(36) Teare, H.; Robins, E. G.; Kirjavainen, A.; Forsback, S.; Sandford, G.; Solin, O.; Luthra, S. K.; Gouverneur, V. Radiosynthesis and evaluation of [18F]Selectfluor bis(triflate). *Angew. Chem., Int. Ed.* **2010**, *49*, 6821−4.
(37) Chauhan, M. S.; Yadav, G. D.; Hussain, F.; Singh, S. N-Fluorobenzenaminium tetrafluoroborate generated in situ by aniline and Selectfluor as a reusable catalyst for the ring opening of epoxides with amines under microwave irradiation. *Catal. Sci. Technol.* **2014**, *4*, 3945−3952.
(38) Madani, A.; Anghileri, L.; Heydenreich, M.; Möller, H. M.; Pieber, B. Benzylic fluorination induced by N−F bond activation of Selectfluor with a solvent-dependent selectivity switch. *chemRxiv* **2022**, DOI: 10.26434/chemrxiv-2022-mstv5.

5.1 Specific Contribution

Considering a recently described direct benzylic C(sp^3)–H fluorination that was initiated by a charge-transfer complex involving *N*-heterocyclic substrates and Selectfluor™, I envisioned that a similar mode of activation could be used for the benzylic radical fluorination of phenylacetic acids, yielding α-fluorophenylacetic acids.[1]

My initial experiments using 4-dimethylaminopyridine (4-DMAP) and Selectfluor™ in aqueous media resulted in a mixture of both fluorinated products with selectivity towards the decarboxylated benzyl fluoride. Considerable optimization experiments revealed the selective formation of the decarboxylated product was possible in a mixture of acetone and water (1:1) at elevated temperatures. Carefully optimizing all reaction parameters, I established the ideal conditions, selectively resulting in α-fluorophenylacetic acids. Investigating the scope and limitations of the direct C(sp^3)–H fluorination reaction, I found that the reaction results in good to excellent yields for phenylacetic acid derivatives with electron-deficient and electron-rich benzene moieties, with no preferences regarding ortho-, meta- and para-substitution. Lucia Anghileri optimized the decarboxylative protocol and investigated the scope and limitations of this transformation. We proposed that the mechanism proceeds through generation of $TEDA^{2+\cdot}$, generated in situ by a charge-transfer complex between Selectfluor™ and the electron-rich additive (Figure 5.1). We hypothesize that the radical dicationic species acts as a chain carrier in a single electron transfer (SET) process, triggering the decarboxylation under aqueous conditions. In polar aprotic solvents, however, hydrogen atom transfer (HAT), cleaving the benzylic C(sp^3)–H resulting the key radical species. The switch between the two mechanistic pathways is a consequence of the pK_a values of the phenylacetic acids under the given reaction conditions. In polar aprotic solvents phenylacetic acids show a low acidity, whereas under aqueous conditions the carboxylate species is predominant, increasing the likelihood of the SET pathway.

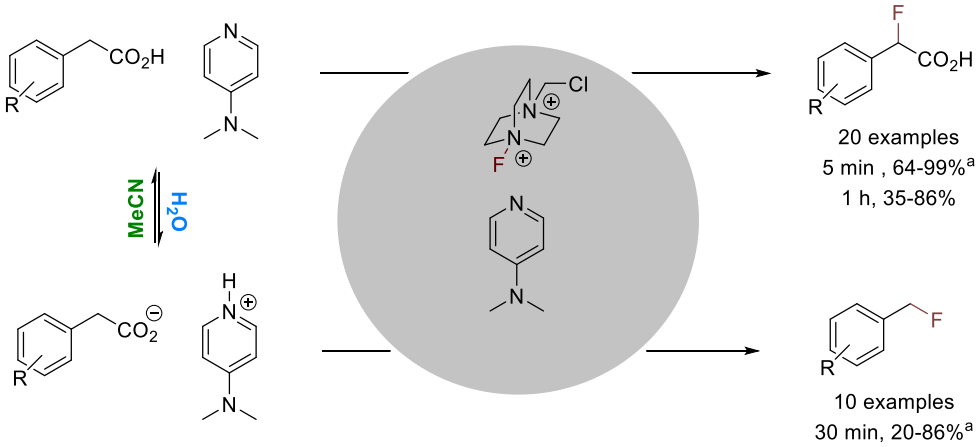

Figure 5.1 Charge transfer complex mediated **A** direct benzylic C(sp^3)-H fluorination reaction and **B** decarboxylative benzylic fluorination of phenylacetic acid derivatives. [a] NMR Yield, determined via ^{1}H NMR spectroscopy, using dimethyl maleate as internal standard.

To gain mechanistic insights, I used in situ ATR-IR to track the direct C–H fluorination, revealing immediate product formation upon addition of all three reagents. Further, consumption of Selectfluor™ in the absence of the substrate underlines the hypothesis of the formation of a reactive species between the fluorinating agent and the pyridine additive. Conducting a competition experiment involving deuterium labelled phenylacetic acid, I identified the C–H cleavage to be the rate determining step.

Finally, I undertook competition experiments using phenylacetic acids with different electronic properties. Analyzing the product distribution, I found that electron-rich phenylacetic acids react slower, rendering a SET event followed by deprotonation to the benzylic radical as unlikely.

5.2 References

(1) Danahy, K. E.; Cooper, J. C.; Van Humbeck, J. F. Benzylic Fluorination of Aza-Heterocycles Induced by Single-Electron Transfer to Selectfluor. *Angew. Chem. Int. Ed.* **2018**, *57* (18), 5134-5138. DOI: https://doi.org/10.1002/anie.201801280.

Chapter 6

Visible-Light-Mediated Oxidative Debenzylation of 3-*O*-Benzyl-1,2:5,6-di-*O*-isopropylidene-α-D-glucofuranose

Madani, A.; † Sletten, E. T.; † Seeberger, P. H.; Pieber, B.

Org. Synth. **2023**, *100*, 271.

†These authors contributed equally

Disclaimer: The protocol reproduced in this Thesis shows the submitted mauscript. After minor revisions, checking by an independent laboratory and editing, the protocol was published.

https://doi.org/10.15227/orgsyn.100.0271

Organic Syntheses

Visible-light-mediated oxidative debenzylation of 3-*O*-benzyl-1,2:5,6-di-*O*-isopropylidene-α-D-glucofuranose

Amiera Madani,† Eric T. Sletten,† Cristian Cavedon, Peter H. Seeberger,* Bartholomäus Pieber*

Department of Biomolecular Systems, Max-Planck-Institute of Colloids and Interfaces, Am Mühlenberg 1, 14476 Potsdam, Germany

†These authors contributed equally

Checked by Jane Doe and Max Mustermann

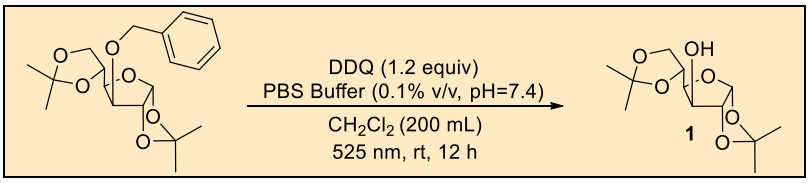

Procedure (Note 1)

1,2:5,6-Di-O-isopropylidene-a-D-glucofuranose (***1***). An oven-dried, single-necked side-armed Schlenk tube (250 mL, 23x4.5 cm) equipped with a football-shaped Teflon-coated magnetic stir bar (2.5 cm) is charged sequentially with 3-*O*-benzyl-1,2:5,6-di-*O*-isopropylidene-α-D-glucofuranose (4.0 g, 11.4 mmol, 1 equiv) (Note 2) and dichloromethane (200 mL, 57 mM) (Note 3). Under ambient atmosphere, 2,3-dichloro-5,6-dicyano-1,4-benzoquinone (DDQ, 3.12 g, 13.6 mmol, 1.2 equiv) (Note 4) and PBS buffer (0.2 mL, 0.1%$_{vol,}$ pH 7.4) (Note 5) is added and the flask is sealed with a rubber septum (Figure 1B). The reaction mixture is stirred at 1400 ppm and irradiated using two green LED lamps (525 nm) (Note 6) at full power while stirring at 1400 rpm (Figure 1C).

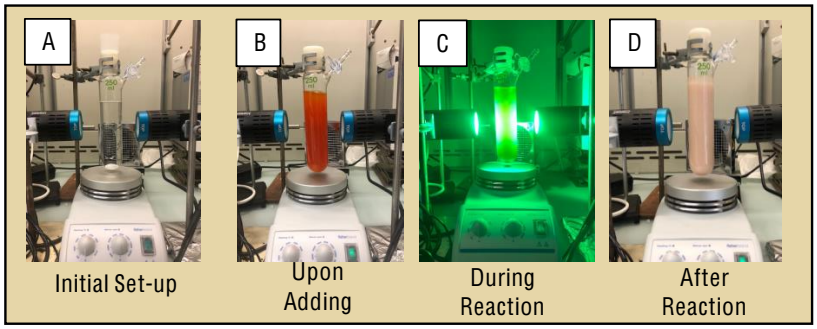

Figure 1. Reaction mixture before (A) and after (B) addition of DDQ, during irradiation (C) and after the reaction (D).

The reaction progress is monitored by TLC analysis (Figure 2B) (Note 7), taking samples (ca. 50 µL) of the crude mixture with a syringe through the rubber septum.

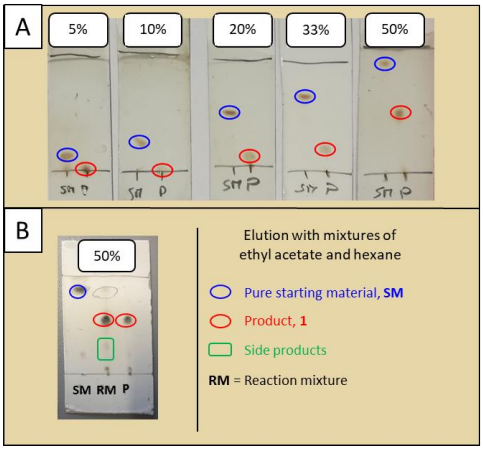

Figure 2. TLC analysis of pure starting material and product using different amounts of ethyl acetate in hexane as mobile phase (A) and analysis of the reaction mixture after 12 h using ethyl acetate : hexane (1:1) (B). TLCs were stained with 10%$_{vol}$ H_2SO_4 in ethanol followed by heating.

After 12 h (Figure 1D), the starting material is almost completely consumed and only small amounts of undesired side-products are formed (Figure 2B). Next, the reaction mixture is vacuum-filtered through a plug of celite (25 g) (Note 8) contained in a fritted funnel (7x6 cm) and collected in a 1000 mL Erlenmeyer flask (Figure 3A). The celite bed is washed with 150 mL of CH_2Cl_2 and the filtrate is transferred into a 500 mL separatory funnel (final volume 350 mL). The solution is then washed with saturated $NaHCO_3$ (150 mL). The aqueous layer becomes orange, while the organic layer is yellow (Figure 3B). After phase-separation, the organic layer is drained and the aqueous layer is extracted with CH_2Cl_2 (2x75 mL) (Note 9). Combined organic layers are dried over Na_2SO_4 (~30 g), filtered and the solvent is removed by rotary evaporation (35 °C, 100 mm Hg).

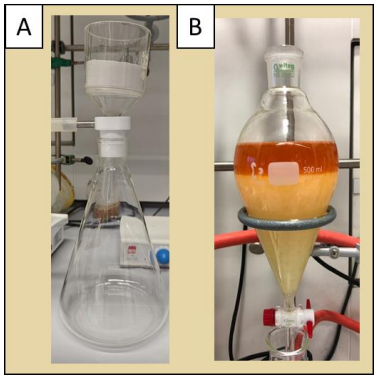

Figure 3. Vacuum filter apparatus used for celite bed (A) and reaction after washing with saturated $NaHCO_3$ (B).

A slurry is prepared from silica (90 g, Note 10) and a mixture of ethyl acetate and hexane (33%$_{vol}$, 300 mL) (Note 11) and loaded into a fritted glass column (5x50 cm) (Figure 4A). The column is packed using pressurized air and an additional layer of sand (25 g) is gently added on the top of the column. The crude product is loaded on the column by dissolving the residue in a minimal amount of toluene (~5 mL) and transferring it with a glass pipette. The round-bottom flask is rinsed with toluene (2x2.5 mL) and the washings are loaded on the column as well.

The loaded crude is pushed into the silica layer using air pressure, then 10 mL of ethyl acetate/hexane mixture (33%$_{vol}$) are gently added to the top of the column and pushed into the silica.

Figure 4. Glass column loaded with a slurry of silica, the crude product, and sea sand, eluted with ethyl acetate and hexane.

A 500 mL reservoir is added to the glass column (Figure 4), filled with the eluent system (ethyl acetate/hexane 33%$_{vol}$) and fractions of 15 mL each (20x150 mm test tubes) were collected (isocratic elution, total volume = 1.5 L). Presence of pure product is detected by TLC analysis in fractions 31 to 60 (Figure 5A). These fractions are combined in a 1000 mL round-bottom flask and the solvent is removed by rotary evaporation (35 °C, 50 mmHg) to obtain the title compound **1** as an off-white amorphous solid (Figure 5B, 2.34 g, 8.9 mmol, yield = 78%, purity = >99%) (Note 12-16).

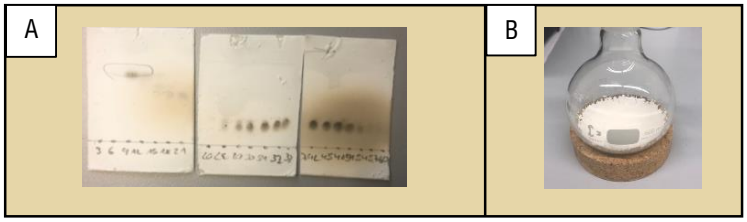

Figure 5. TLC analysis of fractions obtained from chromatography (A) and final product 1 (B).

Organic Syntheses

Notes

1. Prior to performing each reaction, a thorough hazard analysis and risk assessment should be carried out with regard to each chemical substance and experimental operation on the scale planned and in the context of the laboratory where the procedures will be carried out. Guidelines for carrying out risk assessments and for analyzing the hazards associated with chemicals can be found in references such as Chapter 4 of "Prudent Practices in the Laboratory" (The National Academies Press, Washington, D.C., 2011; the full text can be accessed free of charge at https://www.nap.edu/catalog/12654/prudent-practices-in-the-laboratory-handling-and-management-of-chemical. See also "Identifying and Evaluating Hazards in Research Laboratories" (American Chemical Society, 2015) which is available via the associated website "Hazard Assessment in Research Laboratories" at https://www.acs.org/content/acs/en/about/governance/committees/chemicalsafety/hazard-assessment.html. In the case of this procedure, the risk assessment should include (but not necessarily be limited to) an evaluation of the potential hazards associated with 3-*O*-benzyl-1,2:5,6-di-*O*-isopropylidene-α-D-glucofuranose, 2,3-dichloro-5,6-dicyano-1,4-benzoquinone, dichloromethane, ethyl acetate, hexane, sulfuric acid, ethanol, sodium sulfate, sodium bicarbonate, deuterated chloroform, deuterated dimethyl sulfoxide, PBS buffer, celite, silica gel, maleic acid, toluene, sodium chloride, as well as the proper procedures for chromatographic purifications and photochemical experiments. Photochemical experiments should be carried out in a dedicated compartment (fume hood), shielded so that no light is exchanged with the surrounding environment. The operator should use light filtering goggles while such compartment is open for operations.
2. 3-*O*-Benzyl-1,2:5,6-di-*O*-isopropylidene-α-D-glucofuranose, 97% (CAS 18685-18-2) was purchased from Fisher Scientific and used as received.
3. Dichloromethane (stabilized with ethanol) was purchased from VWR Chemicals BDH® and used as received. Alternatively, dichloromethane (unstabilized, HPLC grade) can also be utilized if it can be acquired. Dichloromethane stabilized with amylene should not be used due to reproducibility problems.
4. 2,3-Dichloro-5,6-dicyano-1,4-benzoquinone, 98% (CAS 84-58-2) was purchased from Sigma-Aldrich and used as received.

5. Phosphate-buffered saline (PBS buffer) solution was purchased from Sigma-Aldrich and used as received after verifying the pH value to be 7.4.
6. Two Kessil PR160-525L LED lamps at full power were used for irradiation at 525 nm. Lamps were installed 4 cm away from the reaction flask as shown in Figures 1 and 6. Lamps had linear reflectors that were aligned vertically with the reaction vessel. A high-power computer fan was used for cooling (Figure 6, left).

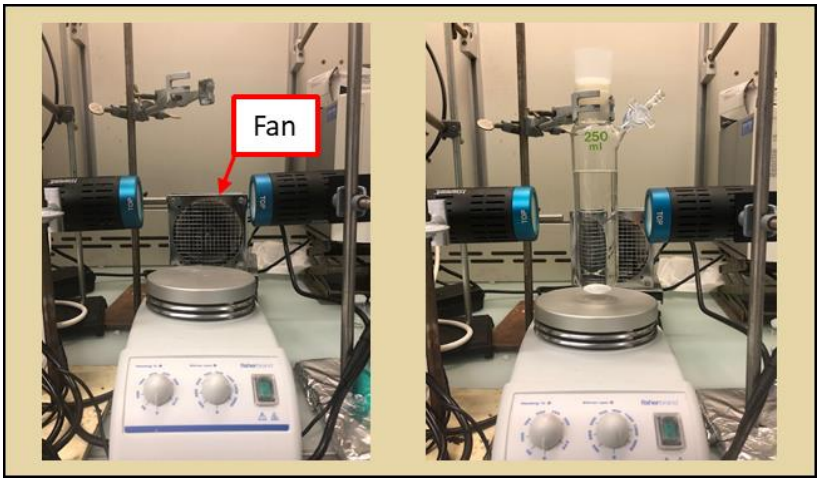

Figure 6. Irradiation setup using two lamps (525 nm) at 4 cm distance to the reaction vessel and a computer fan for cooling.

7. TLC analysis of the crude reaction mixture is performed using pre-coated ALUGRAM Xtra SIL G/UV254 sheets from Macherey-Nagel. TLCs are eluted with 33%$_{vol}$ ethyl acetate/hexane and 50%$_{vol}$ ethyl acetate/hexane and stained using 10%$_{vol}$ of H_2SO_4 in ethanol, followed by gentle heating.

33% ethyl acetate/hexane	**1a** : Rf = 0.73	**1** : Rf = 0.24
50% ethyl acetate/hexane	**1a** : Rf = 0.88	**1** : Rf = 0.47

8. Celite (Celite 535) was purchased from Carl Roth.
9. In case of emulsion formation, 50 mL of saturated brine (NaCl) solution can be added to the aqueous phase.
10. Silica gel (Silica 60, 0.04-0.063 mm) was purchased from Macherey-Nagel.

11. Ethyl acetate (HPLC grade, Fisher Chemical) and hexane (NORMAPUR grade, VWR) were used as received.
12. **^{1}H NMR (400 MHz, $CDCl_3$)** δ 5.95 (d, *J* = 3.6 Hz, 1H), 4.54 (d, *J* = 3.6 Hz, 1H), 4.38 – 4.31 (m, 2H), 4.17 (dd, *J* = 8.6, 6.2 Hz, 1H), 4.07 (dd, *J* = 7.6, 2.8 Hz, 1H), 3.98 (dd, *J* = 8.6, 5.4 Hz, 1H), 2.54 (d, *J* = 3.7 Hz, 1H), 1.50 (s, 3H), 1.44 (s, 3H), 1.36 (s, 3H), 1.32 (s, 3H) ppm.
13. **^{13}C NMR (101 MHz, $CDCl^3$)** δ 111.8, 109.6, 105.2, 85.1, 81.2, 74.8, 73.0, 67.6, 26.8, 26.2, 25.2 ppm.
14. **IR (neat)**: 3428, 2986, 2953, 2936, 2905, 2874, 1457, 1374, 1246, 1220, 1161, 1119, 1090 1059, 1030, 1003, 934, 881, 846, 783 cm^{-1}.
15. A qNMR was conducted of **1** (60 mg) in DMSO-d_6 using maleic acid (0.5 equiv, 13.4 mg) as an internal standard, with relaxation time (D1) set to 30 seconds. Maleic acid (99%) was purchased from ACROS Organics and used as received.
16. The reaction was repeated on the same scale. Yield = 2.07 g, 70%.

Working with Hazardous Chemicals

The procedures in *Organic Syntheses* are intended for use only by persons with proper training in experimental organic chemistry. All hazardous materials should be handled using the standard procedures for work with chemicals described in references such as "Prudent Practices in the Laboratory" (The National Academies Press, Washington, D.C., 2011; the full text can be accessed free of charge at http://www.nap.edu/catalog.php?record_id=12654). All chemical waste should be disposed of in accordance with local regulations. For general guidelines for the management of chemical waste, see Chapter 8 of Prudent Practices.

In some articles in *Organic Syntheses*, chemical-specific hazards are highlighted in red "Caution Notes" within a procedure. It is important to recognize that the absence of a caution note does not imply that no significant hazards are associated with the chemicals involved in that procedure. Prior to performing a reaction, a thorough risk assessment should be carried out that includes a review of the potential hazards associated with each chemical and experimental operation on the scale that is planned for the procedure. Guidelines for carrying out a risk assessment and for analyzing the hazards associated with chemicals can be found in Chapter 4 of Prudent Practices.

Discussion

Complex molecule synthesis relies on protective groups to ensure chemo-, regio-, and stereoselectivity.[2] The construction of well-defined oligosaccharides requires selectively masking and unmasking of hydroxyl groups throughout the synthetic route using a host of protective groups.[3-5] Benzyl ethers are important protective groups in the synthesis of carbohydrates due to their excellent stability over a wide range of conditions.[2] However, benzyl ether cleavage requires harsh reduction/oxidation processes, such as catalytic hydrogenolysis, Birch reduction, or oxidation with ozone or BCl_3, that are hazardous[6, 7] and poorly functional group tolerant[2, 8] Mild, selective, and catalytic cleavage of benzyl ethers would render them more versatile and attractive protective groups, conceptually changing the approach toward the synthesis of complex glycans and other natural products. Compared with benzyl ethers, *p*-methoxybenzyl (PMB) ethers can be selectively cleaved using mild stoichiometric oxidants or common photocatalysts due to their lower oxidation potential ($E_{Bn\text{-}O\text{-}Me}$= 2.20 V vs saturated calomel electrode (SCE)[9] and $E_{PMB\text{-}O\text{-}Me}$= 1.60 V vs SCE[9]).[2, 10-12]

A photooxidant with a sufficiently strong oxidizing excited state could facilitate the oxidative cleavage of benzyl ethers with high functional group tolerance. Indeed, using green light irradiation (LEDs centered at 525 nm) and a stoichiometric amount of 2,3-dichloro-5,6-dicyano-1,4-benzoquinone (DDQ,$E^{3}_{DDQ^*/DDQ^-}$ = 3.18 V vs SCE[15]) in wet dichloromethane, complete conversion of benzyl-protected furanose **1a** and selective formation of the desired product **1** is achieved (Figure 7).[13]

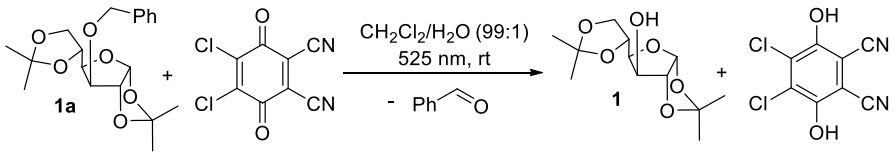

Figure 7. Photooxidative debenzylation with DDQ.

Use of blue lamps (440 nm) resulted in formation of undesired side products.[13] To ease the tedious separation of the stoichiometric byproduct 2,3-dichloro-5,6-dicyano-1,4-hydroquinone ($DDQH_2$), we also developed a catalytic protocol using DDQ (25 mol%) in combination with *tert*-butyl nitrite (TBN, 2 equiv) and air as terminal oxidant (Table 1). [13-21] Both methods were suitable to selectively cleave benzyl ethers on substrates containing acetyl, isopropylidene, and benzoyl protecting groups (**1a**−**4a**) in less than 4 h with excellent yield on a 100 µmol scale (84−96%). Substrates presenting thioethers that potentially cause catalyst poisoning in palladium-catalyzed hydrogenolysis, also reacted smoothly and no sulfoxide or sulfone side-products were identified (**5a**−**11a**). Several common protecting groups that are not tolerated in hydrogenolysis or Birch reduction, such as fluorenylmethoxycarbonyl (Fmoc, **6a, 7a, 8a**), levulinic ester (Lev, **8a**), allyl carbonate (Alloc, **9a**), propargyl carbonate (Poc, **10a**), and benzylidene (**12a**), were well tolerated. Azides are essential handles for bio-orthogonal labeling and are stable to these photooxidative benzyl ether cleavage conditions (**11a**). The high functional group tolerance of the photooxidative debenzylation was key to selectively cleave benzyl ethers in a total synthesis of tetrodotoxin and eribulin B.[22, 23] 2-Naphtylmethylether (NAP, **12a**) is routinely removed using stoichiometric amounts of DDQ in the absence of light. We showed that the protocol using 25 mol% DDQ is also a viable option for NAP cleavage that demands less purification effort. The deprotection of a substrate presenting both benzyl ether and benzyloxycarbonyl (Cbz, **13a**) groups showed that stoichiometric amounts of DDQ are necessary in order to increase the desired reactivity, reduce reaction times and limit the competitive Cbz cleavage. Phenylselenyl (**14a**) and *tert*-butyldimethylsilyl (TBS, **15a**)[24] ethers didn't withstand the photooxidative debenzylation conditions. Deprotection of per-benzylated glucose (**16a**) was not feasible due to precipitation of polar intermediates.

Table 1. Substrate scope of the photooxidative debenzylation protocol.

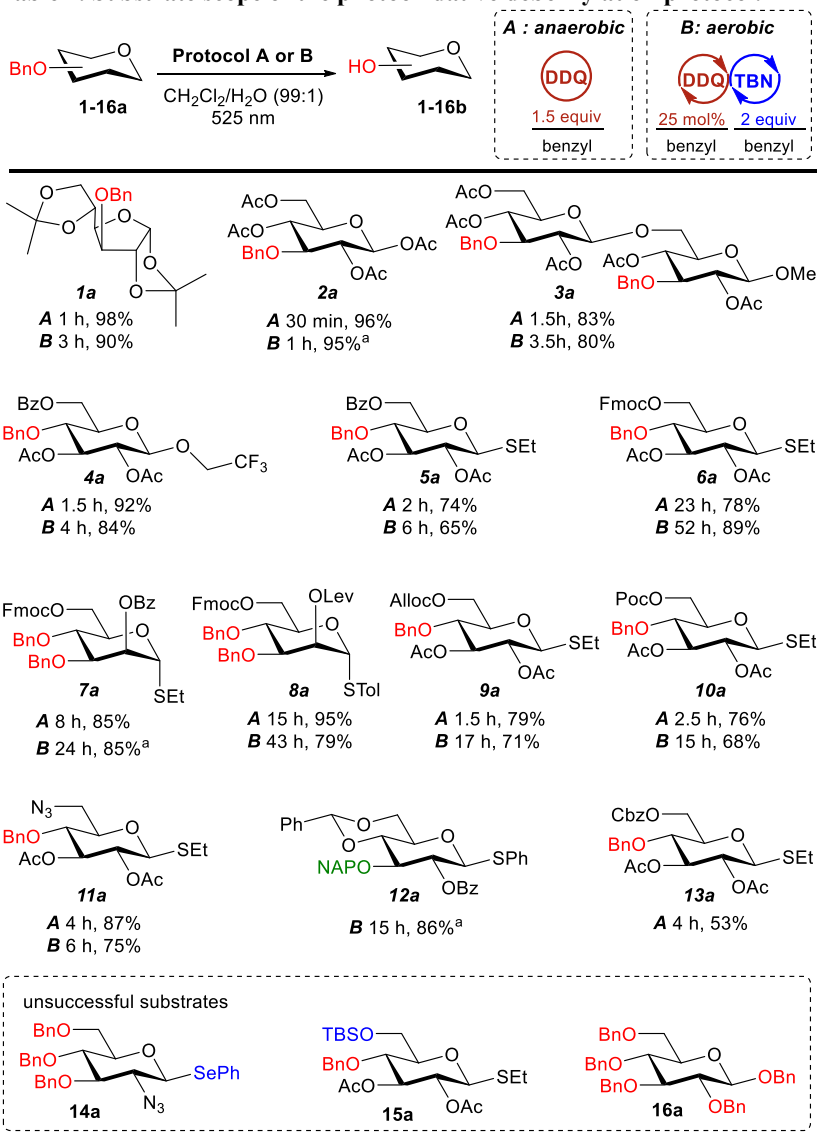

Reaction conditions: benzyl ether (100 µmol), DDQ (protocol A: 150 µmol/benzyl, protocol B: 25 µmol/benzyl), TBN (protocol B, 200 µmol), CH_2Cl_2 (5 mL), H_2O (50 µL), 525 nm irradiation at rt.
[b]Reaction on 50 µmol scale. Isolated yields are reported.

Application of the catalytic methodology (Protocol B) for large-scale debenzylation (11.4 mmol) of **1a** using two 525 nm LED lamps proved ineffective and is accompanied by reproducibility problems, potentially due to poor light penetration. Long reaction times are required and led to cleavage of acid-sensitive isopropylidene groups by interacting with acidic reaction intermediates ($DDQH_2$ and nitrous acid).[25] At this scale, formation of an organic and aqueous layer was observed, which was not the case on the small-scale experiments. The water layer promoted acetal hydrolysis, which was mitigated by lowering the water content (1 to 0.1%) and introducing a buffer (PBS, pH 7.4)[26]. Nevertheless, the low photon flux did not allow for efficient NO_2 generation and precipitation of $DDQH_2$ was observed along with incomplete reactions.

The method using stoichiometric amounts of DDQ (1.2 equiv, Protocol A), on the contrary, can be reproducibly carried out on a 11.4 mmol scale using two LED lamps (Figure 1). Monitoring the transformation by TLC indicated 12 h as the optimal reaction time, with the starting material being nearly consumed and side-products remaining minimal (Figure 2B), ultimately yielding **1** in 78%.

This photooxidative debenzylation strategy overcomes current limitations of benzyl ethers as protecting groups that arise from the harsh conditions necessary for their cleavage. The methodology enables the use of benzyl ethers as orthogonal protective group that is installed and removed throughout the synthesis of complex molecules and clears the path to the development of new synthetic routes in total synthesis.

References

1. Max-Planck-Institute of Colloids and Interfaces, Am Mühlenberg 1, 14476 Potsdam, Germany. Email: Peter.Seeberger@mpikg.mpg.de ORCID 0000-0003-3394-8466**;** Bartholomaeus.Pieber@mpikg.mpg.de ORCID 0000-0001-8689-388X. We gratefully acknowledge the Max-Planck Society for generous financial support. B.P. acknowledges financial support from a Liebig Fellowship of the German Chemical Industry Fund (Fonds der Chemischen Industrie, FCI). E.T.S acknowledges financial support from the Alexander von Humboldt Foundation.

2. Greene, T. W.; Wuts, P. G. M., *Protective Groups in Organic Synthesis*. 1999.
3. Wang, T.; Demchenko, A. V., *Org. Biomol. Chem.* 2019, *17*, 4934-4950.
4. Krasnova, L.; Wong, C. H., *J. Am. Chem. Soc.* 2019, *141*, 3735–3754.
5. Guberman, M.; Seeberger, P. H., *J. Am. Chem. Soc.* 2019, *141*, 5581-5592.
6. Van Ornum, S. G.; Champeau, R. M.; Pariza, R., *Chem. Rev.* 2006, *106*, 2990-3001.
7. Joshi, D. K.; Sutton, J. W.; Carver, S.; Blanchard, J. P., *Org. Process Res. Dev.* 2005, *9*, 997–1002.
8. Crawford, C.; Oscarson, S., *Eur. J. Org. Chem.* 2020, *2020*, 3332-3337.
9. Mayeda, E. A.; Miller, L. L.; Wolf, J. F., *J. Am. Chem. Soc.* 1972, *94*, 6812–6816.
10. Horita, K.; Yoshioka, T.; Tanaka, T.; Oikawa, Y.; Yonemitsu, O., *Tetrahedron* 1986, *42*, 3021-3028.
11. Classon, B.; Garegg, P. J.; Samuelsson, B.; Lawesson, S. O.; Norin, T., *Acta Chem. Scand.* 1984, *38b*, 419-422.
12. Vaino, A. R.; Szarek, W. A., *Synlett* 1995, *1995*, 1157-1158.
13. Cavedon, C.; Sletten, E. T.; Madani, A.; Niemeyer, O.; Seeberger, P. H.; Pieber, B., *Org. Lett.* 2021, *23*, 514-518.
14. Song, C.; Yi, H.; Dou, B.; Li, Y.; Singh, A. K.; Lei, A., *Chem. Commun.* 2017, *53*, 3689-3692.
15. Rusch, F.; Schober, J.-C.; Brasholz, M., *ChemCatChem* 2016, *8*, 2881-2884.
16. Wang, Y.; Wang, S.; Chen, B.; Li, M.; Hu, X.; Hu, B.; Jin, L.; Sun, N.; Shen, Z., *Synlett* 2020, *31*, 261-266.
17. Das, S.; Natarajan, P.; König, B., *Chem. Eur. J.* 2017, *23*, 18161-18165.
18. Pan, D.; Pan, Z.; Hu, Z.; Li, M.; Hu, X.; Jin, L.; Sun, N.; Hu, B.; Shen, Z., *Eur. J. Org. Chem.* 2019, *2019*, 5650-5655.
19. Song, C.; Dong, X.; Yi, H.; Chiang, C.-W.; Lei, A., *ACS Catal.* 2018, *8*, 2195-2199.
20. Shen, Z.; Dai, J.; Xiong, J.; He, X.; Mo, W.; Hu, B.; Sun, N.; Hu, X., *Adv. Synth. Catal.* 2011, *353*, 3031-3038.
21. Shen, Z.; Sheng, L.; Zhang, X.; Mo, W.; Hu, B.; Sun, N.; Hu, X., *Tetrahedron Lett.* 2013, *54*, 1579-1583.
22. Konrad, D. B.; Rühmann, K.-P.; Ando, H.; Hetzler, B. E.; Strassner, N.; Houk, K. N.; Matsuura, B. S.; Trauner, D., *Science* 2022, *377*, 411-415.
23. Nicolaou, K. C.; Pan, S.; Shelke, Y.; Rigol, S.; Bao, R.; Das, D.; Ye, Q., *Proc. Natl. Acad. Sci.* 2022, *119*, e2208938119.

24. Tanemura, K.; Suzuki, T.; Horaguchi, T., *J. Chem. Soc., Perkin Trans. 1* 1992, *22*, 2997-2998.
25. Lloyd, D.; Bylsma, M.; Bright, D. K.; Chen, X.; Bennett, C. S., *J. Org. Chem.* 2017, *82*, 3926-3934.
26. Loka, R. S.; Sletten, E. T.; Barash, U.; Vlodavsky, I.; Nguyen, H. M., *ACS Appl. Mater. Interfaces* 2019, *11*, 244-254.

Appendix
Chemical Abstracts Nomenclature (Registry Number)

Starting material, **1a**: 3-*O*-benzyl-1,2:5,6-di-*O*-isopropylidene-α-D-glucofuranose; (18685-18-2)
DDQ: 2,3-dichloro-5,6-dicyano-1,4-benzoquinone; (84-58-2)
TBN: *tert*-butyl nitrite; (540-80-7)
Product, **1**: 1,2:5,6-di-*O*-isopropylidene-α-D-glucofuranose; (582-52-5)

Amiera Madani completed her undergraduate studies in chemistry at the University of Tübingen (Germany). In 2019 she joined the Max-Planck-Institute of Colloids and Interfaces in Potsdam (Germany) to obtain her doctoral degree in 2022. Her research focuses on the development and mechanistic investigation of reactions involving reactive open-shell intermediates.

Eric T. Sletten completed his undergraduate studies in chemistry at Wartburg College (IA) in 2013. In 2013 he joined the University of Iowa Department of Chemistry and obtained his Ph.D. in 2018. In 2019, he subsequently moved to the Max-Planck-Institute of Colloids and Interfaces in Potsdam (Germany) as a postdoctoral researcher and was awarded Alexander-von-Humboldt postdoctoral research fellowship. His research focuses on the development of methodologies for glycan synthesis.

Cristian Cavedon completed his undergraduate studies in industrial chemistry at the University of Padua (Italy). In 2018 he joined the Max-Planck-Institute of Colloids and Interfaces in Potsdam (Germany) to obtain his doctoral degree in 2021. He is currently a postdoctoral researcher in the Department of Chemistry of the Massachusetts Institute of Technology (USA). His research focuses on the development of organic methodologies using catalysis as well as flow and photochemistry.

Peter H. Seeberger completed his undergraduate studies in chemistry in Erlangen (Germany) and his Ph.D. in biochemistry in Boulder (CO). After postdoctoral research at the Sloan–Kettering Cancer Center in New York (95-97) and positions as Firmenich Associate Professor with tenure at MIT (98–03) and Professor at ETH Zurich (03-09), he is now a Director at the Max–Planck-Institute in Potsdam and Professor at Freie Universität Berlin. His research interests include chemistry, biology, and engineering.

Bart Pieber studied chemistry in Graz (Austria) and received his Ph.D. in 2015. He subsequently moved to the Max-Planck-Institute of Colloids and Interfaces in Potsdam (Germany) for postdoctoral work. In 2018, he was awarded a Liebig fellowship of the German Chemical Industry Funds to start independent research at the same institute. In addition, Bart is a lecturer at the University of Potsdam. His research interests include photocatalysis, reaction and catalyst development, mechanistic investigations and flow chemistry.

Organic Syntheses

^{1}H NMR (400 MHz, $CDCl_3$) of 1:

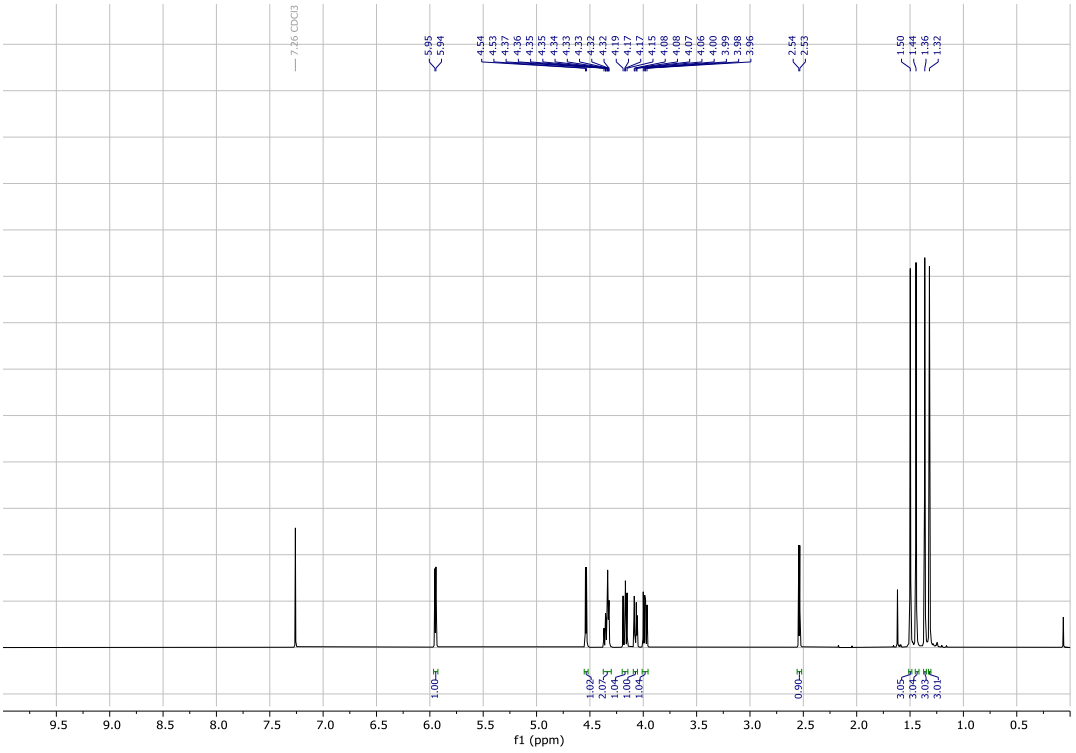

Organic Syntheses

^{13}C NMR (400 MHz, $CDCl_3$) of 1:

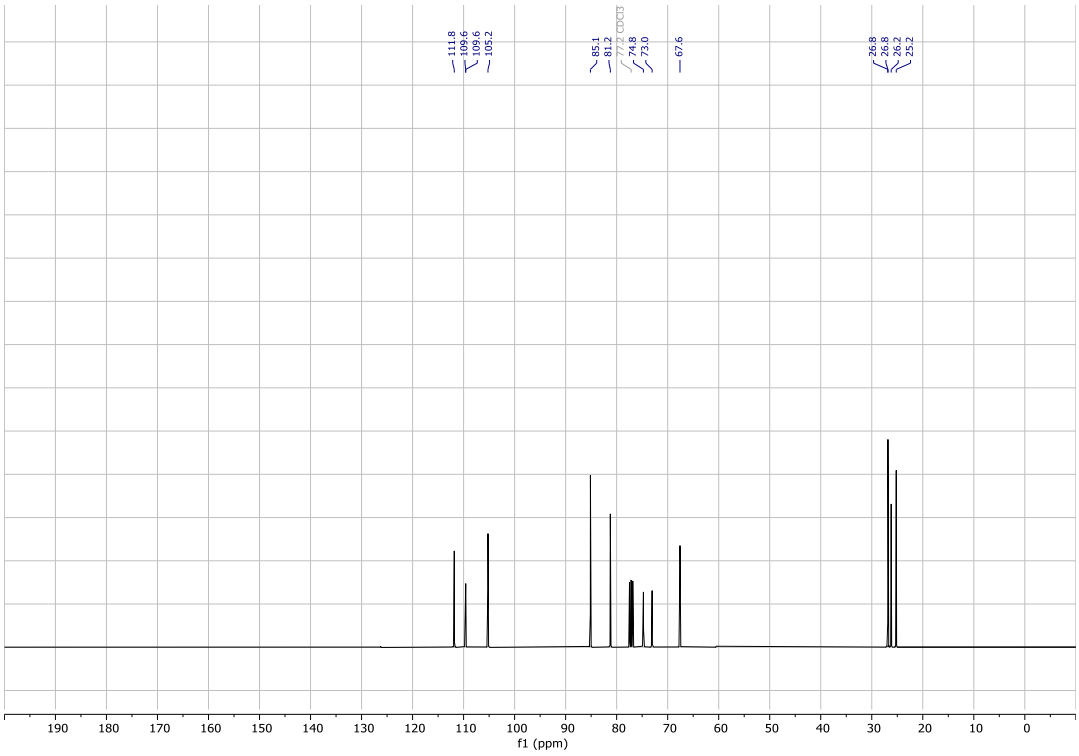

Organic Syntheses

^{1}H qNMR (400 MHz, DMSO-d_6) of 1:

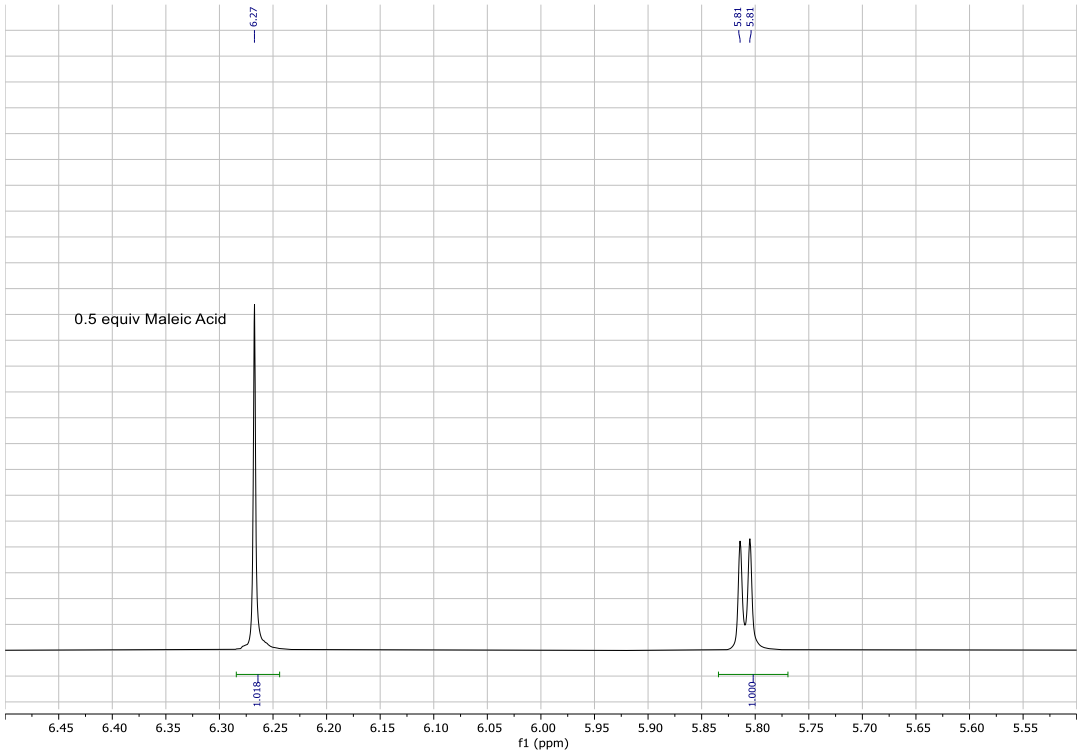

Delay time = 30 sec

6.1 Specific Contribution

We previously developed a visible-light mediated approach to remove benzyl ethers under mild conditions (Chapter 9).[1] A catalytic protocol, using a combination of 2,3-dichloro-5,6-dicyano-1,4-benzoquinone (DDQ) and *tert*-butyl nitrite (TBN) and a stoichiometric version. The preceding chapter above describes our efforts to scale up the protocol to be more widely applicable.

Probing the photocatalytic reaction on large scale (> 2 g), using an experimental setup with two Kessil™ lamps, the debenzylation of 3-*O*-benzyl-1,2:5,6-di-*O*-isopropylidene-α-D-glucofuranose resulted in poor yields and reproducibility issues. Mechanistic knowledge I gained via in situ reaction monitoring helped me identify different factors perturbing the conversion. Low photon flux and small headspace of the pressure-rated flask failed to produce NO_2, necessary to restore DDQ from the hydroquinone $DDQH_2$, rendering the debenzylation inefficient (Figure 6.1 A). Poor light penetration further led to longer reaction times and resulted the cleavage of adjacent isopropylidene protecting groups via interaction with acidic reaction intermediate $DDQH_2$ or nitrous acid, rendering the debenzylation using a complex catalytic system insufficient on large-scale. The formation of an aqueous layer, observed at this scale, further promoted acetal hydrolysis.

Careful investigation of different glassware, lamp position and orientation, and amount of reagents, I was able to find the optimal conditions able to deprotect the sugar in a reproducible fashion, on all scales. Using Phosphate-buffered saline (PBS buffer) and stoichiometric amounts of DDQ (1.2 equiv.) resulted the desired product in good yields (78%) (Figure 6.1 B).

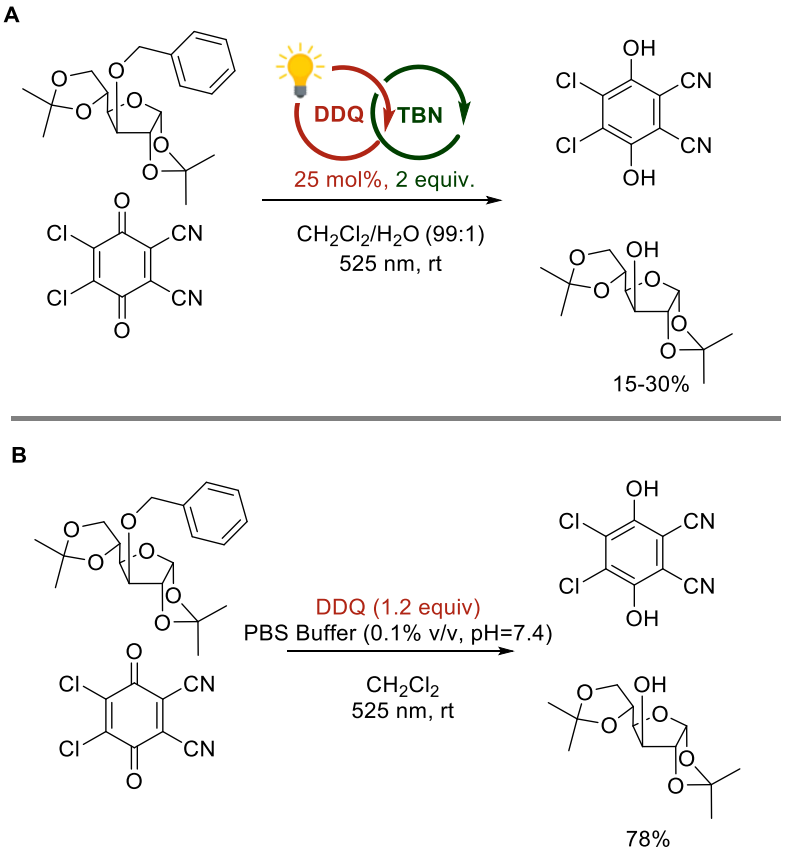

Figure 6.1 Photooxidative debenzylation of 3-*O*-benzyl-1,2:5,6-di-*O*-isopropylidene-α-D-glucofuranose using **A** catalytic amounts of DDQ in combination with TBN and **B** stoichiometric amounts of DDQ.

6.2 References

(1) Cavedon, C.; Sletten, E. T.; Madani, A.; Niemeyer, O.; Seeberger, P. H.; Pieber, B. Visible-Light-Mediated Oxidative Debenzylation Enables the Use of Benzyl Ethers as Temporary Protecting Groups. *Org. Lett.* **2021**, *23* (2), 514-518. DOI: 10.1021/acs.orglett.0c04026.

Chapter 7

Evidence for Photocatalyst Involvement in Oxidative Additions of Nickel-Catalyzed Carboxylate *O*-Arylations

Malik J. A.; **Madani, A**.; Pieber, B.; Seeberger, P. H.

J. Am. Chem. Soc. **2020**, 142, 25, 11042–11049.

https://doi.org/10.1021/jacs.0c02848

JACS
JOURNAL OF THE AMERICAN CHEMICAL SOCIETY

pubs.acs.org/JACS

Article

Evidence for Photocatalyst Involvement in Oxidative Additions of Nickel-Catalyzed Carboxylate *O*-Arylations

Jamal A. Malik, Amiera Madani, Bartholomäus Pieber,* and Peter H. Seeberger*

Cite This: *J. Am. Chem. Soc.* 2020, 142, 11042−11049

Read Online

ACCESS | Metrics & More | Article Recommendations | Supporting Information

ABSTRACT: Dual photocatalysis and nickel catalysis can effect cross-coupling under mild conditions, but little is known about the *in situ* kinetics of this class of reactions. We report a comprehensive kinetic examination of a model carboxylate *O*-arylation, comparing a state-of-the-art homogeneous photocatalyst ($Ir(ppy)_3$) with a competitive heterogeneous photocatalyst (graphitic carbon nitride). Experimental conditions were adjusted such that the nickel catalytic cycle is saturated with excited photocatalyst. This approach was designed to remove the role of the photocatalyst, by which only the intrinsic behaviors of the nickel catalytic cycles are observed. The two reactions did not display identical kinetics. $Ir(ppy)_3$ deactivates the nickel catalytic cycle and creates more dehalogenated side product. Kinetic data for the reaction using $Ir(ppy)_3$ supports a turnover-limiting reductive elimination. Graphitic carbon nitride gave higher selectivity, even at high photocatalyst-to-nickel ratios. The heterogeneous reaction also showed a rate dependence on aryl halide, indicating that oxidative addition plays a role in rate determination. The results argue against the current mechanistic hypothesis, which states that the photocatalyst is only involved to trigger reductive elimination.

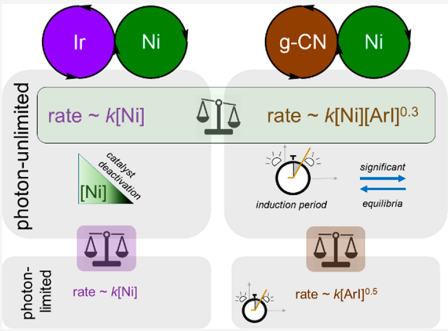

INTRODUCTION

Palladium catalysis is key to many conceptual and practical advances in modern organic chemistry, but the scarcity of palladium bodes poorly for long-term use. As such, transferring well-defined reactivities of palladium to nickel, an isoelectronic and more abundant metal, has been an explicit goal of catalysis for more than 50 years. Low-valent nickel species are capable of undergoing oxidative additions readily, but the subsequent reductive eliminations (REs), particularly for Ni(II) complexes, are thought to be comparatively difficult.[1] Nickel couplings are hence believed to go through higher-valent intermediates,[2,3] accessed by stoichiometric redox modulators, such that the RE is more favorable.[4,5]

The combination of photocatalysis with nickel catalysis has provided an elegant pathway by which nickel can turn over without adding excessive reductants or harsh conditions.[6,7] Iridium polypyridyl complexes were found to act as photocatalysts (PCs) to effect C−N, C−O, C−S, and C−C couplings using nickel(II) precatalysts.[8−11] Subsequent reports showed that the homogeneous iridium photocatalysts can be replaced with heterogeneous graphitic carbon nitride (g-CN) semiconductors, rendering the overall transformations noble-metal-free.[12−16]

The current mechanistic proposal for a relatively well-studied carboxylate *O*-arylation (Figure 1A) in this family of reactions is depicted in Figure 1B.[17] Numerous common nickel(II) precatalysts are viable, which are thought to undergo two single-electron transfers to a bipyridyl Ni(0) **4**. From this reduced species, oxidative addition to form **5** is facile. The catalyst resting state **6** is unable to undergo the necessary reductive elimination. To close the cycle, **6** receives an energy transfer from the excited state of the photocatalyst, which enables C−O bond formation.[18,19] Stern−Volmer quenching studies,[17] transient absorption spectroscopy,[18] and computational studies[19] have been used to support quenching of $Ir(ppy)_3$ by a potential nickel(II) intermediate.

Broadly, the substrate scopes for both homogeneous ($Ir(ppy)_3$) and heterogeneous (g-CN) variations of carbon−heteroatom couplings contain only electron-poor aryl halides and electron-neutral or rich coupling partners (HNR_2, HOR, HSR, etc.). To our knowledge, these limitations have not been explicitly discussed in a mechanistic context. The $Ir(ppy)_3$-catalyzed homogeneous carboxylate *O*-arylation accommodates only electron-withdrawing aryl bromides, and electron-withdrawing carboxylic acids are absent. Such a combination could be explained by arguing that an S_NAr-type reductive elimination is required.

However, tension between the existing mechanism and the resulting substrate scopes surfaced during our development of the heterogeneous congener using graphitic carbon nitride

Received: March 12, 2020
Published: May 29, 2020

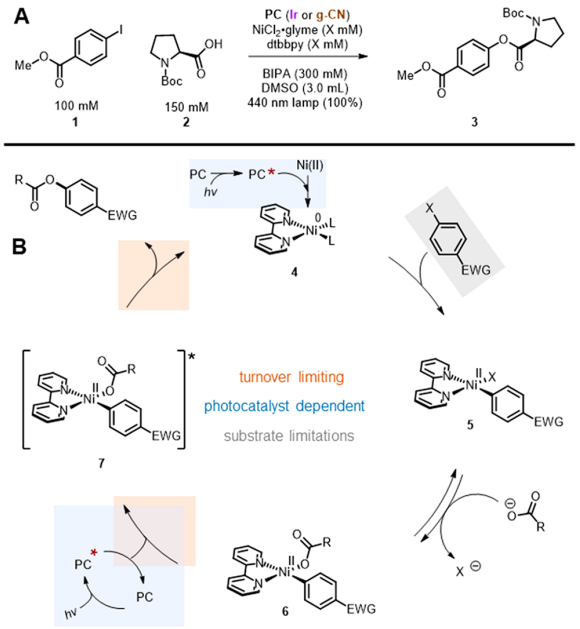

Figure 1. (A) The two dual photocatalyzed and nickel-catalyzed reactions studied in this work. Standard conditions are shown. Deviations from these conditions in any subsequent figure will be noted. (B) Mechanistic hypothesis presented in 2017.[17]

photocatalysts.[12] During a cursory kinetic study, methyl 4-iodobenzoate **1** (96%, 4 h) coupled considerably faster than methyl 4-bromobenzoate (88%, 48 h) with *N*-Boc-proline **2**. Once the nickel catalytic cycle is at the resting state **6**, the differences between an aryl iodide and bromide are irrelevant, as only the aryl ring remains on-cycle. This discrepancy in rate must therefore arise from the oxidative addition or ligand exchange step. As even aryl chlorides show facile proclivities toward oxidative addition with low-valent nickel in non-photochemical reactions,[20] and the homogeneous analogue converted aryl bromides efficiently, we began to question whether the currently accepted mechanism is operational with the heterogeneous congener. Given that we found the same electronic substituent limitations with g-CN as for $Ir(ppy)_3$, albeit with iodides instead of bromides, we further wondered if there were mechanistic commonalities among the two *O*-arylations.

Electron deficiency of an aryl halide can accelerate oxidative additions, as the aryl halide is itself formally reduced. In this vein, aryl halide limitations in this class of reactions could be explained by scission of the aryl halide bond that pushes at the energetic boundaries of photocatalytic reductions. Reduction potentials of common aryl halides range from −1.0 to −3.5 V vs SCE,[21,22] with electron-donating groups and higher-row halides ranking as more difficult. The iridium polypyridyl complex $Ir(ppy)_3$ used in the homogeneous *O*-arylation has a reduction potential of −1.73 V, and substrate limitations could be a marker of the Ir(III)*/Ir(IV) potential within the aforementioned range.[23] Such logic has been invoked for the thioetherification of aryl iodides[24] as well as dehalogenations[25,26] with this exact photocatalyst. Stern−Volmer and transient absorption studies showed that aryl iodides could in fact quench the excited triplet state of $Ir(ppy)_3$,[24] forming an aryl radical.

With these considerations in mind, we set out to answer three basic questions: (1) Do the heterogeneous and homogeneous reactions proceed by the same mechanism? If so, (2) do they both conform to the extant hypothesis, in which reductive elimination is turnover-limiting, and (3) are the turnover-limiting steps and the steps which require a photocatalyst the same?

RESEARCH PLAN AND HYPOTHESES

Numerous mechanistic studies have been undertaken for photocatalytic reactions in general.[27] Inquiries on dual nickel-catalyzed and photocatalyzed carbon−heteroatom cross-couplings have largely focused on the character of the interaction between photocatalyst and metal catalyst.[19,28] However, no in-depth kinetics studies of any of these reactions have been disclosed.

Kinetics studies of catalytic systems that observe native reaction conditions throughout their entire course can afford a wealth of qualitative and quantitative information usually inaccessible from studies of a narrower scope.[29,30] However, "native" reaction conditions are typically based on the methodology studies where the primary aim is the optimization of yield. Studies of dual photocatalytic and nickel catalytic reactions under such conditions may give data obfuscated by rate-limiting processes derived from interaction between the PC and metal catalyst. Kinetically, this may paint an incomplete picture of the reaction, but these data could arguably be useful to synthetic chemists considering using such a method. We therefore sought to observe the homogeneous and heterogeneous dual photo- and nickel-catalyzed *O*-arylations in two regimes each. The first would be closer to the standard conditions obtained during methodology development ("photon-limited"), geared toward understanding overall reaction behavior. The second would be in a regime in which the metal catalyst is saturated with excited photocatalyst species ("photon-unlimited"). Under such conditions, photons are essentially treated as a reagent in high excess. Data obtained in this regime allow us to both evaluate the intrinsic kinetics of the nickel cycle, as well as enable a more rigorous comparison between data sets of different photocatalysts.

As no *in situ* studies exist to date for any dual nickel-catalyzed and photocatalyzed cross-couplings, comparison of the photon-limited and photon-unlimited regimes with each other for the two reactions would be of general interest. We anticipated that we would see differences between the photon-limited and photon-unlimited regimes, potentially in the magnitude of the reagents' coefficients in the rate laws.

Most importantly, the intrinsic, photon-unlimited kinetics of both reactions should be compared with each other and to the extant mechanistic hypothesis. The kinetics in photon-unlimited regimes of the homogeneous and heterogeneous reactions should be identical since the PC should drop out of the rate law. The extant hypothesis for the dual photo- and nickel-catalyzed carboxylate *O*-arylation, congruent with the accrued understanding of nickel catalysis, is that the PC enables a turnover-limiting reductive elimination.[17] Thus, we predicted that the photon-unlimited regime for both reactions would give rate $\sim k[\mathrm{Ni}]$.

RESULTS

Heterogeneous (Graphitic Carbon Nitride) PC. *Photon-Limited (3.33 mg/mL g-CN, 5 mM Ni·L, 50% Lamp Power).* First, the kinetics of the carboxylate *O*-arylation of aryl iodides using the graphitic carbon nitride CN-OA-m[31] as a photocatalyst in photon-limited conditions were analyzed. These photocatalytic reactions can be tracked by attaching a custom vial to an *in situ* infrared probe.[12] Using a stronger LED lamp for increased photon flux and improved reproducibility, we ensured that the infrared technique tracked reaction progress by verification with an orthogonal method (Figure S2).

https://dx.doi.org/10.1021/jacs.0c02848
J. Am. Chem. Soc. 2020, 142, 11042−11049

From a cursory, qualitative glance, these reactions at the native conditions display no unusual behavior, except for exhibiting a short induction period. A series of experiments were conducted to assess which reagents were responsible for this induction (Figure S5). Delaying the injection of $NiCl_2$·glyme and its bipyridyl ligand or aryl iodide **1** resulted in immediate productive catalysis. Delayed injection of carboxylic acid **2** retained the induction period. Conspicuously, delaying addition of the base *N-tert*-butylisopropylamine (BIPA) resulted in a reaction profile slightly suggestive of catalyst activation,[32] indicating that the secondary amine plays a role more significant than simply that of a Brønsted base.

Varying the nickel concentration from 5 to 20 mM unsurprisingly resulted in no rate change (Figure S6). At 5 mM Ni, no catalyst deactivation or product inhibition was observed (Figure S8), which is expected at such a high metal catalyst concentration. Surprisingly, modulation in [**1**] resulted in a fractionally positive order (Figure S9) for the aryl iodide. Carboxylic acid **2** showed a zero-order dependence (Figure S10). Reagent orders obtained in this regime should be considered with some measure of caution as the interactions between PC and Ni are ill-defined. However, we were curious if the reagent order of the aryl iodide would persist in the photon-unlimited regime, as it would be a significant clue to help resolve the questions posed above.

Photon-Unlimited (3.33 mg/mL g-CN, 0.2 mM Ni·L, 100% Lamp Power). To switch from the photon-limited to the photon-unlimited regime, we needed to increase the ratio of photons and/or PC to nickel. Although numerous photocatalytic reactions with metal centers have been tracked with *in situ* apparatuses,[33] to our knowledge only one study has described finding a region in which the metal's access to excitation is carefully controlled to be unimpeded.[34] In the work of Lehnherr et al., light directly excited a metal catalyst, with no photocatalytic intermediary. To find a region in which their metal catalyst was not limited by throughput of photons, initial rate was plotted against catalyst concentration, and at lower concentrations a roughly linear correlation is apparent. To make a comparable plot, we retained a high PC loading and maximum lamp power (Figure 2A).

Moving from high to low nickel concentrations along this plot surprisingly did not provide an identical shape to that of the literature precedent. Specifically, we observed an unexpected "peak" where catalysis has a much higher rate, around 1 mM. Although further studies are required to account for this behavior, it is possible that, above a certain threshold, the metal catalyst engages in some combination of comproportionation[35,36] and/or higher-order nickel species thought to be catalytically relevant.[37,38]

The area at very low concentration of nickel would likely provide a regime in which the nickel catalytic cycle was not limited by access to an excited photocatalytic species. To confirm this was the case, at low concentrations we used variable time normalization analysis (VTNA)[39] to find a first-order dependence on nickel between 0.15−0.25 mM (Figure S11). Kinetic studies in this area are expected to produce data that reflect the intrinsic characteristics of the nickel cycle.

To probe the robustness of the nickel catalyst, two "same-excess" experiments were conducted[29,40] under photon-unlimited conditions and the less concentrated was time-shifted on the *x*-axis (Figure 2B). Overlay here indicates that the product does not inhibit catalysis, nor does meaningful or disproportionate catalyst deactivation occur.

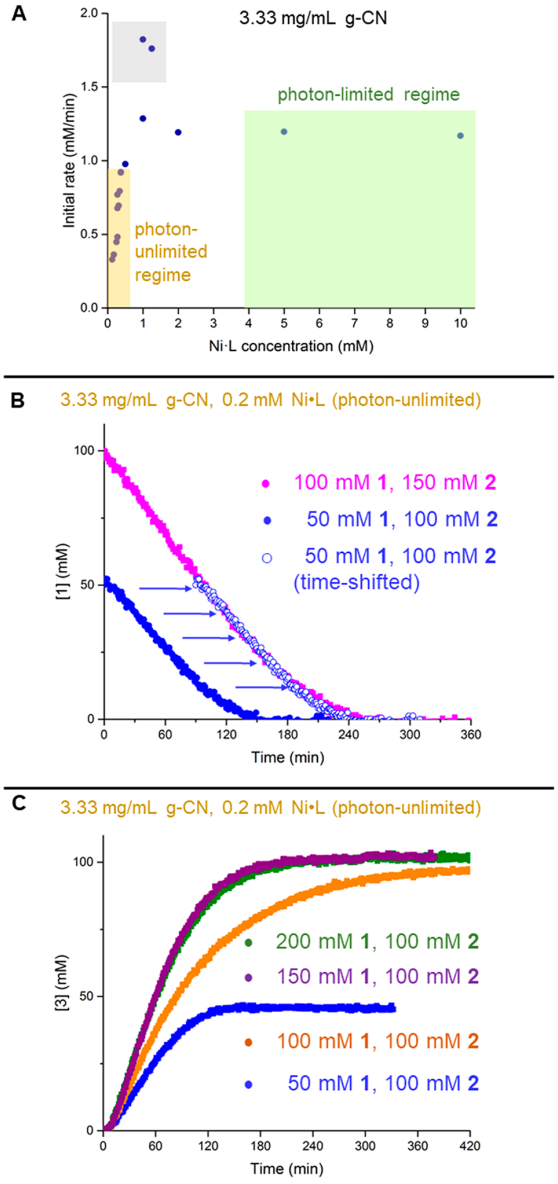

Figure 2. Key experiments of heterogeneous congener. (A) Overview of where the photon-limited and unlimited regimes could be identified. (B) Time-shifted same excess experiments. Overlay indicates lack of catalyst deactivation or product inhibition. (C) Positive-order dependence of aryl iodide observed.

Experiments to determine the reagent orders of the substrates revealed that aryl iodide again exhibited a positive order dependence (Figure 2C). Due to the induction period, first attempts at VTNA overlay were found to be problematic (Figure S12). Elegant mathematical solutions to this common issue have been disclosed,[41] but the most rigorous would require spectroscopic determination of the active catalyst concentration. Repeating the different excess experiments with delayed catalyst injections (Figure S13), which bypass the induction period as described above, cleanly leads to a reagent order of 0.3 under 150 mM [**1**].

https://dx.doi.org/10.1021/jacs.0c02848
J. Am. Chem. Soc. 2020, 142, 11042−11049

Examination of the dependence on reagents' concentrations for **2**, the base, and the photocatalyst provided a much less straightforward picture. All three reagents exhibit positive order dependence at lower concentrations and inhibitory effects at higher concentrations (Figures S14–S16).

Homogeneous ($Ir(ppy)_3$) PC. We began the homogeneous studies by attempting to determine a proper photocatalyst loading that would enable photon-limited conditions. Initial experiments with 0.1 mM Ni·L and the standard (1 mM) photocatalyst concentration[17] gave unsatisfactory yields. We observed dehalogenation accompanying productive catalysis (Table 1). Formation of the phenol side product **9** appears to be independent of an unfavorable PC-to-Ni ratio.

Table 1. Screening to Determine Photocatalyst Loading for Photon-Limited Regimes of the Homogeneous Reaction[a]

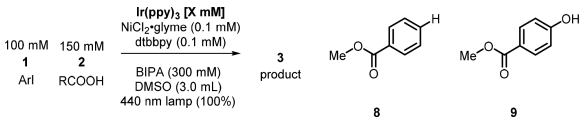

mM PC	3	1	8	9	Mass balance
1	62	0	18	6	86
0.5	83	0	10	4	97
0.25	82	0	8	3	94
0.125	90	0	5	5	100

[a]Final concentrations of product and side products were determined by ^1H NMR using 1,3,5-trimethoxybenzene as an internal standard.

High concentrations of $Ir(ppy)_3$ accelerate the consumption of **1** but not significantly the rate of product formation (Figure 3A). This finding is in striking contrast to the heterogeneous analogue, where slower product formation is a function of slower consumption of **1** at higher PC loading (Figure S16). Experiments with 0.125 mM PC loading (Figure 3A, blue) appear to be limited by the relay of energy from PC to Ni (Figure S17), and are the basis for the photon-limited studies.

Photon-Limited (0.125 mM $Ir(ppy)_3$, 0.1 mM Ni·L, 100% Lamp Power). The first noteworthy qualitative observation of iridium-catalyzed *O*-arylations is the lack of induction period. Catalysis begins immediately in a positive-order fashion. Increasing concentration of nickel leads to increased rate, which was determined to be a first-order dependence by VTNA (Figure S18). A same-excess experiment shows no deactivation of the nickel throughout the course of the reaction (Figure S19). In contrast to the heterogeneous congener, no rate dependence was found for **1** or **2** (Figure S20). Interestingly, increasing concentration of base increases the rate (Figure S21). Again, some caution is advised in mechanistic interpretation from these data, as these conditions are designed to maximize yield. However, the lack of rate dependence on aryl iodide could be a significant finding if it persisted in photon-unlimited conditions.

Photon-Unlimited (1 mM $Ir(ppy)_3$, 0.2 mM Ni·L, 100% Lamp Power). In order to draw meaningful comparisons between the two photon-unlimited data sets, we sought to use the same $[Ni]_{t=0}$ as was used for the heterogeneous system. As such, finding the photon-unlimited regime for the homogeneous reaction occurred through a reverse process from the heterogeneous case. A short series of experiments was conducted in which the nickel concentration was kept constant and the photocatalyst concentration was raised, similar to

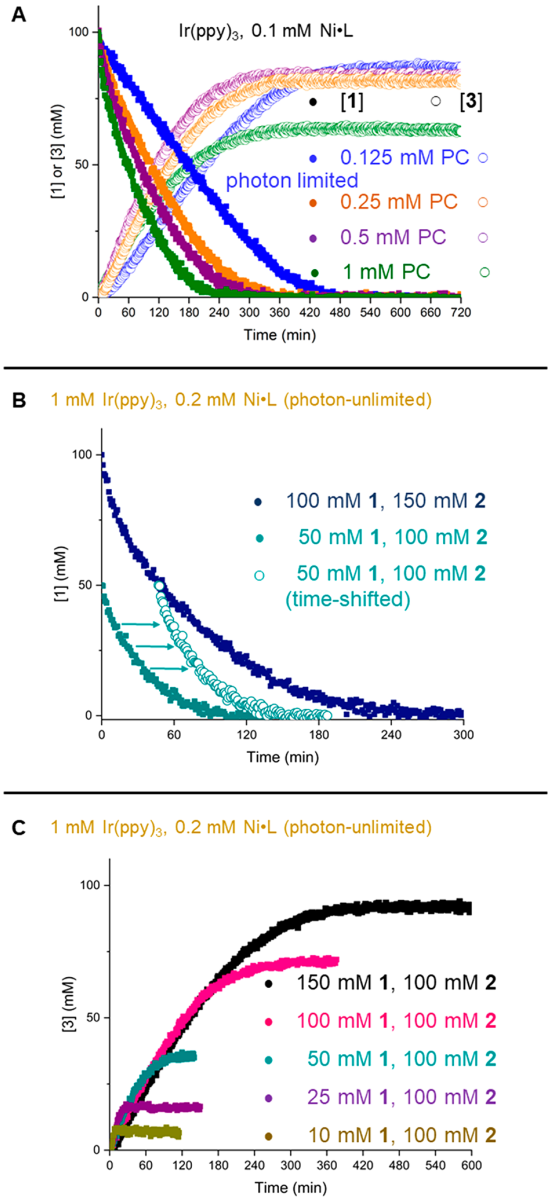

Figure 3. Key experiments of homogeneous congener. (A) Identification of photon-limited regime by reaction fingerprint; reactions progress of blue curve appears to be limited by interaction between PC and Ni. (B) Same excess experiment shows catalyst deactivation intrinsic to iridium-catalyzed *O*-arylations. (C) Rate is independent of [**1**].

Figure 3A (Figure S22). VTNA analysis showed first-order nickel dependence in the concentration range around 0.2 mM Ni at 1 mM $Ir(ppy)_3$ (Figure S24). Corroboration that this approach gives a photon-unlimited regime was found through data obtained in a similar regime derived from an initial-rate plot (Figures S27–S31).

A major difference between the heterogeneous and homogeneous reaction was apparent from the same-excess experiment, where no overlay was observed (Figure 3B). Should the product inhibit catalysis, an effect in the

https://dx.doi.org/10.1021/jacs.0c02848
J. Am. Chem. Soc. 2020, 142, 11042–11049

heterogeneous reaction would have been observed, so we can attribute this behavior to catalyst deactivation.

Experiments varying the amounts of substrate and coupling partner were conducted to obtain the reagent orders of our reactants. In contrast to the heterogeneous reaction, we found the rate to be essentially independent of the concentration of **1** (Figure 3C). The dependence on [**2**] was not found to be significant (Figure S25). Last, we modified the amount of base while keeping all other reagents constant. Similar to the observation from the photon-limited data set, this change was the sole factor that accelerates the homogeneous reaction (Figure S26).

DISCUSSION

The most conspicuous finding of this study was the rejection of the hypothesis that the kinetics of both systems would give identical rate laws. In other words, as particular care was taken such that the nickel cycle was saturated with excited photocatalyst species for both systems, the intrinsic kinetics of a nickel cross-coupling cycle should have been identical between the two had the mechanisms been the same.

The chief quantitative finding of this study is the fractional dependence of aryl iodide **1** in the heterogeneous rate law. To some degree in the heterogeneous congener, oxidative addition is turnover-limiting. We propose that this is a result of direct photocatalytic activation of the substrate (Figure 4B). The fractional order arises as this activation occurs off of the nickel cycle. Nickel is first-order as it intercepts the radical species on the nickel catalytic cycle.

This process may have been overlooked because it is not necessarily turnover-limiting. The reduction potential of Ir(III)*/Ir(IV), −1.73 V, is sufficient to donate an electron to the aryl halide **1**;[25,42,43] this step is photocatalyst-dependent but fast for aryl iodides (Figure 4B). In contrast, the analogous excited state of the graphitic carbon nitride used in this study is less reducing (up to −1.65 V vs SCE). The capacity for electron transfer is worse, and therefore even in conditions that can be considered photon-unlimited, formation of oxidative addition intermediate **5** is still limited by the kinetically relevant halide fragmentation.

We reject the hypothesis that photocatalysts are required only as a late-cycle trigger for RE. We contend that the photocatalyst is required for at *least* one additional point on the catalytic cycle, namely for single-electron transfer to the aryl halide. Substrate limitations for dual photo- and nickel-catalyzed carbon−heteroatom cross-couplings derive from this elementary step. The most obvious example is the far superior conversion of aryl bromides in this homogeneous *O*-arylation compared to the heterogeneous congener. Such a framework also harmonizes the mechanisms by which these transformations occur with the existing body of photocatalytic dehalogenations and radical-based transformations.[25,26]

To augment our understanding of the heterogeneous reaction, we created a Hammett plot examining rate dependencies on aryl iodides with substituents of varying electronic character (Figure 4C). Qualitatively, this shape is also seen for the oxidative addition of tris(triphenylphosphine)nickel(0) to aryl chlorides.[20] Our ρ value (2.1) is far below that of this more traditional oxidative addition (8.8), thought to proceed through an S_NAr-type mechanism. This could be explained by differences in ligand systems and halides, but also could point to a lowered dependence on the electronic substituent due to a non-concerted oxidative addition.

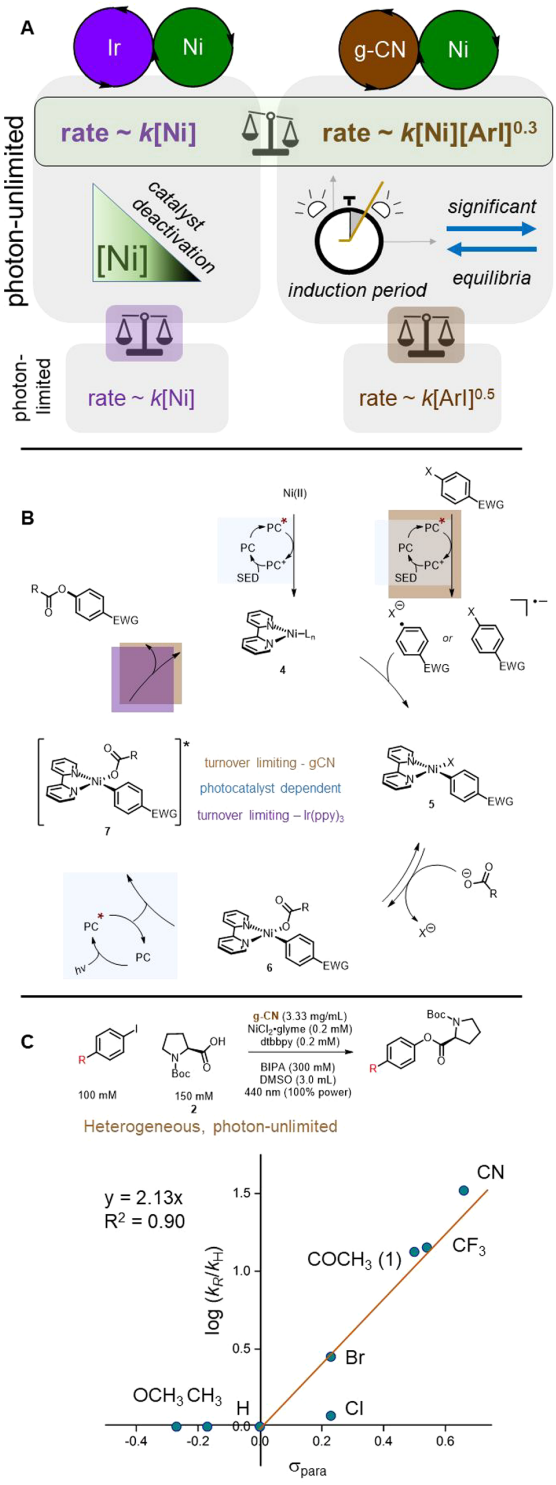

Figure 4. (A) Key findings of this study. (B) Updated mechanistic proposal. Secondary amine base is proposed to close the photoredox cycle by serving as single electron donor (SED). (C) Hammett plot for heterogeneous congener supports that oxidative addition is to some degree turnover-limiting.

https://dx.doi.org/10.1021/jacs.0c02848
J. Am. Chem. Soc. 2020, 142, 11042−11049

With a rate law proportional only to the nickel concentration, data for the homogeneous reaction could reasonably fit three turnover-limiting steps: a unimolecular rearrangement, ligand dissociation, or reductive elimination. We have observed nothing to support or reject the first two. Given that the incumbent hypothesis is that RE is turnover-limiting, our data support the existing proposals. As we had originally predicted, our kinetic data here likely reflects the limitations inherent to nickel catalysis.

Whether or not **6** requires a photocatalyst to trigger RE likely depends on the oxidation state of this intermediate. It has been clearly demonstrated that a Ni(II) resting state cannot undergo RE without photocatalytic excitation.[17−19] However, extensive literature precedent points to the viability of multiple nickel oxidation states in cross-coupling reactions across very different conditions,[35,44,45] and the oxidation state of the on-cycle intermediate for these photochemical reactions has yet to be convincingly resolved. Should this intermediate require activation via energy/electron transfer in the homogeneous reactions, it would not be turnover-limiting, given the photon-unlimited environment.

Of note is the fact that the only way to accelerate the homogeneous reaction was by addition of more secondary amine base, which is already in large excess. We offer three potential explanations. First, and most likely, the secondary amine donates an electron to $[Ir(ppy)_3]^+$ to regenerate the photocatalytic cycle. We can assume that the concentration of **2** requires equimolar amounts of base for deprotonation, and extra amine beyond that point fulfills various roles including weak ligand and electron source. Second, the base is potentially involved in the organization of the nickel catalyst to some degree, evinced by the "reaction fingerprint" of the heterogeneous reaction when the base is injected after a delay (Figure S5). As such, it is possible that its presence does not outright accelerate the reaction as much as it is as guard against decelerating or deactivating processes. Alternatively, or additionally, weak coordination of the base to the square planar pre-RE complex could create a more encumbered five-coordinate complex that is more prone to elimination,[46,47] or is better tuned to absorb an energy transfer.[28]

Qualitatively, two main observations stand out for iridium-catalyzed carboxylate *O*-arylations. First, this system inherently tends to be less selective. In the photon-unlimited regime, at reactions with reasonable concentrations of substrates, yields were frequently in the 70−80% range, often accompanied by significant dehalogenation of the aryl iodide. We believe that this results from speeding up photocatalytic activation of the aryl iodide beyond the capacity of the nickel species to trap the radical on-cycle.

Second, the homogeneous reactions have an intrinsic propensity for catalyst deactivation. Kinetics for the photon-limited and photon-unlimited regimes were essentially the same outside of the fact that catalyst deactivation was not observed in the photon-limited regime. We contend that dual iridium- and nickel-catalyzed processes operate at inflated nickel concentrations to compensate for this inherent deactivation.

Qualitatively, the induction period in the heterogeneous congener notably differs from the homogeneous reaction. We observe small amounts of consumption of aryl iodide during the delay before product begins to form. If reduction of the Ni(II) precatalyst to a lower-valent species is requisite for productive catalysis, it is possible that this reduction is parallel to or intertwined with dehalogenation.

An unexpected revelation of the heterogeneous reaction is seen in the studies modulating the photocatalyst loading (Figure S16). In contrast to the homogeneous reaction, in which additional PC accelerates consumption of **1** indiscriminately, excess g-CN loading shows slower catalysis but with reasonable preservation of selectivity. We again attribute this to the weaker reduction potential of graphitic carbon nitrides, and is a potential upside to the more limited scope. Such a finding portends well for scalability as well as for sensitive or late-stage functionalization. Careful optimization of the ratios of photocatalyst, nickel, and substrate is less likely to be necessary with graphitic carbon nitrides.

■ CONCLUSION

Efforts to swap photocatalysts in dual photocatalytic and metal catalytic systems may not preserve the inherent reactivity of the metal catalytic cycle. Homogeneous and heterogeneous esterifications differ primarily in that the heterogeneous congener showed a rate dependence on the aryl halide substrate. We ascribe this to the nickel trapping an off-cycle radical anion generated by the photocatalyst and the aryl halide. In this sense, the requirements for electron-withdrawing substrates may be ascribed to an energetic barrier that is independent of the nickel catalytic cycle. Overcoming such limitations likely must occur through photocatalyst development and tuning to maximize the reduction potential of the excited PC. Alternatively, methods to front-load the energetic relay from external source to photocatalyst to substrate show great promise.[48] However, as our PC and nickel screenings to find different regimes show, using a PC that is too reducing for the chosen substrate and/or metal catalyst can lead to over-reduction and catalyst deactivation. Countering this requires careful modulation of PC and metal catalyst concentrations. Hence, for the $Ir(ppy)_3$-catalyzed *O*-arylation shown here, a photon-limited approach is desirable. Optimization of the graphitic carbon nitride conditions did not require such considerations. At least partially due to the reduction potential of the PC*, nickel catalyst concentration could be lowered up to 50 times from what was used in methodological development without observing a significant amount of nickel catalyst deactivation. Additionally, peak catalytic activity was found at a much lower concentration of nickel than used in method development. The choice of photocatalyst may, among other things, be determined by the electronic character of the substrate, as less dehalogenation was observed in the g-CN case. We believe that photocatalysts with weaker reduction potentials, such as graphitic carbon nitrides, are less likely to participate in a Ni(0)/Ni(II) cycle.

■ ASSOCIATED CONTENT

Supporting Information

The Supporting Information is available free of charge at https://pubs.acs.org/doi/10.1021/jacs.0c02848.

Experimental procedures and data (PDF)

■ AUTHOR INFORMATION

Corresponding Authors

Bartholomäus Pieber − *Department of Biomolecular Systems, Max-Planck-Institute of Colloids and Interfaces, 14476*

https://dx.doi.org/10.1021/jacs.0c02848
J. Am. Chem. Soc. 2020, 142, 11042−11049

Potsdam, Germany; orcid.org/0000-0001-8689-388X; Email: bartholomaeus.pieber@mpikg.mpg.de

Peter H. Seeberger − *Department of Biomolecular Systems, Max-Planck-Institute of Colloids and Interfaces, 14476 Potsdam, Germany; Department of Chemistry and Biochemistry, Freie Universität Berlin, 14195 Berlin, Germany;* orcid.org/0000-0003-3394-8466; Email: peter.seeberger@mpikg.mpg.de

Authors

Jamal A. Malik − *Department of Biomolecular Systems, Max-Planck-Institute of Colloids and Interfaces, 14476 Potsdam, Germany;* orcid.org/0000-0003-3726-5902

Amiera Madani − *Department of Biomolecular Systems, Max-Planck-Institute of Colloids and Interfaces, 14476 Potsdam, Germany; Department of Chemistry and Biochemistry, Freie Universität Berlin, 14195 Berlin, Germany;* orcid.org/0000-0001-8995-0966

Complete contact information is available at: https://pubs.acs.org/10.1021/jacs.0c02848

Notes

The authors declare no competing financial interest.

■ ACKNOWLEDGMENTS

We gratefully acknowledge the Max-Planck Society for generous financial support. A.M. and B.P. acknowledge the Deutsche Forschungsgemeinschaft (DFG, German Research Foundation) under Germany's Excellence Strategy−EXC 2008/1 (UniSysCat)−390540038 for financial support. B.P. acknowledges financial support by a Liebig Fellowship from the German Chemical Industry Fund (Fonds der Chemischen Industrie, FCI). We also gratefully thank Dr. Matt Mower (Janssen Pharmaceutical), Prof. Keary Mark Engle (TSRI), and anonymous reviewers for helpful discussions. A version of this research was previously posted to ChemRxiv: DOI: 10.26434/chemrxiv.11973141.v1

■ REFERENCES

(1) Tasker, S. Z.; Standley, E. A.; Jamison, T. F. Recent advances in homogeneous nickel catalysis. *Nature* **2014**, *509*, 299−309.

(2) Schultz, J. W.; Fuchigami, K.; Zheng, B.; Rath, N. P.; Mirica, L. M. Isolated Organometallic Nickel(III) and Nickel(IV) Complexes Relevant to Carbon-Carbon Bond Formation Reactions. *J. Am. Chem. Soc.* **2016**, *138*, 12928−12934.

(3) Jones, G. D.; Martin, J. L.; McFarland, C.; Allen, O. R.; Hall, R. E.; Haley, A. D.; Brandon, R. J.; Konovalova, T.; Desrochers, P. J.; Pulay, P.; Vicic, D. A. Ligand Redox Effects in the Synthesis, Electronic Structure, and Reactivity of an Alkyl-Alkyl Cross-Coupling Catalyst. *J. Am. Chem. Soc.* **2006**, *128*, 13175−13183.

(4) Colon, I.; Kelsey, D. R. Coupling of aryl chlorides by nickel and reducing metals. *J. Org. Chem.* **1986**, *51*, 2627−2637.

(5) Meucci, E. A.; Ariafard, A.; Canty, A. J.; Kampf, J. W.; Sanford, M. S. Aryl-Fluoride Bond-Forming Reductive Elimination from Nickel(IV) Centers. *J. Am. Chem. Soc.* **2019**, *141*, 13261−13267.

(6) Skubi, K. L.; Blum, T. R.; Yoon, T. P. Dual Catalysis Strategies in Photochemical Synthesis. *Chem. Rev.* **2016**, *116*, 10035−10074.

(7) Cavedon, C.; Seeberger, P. H.; Pieber, B. Photochemical Strategies for Carbon-Heteroatom Bond Formation. *Eur. J. Org. Chem.* **2020**, *2020*, 1379−1392.

(8) Twilton, J.; Le, C.; Zhang, P.; Shaw, M. H.; Evans, R. W.; MacMillan, D. W. C. The Merger of Transition Metal and Photocatalysis. *Nat. Rev. Chem.* **2017**, *1*, 0052.

(9) Milligan, J. A.; Phelan, J. P.; Badir, S. O.; Molander, G. A. Alkyl Carbon-Carbon Bond Formation by Nickel/Photoredox Cross-Coupling. *Angew. Chem., Int. Ed.* **2019**, *58*, 6152−6163.

(10) Oderinde, M. S.; Frenette, M.; Robbins, D. W.; Aquila, B.; Johannes, J. W. Photoredox Mediated Nickel Catalyzed Cross-Coupling of Thiols With Aryl and Heteroaryl Iodides via Thiyl Radicals. *J. Am. Chem. Soc.* **2016**, *138*, 1760−1763.

(11) Oderinde, M. S.; Jones, N. H.; Juneau, A.; Frenette, M.; Aquila, B.; Tentarelli, S.; Robbins, D. W.; Johannes, J. W. Highly Chemoselective Iridium Photoredox and Nickel Catalysis for the Cross-Coupling of Primary Aryl Amines with Aryl Halides. *Angew. Chem., Int. Ed.* **2016**, *55*, 13219−13223.

(12) Pieber, B.; Malik, J. A.; Cavedon, C.; Gisbertz, S.; Savateev, A.; Cruz, D.; Heil, T.; Zhang, G.; Seeberger, P. H. Semi-heterogeneous Dual Nickel/Photocatalysis using Carbon Nitrides: Esterification of Carboxylic Acids with Aryl Halides. *Angew. Chem., Int. Ed.* **2019**, *58*, 9575−9580.

(13) Cavedon, C.; Madani, A.; Seeberger, P. H.; Pieber, B. Semiheterogeneous Dual Nickel/Photocatalytic (Thio)etherification Using Carbon Nitrides. *Org. Lett.* **2019**, *21*, 5331−5334.

(14) Ghosh, I.; Khamrai, J.; Savateev, A.; Shlapakov, N.; Antonietti, M.; König, B. Organic Semiconductor Photocatalyst Can Bifunctionalize Arenes and Heteroarenes. *Science* **2019**, *365*, 360−366.

(15) Khamrai, J.; Ghosh, I.; Savateev, A.; Antonietti, M.; König, B. Photo-Ni-Dual-Catalytic $C(sp^2)$-$C(sp^3)$ Cross-Coupling Reactions with Mesoporous Graphitic Carbon Nitride as a Heterogeneous Organic Semiconductor Photocatalyst. *ACS Catal.* **2020**, *10*, 3526−3532.

(16) Gisbertz, S.; Reischauer, S.; Pieber, B. Overcoming Limitations in Dual Photoredox/Nickel catalyzed C-N Cross-Couplings due to Catalyst Deactivation. *ChemRxiv* **2019**, 10298735.

(17) Welin, E. R.; Le, C.; Arias-Rotondo, D. M.; McCusker, J. K.; MacMillan, D. W. C. Photosensitized, energy transfer-mediated organometallic catalysis through electronically excited nickel(II). *Science* **2017**, *355*, 380−385.

(18) Tian, L.; Till, N. A.; Kudisch, B.; MacMillan, D. W. C.; Scholes, G. D. Transient Absorption Spectroscopy Offers Mechanistic Insights for an Iridium/Nickel-Catalyzed C-O Coupling. *J. Am. Chem. Soc.* **2020**, *142*, 4555−4559.

(19) Ma, P.; Wang, S.; Chen, H. Reactivity of Transition-Metal Complexes in Excited States: C-O Bond Coupling Reductive Elimination of a Ni(II) Complex Is Elicited by the Metal-to-Ligand Charge Transfer State. *ACS Catal.* **2020**, *10*, 1−6.

(20) Foà, M.; Cassar, L. Oxidative addition of aryl halides to tris(triphenylphosphine)nickel(0). *J. Chem. Soc., Dalton Trans.* **1975**, 2572−2576.

(21) Roth, H. G.; Romero, N. A.; Nicewicz, D. A. Experimental and Calculated Electrochemical Potentials of Common Organic Molecules for Applications to Single-Electron Redox Chemistry. *Synlett* **2016**, *27*, 714−723.

(22) All redox potentials in this article are given in reference to the saturated calomel electrode (SCE).

(23) These values may not serve as a hard limit and are often found to be surpassed in reaction conditions. See the following for a seminal discussion, and refs 24 and 25 for examples: King, K. A.; Spellane, P. J.; Watts, R. J. Excited-State Properties of a Triply Ortho-metalated Iridium(III) Complex. *J. Am. Chem. Soc.* **1985**, *107*, 1431−1432.

(24) Czyz, M. L.; Weragoda, G. K.; Monaghan, R.; Connell, T. U.; Brzozowski, M.; Scully, A. D.; Burton, J.; Lupton, D. W.; Polyzos, A. A visible-light photocatalytic thiolation of aryl, heteroaryl and vinyl iodides. *Org. Biomol. Chem.* **2018**, *16*, 1543−1551.

(25) Nguyen, J. D.; D'Amato, E. M.; Narayanam, J. M. R.; Stephenson, C. R. J. Engaging unactivated alkyl, alkenyl and aryl iodides in visible-light-mediated free radical reactions. *Nat. Chem.* **2012**, *4*, 854−859.

(26) Discekici, E. H.; Treat, N. J.; Poelma, S. O.; Mattson, K. M.; Hudson, Z. M.; Luo, Y.; Hawker, C. J.; de Alaniz, J. R. A highly reducing metal-free photoredox catalyst: design and application in radical dehalogenations. *Chem. Commun.* **2015**, *51*, 11705−11708.

(27) Buzzetti, L.; Crisenza, G. E. M.; Melchiorre, P. Mechanistic Studies in Photocatalysis. *Angew. Chem., Int. Ed.* **2019**, *58*, 3730−3747.
(28) Kudisch, M.; Lim, C.-H.; Thordarson, P.; Miyake, G. M. Energy Transfer to Ni-Amine Complexes in Dual Catalytic, Light-Driven C-N Cross-Coupling Reactions. *J. Am. Chem. Soc.* **2019**, *141*, 19479−19486.
(29) Blackmond, D. G. Kinetic Profiling of Catalytic Organic Reactions as a Mechanistic Tool. *J. Am. Chem. Soc.* **2015**, *137*, 10852−10866.
(30) As an example, *ex situ* mechanistic studies with the same techniques are able to support the two competing hypotheses in the Introduction, with no real way to resolve the discrepancy.
(31) Zhang, G.; Li, G.; Lan, Z.-A.; Lin, L.; Savateev, A.; Heil, T.; Zafeiratos, S.; Wang, X.; Antonietti, M. Optimizing Optical Absorption, Exciton Dissociation, and Charge Transfer of a Polymeric Carbon Nitride with Ultrahigh Solar Hydrogen Production Activity. *Angew. Chem., Int. Ed.* **2017**, *56*, 13445−13449.
(32) Mower, M. P.; Blackmond, D. G. Mechanistic Rationalization of Unusual Sigmoidal Kinetic Profiles in the Machetti-De Sarlo Cycloaddition Reaction. *J. Am. Chem. Soc.* **2015**, *137*, 2386−2391.
(33) Ji, Y.; DiRocco, D. A.; Kind, J.; Thiele, C. M.; Gschwind, R. M.; Reibarkh, M. LED-Illuminated NMR Spectroscopy: A Practical Tool for Mechanistic Studies of Photochemical Reactions. *ChemPhotoChem.* **2019**, *3*, 984−992.
(34) Lehnherr, D.; Ji, Y.; Neel, A. J.; Cohen, R. D.; Brunskill, A. P. J.; Yang, J.; Reibarkh, M. Discovery of a Photoinduced Dark Catalytic Cycle Using in Situ LED-NMR Spectroscopy. *J. Am. Chem. Soc.* **2018**, *140*, 13843−13853.
(35) Sun, R.; Qin, Y.; Ruccolo, S.; Schnedermann, C.; Costentin, C.; Nocera, D. G. Elucidation of a Redox-Mediated Reaction Cycle for Nickel-Catalyzed Cross Coupling. *J. Am. Chem. Soc.* **2019**, *141*, 89−93.
(36) Sun, R.; Qin, Y.; Nocera, D. G. General Paradigm in Photoredox Nickel-Catalyzed Cross-Coupling Allows for Light-Free Access to Reactivity. *Angew. Chem., Int. Ed.* **2020**, *59*, 9527−9533.
(37) Somerville, R. J.; Hale, L. V. A.; Gómez-Bengoa, E.; Burés, J.; Martin, R. Intermediacy of Ni-Ni Species in sp^2 C-O Bond Cleavage of Aryl Esters: Relevance in Catalytic C-Si Bond Formation. *J. Am. Chem. Soc.* **2018**, *140*, 8771−8780.
(38) Mohadjer Beromi, M.; Brudvig, G. W.; Hazari, N.; Lant, H. M. C.; Mercado, B. Q. Synthesis and Reactivity of Paramagnetic Nickel Polypyridyl Complexes Relevant to $C(sp^2)$-$C(sp^3)$Coupling Reactions. *Angew. Chem., Int. Ed.* **2019**, *58*, 6094−6098.
(39) Nielsen, C. D. T.; Burés, J. Visual kinetic analysis. *Chem. Sci.* **2019**, *10*, 348−353.
(40) Blackmond, D. G. Reaction Progress Kinetic Analysis: A Powerful Methodology for Mechanistic Studies of Complex Catalytic Reactions. *Angew. Chem., Int. Ed.* **2005**, *44*, 4302−4320.
(41) Martínez-Carrión, A.; Howlett, M. G.; Alamillo-Ferrer, C.; Clayton, A. D.; Bourne, R. A.; Codina, A.; Vidal-Ferran, A.; Adams, R. W.; Burés, J. Kinetic Treatments for Catalyst Activation and Deactivation Processes based on Variable Time Normalization Analysis. *Angew. Chem., Int. Ed.* **2019**, *58*, 10189−10193.
(42) Ghosh, I.; Marzo, L.; Das, A.; Shaikh, R.; König, B. Visible Light Mediated Photoredox Catalytic Arylation Reactions. *Acc. Chem. Res.* **2016**, *49*, 1566−1577.
(43) Cheng, Y.; Gu, X.; Li, P. Visible-Light Photoredox in Homolytic Aromatic Substitution: Direct Arylation of Arenes with Aryl Halides. *Org. Lett.* **2013**, *15*, 2664−2667.
(44) Manzoor, A.; Wienefeld, P.; Baird, M. C.; Budzelaar, P. H. M. Catalysis of Cross-Coupling and Homocoupling Reactions of Aryl Halides Utilizing Ni(0), Ni(I), and Ni(II) Precursors; Ni(0) Compounds as the Probable Catalytic Species but Ni(I) Compounds as Intermediates and Products. *Organometallics* **2017**, *36*, 3508−3519.
(45) Kawamata, Y.; Vantourout, J. C.; Hickey, D. P.; Bai, P.; Chen, L.; Hou, Q.; Qiao, W.; Barman, K.; Edwards, M. A.; Garrido-Castro, A. F.; deGruyter, J. N.; Nakamura, H.; Knouse, K.; Qin, C.; Clay, K. J.; Bao, D.; Li, C.; Starr, J. T.; Garcia-Irizarry, C.; Sach, N.; White, H. S.; Neurock, M.; Minteer, S. D.; Baran, P. S. Electrochemically Driven, Ni-Catalyzed Aryl Amination: Scope, Mechanism, and Applications. *J. Am. Chem. Soc.* **2019**, *141*, 6392−6402.
(46) Johnson, J. B.; Rovis, T. More than Bystanders: The Effect of Olefins on Transition-Metal-Catalyzed Cross-Coupling Reactions. *Angew. Chem., Int. Ed.* **2008**, *47*, 840−871.
(47) Ujaque, G.; Maseras, F.; Eisenstein, O.; Liable-Sands, L.; Rheingold, A. L.; Yao, W.; Crabtree, R. H. Breaking an Electronically Preferred Symmetry by Steric Effects in a Series of $[Ir(biph)X(QR_3)_2]$ Compounds (X = Cl or I, Q = P or As). *New J. Chem.* **1998**, *22*, 1493−1498.
(48) Cowper, N. G. W.; Chernowsky, C. P.; Williams, O. P.; Wickens, Z. K. Potent Reductants via Electron-Primed Photoredox Catalysis: Unlocking Aryl Chlorides for Radical Coupling. *J. Am. Chem. Soc.* **2020**, *142*, 2093−2099.

https://dx.doi.org/10.1021/jacs.0c02848
J. Am. Chem. Soc. 2020, 142, 11042−11049

7.1 Specific Contribution

To conduct the first in situ kinetic analysis of a nickel metallaphotoredox reaction, we compared a state-of-the-art Ir phototocatalyst, $Ir(ppy)_3$, with a graphitic carbon nitride photocatalyst (CN-OA-m), using a model esterification. The reaction progress was tracked with in situ ATR-IR spectroscopy, using a fixed setup to ensure reproducibility of the data. Using a graphical analysis technique, variable time normalization analysis (VTNA), we determined reagent orders from the reaction progress profiles. Dr. Jamal A. Malik and Dr. Bartholomäus Pieber conceived the idea behind the project. I discussed and planned all of the experiments together with the other co-authors.

Taking into consideration that the data which is obtained under the typical reaction conditions might be obscured by turnover-limiting interactions between the photocatalyst (PC) and the nickel catalytic cycle, we adjusted experimental parameters to study both reactions i) under native reaction conditions and ii) within a concentration regime in which the nickel catalytic cycle is fully saturated with the excited photocatalytic species, imparting information of the intrinsic kinetics.

Dr. Jamal A. Malik collected, analysed and interpreted the majority of the kinetic data of the semi-heterogenous reaction under native conditions and most experiments in the intrinsic kinetics regime. I conducted a share of the initial rate studies for the CN-OA-m catalyzed system, to find the intrinsic kinetics regime and some of the experiments in the "intrinsic kinetics regime".[1]

I undertook the majority of experiments of the homogenous $Ir(ppy)_3$ system under both, native and intrinsic kinetics regime, including initial rate studies to assess the "intrinsic kinetic regime", "different excess" experiments, obtaining reagent orders of all reagents in both concentration regimes. I analysed and interpreted the results together with Dr. Jamal A. Malik.

Further, I evaluated the robustness of the catalyst in the $Ir(ppy)_3$ catalysed system, applying a "same excess" experiment and interpreted the data together with Dr. Jamal A. Malik. In contrast to the semi-heterogeneous congener, catalyst deactivation was observed under "intrinsic kinetic" reaction conditions. Product inhibition could be excluded, given the absence of inhibitory behaviour in the g-CN-OA-m catalysed *O*-arylation.

Ultimately, different rate laws were identified for the homogeneous- and semi-heterogeneous cross couplings, which suggests they follow dissimilar mechanistic scenarios (Figure 7.1). With a rate law only depending on the nickel concentration, our data supports the incumbent mechanistic hypothesis, suggesting the reductive elimination to be the only turnover-limiting step for the $Ir(ppy)_3$ catalysed reaction (Figure 7.1 A). However, we now provide evidence for the involvement of the photocatalyst in the oxidative addition of the aryl iodide.

Given the rate dependency of the aryl iodide in a fractionally positive fashion, we hypothesized that the PC activates the aryl halide prior to the oxidative addition to the nickel complex, which in the CN-OA-m is a turnover-limiting factor (Figure 7.1 B).

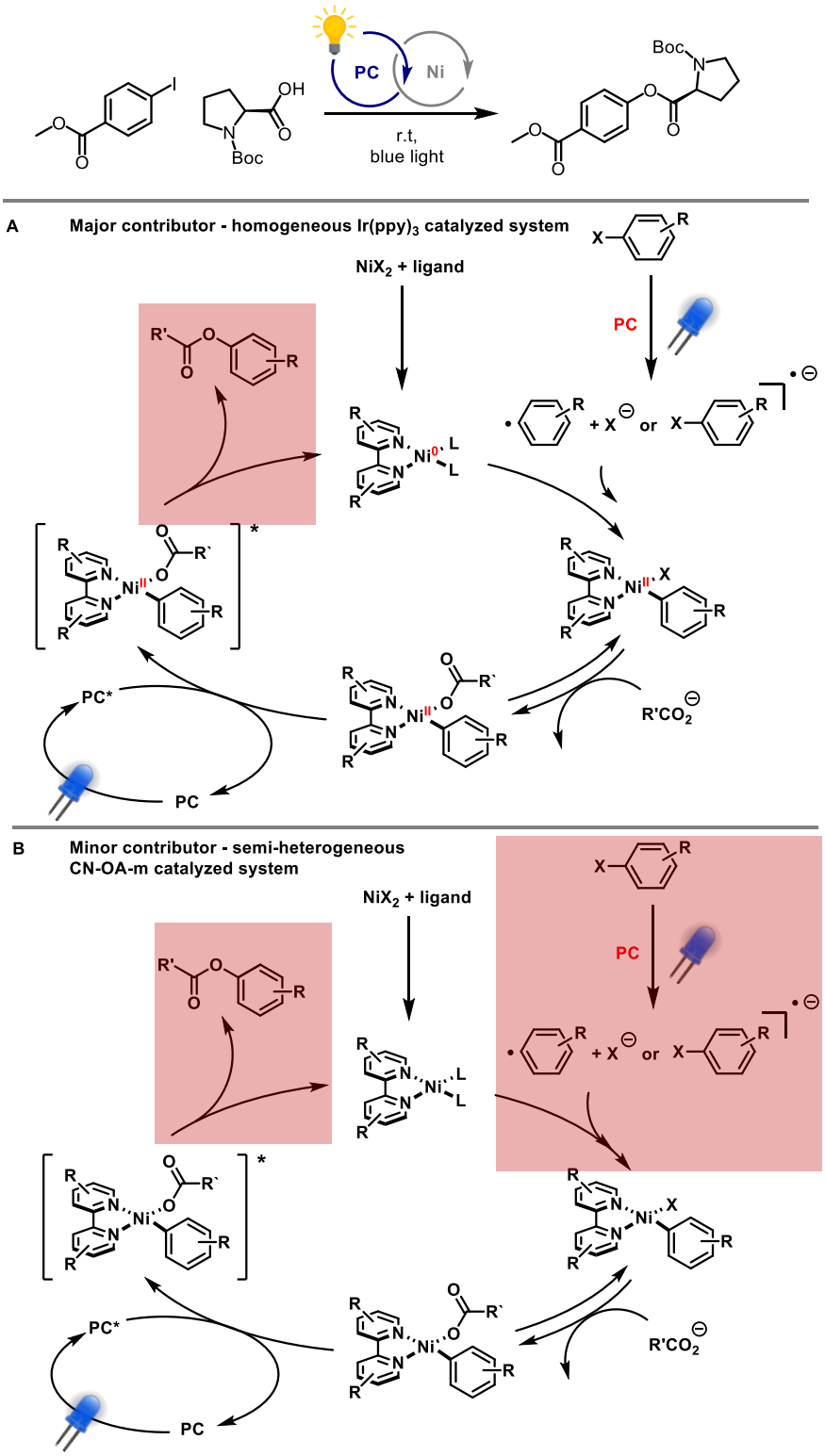

Figure 7.1 Proposed mechanistic pathways for the nickel catalyzed carboxylate *O*-arylation, based on evidence found in this kinetic study and taking the then-current mechanistic hypothesis into consideration.[2] **A** Homogeneous $Ir(ppy)_3$ catalyzed system, with a rate-law solely depending on the nickel concentration; oxidation numbers were adopted.[2] **B** Semi-heterogenous CN-OA-m catalyzed reaction. Turnover-limiting steps are marked in red.

7.2 References

(1) Ji, Y.; DiRocco, D. A.; Kind, J.; Thiele, C. M.; Gschwind, R. M.; Reibarkh, M. LED-Illuminated NMR Spectroscopy: A Practical Tool for Mechanistic Studies of Photochemical Reactions. *ChemPhotoChem* **2019**, *3* (10), 984-992. DOI: https://doi.org/10.1002/cptc.201900109.
(2) Welin, E. R.; Le, C.; Arias-Rotondo, D. M.; McCusker, J. K.; MacMillan, D. W. Photosensitized, energy transfer-mediated organometallic catalysis through electronically excited nickel(II). *Science* **2017**, *355* (6323), 380-385. DOI: 10.1126/science.aal2490 From NLM.

Chapter 8

Semi-Heterogeneous Dual Nickel/Photocatalytic (Thio)Etherification Using Carbon Nitrides

Cavedon. C.; **Madani A.;** Seeberger P. H., Pieber B

Org. Lett. **2019**, 21, 13, 5331-5334.

https://doi.org/10.1021/acs.orglett.9b01957

OL | Organic Letters

Letter

Cite This: Org. Lett. 2019, 21, 5331−5334

pubs.acs.org/OrgLett

Semiheterogeneous Dual Nickel/Photocatalytic (Thio)etherification Using Carbon Nitrides

Cristian Cavedon,[†,‡] Amiera Madani,[†,‡] Peter H. Seeberger,[†,‡] and Bartholomäus Pieber*[,†]

[†]Department of Biomolecular Systems, Max Planck Institute of Colloids and Interfaces, Am Mühlenberg 1, 14476 Potsdam, Germany

[‡]Department of Chemistry and Biochemistry, Freie Universität Berlin, Arnimallee 22, 14195 Berlin, Germany

Supporting Information

ABSTRACT: A carbon nitride material can be combined with homogeneous nickel catalysts for light-mediated cross-couplings of aryl bromides with alcohols under mild conditions. The metal-free heterogeneous semiconductor is fully recyclable and couples a broad range of electron-poor aryl bromides with primary and secondary alcohols as well as water. The application for intramolecular reactions and the synthesis of active pharmaceutical ingredients was demonstrated. The catalytic protocol is applicable for the coupling of aryl iodides with thiols as well.

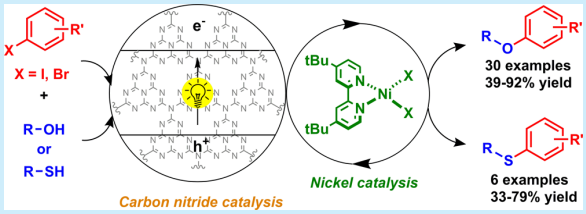

Alkyl aryl ethers are a common structural motif in many active pharmaceutical ingredients (APIs), such as Fluoxetine, Ketoconazole, Raloxifene, and Flecainide (Figure 1).[1,2]

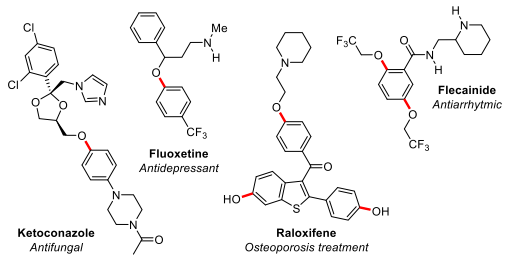

Figure 1. Examples of APIs containing the alkyl aryl ether motif.

Nucleophilic substitution of alkyl halides with phenolates (Williamson ether synthesis) traditionally used to synthesize these scaffolds, suffers from functional group incompatibilities due to the harsh conditions it requires. Catalytic strategies for the synthesis of ethers were developed to overcome these drawbacks. Copper can catalyze the coupling of phenols and aryl halides (Ullmann-type reaction),[3,4] as well as aryl boronic acids and alcohols (Chan−Evans−Lam coupling).[5] Palladium-catalyzed *O*-arylations of alcohols via Buchwald−Hartwig-type cross-coupling reactions broaden the substrate scope.[6,7] Strongly basic conditions and well-designed biaryl phosphine ligands are required for efficient cross-coupling reactions.[8]

Nickel catalysis gained increasing interest due to its significantly higher abundance compared to noble metals.[9,10] The low electronegativity of Ni enables facile oxidative addition into carbon−halide bonds, whereas reductive elimination, especially in case of C−O couplings, is difficult.[11−13] Thermolysis of Ni(II) oxametallacycles, for example, results in *β*-hydride elimination of undesired carbonyl compounds, whereas oxidation to Ni(III) complexes via single electron transfer (SET) with stoichiometric oxidants can induce reductive elimination resulting in C−O bond formation.[14] Combining nickel with photoredox catalysis,[15−17] enables the coupling of aryl bromides with alcohols[18,19] or water[20] without stoichiometric SET oxidants.

Photoredox catalysis is dominated by expensive, homogeneous iridium, and ruthenium complexes. Noble-metal-free, homogeneous photoredox catalysts, such as boron-dipyrromethene derivatives (BODIPY),[20] require tedious purification procedures and are prone to degradation.[21] Heterogeneous semiconductors are a recyclable alternative to common homogeneous photoredox catalysts.[22−25] CdSe quantum dots[26] and CdS[27] were used for carbon−heteroatom couplings via the dual nickel/photoredox catalytic approach. Cadmium, however, is among the most toxic elements[28] and strictly regulated.[29] Its application in the synthesis of APIs is therefore not desirable.

Carbon nitride (CN) materials, a class of stable and metal-free semiconductors with low toxicity[30] that can be easily made from commodity chemicals, are able to activate Ni complexes via photosensitization.[31] Here, we show that these materials are also able to catalyze alkyl aryl ether synthesis, likely by triggering reductive elimination via SET modification of the oxidation state of Ni complexes.[32]

The etherification of methyl 4-bromobenzoate with 1-hexanol served as a model reaction for initial studies (Table 1). A careful optimization of all reaction parameters showed that a carbon

Received: June 6, 2019
Published: June 24, 2019

DOI: 10.1021/acs.orglett.9b01957
Org. Lett. 2019, 21, 5331−5334

Table 1. Optimized Conditions and Control Experiments[a]

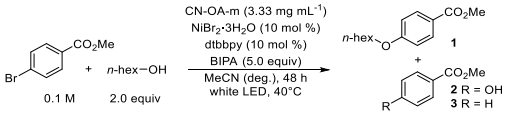

entry	conditions	1 (%)[b]	2 (%)[b]	3 (%)[b]
1	as shown	96	3	1
2	CN-OA-m (1.66 mg mL^{-1})	90	6	n.d.
3	24 h	55	3	n.d.
4	24 h with 10 mol % quinuclidine	61	2	n.d.
5	methyl 4-chlorobenzoate	4	n.d.	n.d.
6	no light	n.d.	n.d.	n.d.
7	no CN-OA-m	n.d.	n.d.	n.d.
8	no $NiBr_2{\cdot}3H_2O$	n.d.	n.d.	n.d.
9	no dtbbpy	n.d.	n.d.	n.d.
10	no BIPA	n.d.	n.d.	n.d.
11	no degassing	n.d.	n.d.	n.d.

[a]Reaction conditions: methyl 4-bromobenzoate (0.3 mmol), 1-hexanol (0.6 mmol), CN-OA-m (10 mg), $NiBr_2{\cdot}3H_2O$ (30 μmol), dtbbpy (30 μmol), BIPA (1.5 mmol), MeCN (3.0 mL), white LEDs at 40 °C for 48 h. [b]Determined by ^{1}H NMR using 1,3,5-trimethoxybenzene as internal standard. n.d. = not detected.

nitride material prepared by polymerization of urea and oxamide (CN-OA-m)[33] in combination with catalytic amounts of $NiBr_2{\cdot}3H_2O$ and di-*tert*-butylbipyridyl (dtbbpy) results in the selective synthesis of the desired ether (**1**) after 48 h irradiation with white LEDs in acetonitrile under mildly basic conditions (entry 1–2). The only side-products were small amounts of the corresponding phenol (**2**) from the cross-coupling with water and dehalogenated methyl benzoate (**3**). In homogeneous dual catalysis, the addition of catalytic amounts of quinuclidine was reported to accelerate the reaction.[18,19] For similar reasons, an amine-modified organonickel complex was used in combination with photoredox catalysis for the synthesis of phenols from aryl halides and water.[20] The semiheterogeneous protocol did not result in significant rate enhancement when 10 mol % quinuclidine was added (entries 3–4). The utilization of 6,6′-diamino-2,2′-bipyridyl instead of dtbbpy drastically reduced the efficacy of the C–O coupling in our model system (see Table S4). A reaction with methyl 4-chlorobenzoate as substrate resulted in very low amounts of the desired ether product under optimized conditions (Table 1, entry 5). No reaction was detected in the case of the mesyltate, triflate, or tosylate derivatives (see Table S10). Control experiments proved that light, CN-OA-m, $NiBr_2{\cdot}3H_2O$, dtbbpy, *N*-*tert*-butylisopropylamine (BIPA), and oxygen-free conditions are essential for successful C–O cross-couplings (entries 6–11).

With the optimized conditions in hand, the versatility of the semiheterogeneous cross-coupling was investigated (Scheme 1). Aryl bromides substituted with electron withdrawing groups in *para*-position were generally isolated in good to excellent yields. A broad range of functional groups including esters (**1**), nitriles (**4**), aldehydes (**5**), ketones (**6**, **15**), phenylboronic acid pinacol esters (**14**), chlorides (**10**), and trifluoromethyl- (**13**) as well as methylsulfonyl-groups (**16**) were tolerated. Substrates with electron withdrawing meta-substituents (**7**, **8**) did also yield the desired products, although with lower efficiency. Ortho-substituted aryl bromides (**11**, **12**) resulted in a drastically decreased reactivity. Coupling of 1,4-dibromobenzene with 1-hexanol gave a selective monoetherification as the resulting aryl alkyl ether (**9**) deactivates the second bromide functionality.

Scheme 1. Scope and Limitations of the Semiheterogeneous Etherification[a]

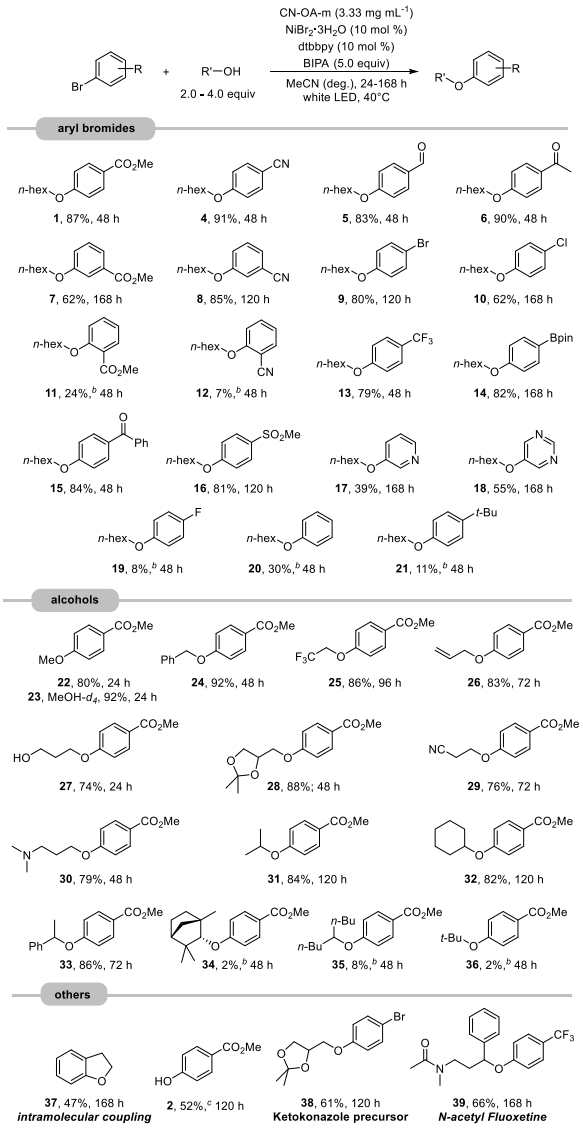

[a]Reaction conditions: aryl bromide (1.2 mmol), alcohol (2.4–4.8 mmol), CN-OA-m (20 mg), $NiBr_2{\cdot}3H_2O$ (120 μmol), dtbbpy (120 μmol), BIPA (6.0 mmol), MeCN (6.0 mL), white LEDs at 40 °C. [b]Determined by ^{1}H NMR using 1,3,5-trimethoxybenzene as internal standard. [c]DMF was used as solvent.

Heteroaryl bromides (**17**, **18**) were successfully coupled under these conditions. Substrates lacking a strong electron withdrawing group gave very low amounts of the desired C–O coupling products (**20**, **21**) within 48 h.

Electronic effects dictate the reactivity of *para*- and *meta*-substituted aryl bromides, whereas steric effects influence the reactivity of *ortho*-substituted analogs and are responsible for the scope and limitations of aliphatic alcohols (Scheme 1). Coupling of methyl 4-bromobenzoate with methanol (**22**) was completed within 24 h under standard conditions and within 8 h when MeOH was used as solvent (see the Supporting Information). The semiheterogeneous methodology provides an effective

DOI: 10.1021/acs.orglett.9b01957
Org. Lett. 2019, 21, 5331–5334

method to prepare deuterium-labeled anisoles (**23**) in excellent yield. Primary alcohols with benzyl (**24**), allyl (**26**), nitrile (**29**), trifluoromethyl (**25**), and tertiary amine (**30**) groups were coupled with high selectivity. The secondary alcohols isopropanol (**31**), cyclohexanol (**32**), and 1-phenylethanol (**33**) reacted efficiently as well. Sterically encumbered secondary (**34**, **35**) and tertiary (**36**) alcohols resulted in low amounts of the desired ether products within 48 h. Formation of diaryl ethers from the reaction of aryl bromides and phenols was not observed, presumably due to the low nucleophilicity of aromatic alcohols.

Coupling of methyl 4-bromobenzoate with water as nucleophile gave phenol **2** in moderate isolated yield by switching to DMF as a solvent (for details, see Table S12). The ortho-substituted, electron-rich aryl bromide 2-(2-bromophenyl)ethanol did undergo an intramolecular C−O coupling, resulting in 2,3-dihydrobenzofurane (**37**).[34] An analogous preparation of chromane and 1,4-benzodioxane was not feasible (see Table S11). The reason for this remains unclear, especially because chromanes were previously synthesized by reductive elimination from the corresponding nickel(II) oxametallacycles.[14] The semiheterogeneous dual catalytic reaction of 1,4-dibromobenzene and isopropylideneglycerol afforded **38**, a potential intermediate for the preparation of ketoconazole (Figure 1), itraconazole, terconazole, and their derivatives.[35] The antidepressant Fluoxetine can be synthesized using this method. *N*-Protected 3-methylamino-1-phenylpropanol reacted with 1-bromo-4-(trifluoromethyl)benzene resulting in *N*-acetyl fluoxetine (**39**) in 66%.

The same catalytic system was evaluated for the coupling of thiols with aryl halides (Scheme 2).[36−40] The reaction of aryl bromides and thiols usually requires strongly reducing photoredox catalysts,[39] whereas aryl iodides can be successfully coupled using weaker reductants.[38] When the optimized semiheterogeneous protocol (the conduction band minimum of CN-OA-m was reported to be at −1.6 V vs Ag/AgCl[33]) was applied on the reaction of methyl 4-bromobenzoate with methyl 3-mercaptopropionate, only 4% of the desired thioether were formed after 48 h (Table S15). The analogous reaction using methyl 4-iodobenzoate went to completion within 48 h resulting in 79% isolated yield of the desired thioether (**40**). When 2-mercaptoethanol was used, a selective C−S bond formation (**41**), with no detectable amount of the corresponding etherification product was obtained. In contrast to the C−O coupling, the semiheterogeneous C−S bond formation is not limited to primary and secondary thiols (**40**−**42**). Tertiary (**43**) and aromatic thiols (**44**, **45**) also gave the desired thioethers in moderate isolated yields. This finding can be rationalized by the formation of highly reactive thiyl radicals, which are proposed to add to Ni(I) intermediates in the dual catalytic thioether synthesis.[38,39]

The reaction rate was significantly increased by using blue LEDs with higher light intensity (for details, see Supporting Information). The coupling of methyl 4-bromobenzoate and methanol, for example, was complete after 16 h instead of 24 using a modified setup. These intensified conditions were used for studying the recyclability of the heterogeneous carbon nitride material (Figure 2). CN-OA-m was recycled six times, without losing its catalytic activity (Figure 2), proofing its high potential for sustainable photocatalysis.

Scheme 2. Scope of Semiheterogeneous Thioetherification[a]

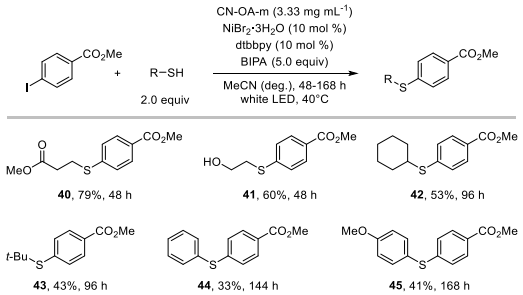

[a]Reaction conditions: methyl 4-iodobenzoate (1.2 mmol), thiol (2.4 mmol), CN-OA-m (20 mg), $NiBr_2{\cdot}3H_2O$ (120 μmol), dtbbpy (120 μmol), BIPA (6.0 mmol), MeCN (6.0 mL), white LEDs at 40 °C.

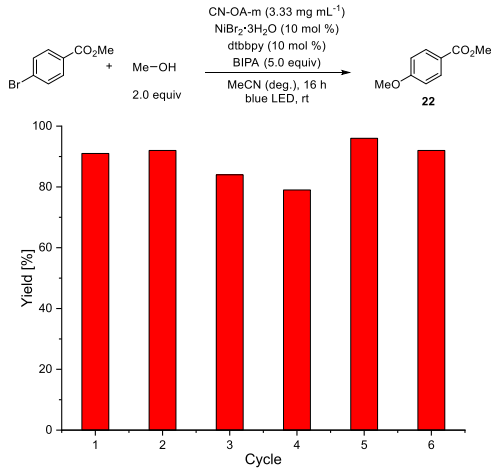

Figure 2. Recycling of CN-OA-m in the semiheterogeneous etherification.

Analysis of the recycled photocatalyst showed Ni deposition (see the Supporting Information). Attempts to use the recycled photocatalyst in absence of additional Ni(II) salts showed that the immobilized Ni species is not catalytically active in the model reaction.

In conclusion, a dual Ni/photocatalytic C−O coupling was developed using a carbon nitride semiconductor as recyclable photocatalyst with low toxicity. The semiheterogeneous nickel/carbon nitride catalysis is an inexpensive, sustainable alternative to homogeneous protocols. The method selectively couples a broad range of electron-poor aryl bromides with primary and secondary alcohols as well as water in good to excellent isolated yields. The application of this protocol for intramolecular reactions and API synthesis was demonstrated. The same catalytic protocol can be utilized to couple aryl iodides with thiols.

■ ASSOCIATED CONTENT

Supporting Information

The Supporting Information is available free of charge on the ACS Publications website at DOI: 10.1021/acs.orglett.9b01957.

Experimental procedures and characterization data (PDF)

DOI: 10.1021/acs.orglett.9b01957
Org. Lett. 2019, 21, 5331−5334

AUTHOR INFORMATION

Corresponding Author

*E-mail: bartholomaeus.pieber@mpikg.mpg.de.

ORCID

Bartholomäus Pieber: 0000-0001-8689-388X

Author Contributions

The manuscript was written through contributions of all authors. All authors have given approval to the final version of the manuscript.

Notes

The authors declare no competing financial interest.

A version of this research was previously posted to ChemRxiv: Cavedon, Cristian; Madani, Amiera; Seeberger, Peter H.; Pieber, Bartholomäus (2019): Semi-Heterogeneous Dual Nickel/Photocatalytic (Thio)Etherification using Carbon Nitrides. *ChemRxiv*. Preprint. June 6, 2019. https://doi.org/10.26434/chemrxiv.8231144.v1

ACKNOWLEDGMENTS

We gratefully acknowledge the Max-Planck Society for generous financial support. B.P. acknowledges financial support by a Liebig Fellowship of the German Chemical Industry Fund (Fonds der Chemischen Industrie, FCI). A.M. and B.P. acknowledge the Deutsche Forschungsgemeinschaft (DFG, German Research Foundation) under Germany's Excellence Strategy—EXC 2008/1 (UniSysCat)—390540038 for financial support. We thank our colleagues Xuan Pham (FU Berlin) and Katharina ten Brummelhuis (MPIKG) for analytical support.

REFERENCES

(1) Evano, G.; Wang, J.; Nitelet, A. *Org. Chem. Front.* **2017**, *4*, 2480−2499.

(2) McGrath, N. A.; Brichacek, M.; Njardarson, J. T. *J. Chem. Educ.* **2010**, *87*, 1348−1349.

(3) Bhunia, S.; Pawar, G. G.; Kumar, S. V.; Jiang, Y.; Ma, D. *Angew. Chem., Int. Ed.* **2017**, *56*, 16136−16179.

(4) Monnier, F.; Taillefer, M. *Angew. Chem., Int. Ed.* **2009**, *48*, 6954−6971.

(5) Allen, S. E.; Walvoord, R. R.; Padilla-Salinas, R.; Kozlowski, M. C. *Chem. Rev.* **2013**, *113*, 6234−6458.

(6) Enthaler, S.; Company, A. *Chem. Soc. Rev.* **2011**, *40*, 4912−4924.

(7) Schlummer, B.; Scholz, U. *Adv. Synth. Catal.* **2004**, *346*, 1599−1626.

(8) Zhang, H.; Ruiz-Castillo, P.; Buchwald, S. L. *Org. Lett.* **2018**, *20*, 1580−1583.

(9) Rosen, B. M.; Quasdorf, K. W.; Wilson, D. A.; Zhang, N.; Resmerita, A.-M.; Garg, N. K.; Percec, V. *Chem. Rev.* **2011**, *111*, 1346−1416.

(10) Tasker, S. Z.; Standley, E. A.; Jamison, T. F. *Nature* **2014**, *509*, 299.

(11) Matsunaga, P. T.; Mavropoulos, J. C.; Hillhouse, G. L. *Polyhedron* **1995**, *14*, 175−185.

(12) Koo, K.; Hillhouse, G. L. *Organometallics* **1995**, *14*, 4421−4423.

(13) Matsunaga, P. T.; Hillhouse, G. L.; Rheingold, A. L. *J. Am. Chem. Soc.* **1993**, *115*, 2075−2077.

(14) Han, R.; Hillhouse, G. L. *J. Am. Chem. Soc.* **1997**, *119*, 8135−8136.

(15) Twilton, J.; Le, C.; Zhang, P.; Shaw, M. H.; Evans, R. W.; MacMillan, D. W. C. *Nat. Rev. Chem.* **2017**, *1*, 0052.

(16) Skubi, K. L.; Blum, T. R.; Yoon, T. P. *Chem. Rev.* **2016**, *116*, 10035−10074.

(17) Milligan, J. A.; Phelan, J. P.; Badir, S. O.; Molander, G. A. *Angew. Chem., Int. Ed.* **2019**, *58*, 6152−6163.

(18) Terrett, J. A.; Cuthbertson, J. D.; Shurtleff, V. W.; MacMillan, D. W. C. *Nature* **2015**, *524*, 330−334.

(19) Zhu, B.; Yan, L.-K.; Geng, Y.; Ren, H.; Guan, W.; Su, Z.-M. *Chem. Commun.* **2018**, *54*, 5968−5971.

(20) Yang, L.; Huang, Z.; Li, G.; Zhang, W.; Cao, R.; Wang, C.; Xiao, J.; Xue, D. *Angew. Chem., Int. Ed.* **2018**, *57*, 1968−1972.

(21) Yang, L.; Simionescu, R.; Lough, A.; Yan, H. *Dyes Pigm.* **2011**, *91*, 264−267.

(22) Savateev, A.; Ghosh, I.; König, B.; Antonietti, M. *Angew. Chem., Int. Ed.* **2018**, *57*, 15936−15947.

(23) Lang, X.; Chen, X.; Zhao, J. *Chem. Soc. Rev.* **2014**, *43*, 473−486.

(24) Chen, J.; Cen, J.; Xu, X.; Li, X. *Catal. Sci. Technol.* **2016**, *6*, 349−362.

(25) Friedmann, D.; Hakki, A.; Kim, H.; Choi, W.; Bahnemann, D. *Green Chem.* **2016**, *18*, 5391−5411.

(26) Caputo, J. A.; Frenette, L. C.; Zhao, N.; Sowers, K. L.; Krauss, T. D.; Weix, D. J. *J. Am. Chem. Soc.* **2017**, *139*, 4250−4253.

(27) Liu, Y.-Y.; Liang, D.; Lu, L.-Q.; Xiao, W.-J. *Chem. Commun.* **2019**, *55*, 4853−4856.

(28) Godt, J.; Scheidig, F.; Grosse-Siestrup, C.; Esche, V.; Brandenburg, P.; Reich, A.; Groneberg, D. A. *J. Occup. Med. Toxicol.* **2006**, *1*, 22−22.

(29) Directive 2011/65/EU on the restriction of the use of certain hazardous substances in electrical and electronic equipment. **2011**,*Official Journal of the European Union*, *L174*, 88−110.

(30) Dong, Q.; Mohamad Latiff, N.; Mazánek, V.; Rosli, N. F.; Chia, H. L.; Sofer, Z.; Pumera, M. *ACS Appl. Nano Mater.* **2018**, *1*, 4442−4449.

(31) Pieber, B.; Malik, J. A.; Cavedon, C.; Gisbertz, S.; Savateev, A.; Cruz, D.; Heil, T.; Zhang, G.; Seeberger, P. H. *Angew. Chem., Int. Ed.* **2019**, DOI: 10.1002/anie.201902785.

(32) The etherification was proposed to proceed via SET oxidation/reduction of Ni intermediates (ref 18). However, a photosensitization pathway cannot be excluded: Welin, E. R.; Le, C.; Arias-Rotondo, D. M.; McCusker, J. K.; MacMillan, D. W. *Science* **2017**, *355*, 380−385.

(33) Zhang, G.; Li, G.; Lan, Z.-A.; Lin, L.; Savateev, A.; Heil, T.; Zafeiratos, S.; Wang, X.; Antonietti, M. *Angew. Chem.* **2017**, *129*, 13630−13634.

(34) During the preparation of this manuscript, an intramolecular dual nickel/photoredox C−O bond formation was described: Lee, H.; Boyer, N. C.; Deng, Q.; Kim, H.-Y.; Sawyer, T. K.; Sciammetta, N. *Chem. Sci.* **2019**, *10*, 5073−5078.

(35) Liu, Y.; Liu, Z.; Cao, X.; Liu, X.; He, H.; Yang, Y. *Bioorg. Med. Chem. Lett.* **2011**, *21*, 4779−4783.

(36) Marzo, L.; Pagire, S. K.; Reiser, O.; König, B. *Angew. Chem., Int. Ed.* **2018**, *57*, 10034−10072.

(37) Jouffroy, M.; Kelly, C. B.; Molander, G. A. *Org. Lett.* **2016**, *18*, 876−879.

(38) Oderinde, M. S.; Frenette, M.; Robbins, D. W.; Aquila, B.; Johannes, J. W. *J. Am. Chem. Soc.* **2016**, *138*, 1760−1763.

(39) Du, Y.; Pearson, R. M.; Lim, C.-H.; Sartor, S. M.; Ryan, M. D.; Yang, H.; Damrauer, N. H.; Miyake, G. M. *Chem. - Eur. J.* **2017**, *23*, 10962−10968.

(40) Santandrea, J.; Minozzi, C.; Cruché, C.; Collins, S. K. *Angew. Chem., Int. Ed.* **2017**, *56*, 12255−12259.

DOI: 10.1021/acs.orglett.9b01957
Org. Lett. 2019, 21, 5331−5334

8.1 Specific Contribution

Combining a nickel catalyst with a graphitic carbon nitride (gCN, more precisely CN-OA-m), we developed a photocatalyzed C−O and C−S cross-coupling reaction, which overcomes the sustainability limitations commonly associated with state-of-the-art organometallic-based photocatalyst. We prepared the semiconductor (CN-OA-m) via calcination of oxamide and urea at 500 °C followed by anaerobic polymerization using molten potassium salts as a structural template. The resulting yellow powder absorbs light in the visible region up to 700 nm. Cristian Cavedon and Bartholomäus Pieber conceived the idea behind this project. C. Cavedon investigated the feasibility of this transformation, finding that a mixture of CN-OA-m and a nickel-bipyridine complex successfully couples electron-poor aryl bromides with alcohols in moderate to excellent yields (Figure 8.1). As for the alcohol counterpart, limitations arise based on the nucleophilicity: while two equivalents of a primary alcohol resulted in excellent product yields within 24-96 h, four equivalents of a secondary alcohol is required to maintain a reaction time under 120 h. Only traces of the desired product were obtained using tertiary alcohols.

I investigated the scope and limitations of the C−S cross-coupling of an aryl iodide with thiols (Figure 8.1). 4-Iodobenzoate was readily combined with primary, secondary, and tertiary thiols, as well as a neutral and electron-rich aromatic thiophenols, in moderate to good yields.

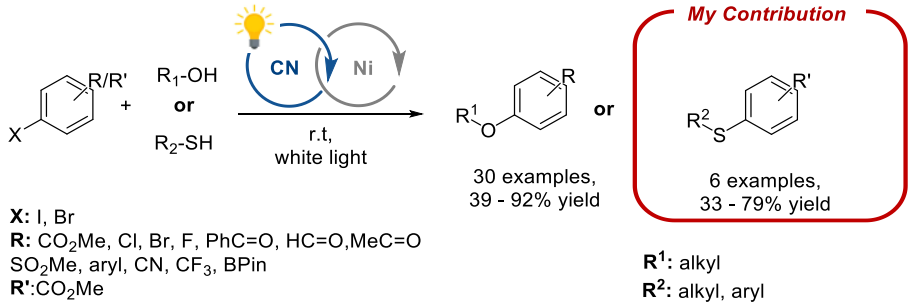

Figure 8.1 Dual nickel- and photocatalyzed etherification and thioetherification reaction. My specific contribution, experimentally, is highlighted in red.

The significant difference in the scope of the thio- and etherification indicates that the two reactions proceed via different mechanistic pathways.

Johannes and coworkers reported a photocatalyzed C–S cross-coupling mediated by an Ir^{III} photocatalyst in combination with a nickel salt.[1] The mechanistic proposal, shown in Chapter 1.3 (Figure 1.12), suggests the formation of an *S*-centered radical, formed via reductive quenching of the excited photocatalyst. In contrast, the mechanism for the etherification reaction was thought to proceed via a mechanism where the photocatalyst only modulates the oxidation state of nickel.[2]

8.2 References

(1) Oderinde, M. S.; Frenette, M.; Robbins, D. W.; Aquila, B.; Johannes, J. W. Photoredox Mediated Nickel Catalyzed Cross-Coupling of Thiols With Aryl and Heteroaryl Iodides via Thiyl Radicals. *J. Am. Chem. Soc.* **2016**, *138* (6), 1760-1763. DOI: 10.1021/jacs.5b11244.

(2) Terrett, J. A.; Cuthbertson, J. D.; Shurtleff, V. W.; MacMillan, D. W. C. Switching on elusive organometallic mechanisms with photoredox catalysis. *Nature* **2015**, *524* (7565), 330-334. DOI: 10.1038/nature14875.

Chapter 9

Visible Light-Mediated Oxidative Debenzylation Enables the Use of Benzyl Ethers as Temporary Protecting Groups

Cavedon, C.; Sletten, E. T.; **Madani, A.;** Niemeyer, O.; Seeberger, P. H.; Pieber, B.
Org. Lett. **2021**, *23*, 514-518.

https://doi.org/10.1021/acs.orglett.0c04026

OL Organic Letters

pubs.acs.org/OrgLett Letter

Visible-Light-Mediated Oxidative Debenzylation Enables the Use of Benzyl Ethers as Temporary Protecting Groups

Cristian Cavedon, Eric T. Sletten, Amiera Madani, Olaf Niemeyer, Peter H. Seeberger,* and Bartholomäus Pieber*

Cite This: *Org. Lett.* 2021, 23, 514–518 Read Online

ACCESS | Metrics & More | Article Recommendations | Supporting Information

ABSTRACT: The cleavage of benzyl ethers by catalytic hydrogenolysis or Birch reduction suffers from poor functional group compatibility and limits their use as a protecting group. The visible-light-mediated debenzylation disclosed here renders benzyl ethers temporary protective groups, enabling new orthogonal protection strategies. Using 2,3-dichloro-5,6-dicyano-1,4-benzoquinone (DDQ) as a stoichiometric or catalytic photooxidant, benzyl ethers can be cleaved in the presence of azides, alkenes, and alkynes. The reaction time can be reduced from hours to minutes in continuous flow.

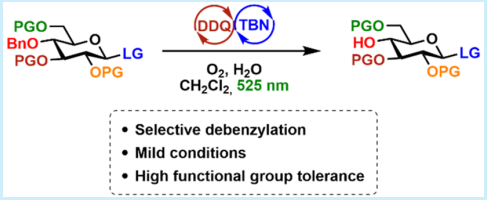

The synthesis of complex molecules such as biopolymers relies on protective groups to ensure chemo-, regio-, and stereoselectivity.[1] Protecting groups are of central importance to carbohydrate construction, where a host of hydroxyl groups have to be masked. Installation and selective removal are the basis for orthogonal protecting group strategies that are key to the synthesis of well-defined oligosaccharides.[2−4] Benzyl ethers are stable over a wide range of conditions, making them an ideal protecting group that is removed only at the very end of the synthesis.[1] For this very reason, however, benzyl ether cleavage requires harsh reduction/oxidation processes, such as catalytic hydrogenolysis, Birch reduction, or oxidation with ozone or BCl_3, which are incompatible with many functional groups[1,5] and are hazardous.[6,7] Methods for the mild and selective cleavage of benzyl ethers would render them attractive temporary protective groups that would conceptually change the strategic approach toward the synthesis of complex glycans.

Compared with benzyl ethers, *p*-methoxybenzyl (PMB) ethers can be selectively cleaved using mild stoichiometric oxidants.[1,8−10] Photoredox catalysis was used to selectively cleave PMB ethers (Scheme 1a).[11−13] Benzyl ethers ($E_{Bn\text{-}O\text{-}Me}$ = 2.20 V vs saturated calomel electrode (SCE)[14]) have a significantly higher oxidation potential compared with PMB ethers ($E_{PMB\text{-}O\text{-}Me}$ = 1.60 V vs SCE[14]) and are stable during the photocatalytic PMB cleavage.[11−13]

A photocatalyst (PC) with a sufficiently strong oxidizing excited state could facilitate the oxidative cleavage of benzyl ethers with high functional group tolerance (Scheme 1b). To move this concept to practice, a suitable PC, H-atom acceptor, and terminal oxidant had to be identified using the debenzylation of C(3)-*O*-benzyl-tetraacetylglucoside (**1a**) as a model reaction. Initial efforts with common PCs were not successful. A combination of 4 mol % 9-mesityl-10-methylacridinium as the PC and 5.0 equiv of CBr_4, for example, was capable of hydrolyzing the benzyl ether, but concomitant product degradation resulted in low yields (Table S2).

Scheme 1. Visible-Light-Mediated Oxidative Deprotection Strategies of PMB and Benzyl Ethers

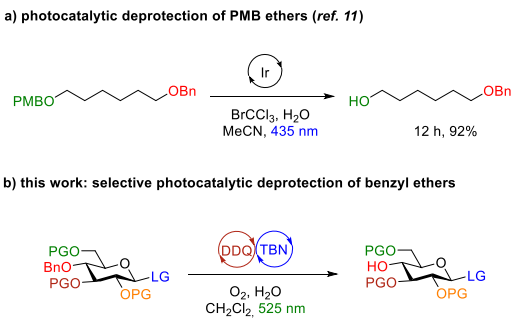

Full conversion of the starting material and excellent selectivity toward the desired product (**1b**) were achieved using stoichiometric amounts of 2,3-dichloro-5,6-dicyano-1,4-benzoquinone (DDQ) ($E^{3}_{DDQ^*/DDQ^{-\bullet}}$ = 3.18 V vs SCE[15]) and green-light irradiation (525 nm) in wet dichloromethane (Table 1, entry 1). In contrast with photochemical PMB deprotection,[11−13] an additional H-atom acceptor is not required, as the single electron transfer oxidation and the hydrogen abstraction are executed by DDQ upon irradiation.[16]

Received: December 4, 2020
Published: January 5, 2021

https://doi.org/10.1021/acs.orglett.0c04026
Org. Lett. 2021, 23, 514–518

Table 1. Optimized Conditions and Control Experiments for the Visible-Light-Mediated Oxidative Debenzylation Using Catalytic and Stoichiometric Amounts of DDQ[a]

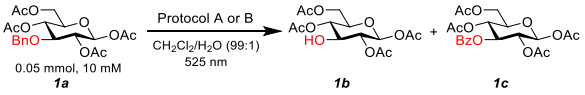

	entry	variation	time	1a [%][b]	1b [%][b]	1c [%][b]
DDQ, O_2-free, 1.5 equiv	1	none	30 min	n.d.[c]	96	<2
	2	440 nm	10 min	n.d.	78	16
	3	no light	24 h	99	n.d.	n.d.
DDQ, TBN, air, 25 mol% 25 mol%	4	none	2 h	n.d.	97	<2
	5	440 nm	30 min	n.d.	87	11
	6	no light	2 h	98	<2	n.d.
	7	no DDQ	2 h	100	n.d.	n.d.
	8	no TBN	2 h	77	23	n.d.
	9	degassed	2 h	57	40	<2

[a]Reaction conditions: **1a** (50 μmol), DDQ (Protocol A: 75 μmol, Protocol B: 12.5 μmol), TBN (Protocol B: 12.5 μmol), CH_2Cl_2 (5 mL), H_2O (50 μL), 525 nm irradiation at rt. [b]Determined by ^{1}H NMR using maleic acid as the internal standard. [c]Not detected.

The irradiation source is crucial for achieving high selectivity. Shorter wavelengths (440 nm) result in the formation of significant amounts of the corresponding benzoyl ester **1c** (entry 2). The cleavage of benzyl ethers using simple substrates was previously reported using stoichiometric amounts of DDQ under UV irradiation but suffered from low functional group compatibility.[17]

To avoid the tedious separation of the stoichiometric byproduct 2,3-dichloro-5,6-dicyano-1,4-hydroquinone ($DDQH_2$), we ultimately developed a catalytic protocol using DDQ (25 mol %), *tert*-butyl nitrite (TBN, 25 mol %) as the cocatalyst, and air as the terminal oxidant (Table 1, entry 4).[18−25] The nitrite thermally or photochemically releases NO that is oxidized by O_2 to NO_2 and reoxidizes $DDQH_2$ to DDQ.[16] Similar to the protocol with stoichiometric amounts of DDQ, lower selectivities were observed at shorter wavelengths (entry 5). Control studies confirmed that photons and DDQ are necessary for productive catalysis (entries 3, 6, and 7). Monitoring the reaction using an LED-NMR setup supported the notion that the reaction ceases upon light source removal (Figure 1a).[26] When DDQ is used in catalytic amounts and no TBN is added, the reaction stops after one turnover (Table 1, entry 8). The late addition of TBN can restore DDQ, and the reaction smoothly proceeds until completion (Figure 1b). Under anaerobic conditions, the reaction did not go to completion, confirming that O_2 is required (Table 1, entry 9).

Both protocols were evaluated using carbohydrate substrates that carry multiple protecting groups (Scheme 2). The protocol using catalytic amounts of DDQ (protocol B) was slightly modified (2 equiv of TBN) to avoid long reaction times. Substrates containing acetyl, isopropylidine, and benzoyl protecting groups (**1a**−**4a**) were smoothly deprotected in <4 h using both protocols and were isolated in excellent yield (84−96%). Thioethers that could potentially poison palladium catalysts during hydrogenolysis were unproblematic using both

a) light on/off experiment

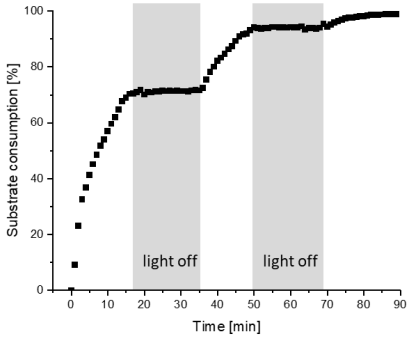

b) delayed TBN addition

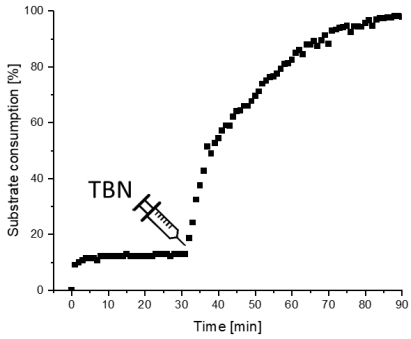

Figure 1. *In situ* NMR studies using an LED-NMR setup. For experimental details, see the Supporting Information.

photooxidative protocols, and no sulfoxide or sulfone side products were identified (**5a**−**11a**). Several common protecting groups that are not tolerated in hydrogenolysis or Birch reduction, such as fluorenylmethoxycarbonyl (**6a**, **7a**, **8a**), levulinic ester (**8a**), allyl carbonate (**9a**), propargyl carbonate (**10a**), and benzylidene (**12a**), were well tolerated. Azides (**11a**), which are essential for biorthogonal labeling, are stable to the photooxidative benzyl ether cleavage. 2-Naphtylmethyl ether (NAP, **12a**) is routinely removed using stoichiometric amounts of DDQ in the absence of light. The light-mediated protocol using 25 mol % DDQ (protocol B) provides a valuable alternative to avoid stoichiometric amounts of organic oxidant. The benzyloxycarbonyl (Cbz) group was partially cleaved using stoichiometric amounts of DDQ (protocol A), resulting in a modest isolated yield of the desired product **13b**. Using the catalytic method (protocol B), longer reaction times resulted in significant cleavage of the Cbz group. (See the Supporting Information.) Phenylselenyl (**14a**) and *tert*-butyldimethylsilyl (TBS, **15a**)[27] groups are not stable under the conditions applied. Whereas the photocatalytic protocol enables the use of benzyl ethers as temporary protective groups, it is not the method of choice to globally deprotect carbohydrates. Full deprotection of perbenzylated glucose

https://doi.org/10.1021/acs.orglett.0c04026
Org. Lett. 2021, 23, 514−518

Scheme 2. Substrate Scope and Limitations for the Visible-Light-Mediated Oxidative Cleavage of Benzyl Ethers[a]

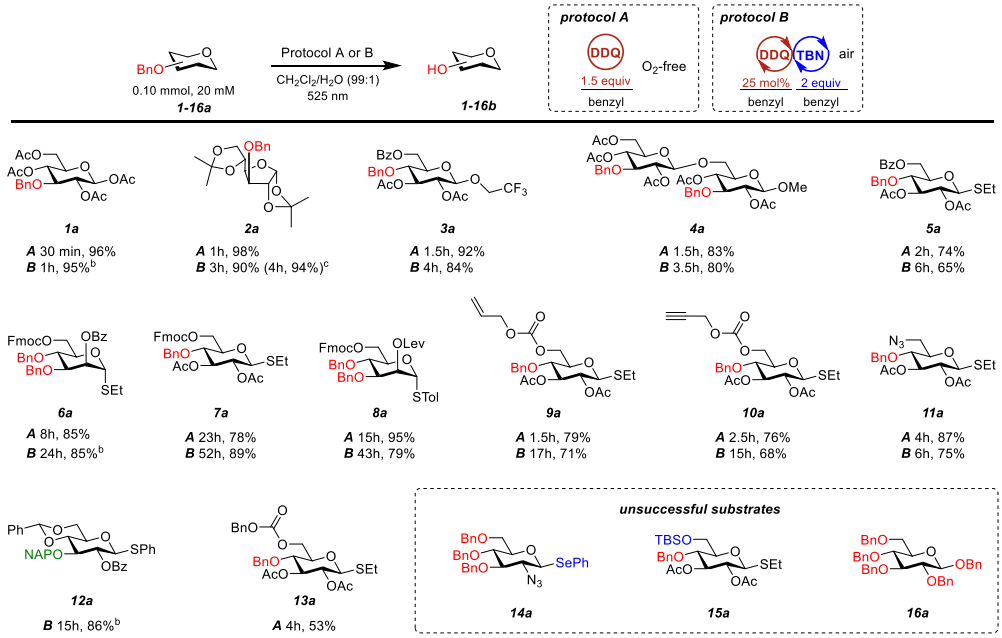

[a]Reaction conditions: benzyl ether (100 μmol), DDQ (protocol A: 150 μmol/benzyl, protocol B: 25 μmol/benzyl), TBN (protocol B, 200 μmol), CH_2Cl_2 (5 mL), H_2O (50 μL), 525 nm irradiation at rt. [b]Reaction on a 50 μmol scale. [c]Reaction on a 1.5 mmol scale. Isolated yields are reported.

(**16a**) was not feasible, and a complex mixture of partially deprotected derivatives precipitated during the reaction.

The relatively long reaction times for some substrates are a major limitation, especially using the catalytic protocol. This is a result of the long wavelengths used, as DDQ absorbs only weakly above 450 nm (Figure S9). When a 440 nm irradiation source was applied, we observed significantly shorter reaction times but had severe selectivity issues due to overoxidation and product degradation.

Slowing down a chemical reaction to avoid selectivity problems is a common strategy in batch. Continuous-flow chemistry can help to overcome selectivity issues, as it offers precise control over the reaction time and better irradiation.[28,29] A two-feed setup introduced the homogeneous reaction mixture and air into the reactor unit, which consisted of fluorinated ethylene propylene (FEP) tubing (0.8 mm i.d.) and a 440 nm light source. A short optimization study using C(3)-*O*-benzyl-glucofuranose **2a** resulted in a significant reduction of the reaction time (2.5 min in flow at 440 nm versus 3 h in batch at 525 nm) while maintaining excellent selectivity (Figure 2a). An experiment using a longer residence time showed that selectivity issues indeed arise from prolonged reaction times at low wavelengths (Figure 2b)

The flow approach was subsequently tested for other substrates (Figure 2c). The reaction time for the debenzylation of **10a** was significantly reduced to 3 min, whereas dibenzylated compounds **4a** and **6a** required 10 min.

In conclusion, we developed a mild, photocatalytic debenzylation protocol that is significantly more functional-group-tolerant than traditional methods. The proper choice of irradiation source is crucial for reaching high selectivities of benzyl ether cleavage in batch. Green-light irradiation (525 nm) was superior over blue light (440 nm) in suppressing the formation of side products during batch reactions. A biphasic

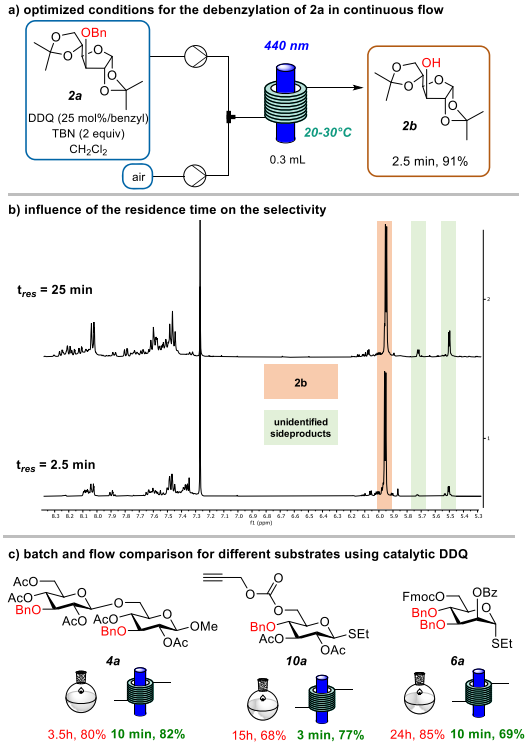

Figure 2. Visible-light-mediated oxidative cleavage of benzyl ethers using a continuous-flow system.

continuous-flow system helped to reduce the reaction times. Precise control of the reaction time and efficient irradiation in

https://doi.org/10.1021/acs.orglett.0c04026
Org. Lett. 2021, 23, 514−518

flow enabled the use of 440 nm to significantly reduce reaction times while maintaining high selectivities. The photooxidative debenzylation overcomes the current limitations of benzyl ethers as protecting groups that arise from the harsh conditions necessary for their cleavage. The methodology enables the use of benzyl ethers as a temporary protective group and is attractive for the development of new synthetic routes in glycan synthesis.

■ ASSOCIATED CONTENT

Supporting Information

The Supporting Information is available free of charge at https://pubs.acs.org/doi/10.1021/acs.orglett.0c04026.

Detailed experimental procedures and characterization data for all compounds (PDF)

■ AUTHOR INFORMATION

Corresponding Authors

Bartholomäus Pieber − *Department of Biomolecular Systems, Max Planck Institute of Colloids and Interfaces, 14476 Potsdam, Germany;* orcid.org/0000-0001-8689-388X; Email: bartholomaeus.pieber@mpikg.mpg.de

Peter H. Seeberger − *Department of Biomolecular Systems, Max Planck Institute of Colloids and Interfaces, 14476 Potsdam, Germany; Department of Chemistry and Biochemistry, Freie Universität Berlin, 14195 Berlin, Germany*; Email: peter.seeberger@mpikg.mpg.de

Authors

Cristian Cavedon − *Department of Biomolecular Systems, Max Planck Institute of Colloids and Interfaces, 14476 Potsdam, Germany; Department of Chemistry and Biochemistry, Freie Universität Berlin, 14195 Berlin, Germany*

Eric T. Sletten − *Department of Biomolecular Systems, Max Planck Institute of Colloids and Interfaces, 14476 Potsdam, Germany*

Amiera Madani − *Department of Biomolecular Systems, Max Planck Institute of Colloids and Interfaces, 14476 Potsdam, Germany; Department of Chemistry and Biochemistry, Freie Universität Berlin, 14195 Berlin, Germany*

Olaf Niemeyer − *Department of Biomolecular Systems, Max Planck Institute of Colloids and Interfaces, 14476 Potsdam, Germany*

Complete contact information is available at: https://pubs.acs.org/10.1021/acs.orglett.0c04026

Author Contributions

The manuscript was written through contributions of all authors. All authors have given approval to the final version of the manuscript.

Notes

A preprint of this research was previously posted to ChemRxiv on October 27, 2020: Cavedon, C.; Sletten, E. T.; Madani, A.; Niemeyer, O.; Seeberger, P. H.; Pieber, B. Visible Light-Mediated Oxidative Debenzylation. *ChemRxiv* 2020, DOI: 10.26434/chemrxiv.13135814.

The authors declare no competing financial interest.

■ ACKNOWLEDGMENTS

We gratefully acknowledge the Max-Planck Society for generous financial support. A.M. and B.P. acknowledge the Deutsche Forschungsgemeinschaft (DFG, German Research Foundation) under Germany's Excellence Strategy−EXC 2008/1 (UniSysCat)−390540038 for financial support. B.P. acknowledges financial support from a Liebig Fellowship of the German Chemical Industry Fund (Fonds der Chemischen Industrie, FCI). E.T.S. acknowledges financial support from the Alexander von Humboldt Foundation.

■ REFERENCES

(1) Greene, T. W.; Wuts, P. G. M. *Protective Groups in Organic Synthesis*, 3rd ed.; Wiley: New York, 1999.

(2) Wang, T.; Demchenko, A. V. Synthesis of carbohydrate building blocks via regioselective uniform protection/deprotection strategies. *Org. Biomol. Chem.* **2019**, *17*, 4934−4950.

(3) Krasnova, L.; Wong, C.-H. Oligosaccharide Synthesis and Translational Innovation. *J. Am. Chem. Soc.* **2019**, *141*, 3735−3754.

(4) Guberman, M.; Seeberger, P. H. Automated Glycan Assembly: A Perspective. *J. Am. Chem. Soc.* **2019**, *141*, 5581−5592.

(5) Crawford, C.; Oscarson, S. Optimized Conditions for the Palladium-Catalyzed Hydrogenolysis of Benzyl and Naphthylmethyl Ethers: Preventing Saturation of Aromatic Protecting Groups. *Eur. J. Org. Chem.* **2020**, *2020*, 3332−3337.

(6) Van Ornum, S. G.; Champeau, R. M.; Pariza, R. Ozonolysis Applications in Drug Synthesis. *Chem. Rev.* **2006**, *106*, 2990−3001.

(7) Joshi, D. K.; Sutton, J. W.; Carver, S.; Blanchard, J. P. Experiences with Commercial Production Scale Operation of Dissolving Metal Reduction Using Lithium Metal and Liquid Ammonia. *Org. Process Res. Dev.* **2005**, *9*, 997−1002.

(8) Horita, K.; Yoshioka, T.; Tanaka, T.; Oikawa, Y.; Yonemitsu, O. On the selectivity of deprotection of benzyl, mpm (4-methoxybenzyl) and dmpm (3,4-dimethoxybenzyl) protecting groups for hydroxy functions. *Tetrahedron* **1986**, *42*, 3021−3028.

(9) Classon, B.; Garegg, P. J.; Samuelsson, B.; Lawesson, S.-O.; Norin, T. The p-Methoxybenzyl Group as Protective Group of the Anomeric Centre. Selective Conversions of Hydroxy Groups into Bromo Groups in p-Methoxybenzyl 2-Deoxy-2-phthalimido-beta-D-glucopyranoside. *Acta Chem. Scand.* **1984**, *38b*, 419−422.

(10) Vaino, A. R.; Szarek, W. A. Iodine in Methanol: a Simple Selective Method for the Cleavage of p-Methoxybenzyl Ethers. *Synlett* **1995**, *1995*, 1157−1158.

(11) Tucker, J. W.; Narayanam, J. M. R.; Shah, P. S.; Stephenson, C. R. J. Oxidative photoredox catalysis: mild and selective deprotection of PMB ethers mediated by visible light. *Chem. Commun.* **2011**, *47*, 5040−5042.

(12) Liu, Z.; Zhang, Y.; Cai, Z.; Sun, H.; Cheng, X. Photoredox Removal of p-Methoxybenzyl Ether Protecting Group with Hydrogen Peroxide as Terminal Oxidant. *Adv. Synth. Catal.* **2015**, *357*, 589−593.

(13) Ahn, D. K.; Kang, Y. W.; Woo, S. K. Oxidative Deprotection of p-Methoxybenzyl Ethers via Metal-Free Photoredox Catalysis. *J. Org. Chem.* **2019**, *84*, 3612−3623.

(14) Mayeda, E. A.; Miller, L. L.; Wolf, J. F. Electrooxidation of benzylic ethers, esters, alcohols, and phenyl epoxides. *J. Am. Chem. Soc.* **1972**, *94*, 6812−6816.

(15) Ohkubo, K.; Fujimoto, A.; Fukuzumi, S. Visible-Light-Induced Oxygenation of Benzene by the Triplet Excited State of 2,3-Dichloro-5,6-dicyano-p-benzoquinone. *J. Am. Chem. Soc.* **2013**, *135*, 5368−5371.

(16) For a discussion of possible mechanisms, see the Supporting Information.

(17) Rahim, M. A.; Matsumura, S.; Toshima, K. Deprotection of benzyl ethers using 2,3-dichloro-5,6-dicyano-p-benzoquinone (DDQ) under photoirradiation. *Tetrahedron Lett.* **2005**, *46*, 7307−7309.

https://doi.org/10.1021/acs.orglett.0c04026
Org. Lett. 2021, 23, 514−518

(18) Song, C.; Yi, H.; Dou, B.; Li, Y.; Singh, A. K.; Lei, A. Visible-light-mediated C2-amination of thiophenes by using DDQ as an organophotocatalyst. *Chem. Commun.* **2017**, *53*, 3689−3692.
(19) Rusch, F.; Schober, J.-C.; Brasholz, M. Visible-Light Photocatalytic Aerobic Benzylic C(sp3)−H Oxygenations with the 3DDQ*/tert-Butyl Nitrite Co-catalytic System. *ChemCatChem* **2016**, *8*, 2881−2884.
(20) Wang, Y.; Wang, S.; Chen, B.; Li, M.; Hu, X.; Hu, B.; Jin, L.; Sun, N.; Shen, Z. Visible-Light-Induced Arene C(sp2)−H Lactonization Promoted by DDQ and tert-Butyl Nitrite. *Synlett* **2020**, *31*, 261−266.
(21) Das, S.; Natarajan, P.; König, B. Teaching Old Compounds New Tricks: DDQ-Photocatalyzed C−H Amination of Arenes with Carbamates, Urea, and N-Heterocycles. *Chem. - Eur. J.* **2017**, *23*, 18161−18165.
(22) Pan, D.; Pan, Z.; Hu, Z.; Li, M.; Hu, X.; Jin, L.; Sun, N.; Hu, B.; Shen, Z. Metal-Free Aerobic Oxidative C−O Coupling of C(sp3)−H with Carboxylic Acids Catalyzed by DDQ and tert-Butyl Nitrite. *Eur. J. Org. Chem.* **2019**, *2019*, 5650−5655.
(23) Song, C.; Dong, X.; Yi, H.; Chiang, C.-W.; Lei, A. DDQ-Catalyzed Direct C(sp3)−H Amination of Alkylheteroarenes: Synthesis of Biheteroarenes under Aerobic and Metal-Free Conditions. *ACS Catal.* **2018**, *8*, 2195−2199.
(24) Shen, Z.; Dai, J.; Xiong, J.; He, X.; Mo, W.; Hu, B.; Sun, N.; Hu, X. 2,3-Dichloro-5,6-dicyano-1,4-benzoquinone (DDQ)/tert-Butyl Nitrite/Oxygen: A Versatile Catalytic Oxidation System. *Adv. Synth. Catal.* **2011**, *353*, 3031−3038.
(25) Shen, Z.; Sheng, L.; Zhang, X.; Mo, W.; Hu, B.; Sun, N.; Hu, X. Aerobic oxidative deprotection of benzyl-type ethers under atmospheric pressure catalyzed by 2,3-dichloro-5,6-dicyano-1,4-benzoquinone (DDQ)/tert-butyl nitrite. *Tetrahedron Lett.* **2013**, *54*, 1579−1583.
(26) Feldmeier, C.; Bartling, H.; Riedle, E.; Gschwind, R. M. LED based NMR illumination device for mechanistic studies on photochemical reactions − Versatile and simple, yet surprisingly powerful. *J. Magn. Reson.* **2013**, *232*, 39−44.
(27) Tanemura, K.; Suzuki, T.; Horaguchi, T. Deprotection of silyl ethers using 2,3-dichloro-5,6-dicyano-p-benzoquinone. *J. Chem. Soc., Perkin Trans. 1* **1992**, *22*, 2997−2998.
(28) Plutschack, M. B.; Pieber, B.; Gilmore, K.; Seeberger, P. H. The Hitchhiker's Guide to Flow Chemistry. *Chem. Rev.* **2017**, *117*, 11796−11893.
(29) Cambié, D.; Bottecchia, C.; Straathof, N. J. W.; Hessel, V.; Noël, T. Applications of Continuous-Flow Photochemistry in Organic Synthesis, Material Science, and Water Treatment. *Chem. Rev.* **2016**, *116*, 10276−10341.

■ NOTE ADDED AFTER ISSUE PUBLICATION

This article was initially published with an incorrect copyright statement and was corrected on or around May 5, 2021.

https://doi.org/10.1021/acs.orglett.0c04026
Org. Lett. 2021, 23, 514−518

9.1 Specific Contribution

Using photoredox catalysis, we developed a novel synthetic methodology, allowing for the removal of benzyl protecting groups under mild conditions. To gain mechanistic insights, I used a fibre optic LED-NMR setup for time-resolved studies of the photocatalytic deprotection of acetyl 2,4,6-tri-*O*-acetyl-3-*O*-benzyl-β-D-glucopyranose under adjusted reaction conditions.[1] Tracking the debenzylation reaction over its whole course resulted a progress profile indicative for overall first order kinetics. To investigate the reaction's dependency on light, I designed and conducted a chopped illumination experiment, which resulted in a stalled progress profile in the absence of light (Figure 9.1). I analysed and interpreted the data, which suggested a short-lived active photogenerated species. Furthermore, this finding helped me to rule out a radical-chain reaction mechanism. My expertise in real-time reaction monitoring of photocatalytic transformations, gained during my work described in Chapter 6, allowed me to design experiments that help unravel mechanistic details.[2] The role of *tert*-butyl nitrite (TBN) as a cocatalyst to restore 2,3-dichlor-5,6-dicyano-1,4-benzoquinone (DDQ) was confirmed by a delayed addition experiment, showcasing the stagnation of product formation after one turnover of DDQ, resulting in $DDQH_2$.

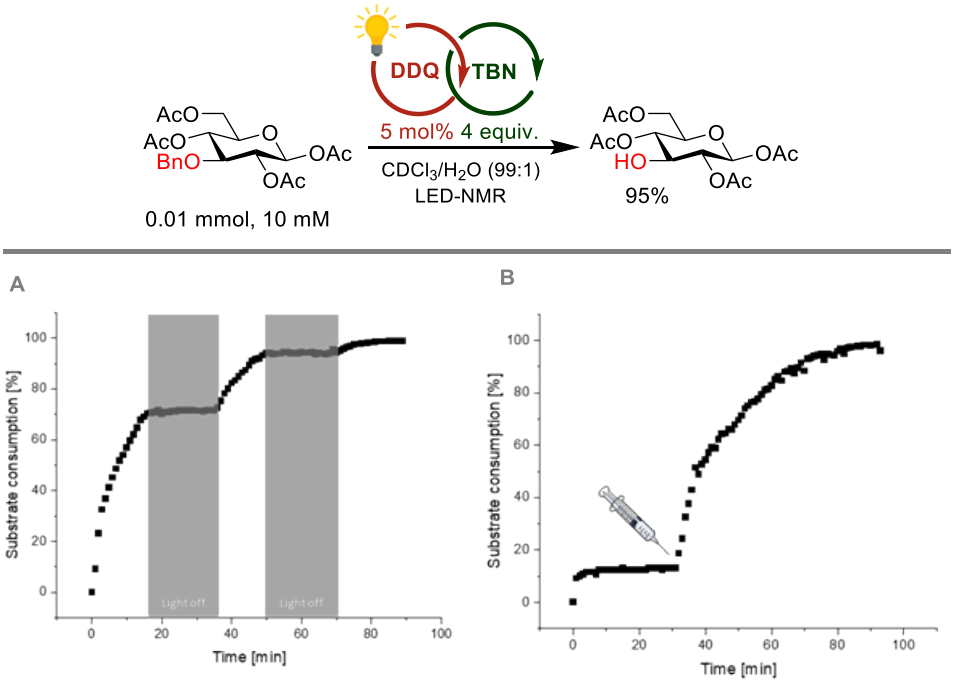

Figure 9.1 In situ monitoring of the photocatalytic cleavage of a benzyl ether protection group under **A** interrupted illumination and **B** delayed addition of TBN.

9.2 References

(1) Feldmeier, C.; Bartling, H.; Riedle, E.; Gschwind, R. M. LED based NMR illumination device for mechanistic studies on photochemical reactions--versatile and simple, yet surprisingly powerful. *J. Magn. Reson.* **2013**, *232*, 39-44. DOI: 10.1016/j.jmr.2013.04.011 From NLM.
(2) Malik, J. A.; Madani, A.; Pieber, B.; Seeberger, P. H. Evidence for Photocatalyst Involvement in Oxidative Additions of Nickel-Catalyzed Carboxylate O-Arylations. *J. Am. Chem. Soc.* **2020**, *142* (25), 11042-11049. DOI: 10.1021/jacs.0c02848.

Chapter 10

Outlook

Radicals play a vital role in synthetic organic chemistry, therefore, the development and understanding of new synthetic methodologies to access these reactive open-shell intermediates in a practical fashion is of interest. Over the course of my doctoral effort, I worked to mechanistically understand and utilize the power of these open-shell intermediates for various organic transformations.

These studies highlight the value of in situ monitoring for the visualization and mechanistic investigation of complex photocatalytic systems. However, the development of analytical tools, capable of studying such transformations, has not paralleled the surge of activity in visible-light photocatalysis. The lack of instruments capable of detecting transient species in a low concentration, while offering rich structural information still creates a blind spot. Using multiple, orthogonal monitoring techniques, sequentially or simultaneously, could circumvent this limitation, while cross-validating assures accuracy of the obtained data.[1] Further, the combination of real-time monitoring with kinetic modelling can predict the dynamic behavior of complex photocatalytic reactions more precisely and enhance result-based decision making.[2]

Quickly upon the development and mechanistic study of the photooxidative cleavage of a benzyl ether methodology, the community applied it to several multistep organic syntheses including several complex medical relevant biomolecules.[3]

However, there are still shortcomings of the method, that need to be overcome including global deprotection of highly polar molecules such as glycans has so far not been feasible. The next logical step would therefore be the optimization of the reactions protocol addressing the solubility issues rendering the reaction inefficient for the simultaneous deprotection of more than two benzyl ether groups. Additionally, a less toxic alternative for photocatalyst, DDQ would be desirable.

Though I was able to develop a divergent strategy for the fluorination of phenylacetic acid derivatives solely induced by a charge-transfer complex, unfortunately the methodology has limited functional group tolerance, which constricts its applicability.

To improve this fact, careful modulation of the donor and acceptor moiety of the charge-transfers complex should be considered.[4] Currently, the methodologies applicability in the deoxygenative fluorination of primary, secondary and tertiary alcohols via the respective oxalates, is investigated in our group, overcoming the scopes limitation to phenylacetic acids. Though given the simplicity of the method and short reaction time (1-30 mins), it has high potential applicability in radiosynthesis, using [^{18}F]-labeled Selectfluor™. ^{18}F-Radiopharmaceuticals are the most frequently used for molecular imaging studies for in vivo positron emitting tomography (PET).[5] Therefore, the demand for efficient and straightforward synthetic strategies yielding clinically relevant radiopharmaceuticals is increasing.

References

(1) Chung, R.; Hein, J. E. The More, The Better: Simultaneous In Situ Reaction Monitoring Provides Rapid Mechanistic and Kinetic Insight. *Top. Catal.* **2017**, *60* (8), 594-608. DOI: 10.1007/s11244-017-0737-9.
(2) Ben-Tal, Y.; Lloyd-Jones, G. C. Kinetics of a Ni/Ir-Photocatalyzed Coupling of ArBr with RBr: Intermediacy of ArNiII(L)Br and Rate/Selectivity Factors. *J. Am. Chem. Soc.* **2022**, *144* (33), 15372-15382. DOI: 10.1021/jacs.2c06831.
(3) Nicolaou, K. C.; Pan, S.; Shelke, Y.; Rigol, S.; Bao, R.; Das, D.; Ye, Q. A unified strategy for the total syntheses of eribulin and a macrolactam analogue of halichondrin B. *Proc. Natl. Acad. Sci.* **2022**, *119* (32), e2208938119. DOI: doi:10.1073/pnas.2208938119. Konrad, D. B.; Rühmann, K.-P.; Ando, H.; Hetzler, B. E.; Strassner, N.; Houk, K. N.; Matsuura, B. S.; Trauner, D. A concise synthesis of tetrodotoxin. *Science* **2022**, *377* (6604), 411-415. DOI: doi:10.1126/science.abn0571.
(4) Hua, A. M.; Bidwell, S. L.; Baker, S. I.; Hratchian, H. P.; Baxter, R. D. Experimental and Theoretical Evidence for Nitrogen–Fluorine Halogen Bonding in Silver-Initiated Radical Fluorinations. *ACS Catal.* **2019**, *9* (4), 3322-3326. DOI: 10.1021/acscatal.9b00623.
(5) Jacobson, O.; Kiesewetter, D. O.; Chen, X. Fluorine-18 Radiochemistry, Labeling Strategies and Synthetic Routes. *Bioconjugate Chem.* **2015**, *26* (1), 1-18. DOI: 10.1021/bc500475e.

Supporting Information - Chapter 5

Benzylic Fluorination Induced by a Charge-Transfer Complex with a Solvent-Dependent Selectivity Switch

Madani, A.; Anghileri, L.; Heydenreich, M.; Möller, H. M.; Pieber, B.
Organic Letters **2022**, *24*, 29, 5376-5380.

https://doi.org/10.1021/acs.orglett.2c02050

Benzylic fluorination induced by a charge-transfer complex with a solvent-dependent selectivity switch

Amiera Madani, [†,‡] Lucia Anghileri, [†,‡] Matthias Heydenreich, [§] Heiko M. Möller, [§] and Bartholomäus Pieber[*†]

[†] Department of Biomolecular Systems, Max-Planck-Institute of Colloids and Interfaces, Am Mühlenberg 1, 14476 Potsdam, Germany

[‡] Department of Chemistry and Biochemistry, Freie Universität Berlin, Arnimallee 22, 14195 Berlin, Germany

[§] Institute of Chemistry/Analytical Chemistry, University of Potsdam, Karl-Liebknecht-Strasse 24–25, 14476 Potsdam, Germany

Correspondence to: bartholomaeus.pieber@mpikg.mpg.de

1. General remarks

Substrates, reagents, and solvents were purchased from commercial suppliers and used without further purification. NMR spectra were recorded using a Varian 400 MHz (400, 100 and 376 MHz respectively for ^{1}H-, ^{13}C- and ^{19}F-NMR) or a Bruker NEO 500 MHz spectrometer equipped with a H/F/C/N-TCI-Prodigy probe and are reported in ppm relative to the residual solvent peaks. Peaks are reported as: s = singlet, d = doublet, t = triplet, q = quartet, m = multiplet or unresolved, with coupling constants in Hz. Reaction monitoring via FTIR analysis was performed with a ReactIR^{TM} 15 (Mettler-Toledo) console, with a DST 9.5mm SiComp^{TM} probe attached. Analytical thin layer chromatography (TLC) was carried out using pre-coated TLC-sheets, ALUGRAM Xtra SIL G/UV254 sheets (Macherey-Nagel) and visualized with 254 nm light. Purification of synthesized compounds was carried out by flash chromatography on a Reveleris X2 Flash Chromatography System from GRACE. A prepacked column with 12 g, 40 µm silica gel was used at a 30 mL/min elution flow rate. Silica 60 M (0.04-0.063 mm) silica gel (Macherey-Nagel) was used for dry loading of the crude compounds. High resolution mass spectra (HRMS, *m/z*) were recorded on a Bruker MicroTOF spectrometer using positive electrospray ionization (ESI).

2. Initial experiments

Table S1. Initial experiments[a]

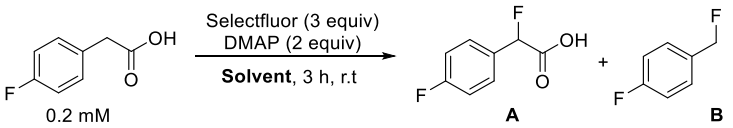

Entry	Solvent	Conversion [%][b]	A [%][c]	B [%][c]
1	MeCN	66	66	n.d.
2	MeCN:H_2O (1:1)	73	7	33

[a]Reaction conditions: 4-fluorophenylacetic acid (0.3 mmol), Selectfluor (0.9 mmol), DMAP (0.6 mmol), solvent (1.5 mL, degassed) under nitrogen atmosphere at r.t for 3 h. [b]Conversion of 4-biphenylacetic acid determined by ^{1}H-NMR using dimethyl maleate as an internal standard. [c]NMR yield determined by ^{1}H-NMR using dimethyl maleate as an internal standard. n.d. = not detected.

Table S2. Control studies in MeCN[a]

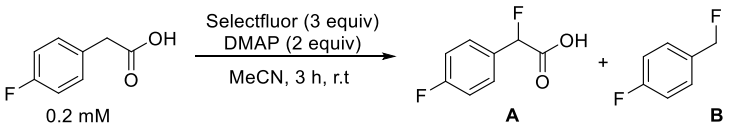

Entry	Variation	Conversion [%][b]	A [%][c]	B [%][c]
1	No degassing	80	80	n.d
2	No Selectfluor	n.d	n.d	n.d
3	No DMAP	n.d	n.d	n.d

[a]Reaction conditions: 4-fluorophenylacetic acid (0.3 mmol), Selectfluor (0.9 mmol), DMAP (0.6 mmol) in acetonitrile (anhydrous, 1.5 mL) at r.t for 3 h. [b]Conversion of 4-biphenylacetic acid determined by ^{1}H-NMR using dimethyl maleate as an internal standard. [c]NMR yield determined by n.d = not detected.

Table S3. Control studies in MeCN:H_2O[a]

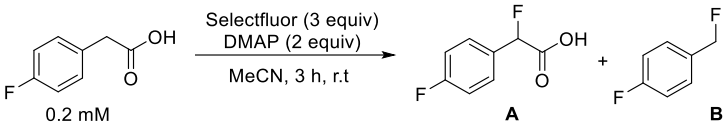

Entry	Variation	Conversion [%][b]	A [%][c]	B [%][c]
1	No degassing	17	6	11
2	No Selectfluor	n.d	n.d	n.d
3	No DMAP	n.d	n.d	n.d

[a]Reaction conditions: 4-fluorophenylacetic acid (0.3 mmol), Selectfluor (0.9 mmol), DMAP (0.6 mmol) in solvent (anhydrous, 1.5 mL) at r.t for 3 h. [b]Conversion of 4-biphenylacetic acid determined by ^{1}H-NMR using dimethyl maleate as an internal standard. [c]NMR yield determined by n.d = not detected.

3. Decarboxylative fluorination

General experimental procedure for optimization experiments. An oven dried crimp top vial (19 x 100 mm) equipped with a stir bar was charged with with 4-biphenylacetic acid and Selectfluor®. The solvent mixture was added and the mixture was stirred and sonicated for 5 min. Subsequently, 4-dimethylaminopyridine (and, if indicated, the additive) was added. The vial was sealed and the reaction mixture was stirred and sonicated for 5 min. The mixture was degassed by bubbling Argon for 10 min. The reaction mixture was stirred in an oil bath at 70 °C for the respective time. Afterwards, dimethyl maleate (1 equiv.) was added. The reaction mixture was quenched with HCl (1 M, 1 mL) and extracted with $CDCl_3$ (1 mL). An aliquote (~200 µL) of the organic phase was subsequently subjected to ^{1}H NMR analysis.

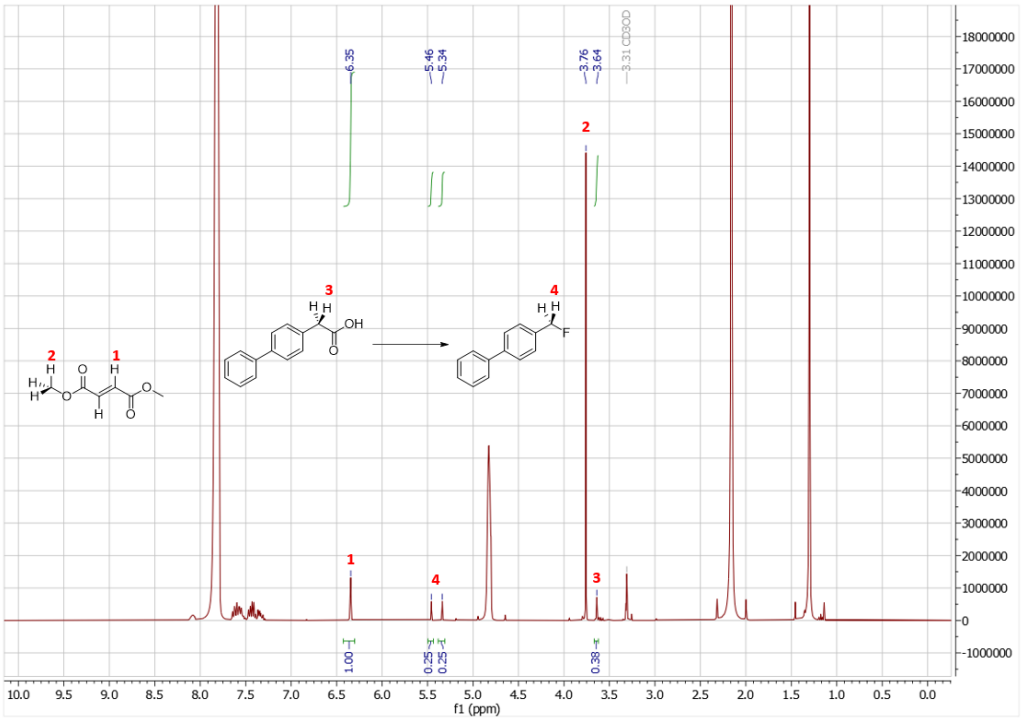

Figure S1. Example of a ^{1}H-NMR spectrum for determining NMR yields.

3.1 Solvent screening

Table S4. Initial solvent screening[a]

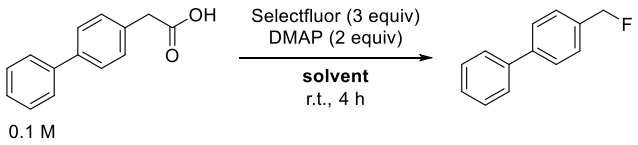

Entry	Solvent	Conversion [%][b]	Yield [%][c]
1	MeCN/H_2O 1:1	33	28
2	**Acetone/ H_2O 1:1**	**41**	**40**
3	EtOH/ H_2O 1:1	n.d.o[d]	18
4	THF/ H_2O 1:1	14	8
5	DMF/ H_2O 1:1	44	36
6	H_2O	39	26

[a]Reaction conditions: 4-biphenylacetic acid (0.1 mmol), Selectfluor (0.3 mmol), DMAP (0.2 mmol), solvent (1 mL), r.t, 4 h. [b]Conversion of 4-biphenylacetic acid determined by ^{1}H-NMR using dimethyl maleate as an internal standard. [c]NMR yield determined by ^{1}H-NMR using dimethyl maleate as an internal standard [d]Not determined due to overlapping signals.

Table S5. Initial solvent screening[a]

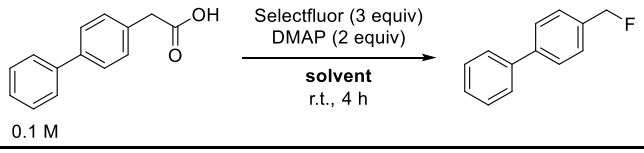

Entry	Acetone:H_2O	Conversion [%][b]	Yield [%][c]
1	1:2	34	33
2	**1:1**	**41**	**40**
3	2:1	20	20
4	5:1	12	10

[a]Reaction conditions: 4-biphenylacetic acid (0.1 mmol), Selectfluor (0.3 mmol), DMAP (0.2 mmol), solvent (1 mL), r.t, 4 h. [b]Conversion of 4-biphenylacetic acid determined by ^{1}H-NMR using dimethyl maleate as an internal standard. [a]NMR yield determined by ^{1}H-NMR using dimethyl maleate as an internal standard

3.2 Temperature & Additive screening

Table S6. Temperature screening[a]

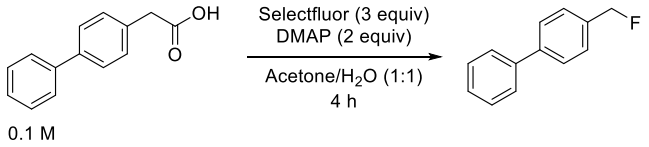

Entry	Temperature [°C]	Conversion [%][b]	Yield [%][c]
1	r.t.	41	40
2	50	47	44
3	**70**	**62**	**50**
4	90	43	16

[a]Reaction conditions: 4-biphenylacetic acid (0.1 mmol), Selectfluor (0.3 mmol), DMAP (0.2 mmol), acetone/H_2O (1:1, 1 mL), 4 h. [b]Conversion of 4-biphenylacetic acid determined by ^{1}H-NMR using dimethyl maleate as an internal standard. [a]NMR yield determined by ^{1}H-NMR using dimethyl maleate as an internal standard

Table S7. Additive screening[a]

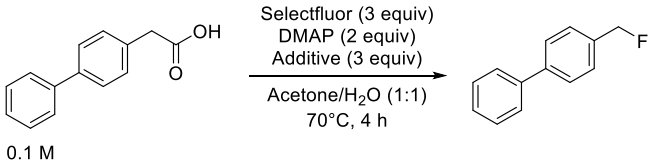

Entry	Additive	Conversion [%][b]	Yield [%][c]
1	--	62	50
2	$NaHCO_3$	33	22
3	Cs_2CO_3	13	traces
4	Li_2CO_3	23	traces
5	K_2CO_3	17	traces
6	KF	84	56
7	CsF	84	62
8	K_3PO_4	21	traces
9	K_2HPO_4	42	34
10	LiF	70	56
11	MgF_2	64	54
12	CaF_2	61	52
13	$(t\text{Bu})_4\text{NF}$	31	30
14	**NaF**	**75**	**66**
15	NH_4F	76	60

[a]Reaction conditions: 4-biphenylacetic acid (0.1 mmol), Selectfluor (0.3 mmol), DMAP (0.2 mmol), acetone/H_2O (1:1, 1 mL), 70°C, 4 h. [b]Conversion of 4-biphenylacetic acid determined by ^{1}H-NMR using dimethyl maleate as an internal standard. [a]NMR yield determined by ^{1}H-NMR using dimethyl maleate as an internal standard

3.3 Reaction time and concentration

Table S8. Optimization of reaction time and concentration[a]

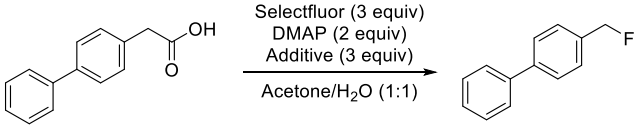

Entry	Additive	Concentration [M]	Time	T [ºC]	Conversion [%][b]	Yield [%][c]
1	-	0.1	4 h	r.t.	41	40
2	-	0.2	4 h	r.t.	48	48
3	-	0.2	4 h	70 ºC	80	70
4	NaF	0.2	4 h	70 ºC	88	86
5	NaF	0.2	1 h	70 ºC	90	86
6	NaF	0.2	30 min	70 ºC	86	85
7	NaF	0.2	10 min	70 ºC	85	82

[a]Reaction conditions: 4-biphenylacetic acid (0.1 mmol), Selectfluor (0.3 mmol), DMAP (0.2 mmol), acetone/H_2O (1:1). [b]Conversion of 4-biphenylacetic acid determined by ^{1}H-NMR using dimethyl maleate as an internal standard. [a]NMR yield determined by ^{1}H-NMR using dimethyl maleate as an internal standard

3.4 Control studies

Table S9. Control studies[a]

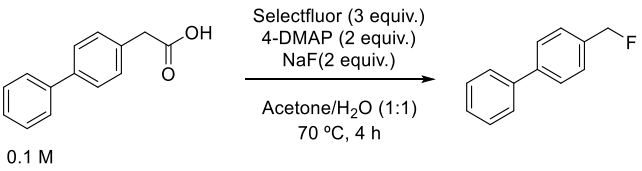

Entry	Variation	Conversion [%][b]	Yield [%][c]
1	none	88	86
2	Selectfluor (2 equiv)	64	42
3	DMAP (1 equiv)	95	86[c]
4	DMAP (10 mol%)	48	30
5	NaF (1 equiv)	67	56
6	Temperature (r.t.)	40	32

[a]Reaction conditions: 4-biphenylacetic acid (0.1 mmol), Selectfluor, DMAP and NaF in acetone/water under N_2 atmosphere for 4 h. [b]Determined by ^{1}H-NMR using dimethyl maleate as an internal standard. [c]The use of 1 equiv. of DMAP generated an unidentified side product.

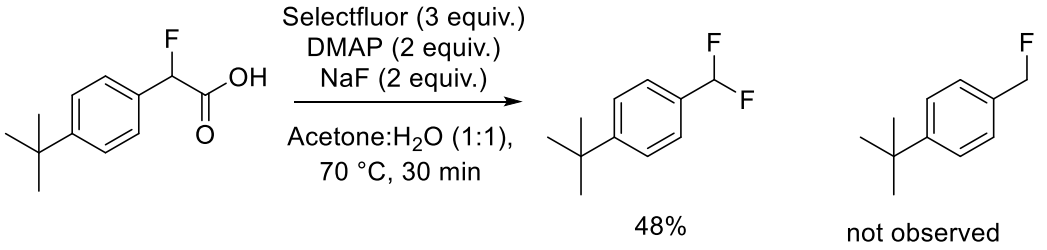

Scheme S1. Decarboxylative fluorination reaction of 2-(4-(tert-butyl)phenyl)-2-fluoroacetic acid

3.5 Scope

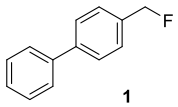

1

General experimental procedure for the synthesis of 4-(fluoromethyl)-1,1'-biphenyl (1). An oven dried vessel equipped with a stir bar was charged with substrate (424.5 mg, 2 mmol, 0.2 mM) and Selectfluor® (2.13 g, 6 mmol, 3 equiv.). Aceton:H_2O (10 mL, 1:1) was added and the mixture was stirred and sonicated for 5 min. Subsequently, 4-dimethylaminopyridine (488.7 mg, 4 mmol, 2 equiv.) and NaF (167.9 mg, 4 mmol, 2 equiv.) were added. The vial was sealed and the reaction mixture was stirred and sonicated for 5 min. The mixture was degassed by bubbling Argon for 10 min. The reaction mixture was stirred in an oil bath at 70 °C for the respective time. The reaction mixture was quenched with HCl (1 M, 10 mL) and extracted with $CHCl_3$ (3 x 10 mL). The combined organic phases were washed with brine (10 mL), dried over $MgSO_4$ under concentrated under reduced pressure. Purification was performed by column chromatography using hexane. The title compound was isolated as a colorless solid (267.9 mg, 1.44 mmol, 72%). ^{1}H NMR (400 MHz, CDCl3) δ. 7.71 – 7.66 (m, 4H), 7.54 – 7.50 (m, 4H), 7.47 – 7.41 (m, 1H). 7.47 – 7.41 (m, 1H), 5.48 (d, J = 47.8 Hz, 1H). ^{13}C NMR (400 MHz, $CDCl_3$) δ ppm 141.9, 140.7, 135.3 (d, J = 17.2 Hz), 129.0, 128.3 (d, J = 5.9 Hz), 127.7, 127.5, 127.3, 84.6 (d, J = 166.2 Hz). ^{19}F NMR (400 MHz, $CDCl_3$) δ ppm -206.2 (t, J = 47.9 Hz). These data are in full agreement with those previously published in the literature.[1]

General experimental procedure products that were not isolated due to their low boiling point. An oven dried crimp top vial (19 x 100 mm) equipped with a stir bar was charged with substrate (0.1 mmol, 0.2 mM) and Selectfluor® (0.3 mmol, 3 equiv.). Aceton:H_2O (2 mL, 1:1) was added and the mixture was stirred and sonicated for 5 min. Subsequently, 4-dimethylaminopyridine (0.2 mmol, 2 equiv.) and NaF (0.2 mmol, 2 equiv.) were added. The vial was sealed and the reaction mixture was stirred and sonicated for 5 min. The mixture was degassed by bubbling Argon for 10 min. The reaction mixture was stirred in an oil bath at 70 °C for the respective time. Upon completion, dimethyl maleate (12.4 µL, 0.1 mmol, 1 equiv.) was added. The reaction mixture was quenched with HCl (1 M, 1 mL) and extracted with $CDCl_3$ (1 mL). An aliquote (~200 µL) of the organic phase was subsequently subjected to ^{1}H NMR analysis.

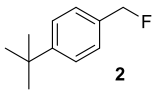

1-(tert-butyl)-4-(fluoromethyl)benzene (2). The compound was synthesized following the general procedure. An NMR yield of 84% was determined using dimethyl maleate as an internal standard. The product was not isolated due to its low boiling point.

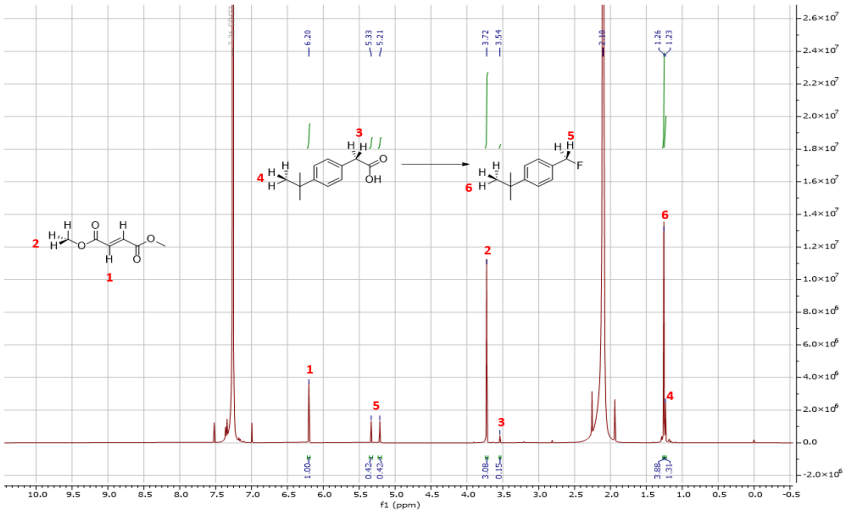

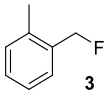

1-(fluoromethyl)-2-methylbenzene (3). The compound was synthesized following the general procedure. An NMR yield of 80% was determined using dimethyl maleate as an internal standard. The product was not isolated due to its low boiling point.

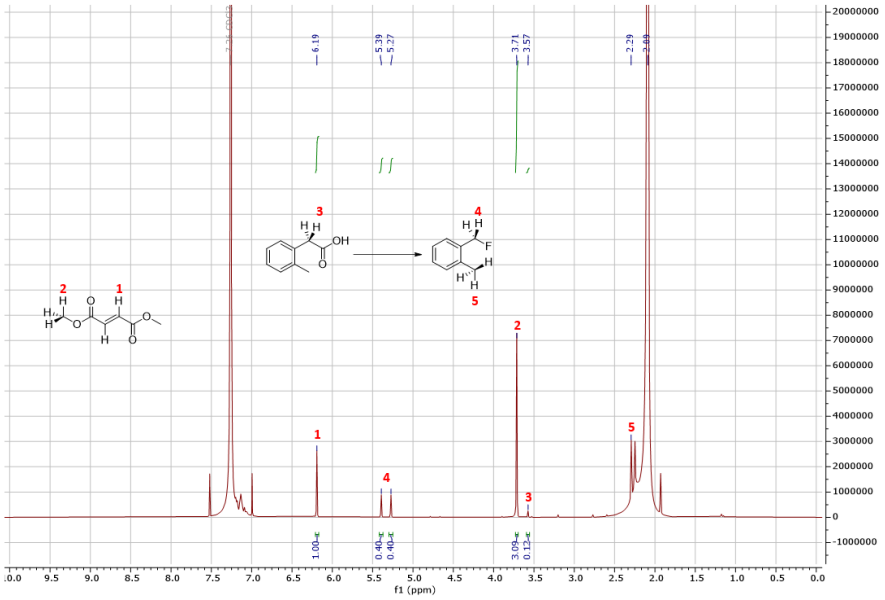

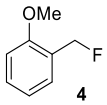

4

2-(2-methoxyphenyl)acetic acid (4). The compound was synthesized following the general procedure. An NMR yield of 56% was determined using dimethyl maleate as an internal standard. The product was not isolated due to its low boiling point.

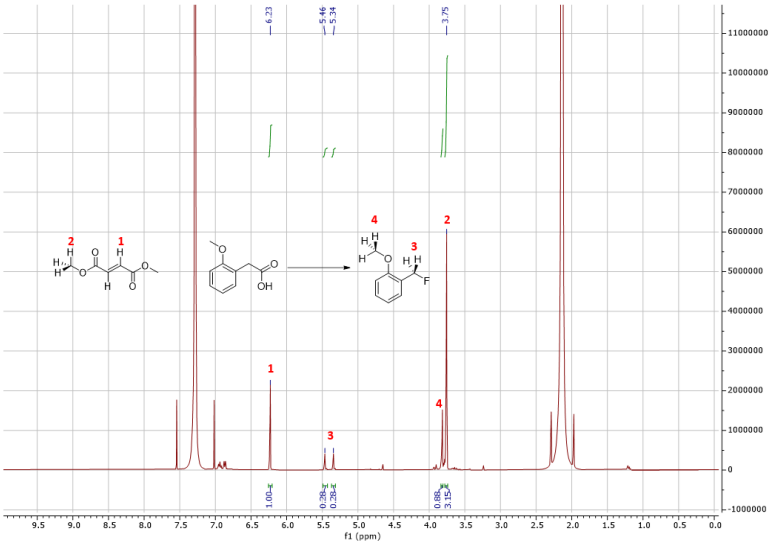

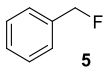

5

(Fluoromethyl)benzene (5). The compound was synthesized following the general procedure. An NMR yield of 60% was determined using dimethyl maleate as an internal standard. The product was not isolated due to its low boiling point.

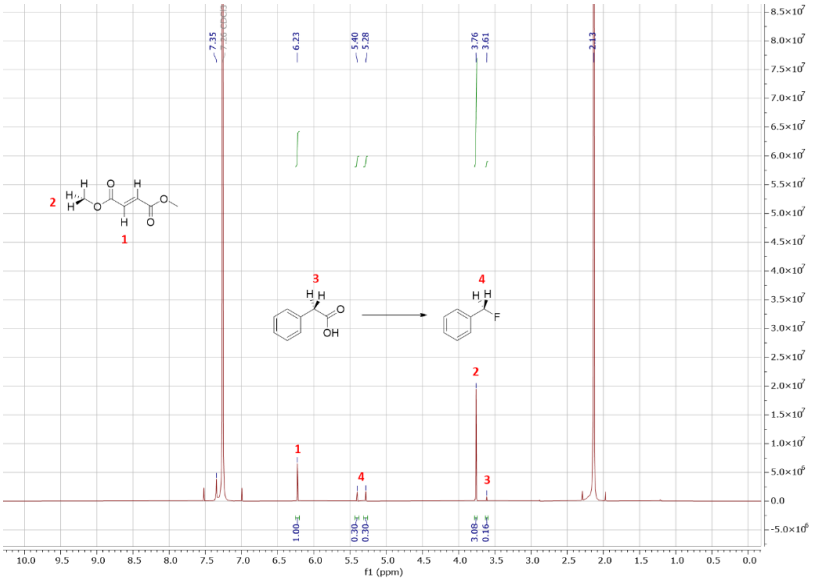

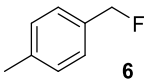

6

1-(fluoromethyl)-4-methylbenzene (6). The compound was synthesized following the general procedure. An NMR yield of 66% was determined using dimethyl maleate as an internal standard. The product was not isolated due to its low boiling point.

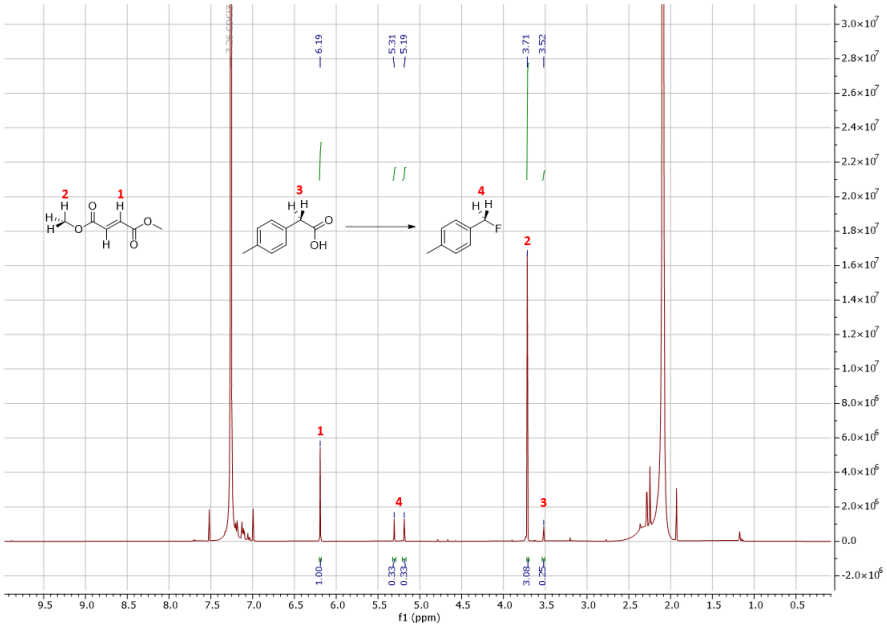

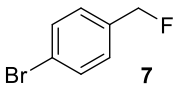

7

1-bromo-4-(fluoromethyl)benzene (7). The compound was synthesized following the general procedure. An NMR yield of 50% was determined using dimethyl maleate as an internal standard. The product was not isolated due to its low boiling point.

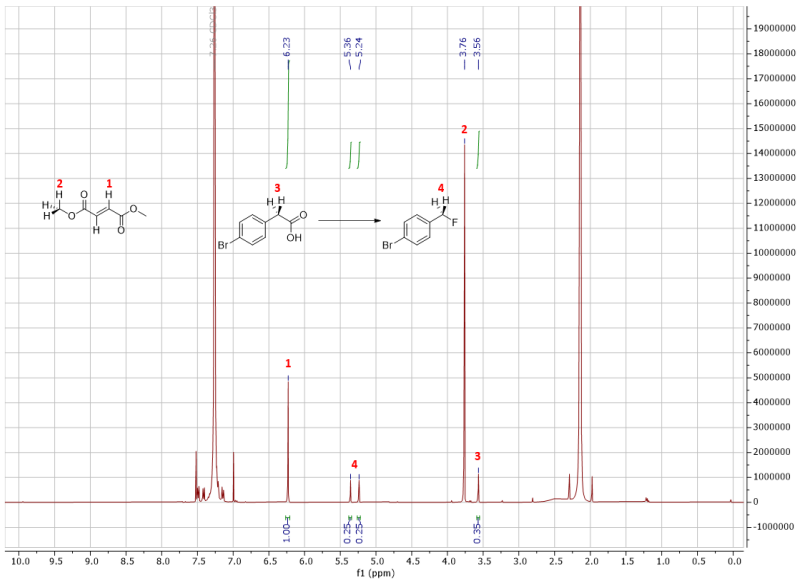

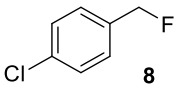

8

1-chloro-4-(fluoromethyl)benzene (8). The compound was synthesized following the general procedure. An NMR yield of 60% was determined using dimethyl maleate as an internal standard. The product was not isolated due to its low boiling point.

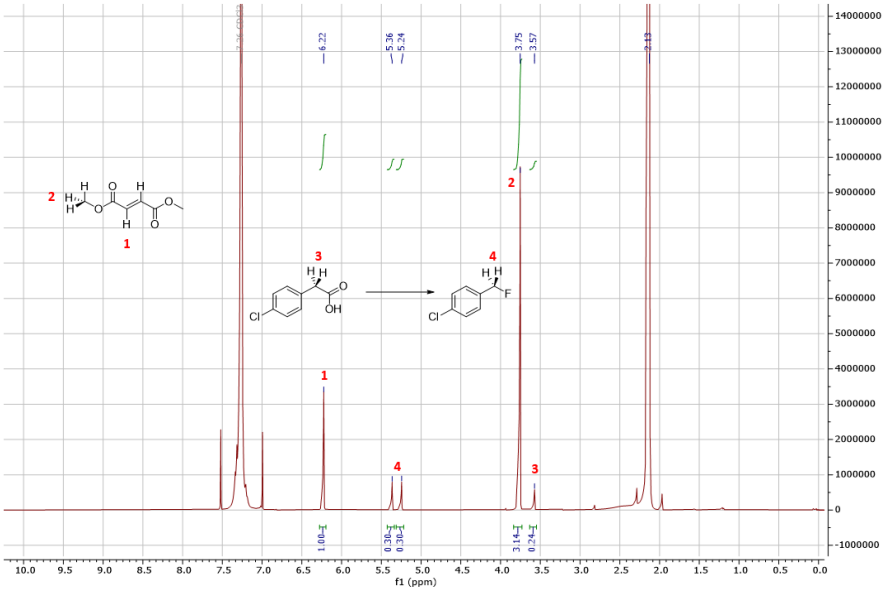

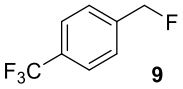

9

1-(fluoromethyl)-4-(trifluoromethyl)benzene (9). The compound was synthesized following the general procedure. An NMR yield of 20% was determined using dimethyl maleate as an internal standard. The product was not isolated due to its low boiling point.

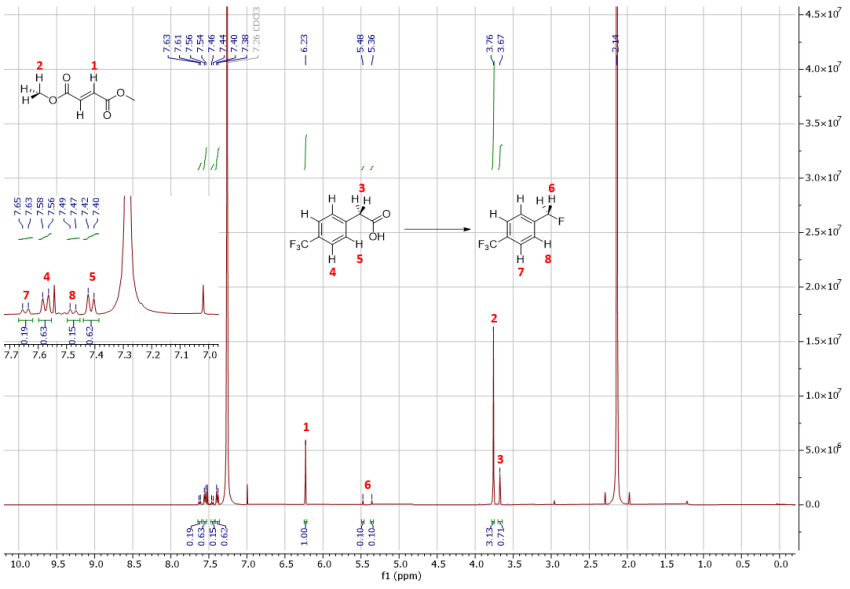

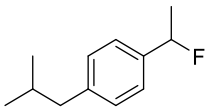

40

1-(1-fluoroethyl)-4-isobutylbenzene (10). The compound was synthesized following the general procedure. An NMR yield of 44% was determined using dimethyl maleate as an internal standard. The product was not isolated due to its low boiling point.

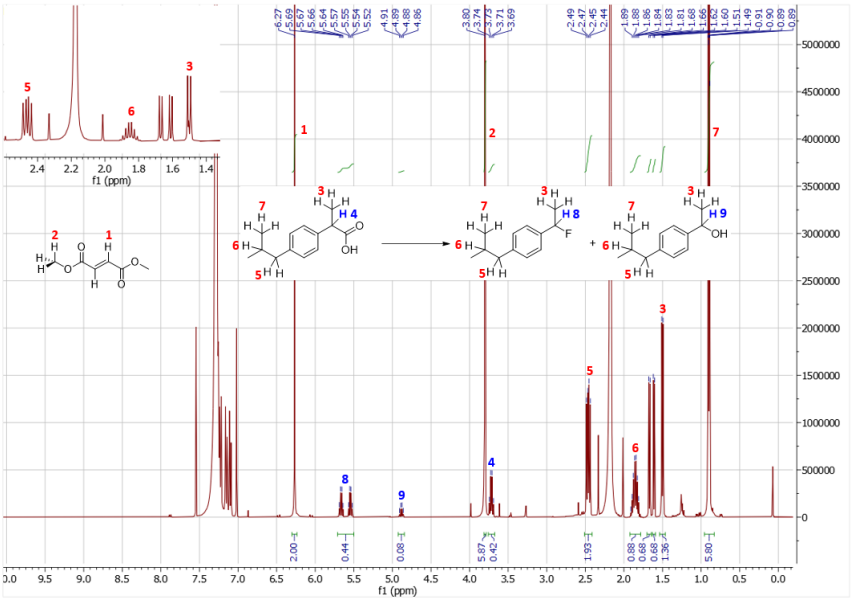

4. α-fluorination

General experimental procedure for optimization experiments. An oven-dried vessel (19 x 100 mm) equipped with a stir bar was charged with 4-fluorophenylacetic acid (or, if indicated another phenylacetic acid derivative), 4-dimethylaminopyridine and Selectfluor®. Solvent was added, the vessel was sealed with a septum and sonicated for 5 minutes. The mixture was stirred at room temperature for the respective reaction time. Upon completion, dimethyl maleate (1 equiv.) was added The reaction mixture was quenched with HCl (1 M, 1 mL) and extracted with $CDCl_3$ (1 mL). An aliquote (~200 µL) of the organic phase was subsequently subjected to ^{1}H NMR analysis. NMR spectra were taken in $CDCl_3$ or MeOD-d_3. A representative ^{1}H NMR spectrum for determining the yield is shown in Figure S2.

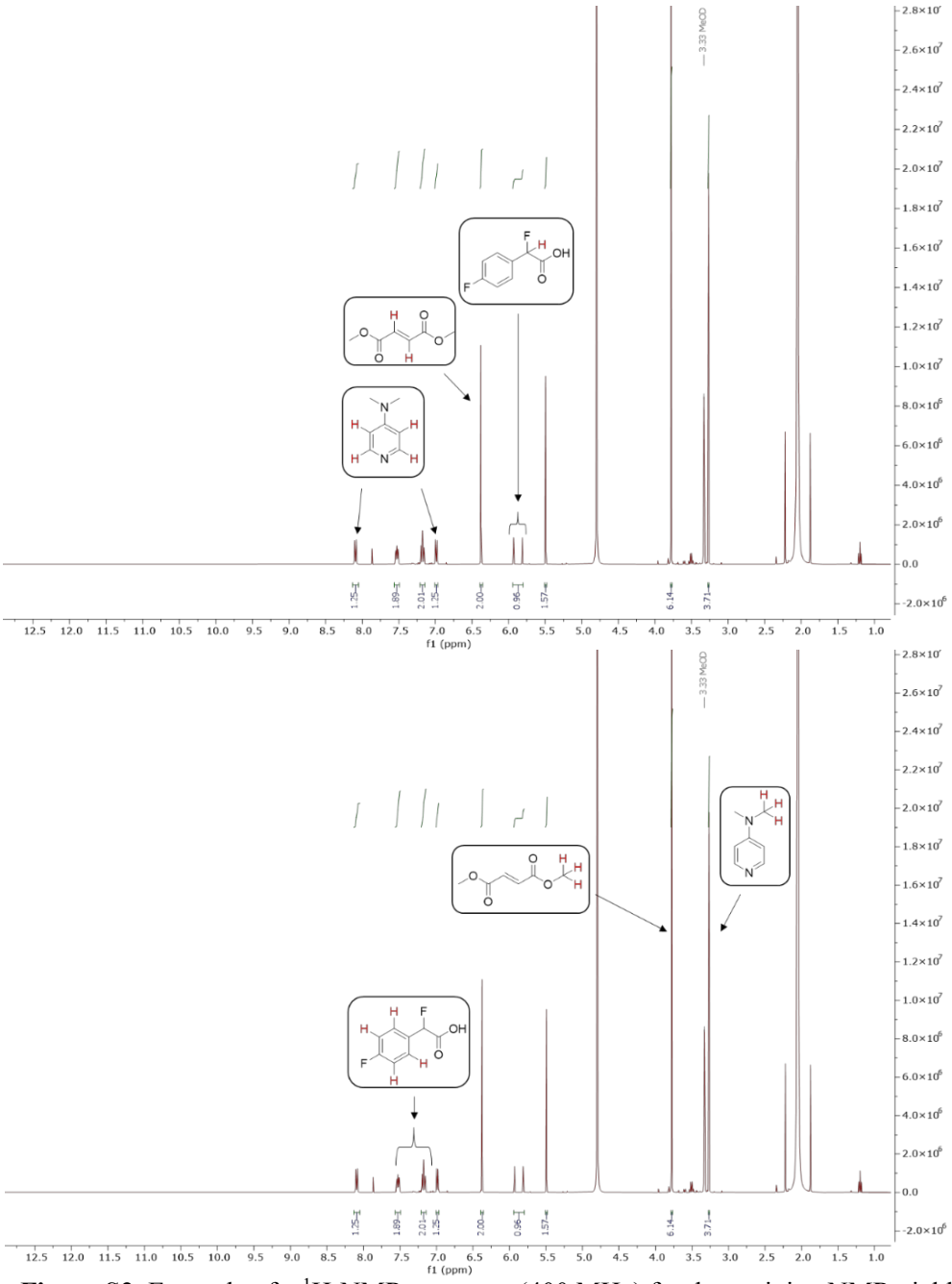

Figure S2. Example of a ^{1}H-NMR spectrum (400 MHz) for determining NMR yields.

4.1 N–F Reagents

Table S10. Tests using different fluorinating agents[a]

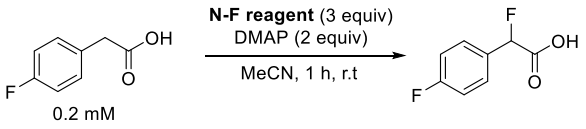

0.2 mM

Entry	Additive	Conversion [%][b]	Yield [%][c]
1	**Selectfluor**	**80**	**80**
2	NFSI	40	40
3	NFpy	-	-

[a]Reaction conditions: 4-fluorophenylacetic acid (0.3 mmol), N-F reagent (0.9 mmol), DMAP (0.6 mmol) in MeCN (anhydrous, 1.5 mL), r.t for 1 h. [b]Conversion of 4-biphenylacetic acid determined by ^{1}H-NMR using dimethyl maleate as an internal standard. [c]NMR yield determined by ^{1}H-NMR using dimethyl maleate as an internal standard

4.2 Solvent screening

Table S11. Solvent screening[a]

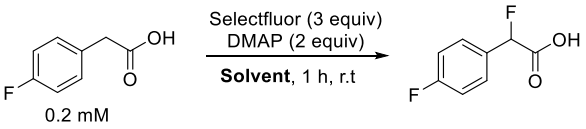

0.2 mM

Entry	Additive	Conversion [%][b]	Yield [%][c]
1	**MeCN**	**80**	**80**
2	Acetone	56	56
3	DMF	73	73
4	MeOH	75	n.d
5	THF	0	n.d
6	$CHCl_3$	0	n.d
7	DCM	0	n.d

[a]Reaction conditions: 4-fluorophenylacetic acid (0.3 mmol), Selectfluor (0.9 mmol), DMAP (0.6 mmol) in solvent (anhydrous, 1.5 mL), r.t for 1 h. [b]Conversion of 4-biphenylacetic acid determined by ^{1}H-NMR using dimethyl maleate as an internal standard. [c]NMR yield determined by ^{1}H-NMR using dimethyl maleate as an internal standard

4.3 Optimization of the equivalents of Selectfluor and DMAP

Table S12. Optimization experiments of the equivalents of Selectfluor and DMAP[a]

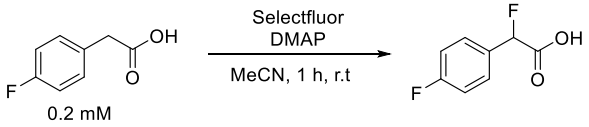

0.2 mM

Entry	Selectfluor (equiv)	DMAP (equiv)	Conversion [%][b]	Yield [%][c]
1	3	2	80	80
2	3	1	38	38
3	3	0.5	3	3
4	3	0.1	2	2
5	3	2	80	80
6	2	2	89	89
7	**1.2**	**2**	**97**	**97**

[a]Reaction conditions: 4-fluorophenylacetic acid (0.3 mmol), Selectfluor and DMAP in MeCN (anhydrous, 1.5 mL), r.t for 1 h. [b]Conversion of 4-biphenylacetic acid determined by ^{1}H-NMR using dimethyl maleate as an internal standard. [c]NMR yield determined by ^{1}H-NMR using dimethyl maleate as an internal standard

4.4 Screening of different activators

Table S13. Activator screening[a]

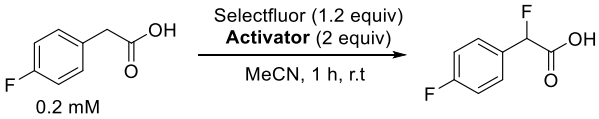

0.2 mM

Entry	Activator	Conversion [%][b]	Yield [%][c]
1	**DMAP**	**97**	**97**
2	*N,N*-Dimethylanilin	0	n.d
3	Pyridine	9	9
4	4-Methoxypyridine	66	66
5	4-Aminopyridine	82	82
6	2-Phenylpyridine	0	n.d
7	Quinoline	0	n.d
8	3-Hydroxypyridine	0	n.d
9	6-Cyanopyridine	0	n.d
10	2-Chloropyridine	0	n.d
11	2,6-Lutidine	52	n.d
12	DABCO	0	n.d

[a]Reaction conditions: 4-fluorophenylacetic acid (0.3 mmol), Activator (0.36 mmol), DMAP (0.6 mmol) in solvent (anhydrous, 1.5 mL), r.t for 1 h. [b]Conversion of 4-biphenylacetic acid determined by ^{1}H-NMR using dimethyl maleate as an internal standard. [c]NMR yield determined by ^{1}H-NMR using dimethyl maleate as an internal standard

4.5 Concentration and reaction time studies

Table S14. Concentration/time studies[a]

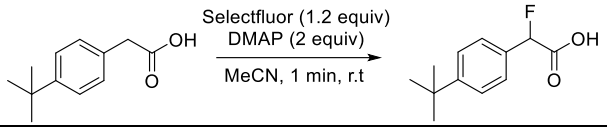

Entry	Concentration [mM]	Conversion [%][b]	Yield [%][c]	
			1 min	5 min
1	0.2	92	92	92
2	0.1	85	85	91
3	0.05	58	58	72
4	0.2[d]	79	79	-

[a]Reaction conditions: 4-*tert*-Butylphenylacetic acid (0.3 mmol), Selectfluor (0.36 mmol), DMAP (0.6 mmol) in MeCN (anhydrous), r.t for 1 min [b]Conversion of 4-biphenylacetic acid determined by ^{1}H-NMR using dimethyl maleate as an internal standard. [c]NMR yield determined by ^{1}H-NMR using dimethyl maleate as an internal standard. [d]0°C

Table S15. One minute experiments using different substrates[a]

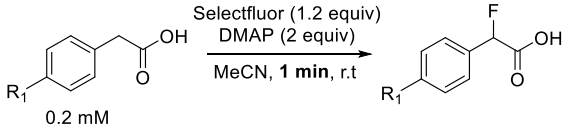

Entry	Substrate	Conversion [%][b]	Yield [%][c]
1	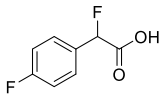	96	96
2	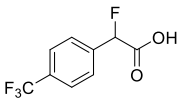	89	89
3	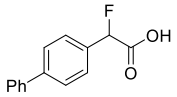	93	93
4	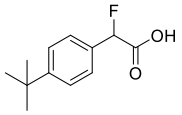	92	92
5	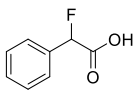	99	99

[a]Reaction conditions: Phenylacetic acid derivative (0.3 mmol), Selectfluor (0.36 mmol), DMAP (0.6 mmol) in MeCN (anhydrous, 1.5 mL), r.t for 1 min. min [b]Conversion of 4-biphenylacetic acid determined by ^{1}H-NMR using dimethyl maleate as an internal standard. [c]NMR yield determined by ^{1}H-NMR using dimethyl maleate as an internal standard.

4.6 Mechanistic investigations

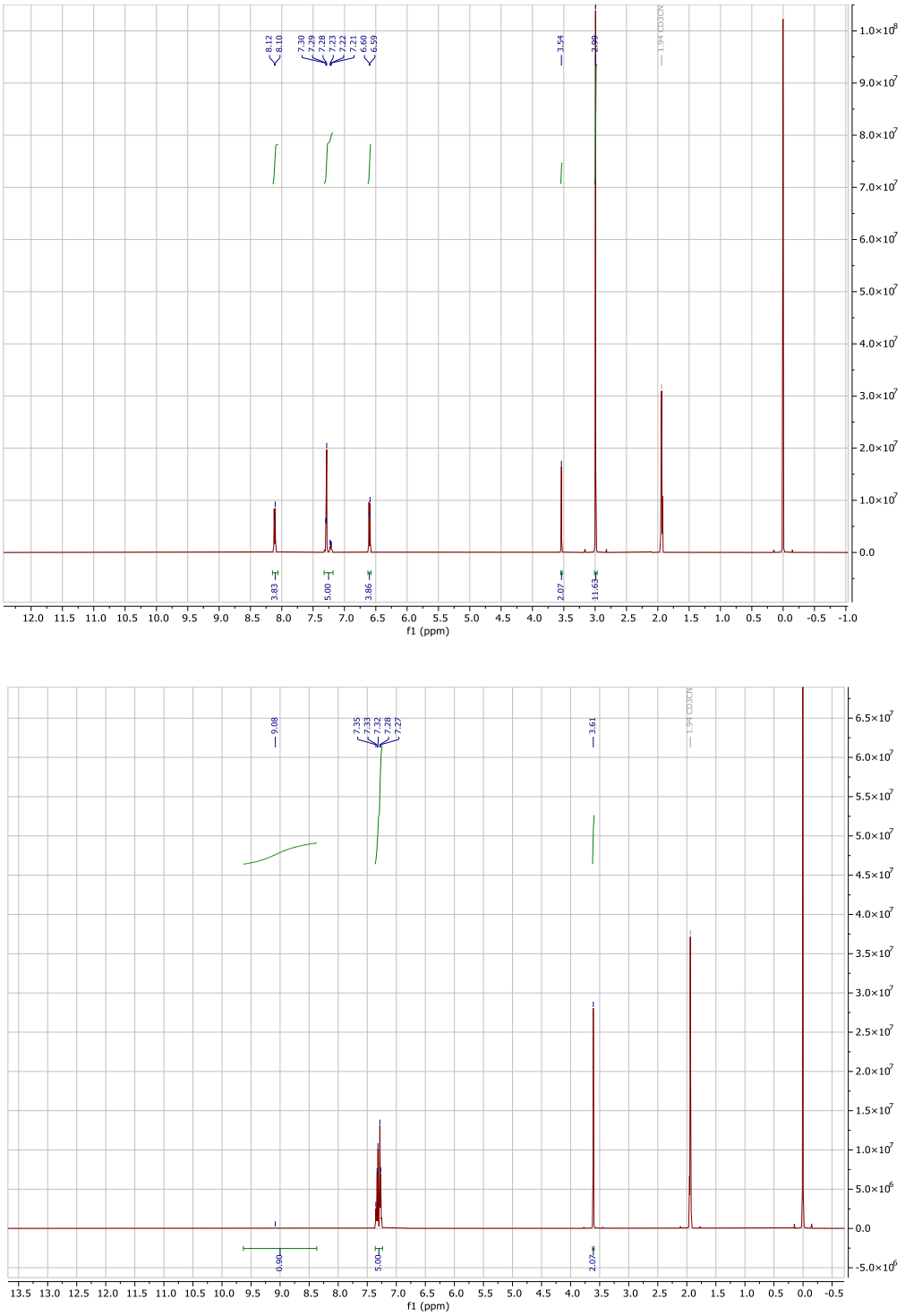

Figure S3. ^{1}H spectrum (400 MHz) of phenylacetic acid (bottom), and a mixture of phenylacetic acid and DMAP (2 equiv.) in CD_3CN.

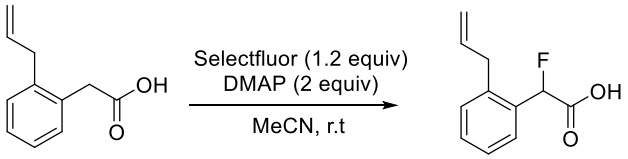

Scheme S2. Radical clock experiment. The substrate was synthesized according to literature.[2]

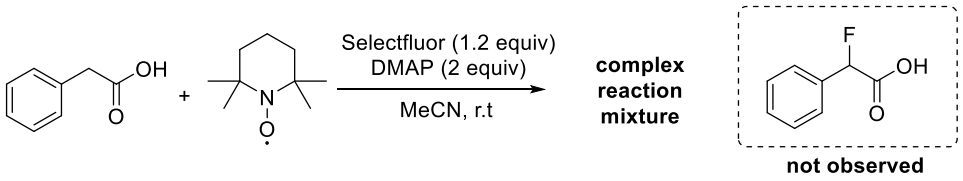

Scheme S3. Experiment in presence of TEMPO.

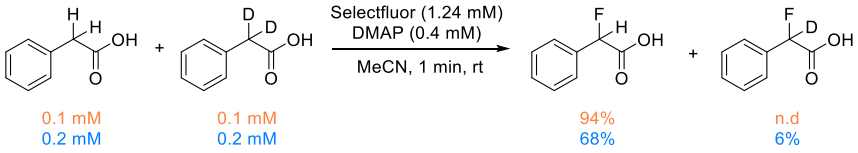

Scheme S4. Competition experiment between phenylacetic acid and deuterium-labelled phenylacetic acid. The labelled compound was synthesized according to a literature procedure.[3]

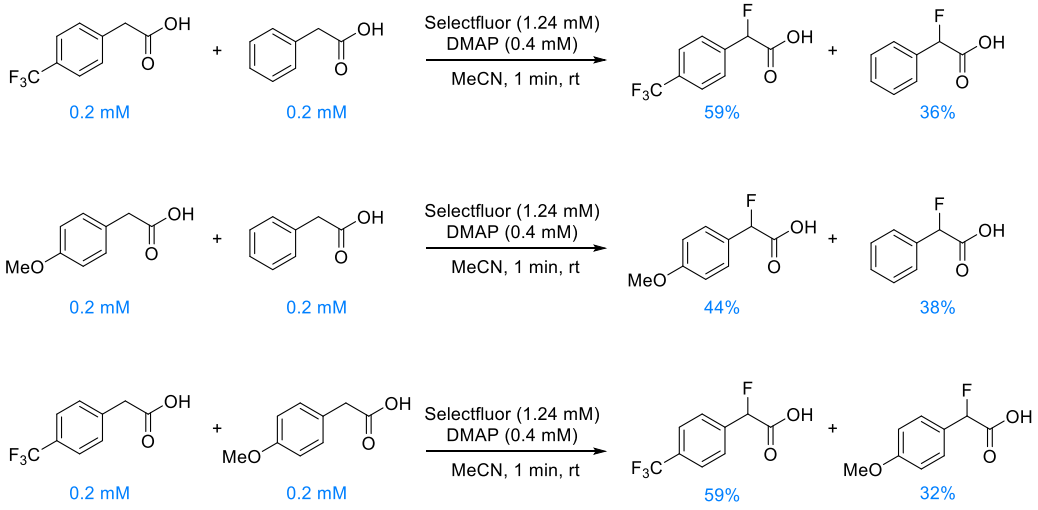

Scheme S5. Competitive experiments between phenylacetic acids derivatives.

4.7 Delayed addition experiments

Table S16. Delayed addition experiments[a]

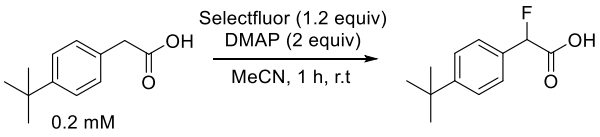

Entry	Compound added after 30 min	Conversion [%][b]	Yield [%][c]
1	**Substrate**	**n.d**	**n.d**
2	Selectfluor	100	100
3	DMAP	88	88

[a]Reaction conditions: 4-*tert*-Butylphenylacetic acid (0.3 mmol), Selectfluor (0.36 mmol), DMAP (0.6 mmol) in MeCN (anhydrous, 1.5 mL), r.t. for 1 h. [b]Conversion of 4-biphenylacetic acid determined by ^{1}H-NMR using dimethyl maleate as an internal standard. [c]NMR yield determined by ^{1}H-NMR using dimethyl maleate as an internal standard.

4.8 Reaction monitoring using a ReactIR

To maintain a constant operating temperature, the ReactIR console was filled with liquid nitrogen every 12 hours. Prior to each experiment, a background spectrum was recorded before attaching the reaction vessel. The raw ReactIR data was treated with a negative second derivative function, to aid in separation of peaks. The reference spectrum of the solvent was subtracted. The product peak appeared at ~1648 cm^{-1} (C-H bending, aromatic), Selectfluor was detected at 1005 cm^{-1} (*N*-F bond) and the consumption of DMAP was observed at 1608 cm^{-1} (C=C semicircle stretch).[4-5] Data obtained from the iCiR was processed using OriginPro2021.

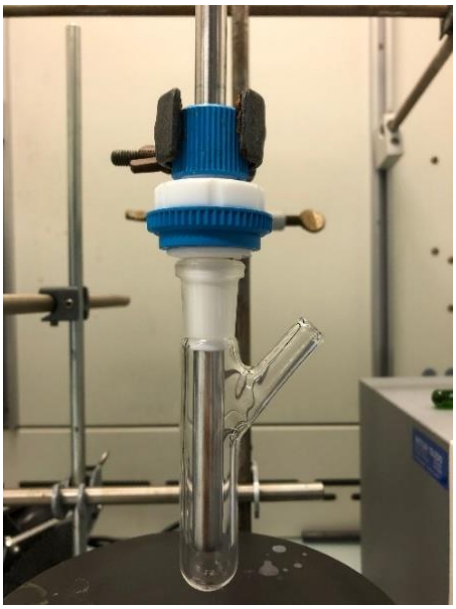

Figure S4. ReactIR setup shown with reaction vessel attached to the probe. The custom-made sidearm allows the delayed addition of reagents, degassing or sampling.

Experimental procedure for reaction monitoring. A custom-made reaction vessel (19 x 100 mm) with a sidearm (Figure S4) was equipped with a stir bar and charged with 4-tert-butylphenylacetic acid (115. 35 mg, 0.2 mM, 0.6 mmol) and 4-dimethylaminopyridine (146.6 mg, 1.2 mmol, 2 equiv.). MeCN (3 mL) was added, the vessel was sealed and sonicated for 5 minutes. The reaction vessel was attached to a PTFE adapter affixed to the ReactIRs probe (Figure S3). The reaction mixture was stirred for 30 min while collecting data (Figure S4). After this period, Selectfluor (255.06 mg, 0.72 mmol, 1.2 equiv.) was added and the mixture was stirred for 1 h at r.t.

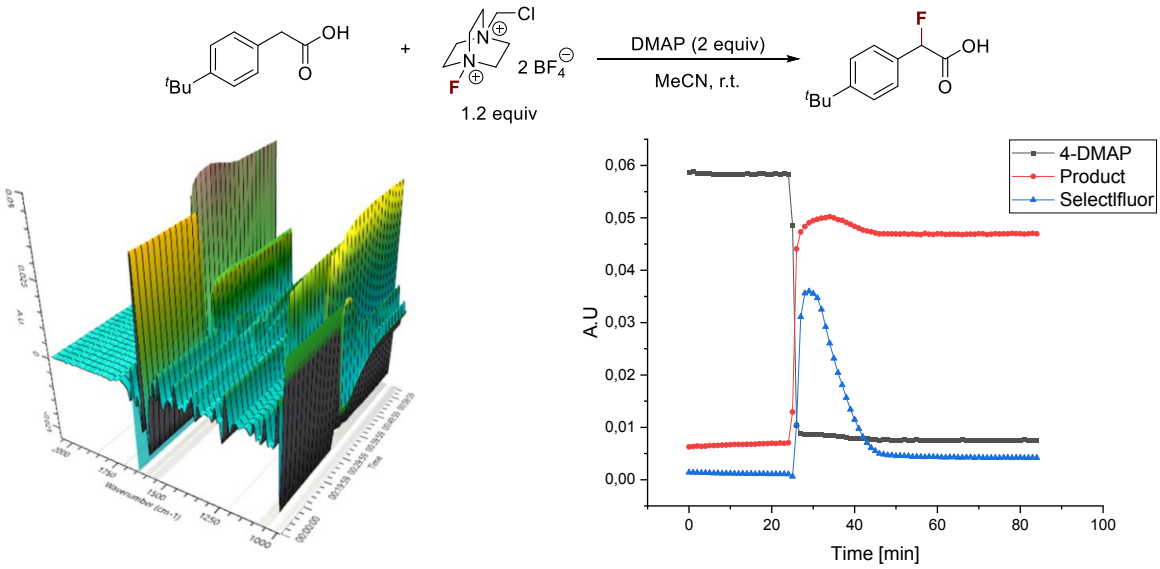

Figure S5. Reaction monitoring of the fluorination of 2-(4-(*tert*-butyl)phenyl)acetic acid using ReactIR. Raw data output (left) and processed reaction profile ((right).

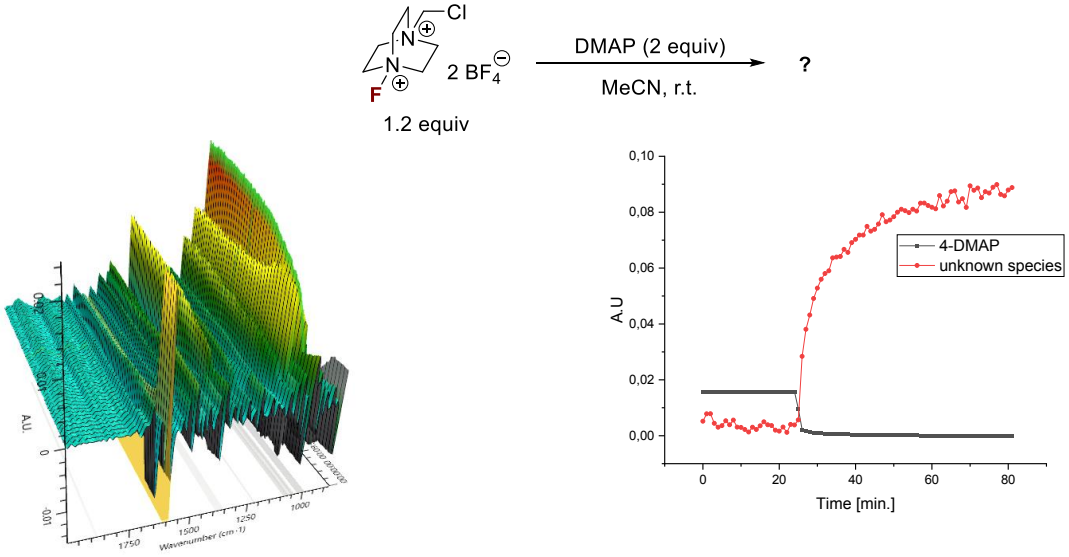

Figure S6. Monitoring of the reaction of DMAP and Selectfluor in absence of starting material using ReactIR. Raw data output (left) and processed reaction profile ((right).

4.9 NMR experiments

Initial NMR experiments with SelectFluor and DMAP in absence of starting material indicated that HF (signs of glass etching of the NMR tubes). To prevent glass etching and consumption of HF by this process, we used poly propylene micro reaction caps and Teflon NMR inserts for further measurements.
DMAP forms an adduct with HF (Figure S7 and S8). The triplet signal at 11.42 ppm shows a long-range coupling to the pyridinium nitrogen in the ^{1}H-^{15}N-HMBC spectrum (Figure S8). Similar pyridinium polyhydrogen fluorides are known, such as Olahs reagent.[6]

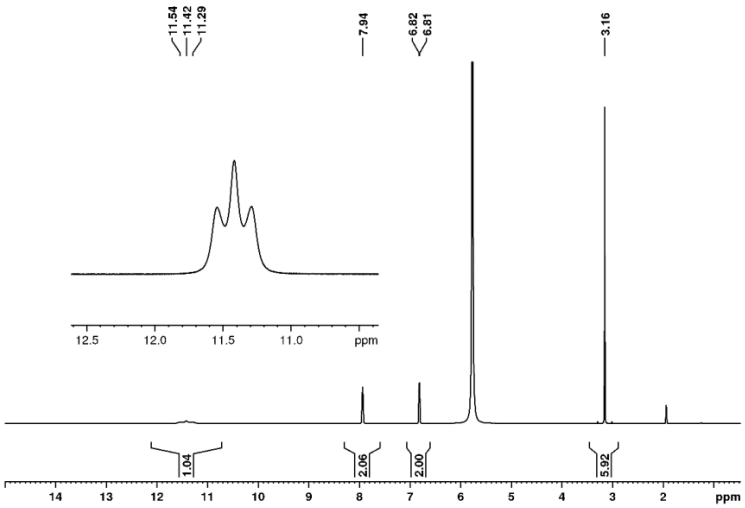

Figure S7. ^{1}H NMR spectrum (500 MHz) of DMAP in presence of HF in CD_3CN. HF (48%, 0.038 mL, 1.06 mmol) was added to DMAP (6.1 mg, 0.05 mmol) in CD_3CN (0.35 mL). DMAP forms an adduct with HF. The triplet at 11.4 ppm originates from $(F\text{-}H\text{-}F)^-$ coordinated to the pyridine nitrogen of DMAP. The two ^{19}F coupling partners lead to a triplet splitting of the ^{1}H signal.

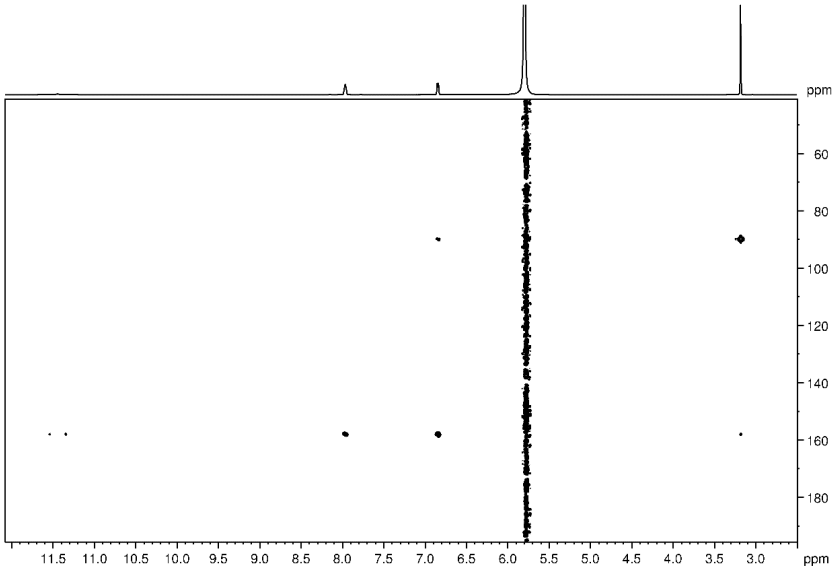

Figure S8. ^{15}N-^{1}H-HMBC spectrum of DMAP in presence of HF in $CDCN_3$. HF (48%, 0.038 mL, 1.06 mmol) was added to DMAP (6.1 mg, 0.05 mmol) in CD_3CN (0.35 mL).

In the ^{1}H NMR spectrum of a mixture of SelectFluor with DMAP, we observed the same triplet signal indicative of a pyridinium HF adduct (Figure S9 and S10).

The superposition of the ^{1}H-^{15}N-HMBC spectra of the DMAP/HF mixture with the reaction mixture of SelectFluor/DMAP shows that, also when using SelectFluor, the pyridinium nitrogen resonance shifts to ca. 160 ppm indicative of the formation of the (F-H-F)-adduct. In this case, however, the (F-H-F)-Triplett is too broad such that the long-range correlation signal could not be detected.

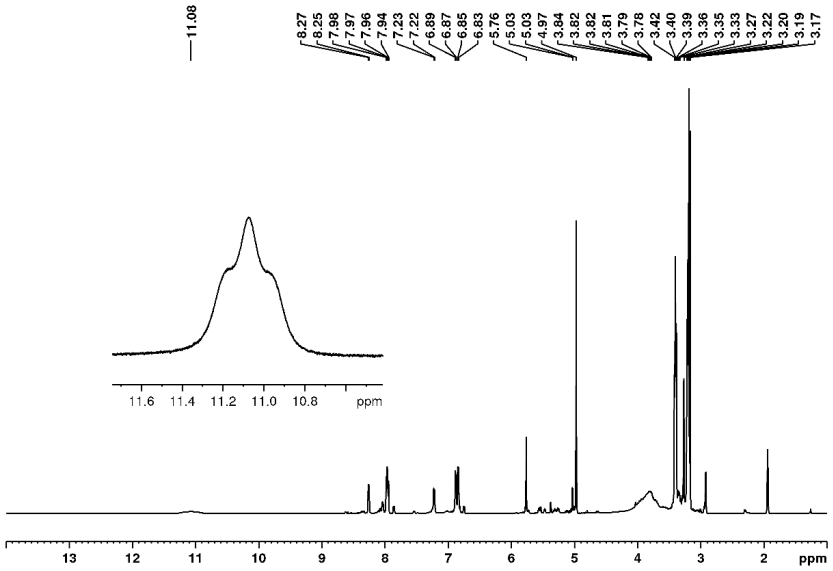

Figure S9: ^{1}H NMR spectrum (500 MHz) of a reaction mixture of Selectfluor (17.7 mg, 0.05 mmol) and DMAP (6.1 mg, 0.05 mmol) in CD_3CN (0.35 mL) after a reaction time of three days.

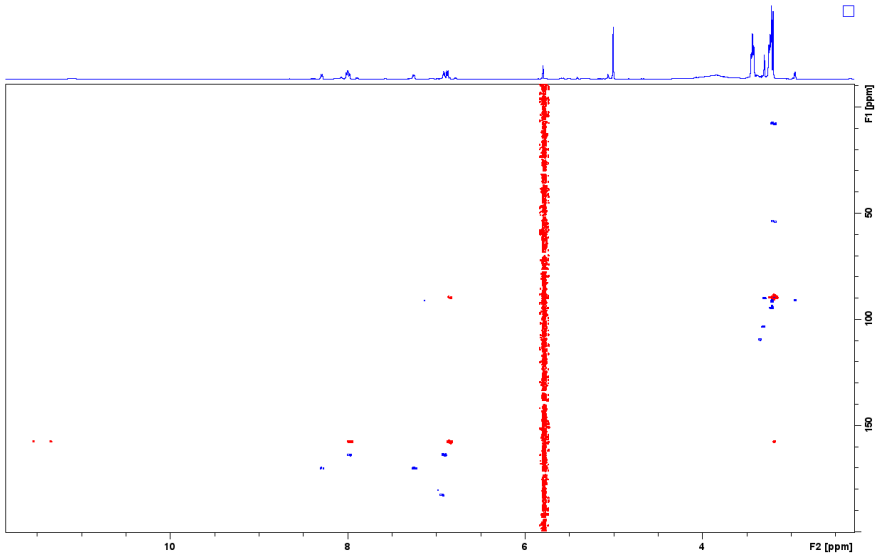

Figure S10. Superposition of ^{1}H-^{15}N-HMBC spectra. Red: HF (48%, 0.038 mL, 1.06 mmol) was added to DMAP (6.1 mg, 0.05 mmol) in CD_3CN (0.35 mL). Blue: Selectfluor (17.7 mg, 0.05 mmol) and DMAP (6.1 mg, 0.05 mmol) in CD_3CN (0.35 mL) after a reaction time of 3 days.

^{19}F NMR measurements show that HF is liberated very early after mixing the reactants (δ_{19F} = -166 ppm, see Figure S10). Right after mixing, additional, transient signals (δ_{19F} = -19 and -14 ppm, respectively) are observed in the ^{19}F NMR spectrum. These might originate from *N*-fluorinated species. However, we have not been able to prove this beyond doubt. After a reaction time of (here) several days, these transient signals have disappeared, and the ^{19}F signal of HF has shifted slightly to (δ_{19F} = -177 ppm, Figure S11). In this regard, it has to be noted that the ^{19}F chemical shift of HF depends strongly on its concentration, the presence of H^+ and other coordinating agents.

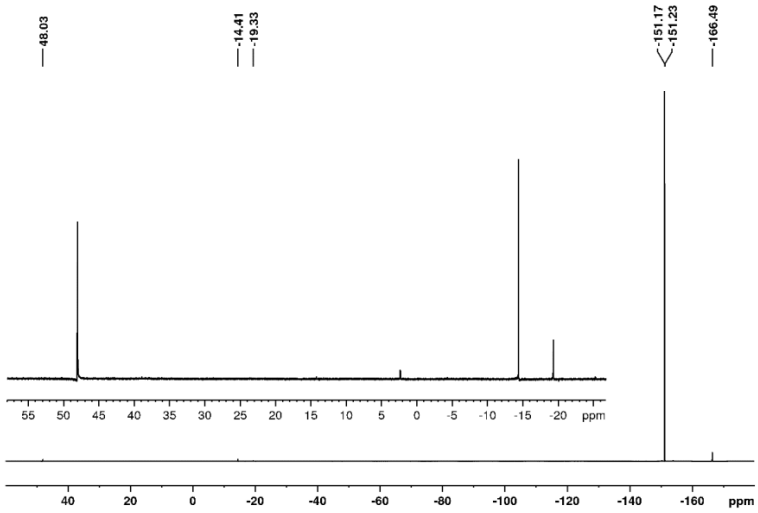

Figure S11. ^{19}F NMR (471 MHz) spectrum directly after mixing Selectfluor (17.7 mg, 0.05 mmol) and DMAP (6.1 mg, 0.05 mmol) in CD_3CN (0.35 mL). The large signal at ca. -150 ppm originates from BF_4^-.

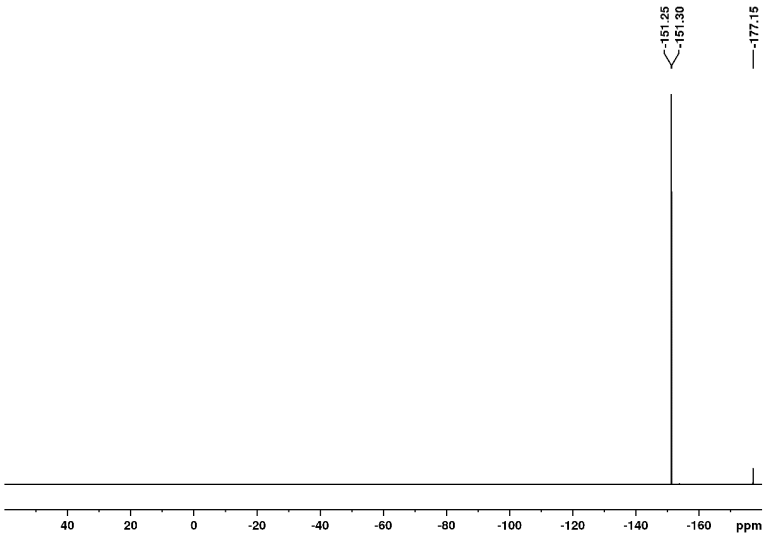

Figure S12. ^{19}F NMR spectrum (471 MHz) of a reaction mixture of Selectfluor (17.7 mg, 0.05 mmol) and DMAP (6.1 mg, 0.05 mmol) in CD_3CN (0.35 mL) after three days. Transient ^{19}F signals, observed right after mixing, have disappeared. Only the large signals of BF_4^- at ca. -150 ppm and HF at -177 ppm are visible.

Neutralization with NaOH converts HF into F^-. Applied to the sample shown in Figure S11, still only two ^{19}F signals are observed, confirming the presence of BF_4^- and F^- (Figure S12). The amount of HF and F^-, resp., increases with time. Calibrating the integral of the BF_4^--signal to 100%, the integrals of the HF signals change from 20 % (after mixing), 26 % (after 4h) to 28% and reach 25% for the quenched F^- signal.

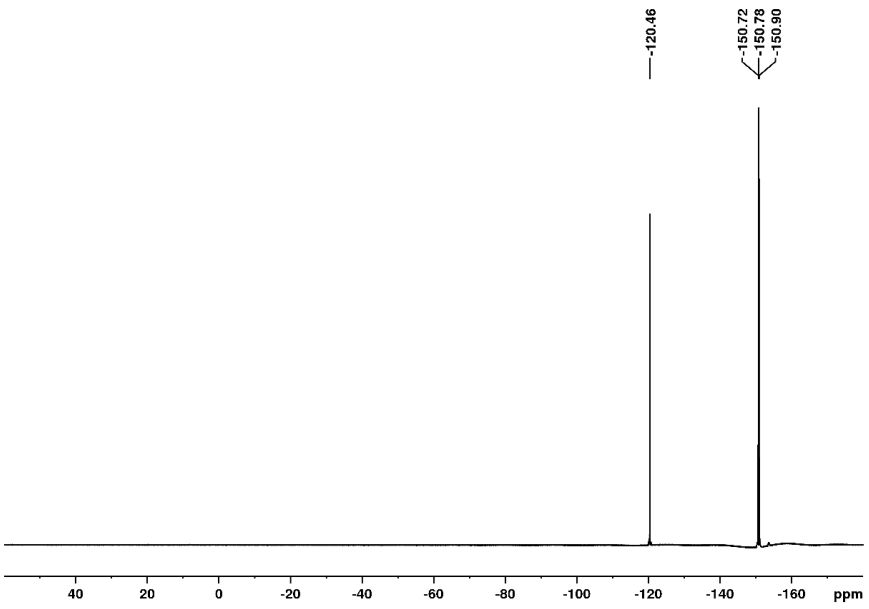

Figure S13: ^{19}F NMR spectrum (471 MHz) of a reaction mixture of Selectfluor (17.7 mg, 0.05 mmol) and DMAP (6.1 mg, 0.05 mmol) in CD_3CN (0.35 mL) after 4 days after adding 0.2 ml 1M NaOH (0.2 mmol) for neutralization. The large signal at -150 ppm originates from of $BF_4^-$and the signal at -120 ppm originates from F^-.

5 Scope

General experimental procedure. An oven-dried vessel (19 x 100 mm) equipped with a stir bar was charged with substrate (1.8 mmol, 1 equiv, 0.2 mM), 4-dimethylaminopyridine (3.6 mmol, 2 equiv.) and Selectfluor. MeCN (9 mL) was added, the vessel was sealed stirred at room temperature for one hour. HCl (10 mL, 1 M) was added and the mixture was extracted with diethylether (3 x 10 mL). The combined organic phases were dried over Na_2SO_4, filtered and concentrated. The product was purified by column chromatography (SiO_2, Hexane/EtOAc or Hexane/MeOH) on a Grace™ Reveleris™ system.

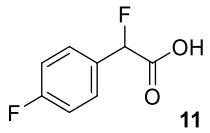

11

2-Fluoro-2-(4-fluorophenyl)acetic acid (11). From 2-(4-fluorophenyl)acetic acid (277.45 mg, 1.8 mmol, 0.2 mM) using 4-(dimethylamino)-pyridine (439.8 mg, 3.6 mmol, 2 equiv.) and 1-chloromethyl-4-fluoro-1,4-diazoniabicyclo[2.2.2]octanebis(tetrafluoroborate) (765.2 mg, 2.16 mmol, 1.2 equiv.) in 9 mL MeCN. The crude mixture was purified over silica with flash chromatography, using an eluent gradient of 5-20% EA in hexane to afford the title compound as a white powder (221.8 mg, 1.3 mmol, 72%).

^{1}H NMR (400 MHz, $CDCl_3$) δ 8.84 (s, 1H), 7.49–7.46 (m, 2H), 7.15 – 7.07 (m, 2H), 5.81 (d, *J* = 47.2 Hz, 1H) ppm. **^{13}C NMR** (101 MHz, $CDCl_3$) δ 173.8 (d, *J* = 28.2 Hz), 163.7 (dd, *J* = 249.5, 2.2 Hz), 129.4 (dd, *J* = 21.1, 3.4 Hz), 129.0 – 128.8 (m), 116.2 (d, *J* = 22.1 Hz), 88.3 (d, *J* = 187.3 Hz) **^{19}F NMR** (376 MHz, $CDCl_3$) δ -110.59– -110.67 (m) -179.54 (d, *J* = 46.8 Hz) ppm.

These data are in full agreement with those previously published in the literature.[7]

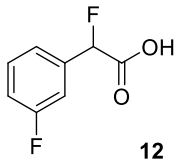

12

2-fluoro-2-(3-fluorophenyl)acetic acid (12). From 2-(3-fluorophenyl)acetic acid (277.45 mg, 1.8 mmol, 0.2 mM) using 4-(dimethylamino)-pyridine (439.8 mg, 3.6 mmol, 2 equiv.) and 1-chloromethyl-4-fluoro-1,4-diazoniabicyclo[2.2.2]octanebis(tetrafluoroborate) (765.2 mg, 2.16 mmol, 1.2 equiv.) in 9 mL MeCN. The crude mixture was purified over silica with flash chromatography, using an eluent gradient of 0–10% EA in hexane to afford the title compound as a yellowish powder (160.0 mg, 0.93 mmol, 52%).

^{1}H NMR (400 MHz, $CDCl_3$) δ 11.56 (s, 1H), 7.40– 7.35 (m, 1H), 7.26– 7.24 (m, 1H), 7.19 (d, *J* = 9.2 Hz, 1H), 7.12– 7.07 (m, 1H), 5.80 (d, *J* = 47.1 Hz, 1H) ppm. ^{13}C NMR (101 MHz, $CDCl_3$) δ 174.3 (d, *J* = 27.5 Hz), 162.9 (d, *J* = 247.9 Hz), 135.6 (dd, *J* = 27.9, 8.9 Hz), 130.8 (d, *J* = 8.2 Hz), 122.3 (dd, *J* = 6.6, 3.1 Hz), 117.1 (dd, *J* = 21.0, 1.8 Hz), 113.8 (dd, *J* = 23.2, 6.9 Hz), 88.1 (dd, *J* = 188.6, 2.2 Hz) ppm. ^{19}F NMR (376 MHz, $CDCl_3$) δ -111.37, -183.17 (d, *J* = 47.3 Hz) ppm. HRMS (ESI) *m/z* calculated [M+2Na-H] 217.0011, found, 217.0012.

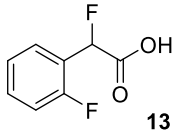

13

2-Fluoro-2-(2-fluorophenyl)acetic acid (13). From 2-(2-fluorophenyl)acetic acid (277.45 mg, 1.8 mmol, 0.2 mM) using 4-(dimethylamino)-pyridine (439.8 mg, 3.6 mmol, 2 equiv.) and 1-chloromethyl-4-fluoro-1,4-diazoniabicyclo[2.2.2]octanebis(tetrafluoroborate) (765.2 mg, 2.16 mmol, 1.2 equiv.) in 9 mL MeCN. The crude mixture was purified over silica with flash chromatography, using an eluent gradient of 0–10% EA in hexane to afford the title compound as a yellowish powder (163.1 mg, 0.95 mmol, 53%).

^{1}H NMR (400 MHz, $CDCl_3$) δ 8.87 (s, 1H), 7.55 – 7.40 (m, 2H), 7.27 – 7.09 (m, 2H), 6.13 (d, J = 48.5 Hz, 1H) ppm. ^{13}C NMR (101 MHz, $CDCl_3$) δ 173.3 (dd, J = 28.1, 1.3 Hz), 160.4 (dd, J = 250.7, 4.4 Hz), 132.1 (dd, J = 8.3, 2.6 Hz), 128.9 (dd, J = 5.1, 2.6 Hz), 124.7 (dd, J = 4.1, 1.2 Hz), 121.2 (dd, J = 20.9, 13.9 Hz), 116.0 (d, J = 20.9 Hz), 83.2 (dd, J = 185.6, 3.9 Hz) ppm. ^{19}F NMR (376 MHz, $CDCl_3$) δ -117.09 (m), -181.17 (d, J = 46.7 Hz) ppm. These data are in full agreement with those previously published in the literature. [7]

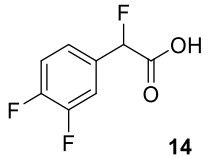

14

2-(3,4-difluorophenyl)-2-fluoroacetic acid (14). From 2-(3,4-difluorophenyl)acetic acid (309.8 mg, 1.8 mmol, 0.2 mM), using 4-(dimethylamino)pyridine (439.8 mg, 3.6 mmol, 2 equiv.) and 1-chloromethyl-4-fluoro-1,4-diazoniabicyclo[2.2.2]octanebis(tetrafluoroborate) (765.2 mg, 2.16 mmol, 1.2 equiv.) in 9 mL MeCN. The crude mixture was purified over silica with flash chromatography, using an eluent gradient of 0-10% EA in hexane to afford the title compound as white crystals (161.6 mg, 0.85 mmol, 47%).

^{1}H NMR (400 MHz, $CDCl_3$) δ 7.39– 7.34 (m, 1H), 7.28 – 7.20 (m, 2H), 5.82 (d, J = 47.0 Hz, 1H) ppm. ^{13}C NMR (101 MHz, $CDCl_3$) δ 174.2 (d, J = 27.8 Hz), 151.4 (ddd, J = 249.8, 10.5, 2.1 Hz), 150.6 (dd, J = 249.7, 12.1 Hz), 130.2 (ddd, J = 21.6, 5.8, 3.9 Hz), 123.2 (td, J = 6.7, 3.8 Hz), 118.1 (d, J = 17.8 Hz), 116.0 (dd, J = 18.9, 6.6 Hz), 87.6 (dd, J = 188.8, 1.5 Hz) ppm. ^{19}F NMR (376 MHz, $CDCl_3$) δ -135.10 – -135.16 (m), -135.54 – -135.63 (m), -181.48 (d, J = 47.2 Hz) ppm. HRMS (ESI) *m/z* calculated [M+2Na-H] 234.9911, found, 234.9918.

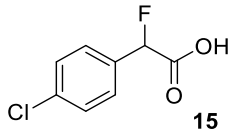

15

2-(4-chlorophenyl)-2-fluoroacetic acid (15). From 2-(4-chlorophenyl)acetic acid (307.8 mg, 1.8 mmol, 0.2 mM), using 4-(dimethylamino)pyridine (439.8 mg, 3.6 mmol, 2 equiv.) and 1-chloromethyl-4-fluoro-1,4-diazoniabicyclo[2.2.2]octanebis(tetrafluoroborate) (765.2 mg, 2.16 mmol, 1.2 equiv.) in 9 mL MeCN. The crude mixture was purified over silica with flash chromatography, using an eluent gradient of 0–10% EA in hexane to afford the title compound as a white solid (286.7 mg, 1.5 mmol, 84%).

^{1}H NMR (400 MHz, $CDCl_3$) δ 10.98 – 10.64 (m, 1H), 7.49 – 7.38 (m, 4H), 5.83 (d, J = 47.5 Hz, 1H) ppm. ^{13}C NMR (101 MHz, $CDCl_3$) δ 174.1 (d, J = 32.3 Hz), 136.1 (d, J = 2.5 Hz), 131.8 (d, J = 21.1 Hz), 129.2, 127.9 (d, J = 6.2 Hz), 88.0 (d, J = 188.2 Hz) ppm. ^{19}F NMR (376 MHz, $CDCl_3$) δ -181.97 (d, J = 47.2 Hz) ppm. These data are in full agreement with those previously published in the literature.[7]

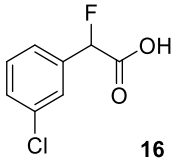

16

2-(3-chlorophenyl)-2-fluoroacetic acid (16). From 2-(3-chlorophenyl)acetic acid (307.8 mg, 1.8 mmol, 0.2 mM) using 4-(dimethylamino)pyridine (439.8 mg, 3.6 mmol, 2 equiv.) and 1-chloromethyl-4-fluoro-1,4-diazoniabicyclo[2.2.2]octanebis(tetrafluoroborate) (765.2 mg, 2.16 mmol, 1.2 equiv.) in 9 mL MeCN. The crude mixture was purified over silica with flash chromatography (30% EA in hexane) to afford the title compound as a yellow oil (164.5 mg, 0.87 mmol, 48%).

^{1}H NMR (400 MHz, $CDCl_3$) δ 7.47 (s, 1H), 7.39 – 7.34 (m, 3H), 5.77 (d, J = 47.3 Hz, 1H) ppm. ^{13}C NMR (101 MHz, $CDCl_3$) δ 168.6 (d, J = 27.3 Hz), 136.1 (d, J = 21.0 Hz), 134.9, 130.23, 129.9 (d, J = 1.8 Hz), 126.8 (d, J = 6.8 Hz), 124.8 (d, J = 6.3 Hz), 88.6 (d, J = 187.2 Hz) ppm. ^{19}F NMR (376 MHz, $CDCl_3$) δ -182.24 (d, J = 47.4 Hz) ppm. These data are in full agreement with those previously published in the literature.[7]

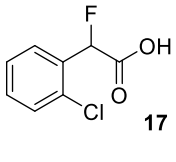

17

2-(2-chlorophenyl)-2-fluoroacetic acid (17). From 2-(2-chlorophenyl)acetic acid (307.8 mg, 1.8 mmol, 0.2 mM) using 4-(dimethylamino)pyridine (439.8 mg, 3.6 mmol, 2 equiv.) and 1-chloromethyl-4-fluoro-1,4-diazoniabicyclo[2.2.2]octanebis(tetrafluoroborate) (765.2 mg, 2.16 mmol, 1.2 equiv.) in 9 mL MeCN. The crude mixture was purified over silica with flash chromatography (30% EA in hexane) to afford the title compound as a yellowish powder (274.5 mg, 1.5 mmol, 81%).

^{1}H NMR (400 MHz, MeOD-d_4): δ 7.57–7.35 (m, 4H), 6.24 (d, J = 46.8 Hz, 1H) ppm. ^{13}C NMR (100 MHz, MeOD-d_4): δ 170.1 (d, J = 27.4 Hz), 133.5 (d, J = 4.1 Hz), 132.9 (d, J = 20.2 Hz), 130.9 (d, J = 2.6 Hz), 129.7 (d, J = 1.1 Hz), 128.8 (d, J = 5.5 Hz), 127.2 (d, J = 1.2 Hz), 86.1 (d, J = 182.1 Hz) ppm. ^{19}F NMR (376 MHz, MeOD-d_4): δ -180.44 (d, J = 45.7 Hz) ppm. HRMS (ESI) *m/z* calculated [M+2Na-H] 232.9711, found, 232.9720.

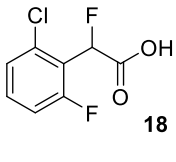

18

2-(2-chloro-6-fluorophenyl)-2-fluoroacetic acid (18). From2-(2-chloro-6-fluorophenyl)acetic acid (339.44 mg, 1.8 mmol, 0.2 mM), using 4-(dimethylamino)pyridine (439.8 mg, 3.6 mmol, 2 equiv.) and 1-chloromethyl-4-fluoro-1,4-diazoniabicyclo[2.2.2]octanebis(tetrafluoroborate) (765.2 mg, 2.16 mmol, 1.2 equiv.) in 9 mL MeCN. A yield of 64% was determined by ^{1}H NMR, using dimethyl maleate as an internal standard. The product could not be separated from the substrate by column chromatography.

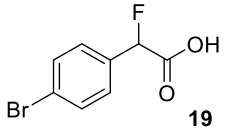

19

2-(4-bromophenyl)-2-fluoroacetic acid (19). From 2-(4-bromophenyl)acetic acid (387.9 mg, 1.8 mmol, 0.2 mM), using 4-(dimethylamino)pyridine (439.8 mg, 3.6 mmol, 2 equiv.) and 1-chloromethyl-4-fluoro-1,4-diazoniabicyclo[2.2.2]octanebis(tetrafluoroborate) (765.2 mg, 2.16 mmol, 1.2 equiv.) in 9 mL MeCN. The crude mixture was purified over silica with flash chromatography (40% EA in hexane) to afford the title compound as white powder (254.5 mg, 1.2 mmol, 61%).

^{1}H NMR (400 MHz, $CDCl_3$): δ 7.58 (d, *J* = 7.8 Hz, 2H), 7.38 (d, *J* = 8.2 Hz, 2H) 5.81 (d, *J* = 47.0 Hz, 1H) ppm. ^{13}C NMR (101 MHz, $CDCl_3$) δ 172.8 (d, *J* = 27.8 Hz), 133.1 (d, *J* = 20.8 Hz), 132.7 (d, *J* = 21.0 Hz), 132.2, 128.3 (d, *J* = 5.8 Hz), 124.3 (d, *J* = 2.5 Hz), 88.8 (d, *J* = 186.4 Hz), 88.3 (d, *J* = 187.2 Hz) ppm. ^{19}F NMR (376 MHz, $CDCl_3$) δ -182.43 (d, *J* = 49 Hz) ppm. These data are in full agreement with those previously published in the literature.[8]

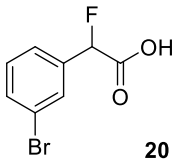

20

2-(3-bromophenyl)-2-fluoroacetic acid (20). From 2-(3-bromophenyl)acetic acid (387.9 mg, 1.8 mmol, 0.2 mM), using 4-(dimethylamino)pyridine (439.8 mg, 3.6 mmol, 2 equiv.) and 1-chloromethyl-4-fluoro-1,4-diazoniabicyclo[2.2.2]octanebis(tetrafluoroborate) (765.2 mg, 2.16 mmol, 1.2 equiv.) in 9 mL MeCN. The crude mixture was purified over silica with flash chromatography (40% EA in hexane) to afford the title compound as white powder (157.6 mg, 0.68 mmol, 38%).

^{1}H NMR (400 MHz, $CDCl_3$) δ 10.94 (s, 1H), 7.61 (s, 1H), 7.53– 7.51 (m, 1H), 7.40– 7.37 (m, 1H), 7.28–7.24 (m, 1H) 5.76 (d, *J* = 47.1 Hz, 1H) ppm. ^{13}C NMR (101 MHz, $CDCl_3$) δ 174.0 (d, *J* = 27.7 Hz), 135.5 (d, *J* = 20.8 Hz), 133.2 (d, *J* = 1.8 Hz), 130.6, 129.6 (d, *J* = 6.8 Hz), 125.2 (d, *J* = 6.3 Hz), 123.0, 87.9 (d, *J* = 188.8 Hz) ppm. ^{19}F NMR (376 MHz, $CDCl_3$) δ -183.16 (d, *J* = 46.9 Hz) ppm. These data are in full agreement with those previously published in the literature.[8]

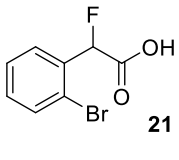

21

2-(2-bromophenyl)-2-fluoroacetic acid (21). From 2-(2-bromophenyl)acetic acid (387.9 mg, 1.8 mmol, 0.2 mM), using 4-(dimethylamino)pyridine (439.8 mg, 3.6 mmol, 2 equiv.) and 1-chloromethyl-4-fluoro-1,4-diazoniabicyclo[2.2.2]octanebis(tetrafluoroborate) (765.2 mg, 2.16 mmol, 1.2 equiv.) in 9 mL MeCN. The crude mixture was purified over silica with flash chromatography (40% EA in hexane) to afford the title compound as white powder (212.6 mg, 0.91 mmol, 51%).

^{1}H NMR (400 MHz, $CDCl_3$) δ 7.63 (d, *J* = 8.1 Hz, 1H), 7.54 –7.51 (m, 1H), 7.42 – 7.37 (m, 1H), 7.32 – 7.28 (m, 1H), 6.28 (d, *J* = 46.3 Hz, 1H) ppm. ^{13}C NMR (101 MHz, $CDCl_3$) δ 172.9 (d, *J* = 28.1 Hz), 133.4, 133.3 (d, *J* = 20.7 Hz), 131.5 (d, *J* = 2.5 Hz), 128.7 (d, *J* = 6.2 Hz), 128.0, 123.4 (d, *J* = 4.7 Hz), 87.9 (d, *J* = 186.9 Hz) ppm. ^{19}F NMR (376 MHz, $CDCl_3$) δ -180.05 (d, *J* = 46.2 Hz) ppm. HRMS (ESI) *m/z* calculated [M+2Na-H] 276.9211, found, 278.9203.

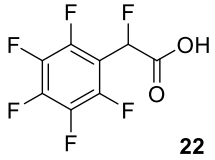

22

2-Fluoro-2-(perfluorophenyl)acetic acid (22). From 2-(perfluorophenyl)acetic acid (406.9 mg, 1.8 mmol, 0.2 mM), using 4-(dimethylamino)pyridine (439.8 mg, 3.6 mmol, 2 equiv.) and 1-chloromethyl-4-fluoro-1,4-diazoniabicyclo[2.2.2]octanebis(tetrafluoroborate) (765.2 mg, 2.16 mmol, 1.2 equiv.) in 9 mL MeCN. The crude mixture was purified over silica with flash chromatography, using an eluent gradient of 0-10% EA in hexane to afford the title compound as yellow oil (163.8 mg, 0.67 mmol 38%).

^{1}H NMR (400 MHz, DMSO) δ 14.17 (s, 1H), 6.48 (d, J = 44.7 Hz, 1H) ppm. ^{13}C NMR (101 MHz, DMSO) δ 167.5 (d, J = 26.0 Hz), 146.1, 143.6, 140.7, 138.5, 136.02 109.4 (d, J = 17.0 Hz), 78.6 (d, J = 185.2 Hz) ppm. ^{19}F NMR (376 MHz, DMSO) δ -142.28 – -142.42 (m), -149.81 – -151.43 (m), -160.86 – -161.85 (m), -180.97 (d, J = 44.5 Hz) ppm. HRMS (ESI) *m/z* calculated [M+2Na-H], 288.9711 found, 288.9639.

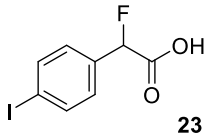

23

2-fluoro-2-(4-iodophenyl)acetic acid (23). From 2-(4-iodophenyl)acetic acid (225.8 mg, 1.8 mmol, 0.2 mM), using 4-(dimethylamino)pyridine (439.8 mg, 3.6 mmol, 2 equiv.) and 1-chloromethyl-4-fluoro-1,4-diazoniabicyclo[2.2.2]octanebis(tetrafluoroborate) (765.2 mg, 2.16 mmol, 1.2 equiv.) in 9 mL MeCN. The crude mixture was purified over silica with flash chromatography, using an eluent gradient of 0–10% EA in hexane to afford the title compound as a white solid (86.2 mg, 0.31 mmol, 35%).

^{1}H NMR (400 MHz, $CDCl_3$) δ 7.80 (d, J = 7.6 Hz, 2H), 7.26 (d, J = 8.7 Hz, 2H), 5.81 (d, J = 47.2 Hz, 1H) ppm. ^{13}C NMR (101 MHz, $CDCl_3$) δ 173.9 (d, J = 27.6 Hz), 138.2, 133.1 (d, J = 20.9 Hz), 128.4 (d, J = 6.2 Hz), 96.3 (d, J = 2.7 Hz), 88.3 (d, J = 188.1 Hz) ppm. ^{19}F NMR (376 MHz, $CDCl_3$) δ -182.15 (d, J = 47.0 Hz) ppm. HRMS (ESI) *m/z* calculated [M+2Na-H] 324.9111, found, 324.9089.

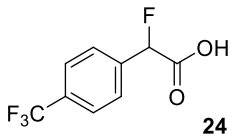

24

2-Fluoro-2-(4-(trifluoromethyl)phenyl)acetic acid (24). From 2-(4-(trifluoromethyl)phenyl)acetic acid (367.47 1.8 mmol, 0.2 mM) using 4-(dimethylamino) pyridine (439.8 mg, 3.6 mmol, 2 equiv.) and 1-chloromethyl-4-fluoro-1,4-diazoniabicyclo[2.2.2]octanebis(tetrafluoroborate) (765.2 mg, 2.16 mmol, 1.2 equiv.) in 9 mL MeCN. The crude mixture was purified over silica with flash chromatography (10% EA in hexane) to afford the title compound as yellow crystals (343.3 mg, 1.55 mmol, 86%).

^{1}H NMR (400 MHz, $CDCl_3$) δ 11.54 (s, 1H), 7.83 – 7.50 (m, 4H), 5.90 (d, J = 47.1 Hz, 1H) ppm. ^{13}C NMR (101 MHz, $CDCl_3$) δ 173.9 (d, J = 27.2 Hz), 137.2 (d, J = 21.1 Hz), 132.7–131.7 (m), 126.9 (d, J = 6.7 Hz), 126.0 (d, J = 3.8 Hz), 88.1 (d, J = 189.0 Hz) ppm. ^{19}F NMR (376 MHz, $CDCl_3$) δ -62.95, -185.25 (d, J = 47.3 Hz) ppm. These data are in full agreement with those previously published in the literature.[8]

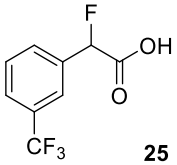

25

2-fluoro-2-(3-(trifluoromethyl)phenyl)acetic acid (25). From 2-(3-(trifluoromethyl)phenyl)acetic acid (367.47 mg, 1.8 mmol, 0.2 mM) using 4-(dimethylamino)-pyridine (439.8 mg, 3.6 mmol, 2 equiv.) and 1-chloromethyl-4-fluoro-1,4-diazoniabicyclo[2.2.2]octanebis(tetrafluoroborate) (765.2 mg, 2.16 mmol, 1.2 equiv.) in 9 mL MeCN. The crude mixture was purified over silica with flash chromatography using an eluent gradient of 0-20% EA in hexane to afford the title compound as a yellowish powder (126.6 mg, 0.57 mmol, 32%).

^{1}H NMR (400 MHz, $CDCl_3$) δ 9.67 (s, 1H), 7.79 (s, 1H), 7.72 (d, J = 7.9 Hz, 2H), 7.59 (t, J = 7.8 Hz, 1H), 5.93 (d, J = 47.2, 1H) ppm. ^{13}C NMR (101 MHz, $CDCl_3$) δ 173.2 (d, J = 27.2 Hz), 134.3 (d, J = 21.4 Hz), 131.3 (q, J = 32.9 Hz), 129.7 (d, J = 6.5 Hz), 129.5, 126.8– 126.7 (m), 123.2– 123.3 (m), 87.9 (d, J = 188.9 Hz) ppm.^{19}F NMR (376 MHz, $CDCl_3$) δ -62.81, -184.25 (d, J = 46.7 Hz) ppm. HRMS (ESI) *m/z* calculated [M+2Na-H] 267.0011, found, 266.9985.

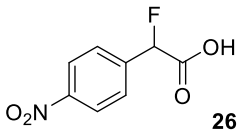

26

2-fluoro-2-(4-nitrophenyl)acetic acid (26). From 2-fluoro-2-(4-nitrophenyl)acetic acid (326.07 mg, 1.8 mmol, 0.2 mM) using 4-(dimethylamino)pyridine (439.8 mg, 3.6 mmol, 2 equiv.) and 1-chloromethyl-4-fluoro-1,4-diazoniabicyclo[2.2.2]octanebis(tetrafluoroborate) (765.2 mg, 2.16 mmol, 1.2 equiv.) in 9 mL MeCN. A yield of 87% was determined by ^{1}H NMR, using dimethyl maleate as an internal standard. Isolation was not possible, because the title compound decomposed during column chromatography.

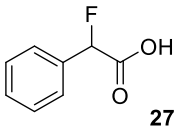

27

2-fluoro-2-phenylacetic acid (27). From 2-phenylacetic acid (245.07 mg, 1.8 mmol, 0.2 mM), using 4-(dimethylamino)pyridine (439.8 mg, 3.6 mmol, 2 equiv.) and 1-chloromethyl-4-fluoro-1,4-diazoniabicyclo[2.2.2]octanebis(tetrafluoroborate) (765.2 mg, 2.16 mmol, 1.2 equiv.) in 9 mL MeCN. The crude mixture was purified over silica with flash chromatography (5% EA in hexane) to afford the title compound as white crystals (136.8 mg, 0.89 mmol, 49%).

^{1}H NMR (400 MHz, $CDCl_3$): δ 10.40 (s, 1H) 7.61–7.33 (m, 5H), 5.86 (d, J = 47.4 Hz, 1H) ppm. ^{13}C NMR (101 MHz, $CDCl_3$) δ 174.6 (d, J = 28.0 Hz), 133.5 (d, J = 20.4 Hz), 130.1 (d, J = 2.2 Hz), 129.0, 126.8 (d, J = 6.1 Hz), 88.9 (d, J = 186.6Hz) ppm. ^{19}F NMR (376 MHz, $CDCl_3$): δ -180.82 (d, J = 47.5 Hz) ppm. These data are in full agreement with those previously published in the literature.[8]

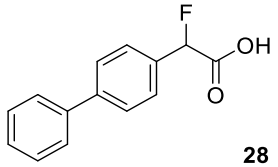

28

2-([1,1'-biphenyl]-4-yl)-2-fluoroacetic acid) (28). From 2-([1,1'-biphenyl]-4-yl)acetic acid (382.05 mg, 1.8 mmol, 0.2 mM) using 4-(dimethylamino)-pyridine (439.8 mg, 3.6 mmol, 2 equiv.) and 1-chloromethyl-4-fluoro-1,4-diazoniabicyclo[2.2.2]octanebis(tetrafluoroborate) (765.2 mg, 2.16 mmol, 1.2 equiv.) in 9 mL MeCN. The crude mixture was purified over silica with flash chromatography using an eluent gradient of 5–10 % EA in hexane to afford the title compound as a yellowish powder (308.7 mg, 1.34 mmol, 75%).

^{1}H NMR (400 MHz, MeOD) δ 7.68 (d, *J* = 7.7 Hz, 2H), 7.63 (d, *J* = 8.3 Hz, 2H), 7.55 (d, *J* = 8.0 Hz, 2H), 7.44 (t, *J* = 7.3 Hz, 2H), 7.35 (t, *J* = 6.6 Hz, 1H), 5.90 (d, *J* = 47.9 Hz, 1H). ^{13}C NMR (100 MHz, MeOD-d_4): δ 170.8 (d, *J* = 28.0 Hz), 141.2 (d, *J* = 214.3 Hz), 134.0 (d, *J* = 20.4 Hz), 128.6 – 126.6 (m), 88.9 (d, *J* = 182.1 Hz) ppm. ^{19}F NMR (376 MHz, MeOD-d_4): δ -179.43 (d, *J* = 47.5 Hz) ppm. These data are in full agreement with those previously published in the literature.[7]

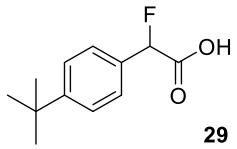

29

2-(4-(*tert*-butyl)phenyl)-2-fluoroacetic acid (29). From 2-(4-(tert-butyl)phenyl)acetic acid (346.06mg, 1.8 mmol, 0.2 mM), using 4-(dimethylamino)pyridine (439.8 mg, 3.6 mmol, 2 equiv.) and 1-chloromethyl-4-fluoro-1,4-diazoniabicyclo[2.2.2]octanebis(tetrafluoroborate) (765.2 mg, 2.16 mmol, 1.2 equiv.) in 9 mL MeCN. The crude mixture was purified over silica with flash chromatography, using an eluent gradient of 0–10% EA in hexane to afford the title compound as white crystals (185.4 mg, 0.88 mmol, 49%).

^{1}H NMR (400 MHz, $CDCl_3$) δ 10.50 (s, 1H), 7.48 – 7.39 (m, 4H), 5.80 (d, *J* = 47.5 Hz, 1H) 1.33 (s, 9H) ppm. ^{13}C NMR (101 MHz, $CDCl_3$) δ 174.7 (d, *J* = 28.3 Hz), 153.4 (d, *J* = 2.3 Hz), 130.5 (d, *J* = 20.6 Hz), 126.7 (d, *J* = 5.7 Hz), 126.0, 88.8 (d, *J* = 186.1 Hz), 34.9, 31.3 ppm. ^{19}F NMR (376 MHz, $CDCl_3$) δ -179.39 (d, *J* = 47.5 Hz) ppm. These data are in full agreement with those previously published in the literature.[8]

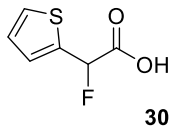

30

2-fluoro-2-(thiophen-2-yl)acetic acid (30). From 2-(thiophen-2-yl)acetic acid (255.02 mg, 1.8 mmol, 0.2 mM), using 4-(dimethylamino)pyridine (439.8 mg, 3.6 mmol, 2 equiv.) and 1-chloromethyl-4-fluoro-1,4-diazoniabicyclo[2.2.2]octanebis(tetrafluoroborate) (765.2 mg, 2.16 mmol, 1.2 equiv.) in 9 mL MeCN. The yield of 83% was determined by ^{1}H NMR, using dimethyl maleate as an internal standard. Isolation was not possible, because the title compound decomposed during column chromatography.

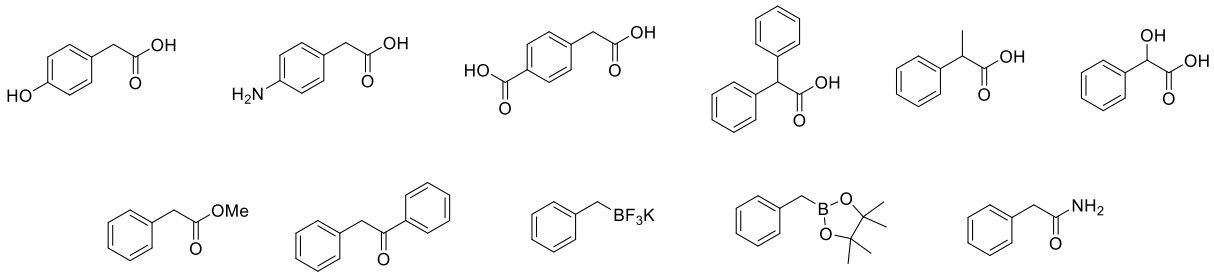

Scheme S6. Unsuccessful substrates

6 References

(1) Blessley, G.; Holden, P.; Walker, M.; Brown, J. M.; Gouverneur, V. Palladium-Catalyzed Substitution and Cross-Coupling of Benzylic Fluorides. *Org. Lett.* **2012**, *14*, 2754-2757.

(2) Tanaka, T.; Yazaki, R.; Ohshima, T. Chemoselective Catalytic α-Oxidation of Carboxylic Acids: Iron/Alkali Metal Cooperative Redox Active Catalysis. *J. Am. Chem. Soc.* **2020**, *142*, 4517-4524.

(3) Ye, L.; Tian, Y.; Meng, X.; Gu, Q.-S.; Liu, X.-Y. Enantioselective Copper(I)/Chiral Phosphoric Acid Catalyzed Intramolecular Amination of Allylic and Benzylic C−H Bonds. *Angew. Chem. Int. Ed.* **2020**, *59*, 1129-1133.

(4) Hua, A. M.; Bidwell, S. L.; Baker, S. I.; Hratchian, H. P.; Baxter, R. D. Experimental and Theoretical Evidence for Nitrogen‐Fluorine Halogen Bonding in Silver-Initiated Radical Fluorinations. *ACS Catal.* **2019**, *9*, 3322-3326.

(5) Sundaraganesan, N.; Kalaichelvan, S.; Meganathan, C.; Joshua, B. D.; Cornard, J. FT-IR, FT-Raman spectra and ab initio HF and DFT calculations of 4-N,N′-dimethylamino pyridine. *Spectrochim. Acta A Mol. Biomol. Spectros.* **2008**, *71*, 898-906.

(6) Olah, G. A.; Welch, J. T.; Vankar, Y. D.; Nojima, M.; Kerekes, I.; Olah, J. A. Synthetic methods and reactions. 63. Pyridinium poly(hydrogen fluoride) (30% pyridine-70% hydrogen fluoride): a convenient reagent for organic fluorination reactions. *J. Org. Chem.* **1979**, *44*, 3872-3881.

(7) Wang, H.; Liu, C.-F.; Song, Z.; Yuan, M.; Ho, Y. A.; Gutierrez, O.; Koh, M. J. Engaging α-Fluorocarboxylic Acids Directly in Decarboxylative C‐C Bond Formation. *ACS Catal.* **2020**, *10*, 4451-4459.

(8) Sap, J. B. I.; Wilson, T. C.; Kee, C. W.; Straathof, N. J. W.; Ende, C. W. a.; Mukherjee, P.; Zhang, L.; Genicot, C.; Gouverneur, V. Synthesis of 18F-difluoromethylarenes using aryl boronic acids, ethyl bromofluoroacetate and [18F]fluoride. *Chem. Sci.* **2019**, *10*, 3237-3241.

Copies of NMR spectra of isolated compounds

Copies of NMR spectra of isolated compounds are available in the Supporting Information through the website of the Publisher. https://doi.org/10.1021/acs.orglett.2c02050

Supporting Information – Chapter 7

Evidence for Photocatalyst Involvement in Oxidative Additions of Nickel-Catalyzed Carboxylate *O*-Arylations

Malik A. Jamal.; **Madani, A**.; Pieber, B.; Seeberger, P. H.
J. Am. Chem. Soc. **2020**, 142, 25, 11042–11049.

https://doi.org/10.1021/jacs.002848

Evidence for Photocatalyst Involvement in Oxidative Additions of Nickel-Catalyzed Carboxylate *O*-Arylations

Jamal A. Malik,[†] Amiera Madani,[†‡] Bartholomäus Pieber,*[†] and Peter H. Seeberger*[†‡]

[†]Department of Biomolecular Systems, Max-Planck-Institute of Colloids and Interfaces, Am Mühlenberg 1, 14476 Potsdam, Germany.

‡Department of Chemistry and Biochemistry, Freie Universität Berlin, Arnimallee 22, 14195 Berlin, Germany.

SUPPORTING INFORMATION

TABLE OF CONTENTS

1. General remarks

Substrates, reagents, and solvents were purchased from commercial suppliers and used without further purification unless otherwise noted. *N*-Boc proline was lyophilized for 24h prior to use to remove residual water. *N-tert*-butylisopropylamine (BIPA) was prepared according to literature procedure.[1] ^{1}H- and ^{13}C-NMR spectra were obtained using a Varian 400 spectrometer (400 MHz, Agilent), an Ascend^{TM} 400 spectrometer (400 MHz, cryoprobe, Bruker) and a Varian 600 spectrometer (600 MHz, Agilent) at 298 K, and are reported in ppm relative to the residual solvent peaks. Standard NMR quantification was through Varian 400 MHz spectrometer, with the following settings: Acquisition points (complex points) 16384; Acquisition time 2.556s; Relaxation delay 1.000s; Receiver gain as autogain (default 30); Spectral width 16.0 ppm; 128 scans. Peaks are reported as: s = singlet, d = doublet, t = triplet, q = quartet, m = multiplet or unresolved, with coupling constants in Hz. No thin-layer or otherwise silica-based chromatography was performed in the course of these experiments. Lamps (A160, 40W maximum) were purchased from Kessil and used as received. *In situ* FTIR analysis was performed with a ReactIR^{TM} 15 (Mettler-Toledo) console, with a DST 9.5mm SiComp^{TM} probe attached. Data processing from *in situ* FTIR analysis was performed in Microsoft Excel. Graphs were presented in Microsoft Excel or Origin.

2. General procedures and analysis for *in situ* ReactIR experiments

2.1.1 Considerations before experiments

Roughly two hours prior to each experiment, the ReactIR console was purged and filled with liquid nitrogen. A background spectrum was recorded shortly before attaching the reaction vessel to the ReactIR probe. To maintain a constant operating temperature during the course of longer experiments, the ReactIR console was replenished with new liquid nitrogen every 12 hours.
The 440 nm lamp was permanently affixed to a metal rod such that the edge of the lamp was 3.5 cm from the middle of the diameter of the ReactIR probe. During our initial studies we found that the greatest source of error derived from inconsistencies in lamp distance and orientation. As such, neither the 440 nm lamp nor ReactIR probe were moved nor disturbed during the months required for data collection.

2.1.2 General experimental procedure

A custom-made vial with a sidearm attached (19 x 100 mm, see Figure S1) was equipped with a stir bar and charged with photocatalyst, *N*-Boc proline, and aryl iodide. Subsequently, DMSO (anhydrous, 3 mL), $NiCl_2$·glyme and dtbbpy from a stock solution, and BIPA were added. Both necks of the vial were sealed with septa and Parafilm. The reaction mixture was sonicated for 5 min followed by stirring for 5-10 min until fine dispersion of the solids was achieved. The flask was then transported to the ReactIR where the larger septum was removed and the vessel immediately attached to the probe. To ensure an airtight seal, a PTFE adapter was affixed to the probe, to which the vessel was snugly attached. The vessel was continually degassed with Ar for 15 minutes through the sidearm with thin needles. The mixture was stirred for 5 minutes again to re-ensure mixing of the components while data collection started on the ReactIR. After this period the 440 nm lamp was turned on, and this initiation time was marked with the ReactIR proprietary software.

2.1.3 General experimental procedure for delayed injection experiments

A custom-made vial with a sidearm attached (19 x 100 mm, see Figure S1) was equipped with a stir bar and charged with all reaction components except for one. Both necks of the vial were sealed with septa and Parafilm. The reaction mixture was sonicated for 5 min followed by stirring for 5-10 min until fine dispersion of the solids was achieved. The flask was then transported to the ReactIR, where the larger septum was removed and the vessel immediately attached to the probe. To ensure an airtight seal, a PTFE adapter was affixed to the probe, to which the vessel was snugly attached. The vessel was continually degassed with Ar for 15 minutes through the sidearm with thin needles. The mixture was stirred for 5 minutes again to re-ensure mixing of the components while data collection started on the ReactIR. After this period the 440 nm lamp was turned on to 100% power, and this initiation time was marked with the ReactIR proprietary software. After five minutes, the last component (in a DMSO solution) was injected.

2.1.4 Considerations after experiments

To aid in separation of peaks, a negative second derivative function was applied to the raw ReactIR absorbance data. After subtraction of reference spectra, the product peak arrives at ~1764 cm^{-1} while disappearance of the starting material can be observed at a peak around ~761 cm^{-1}. Raw data from iCiR was ported to Excel (Microsoft) for processing. Final data were then plotted in Excel (Microsoft) or OriginPro 2015 (OriginLab).

Initial concentrations of all starting materials were determined from reaction stoichiometry. Final concentration of the product was determined from ^{1}H-NMR analysis. This method was validated as described in Section 3.

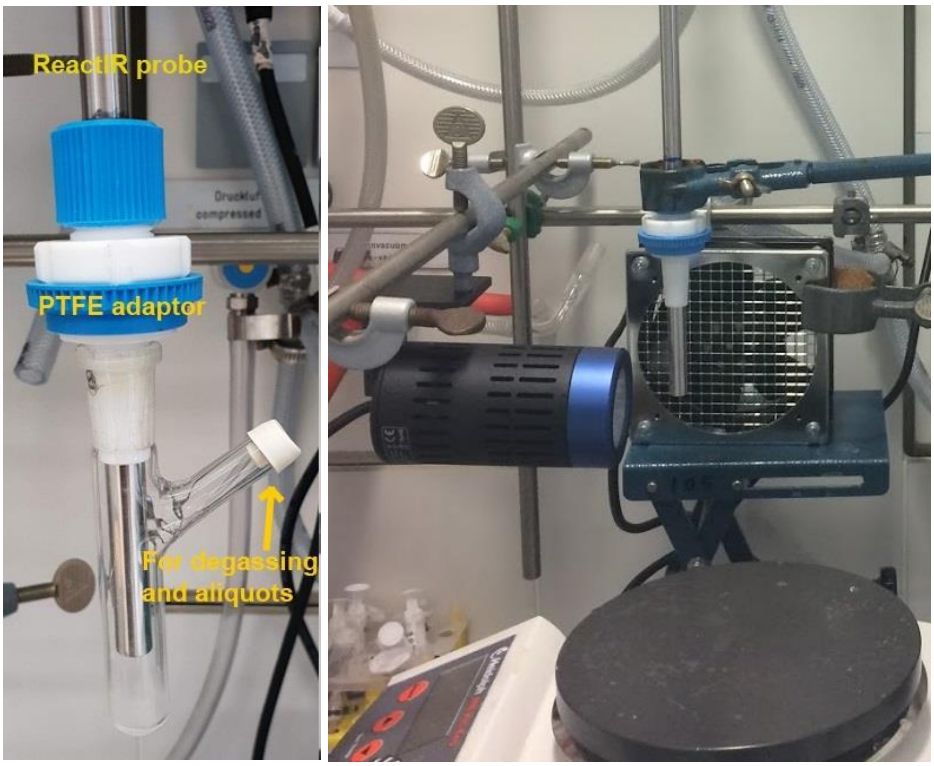

Figure S1. (A) Vessel used for kinetics experiments with sidearm attached to enable degassing after attachment to the ReactIR probe. (B) Setup shown without attached vessel. As our largest source of error was found to derive from inconsistency in lamp placement, a secured lamp and probe were left unchanged for all experiments in this study.

2.2 NMR analysis of reactants, products, and side products

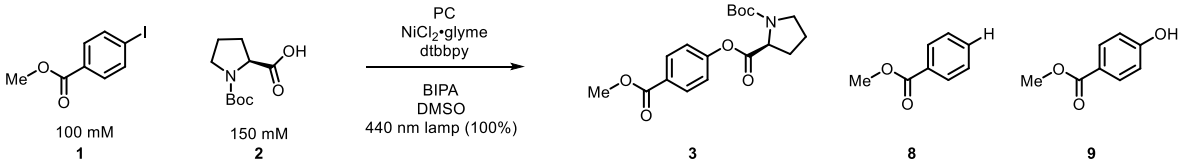

Sample NMRs are shown below.

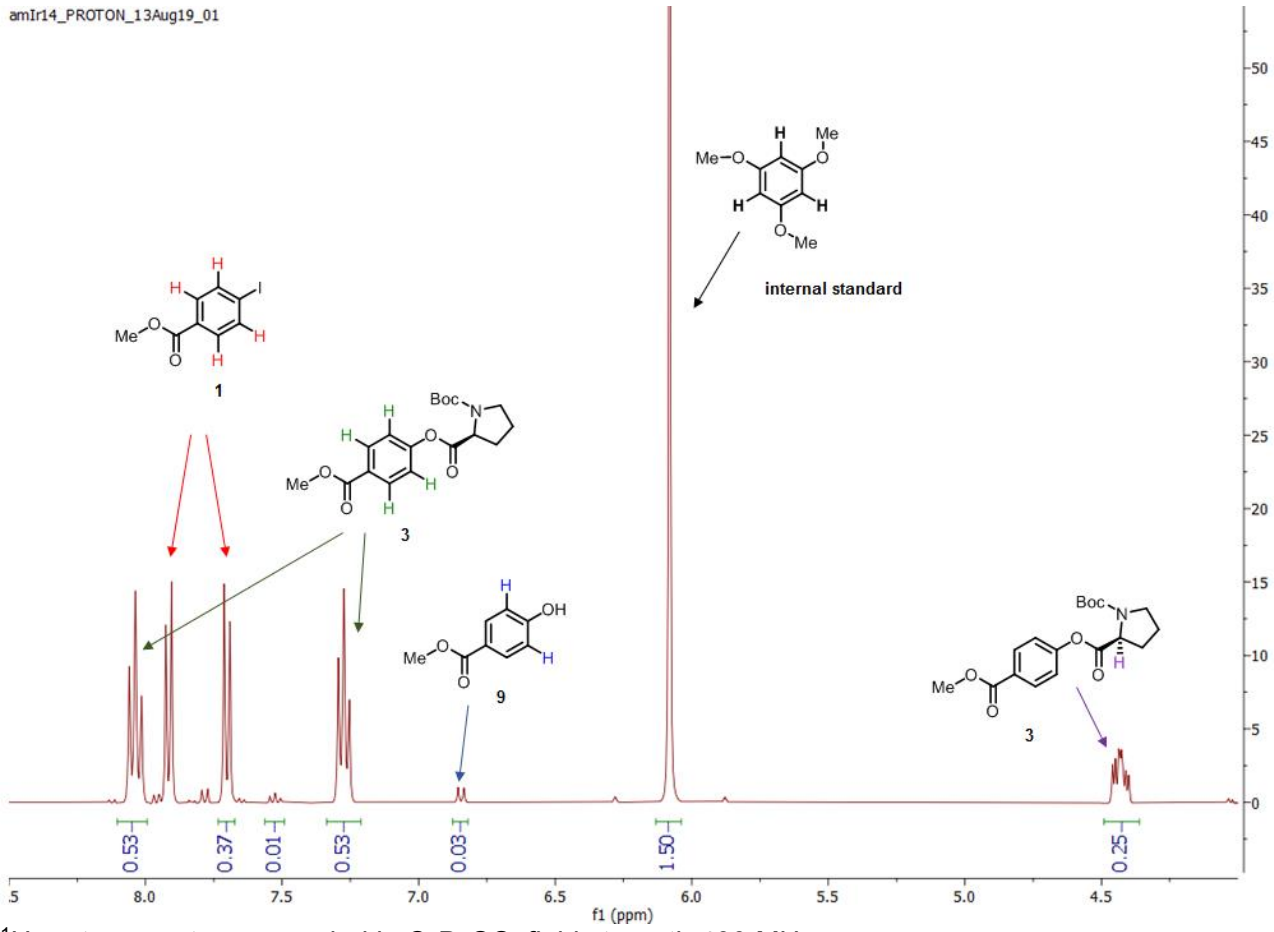

^{1}H proton spectrum recorded in C_2D_6OS, field strength 400 MHz.

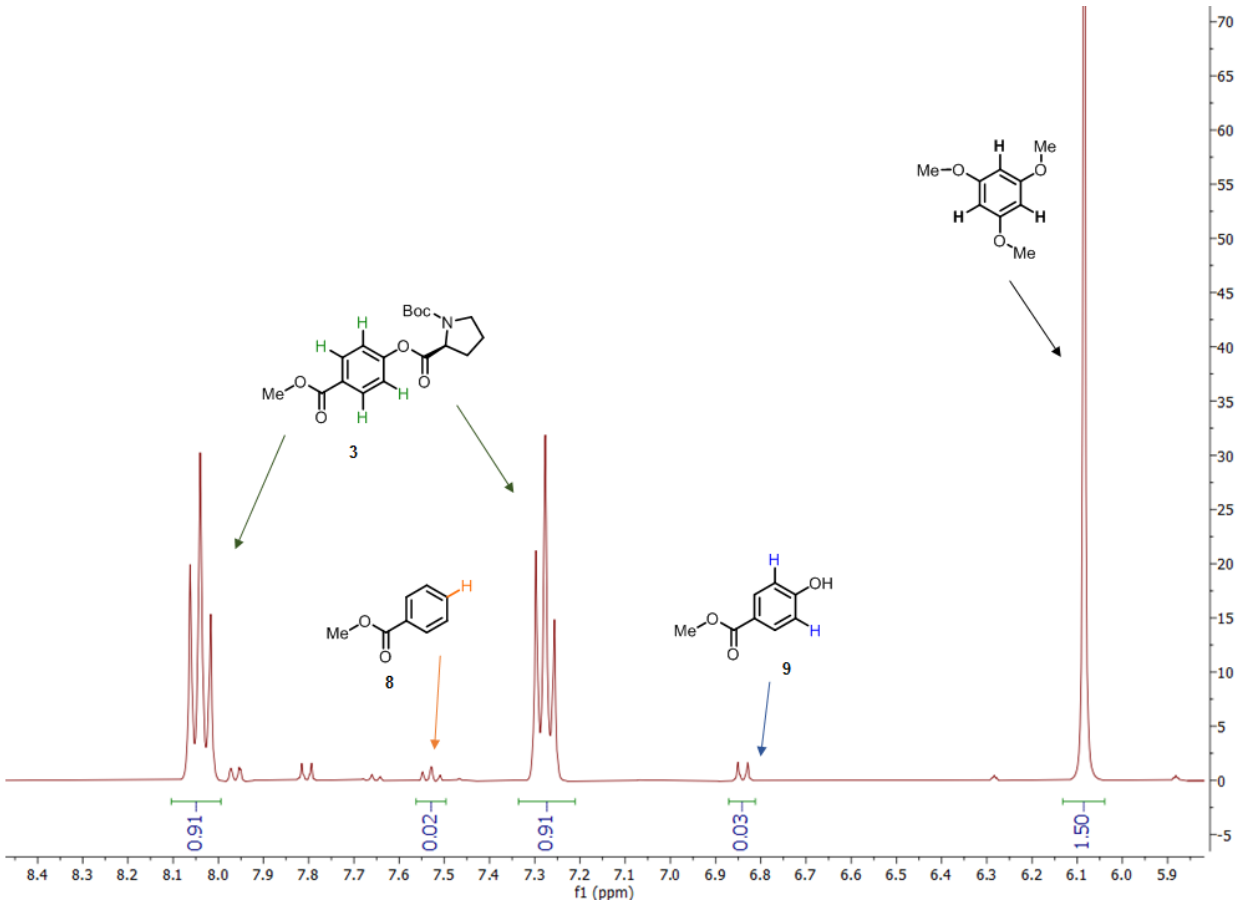

^{1}H proton spectrum recorded in C_2D_6OS, field strength 400 MHz.

Sample completed, selective reaction.

3. On the validity and reproducibility of data

3.1 Ensuring validity of data

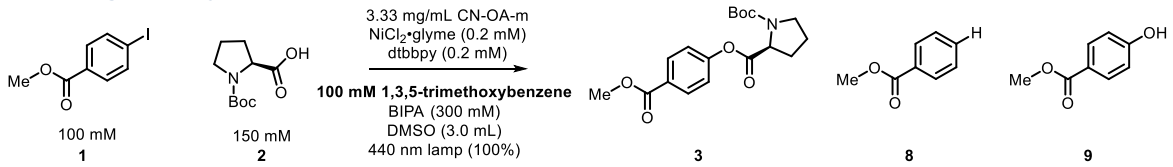

Scheme S1. Experiment to independently validate the method.

An experiment following the general procedure outlined (see 2.1.2) above was conducted, according to the stoichiometry in Scheme 1. Notably, added to the normal reaction mixture was 100 mM 1,3,5-trimethoxybenzene, the internal standard used for all *ex situ* NMRs.

Upon initiation of light and periodically thereafter, small aliquots were withdrawn. The timepoints of these aliquots were noted, and each aliquot was analyzed with ^{1}H-NMR.

Previously we have demonstrated that final NMR yield of these reactions is accurately reflected by isolated yield.[2] As such, NMR can be considered a reliable benchmark for comparison of our *in situ* method.

ReactIR yield was calculated from raw absorbance data that was normalized and scaled, tethered to the final NMR yield. The overlay below between two completely independent methods indicates that ReactIR is a competent measure of reaction progress.

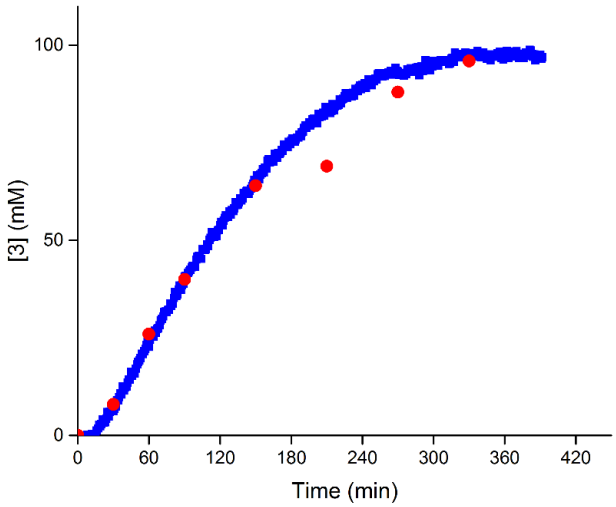

Figure S2. Correlation of NMR and IR yield.

Time (min)	NMR Yield	IR Yield	Difference	NMR SM	Total mass balance
0	0	0	0	98	98
30	8	6.2	1.8	87	95
60	26	22.7	3.3	72	98
90	40	40.7	-0.7	57	97
150	64	64.4	-0.4	33	97
210	69	83	-14	18	87
270	88	93.2	-5.2	6	94
330	96	97.7	-1.7	2	98

Table S1. NMR was used to validate *in situ* infrared tracking as a valid experimental technique to determine reaction progress.

3.2 Ensuring reproducibility of data

Frequently experiments were repeated to ensure that data was reproducible. Below are shown one example of such a data set.

In general, for data sets that were to be compared with one another, the same stock solution of $NiCl_2$•glyme and dtbbpy was used. As stated above, the lamp was secured and unmoved during the course of all experiments for this work. Those two factors were paramount for reproducible data collection.

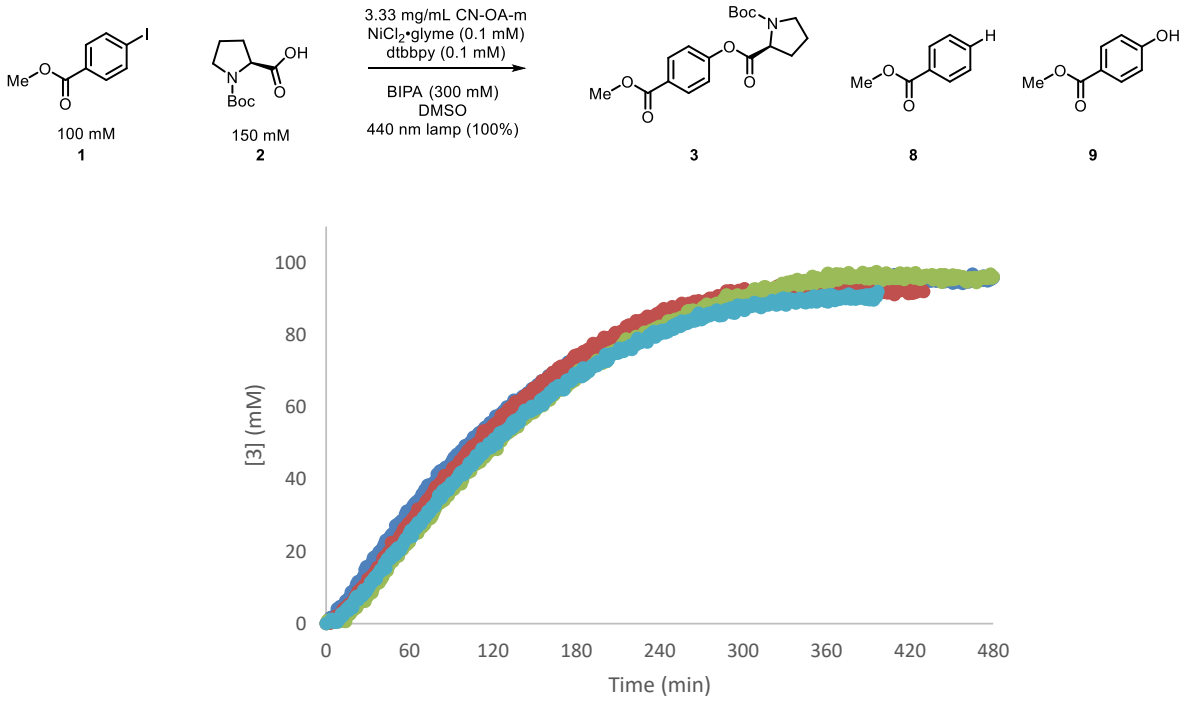

Figure S3. Photon-unlimited, heterogeneous reactions run in quadruplicate to verify reproducibility.

Entry	[1]	[3]	[8]	[9]	Total
jam260	0	91	4	4	99
jam264	0	92	4	4	100
jam266	0	91	4	5	100
jam267	3	89	3	2	97

Table S2. Tabulated yields and side products from quadruplicate quality control testing.

Two of these NMRs are shown below.

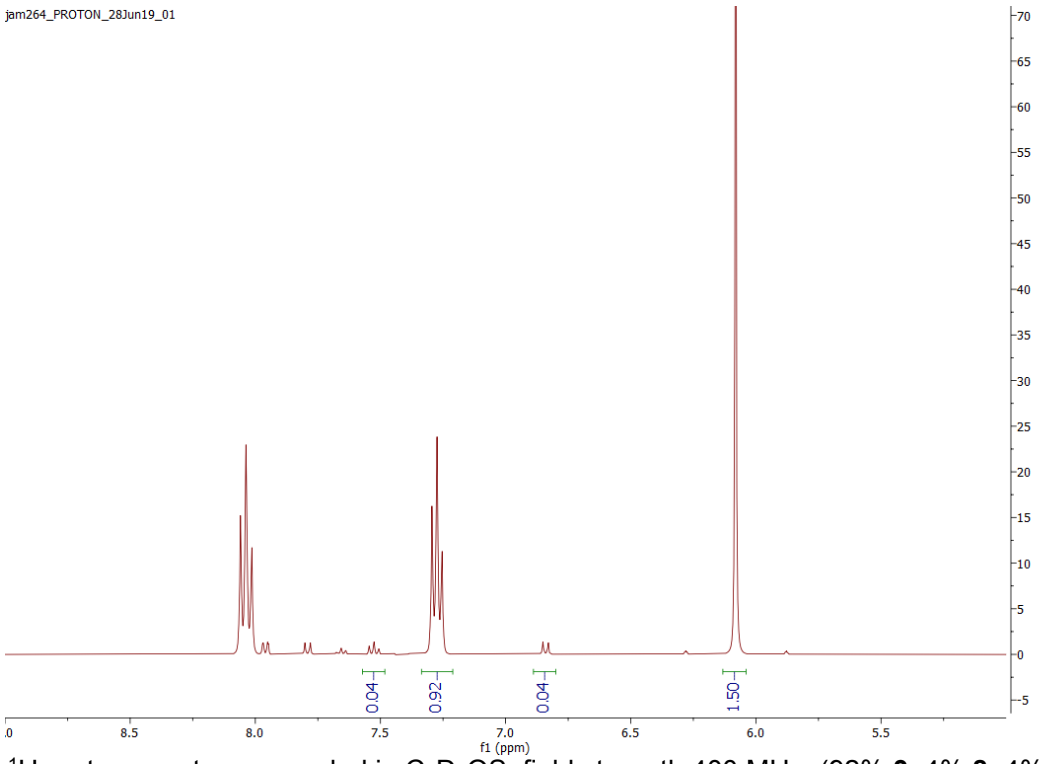

^{1}H proton spectrum recorded in C_2D_6OS, field strength 400 MHz. (92% **3**, 4% **8**, 4% **9**)

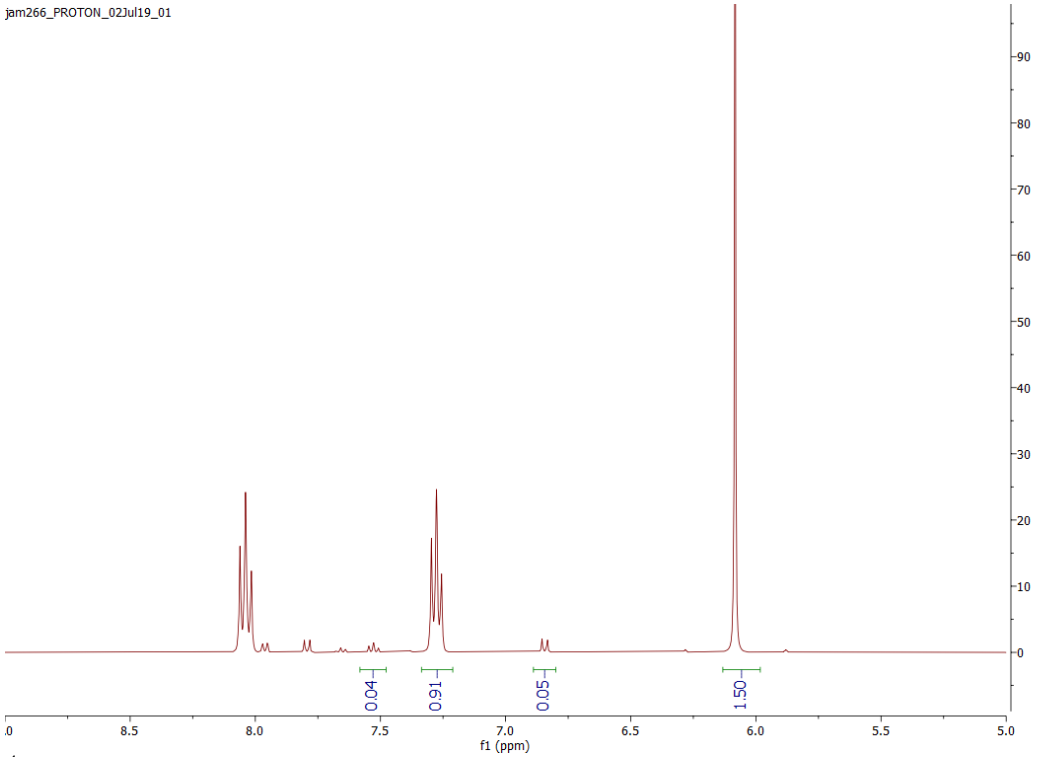

^{1}H proton spectrum recorded in C_2D_6OS, field strength 400 MHz. (91% **3**, 4% **8**, 5% **9**)

S11

4. Graphitic carbon nitride (heterogeneous) as photocatalyst: Photon-limited regime

4.1 Effect of lamp power

Following the general procedure outlined above, the four different settings on the 440 nm lamp were tested.

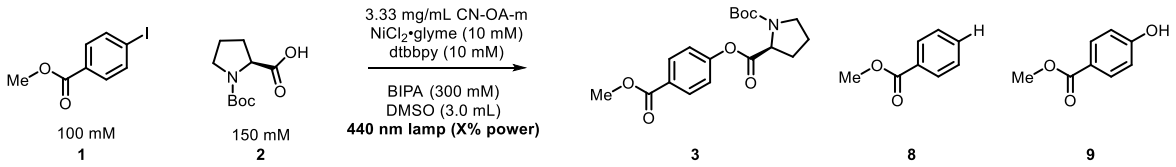

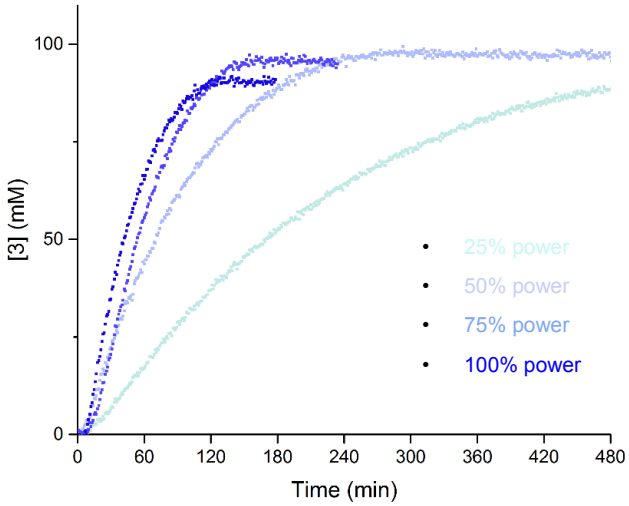

Figure S4. Effect of lamp power on reaction speed. In order to best saturate the nickel catalyst with excited photocatalytic species, the highest lamp setting was chosen for "photon-unlimited" experiments in this study. 50% power was used for the "photon-limited" studies due to slightly advantageous yield.

Entry	Lamp	[1]	[3]	[8]	[9]	Total
jam176	**25**	0	89	3	3	95
jam178	**50**	0	94	2	3	99
jam179	**75**	0	89	3	2	94
jam180	**100**	0	90	3	2	95

Table S3. Tabulated yields and side products from screening lamp power.

4.2 Cursory examination of induction period

A custom-made vial with a sidearm attached (19 x 100 mm, see Figure S1) was equipped with a stir bar and charged with all reaction components except for one. Both necks of the vial were sealed with septa and Parafilm. The reaction mixture was sonicated for 5 min followed by stirring for 5-10 min until fine dispersion of the solid photocatalyst was achieved. The flask was then transported to the ReactIR, where the larger septum was removed and the vessel immediately attached to the probe. To ensure an airtight seal, a PTFE adapter was affixed to the probe, to which the vessel was snugly attached. The vessel was continually degassed with Ar for 15 minutes through the sidearm with thin needles. The mixture was stirred for 5 minutes again to re-ensure mixing of the components while data collection started on the ReactIR. After this period the 440 nm lamp was turned on to 100% power, and this initiation time was marked with the ReactIR proprietary software. After five minutes, the last component (in a DMSO solution) was injected.

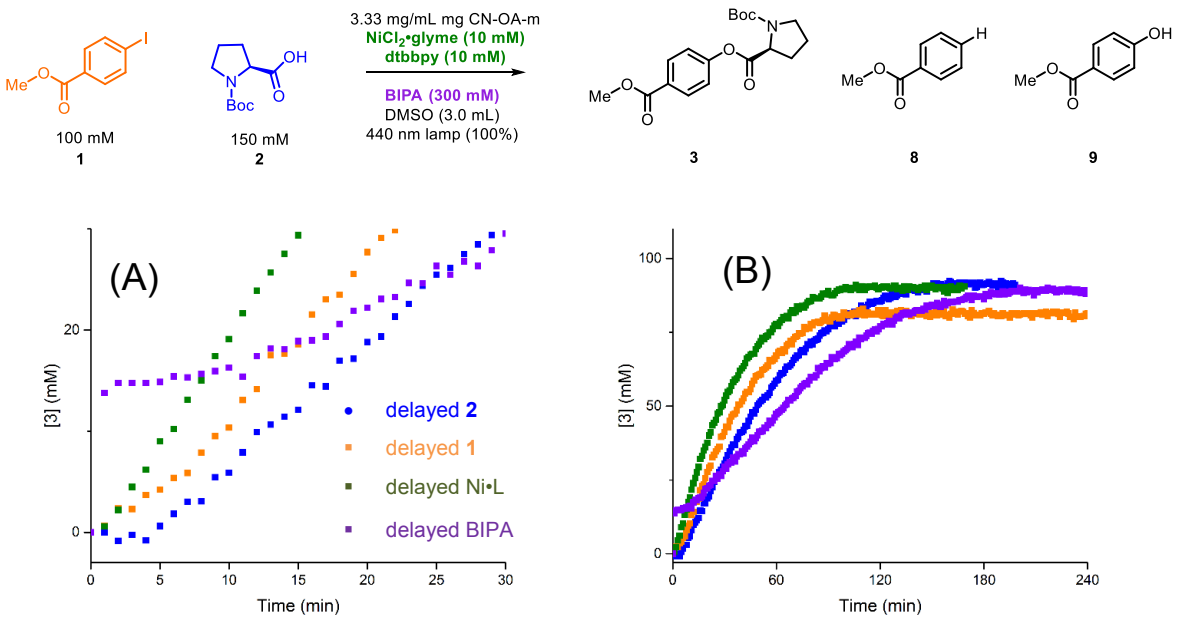

Figure S5. Delayed injection experiments in order to obtain rough information about what contributes to the induction period. Immediate, positive-order kinetics are observed upon delayed injection of the nickel and of the aryl iodide. Delayed injection of proline retains the induction period. Delayed injection of the base results in catalyst activation-type behavior. (A) First 30m, zoomed. (B) Complete reaction.

Entry	Delayed reagent	[1]	[3]	[8]	[9]	Total
jam183	aryl iodide (**1**)	0	80	4	3	87
jam182	N-Boc proline (**2**)	0	91	3	1	95
jam184	Ni • L	0	90	3	2	95
jam185b	Base (BIPA)	0	91	3	1	95

Table S4. Tabulated yields and side products from delaying injections of reagents.

4.3 Order of catalyst, photon-limited

Following the delayed injection procedure (see section 2.1.3 – Ni•L delayed) described above, experiments were conducted varying only the concentration of nickel and ligand.

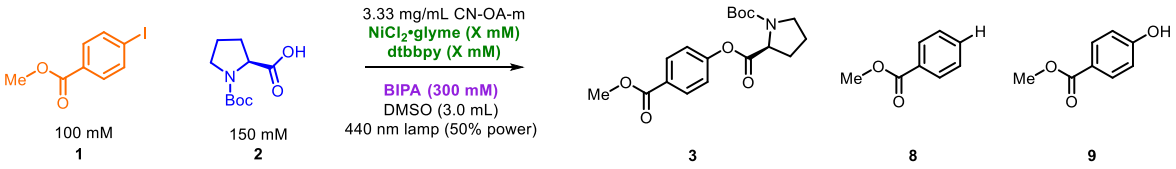

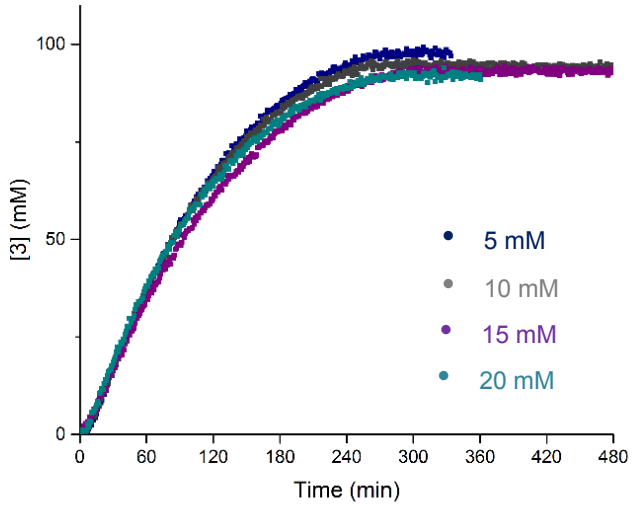

Figure S6. In the photon-limited regime, catalyst concentration has no effect on product-forming rate, and is therefore zero-order. Delayed injection of $NiCl_2$•glyme and dtbbpy solution was used to assist potential VTNA manipulations, which were not used in this instance.

Entry	[Ni•L]	[1]	[3]	[8]	[9]	Total
jam209	5	0	96	3	2	101
jam208b	10	0	92	3	3	98
jam210	15	0	94	2	2	98
jam211	20	0	91	3	2	96

Table S5. Tabulated yields and side products from varying catalyst order in photon-limited regime.

4.4 Effect of photocatalyst

Following the delayed injection procedure (see section 2.1.3 – Ni•L delayed), two experiments were conducted varying only the amount of photocatalyst.

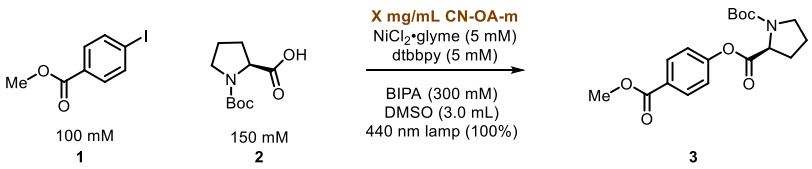

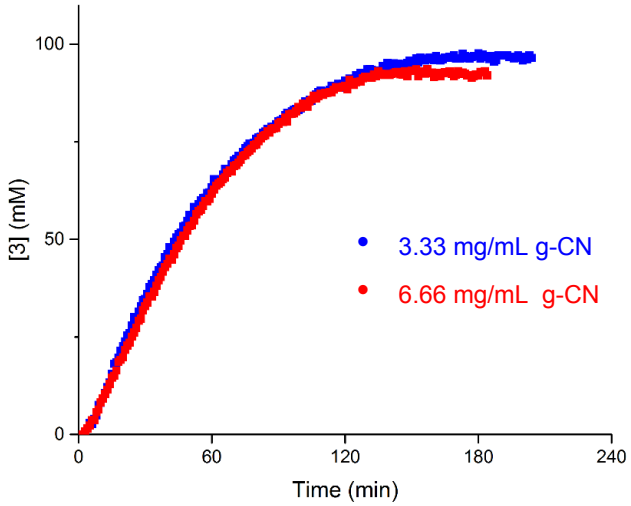

Figure S7. In the photon-limited regime, doubling the amount of photocatalyst has no effect on reaction rate. Delayed injection of $NiCl_2$•glyme and dtbbpy solution was used to assist potential VTNA manipulations, which were not used in this instance.

Entry	PC loading	[1]	[3]	[8]	[9]	Total
jam220	3.33 mg/mL	0	95	2	1	98
jam221	6.66 mg/mL	0	91	4	3	98

Table S6. Tabulated yields and side products from varying photocatalyst loading.

4.5 Same excess

Following the delayed injection procedure (see section 2.1.3 – Ni•L delayed), two experiments were conducted with the same "excess" (50 mM) between $[1]_0$ and $[2]_0$.

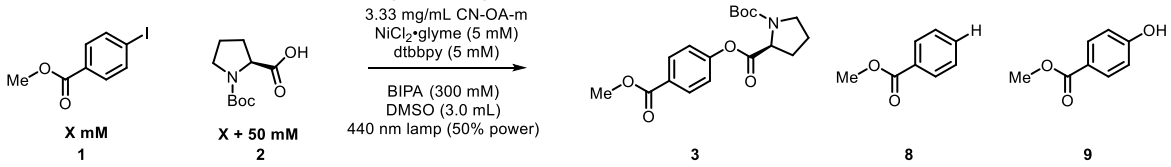

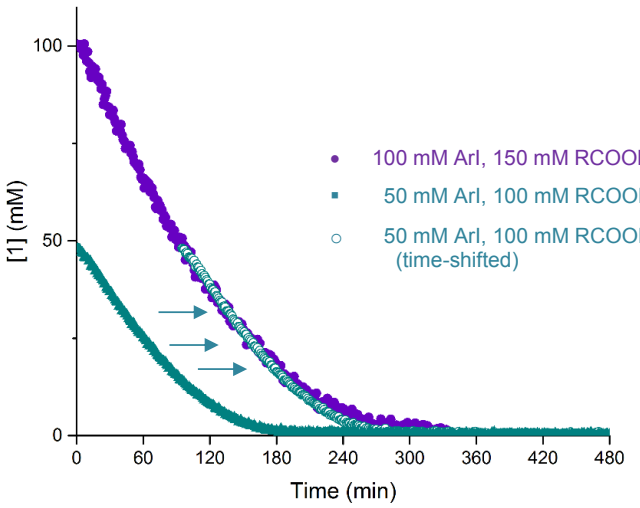

Figure S8. Overlay indicates no significant amount of catalyst deactivation or product inhibition in conditions outside of the linear absorption regime.

Entry	$[1]_0$	[1]	[3]	[8]	[9]	Total
jam209	100	0	96	3	2	101
jam214	50	0	45	2	2	49

Table S7. Tabulated yields and side products from photon-limited same excess experiment.

4.6 Different excess, aryl iodide

Following the delayed injection procedure (see section 2.1.3 – Ni•L delayed), experiments were conducted varying only the concentration of [**1**].

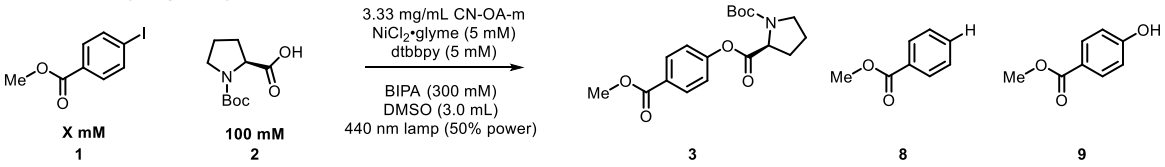

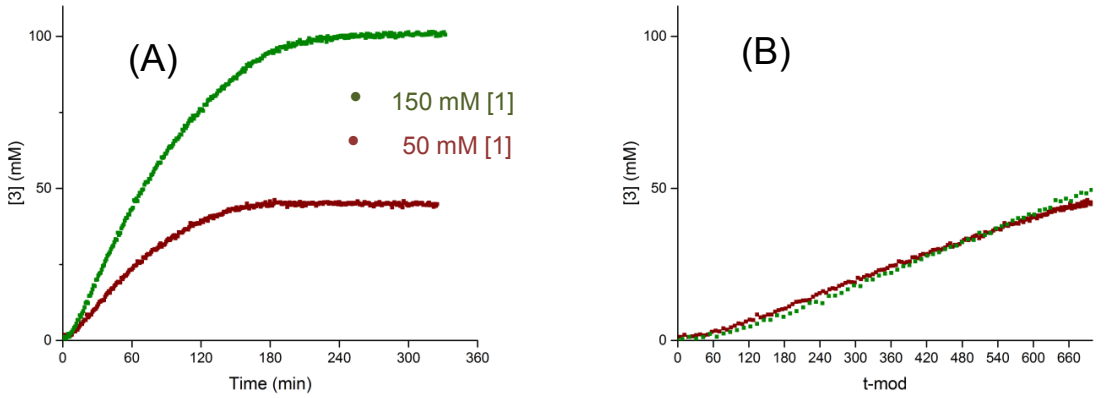

Figure S9. (A) Different excess experiments in the photon-limited regime show a positive-order dependence on [1]. (B) VTNA analysis shows best overlay at a coefficient of 0.5, indicating that rate ~[ArI]$^{0.5}$

Entry	$[1]_0$	[1]	[3]	[8]	[9]	Total
jam214	50	0	45	2	2	49
jam216	150	26	99	2	15	142

Table S8. Tabulated yields and side products from photon-limited different excess experiment.

4.7 Different excess, *N*-Boc proline

Following the delayed injection procedure (see section 2.1.3 – Ni•L delayed), experiments were conducted varying only the concentration of [2].

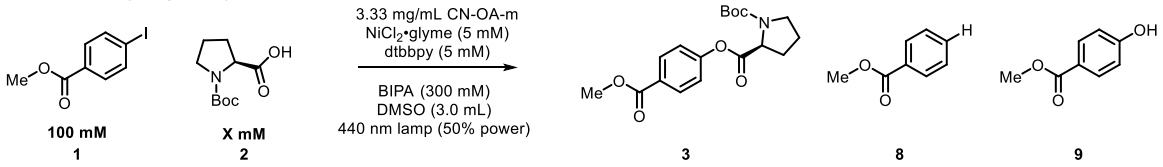

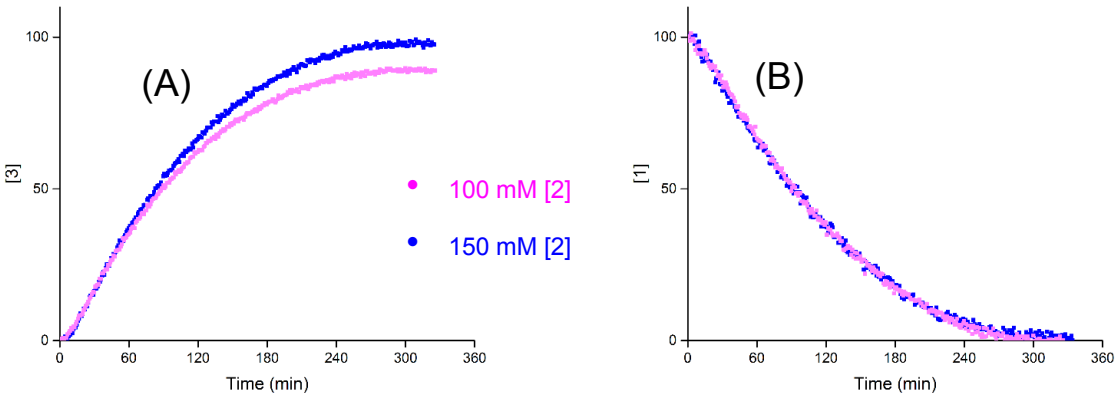

Figure S10. Different excess experiments in the photon-limited regime show a likely zero-order dependence on [2]. (A) Product formation. (B) Disappearance of substrate **1**.

Entry	$[2]_0$	[1]	[3]	[8]	[9]	Total
jam209	150	0	96	3	2	101
jam215	100	0	83	2	1	86

Table S9. Tabulated yields and side products from photon-limited different excess experiment.

5. Graphitic carbon nitride (heterogeneous) as photocatalyst: Photon-unlimited regime

5.1 Towards a photon-unlimited regime

Following the general procedure described above (see section 2.1.2), experiments were conducted varying only the concentration of nickel and ligand. Initial rates were determined with a Savitsky-Golay filter at the t = 15 min data point.

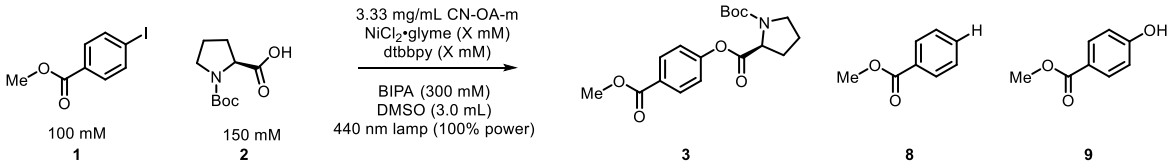

(Plot shown in Figure 2A.)

5.2 Catalyst order

Following the general procedure described above (see section 2.1.2), experiments were conducted varying only the concentration of nickel and ligand.

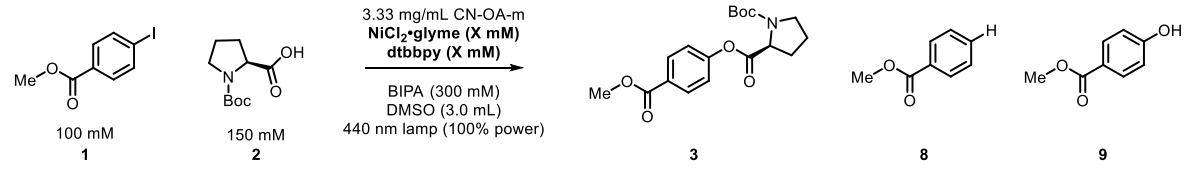

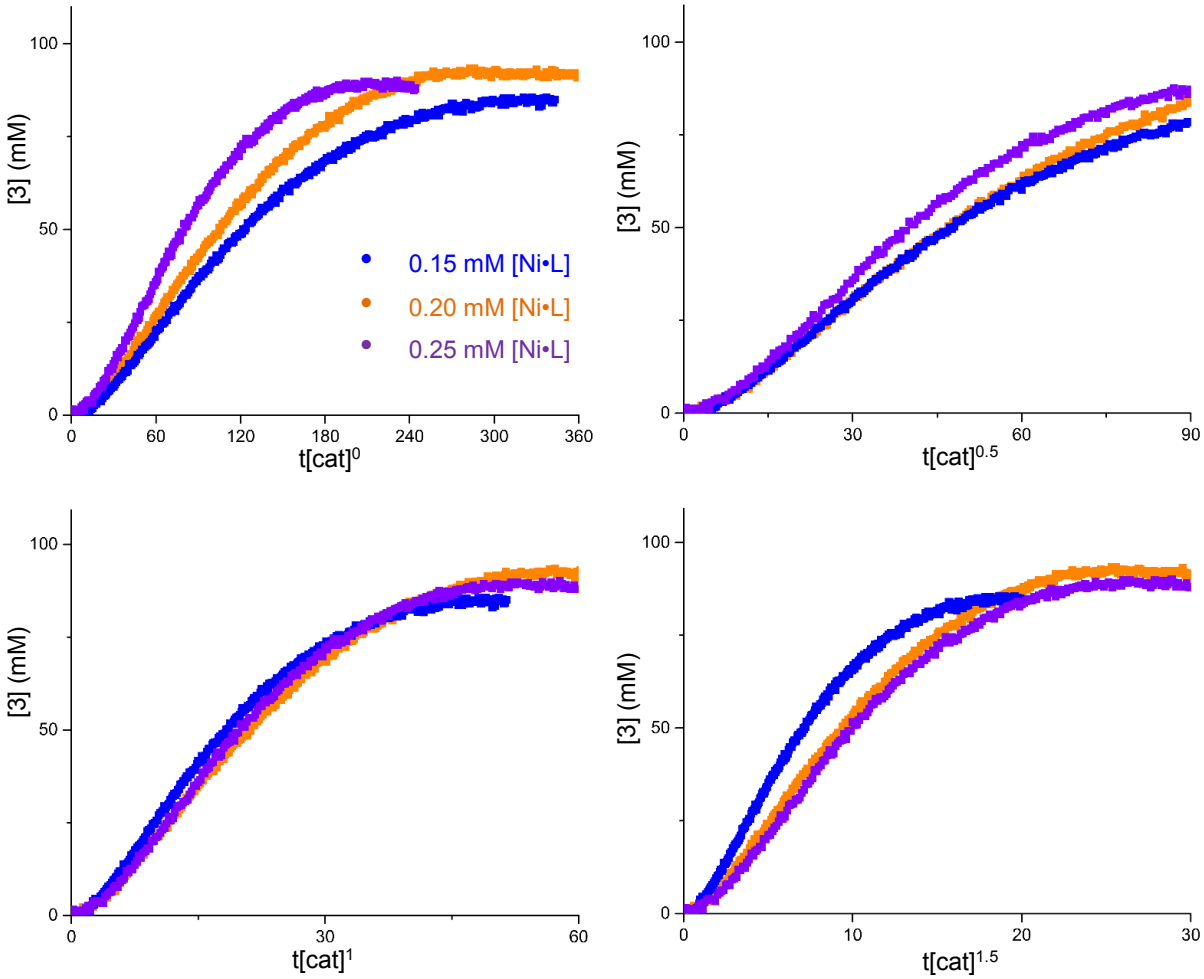

Figure S11. VTNA overlay indicates Ni•L is first order.

Entry	[Ni•L] (mM)	[1]	[3]	[8]	[9]	Total
jam281	0.15	0	85	5	5	95
jam278	0.20	0	88	5	6	99
jam284	0.25	0	87	4	5	96

Table S10. Tabulated yields and side products from photon-unlimited catalyst order experiments.

5.3 Same excess

Following the general procedure described above (see Section 2.1.2), experiments were conducted with the same excess (defined as $[\mathbf{2}]_0 - [\mathbf{1}]_0$; in this case 50 mM) but different initial concentrations.

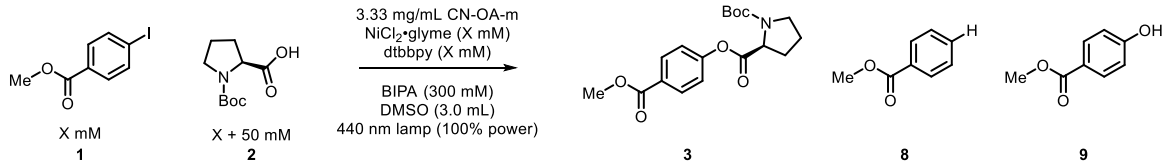

(Plot shown in Figure 2B.)

Entry	$[1]_0$	[1]	[3]	[8]	[9]	Total
jam278	100	0	88	5	6	99
jam287	50	0	41	4	4	49

Table S11. Tabulated yields and side products from photon-unlimited same excess experiments.

5.4 Different excess experiments, aryl iodide

5.4a General procedure

Following the general procedure described above (see Section 2.1.2), experiments were conducted varying only the concentration of [ArI].

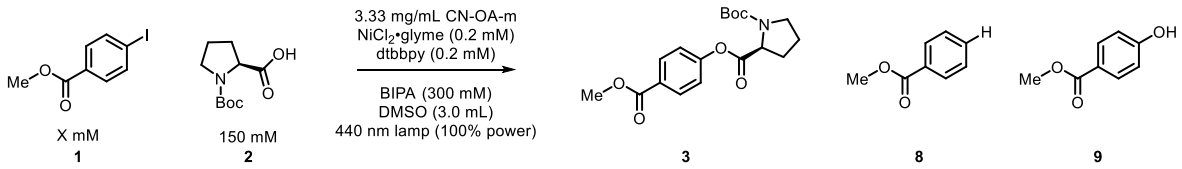

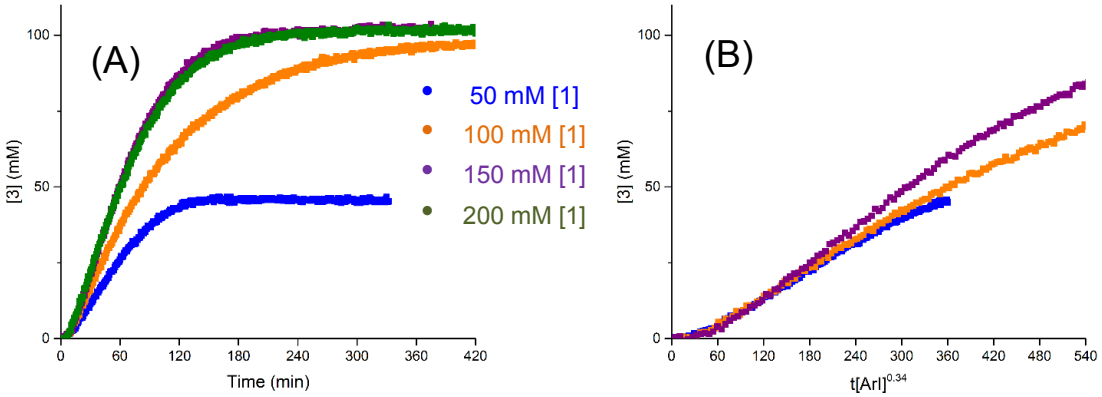

Figure S12. Attempted VTNA overlay was found to be difficult, likely due to the presence of an induction period. (A) Unprocessed [3] vs t data. (B) Best VTNA fit between coefficient 0.3 and 0.4.

Entry	$[1]_0$	[1]	[3]	[4]	[5]	Total
amCN6	50	0	45	3	3	51
amCN4	100	0	96	3	4	103
amCN5	150	25	102	6	14	147
amCN9	200	87	102	3	7	199

Table S12. Tabulated yields and side products from photon-unlimited aryl iodide order experiments.

5.4b Delayed injection procedure

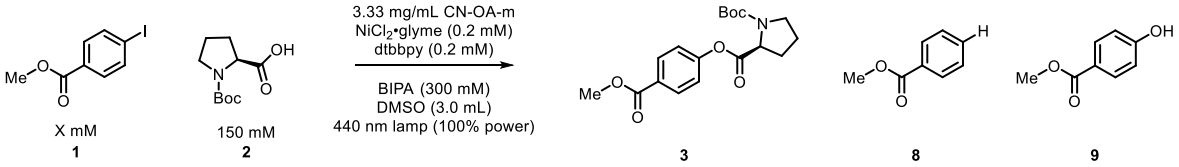

Following the delayed injection procedure (see section 2.1.3 – Ni•L delayed) described above, experiments were conducted varying only the concentration of [ArI]. Procedure B (delayed injection) was used.

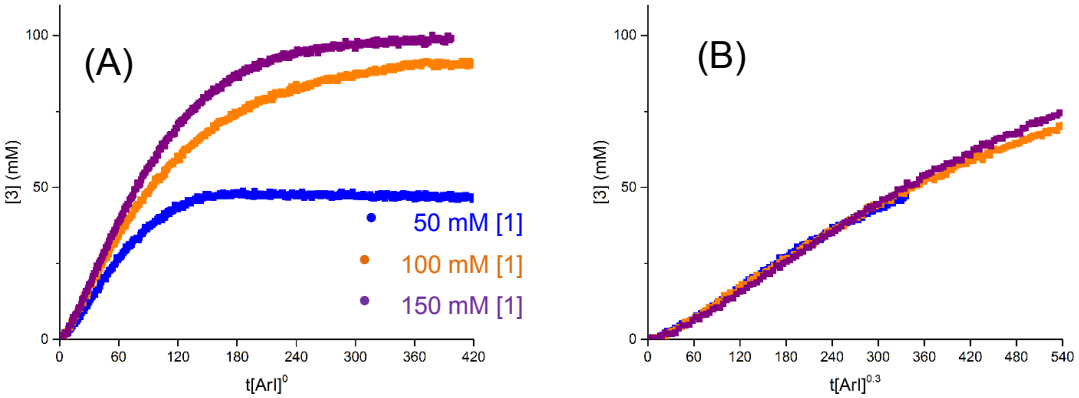

Figure S13. After delayed injection procedure, VTNA overlay found order of aryl iodide to be 0.3.

Entry	$[1]_0$	[1]	[3]	[8]	[9]	Total
amCN15	50	0	46	3	4	53
amCN12	100	0	91	3	5	99
amCN13	150	43	99	3	4	149

Table S13. Tabulated yields and side products from photon-unlimited aryl iodide order experiments, using a delayed injection to bypass the induction period and facilitate VTNA manipulation.

5.5 Different excess, *N*-Boc proline

Following the general procedure described above (see section 2.1.2), experiments were conducted varying only the concentration of carboxylic acid [**2**].

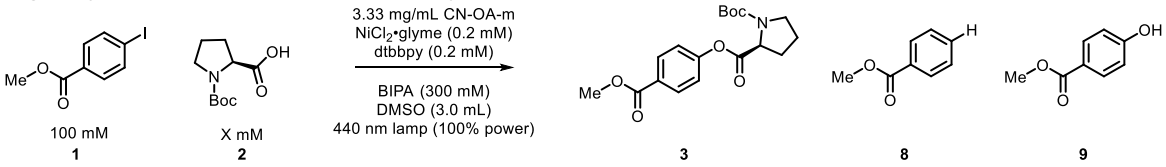

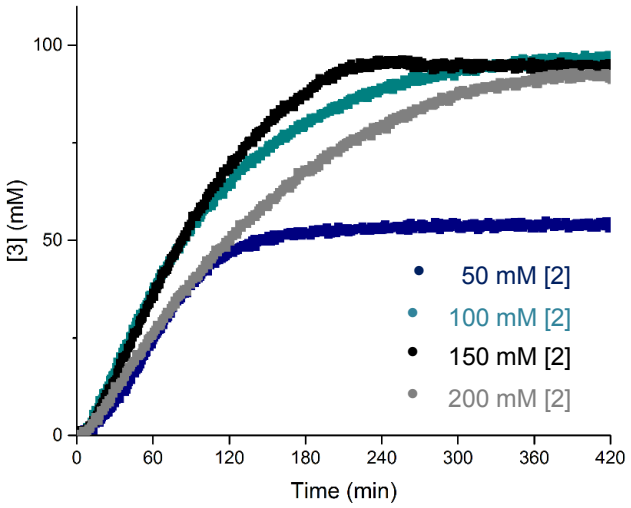

Figure S14. No VTNA manipulations were performed as the dependence on [2] is positive order until a threshold, after which point it becomes inhibitory.

Entry	$[2]_0$	[1]	[3]	[8]	[9]	Total
amCN20	50	17	52	20	8	97
amCN4	100	0	96	3	4	103
amCN3	150	0	93	4	4	101
amCN10	200	0	92	4	2	98

Table S14. Tabulated yields and side products from photon-unlimited experiments to determine rate dependence on [**2**].

5.6 Base experiments

Following the general procedure described above, experiments were conducted varying only the concentration of the secondary base *N-tert*-butylisopropylamine.

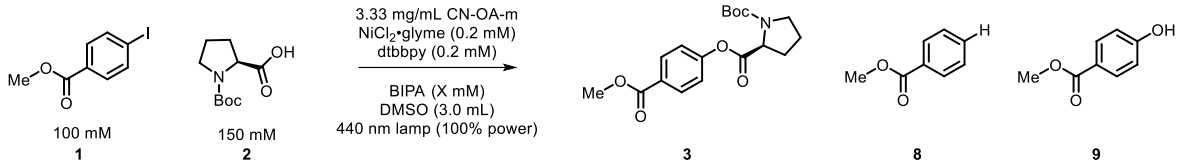

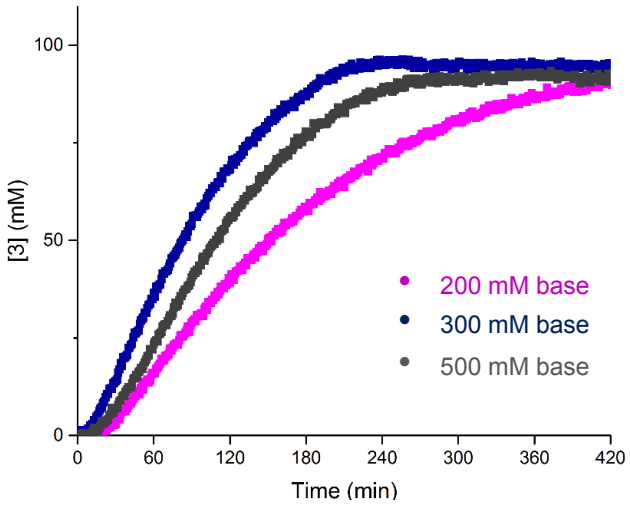

Figure S15. No VTNA manipulations were performed as the dependence on base is positive order until a threshold, after which point it becomes inhibitory.

Entry	[BIPA]	[1]	[3]	[8]	[9]	Total
amCN28	200	0	95	4	2	101
amCN3	300	0	93	4	4	101
amCN27	500	0	91	3	6	100

Table S15. Tabulated yields and side products from photon-unlimited experiments to determine rate dependence on base.

5.7 Photocatalyst experiments

Following the general procedure described above (see section 2.1.2), experiments were conducted varying only the loading of the photocatalyst.

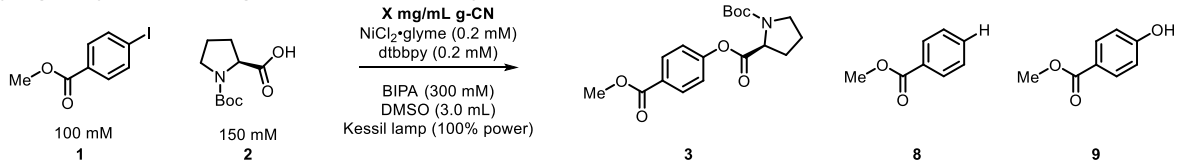

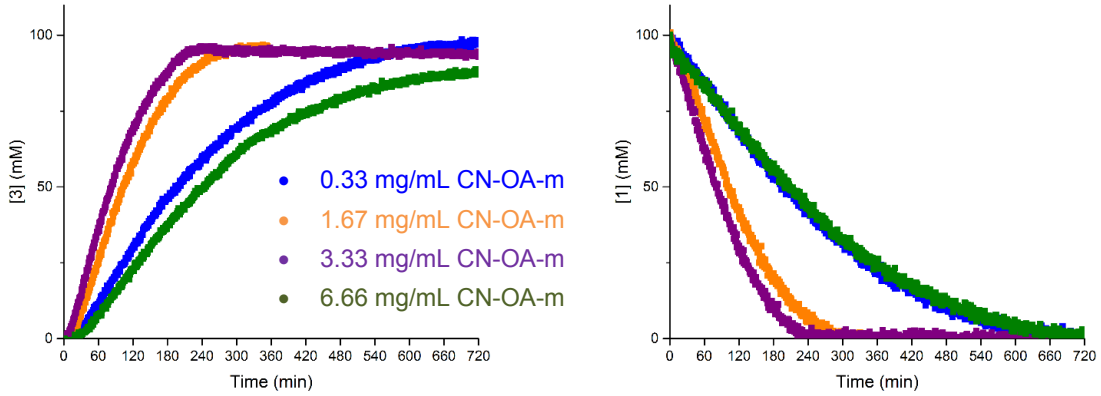

Figure S16. No VTNA manipulations were performed as the dependence on photocatalyst loading is positive order until a threshold, after which point it becomes inhibitory.

Entry	PC	[1]	[3]	[8]	[9]	Total
amCN39	0.33	0	97	2	0	99
amCN38	1.67	0	95	2	3	100
amCN3	3.33	0	93	4	4	101
amCN37	6.66	0	87	6	3	96

Table S16. Tabulated yields and side products from photon-unlimited experiments to determine rate dependence on heterogeneous photocatalyst loading.

5.8 Hammett plot

Following the general procedure described above (see section 2.1.2), experiments were conducted varying only the aryl iodide. Initial rates were determined with a Savitsky-Golay filter after the end of the induction period, which varied among halides in this series.

As in situ IR is an integral measurement,[3] obtaining rate data inherently produces lots of noise. As such, finding one 'initial rate' data point for extremely slow reactions is not possible with any reasonable amount of accuracy. For reactions that proceeded at a negligible pace, the initial rate was simply approximated as zero. For example, the most processed or smoothed (Savitsky-Golay filter, 19pt) rate data for the *p*-CH_3 substituent is shown below, from which any chosen value would have little significance.

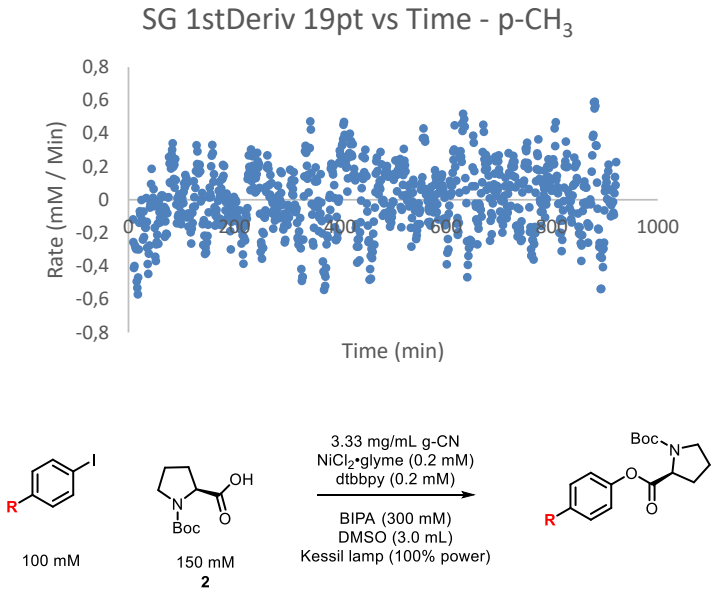

(Data shown graphically in Figure 4C.)

R	σ_{para}	Initial rate	log (k_R/k_H)
OCH3	-0.27	0	0
CH3	-0.17	0	0
H	0	0.06	0.00
Br	0.23	0.16	0.45
Cl	0.23	0.07	0.07
COCH3	0.5	0.76	1.12
CF3	0.54	0.81	1.15
CN	0.66	1.88	1.52

Table S17. Data used in Hammett study. Sigma para values obtained from literature.[4] Initial rates obtained from Savitsky-Golay filter applied to [**3**] vs t data. Concentrations of products obtained from NMR data that matches literature.[2]

6. $Ir(ppy)_3$ (homogeneous) as photocatalyst: Photon-limited regime

6.1 Determination of photocatalyst loading

Following the general procedure described above (see section 2.1.2), experiments were conducted varying only the concentration of photocatalyst.

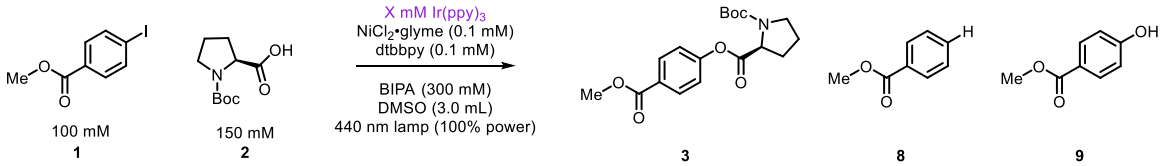

(Results of the reaction are presented in tabular form in Table 1 and graphical form in Figure 3A.)

When normalized [1] vs normalized [t] is plotted, the curvature change between the experiments becomes clearer:

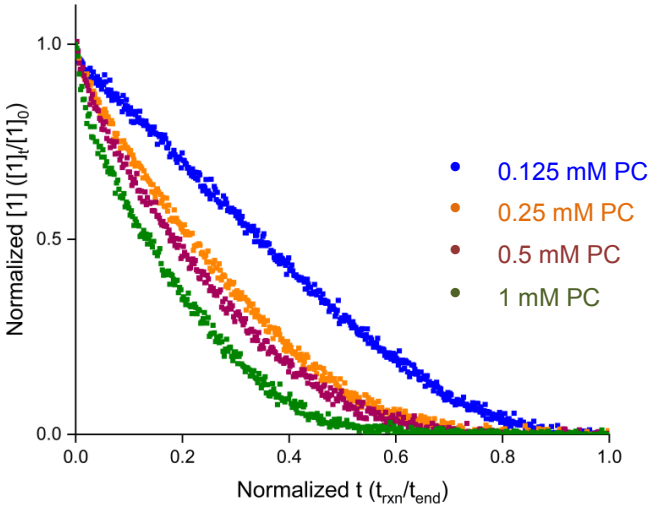

Figure S17. Flatter curvature of the lower photocatalytic loading is indicative of lower-order overall kinetics and a higher likelihood that rate is limited by photon-related processes.

6.1 Determination of nickel order

Following the general procedure described above (see section 2.1.2), experiments were conducted varying only the concentration of nickel and ligand.

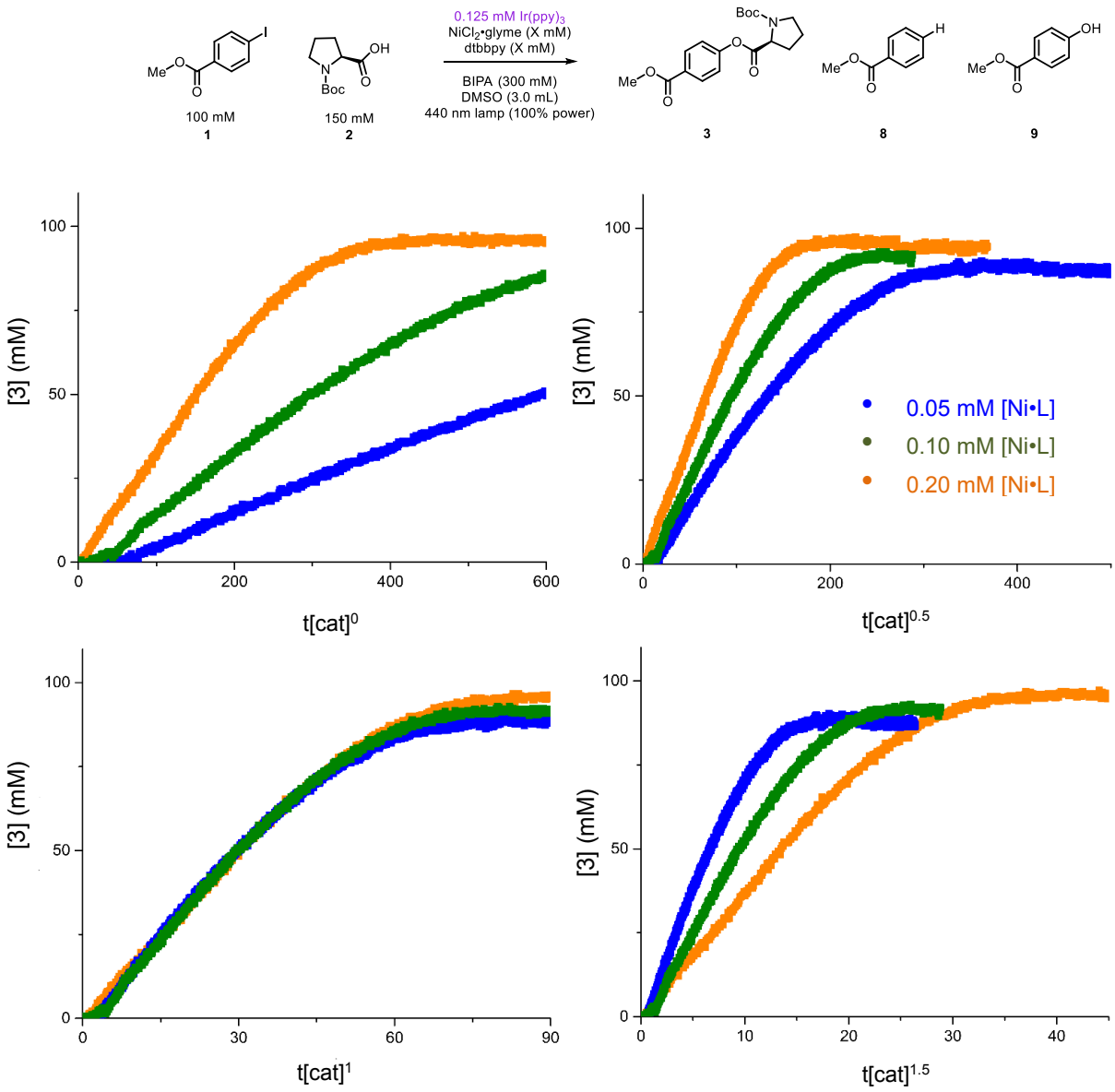

Figure S18. VTNA indicates that catalyst is first-order in the photon-limited regime of the homogeneous reaction.

Entry	[Ni•L]	[1]	[3]	[8]	[9]	Total
amIr21	0.05	0	87	5	3	95
amIr17	0.10	0	92	4	3	99
amIr16	0.20	0	94	3	4	101

Table S18. Tabulated yields and side products from photon-unlimited experiments assessing catalyst order.

6.2 Same excess

Following the general procedure outlined above (see section 2.1.2), two experiments were conducted with the same "excess" (50 mM) between $[1]_0$ and $[2]_0$.

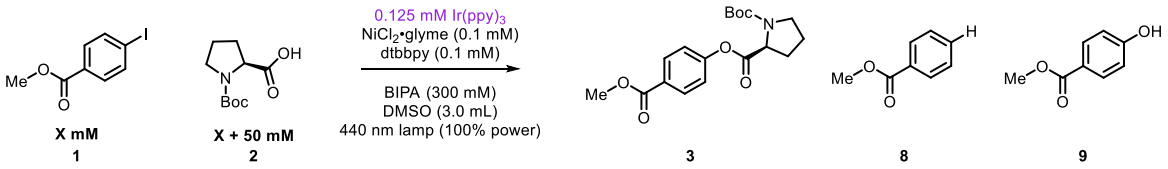

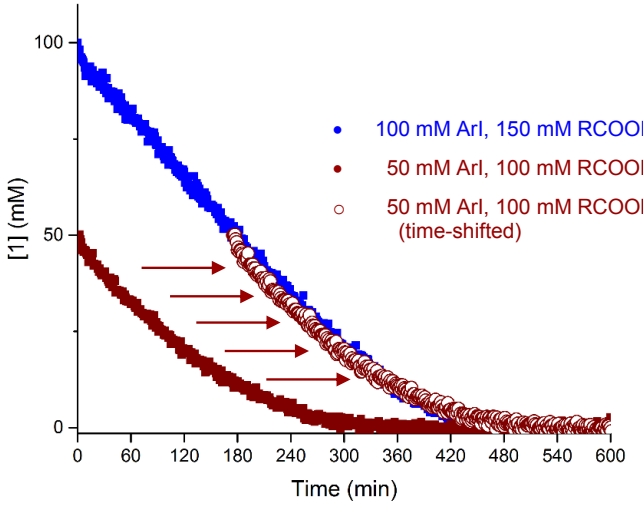

Figure S19. Same excess experiment for the photon-limited homogeneous reaction, in contrast to the photon-unlimited regime, shows no significant amounts of catalyst deactivation.

Entry	$[1]_0$	[1]	[3]	[8]	[9]	Total
amIr29	100	0	86	5	5	96
amIr28	50	1	41	3	3	48

Table S19. Tabulated yields and side products from homogeneous photon-limited same excess experiment.

6.3 Different excess experiments

Following the general procedure described above (see section 2.1.2), experiments were conducted varying only the concentrations of aryl iodide **1** and carboxylic acid **2**.

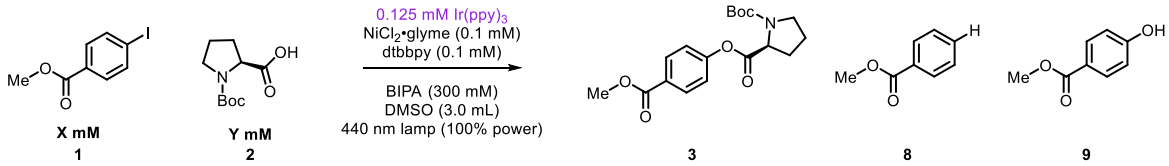

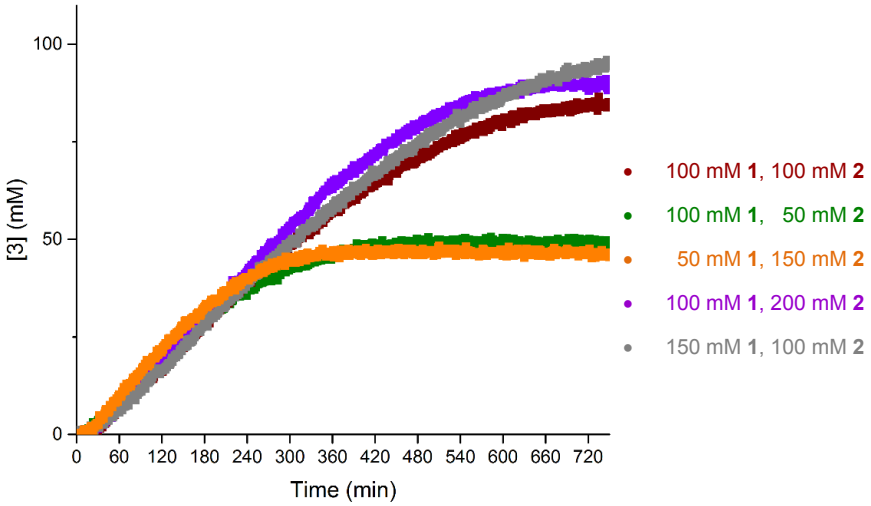

Figure S20. Different excess experiments varying the starting concentrations of **1** and **2** show dependence on neither.

Entry	[1]$_0$	[2]$_0$	[1]	[3]	[8]	[9]	Total
amIr31	100	100	1	88	4	7	100
amIr33	100	50	22	50	6	19	97
amIr41	50	150	0	47	3	1	51
amIr42	100	200	0	93	5	3	101
amIr43	150	100	26	100	6	16	148

Table S20. Tabulated yields and side products from homogeneous photon-limited different excess experiments.

6.4 Base experiments

Following the general procedure described above (see section 2.1.2), experiments were conducted varying only the concentrations of base.

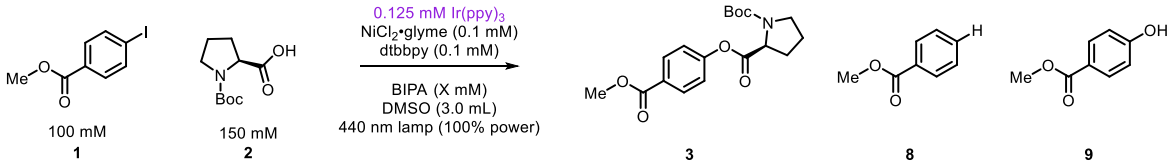

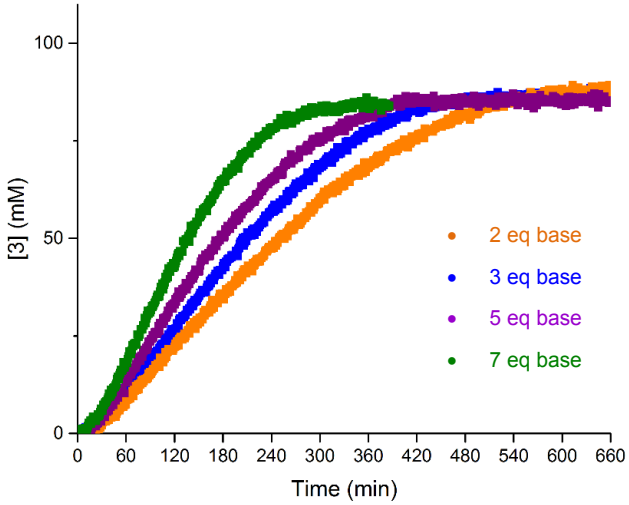

Figure S21. Varying concentration of base was the only factor that could accelerate the homogeneous reaction in the photon-limited regime.

Entry	[BIPA]	[1]	[3]	[8]	[9]	Total
amIr49	200	0	89	5	1	95
amIr29	300	0	86	5	5	96
amIr48	500	0	83	7	4	94
amIr50	700	0	84	7	6	97

Table S21. Tabulated yields and side products from base studies of the homogeneous photon-limited regime.

7. $Ir(ppy)_3$ (homogeneous) as photocatalyst: Photon-unlimited regime, 0.2 mM [Ni•L]

7.1 Determination of photocatalyst loading

Following the general procedure described above (see section 2.1.2), experiments were conducted varying only the concentration of photocatalyst.

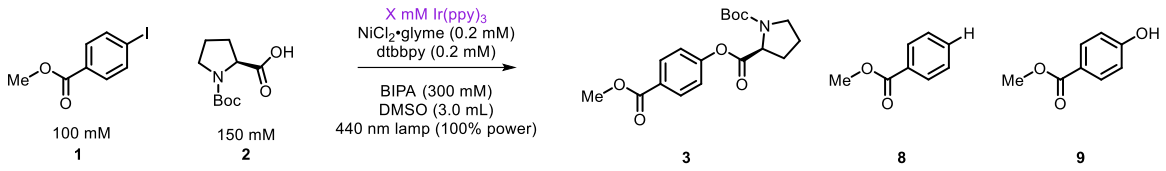

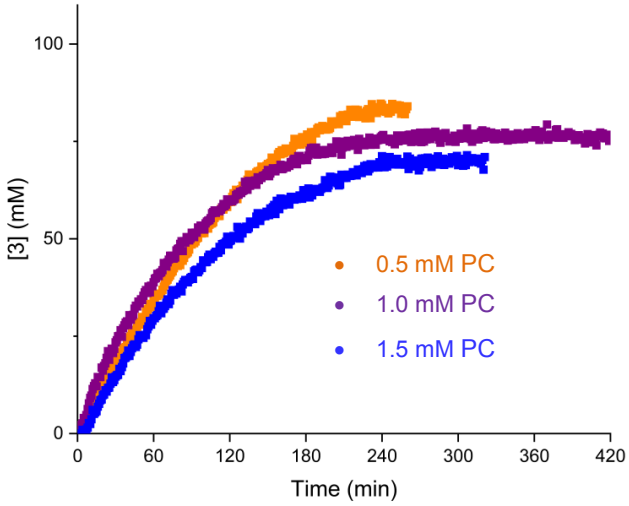

Figure S22. Varying concentration of PC to find regime in which nickel catalyst would be saturated with excited photocatalyst species.

Entry	[PC]	[1]	[3]	[8]	[9]	Total
jam325	0.5	0	84	6	2	92
jam326	1.0	0	73	11	3	87
jam327	1.5	0	71	11	2	84

Table S22. Tabulated yields and side products from PC studies of the homogeneous O-arylation.

7.1.1 Towards a photon-unlimited regime – VTNA test, 0.5 mM PC

It appeared that both 0.5 mM and 1.0 mM PC were candidates for a photon-unlimited regime with 0.2 mM Ni•L. The lowest possible PC loading would be preferable as higher PC loadings gave more side product. To test if we were in a photon-unlimited regime, we performed VTNA on experiments varying nickel concentrations, similar to sections 4.3, 5.2, and 6.2; if nickel is first-order, we are in such a regime.

Following the general procedure described above (see section 2.1.2), experiments were conducted varying only the concentration of nickel and ligand.

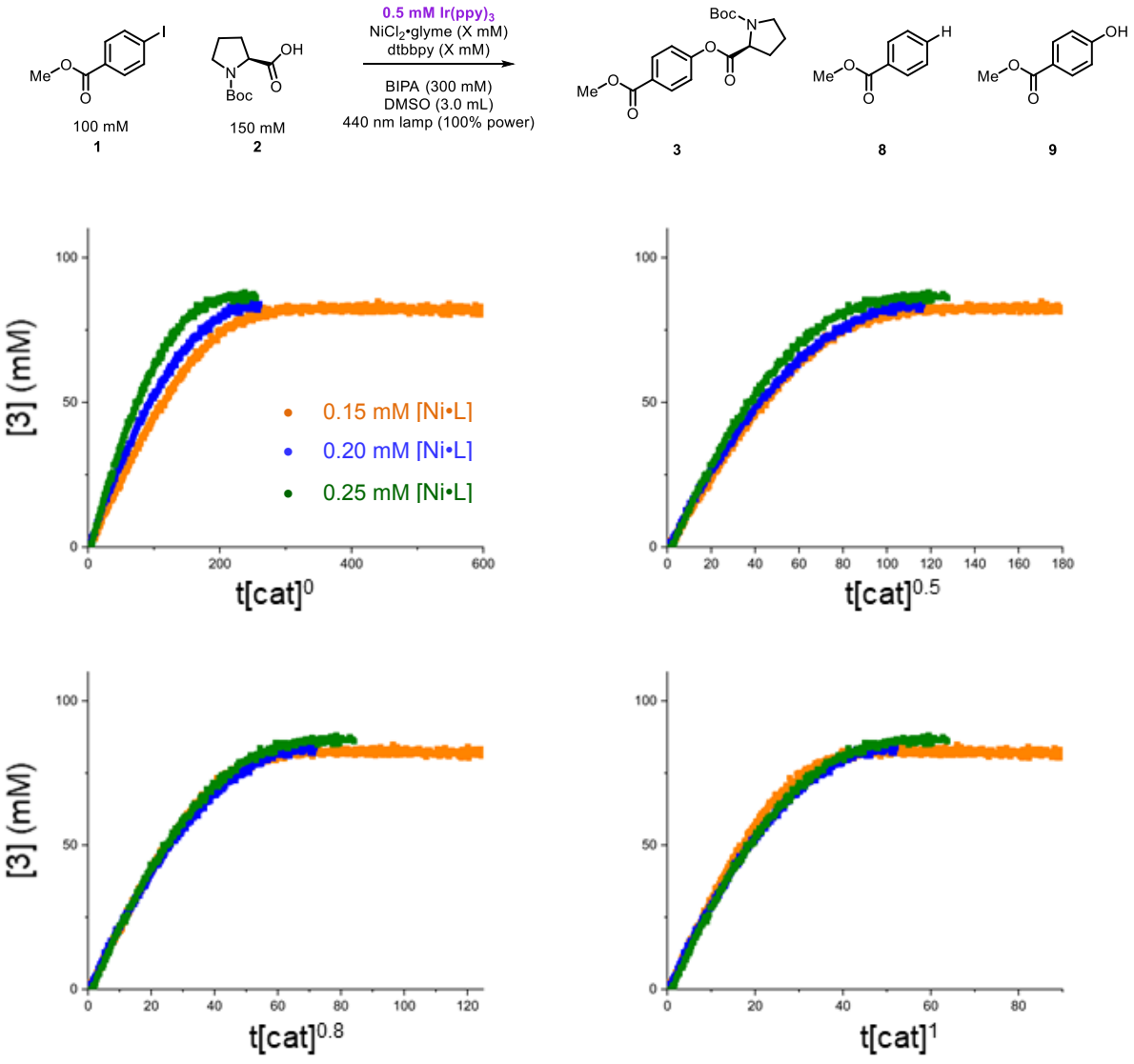

Figure S23. At 0.5 mM PC, nickel could be considered first-order around 0.20 mM, but high fractional was the most accurate overlay.

Entry	[Ni•L]	[1]	[3]	[8]	[9]	Total
jam328	0.15	0	80	8	4	92
jam325	0.20	0	84	6	2	92
jam329	0.25	0	86	5	2	93

Table S23. Tabulated yields and side products from experiments assessing catalyst order at 0.5 mM $Ir(ppy)_3$.

7.1.2 Towards a photon-unlimited regime – VTNA test, 1.0 mM PC

While a photocatalyst loading of 0.5 mM $Ir(ppy)_3$ showed high fractional order for Ni•L around 0.2 mM, it was theorized that increasing the PC loading would ensure first-order kinetics.

Following the general procedure described above (see section 2.1.2), experiments were conducted varying only the concentration of nickel and ligand.

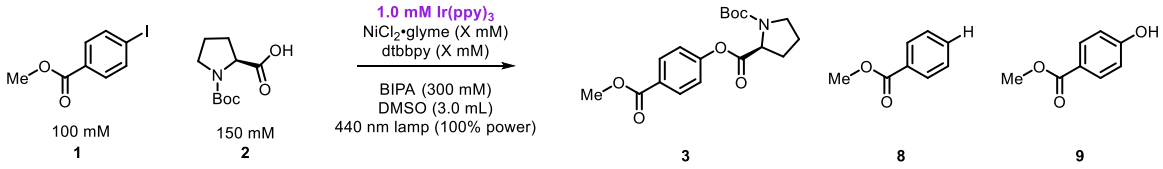

S35

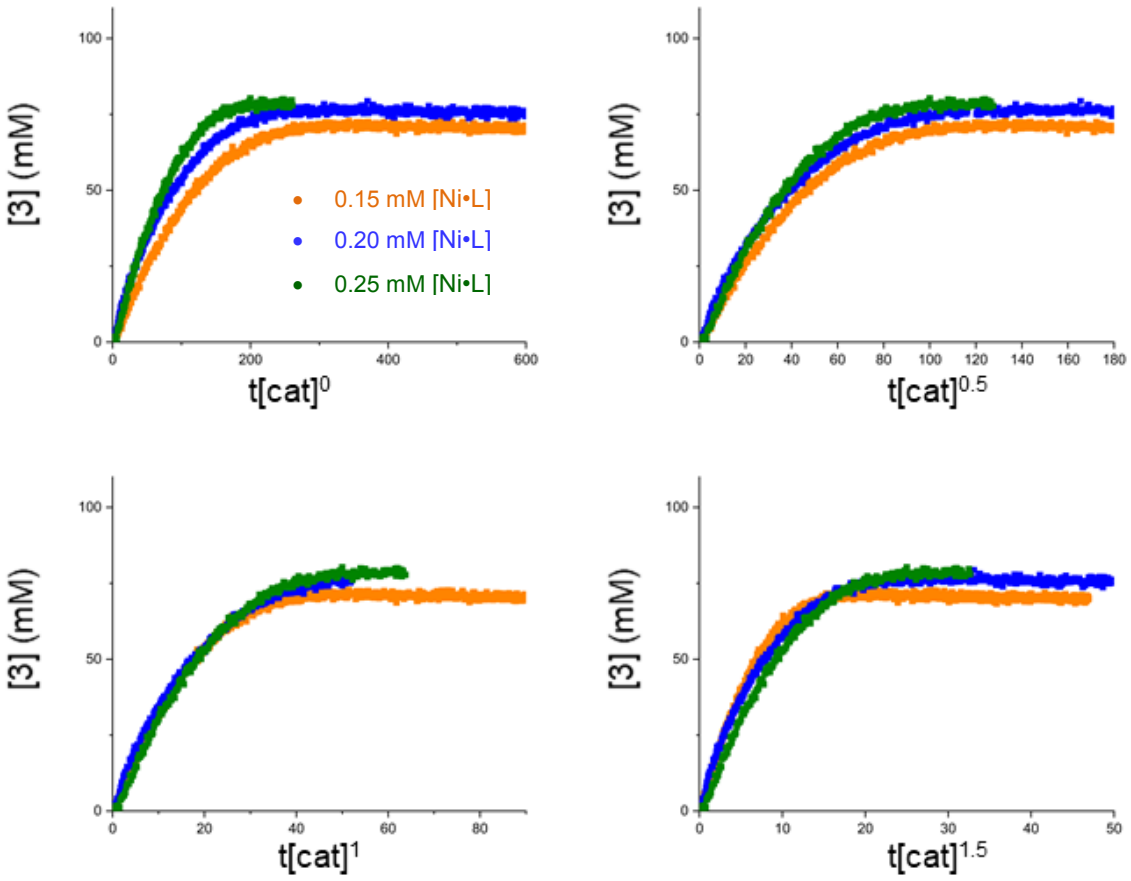

Figure S24. VTNA indicates that nickel catalyst is first-order at 1.0 mM $Ir(ppy)_3$.

Entry	[Ni•L]	[1]	[3]	[8]	[9]	Total
jam330	0.15	0	70	11	3	84
jam326	0.20	0	73	11	3	87
jam331	0.25	0	78	9	3	90

Table S24. Tabulated yields and side products from experiments assessing catalyst order at 1.0 mM $Ir(ppy)_3$.

7.2 Same excess

Following the general procedure outlined above (see section 2.1.2), two experiments were conducted with the same "excess" (50 mM) between $[1]_0$ and $[2]_0$.

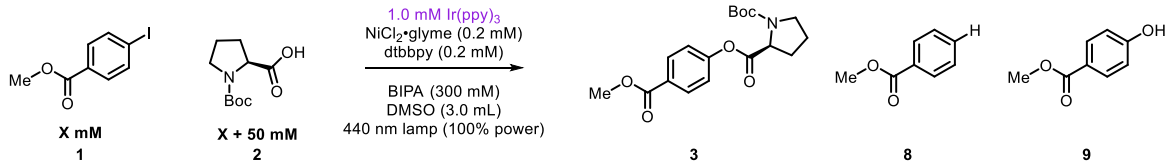

(Plot shown in Figure 3B.)

Entry	$[1]_0$	[1]	[3]	[8]	[9]	Total
jam326	100	0	73	11	3	87
jam332	50	0	35	5	2	42

Table S25. Tabulated yields and side products from homogeneous photon-unlimited same excess experiment.

7.3 Different excess experiments, aryl iodide

Following the general procedure outlined above (see section 2.1.2), experiments were conducted varying only the concentration of aryl iodide **1**.

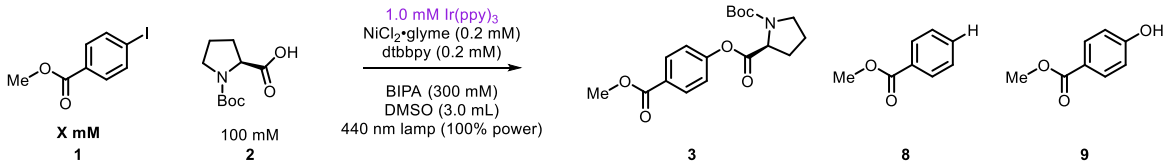

(Plot shown in Figure 3C.)

Entry	$[1]_0$	[1]	[3]	[8]	[9]	Total
jam334	150	6	92	16	14	128
jam333	100	0	72	11	5	88
jam335	50	0	35	5	2	42
jam338	25	0	16	2	4	22
jam339	10	0	6	1	1	8

Table S26. Tabulated yields and side products from homogeneous photon-unlimited different excess experiments varying $[1]_0$.

7.4 Different excess experiments, N-Boc proline

Following the general procedure outlined above (see section 2.1.2), experiments were conducted varying only the concentration of *N*-Boc proline **2**.

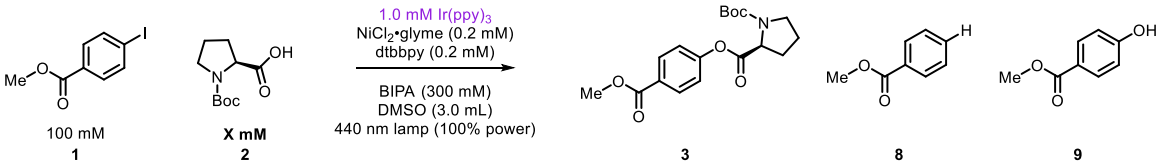

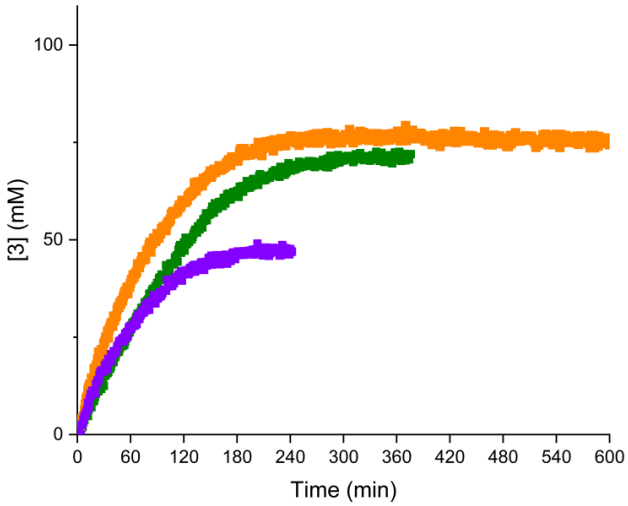

Figure S25. The dependence on [2] is not solvable through VTNA analysis.

Entry	$[2]_0$	[1]	[3]	[8]	[9]	Total
jam326	150	0	73	11	3	87
jam333	100	0	72	11	5	88
jam337	50	10	47	13	14	84

Table S27. Tabulated yields and side products from homogeneous photon-unlimited different excess experiments varying $[2]_0$.

7.5 Base experiments

Following the general procedure outlined above (see section 2.1.2), experiments were conducted varying only the concentration of base.

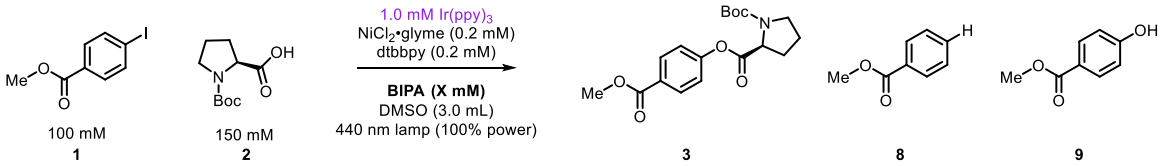

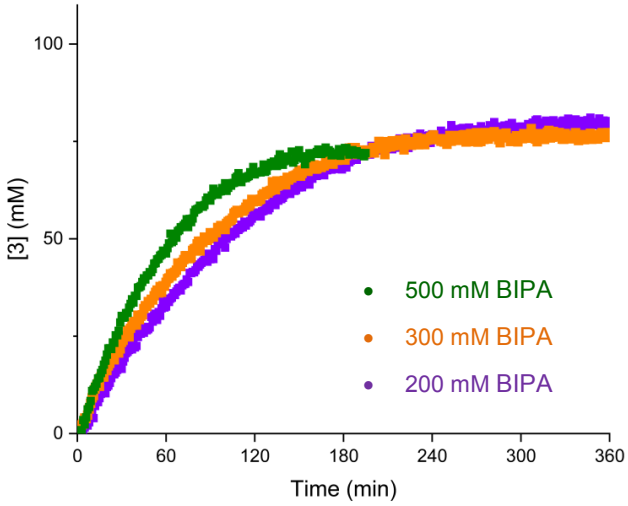

Figure S26. Increasing concentration of base accelerates the homogeneous reaction in the photon-unlimited regime.

Entry	[BIPA]	[1]	[3]	[8]	[9]	Total
jam336	200	0	80	9	3	92
jam326	300	0	73	11	3	87
jam335	500	0	72	12	6	90

Table S28. Tabulated yields and side products from homogeneous photon-unlimited different excess experiments varying [base].

8. $Ir(ppy)_3$ (homogeneous) as photocatalyst: Photon-unlimited regime, classically derived [Ni•L]

The purpose of this section was to corroborate the data from Section 7 through finding the linear-absorption (photon-unlimited) regime through the same procedure that was used in the *heterogeneous* case. These data sets are the same as Section 7 but with a lower [PC] and [Ni]. Agreement between Sections 7 and 8 helps reinforce that the regime is photon-unlimited. The reaction times are longer in this section, but otherwise the trends are the same as Section 7. This remains as a note for researchers that the photon-unlimited regime can be accessed through either procedure.

8.1 Toward a photon-unlimited regime: Initial rate studies, 0.5 mM $Ir(ppy)_3$

Following the general procedure described above (see section 2.1.2), experiments were conducted varying only the concentration of nickel and ligand. Initial rates were determined from product formation with a Savitsky-Golay filter at the t = 10 min data point.

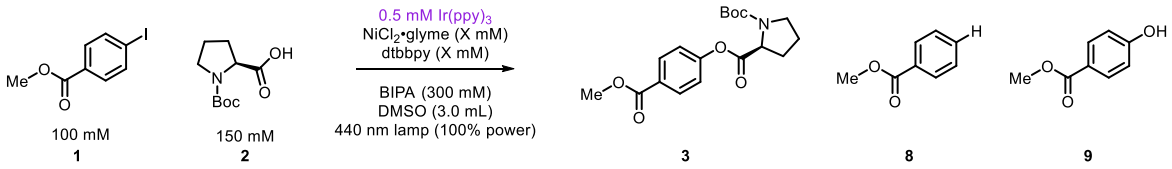

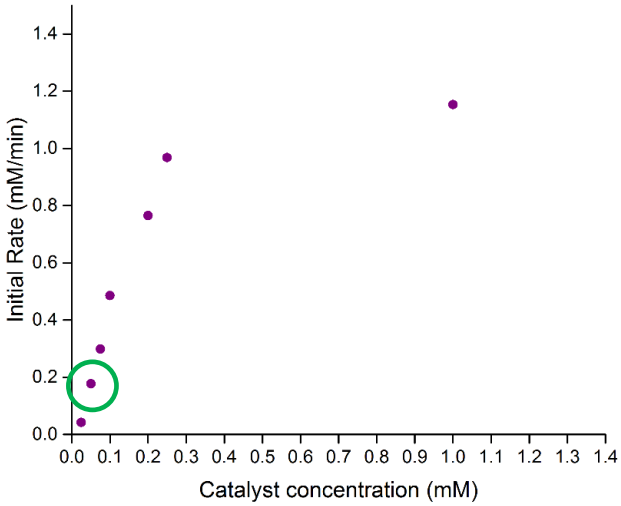

Figure S27. Initial rate studies performed to determine region in which nickel catalyst is not limited by transfer from excited photocatalytic species.

8.2 Order of nickel catalyst, photon-unlimited

Following the general procedure described above (see section 2.1.2), experiments were conducted varying only the concentration of nickel and ligand.

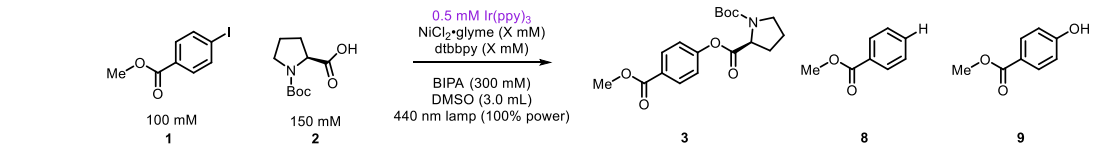

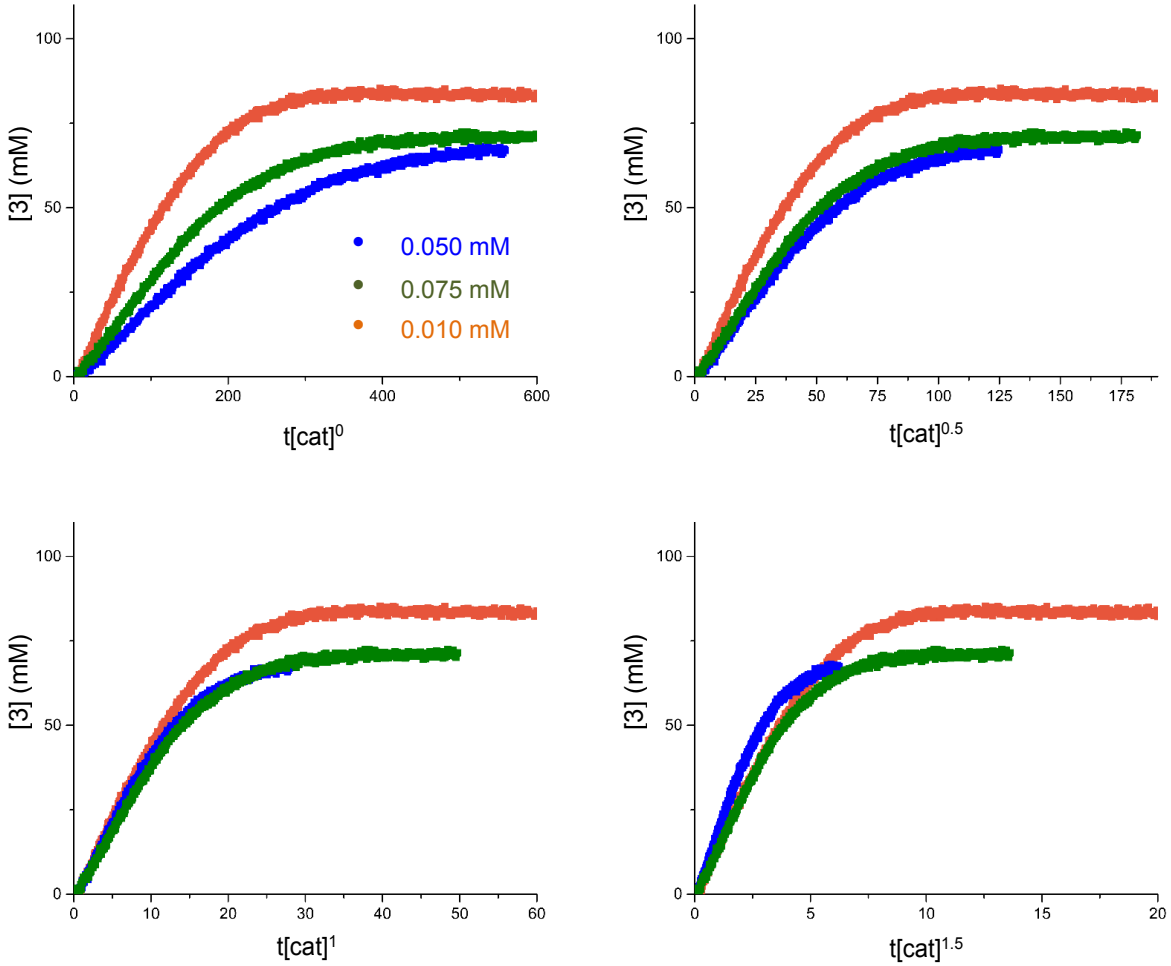

Figure S28. VTNA indicates that catalyst is first-order.

Entry	[Ni]	[1]	[3]	[8]	[9]	Total
amIr63	0.050	1	67	12	2	82
amIr61	0.075	0	73	11	3	87
amIr51	0.100	0	82	8	3	93

Table S29. Tabulated yields and side products from photon-unlimited catalyst order experiments.

8.3 Same excess

Following the general procedure described above (see Section 2.1.2), experiments were conducted with the same excess (defined as $[\mathbf{2}]_0 - [\mathbf{1}]_0$; in this case 50 mM) but different initial concentrations.

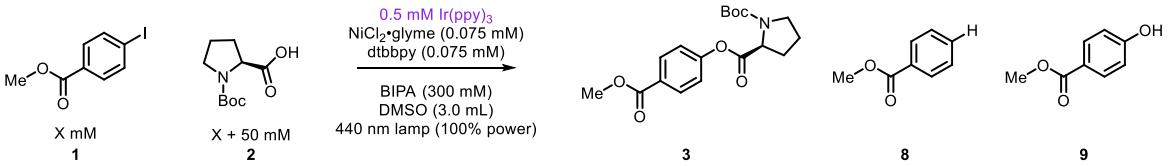

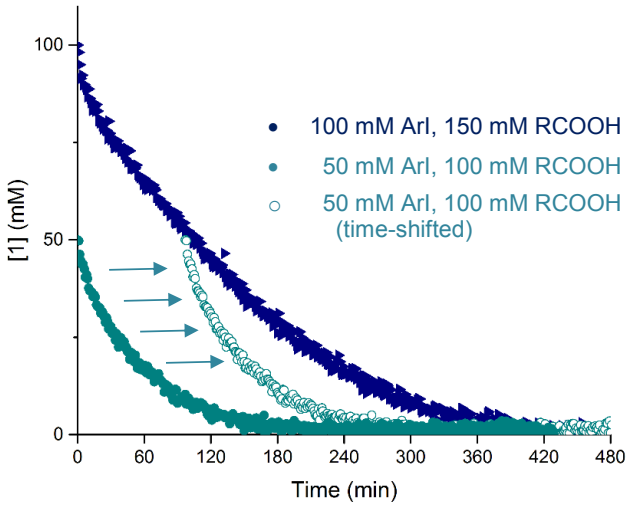

Figure S29. Same excess experiment indicates catalyst deactivation occurs in the photon-unlimited regime for the homogeneous reaction.

Entry	$[1]_0$	[1]	[3]	[8]	[9]	Total
amIr64	50	0	35	7	2	44
amIr61	100	0	73	11	3	87

Table S30. Tabulated yields and side products from photon-unlimited same excess experiments.

8.4 Different excess

Following the general procedure described above (see section 2.1.2), experiments were conducted varying only the concentrations of aryl iodide **1** and carboxylic acid **2**.

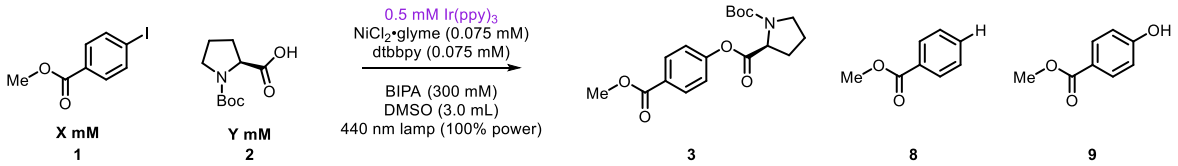

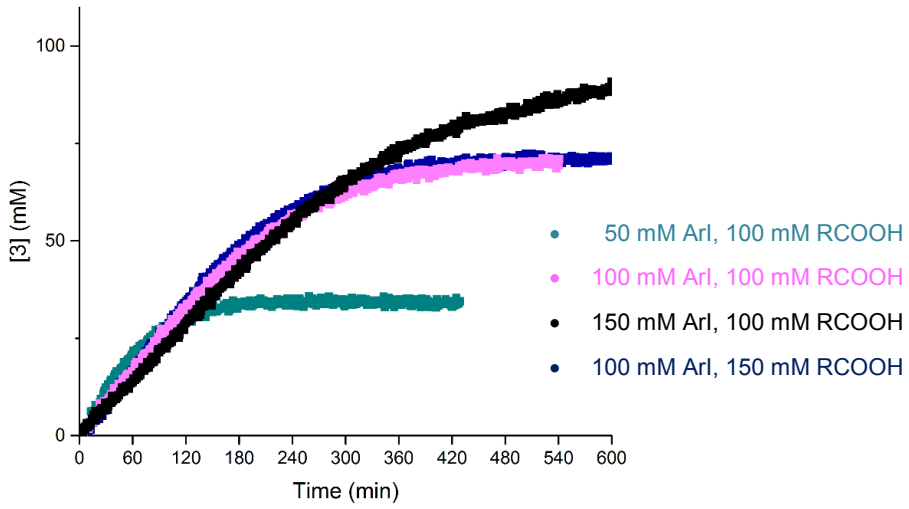

Figure S30. Different excess experiments indicate a lack of rate dependence on [1] or [2] for photon-unlimited homogeneous reactions.

Entry	$[1]_0$	$[2]_0$	[1]	[3]	[4]	[5]	Total
amIr64	50	100	0	35	7	2	44
amIr65	100	100	0	71	12	4	87
amIr66	150	100	17	92	17	8	134
amIr61	100	150	0	73	11	3	87

Table S31. Tabulated yields and side products from photon-unlimited experiments assessing reagent orders of substrates.

8.5 Base experiments

Following the general procedure described above, experiments were conducted varying only the concentration of base.

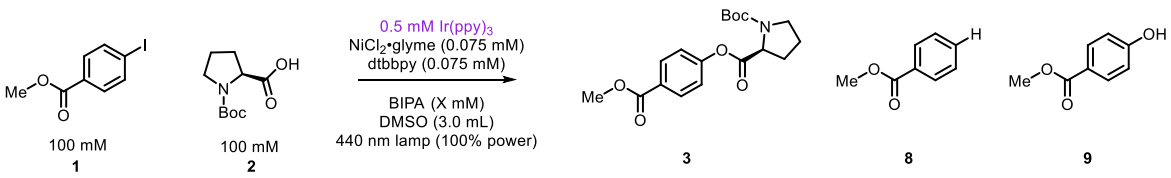

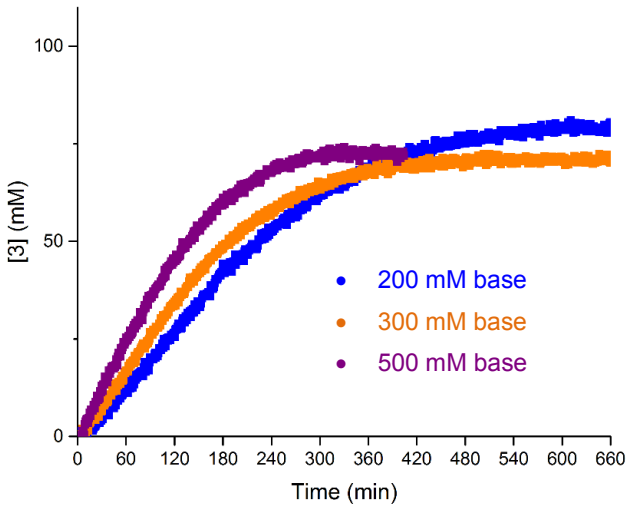

Figure S31. Experiments varying the amount of base in the photon-unlimited, homogeneous reaction.

Entry	[BIPA] (mM)	[1]	[3]	[8]	[9]	Total
amIr68	200	0	80	10	2	92
amIr61	300	0	73	11	3	87
amIr69	500	0	72	14	5	91

Table S32. Tabulated yields and side products from photon-unlimited experiments assessing role of base.

[1] *J. Org. Chem.* **1999**, *64*, 6263
[2] *Angew. Chem. Int. Ed.* **2019**, *58*, 9575
[3] *Angew. Chem. Int. Ed.* **2005**, *44*, 4302
[4] *Chem. Rev.* **1991**, *91*, 165.

Supporting Information - Chapter 8

Semi-Heterogeneous Dual Nickel/Photocatalytic (Thio)Etherification using Carbon Nitrides

Cavedon. C.; **Madani A.;** Seeberger P. H., Pieber B
Orag. Lett. **2019**, 21, 13, 5331-5334.

https://doi.org/10.1021/acs.orglett.9b01957

Semi-Heterogeneous Dual Nickel/Photocatalytic (Thio)Etherification using Carbon Nitrides

Cristian Cavedon,[†‡] Amiera Madani,[†‡] Peter H. Seeberger,[†‡] and Bartholomäus Pieber*[,†]

[†]Department of Biomolecular Systems, Max Planck Institute of Colloids and Interfaces, Am Mühlenberg 1, 14476 Potsdam, Germany

[‡]Department of Chemistry and Biochemistry, Freie Universität Berlin, Arnimallee 22, 14195 Berlin, Germany

Correspondence to: bartholomaeus.pieber@mpikg.mpg.de

TABLE OF CONTENTS

1. General remarks

Substrates, reagents, and solvents were purchased from commercial suppliers and used without further purification. N-*tert*-butylisopropylamine (BIPA),[1] 6,6'-diamino-2,2'-bipyridyl,[2, 3] methyl 4-(((trifluoromethyl)sulfonyl)oxy)benzoate,[4] methyl 4-(tosyloxy)benzoate,[5] methyl 4-((methylsulfonyl)oxy)benzoate,[6] (2-bromophenoxy)ethanol,[7] (2-bromophenyl)propanol[8] and *N*-(3-hydroxy-3-phenylpropyl)-*N*-methylacetamide[9] were prepared according to literature procedures. ^{1}H-, ^{13}C- and ^{19}F-NMR spectra were obtained using a Varian 400 spectrometer (400 MHz, Agilent), an Ascend^{TM} 400 spectrometer (400 MHz, cryoprobe, Bruker) and a Varian 600 spectrometer (600 MHz, Agilent) at 298 K, and are reported in ppm relative to the residual solvent peaks. Peaks are reported as: s = singlet, d = doublet, t = triplet, q = quartet, m = multiplet or unresolved, with coupling constants in Hz. Analytical thin layer chromatography (TLC) was performed on pre-coated TLC-sheets, ALUGRAM Xtra SIL G/UV$_{254}$ sheets (Macherey-Nagel) and visualized with 254 nm light or staining solutions followed by heating. Purification of final compounds was carried out by flash chromatography on the Reveleris X2 Flash Chromatography System from GRACE using prepacked columns with 40 μm silica gel. Silica 60 M (0.04-0.063 mm) silica gel (Sigmal Aldrich) was used for dry loading of the crude compounds on the flash chromatography system. Centrifugation was carried out using an Eppendorf 5430 centrifuge. High-resolution mass spectral data were obtained using a HR-EI-MS (Waters Autospec Premier) and a Waters XEVO G2-XS 4K spectrometer with the XEVO G2-XS QTOF capability kit. Emission spectra of LED lamps were recorded using 10 in. (24.5 cm) integrating sphere (Labsphere, Inc. Model LMS 1050) equipped with a diode array detector (International Light, Model RPS900). The UV/Vis spectrum of Ir[dF(CF$_3$)ppy]$_2$(dtbbpy)PF$_6$ was recorded using a UVmini-1240 spectrometer (Shimadzu). The UV/Vis spectrum of CN-OA-m was recorded using a UV2600 spectrometer (Shimadzu) equipped with an integrating sphere. Inductively coupled plasma - optical emission spectrometry (ICP-OES) was carried out using a Horiba Ultra 2 instrument equipped with photomultiplier tube detection.

2. Preparation of CN-OA-m

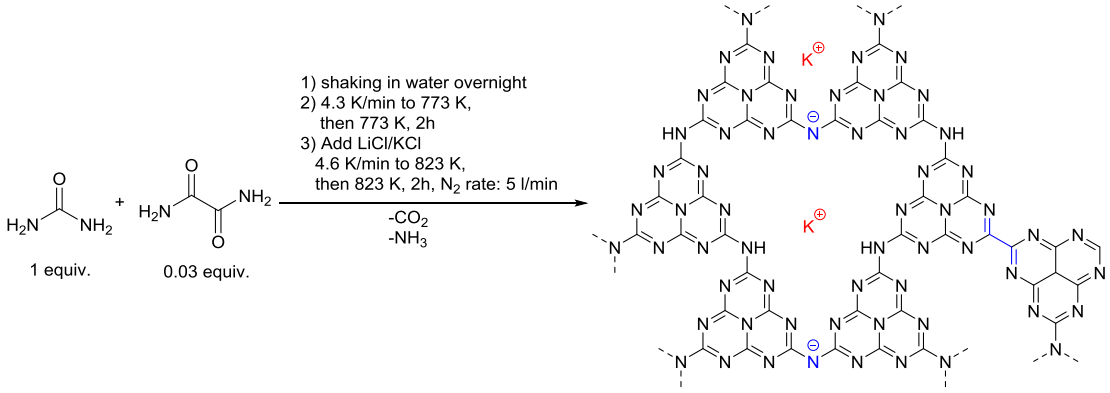

Scheme S1. Synthesis of CN-OA-m

The synthesis for CN-OA-m was carried out using a slightly adapted version of the literature procedure (Scheme S1)[10]: for each batch of the photocatalyst, urea (10 g, 166.5 mmol) and oxamide (0.5 g, 5.7 mmol) were mixed in 10 mL of DI water to generate a homogeneous mixture. After drying at 373 K, the resulting solids were grinded, transferred into a crucible with a cover and heated up in an air-oven with a heating rate of 4.3 K/min to 773 K. After keeping the mixture for 2h at 773 K, the sample was allowed to cool to room temperature. Subsequently, KCl (3.3 g, 44.3 mmol) and LiCl (2.7 g, 63.7 mmol) were added and the solids were grinded to obtain a homogeneous mixture which was heated in an inert atmosphere (N_2 flow: 5 mL/min) to 823 K with a heating rate of 4.6 K/min. After keeping the mixture for 2 h at 823 K, the sample was allowed to cool to room temperature and the resulting solids were collected on a filter paper and washed with H_2O (3 x 100 mL). The resulting yellow material was dried at 373 K (average yield per batch: ~400 mg).

Each batch was tested under the same set of conditions and obtaining always similar catalytic activities (+/-5% based on ^{1}H-NMR with internal standard).

The cost of CN-OA-m was calculated to be 4.2 € g^{-1} based on the prices of urea, oxamide, LiCl and KCl from Sigma-Aldrich (Merck).[11] As a comparison, the price of $Ir(ppy)_3$ is 2124 € g^{-1}.[11]

The UV/Vis spectrum of CN-OA-m shows a strong absorption up to ~460 nm and a comparably weaker absorption band up to ~700 nm (Figure S1, A) which are attributed to the π-π* electron transition of the sp^2 hybridization of C and N in the heptazine framework and n-π* electron transition involving the lone pairs of the edge nitrogen atoms in the heptazine units, respectively.[10] The capability of harvesting low energy light is therefore superior compared to Ir and Ru photocatalysts (see Figure S1, B for the UV/Vis spectrum of $Ir[dF(CF_3)ppy]_2(dtbbpy)PF_6$ as a representative example) which have only a low absorption band between 400 and 500 nm in the visible region, which corresponds to the metal-to-ligand charge transfer transition.

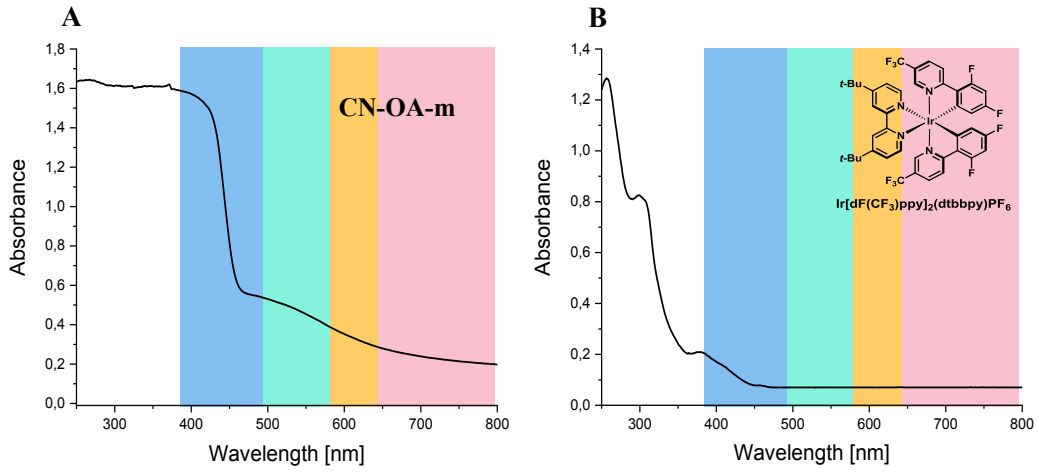

Figure S1. UV/Vis absorption spectra of CN-OA-m (**A**) and Ir[dF(CF_3)ppy]$_2$(dtbbpy)PF_6 (**B**).

3. Setups for photochemical reactions

3.1. RGB photoreactor (low intensity)

A flexible, red/green/blue LED strip[12] (RGB, 5m, 24 W/strip; Tween Light, BAHAG AG, Germany) was wrapped around a 115 mm borosilicate crystallization dish (Figure S2). White light (illumination of all three LED colors - red/green/blue) was used at full power (For emission spectra of a single diode, see Figure S3). The evaporating dish was filled with ethylene glycol and the temperature was set to 40°C to maintain a constant temperature. The sealed reaction vessels were placed at the same distance from the LED strip during all experiments (Figure S2). All reactions were performed with a stirring speed of 1400 rpm.

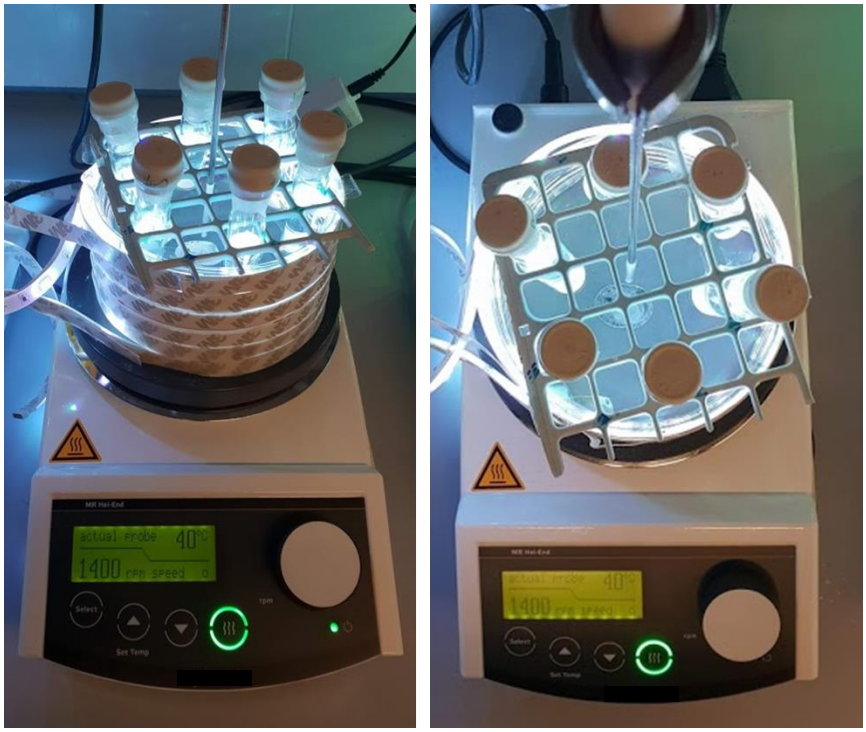

Figure S2. Experimental setup of the RGB photoreactor (low intensity)

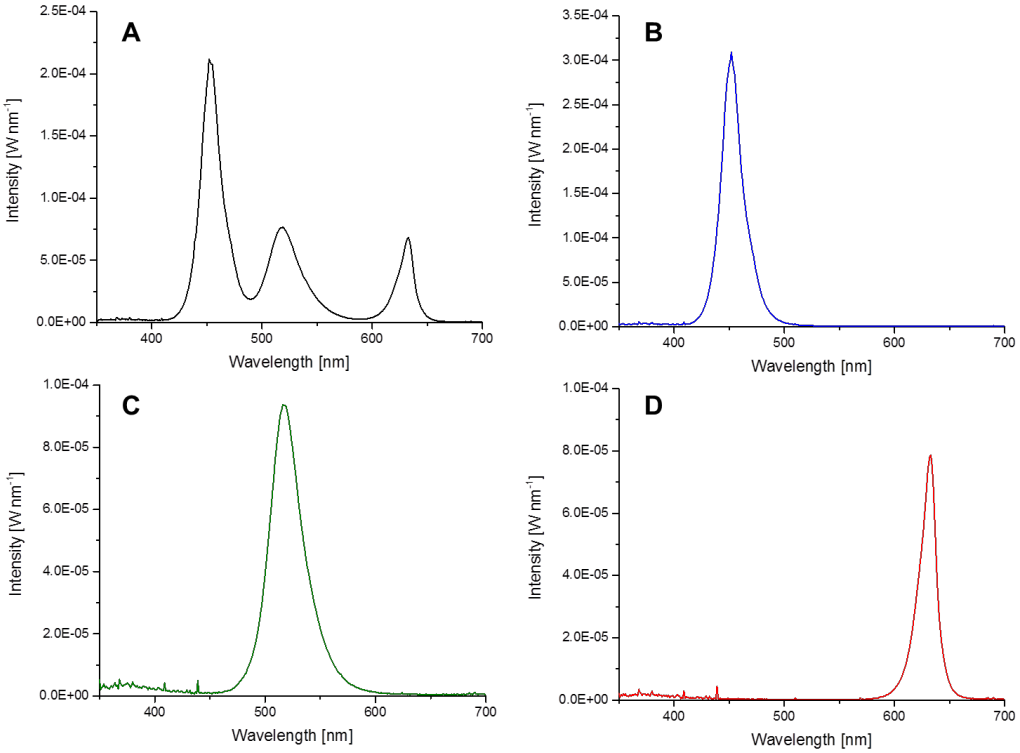

Figure S3. Emission spectra of the LED strips used in the RGB photoreactor (low intensity) for photochemical reactions. All experiments were carried out at maximum power. **A**: white light. **B**: blue light only. **C**: green light only. **D**: red light only.

3.2. 440 nm photoreactor (high intensity)

Blue LED lamps[13] at 50% power (440 nm, 40W, PR160, Kessil Photoredox, for emission spectrum, see Figure S5) were used for experiments on CN-OA-m recycling (Figure S4). Two sealed reaction vessels were placed on a stirring plate 4.5 cm away from a single lamp. To avoid heating of the reaction mixture, a fan was used for cooling. All reactions were performed with maximum stirring speed.

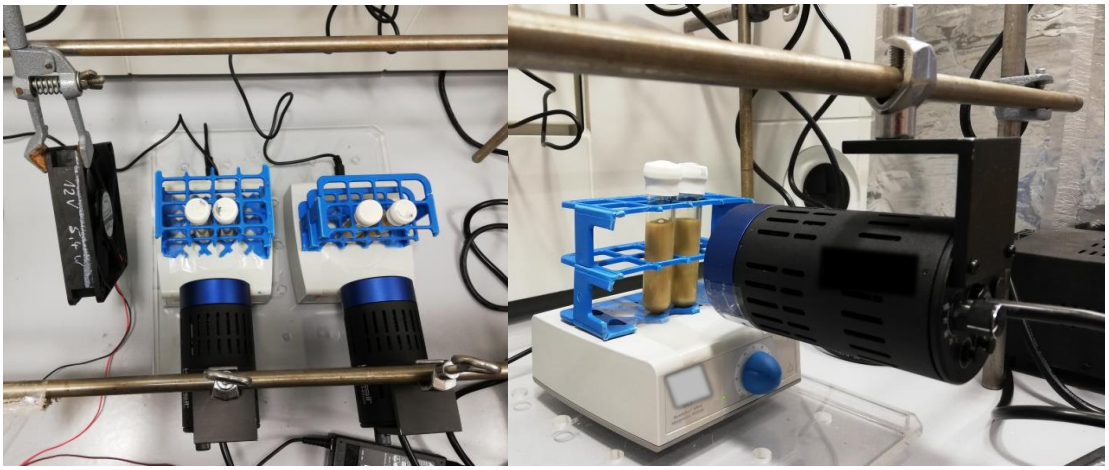

Figure S4. Experimental setup of the 440 nm photoreactor (high intensity).

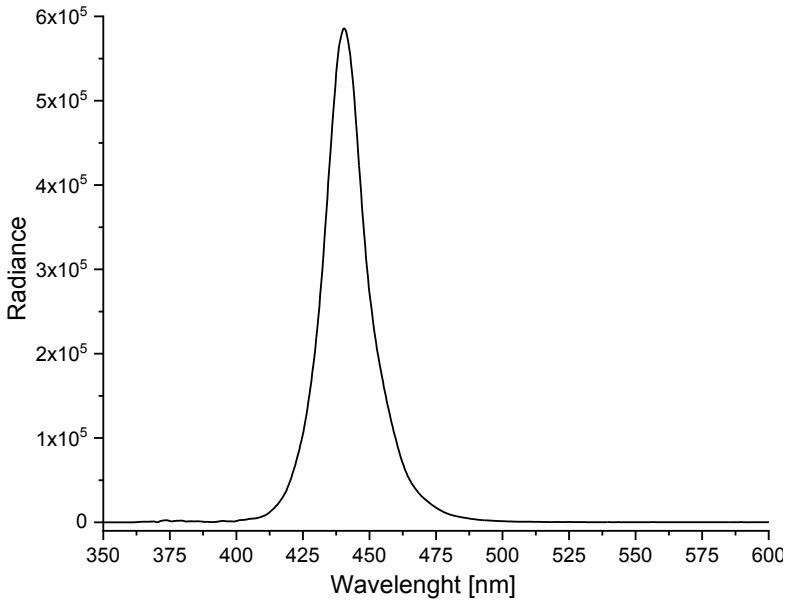

Figure S5. Emission spectrum of Kessil PR160-440 lamps.

4. Reaction optimization of the coupling of aryl bromides and alcohols

4.1. General experimental procedure for screening experiments

An oven dried vial (19 x 100 mm) equipped with a stir bar was charged with the Ni^{II} source (30 µmol, 10 mol%), the ligand (30 µmol, 10 mol%), the CN material (10 mg) and methyl 4-bromobenzoate (64.5 mg, 0.3 mmol, 1.0 equiv). Subsequently, the solvent (3.0 mL), the base (3.0 - 5.0 equiv) and 1-hexanol (2.0 - 3.0 equiv) were added and the vial was sealed with a septum and Parafilm. The reaction mixture was sonicated for 5 - 10 min, followed by stirring for 5 min until a fine dispersion of the solids was achieved. Thereafter, the mixture was degassed by bubbling argon for 10 min. The final reaction mixture was irradiated in the low intensitiy RGB photoreactor with white light at 40 °C with rapid stirring (1400 rpm). After the respective reaction time, one equivalent of 1,3,5-trimethoxybenzene (50.5 mg, 0.3 mmol) was added. An aliquot of the reaction mixture (~200 µL) was filtered, diluted with DMSO-d_6 and subjected to ^{1}H-NMR analysis. For representative NMR spectra, see Figure S6.

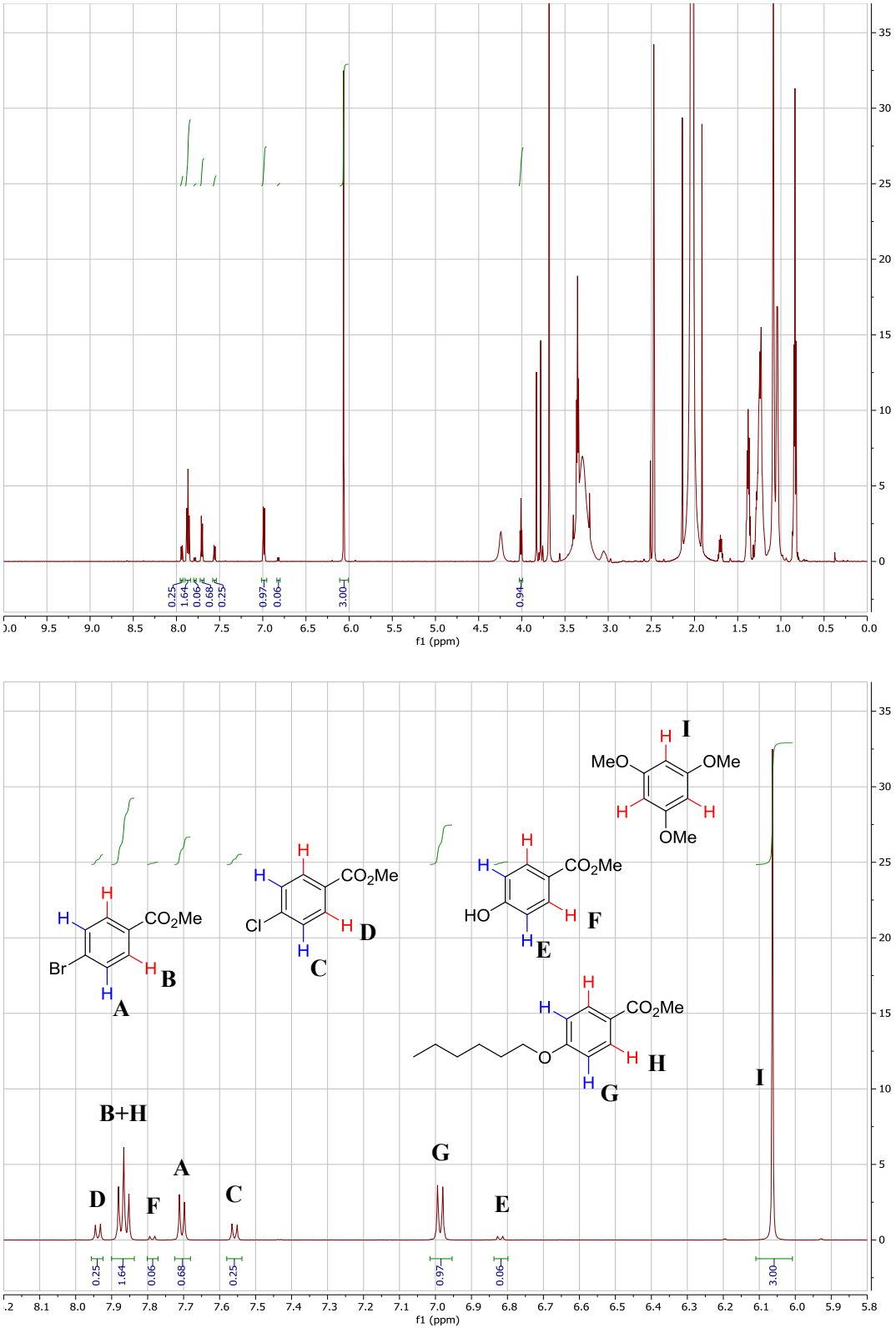

Figure S6. Example of a crude ^{1}H-NMR spectrum of the C-O coupling of methyl 4-bromobenzoate and 1-hexanol.

S10

4.2. Solvent screening

Table S1. Solvent screening.[a]

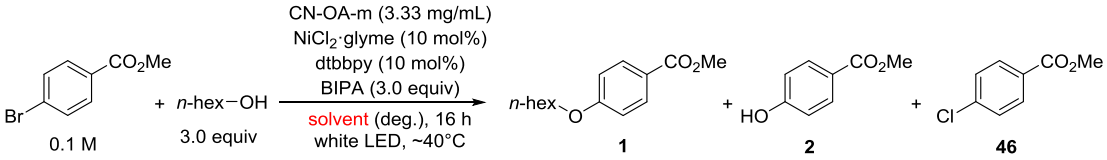

Entry	Solvent	Conversion [%][b]	1 [%][c]	2 [%][c]	46 [%][c]
1	MeCN	68	51	3	13
2	DMF	50	25	9	16
3	THF	41	22	2	17
4	Diglyme	28	11	2	15
5	DMAc	42	11	6	24
6	DMSO	15	4	5	6

[a]Reaction conditions: methyl 4-bromobenzoate (0.3 mmol), 1-hexanol (0.9 mmol), CN-OA-m (10 mg), $NiCl_2$·glyme (30 µmol), dtbbpy (30 µmol), BIPA (0.9 mmol), solvent (anhydrous, 3.0 mL), white LEDs at 40 °C for 16 h. [b]Conversion of methyl 4-bromobenzoate determined by ^{1}H-NMR using 1,3,5-trimethoxybenzene as internal standard. [c]NMR yields determined by ^{1}H-NMR using 1,3,5-trimethoxybenzene as internal standard.

Acetonitrile showed highest conversion and selectivity. HPLC grade MeCN gave identical results compared to high purity, anhydrous MeCN.

4.3. Screening of carbon nitride materials

Table S2. Screening of carbon nitride materials.[a]

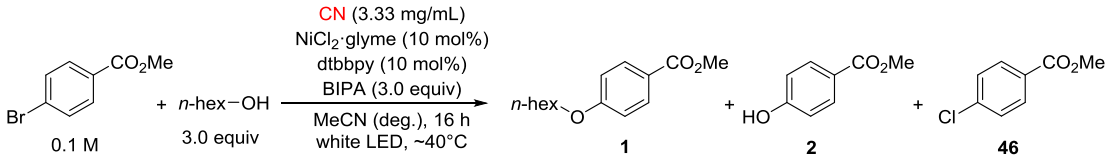

Entry	CN material	Conversion [%][b]	1 [%][c]	2 [%][c]	46 [%][c]
1	CN-OA-m	68	51	3	13
2	$CMB_{0.05}$-CN	28	18	1	9
3	mpg-CN	22	14	1	7
4	$CMB_{0.10}$-CN	4	2	n.d. [d]	2
5	K-PHI	1	traces	n.d.	n.d.
6	CNS_{600}	<1	n.d.	n.d.	n.d.

[a]Reaction conditions: methyl 4-bromobenzoate (0.3 mmol), 1-hexanol (0.9 mmol), CN material (10 mg), $NiCl_2$·glyme (30 µmol), dtbbpy (30 µmol), BIPA (0.9 mmol), MeCN (3.0 mL), white LEDs at 40 °C for 16 h. [b]Conversion of methyl 4-bromobenzoate determined by ^{1}H-NMR using 1,3,5-trimethoxybenzene as internal standard. [c]NMR yields determined by ^{1}H-NMR using 1,3,5-trimethoxybenzene as internal standard. [d]not detected.

Several carbon nitride materials were tested: mesoporous graphitic carbon nitride (mpg-CN),[14] two modified carbon nitrides derived from a cyanuric acid/melamide/barbituric acid complex ($CMB_{0.05}$-CN and $CMB_{0.10}$-CN),[15] a sulfur-doped material (CNS_{600}),[16] a strongly oxidizing potassium poly(heptazine imide) (K-PHI),[17] and a carbon nitride derivative prepared *via* co-condensation of urea and oxamide followed by post-calcination in a molten salt (CN-OA-m).[10]

4.4. Screening of Ni^{II} sources

Table S3. Screening of Ni^{II} sources.[a]

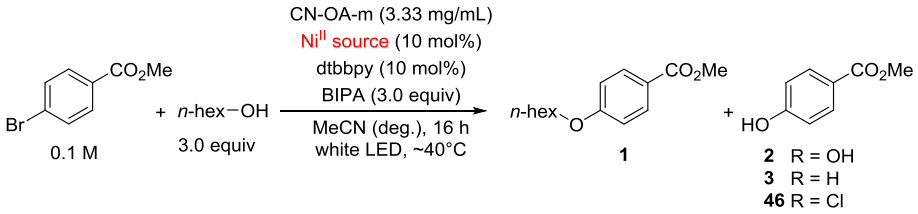

Entry	Ni^{II} source	Conversion [%][b]	1 [%][c]	2 [%][c]	3 [%][c]	46 [%][c]	Price [€ mol^{-1}][d]
1	$Ni(OTf)_2$	60	52	3	2	n.d.[e]	12917
2	$NiCl_2$·glyme	68	51	3	n.d.	13	4161
3	$NiCl_2$	55	41	3	n.d.	11	110
4	$NiBr_2$·glyme	42	39	2	n.d.	n.d.	10431
5	$NiBr_2 \cdot 3H_2O$	40	36	3	n.d.	n.d.	116
6[f]	$Ni(OAc)_2 \cdot 4H_2O$	14	5	2	3	n.d.	28
7	$NiBr_2$	7	5	1	n.d.	n.d.	411
8	$NiCl_2 \cdot 6H_2O$	4	2	n.d.	2	n.d.	71
9	NiI_2	15	14	1	n.d.	n.d.	2063
10	$Ni(acac)_2$	4	1	n.d.	3	n.d.	620

[a]Reaction conditions: methyl 4-bromobenzoate (0.3 mmol), 1-hexanol (0.9 mmol), CN-OA-m (10 mg), Ni^{II} source (30 µmol), dtbbpy (30 µmol), BIPA (0.9 mmol), MeCN (3.0 mL), white LEDs at 40 °C for 16 h. [b]Conversion of methyl 4-bromobenzoate determined by ^{1}H-NMR using 1,3,5-trimethoxybenzene as internal standard. [c]NMR yields determined by ^{1}H-NMR using 1,3,5-trimethoxybenzene as internal standard. [d]Prices according to Sigma Aldrich (Merck).[11] [e]not detected. [f]methyl 4-acetoxybenzoate (4%) was formed as additional side product.

The selection of $NiBr_2 \cdot 3H_2O$ for further studies was based on reactivity, price (significantly cheaper compared to $Ni(OTf)_2$ and $NiBr_2$·glyme) and selectivity (formation methyl 4-chlorobenzoate in case of $NiCl_2$).

4.5. Screening of ligands

Table S4. Ligand screening.[a]

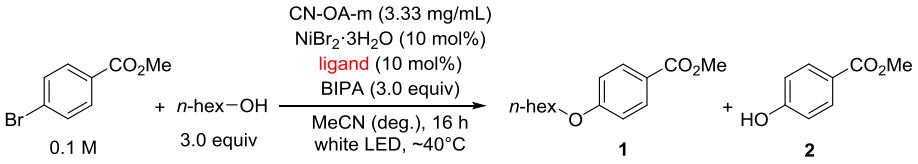

Entry	Ligand	Conversion [%][b]	1 [%][c]	2 [%][c]
1	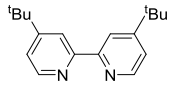	62	57	3
2	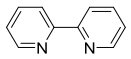	45	42	3
3	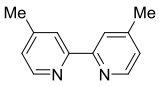	50	47	3
5	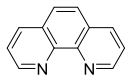	26	23	2
6	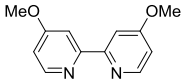	52	48	4
7	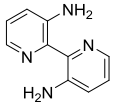	12	6	5

[a]Reaction conditions: methyl 4-bromobenzoate (0.3 mmol), 1-hexanol (0.9 mmol), CN-OA-m (10 mg), $NiBr_2 \cdot 3H_2O$ (30 µmol), ligand (30 µmol), BIPA (0.9 mmol), MeCN (3.0 mL), white LEDs at 40 °C for 16 h. [b]Conversion of methyl 4-bromobenzoate determined by ^{1}H-NMR using 1,3,5-trimethoxybenzene as internal standard. [c] determined by ^{1}H-NMR using 1,3,5-trimethoxybenzene as internal standard.

During the study it was observed that the LED strips used in the RGB photoreactor become less efficient as they are used. As reactivity depends on the light intensity, periodic replacement of the LED strips was found to be necessary. Results reported in Table S4 were obtained right after replacing the light source, and are therefore higher than those obtained in the same conditions from the previous experiement (Table S3, entry 5).

6,6'-diamino-2,2'-bipyridyl (Entry 7) was tested because it was reported to improve the reaction when water is used as coupling partner in the nickel/photoredox catalyzed formation of phenols.[18]

4.6. Base screening

Table S5. Base screening.[a]

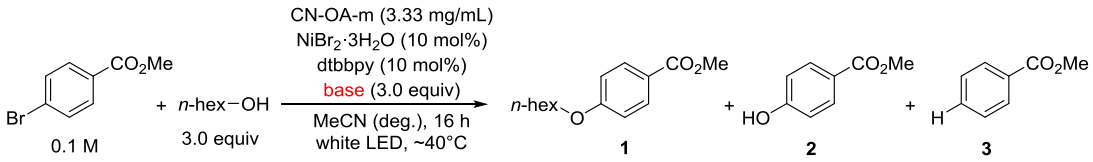

Entry	Base	Conversion [%][b]	1 [%][c]	2 [%][c]	3 [%][c]
1	BIPA + quinuclidine (10 mol%)	78	73	4	n.d.[d]
2	BIPA	62	57	3	n.d.
3	DBU[e]	10	4	n.d.	5
4	Et_3N	23	17	2	4
5	DIPEA[f]	16	7	1	8
6	tetramethyguanidine	4	4	n.d.	n.d.
7	DABCO[g]	<1	n.d.	n.d.	n.d.
8	DMAP[h]	<1	n.d.	n.d.	n.d.
9	CsOAc	<1	n.d.	n.d.	n.d.
10	CsF	<1	n.d.	n.d.	n.d.
11	Cs_2CO_3	<1	n.d.	n.d.	n.d.
12	K_2CO_3	<1	n.d.	n.d.	n.d.
13	K_3PO_4	<1	n.d.	n.d.	n.d.

[a]Reaction conditions: methyl 4-bromobenzoate (0.3 mmol), 1-hexanol (0.9 mmol), CN-OA-m (10 mg), $NiBr_2 \cdot 3H_2O$ (30 µmol), dtbbpy (30 µmol), base (0.9 mmol), MeCN (3.0 mL), white LEDs at 40 °C for 16 h. [b]Conversion of methyl 4-bromobenzoate determined by ^{1}H-NMR using 1,3,5-trimethoxybenzene as internal standard. [c]NMR yields determined by ^{1}H-NMR using 1,3,5-trimethoxybenzene as internal standard. [d]not detected. [e]1,8-Diazabicyclo[5.4.0]undec-7-ene [f]*N,N*-Diisopropylethylamine. [g]1,4-Diazabicyclo[2.2.2]octane. [h]4-(dimethylamino)pyridine.

N-tert-butylisopropylamine (BIPA) performed best during the screening of different bases (Table S5). No conversion of the starting material was detected using common inorganic bases (Table S5, entries 9-13). The addition of quinuclidine (10 mol%, Sigma Aldrich, 13786 € mol^{-1}) increased the product formation by only 15% and was therefore not used in the subsequent tests.[11]

4.7. Screening of reaction conditions

4.7.1. Time

Table S6. Time study.[a]

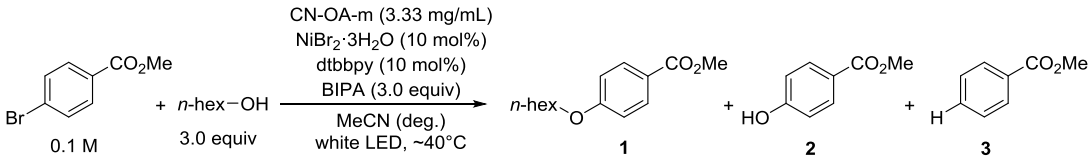

Entry	Time [h]	Conversion [%][b]	1 [%][c]	2 [%][c]	3 [%][c]
1	4	16	13	2	n.d.[d]
2	8	38	35	2	n.d.
3	16	62	57	3	n.d.
4	24	70	66	4	n.d.
5	32	75	69	4	2
6	48	97	91	5	n.d.

[a]Reaction conditions: methyl 4-bromobenzoate (0.3 mmol), 1-hexanol (0.9 mmol), CN-OA-m (10 mg), $NiBr_2 \cdot 3H_2O$ (30 µmol), dtbbpy (30 µmol), BIPA (0.9 mmol), MeCN (3.0 mL), white LEDs at 40 °C for the indicated time. [b]Conversion of methyl 4-bromobenzoate determined by ^{1}H-NMR using 1,3,5-trimethoxybenzene as internal standard. [c]NMR yields determined by ^{1}H-NMR using 1,3,5-trimethoxybenzene as internal standard. [d]not detected.

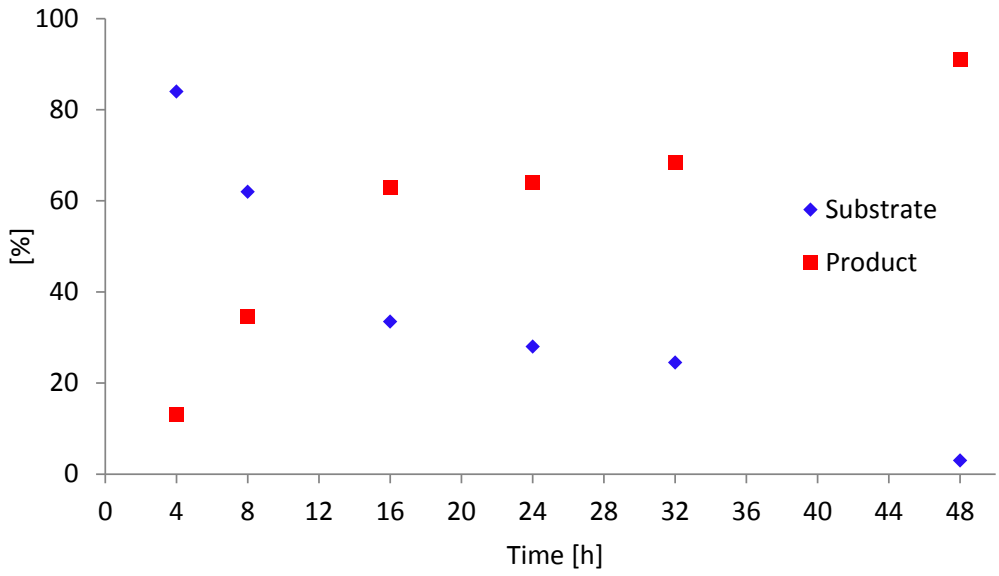

Figure S7: Time study (data from Table S6).

4.7.2. Stoichiometry optimization

Table S7. Optimization of stoichiometry of alcohol and base.[a]

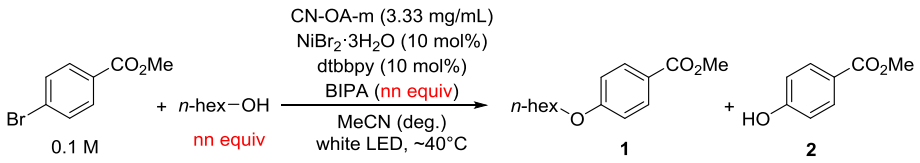

Entry	1-hexanol [equiv]	BIPA [equiv]	Time [h]	Conversion [%][b]	1 [%][c]	2 [%][c]
1	3.0	3.0	16	62	57	3
1	3.0	3.0	24	70	66	4
1	3.0	3.0	48	97	91	5
2	2.0	3.0	16	55	51	4
3	2.0	5.0	16	65	59	5
3	2.0	5.0	24	95	86	8
4	2.0	5.0	48	>99	92	7

[a]Reaction conditions: methyl 4-bromobenzoate (0.3 mmol), 1-hexanol (0.6 or 0.9 mmol), CN-OA-m (10 mg), $NiBr_2 \cdot 3H_2O$ (30 µmol), dtbbpy (30 µmol), BIPA (0.9 or 1.5 mmol), MeCN (3.0 mL), white LEDs at 40 °C for 16 to 48h. [b]Conversion of methyl 4-bromobenzoate determined by ^{1}H-NMR using 1,3,5-trimethoxybenzene as internal standard. [c]NMR yields determined by ^{1}H-NMR using 1,3,5-trimethoxybenzene as internal standard. [d]not detected.

A reduction of the amount of alcohol was realized using a higher amount of BIPA (Table S7, entry 3).

Table S8. Optimization of the stoichiometry of the Ni catalyst and carbon nitride material.[a]

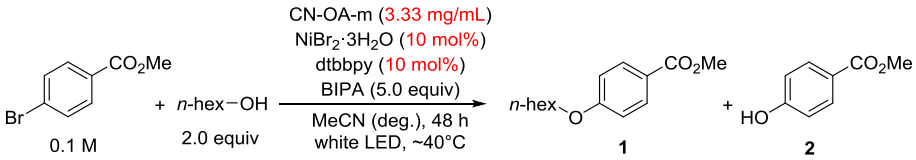

Entry	Deviation from standard conditions	Conversion [%][b]	1 [%][c]	2 [%][c]
1	None	>99	92	7
2	$NiBr_2 \cdot 3H_2O$ (5 mol%) with dtbbpy (5 mol%)	83	77	6
3	CN-OA-m (1.66 mg/ml)	94	90	4

[a]Reaction conditions: methyl 4-bromobenzoate (0.3 mmol), 1-hexanol (0.6 mmol), CN-OA-m (5 or 10 mg), $NiBr_2 \cdot 3H_2O$ (15 or 30 µmol), dtbbpy (15 or 30 µmol), BIPA (1.5 mmol), MeCN (3.0 mL), white LEDs at 40 °C for 48 h. [b]Conversion of methyl 4-bromobenzoate determined by ^{1}H-NMR using 1,3,5-trimethoxybenzene as internal standard. [c]NMR yields determined by ^{1}H-NMR using 1,3,5-trimethoxybenzene as internal standard.

Reducing the amount of the Nickel catalyst resulted in significantly lower conversion within 48 hours. The CN-OA-m (Table S8, entry 3) can be reduced resulting in slightly lower yields. Since the photocatalyst is inexpensive and recyclable, 3.33 mg ml^{-1} was maintained as loading for further experiments.

4.8. Control studies

Table S9. Control studies.[a]

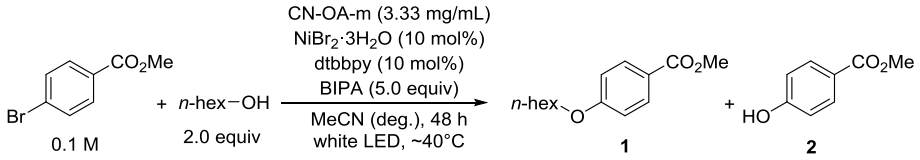

Entry	Deviation from standard conditions	Conversion [%][b]	1 [%][c]	2 [%][c]
1	None	>99	92	7
2	No CN-OA-m	<1	n.d.[d]	n.d.
3	No $NiBr_2 \cdot 3H_2O$	6	n.d.	n.d.
4	No dtbbpy	5	n.d.	n.d.
5	No BIPA	<1	n.d.	n.d.
6	No light	<1	n.d.	n.d.
7	No degassing	<1	n.d.	n.d.

[a]Reaction conditions: methyl 4-bromobenzoate (0.3 mmol), 1-hexanol (0.6 mmol), CN-OA-m (10 mg), $NiBr_2 \cdot 3H_2O$ (30 µmol), dtbbpy (30 µmol), BIPA (1.5 mmol), MeCN (3.0 mL), white LEDs at 40 °C for 48 h. [b]Conversion of methyl 4-bromobenzoate determined by ^{1}H-NMR using 1,3,5-trimethoxybenzene as internal standard. [c]NMR yields determined by ^{1}H-NMR using 1,3,5-trimethoxybenzene as internal standard. [d]not detected.

4.9. Screening of aryl (pseudo)halides

Table S10. Screening of aryl (pseudo)halides.[a]

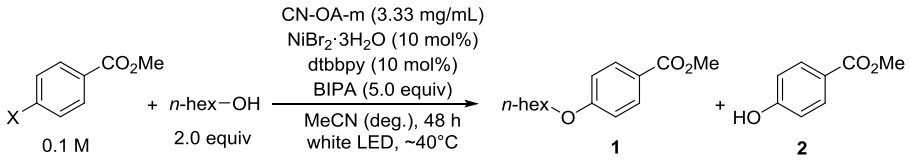

Entry	X	Conversion [%][b]	1 [%][c]	2 [%][c]
1	Br	>99	92	7
2	I	13	13	n.d.[d]
3	Cl	6	4	n.d.
4	OMs	<1	n.d.	n.d.
5	OTs	<1	n.d.	n.d.
6	OTf	<1	n.d.	n.d.

[a]Reaction conditions: aryl (pseudo)halide (0.3 mmol), 1-hexanol (0.6 mmol), CN-OA-m (10 mg), $NiBr_2 \cdot 3H_2O$ (30 µmol), dtbbpy (30 µmol), BIPA (1.5 mmol), MeCN (3.0 mL), white LEDs at 40 °C for 48 h. [b]Conversion of methyl 4-bromobenzoate determined by ^{1}H-NMR using 1,3,5-trimethoxybenzene as internal standard. [c]NMR yields determined by ^{1}H-NMR using 1,3,5-trimethoxybenzene as internal standard. [d]not detected.

4.10. Intramolecular etherification

Table S11. Intramolecular etherification for the formation of oxygen heterocycles.[a]

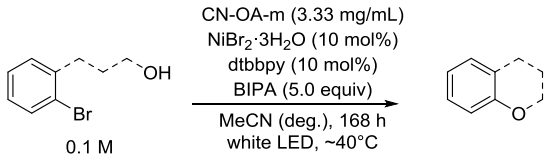

Entry	Substrate	Product	Substrate/Product[b]
1[c]	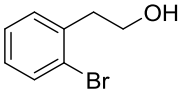	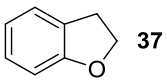 **37**	34/56
2	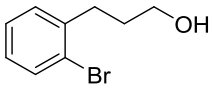	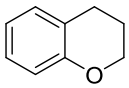	>99/0
3	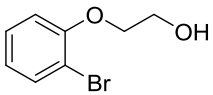	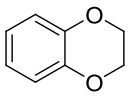	>99/0

[a]Reaction conditions: substrate (0.6 mmol), CN-OA-m (20 mg), $NiBr_2 \cdot 3H_2O$ (60 µmol), dtbbpy (60 µmol), BIPA (3.0 mmol), MeCN (6.0 mL), white LEDs at 40 °C for 168 h. [b]Ratio calculated from ^1H NMR analysis. [c]No product formation was detected in absence of CN-OA-m, $NiBr_2 \cdot 3H_2O$, dtbbpy, BIPA or light.

5. Reaction optimization for the coupling of aryl bromides and water

5.1. General experimental procedure for screening experiments

An oven dried vial (19 x 100 mm) equipped with a stir bar was charged with $NiBr_2 \cdot 3H_2O$ (8.2 mg, 30 µmol, 10 mol%), the ligand (8.1 mg, 30 µmol, 10 mol%), the CN-OA-m (10 mg) and methyl 4-bromobenzoate (64.5 mg, 0.3 mmol, 1.0 equiv). Subsequently, the solvent (3.0 mL), BIPA (172.8 mg, 1.5 mmol, 5.0 equiv) and H_2O (5.4 – 108.0 mg, 0.3 – 6.0 mmol, 1 - 20 equiv) were added and the vial was sealed with a septum and Parafilm. The reaction mixture was sonicated for 5 - 10 min, followed by stirring for 5 min until a fine dispersion of the solids was achieved. Thereafter, the mixture was degassed by bubbling argon for 10 min. The final reaction mixture was irradiated in the low intensitiy RGB photoreactor with white light at 40 °C with rapid stirring (1400 rpm). After the respective reaction time, one equivalent of 1,3,5-trimethoxybenzene (50.5 mg, 0.3 mmol) was added. An aliquot of the reaction mixture (~200 µL) was filtered, diluted with DMSO-d_6 and subjected to ^{1}H-NMR analysis.

5.2. Solvent screening

Table S12. Solvent screening.[a]

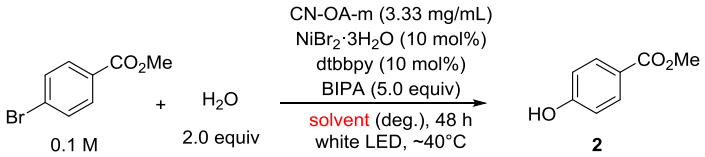

Entry	Solvent	Conversion [%][b]	2 [%][c]
1	MeCN	<1	n.d.[d]
2	MeCN/DMF (1:1)	23	22
3	DMF	50	49

[a]Reaction conditions: methyl 4-bromobenzoate (0.3 mmol), H_2O (0.6 mmol), CN-OA-m (10 mg), $NiBr_2 \cdot 3H_2O$ (30 µmol), dtbbpy (30 µmol), BIPA (1.5 mmol), solvent (3.0 mL), white LEDs at 40 °C for 48 h. [b]Conversion of methyl 4-bromobenzoate determined by ^{1}H-NMR using 1,3,5-trimethoxybenzene as internal standard. [c]NMR yields determined by ^{1}H-NMR using 1,3,5-trimethoxybenzene as internal standard. [d]not detected.

5.3. Ligand screening

Table S13. Ligand screening.[a]

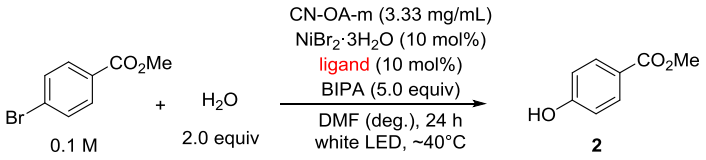

Entry	Ligand	Conversion [%][b]	2 [%][c]
1	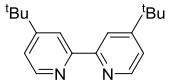	43	42
2	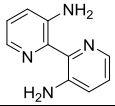	38	37

[a]Reaction conditions: methyl 4-bromobenzoate (0.3 mmol), H_2O (0.6 mmol), CN-OA-m (10 mg), $NiBr_2 \cdot 3H_2O$ (30 µmol), ligand (30 µmol), BIPA (1.5 mmol), DMF (3.0 mL), white LEDs at 40 °C for 24 h. [b]Conversion of methyl 4-bromobenzoate determined by ^{1}H-NMR using 1,3,5-trimethoxybenzene as internal standard. [c]NMR yields determined by ^{1}H-NMR using 1,3,5-trimethoxybenzene as internal standard.

5.4. Stoichiometry optimization

Table S14. Optimization of stoichiometry of water.[a]

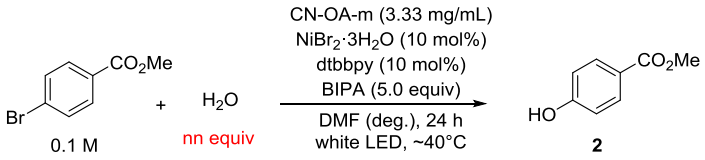

Entry	H_2O [equiv]	Conversion [%][b]	2 [%][c]
1	1	45	45
2	2	43	42
3	5	47	47
4	10	35	30
5	20	29	23

[a]Reaction conditions methyl 4-bromobenzoate (0.3 mmol), H_2O (0.3 to 6.0 mmol), CN-OA-m (10 mg), $NiBr_2 \cdot 3H_2O$ (30 µmol), dtbbpy (30 µmol), BIPA (1.5 mmol), DMF (3.0 mL), white LEDs at 40 °C for 24 h. [b]Conversion of methyl 4-bromobenzoate determined by ^{1}H-NMR using 1,3,5-trimethoxybenzene as internal standard. [c]NMR yields determined by ^{1}H-NMR using 1,3,5-trimethoxybenzene as internal standard.

6. Reaction optimization for the coupling of aryl iodides and thiols

6.1. General experimental procedure for screening experiments

An oven dried vial (19 x 100 mm) equipped with a stir bar was charged with $NiBr_2 \cdot 3H_2O$ (8.2 mg, 30 µmol, 10 mol%), dtbbpy (8.1 mg, 30 µmol, 10 mol%), the CN-OA-m (10 mg) and methyl 4-iodobenzoate (76.8 mg, 0.3 mmol, 1.0 equiv). Subsequently, MeCN (3.0 mL), BIPA (172.8 mg, 1.5 mmol, 5.0 equiv) and methyl 3-mercaptopropionate (72.1 mg, 0.6 mmol, 2.0 equiv) were added and the vial was sealed with a septum and Parafilm. The reaction mixture was sonicated for 5 - 10 min, followed by stirring for 5 min until a fine dispersion of the solids was achieved. Thereafter, the mixture was degassed by bubbling argon for 10 min. The final reaction mixture was irradiated in the low intensitiy RGB photoreactor with white light at 40 °C with rapid stirring (1400 rpm). After the respective reaction time, one equivalent of 1,3,5-trimethoxybenzene (50.5 mg, 0.3 mmol) was added. An aliquot of the reaction mixture (~200 µL) was filtered, diluted with DMSO-d_6 and subjected to ^{1}H-NMR analysis. For a representative NMR spectrum, see Figure S8.

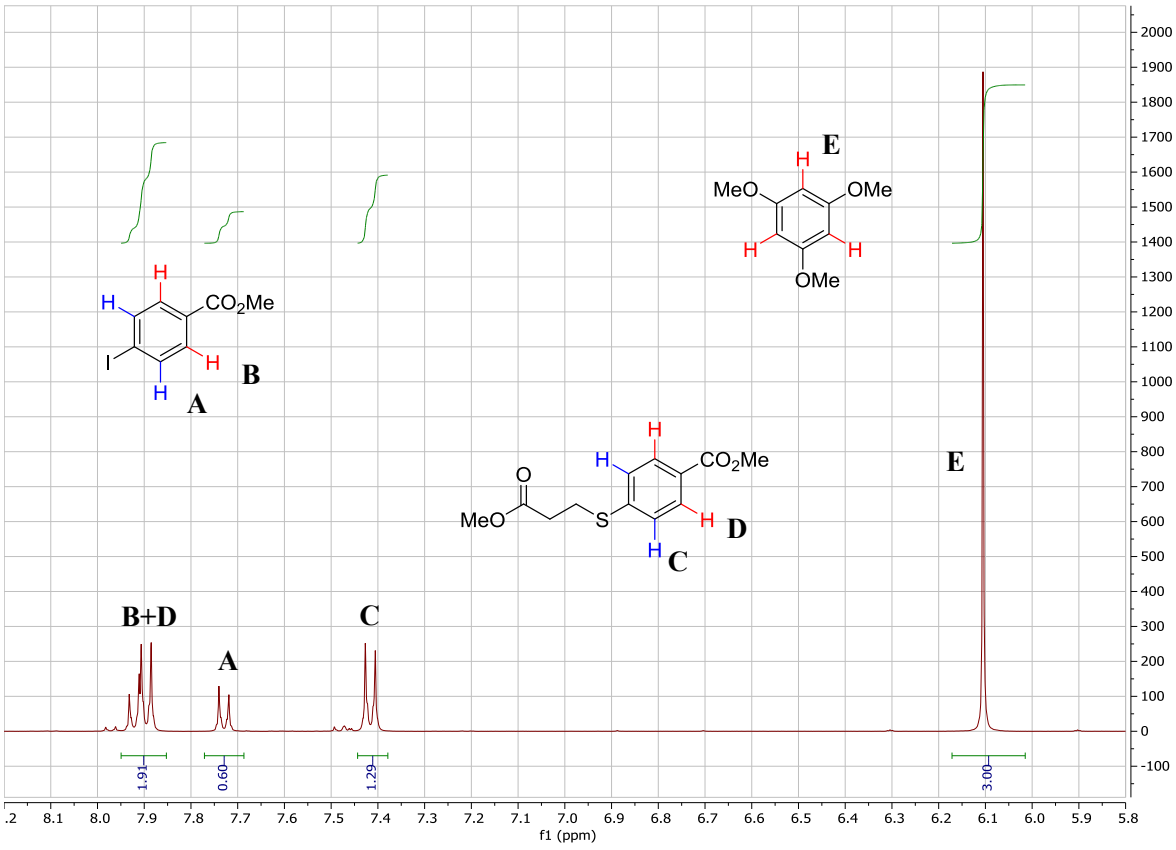

Figure S8. Example of a crude ^{1}H-NMR spectrum of the reaction between methyl 4-iodobenzoate and methyl 3-mercaptopropionate.

Table S15. Studies on the thioetherification of methyl 4-iodobenzoate and methyl 3-mercaptopropionate.[a, b]

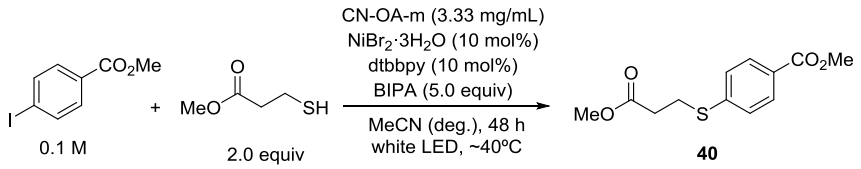

Entry	Deviation from standard conditions	Conversion [%][c]	40 [%][d]
1	None	>99	94
2	Methyl 4-bromobenzoate as substrate	5	4
3	1.0 equiv of thiol	50	46
4	Pyridine (5.0 equiv) as base	43	n.d.o.[e]
5	DBU (5.0 equiv) as base	35	n.d.[f]
6	Reaction time 24 hours	93	92
7	Reaction time 16 hours	70	65
8	No CN-OA-m	5	3
9	No $NiBr_2 \cdot 3H_2O$	13	6
10	No dtbbpy	4	n.d.
11	No BIPA	3	n.d.
12	No light	4	1
13	No degassing	79	68

[a]Reaction conditions: methyl 4-iodobenzoate (0.3 mmol), methyl 3-mercaptopropionate (0.6 mmol), CN-OA-m (10 mg), $NiBr_2 \cdot 3H_2O$ (30 µmol), dtbbpy (30 µmol), BIPA (1.5 mmol), MeCN (3.0 mL), white LEDs at 40 °C for 48 h. [b]An unidentified side product was detected in all experiments (1 to 20%). [c]Conversion of methyl 4-iodobenzoate determined by ^{1}H-NMR using 1,3,5-trimethoxybenzene as internal standard. [d]NMR yields determined by ^{1}H-NMR using 1,3,5-trimethoxybenzene as internal standard. [e]not detected because overlapping with pyridine signals. [f]not detected.

7. Recycling of CN-OA-m

An oven dried vial (19 x 100 mm) equipped with a stir bar was charged with CN-OA-m (20 mg), $NiBr_2 \cdot 3H_2O$ (32.7 mg, 120 µmol, 10 mol%), dtbbpy (32.2 mg, 120 µmol, 10 mol%) and methyl 4-bromobenzoate (258.0 mg, 1.2 mmol, 1.0 equiv). Subsequently, MeCN (6 mL), BIPA (691.3 mg, 6.0 mmol, 5.0 equiv) and methanol (64.9 mg, 2.4 mmol, 2.0 equiv) were added and the vial was sealed with a septum and Parafilm. The reaction mixture was sonicated for 5-10 min, followed by stirring for 5 min until fine dispersion of the solids was achieved. Thereafter, the mixture was degassed by bubbling argon for 10 min. The final reaction mixture was irradiated in the high intensity 440 nm photoreactor with rapid stirring. After 16 hours, one equivalent of 1,3,5-trimethoxybenzene (201.8 mg, 1.2 mmol) was added and the mixture was stirred for 5 min. The reaction mixture was centrifuged at 3500 rpm for 60 min and the liquid phase was carefully separated and analyzed by ^{1}H-NMR. The solid was washed twice with MeCN (6 mL, followed by centrifugation at 3500 rpm for 30 min and separation of the liquid phase), lyophilized (overnight) and reused in the next reaction.

Table S16. Recycling of CN-OA-m.[a]

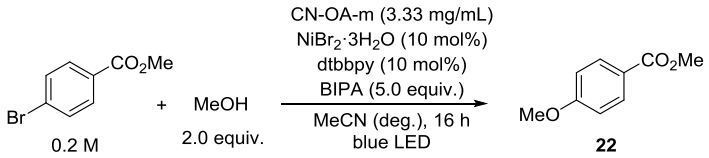

Cycle	Yield [%][b]
1	91
2	92
3	84
4	79
5	96
6	92

[a]Reaction conditions: methyl 4-bromobenzoate (1.2 mmol), methanol (2.4 mmol), CN-OA-m (20 mg), $NiBr_2 \cdot 3H_2O$ (120 µmol), dtbbpy (120 µmol), BIPA (6.0 mmol), MeCN (6.0 mL), blue LEDs for 16 h. [b]NMR yields determined by ^{1}H-NMR using 1,3,5-trimethoxybenzene as internal standard.

Figure S9. Fresh CN-OA-m (**A**) and CN-OA-m after six recycling experiments (**B**).

Measurement	Nickel concentration [mg/g]
1	217
2	214
3	219
Average	217

Table S17. ICP-OES analysis of recovered CN-OA-m after the recycling study.

8. Scope and Limitations

8.1. General procedure for the semi-heterogeneous dual nickel/photocatalytic etherification.

An oven dried vial (19 x 100 mm) equipped with a stir bar was charged with the aryl bromide (1.2 mmol, 1.0 equiv), $NiBr_2 \cdot 3H_2O$ (32.7 mg, 120 µmol, 10 mol%), dtbbpy (32.2 mg, 120 µmol, 10 mol%) and CN-OA-m (20 mg). Subsequently, MeCN (6.0 mL), BIPA (691.3 mg, 6.0 mmol, 5.0 equiv) and the alcohol (2.0 – 4.0 equiv) were added and the vial was sealed with a septum and Parafilm. The reaction mixture was sonicated for 5 - 10 min followed by stirring for 5 min until a fine dispersion of the solids was achieved. Thereafter, the mixture was degassed by bubbling argon for 10 min. The final reaction mixture was irradiated in the low intensity RGB photoreactor with white light at 40 °C with rapid stirring (1400 rpm).After the respective reaction time, an aliquot of the reaction mixture (~200 µL) was filtered, diluted with DMSO-*d*$_6$ and subjected to ^{1}H-NMR analysis. Thereafter, the NMR sample was combined with the reaction mixture, diluted with H_2O (40 mL) and extracted with ethyl acetate (3 x 40 mL). The combined organic phases were washed with aqueous NaOH (1M, 2x40 ml) and brine (40 mL), dried over Na_2SO_4 and concentrated. The product was purified by flash column chromatography (SiO_2, Hexane/EtOAc) on a Grace™ Reveleris™ system using a 12 g cartridge.

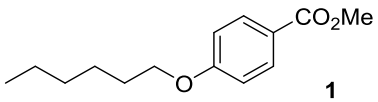

1

Methyl 4-(hexyloxy)benzoate. From methyl 4-bromobenzoate (258.0 mg, 1.2 mmol, 1.0 equiv) and 1-hexanol (245.2 mg, 2.4 mmol, 2.0 equiv). The title compound was isolated after irradiation for 48 hours in 87% yield (246.0 mg, 1.04 mmol) as colorless oil using an elution gradient of 0-4% of ethyl acetate in hexane.

^{1}H NMR (400 MHz, $CDCl_3$) δ 7.97 (d, J = 8.9 Hz, 2H), 6.89 (d, J = 8.9 Hz, 2H), 3.99 (t, J = 6.6 Hz, 2H), 3.87 (s, 3H), 1.84 – 1.74 (m, 2H), 1.51 – 1.39 (m, 2H), 1.37 – 1.28 (m, 4H), 0.97 – 0.77 (m, 3H). ^{13}C NMR (101 MHz, $CDCl_3$) δ 166.92, 162.94, 131.55, 122.26, 114.03, 68.18, 51.84, 31.56, 29.09, 25.68, 22.61, 14.05. These data are in full agreement with those previously published in the literature.[19]

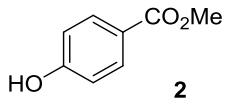

2

Methyl 4-hydroxybenzoate. From methyl 4-bromobenzoate (258.0 mg, 1.2 mmol, 1.0 equiv) and water (108.1 mg, 6.0 mmol, 5.0 equiv), using DMF as solvent. The title compound was isolated after irradiation for 120 hours in 52% yield (93.8 mg, 0.62 mmol) as white solid using an elution gradient of 0-10% of ethyl acetate in hexane.

^{1}H NMR (400 MHz, $CDCl_3$) δ 7.98 (d, J = 8.8 Hz, 2H), 6.91 (d, J = 8.8 Hz, 2H), 6.18 (s, 1H), 3.92 (s, 3H). ^{13}C NMR (101 MHz, $CDCl_3$) δ 167.35, 160.13, 131.98, 122.40, 115.28, 52.12. These data are in full agreement with those previously published in the literature.[18]

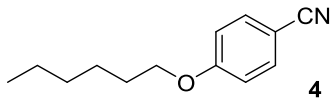

4

4-(hexyloxy)benzonitrile. From 4-bromobenzonitrile (218.4 mg, 1.2 mmol, 1.0 equiv) and 1-hexanol (245.2 mg, 2.4 mmol, 2.0 equiv). The title compound was isolated after irradiation for 48 hours in 91% yield (221.3 mg, 1.09 mmol) as colorless oil using an elution gradient of 0-4% of ethyl acetate in hexane.

^{1}H NMR (400 MHz, $CDCl_3$) δ 7.55 (d, J = 8.8 Hz, 2H), 6.92 (d, J = 8.8 Hz, 2H), 3.98 (t, J = 6.5 Hz, 2H), 1.91 – 1.67 (m, 2H), 1.52 – 1.39 (m, 2H), 1.37 – 1.30 (m, 4H), 0.94 – 0.86 (m, 3H). ^{13}C NMR (101 MHz, $CDCl_3$) δ 162.45, 133.89, 119.31, 115.16, 103.53, 68.39, 31.50, 28.94, 25.61, 22.57, 14.02. These data are in full agreement with those previously published in the literature.[20]

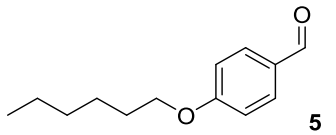

5

4-(hexyloxy)benzaldehyde. From 4-bromobenzaldehyde (222.0 mg, 1.2 mmol, 1.0 equiv) and 1-hexanol (245.2 mg, 2.4 mmol, 2.0 equiv). The title compound was isolated after irradiation for 48 hours in 83% yield (204.5 mg, 0.99 mmol) as yellowish oil using an elution gradient of 0-5% of ethyl acetate in hexane.

^{1}H NMR (600 MHz, $CDCl_3$) δ 9.82 (s, 1H), 7.76 (d, J = 8.8 Hz, 2H), 6.93 (d, J = 8.8 Hz, 2H), 3.98 (t, J = 6.5 Hz, 2H), 1.79 – 1.72 (m, 2H), 1.45 – 1.38 (m, 2H), 1.34 – 1.26 (m, 4H), 0.86 (t, J = 7.1 Hz, 3H). ^{13}C NMR (151 MHz, $CDCl_3$) δ 190.61, 164.19, 131.87, 129.70, 114.68, 68.35, 31.47, 28.97, 25.58, 22.52, 13.95. These data are in full agreement with those previously published in the literature.[21]

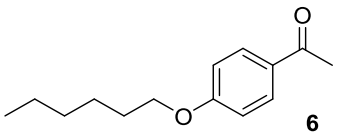

6

1-(4-(hexyloxy)phenyl)ethan-1-one. From 4-bromoacetophenone (238.9 mg, 1.2 mmol, 1.0 equiv) and 1-hexanol (245.2 mg, 2.4 mmol, 2.0 equiv). The title compound was isolated after irradiation for 48 hours in 90% yield (238.0 mg, 1.08 mmol) as colorless oil using an elution gradient of 0-4% of ethyl acetate in hexane.

^{1}H NMR (400 MHz, $CDCl_3$) δ 7.93 (d, J = 8.9 Hz, 2H), 6.93 (d, J = 8.9 Hz, 2H), 4.02 (t, J = 6.6 Hz, 2H), 2.56 (s, 3H), 1.86 – 1.76 (m, 2H), 1.54 – 1.42 (m, 2H), 1.39 – 1.32 (m, 4H), 0.96 – 0.89 (m, 3H). ^{13}C NMR (101 MHz, $CDCl_3$) δ 196.82, 163.12, 130.58, 130.05, 114.11, 68.25, 31.55, 29.07, 26.36, 25.66, 22.60, 14.05. These data are in full agreement with those previously published in the literature.[19]

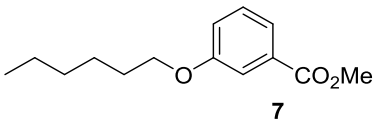

7

Methyl 3-(hexyloxy)benzoate. From methyl 3-bromobenzoate (258.0 mg, 1.2 mmol, 1.0 equiv) and 1-hexanol (245.2 mg, 2.4 mmol, 2.0 equiv). The title compound was isolated after irradiation for 168 hours in 62% yield (175.4 mg, 0.74 mmol) as colorless oil using an elution gradient of 0-5% of ethyl acetate in hexane.

^{1}H NMR (400 MHz, $CDCl_3$) δ 7.59 (d, J = 7.7 Hz, 1H), 7.53 (s, 1H), 7.29 (t, J = 7.9 Hz, 1H), 7.08 – 7.03 (m, 1H), 3.95 (t, J = 6.6 Hz, 2H), 3.87 (s, 3H), 1.80 – 1.71 (m, 2H), 1.48 – 1.39 (m, 2H), 1.35 – 1.29 (m, 4H), 0.89 (t, J = 7.0 Hz, 3H). ^{13}C NMR (101 MHz, $CDCl_3$) δ 166.92, 159.10, 131.32, 129.27, 121.70, 119.83, 114.60, 68.11, 52.03, 31.55, 29.14, 25.68, 22.59, 13.99. These data are in full agreement with those previously published in the literature.[22]

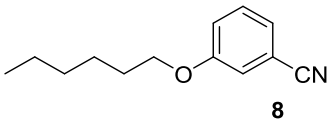

8

3-(hexyloxy)benzonitrile. From 3-bromobenzonitrile (218.4 mg, 1.2 mmol, 1.0 equiv) and 1-hexanol (245.2 mg, 2.4 mmol, 2.0 equiv). The title compound was isolated after irradiation for 120 hours in 85% yield (207.3 mg, 1.02 mmol) as colorless oil using an elution gradient of 0-5% of ethyl acetate in hexane.

^{1}H NMR (600 MHz, $CDCl_3$) δ 7.31 – 7.25 (m, 1H), 7.13 (d, J = 7.6 Hz, 1H), 7.08 – 7.03 (m, 2H), 3.89 (t, J = 6.6 Hz, 2H), 1.79 – 1.66 (m, 2H), 1.44 – 1.36 (m, 2H), 1.33 – 1.25 (m, 4H), 0.86 (t, J = 6.8 Hz,

3H). ^{13}C NMR (151 MHz, $CDCl_3$) δ 159.19, 130.23, 124.07, 119.61, 118.65, 117.34, 113.08, 68.34, 31.47, 28.95, 25.58, 22.53, 13.94. HRMS-EI (m/z) $[M^*]^+$ calcd for $C_{13}H_{17}NO$: 203.1310; found: 203.1313.

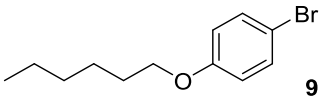

9

1-bromo-4-(hexyloxy)benzene. From 1,4-dibromobenzene (283.1 mg, 1.2 mmol, 1.0 equiv) and 1-hexanol (245.2 mg, 2.4 mmol, 2.0 equiv). The title compound was isolated after irradiation for 120 hours in 80% yield (245.9 mg, 0.96 mmol) as colorless oil using an elution gradient of 0-4% of ethyl acetate in hexane.

^{1}H NMR (600 MHz, $CDCl_3$) δ 7.36 (d, J = 8.9 Hz, 2H), 6.78 (d, J = 8.9 Hz, 2H), 3.90 (t, J = 6.6 Hz, 2H), 1.83 – 1.72 (m, 2H), 1.51 – 1.43 (m, 2H), 1.42 – 1.31 (m, 4H), 0.94 (t, J = 6.8 Hz, 3H). ^{13}C NMR (151 MHz, $CDCl_3$) δ 158.29, 132.18, 116.29, 112.55, 68.23, 31.62, 29.20, 25.73, 22.65, 14.07. These data are in full agreement with those previously published in the literature.[23]

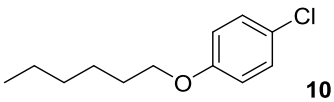

10

1-chloro-4-(hexyloxy)benzene. From 1-bromo-4-chlorobenzene (229.7 mg, 1.2 mmol, 1.0 equiv) and 1-hexanol (245.2 mg, 2.4 mmol, 2.0 equiv). The title compound was isolated after irradiation for 168 hours in 62% yield (156.5 mg, 0.74 mmol) as colorless oil using an elution gradient of 0-1% of ethyl acetate in hexane.

^{1}H NMR (600 MHz, $CDCl_3$) δ 7.21 (d, J = 8.9 Hz, 2H), 6.81 (d, J = 8.9 Hz, 2H), 3.91 (t, J = 6.6 Hz, 2H), 1.80 – 1.72 (m, 2H), 1.48 – 1.40 (m, 2H), 1.37 – 1.30 (m, 4H), 0.91 (t, J = 6.9 Hz, 3H).^{13}C NMR (151 MHz, $CDCl_3$) δ 157.75, 129.22, 125.25, 115.74, 68.31, 31.56, 29.15, 25.67, 22.58, 14.01.

These data are in full agreement with those previously published in the literature.[24]

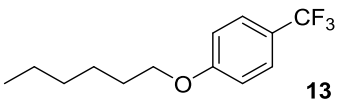

13

1-(hexyloxy)-4-(trifluoromethyl)benzene. From 4-bromobenzotrifluoride (270.0 mg, 1.2 mmol, 1.0 equiv) and 1-hexanol (245.2 mg, 2.4 mmol, 2.0 equiv). The title compound was isolated after irradiation for 48 hours in 79% yield (233.7 mg, 0.95 mmol) as colorless oil using an elution gradient of 0-1% of ethyl acetate in hexane.

^{1}H NMR (600 MHz, $CDCl_3$) δ 7.53 (d, J = 8.5 Hz, 2H), 6.94 (d, J = 8.5 Hz, 2H), 3.98 (t, J = 6.6 Hz, 2H), 1.84 – 1.76 (m, 2H), 1.51 – 1.44 (m, 2H), 1.39 – 1.32 (m, 4H), 0.92 (t, J = 6.7 Hz, 3H). ^{13}C NMR (151 MHz, $CDCl_3$) δ 161.63, 126.77 (q, J = 3.6 Hz), 124.52 (q, J = 270.9 Hz), 122.56 (q, J = 32.6 Hz), 114.38, 68.19, 31.52, 29.04, 25.64, 22.56, 13.93. ^{19}F NMR (564 MHz, $CDCl_3$) δ -61.51. These data are in full agreement with those previously published in the literature.[19]

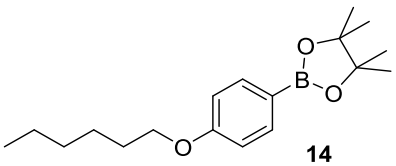

14

2-(4-(hexyloxy)phenyl)-4,4,5,5-tetramethyl-1,3,2-dioxaborolane. From 2-(4-bromophenyl)-4,4,5,5-tetramethyl-1,3,2-dioxaborolane (339.6 mg, 1.2 mmol, 1.0 equiv) and 1-hexanol (245.2 mg, 2.4 mmol, 2.0 equiv). The title compound was isolated after irradiation for 168 hours in 82% yield (298.6 mg, 0.98 mmol) as yellowish oil using an elution gradient of 0-3% of ethyl acetate in hexane.

^{1}H NMR (400 MHz, $CDCl_3$) δ 7.78 (d, J = 8.6 Hz, 2H), 6.91 (d, J = 8.6 Hz, 2H), 3.98 (t, J = 6.6 Hz, 2H), 1.84 – 1.74 (m, 2H), 1.53 – 1.42 (m, 2H), 1.41 – 1.28 (m, 16H), 0.93 (t, J = 6.9 Hz, 3H). ^{13}C NMR (101 MHz, $CDCl_3$) δ 161.78, 136.51, 120.33 (br s), 113.85, 83.47, 67.74, 31.61, 29.20, 25.73, 24.87, 22.63, 14.07. These data are in full agreement with those previously published in the literature.[25]

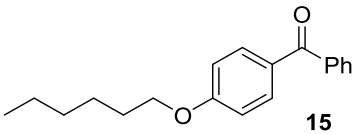

15

(4-(hexyloxy)phenyl)(phenyl)methanone. From (4-bromophenyl)(phenyl)methanone (313.3 mg, 1.2 mmol, 1.0 equiv) and 1-hexanol (245.2 mg, 2.4 mmol, 2.0 equiv). The title compound was isolated after irradiation for 48 hours in 84% yield (286.0 mg, 1.01 mmol) as white solid using an elution gradient of 0-3% of ethyl acetate in hexane.

^{1}H NMR (400 MHz, $CDCl_3$) δ 7.81 (d, J = 8.9 Hz, 2H), 7.75 (d, J = 6.9 Hz, 2H), 7.54 (t, J = 7.4 Hz, 1H), 7.45 (t, J = 7.4 Hz, 2H), 6.94 (d, J = 8.9 Hz, 2H), 4.01 (t, J = 6.5 Hz, 2H), 1.85 – 1.75 (m, 2H), 1.52 – 1.41 (m, 2H), 1.40 – 1.29 (m, 4H), 0.97 – 0.88 (m, 3H). ^{13}C NMR (101 MHz, $CDCl_3$) δ 195.42, 162.87, 138.32, 132.55, 131.84, 129.81, 129.70, 128.17, 114.00, 68.25, 31.58, 29.10, 25.70, 22.63, 14.10. These data are in full agreement with those previously published in the literature.[26]

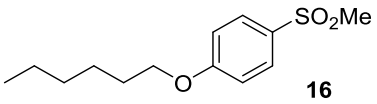

16

1-(hexyloxy)-4-(methylsulfonyl)benzene. From 1-bromo-4-(methylsulfonyl)benzene (282.1 mg, 1.2 mmol, 1.0 equiv) and 1-hexanol (245.2 mg, 2.4 mmol, 2.0 equiv). The title compound was isolated after irradiation for 120 hours in 81% yield (247.4 mg, 0.97 mmol) as white solid using an elution gradient of 0-15% of ethyl acetate in hexane.

^{1}H NMR (600 MHz, $CDCl_3$) δ 7.82 (d, J = 8.8 Hz, 2H), 6.97 (d, J = 8.8 Hz, 2H), 3.99 (t, J = 6.5 Hz, 2H), 2.99 (s, 3H), 1.81 – 1.73 (m, 2H), 1.47 – 1.40 (m, 2H), 1.35 – 1.28 (m, 4H), 0.88 (t, J = 7.0 Hz, 3H). ^{13}C NMR (151 MHz, $CDCl_3$) δ 163.28, 131.93, 129.46, 114.89, 68.55, 44.83, 31.45, 28.91, 25.56, 22.52, 13.97. These data are in full agreement with those previously published in the literature.[19]

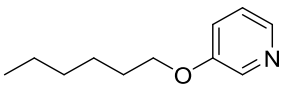

17

3-(hexyloxy)pyridine. From 3-bromopyridine (189.6 mg, 1.2 mmol, 1.0 equiv) and 1-hexanol (245.2 mg, 2.4 mmol, 2.0 equiv). The title compound was isolated after irradiation for 168 hours in 39% yield (84.2 mg, 0.47 mmol) as yellowish oil using an elution gradient of 0-3% of ethyl acetate in hexane.

^{1}H NMR (400 MHz, $CDCl_3$) δ 8.31 (d, J = 2.6, 1.0 Hz, 1H), 8.21 (dd, J = 4.3, 1.8 Hz, 1H), 7.24 – 7.15 (m, 2H), 4.00 (t, J = 6.5 Hz, 2H), 1.89 – 1.73 (m, 2H), 1.54 – 1.42 (m, 2H), 1.41 – 1.30 (m, 4H), 0.92 (t, J = 7.0 Hz, 3H). ^{13}C NMR (101 MHz, $CDCl_3$) δ 155.25, 141.88, 138.04, 123.79, 120.98, 68.30, 31.55, 29.13, 25.64, 22.60, 14.05. HRMS (ESI) m/z calcd for $C_{11}H_{18}NO$ [$(M+H)^+$] 180.1388, found 180.1385.

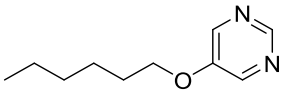

18

5-(hexyloxy)pyrimidine. From 3-bromopyrimidine (190.8 mg, 1.2 mmol, 1.0 equiv) and 1-hexanol (245.2 mg, 2.4 mmol, 2.0 equiv). The title compound was isolated after irradiation for 168 hours in 55% yield (118.6 mg, 0.66 mmol) as yellowish oil using an elution gradient of 0-10% of ethyl acetate in hexane.

^{1}H NMR (400 MHz, $CDCl_3$) δ 8.74 (s, 1H), 8.31 (s, 2H), 3.97 (t, J = 6.5 Hz, 2H), 1.78 – 1.67 (m, 2H), 1.44 – 1.33 (m, 2H), 1.31 – 1.20 (m, 4H), 0.82 (t, J = 6.6 Hz, 3H). ^{13}C NMR (101 MHz, $CDCl_3$) δ 153.02, 151.20, 143.45, 68.66, 31.37, 28.89, 25.41, 22.46, 13.91. These data are in full agreement with those previously published in the literature.[19]

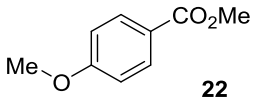

22

Methyl 4-methoxybenzoate. From methyl 4-bromobenzoate (258.0 mg, 1.2 mmol, 1.0 equiv) and methanol (76.9 mg, 2.4 mmol, 2.0 equiv). The title compound was isolated after irradiation for 24 hours in 80% yield (160.1 mg, 0.96 mmol) as white solid using an elution gradient of 0-5% of ethyl acetate in hexane. The reaction can also be carried out in methanol as solvent resulting in 78 % (156.2 mg, 0.94 mmol) of the title compound after 8 hours irradiation.

^{1}H NMR (400 MHz, $CDCl_3$) δ 7.95 (d, J = 8.8 Hz, 2H), 6.87 (d, J = 8.8 Hz, 2H), 3.84 (s, 3H), 3.79 (s, 3H). ^{13}C NMR (101 MHz, $CDCl_3$) δ 166.78, 163.29, 131.53, 122.52, 113.54, 55.32, 51.77. These data are in full agreement with those previously published in the literature.[27]

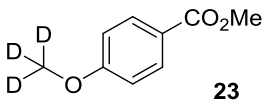

23

Methyl 4-methoxybenzoate-*d*$_3$. From methyl 4-bromobenzoate (258.0 mg, 1.2 mmol, 1.0 equiv) and methanol-*d*$_4$ (84.14 mg, 2.4 mmol, 2.0 equiv). The title compound was isolated after irradiation for 24 hours in 92% yield (185.4 mg, 1.10 mmol) as white solid using an elution gradient of 0-4% of ethyl acetate in hexane.

^{1}H NMR (600 MHz, $CDCl_3$) δ 7.93 (d, J = 9.0 Hz, 2H), 6.85 (d, J = 9.0 Hz, 2H), 3.82 (s, 3H). ^{13}C NMR (151 MHz, $CDCl_3$) δ 166.73, 163.29, 131.50, 122.51, 113.52, 54.47 (hept, J = 21.9 Hz), 51.70. HRMS-EI (m/z) $[M^*]^+$ calcd for $C_9H_7D_3O_3$: 169.0818; found: 169.0816. These data are in full agreement with those previously published in the literature.[28]

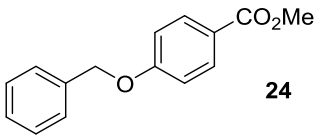

24

Methyl 4-(benzyloxy)benzoate. From methyl 4-bromobenzoate (258.0 mg, 1.2 mmol, 1.0 equiv) and benzyl alcohol (259.5 mg, 2.4 mmol, 2.0 equiv). The title compound was isolated after irradiation for 48 hours in 92% yield (267.4 mg, 1.10 mmol) as white solid using an elution gradient of 0-5% of ethyl acetate in hexane.

^{1}H NMR (400 MHz, $CDCl_3$) δ 8.01 (d, J = 8.9 Hz, 2H), 7.46 – 7.32 (m, 5H), 7.00 (d, J = 8.9 Hz, 2H), 5.12 (s, 2H), 3.89 (s, 3H). ^{13}C NMR (101 MHz, $CDCl_3$) δ 166.83, 162.48, 136.24, 131.62, 128.69, 128.22, 127.51, 122.82, 114.46, 70.08, 51.89. These data are in full agreement with those previously published in the literature.[29]

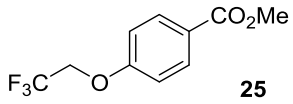

25

Methyl 4-(2,2,2-trifluoroethoxy)benzoate. From methyl 4-bromobenzoate (258.0 mg, 1.2 mmol, 1.0 equiv) and 2,2,2-trifluoroethanol (480.19 mg, 4.8 mmol, 4.0 equiv). The title compound was isolated after irradiation for 96 hours in 86% yield (240.4 mg, 1.03 mmol) as white solid using an elution gradient of 0-15% of ethyl acetate in hexane.

^{1}H NMR (600 MHz, $CDCl_3$) δ 7.98 (d, J = 8.6 Hz, 2H), 6.92 (d, J = 8.6 Hz, 2H), 4.37 (q, J = 8.0 Hz, 2H), 3.86 (s, 3H). ^{13}C NMR (151 MHz, $CDCl_3$) δ 166.35, 160.68, 131.69, 124.41, 123.08 (q, J = 278.3 Hz), 114.30, 65.44 (q, J = 36.3 Hz), 51.88. ^{19}F NMR (564 MHz, $CDCl_3$) δ -74.01. These data are in full agreement with those previously published in the literature.[30]

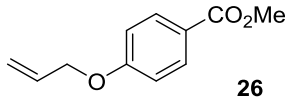

26

Methyl 4-(allyloxy)benzoate. From methyl 4-bromobenzoate (258.0 mg, 1.2 mmol, 1.0 equiv) and allyl alcohol (139.4 mg, 2.4 mmol, 2.0 equiv). The title compound was isolated after irradiation for 72 hours in 83% yield (192.1 mg, 1.00 mmol) as colorless oil using an elution gradient of 0-3% of ethyl acetate in hexane.

^{1}H NMR (400 MHz, $CDCl_3$) δ 7.95 (d, J = 8.9 Hz, 2H), 6.88 (d, J = 8.9 Hz, 2H), 6.06 – 5.93 (m, 1H), 5.38 (d, J = 17.1 Hz, 1H), 5.27 (d, J = 10.6 Hz, 1H), 4.53 (d, J = 5.3 Hz, 2H), 3.84 (s, 3H). ^{13}C NMR (101 MHz, $CDCl_3$) δ 166.72, 162.28, 132.55, 131.52, 122.64, 118.00, 114.25, 68.76, 51.78. These data are in full agreement with those previously published in the literature.[31]

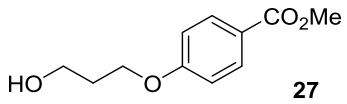

27

Methyl 4-(3-hydroxypropoxy)benzoate. From methyl 4-bromobenzoate (258.0 mg, 1.2 mmol, 1.0 equiv) and 1,3-propandiole (365.3 mg, 4.8 mmol, 4.0 equiv). The title compound was isolated after irradiation for 24 hours in 74% yield (186.5 mg, 0.89 mmol) as colorless oil using an elution gradient of 0-35% of ethyl acetate in hexane.

^{1}H NMR (400 MHz, $CDCl_3$) δ 7.97 (d, J = 8.8 Hz, 2H), 6.91 (d, J = 8.8 Hz, 2H), 4.16 (t, J = 6.1 Hz, 2H), 3.91 – 3.82 (m, 5H), 2.24 – 2.19 (m, 1H), 2.10 – 2.02 (m, 2H).^{13}C NMR (101 MHz, $CDCl_3$) δ 166.98, 162.64, 131.61, 122.53, 114.06, 65.43, 59.77, 51.94, 31.88. HRMS-EI (m/z) $[M^*]^+$ calcd for $C_{11}H_{14}O_4$: 210.0892; found: 210.0883.

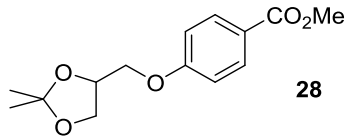

28

methyl 4-((2,2-dimethyl-1,3-dioxolan-4-yl)methoxy)benzoate. From methyl 4-bromobenzoate (258.0 mg, 1.2 mmol, 1.0 equiv) and 1,2-isopropylideneglycerol (317.2 mg, 2.4 mmol, 2.0 equiv). The title compound was isolated after irradiation for 48 hours in 88% yield (279.8 mg, 1.05 mmol) as reddish solid using an elution gradient of 0-15% of ethyl acetate in hexane.

^{1}H NMR (400 MHz, $CDCl_3$) δ 7.98 (d, J = 9.0 Hz, 2H), 6.93 (d, J = 9.0 Hz, 2H), 4.49 (p, J = 5.8 Hz, 1H), 4.20 – 3.88 (m, 4H), 3.88 (s, 3H), 1.46 (s, 3H), 1.40 (s, 3H).^{13}C NMR (101 MHz, $CDCl_3$) δ 166.76, 162.22, 131.59, 123.02, 114.11, 109.90, 73.81, 68.79, 66.68, 51.91, 26.77, 25.32. HRMS-EI (m/z) $[M^*]^+$ calcd for $C_{14}H_{18}O_5$: 266.1154; found: 266.1152.

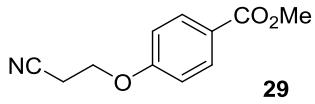

29

Methyl 4-(2-cyanoethoxy)benzoate. From methyl 4-bromobenzoate (258.0 mg, 1.2 mmol, 1.0 equiv) and 3-hydroxypropanenitrile (341.2 mg, 4.8 mmol, 4.0 equiv). The title compound was isolated after irradiation for 72 hours in 76% yield (187.1 mg, 0.91 mmol) as white solid using an elution gradient of 0-2% of ethyl acetate in hexane.

^{1}H NMR (400 MHz, $CDCl_3$) δ 7.97 (d, J = 8.5 Hz, 2H), 6.89 (d, J = 8.5 Hz, 2H), 4.20 (t, J = 6.3 Hz, 2H), 3.86 (s, 3H), 2.84 (t, J = 6.2 Hz, 2H). ^{13}C NMR (101 MHz, $CDCl_3$) δ 166.57, 161.31, 131.67, 123.61, 117.05, 114.14, 62.63, 51.97, 18.55. HRMS-EI (m/z) $[M^*]^+$ calcd for $C_{11}H_{11}NO_3$: 205.0739; found: 205.0746.

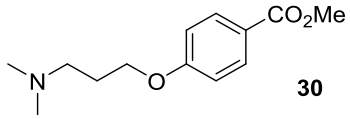

30

Methyl 4-(3-(dimethylamino)propoxy)benzoate. From methyl 4-bromobenzoate (258.0 mg, 1.2 mmol, 1.0 equiv) and *N,N'*-dimethyl-3-hydroxypropylamine (247.6 mg, 2.4 mmol, 2.0 equiv). The title compound was isolated after irradiation for 48 hours in 79% yield (224.3 mg, 0.95 mmol) as yellowish wax using an elution gradient of 0-15% of methanol in dichloromethane.

^{1}H NMR (400 MHz, $CDCl_3$) δ 7.95 (d, J = 8.9 Hz, 2H), 6.88 (d, J = 8.9 Hz, 2H), 4.04 (t, J = 6.4 Hz, 2H), 3.85 (s, 3H), 2.46 (m, 2H), 2.25 (s, 6H), 1.96 (m, 2H).^{13}C NMR (101 MHz, $CDCl_3$) δ 166.85, 162.76, 131.53, 122.38, 114.04, 66.26, 56.13, 51.82, 45.36, 27.22. HRMS-EI (m/z) $[M^*]^+$ calcd for $C_{13}H_{19}NO_3$: 237.1365; found: 237.1358.

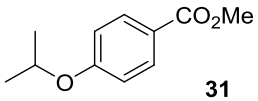

31

Methyl 4-isopropoxybenzoate. From methyl 4-bromobenzoate (258.0 mg, 1.2 mmol, 1.0 equiv) and isopropyl alcohol (288.5 mg, 4.8 mmol, 4.0 equiv). The title compound was isolated after irradiation for 120 hours in 84% yield (196.8 mg, 1.01 mmol) as colorless oil using an elution gradient of 0-3% of ethyl acetate in hexane.

^{1}H NMR (400 MHz, $CDCl_3$) δ 7.93 (d, J = 8.0 Hz, 2H), 6.84 (d, J = 8.0 Hz, 2H), 4.63 – 4.50 (m, 1H), 3.83 (s, 3H), 1.30 (d, J = 6.2 Hz, 6H). ^{13}C NMR (101 MHz, $CDCl_3$) δ 166.78, 161.77, 131.55, 122.03, 114.93, 69.89, 51.69, 21.82. HRMS-EI (m/z) $[M^*]^+$ calcd for $C_{11}H_{14}O_3$: 194.0943; found: 194.0939.

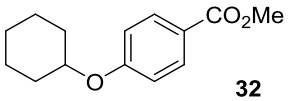

32

Methyl 4-(cyclohexyloxy)benzoate. From methyl 4-bromobenzoate (258.0 mg, 1.2 mmol, 1.0 equiv) and cyclohexanol (480.8 mg, 4.8 mmol, 4.0 equiv). The title compound was isolated after irradiation for 120 hours in 82% yield (230.2 mg, 0.98 mmol) as white solid using an elution gradient of 0-4% of ethyl acetate in hexane.

^{1}H NMR (400 MHz, $CDCl_3$) δ 7.97 (d, J = 8.9 Hz, 2H), 6.89 (d, J = 8.9 Hz, 2H), 4.37 – 4.28 (m, 1H), 3.87 (s, 3H), 2.03 – 1.93 (m, 2H), 1.85 – 1.74 (m, 2H), 1.63 – 1.48 (m, 3H), 1.45 – 1.24 (m, 3H). ^{13}C NMR (101 MHz, $CDCl_3$) δ 166.89, 161.74, 131.58, 122.01, 115.08, 75.30, 51.79, 31.58, 25.51, 23.64. These data are in full agreement with those previously published in the literature.[32]

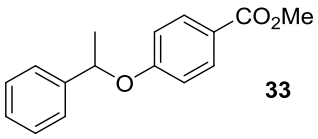

33

Methyl 4-(1-phenylethoxy)benzoate. From methyl 4-bromobenzoate (258.0 mg, 1.2 mmol, 1.0 equiv) and 1-phenylethanol (586.4 mg, 4.8 mmol, 4.0 equiv). The title compound was isolated after irradiation for 72 hours in 86% yield (264.8 mg, 1.03 mmol) as white solid using an elution gradient of 0-4% of ethyl acetate in hexane.

^{1}H NMR (400 MHz, $CDCl_3$) δ 7.94 (d, J = 8.9 Hz, 2H), 7.41 – 7.34 (m, 4H), 7.32 – 7.26 (m, 1H, contains residual solvent signal of $CDCl_3$), 6.91 (d, J = 8.9 Hz, 2H), 5.41 (q, J = 6.4 Hz, 1H), 3.87 (s, 3H), 1.69 (d, J = 6.5 Hz, 3H). ^{13}C NMR (101 MHz, $CDCl_3$) δ 166.85, 161.78, 142.47, 131.49, 128.79, 127.73, 125.49, 122.43, 115.41, 76.17, 51.85, 24.49. HRMS-EI (m/z) $[M^*]^+$ calcd for $C_{16}H_{16}O_3$: 256.1099; found: 256.1091.

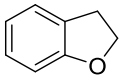

37

2,3-dihydrobenzofurane.

From 2-(2-bromophenyl)ethanol (120.6 mg, 0.6 mmol, 1.0 equiv). The title compound was isolated after irradiation for 168 hours in 47% yield (33.4 mg, 0.28 mmol) as colorless oil using an elution gradient of 0-1% of diethyl ether in pentane.

^{1}H NMR (400 MHz, $CDCl_3$) δ 7.23 (d, J = 6.5 Hz, 1H), 7.14 (t, J = 7.7 Hz, 1H), 6.88 (t, J = 7.0 Hz, 1H), 6.83 (d, J = 8.0 Hz, 1H), 4.59 (t, J = 8.7 Hz, 2H), 3.24 (t, J = 8.7 Hz, 2H). ^{13}C NMR (101 MHz, $CDCl_3$) δ 160.00, 127.95, 126.89, 124.94, 120.35, 109.38, 71.05, 29.76. These data are in full agreement with those previously published in the literature.[33]

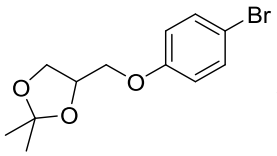

38

4-((4-bromophenoxy)methyl)-2,2-dimethyl-1,3-dioxolane. From 1,4-dibromobenzene (283.1 mg, 1.2 mmol, 1.0 equiv) and 1,2-isopropylideneglycerol (634.4 mg, 4.8 mmol, 4.0 equiv). The title compound was isolated after irradiation for 120 hours in 61% yield (209.6 mg, 0.73 mmol) as white solid using an elution gradient of 0-10% of ethyl acetate in hexane.

^{1}H NMR (400 MHz, $CDCl_3$) δ 7.36 (d, J = 8.7 Hz, 2H), 6.78 (d, J = 8.7 Hz, 2H), 4.45 (p, J = 5.9 Hz, 1H), 4.18 – 3.85 (m, 4H), 1.45 (s, 3H), 1.39 (s, 3H). ^{13}C NMR (101 MHz, $CDCl_3$) δ 157.66, 132.27, 116.32, 113.29, 109.83, 73.88, 68.98, 66.70, 26.78, 25.34. These data are in full agreement with those previously published in the literature.[34]

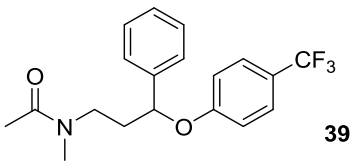

39

N-methyl-N-(3-phenyl-3-(4-(trifluoromethyl)phenoxy)propyl)acetamide. From 4-bromobenzotrifluoride (270.0 mg, 1.2 mmol, 1.0 equiv) and N-(3-hydroxy-3-phenylpropyl)-N-methylacetamide (994.9 mg, 4.8 mmol, 4.0 equiv). After irradiation for 168 hours and ^{1}H NMR analysis, the NMR sample and the reaction mixture were combined, diluted with H_2O (40 mL) and extracted with ethyl acetate (3 x 40 mL). The combined organic phases were washed with brine (40 mL), dried over Na_2SO_4 and concentrated. The title compound was isolated in 66% yield (277.8 mg, 0.79 mmol) as colorless oil using an elution gradient of 0-5% of ethyl acetate in DCM.

^{1}H NMR (600 MHz, $CDCl_3$) rotameric mixture δ 7.42 – 7.36 (m, 2H), 7.34 – 7.27 (m, 4H, contains residual solvent signal of $CDCl_3$), 7.26 – 7.19 (m, 1H), 6.91 – 6.83 (m, 2H), 5.23 – 5.10 (m, 1H), 3.61 – 3.38 (m, 2H), 2.94 – 2.87 (m, 3H), 2.22 – 2.04 (m, 2H), 2.02 – 1.96 (m, 3H). ^{13}C NMR (151 MHz, $CDCl_3$) rotameric mixture, resonances for minor rotamer are enclosed in parenthesis δ 170.61 (170.51), 160.33 (159.94), 140.65 (139.99), (129.00) 128.76, (128.19) 127.89, (126.86 (q, J = 3.7 Hz)) 126.73 (q, J = 3.6 Hz), 125.72 (125.5), 124.36 (q, J = 271.1 Hz) (124.26 (q, J = 271.3 Hz)), 123.14 (q, 32.6 Hz) (122.76 (q, J = 32.6 Hz)), 115.72 (115.64), 78.39 (minor rotamer overlapping with residual solvent signal), (47.03) 44.89, (37.31) 36.50, 36.30 (33.11), 21.84 (20.99). ^{19}F NMR (564 MHz, $CDCl_3$) rotameric mixture, resonances for minor rotamer are enclosed in parenthesis δ -61.53 (-61.61). These data are in full agreement with those previously published in the literature.[35]

8.2. General procedure for the semi-heterogeneous dual nickel/photocatalytic thioetherification.

An oven dried vial (19 x 100 mm) equipped with a stir bar was charged with methyl 4-iodobenzoate (314.4 mg, 1.2 mmol, 1.0 equiv), $NiBr_2 \cdot 3H_2O$ (32.7 mg, 120 µmol, 10 mol%), dtbbpy (32.2 mg, 120 µmol, 10 mol%) and CN-OA-m (20 mg). Subsequently, MeCN (6.0 mL), BIPA (691.3 mg, 6.0 mmol, 5.0 equiv) and the thiol (2.4 mmol, 2.0 equiv) were added and the vial was sealed with a septum and Parafilm. The reaction mixture was sonicated for 5 - 10 min, followed by stirring for 5 min until a fine dispersion of the solids was achieved. Thereafter, the mixture was degassed by bubbling argon for 10 min. The final reaction mixture was irradiated in the low intensity RGB photoreactor with white light at 40 °C with rapid stirring (1400 rpm).After the respective reaction time, an aliquot of the reaction mixture (~200 µL) was filtered, diluted with DMSO-d_6 and subjected to ^{1}H-NMR analysis. Thereafter, the NMR sample was combined with the reaction mixture, diluted with H_2O (40 mL) and extracted with ethyl acetate (3 x 40 mL). The combined organic phases were washed with aqueous NaOH (1M, 2x40 ml) and brine (40 mL), dried over Na_2SO_4 and concentrated. The product was purified by flash column chromatography (SiO_2, Hexane/EtOAc) on a Grace™ Reveleris™ system using a 12 g cartridge.

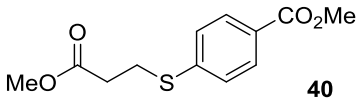

40

Methyl 4-((3-methoxy-3-oxopropyl)thio)benzoate. From methyl 4-iodobenzoate (314.4 mg, 1.2 mmol, 1.0 equiv) and methyl 3-mercaptopropionate (288.4 mg, 2.4 mmol, 2.0 equiv). The title compound was isolated after irradiation for 48 hours in 79% yield (242.1 mg, 0.95 mmol) as white solid using an elution gradient of 0-5% of ethyl acetate in hexane.

^{1}H NMR (400 MHz, $CDCl_3$) δ 7.93 (d, J = 8.6 Hz, 2H), 7.31 (d, J = 8.6 Hz, 2H), 3.89 (s, 3H), 3.69 (s, 3H), 3.25 (t, J = 7.4 Hz, 2H), 2.68 (t, J = 7.4 Hz, 2H). ^{13}C NMR (101 MHz, $CDCl_3$) δ 171.90, 166.67, 142.61, 130.07, 127.24, 126.99, 52.12, 51.99, 33.68, 27.21. HRMS-EI (m/z) $[M^*]^+$ calcd for $C_{12}H_{14}O_4S$: 254.0613; found: 254.0605.

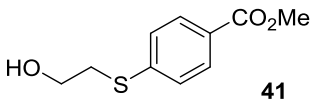

41

Methyl 4-((2-hydroxyethyl)thio)benzoate. From methyl 4-iodobenzoate (314.4 mg, 1.2 mmol, 1.0 equiv) and 2-mercaptoethanol (187.5 mg, 2.4 mmol, 2.0 equiv). The title compound was isolated after irradiation for 48 hours in 60% yield (152.9 mg, 0.72 mmol) as white solid using an elution gradient of 0-25% of ethyl acetate in hexane.

^{1}H NMR (400 MHz, $CDCl_3$) δ 7.91 (d, J = 7.9 Hz, 2H), 7.33 (d, J = 7.9 Hz, 2H), 3.90 (s, 3H), 3.83 (m, 2H), 3.19 (t, J = 6.2 Hz, 2H), 2.66 – 2.56 (m, 1H). ^{13}C NMR (101 MHz, $CDCl_3$) δ 166.83, 142.69, 130.05, 127.15, 127.06, 60.46, 52.20, 35.20. These data are in full agreement with those previously published in the literature.[36]

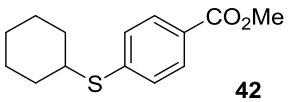

42

Methyl 4-(cyclohexylthio)benzoate. From methyl 4-iodobenzoate (314.4 mg, 1.2 mmol, 1.0 equiv) and cyclohexanethiol (278.9 mg, 2.4 mmol, 2.0 equiv). The title compound was isolated after irradiation for 96 hours in 53% yield (157.8 mg, 0.63 mmol) as colorless oil using an elution gradient of 0-5% of ethyl acetate in hexane.

^{1}H NMR (400 MHz, $CDCl_3$) δ 7.92 (d, J = 8.1 Hz, 2H), 7.34 (d, J = 8.1 Hz, 2H), 3.90 (s, 3H), 3.36 – 3.21 (m, 1H), 2.12 – 1.96 (m, 2H), 1.86 – 1.72 (m, 2H), 1.68 – 1.58 (m, 1H), 1.51 – 1.19 (m, 5H). ^{13}C NMR (101 MHz, $CDCl_3$) δ 166.80, 143.08, 129.88, 128.37, 127.03, 52.06, 44.96, 33.07, 25.95, 25.70.
These data are in full agreement with those previously published in the literature.[37]

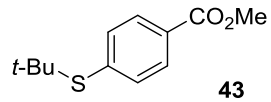

43

Methyl 4-(tert-butylthio)benzoate. From methyl 4-iodobenzoate (314.4 mg, 1.2 mmol, 1.0 equiv) and 2-methylpropanethiol (216.4 mg, 2.4 mmol, 2.0 equiv). The title compound was isolated after irradiation for 96 hours in 43% yield (117.3 mg, 0.52 mmol) as colorless oil using an elution gradient of 0-2% of ethyl acetate in hexane.

^{1}H NMR (400 MHz, $CDCl_3$) δ 7.98 (d, J = 8.5 Hz, 2H), 7.59 (d, J = 8.5 Hz, 2H), 3.92 (s, 3H), 1.31 (s, 9H). ^{13}C NMR (101 MHz, $CDCl_3$) δ 166.72, 138.96, 136.83, 130.05, 129.45, 52.23, 46.74, 31.06. These data are in full agreement with those previously published in the literature.[37]

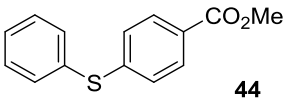

44

Methyl 4-(phenylthio)benzoate. From methyl 4-iodobenzoate (314.4 mg, 1.2 mmol, 1.0 equiv) and thiophenol (264.4 mg, 2.4 mmol, 2.0 equiv). The title compound was isolated after irradiation for 144 hours in 33% yield (98.4 mg, 0.40 mmol) as white solid using an elution gradient of 0-5% of ethyl acetate in hexane.

^{1}H NMR (400 MHz, $CDCl_3$) δ 7.92 (d, J = 8.6 Hz, 2H), 7.55 – 7.48 (m, 2H), 7.45 – 7.36 (m, 3H), 7.23 (d, J = 8.6 Hz, 2H), 3.91 (s, 3H). ^{13}C NMR (101 MHz, $CDCl_3$) δ 166.72, 144.46, 133.77, 132.31, 130.12, 129.69, 128.72, 127.52, 127.43, 52.14. These data are in full agreement with those previously published in the literature.[38]

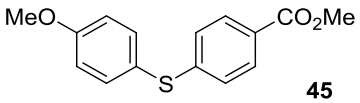

45

Methyl 4-((4-methoxyphenyl)thio)benzoate. From methyl 4-iodobenzoate (314.4 mg, 1.2 mmol, 1.0 equiv) and 4-methoxybenzenethiol (336.5 mg, 2.4 mmol, 2.0 equiv). The title compound was isolated after irradiation for 168 hours in 41% yield (134.2 mg, 0.49 mmol) as white solid using an elution gradient of 0-4% of ethyl acetate in hexane.

^{1}H NMR (400 MHz, $CDCl_3$) δ 7.88 (d, J = 8.6 Hz, 2H), 7.49 (d, J = 8.8 Hz, 2H), 7.10 (d, J = 8.6 Hz, 2H), 6.97 (d, J = 8.8 Hz, 2H), 3.89 (s, 3H), 3.87 (s, 3H). ^{13}C NMR (101 MHz, $CDCl_3$) δ 166.81, 160.61, 146.45, 136.81, 129.97, 126.67, 125.76, 121.52, 115.35, 55.43, 52.06. These data are in full agreement with those previously published in the literature.[39]

9. References

(1) Brown, H. C.; Kanth, J. V. B.; Dalvi, P. V.; Zaidlewicz, M. *J. Org. Chem.* **1999,** *64*, 6263-6274.
(2) Hapke, M.; Staats, H.; Wallmann, I.; Lützen, A. *Synthesis* **2007,** *2007*, 2711-2719.
(3) Kiehne, U.; Bunzen, J.; Staats, H.; Lützen, A. *Synthesis* **2007,** *2007*, 1061-1069.
(4) Yu, P.; Morandi, B. *Angew. Chem., Int. Ed.* **2017,** *56*, 15693-15697.
(5) Wang, J.; Zhao, J.; Gong, H. *Chem. Comm.* **2017,** *53*, 10180-10183.
(6) Maegawa, T.; Kitamura, Y.; Sako, S.; Udzu, T.; Sakurai, A.; Tanaka, A.; Kobayashi, Y.; Endo, K.; Bora, U.; Kurita, T.; Kozaki, A.; Monguchi, Y.; Sajiki, H. *Chem. Eur. J.* **2007,** *13*, 5937-5943.
(7) Viana, H.; Carreiro, E. P.; Goth, A.; Bacalhau, P.; Caldeira, A. T.; Martins, M. d. R.; Burke, A. J. *RSC Adv.* **2016,** *6*, 63214-63223.
(8) Davies, S. G.; Fletcher, A. M.; Houlsby, I. T. T.; Roberts, P. M.; Thomson, J. E.; Zimmer, D. *J. Nat. Prod.* **2018,** *81*, 2731-2742.
(9) Liu, D.; Gao, W.; Wang, C.; Zhang, X. *Angew. Chem., Int. Ed.* **2005,** *44*, 1687-1689.
(10) Zhang, G.; Li, G.; Lan, Z.-A.; Lin, L.; Savateev, A.; Heil, T.; Zafeiratos, S.; Wang, X.; Antonietti, M. *Angew. Chem., Int. Ed.* **2017,** *129*, 13630-13634.
(11) Sigma-Aldrich. https://www.sigmaaldrich.com (Germany, May 25th, 2019).
(12) https://www.bauhaus.info/led-baender/tween-light-led-band/p/22517610?gclid=EAIaIQobChMIoLWto9zl3wIVTZSyCh3YDweqEAQYASABEgJmRfD_BwE&s_kwcid=AL!5677!3!190027496787!!!g!462716337331!&pla_prpaid=462716337331&ef_id=EAIaIQobChMIoLWto9zl3wIVTZSyCh3YDweqEAQYASABEgJmRfD_BwE:G:s&pla_adgrid=41635814775&pla_campid=225980581&pla_prch=online&pla_prid=22517610&cid=PSEGoo225980581_41635814775&pla_adt=pla (Germany, May 25th, 2019).
(13) Kessil Photoredox. https://www.kessil.com/photoredox/Products.php (Germany, May 25th, 2019).
(14) Goettmann, F.; Fischer, A.; Antonietti, M.; Thomas, A. *Angew. Chem., Int. Ed.* **2006,** *45*, 4467-4471.
(15) Shalom, M.; Guttentag, M.; Fettkenhauer, C.; Inal, S.; Neher, D.; Llobet, A.; Antonietti, M. *Chem. Mat.* **2014,** *26*, 5812-5818.
(16) Zhang, J.; Sun, J.; Maeda, K.; Domen, K.; Liu, P.; Antonietti, M.; Fu, X.; Wang, X. *Energy Environ. Sci.* **2011,** *4*, 675-678.
(17) Savateev, A.; Pronkin, S.; Epping, J. D.; Willinger, M. G.; Wolff, C.; Neher, D.; Antonietti, M.; Dontsova, D. *ChemCatChem* **2017,** *9*, 167-174.
(18) Yang, L.; Huang, Z.; Li, G.; Zhang, W.; Cao, R.; Wang, C.; Xiao, J.; Xue, D. *Angew. Chem., Int. Ed.* **2018,** *57*, 1968-1972.
(19) Terrett, J. A.; Cuthbertson, J. D.; Shurtleff, V. W.; MacMillan, D. W. C. *Nature* **2015,** *524*, 330 - 334.
(20) Dang, H.; Cox, N.; Lalic, G. *Angew. Chem., Int. Ed.* **2014,** *53*, 752-756.
(21) Eggers, K.; Fyles, T. M.; Montoya-Pelaez, P. J. *J. Org. Chem.* **2001,** *66*, 2966-2977.
(22) Schoeder, C. T.; Meyer, A.; Mahardhika, A. B.; Thimm, D.; Blaschke, T.; Funke, M.; Müller, C. E. *ACS Omega* **2019,** *4*, 4276-4295.
(23) Song, G.-L.; Zhang, Z.; Da, Y.-X.; Wang, X.-C. *Tetrahedron* **2015,** *71*, 8823-8829.
(24) Kim, J.; Lee, D.-H.; Kalutharage, N.; Yi, C. S. *ACS Catal.* **2014,** *4*, 3881-3885.
(25) Bushby, R. J.; Fisher, J.; Lozman, O. R.; Lange, S.; Lydon, J. E.; McLaren, S. R. *Liquid Crystals* **2006,** *33*, 653-664.
(26) Kawakami, Y.; Sakai, Y.; Okada, A. *Polym. J.* **1990,** *22*, 705.
(27) Lee, Y. H.; Morandi, B. *Nat. Chem.* **2018,** *10*, 1016-1022.
(28) Tzirakis, M. D.; Orfanopoulos, M. *J. Am. Chem. Soc.* **2009,** *131*, 4063-4069.
(29) Kuwano, R.; Kusano, H. *Org. Lett.* **2008,** *10*, 1979-1982.
(30) Pethő, B.; Zwillinger, M.; Csenki, J. T.; Káncz, A. E.; Krámos, B.; Müller, J.; Balogh, G. T.; Novák, Z. *Chem. Eur. J.* **2017,** *23*, 15628-15632.
(31) Scheepstra, M.; Andrei, S. A.; Unver, M. Y.; Hirsch, A. K. H.; Leysen, S.; Ottmann, C.; Brunsveld, L.; Milroy, L.-G. *Angew. Chem., Int. Ed.* **2017,** *56*, 5480-5484.
(32) Mao, R.; Balon, J.; Hu, X. *Angew. Chem., Int. Ed.* **2018,** *57*, 13624-13628.
(33) Alshakova, I. D.; Gabidullin, B.; Nikonov, G. I. *ChemCatChem* **2018,** *10*, 4860-4869.
(34) Kölbel, M.; Beyersdorff, T.; Tschierske, C.; Diele, S.; Kain, J. *Chem. Eur. J.* **2000,** *6*, 3821-3837.
(35) Calow, A. D. J.; Fernández, E.; Whiting, A. *Org. Biomol. Chem.* **2014,** *12*, 6121-6127.
(36) Yoshida, S.; Sugimura, Y.; Hazama, Y.; Nishiyama, Y.; Yano, T.; Shimizu, S.; Hosoya, T. *Chem. Comm.* **2015,** *51*, 16613-16616.
(37) Jin, Y.; Yang, H.; Fu, H. *Chem. Comm.* **2016,** *52*, 12909-12912.
(38) Liu, C.; Szostak, M. *Chem. Comm.* **2018,** *54*, 2130-2133.
(39) Liu, D.; Ma, H.-X.; Fang, P.; Mei, T.-S. *Angew. Chem., Int. Ed.* **2019,** *58*, 5033-5037.

Copies of NMR spectra of isolated compounds

Copies of NMR spectra of isolated compounds are available in the Supporting Information through the website of the Publisher. https://doi.org/10.1021/acs.orglett.9b01957

Supporting Information - Chapter 9

Visible Light-Mediated Oxidative Debenzylation Enables the Use of Benzyl Ethers as Temporary Protecting Groups

Cavedon, C.; Sletten, E. T.; **Madani, A.;** Niemeyer, O.; Seeberger, P. H.; Pieber, B. *Org. Lett.* **2021**, *23*, 514-518.

https://doi.org/10.1021/acs.orglett.0c04026

Visible Light-Mediated Oxidative Debenzylation Enables the Use of Benzyl Ethers as Temporary Protecting Groups

Cristian Cavedon,[†] [‡] Eric T. Sletten,[†] Amiera Madani,[†] [‡] Olaf Niemeyer,[†] Peter H. Seeberger,[†] [‡*] and Bartholomäus Pieber[† *]

[†]Department of Biomolecular Systems, Max Planck Institute of Colloids and Interfaces, Am Mühlenberg 1, 14476 Potsdam, Germany

[‡]Department of Chemistry and Biochemistry, Freie Universität Berlin, Arnimallee 22, 14195 Berlin, Germany

Correspondence to: peter.seeberger@mpikg.mpg.de
bartholomaeus.pieber@mpikg.mpg.de

Table of Contents

1. General remarks

Reagents, and solvents were purchased from commercial suppliers and used without further purification. LED lamps for photocatalytic experiments were purchased from Kessil Lightning.[1] ^{1}H-, ^{13}C-, and ^{19}F spectra were recorded on a Varian 400 spectrometer (400 MHz, Agilent), a Ascend™ 400 spectrometer (400 MHz, cryoprobe, Bruker) and a Varian 600 spectrometer (600 MHz, Agilent) at 298 K, and are reported in ppm relative to the residual solvent peaks. Peaks are reported as: s = singlet, d = doublet, t = triplet, q = quartet, m = multiplet or unresolved, with coupling constants in Hz. Analytical thin layer chromatography (TLC) was performed on pre-coated TLC-sheets, ALUGRAM Xtra SIL G/UV$_{254}$ sheets (Macherey-Nagel) and visualized with 254 nm light or staining solutions followed by heating. Purification of final compounds was carried out by flash chromatography using Silica 60 M (0.04-0.063 mm) silica gel (Sigmal Aldrich). UV/Vis spectra were recorded using a UV-1900 spectrometer (Shimadzu). High-resolution mass spectral data were obtained using a Waters XEVO G2-XS 4K spectrometer with the XEVO G2-XS QTOF capability kit (ESI).

2. Preparation of starting materials

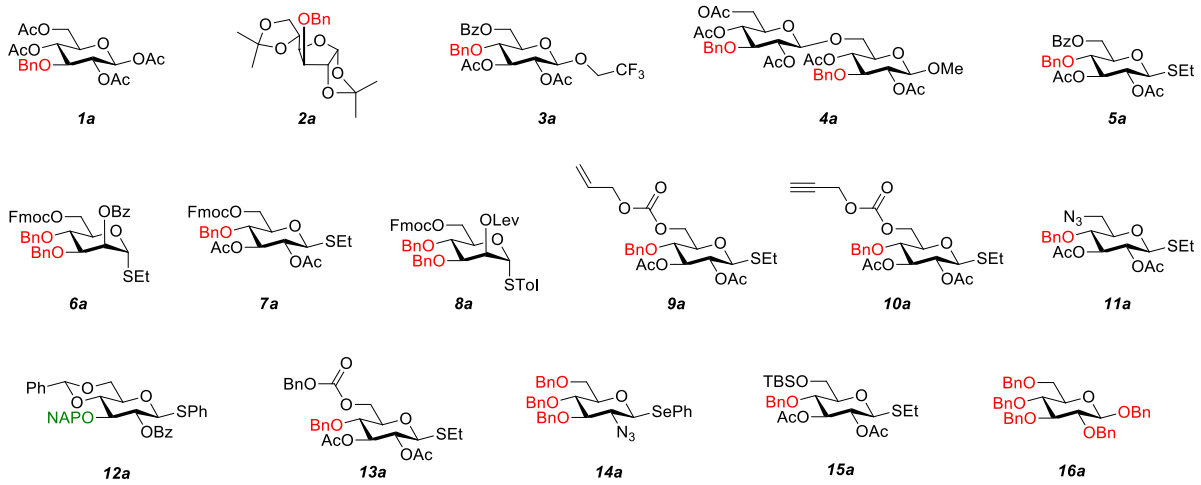

Figure S1: Overview of starting materials.

8a, ***12a*** and ***14a*** are commercially available and were used without further purification.

2a,[2] ***6a***,[3] and ***16a***[4] were prepared according to procedures reported in literature.

5a, ***7a***, ***9a***, ***10a***, ***11a***, ***13a*** and ***15a*** were prepared from a common intermediate ***21***.

Preparation of starting material *1a*

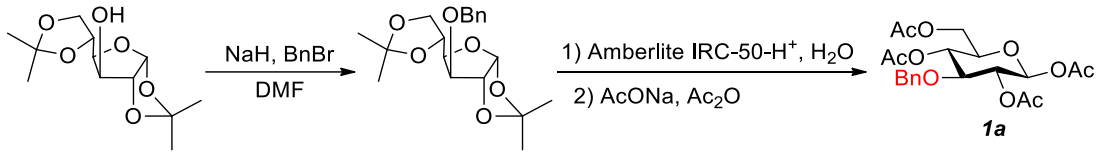

Acetyl 2,4,6-tri-*O*-acetyl-3-*O*-benzyl-β-D-glucopyranose (*1a*): Sodium hydride (3.20 g of a 60% suspension in oil, 80.0 mmol) was added slowly at 0 °C under an argon atmosphere to a suspension of 1,2:5,6-di-*O*-isopropylidene-α-D-glucofuranose (10.40 g, 40.0 mmol) in anhydrous *N*,*N*-dimethylformamide (35 mL). Then benzyl bromide (9.50 mL, 80 mmol) was added slowly and the resulting solution was stirred at room temperature for 2 h. Methanol (10 mL) was added and after 10 min the solution was poured into a mixture of ice and water (100 g) and extracted with diethyl ether (2×100 mL + 2x50 mL). The extract was washed with water (2x100 mL), dried (Na_2SO_4) and concentrated to dryness. Amberlite IRC-50-H^+ (circa 15 g after swelling) was added to a solution of the residue in water (200 mL) before stirring at 70 °C (oil bath) for 4 hours. The resin was filtered off and the solution was concentrated in vacuum and freeze-dried. A solution of the residues (9.12 g) and anhydrous sodium acetate (1.50 g, 18.3 mmol) in acetic anhydride (17.0 mL, 180 mmol) was heated at 110 °C (oil bath) for 5 h and then poured into a mixture of ice and water. The aqueous phase was extracted with ether (3×100 mL) and the extract was washed with water (2x50 mL), dried (Na_2SO_4) and concentrated under vacuum. The residue was purified by flash column chromatography (30% ethyl acetate/hexane) and crystallized from hexane/diethyl ether to obtain the title compound (10.91 g, 24.9 mmol, 62%) as a white solid.

^{1}H NMR (400 MHz, $CDCl_3$) δ 7.36 – 7.27 (m, 3H), 7.23 (d, J = 6.4 Hz, 2H), 5.64 (d, J = 8.2 Hz, 1H), 5.20 – 5.12 (m, 2H), 4.61 (s, 2H), 4.26 – 4.06 (m, 2H), 3.77 – 3.70 (m, 2H), 2.10 (s, 3H), 2.08 (s, 3H), 1.99 – 1.95 (m, 6H). ^{13}C NMR (101 MHz, $CDCl_3$) δ 170.8, 169.3, 169.3, 169.2, 137.5, 128.5, 128.0, 127.9, 92.0, 80.0, 74.2, 73.0, 71.5, 69.0, 61.8, 20.9, 20.8, 20.8, 20.8. HRMS (ESI) m/z: $[M + Na]^+$ Calcd for $C_{21}H_{26}NaO_{10}$ 461.1424; Found 461.1417.

These data are in full agreement with those previously published in the literature.[5]

Preparation of starting material *4a*

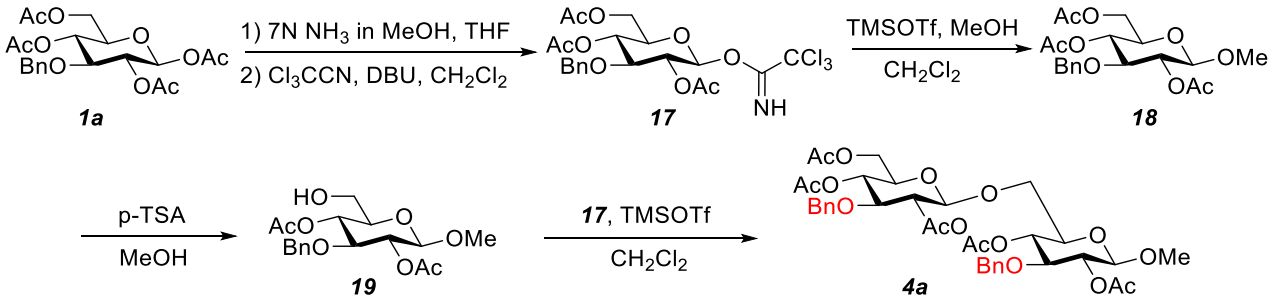

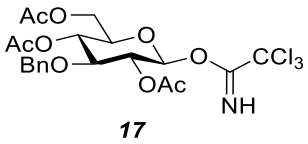

2,4,6-tri-*O*-acetyl-3-*O*-benzyl-β-D-glucopyranosyl trichloroacetimidate (*17*):

Under argon, an oven dried 1000 mL round bottom flask was charged with ***1a*** (10.7 g, 24.4 mmol, 1 equiv), dissolved in THF (750 mL), and sealed with a glass stopper. Slowly, 7N NH_3 in MeOH (30 mL, 15 equiv) was added and the mixture was stirred at room temperature. After each hour, 30 mL 7N NH_3 in MeOH were added until starting material disappeared. After 4 h reaction was complete by TLC (30% ethyl acetate/hexane). Three mL of toluene were added and a stream of air was blown over the surface of the reaction while stirring to remove the ammonia. Once removal of the ammonia was complete, reaction was placed on rotary evaporator and under a slight pressure the remaining ammonia was removed for 10 min. The pressure was slightly increased to remove the THF and then increased to concentrate the reaction to completion.

Residue was dissolved in CH_2Cl_2 (0.1 M, 252 mL) and at 0 °C, DBU (1.92 mL, 12.626 mmol, 0.5 equiv) and trichloroacetonitrile (25.25 mL, 252.5 mmol, 10 equiv) were added. After 3 h of stirring at 0 °C, reaction was complete (TLC-30% ethyl acetate/hexane). The reaction was concentrated and purified by a silica gel chromatography with eluent containing 1% triethylamine to produce ***17*** as an oil (10.2 g, 18.78 mmol, 77%).

^{1}H NMR (400 MHz, $CDCl_3$) δ 8.63 (s, 1H), 7.34 – 7.26 (m, 3H), 7.25 – 7.21 (m, 2H), 6.50 (d, *J* = 3.6 Hz, 1H), 5.18 (t, *J* = 9.8 Hz, 1H), 5.06 (dd, *J* = 10.0, 3.6 Hz, 1H), 4.74 – 4.57 (m, 2H), 4.18 (dd, *J* = 12.7, 4.8 Hz, 1H), 4.11 – 4.00 (m, 3H), 2.04 (s, 3H), 1.96 (s, 3H), 1.96 (s, 3H). ^{13}C NMR (101 MHz, $CDCl_3$) δ 170.9, 169.9, 169.5, 160.8, 137.9, 128.6, 128.0, 127.9, 93.5, 91.0, 76.6, 75.0, 72.2, 70.7, 68.9, 61.8, 20.9, 20.9, 20.7. HRMS (ESI) m/z: $[M + Na]^+$ Calcd for $C_{21}H_{24}Cl_3NNaO_9$ 562.0409; Found 562.0417.

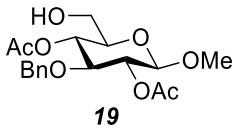

19

Methyl 2,4-di-*O*-acetyl-3-*O*-benzyl-β-D-glucopyranosyl (*19*):

Into an oven dried 250 mL round bottom flask containing ***17*** (3 g, 5.5 mmol, 1 equiv) anhydrous CH_2Cl_2 (0.1 M, 55.5 mL) was added under argon. MeOH (0.67 mL, 16.7 mmol, 3 equiv) was then added and the reaction was cooled to 0 °C. Slowly, TMSOTf (0.1 mL, 0.55 mmol, 0.1 equiv) was added. After stirring at 0 °C for 2 h reaction starting material was consumed (TLC-40% ethyl acetate/hexane). Reaction mixture was quenched with triethylamine, concentrated, and purified by column chromatography to produce ***18*** as a colorless oil (1.6 g, 3.9 mmol, 70%)

In a 250 mL round bottom flask with ***18*** (1.5 g, 3.65 mmol, 1 equiv), MeOH (0.1 M, 36.5 mL) and *p*TSA (695 mg, 3.65 mmol, 1 equiv) were added. Reaction was stirred at room temperature overnight. Upon consumption of the starting material (TLC-40% ethyl acetate/hexane), reaction was concentrated, redissolved in ethyl acetate, and washed with water. Organic phase was then separated, dried with $NaSO_4$, and concentrated. Purification by column chromatography gave ***19*** as a white solid (537 mg, 1.46 mmol, 40%).

^{1}H NMR (400 MHz, $CDCl_3$) δ 7.37 – 7.26 (m, 3H), 7.24 (d, *J* = 6.7 Hz, 2H), 5.07 – 4.97 (m, 2H), 4.62 (s, 2H), 4.37 (d, *J* = 7.9 Hz, 1H), 3.77 – 3.68 (m, 2H), 3.60 (dd, *J* = 12.6, 5.0 Hz, 1H), 3.50 (s, 3H), 3.44 – 3.35 (m, 1H), 2.36 (dd, *J* = 9.2, 5.1 Hz, 1H), 2.01 (d, *J* = 1.9 Hz, 6H). ^{13}C NMR (101 MHz, $CDCl_3$) δ 170.5, 169.5, 138.0, 128.6, 128.0, 127.9, 101.9, 80.1, 74.4, 74.1, 72.6, 70.4, 61.6, 57.0, 21.1, 21.0. HRMS (ESI) m/z: $[M + Na]^+$ Calcd for $C_{18}H_{24}NaO_8$ 391.1363; Found 391.1362.

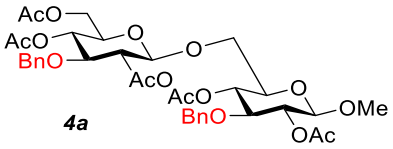

4a

Methyl 2,4,6-tri-*O*-acetyl-3-*O*-benzyl-β-D-glucopyranosyl-(1→6)-2,4,6-tri-*O*-acetyl-3-*O*-benzyl-β-D-glucopyranoside (*4a*):

Into an oven dried 250 mL round bottom flask containing glycosyl acceptor ***19*** (0.6 g, 1.5 mmol, 1 equiv) glycosyl donor ***17*** (0.8 g, 1.6 mmol, 1.1 equiv) was added in anhydrous CH_2Cl_2 (0.1 M, 15 mL) under argon. Reaction was then cooled to 0 °C. Slowly, TMSOTf (0.03 mL, 0.15 mmol, 0.1 equiv) was added. After stirring at 0 °C for 2 h the starting material was consumed (TLC-10% ethyl acetate/CH_2Cl_2). Reaction mixture was quenched with triethylamine, concentrated, and purified by column chromatography to produce ***4a*** as a colorless oil (0.75 g, 1.0 mmol 68%)

^{1}H NMR (400 MHz, $CDCl_3$) δ 7.35 – 7.27 (m, 6H), 7.21 (d, J = 6.2 Hz, 4H), 5.10 (t, J = 9.6 Hz, 1H), 5.07 – 4.95 (m, 2H), 4.87 (t, J = 9.4 Hz, 1H), 4.58 (s, 4H), 4.47 (d, J = 8.0 Hz, 1H), 4.28 (d, J = 8.0 Hz, 1H), 4.25 – 4.19 (m, 1H), 4.08 (dd, J = 12.3, 2.3 Hz, 1H), 3.82 (d, J = 9.2 Hz, 1H), 3.67 (dt, J = 9.4, 4.7 Hz, 2H), 3.62 – 3.51 (m, 3H), 3.47 (s, 3H), 2.08 (s, 3H), 2.01 (s, 3H), 1.98 (s, 9H). ^{13}C NMR (101 MHz, $CDCl_3$) δ 170.9, 169.9, 169.5, 169.5, 169.3, 137.9, 137.8, 128.6, 128.0, 128.0, 128.0, 127.9, 101.8, 101.2, 80.2, 80.1, 77.4, 74.2, 74.1, 73.8, 72.6, 72.5, 72.3, 70.6, 69.6, 68.8, 62.2, 57.0, 21.1, 21.0, 21.0, 20.9, 20.9. HRMS (ESI) m/z: $[M + Na]^+$ Calcd for $C_{37}H_{46}NaO_{16}$ 769.2678; Found 769.2704.

Preparation of common intermediate *21*

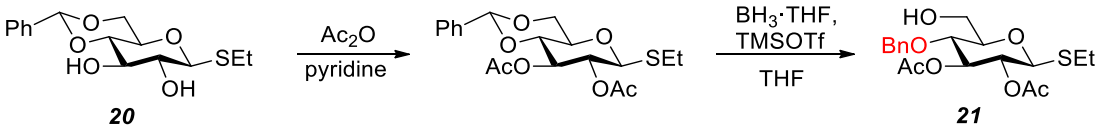

Ethyl 2,3-di-*O*-acetyl-4-*O*-benzyl-β-D-thioglucopyranose (*21*):

To diol ***20*** (8 g, 25.6 mmol, 1 equiv) in a 500 mL round bottom flask, acetic anhydride (24.1 mL, 256 mmol, 10 equiv) and pyridine (80 mL) were added. Reaction stirred overnight at room temperature and monitored for completion by TLC (50% ethyl acetate/hexanes). Upon completion reaction was co-evaporated with toluene (3x200 mL). To the residue (5 g, 12.6 mmol, 1 equiv) anhydrous THF (60 mL) was added under argon and the reaction was cooled to 0 °C. After 30 min, a BH_3 in THF solution (1 M, 25 mL, 25.3 mmol, 2 equiv) followed by TMSOTf (1.25 mL, 12.6 mmol, 1 eqiuv.) were added. Reaction was then slowly warmed up room temperature after 1 h. Upon completion after 3 h (TLC- 20% ethyl acetate/hexanes), reaction was transferred to an Erlenmeyer flask (1000 mL), diluted with 500 mL CH_2Cl_2, and neutralized with $NaHCO_3$ (250 mL). Biphasic mixture was separated in a separatory funnel, dried with $NaSO_4$, concentrated, and purified by column chromatography to produce ***21*** as a colorless oil (3.5 g, 8.82 mmol, 70%).

^{1}H NMR (400 MHz, $CDCl_3$) δ 7.35 – 7.23 (m, 5H), 5.24 (t, *J* = 9.4 Hz, 1H), 4.89 (t, *J* = 9.7 Hz, 1H), 4.62 (q, *J* = 11.4 Hz, 2H), 4.50 (d, *J* = 10.0 Hz, 1H), 3.90 (dd, *J* = 12.3, 2.4 Hz, 1H), 3.75 – 3.66 (m, 2H), 3.46 – 3.40 (m, 1H), 2.78 – 2.58 (m, 2H), 2.28 (s, 1H), 2.03 (s, 3H), 1.92 (s, 3H), 1.24 (t, *J* = 7.5 Hz, 3H). ^{13}C NMR (101 MHz, $CDCl_3$) δ 170.1, 169.8, 137.5, 128.5, 128.0, 128.0, 83.3, 79.5, 75.8, 75.3, 74.8, 70.6, 61.4, 24.3, 20.8, 20.8, 14.9. HRMS (ESI) m/z: $[M + Na]^+$ Calcd for $C_{19}H_{26}NaO_7S$ 421.1291; found 421.1276.

Preparation of starting material *5a*

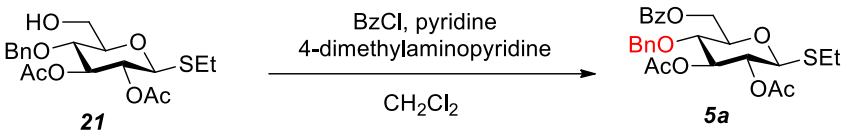

Ethyl 2,3-di-*O*-acetyl-4-*O*-benzyl-6-*O*-benzoyl-β-D-thioglucopyranose (*5a*):

Into a 100 mL round bottom flask with ***21*** (0.8 g, 2 mmol, 1 equiv), CH_2Cl_2 (14 mL) was added followed by pyridine (1.4 mL, 10 mmol, 5 equiv), benzoyl chloride (0.75 mL, 3.5 mmol, 1.75 equiv), and 4-dimethylaminopyridine (16 mg, 0.13 mmol) at 0 °C. Reaction warmed to room temperature and stirred for 2 h while monitoring for completion by TLC (30% ethyl acetate/hexanes). Reaction was then concentrated with toluene and purified by column chromatography to produce ***5a*** as a colorless solid (893 mg, 1.8 mmol, 89%).

^{1}H NMR (400 MHz, $CDCl_3$) δ 8.03 (d, *J* = 7.0 Hz, 2H), 7.59 (t, *J* = 7.5 Hz, 1H), 7.47 (t, *J* = 7.7 Hz, 2H), 7.32 – 7.23 (m, 2H), 7.24 – 7.17 (m, 3H), 5.32 (t, *J* = 8.7 Hz, 1H), 4.98 (t, *J* = 9.7 Hz, 1H), 4.63 – 4.55 (m, 3H), 4.53 (d, *J* = 10.0 Hz, 1H), 4.46 (dd, *J* = 12.1, 3.8 Hz, 1H), 3.82 – 3.66 (m, 2H), 2.79 – 2.52 (m, 2H), 2.07 (s, 3H), 1.99 (s, 3H), 1.23 (t, *J* = 7.4 Hz, 3H). ^{13}C NMR (101 MHz, $CDCl_3$) δ 170.2, 170.0, 166.2, 137.1, 133.4, 129.8, 129.8, 128.7, 128.6, 128.3, 128.2, 83.4, 77.4, 77.3, 76.2, 75.8, 75.0, 70.6, 63.3, 24.4, 21.0, 21.0, 15.1. HRMS (ESI) m/z: $[M + Na]^+$ Calcd for $C_{26}H_{30}NaO_8S$ 525.1553; Found 525.1553.

Preparation of starting material *3a*

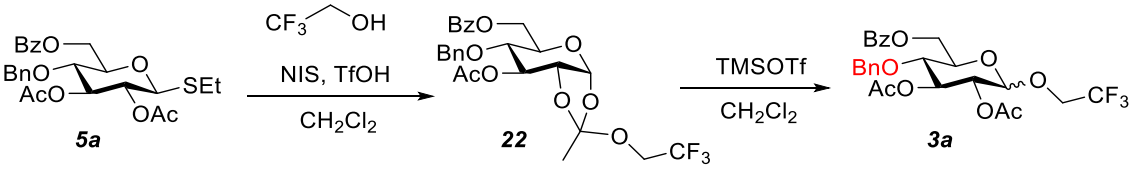

2,2,2-Trifluoroethyl 2,3-di-*O*-acetyl-4-*O*-benzyl-6-*O*-benzoyl-D-glucopyranose (*3a*):

Under an argon atmosphere, CH_2Cl_2 (7 mL) was added in an oven dried flask containing ***5a*** (300.0 mg, 0.75 mmol, 1 equiv), trifluoroethanol (0.11 mL, 1.5 mmol, 2 equiv), and molecular sieves (4 Å, 100 mg/mL). The resulting solution was cooled to 0 ºC and *N*-iodosuccinimide (219 mg, 1.5 mmol, 1.3 equiv) was added. After 30 mins, triflic acid (6 µL, 0.075 mmol, 0.1 equiv) was added slowly. After stirring the resulting solution overnight TLC (30% ethyl acetate/hexanes), the reaction was diluted with CH_2Cl_2 and washed with 10% sodium thiosulfate solution followed by $NaHCO_3$ solution. Combined organic layers were dried over Na_2SO_4 and concentrated under vacuum. The residue was purified by flash column chromatography (30% ethyl acetate/hexane) to obtain orthoester ***22*** as a white solid. Orthoester ***22*** (150 mg, 0.28 mmol, 1 equiv) was then rearranged by subjecting it to TMSOTf (0.01 mL, 0.07 mmol, 0.25 equiv) in CH_2Cl_2 (10 mL) under argon for 1 h (TLC-30% ethyl acetate/hexanes). Reaction was diluted with CH_2Cl_2 and washed with $NaHCO_3$ saturated solution. Organic layer was collected, dried with $NaSO_4$, concentrated, and purified by column chromatography to produce ***3a*** as a colorless solid (120 mg, 0.22 mmol, 80%, α/β 8:92).

Characterization for ***3a*-β**: ^{1}H NMR (400 MHz, $CDCl_3$) δ 8.03 (d, J = 6.9 Hz, 2H), 7.61 (t, J = 7.4 Hz, 1H), 7.49 (d, J = 7.9 Hz, 2H), 7.33 – 7.19 (m, 5H), 5.34 – 5.27 (m, 1H), 4.97 (dd, J = 9.7, 7.9 Hz, 1H), 4.69 – 4.55 (m, 5H), 4.49 (dd, J = 12.2, 4.0 Hz, 1H), 4.16 – 4.03 (m, 1H), 3.99 – 3.87 (m, 1H), 3.84 – 3.69 (m, 2H), 2.06 (s, 3H), 2.00 (s, 3H). ^{13}C NMR (101 MHz, $CDCl_3$) δ 170.1, 170.0, 166.2, 137.0, 133.5, 129.8, 129.7, 128.8, 128.7, 128.4, 128.2, 100.9, 75.5, 75.1, 74.6, 73.6, 71.5, 65.8, 62.7, 21.0, 20.7. ^{19}F NMR (564 MHz, $CDCl_3$) δ -74.46 (t, J = 8.5 Hz). HRMS (ESI) m/z: $[M + Na]^+$ Calcd for $C_{26}H_{27}F_3NaO_9$ 563.1999; Found 563.1511.

Preparation of starting material *7a*

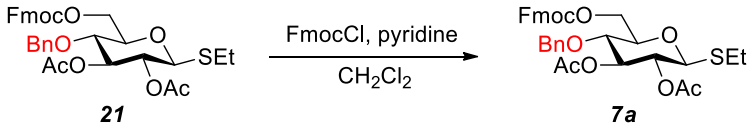

Ethyl 2,3-di-*O*-acetyl-4-*O*-benzyl-6-*O*-(9-fluorenylmethoxycarbonyl)-β-D-thioglucopyranose (*7a*): Under an argon atmosphere, dichloromethane (6 mL) was added in a flask containing ***21*** (300.0 mg, 0.75 mmol). The resulting solution was cooled to 0 ºC and pyridine (300 µL, 3.76 mmol) and Fmoc-Cl (340.4 mg, 1.31 mmol) were added. After stirring the resulting solution overnight, the reaction was quenched by adding water (40 mL) and extracted with dichloromethane (3x40 mL). Combined organic layers were washed with brine (50 mL), dried over Na_2SO_4 and concentrated under vacuum. The residue was purified by flash column chromatography (20% ethyl acetate/hexane) to obtain the title compound (419.8 mg, 0.68 mmol, 90%) as a white solid.

^{1}H NMR (400 MHz, $CDCl_3$) δ 7.78 (d, *J* = 7.6 Hz, 2H), 7.63 (t, *J* = 6.2 Hz, 2H), 7.42 (t, *J* = 7.6 Hz, 2H), 7.36 – 7.29 (m, 5H), 7.28 – 7.24 (m, 2H, contains residual solvent peak), 5.29 (t, *J* = 9.1 Hz, 1H), 4.98 (t, *J* = 9.7 Hz, 1H), 4.64 – 4.56 (m, 2H, 4.53 – 4.44 (m, 2H), 4.41 (m, 2H), 4.32 – 4.23 (m, 2H), 3.75 – 3.61 (m, 2H), 2.77 – 2.60 (m, 2H), 2.07 (s, 3H), 1.98 (s, 3H), 1.25 (t, *J* = 7.5 Hz, 3H). ^{13}C NMR (101 MHz, $CDCl_3$) δ 170.1, 169.9, 155.0, 143.5, 143.3, 141.4, 137.2, 128.7, 128.3, 128.2, 128.1, 127.3, 127.3, 125.3, 125.3, 120.2, 83.4, 77.0, 76.1, 75.7, 75.0, 70.5, 70.1, 66.3, 46.8, 24.4, 21.0, 20.9, 15.1. HRMS (ESI) m/z: $[M + NH_4]^+$ Calcd for $C_{34}H_{40}NO_9S$ 638.2424; Found 638.2449.

Preparation of starting material *9a*

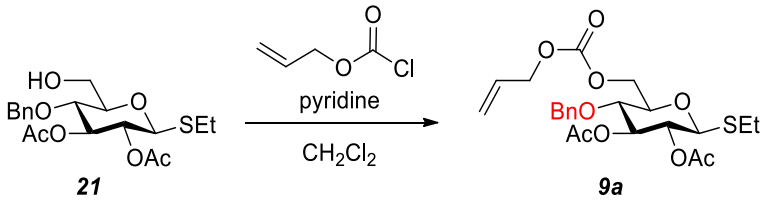

Ethyl 2,3-di-*O*-acetyl-4-*O*-benzyl-6-*O*-allyloxycarbonyl-β-D-thioglucopyranose (*9a*):

Into a 100 mL round bottom flask with ***21*** (0.3 g, 0.75 mmol, 1 equiv), CH_2Cl_2 (5 mL) was added followed by pyridine (0.5 mL, 3.8 mmol, 5 equiv) and allyl chloroformate (0.14 mL, 1.3 mmol, 1.75 equiv) at room temperature. Reaction was stirred overnight and monitored for completion by TLC (30% ethyl acetate/hexanes). Reaction was then concentrated with toluene and purified by column chromatography to produce ***9a*** as a colorless solid (315 mg, 0.65 mmol, 86%).

^{1}H NMR (400 MHz, $CDCl_3$) δ 7.37 – 7.22 (m, 5H), 5.99 – 5.87 (m, 1H), 5.41 – 5.34 (m, 1H), 5.31 – 5.23 (m, 2H), 4.93 (t, *J* = 10.2 Hz, 1H), 4.65 – 4.58 (m, 4H), 4.50 – 4.41 (m, 2H), 4.26 (dd, *J* = 11.7, 4.8 Hz, 1H), 3.72 – 3.57 (m, 2H), 2.77 – 2.59 (m, 2H), 2.05 (s, 3H), 1.96 (s, 3H), 1.24 (t, *J* = 7.5 Hz, 3H). ^{13}C NMR (101 MHz, $CDCl_3$) δ 170.2, 169.9, 154.8, 137.2, 128.7, 128.3, 128.2, 119.3, 83.4, 77.0, 76.1, 75.6, 75.0, 70.5, 68.8, 66.2, 24.3, 21.0, 20.9, 15.0. HRMS (ESI) m/z: $[M + Na]^+$ Calcd for $C_{23}H_{30}NaO_9S$ 505.1503; Found 505.1500.

Preparation of starting material *10a*

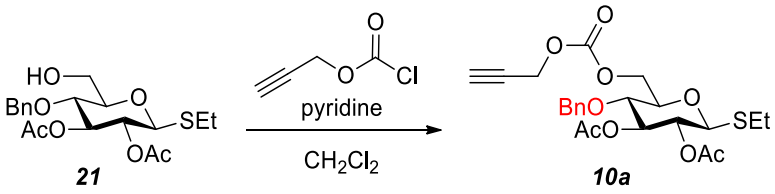

Ethyl 2,3-di-*O*-acetyl-4-*O*-benzyl-6-*O*-propargyloxycarbonyl-β-D-thioglucopyranose (*10a*):

Into a 100 mL round bottom flask with ***21*** (0.3 g, 0.75 mmol, 1 equiv), CH_2Cl_2 (5 mL) was added followed by pyridine (0.5 mL, 3.8 mmol, 5 equiv) and propargyl chloroformate (0.22 mL, 2.3 mmol, 3 equiv) at 0 °C. Reaction was stirred overnight and monitored for completion by TLC (30% ethyl acetate/hexanes). Reaction was then concentrated with toluene and purified by column chromatography to produce ***10a*** as a colorless solid (325 mg, 0.67 mmol, 90%).

^{1}H NMR (400 MHz, $CDCl_3$) δ 7.42 – 7.27 (m, 8H), 7.25 – 7.19 (m, 2H), 5.26 (t, J = 9.1 Hz, 1H), 5.16 (s, 2H), 4.92 (t, J = 9.6 Hz, 1H), 4.56 (q, J = 11.2, 6.7 Hz, 2H), 4.49 – 4.41 (m, 2H), 4.27 (dd, J = 11.7, 4.6 Hz, 1H), 3.71 – 3.56 (m, 2H), 2.75 – 2.57 (m, 2H), 2.04 (s, 3H), 1.96 (s, 3H), 1.23 (t, J = 7.5 Hz, 3H). ^{13}C NMR (101 MHz, $CDCl_3$) δ 170.2, 169.9, 154.9, 137.2, 135.2, 128.8, 128.7, 128.5, 128.3, 128.2, 83.4, 77.4, 77.1, 76.1, 75.6, 75.0, 70.5, 70.0, 66.3, 24.3, 21.0, 20.9, 15.0. HRMS (ESI) m/z: $[M + Na]^+$ Calcd for $C_{23}H_{28}NaO_9S$ 503.1346; Found 503.1326.

Preparation of starting material *11a*

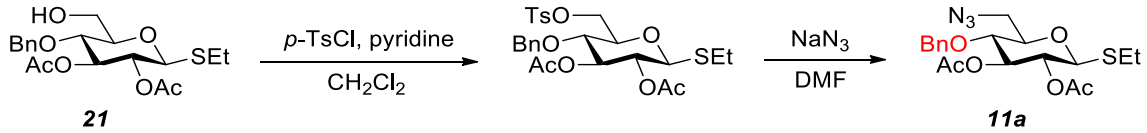

Ethyl 2,3-di-*O*-acetyl-4-*O*-benzyl-6-deoxy-6-azido-β-D-thioglucopyranose (*11a*):

Into a 50 mL round bottom flask with ***21*** (0.3 g, 0.75 mmol, 1 equiv), CH_2Cl_2 (7.5 mL) was added followed by pyridine (0.32 mL, 2.2 mmol, 3 equiv) and 4-toluenesulfonyl chloride (214 mg, 1.1 mmol, 1.5 equiv) at room temperature. Reaction was stirred overnight and monitored for completion by TLC (30% ethyl acetate/hexanes). Reaction was then diluted with CH_2Cl_2 and washed with 10% citric acid solution. Organic layer was collected, dried with $NaSO_4$, concentrated, and purified by column chromatography. Pure residue of previous reaction was dissolved in DMF (10 mL) and NaN_3 (244 mg, 3.7 mmol, 5 equiv) was added. Reaction was stirred overnight at 65 °C (oil bath) and monitored for completion by TLC (30% ethyl acetate/hexanes). Reaction was then diluted with CH_2Cl_2 and washed with water. Organic layer was collected, dried with $NaSO_4$, concentrated, and purified by column chromatography to produce ***11a*** as a colorless solid (193 mg, 0.46 mmol, 61%).

^{1}H NMR (400 MHz, $CDCl_3$) δ 7.38 – 7.28 (m, 3H), 7.26 – 7.22 (m, 2H), 5.25 (t, J = 9.2 Hz, 1H), 4.96 (t, J = 9.7 Hz, 1H), 4.59 (q, J = 11.3 Hz, 2H), 4.49 (d, J = 10.0 Hz, 1H), 3.69 – 3.49 (m, 3H), 3.34 (dd, J = 13.4, 5.2 Hz, 1H), 2.83 – 2.61 (m, 2H), 2.06 (s, 3H), 1.97 (s, 3H), 1.26 (t, J = 7.5 Hz, 3H). ^{13}C NMR (101 MHz, $CDCl_3$) δ 170.2, 169.9, 137.3, 128.8, 128.4, 128.1, 83.0, 78.7, 76.3, 76.0, 75.1, 70.4, 51.1, 23.7, 21.0, 20.9, 14.8. HRMS (ESI) m/z: $[M + Na]^+$ Calcd for $C_{19}H_{25}N_3NaO_6S$ 446.1356; Found 446.1346.

Preparation of starting material *13a*

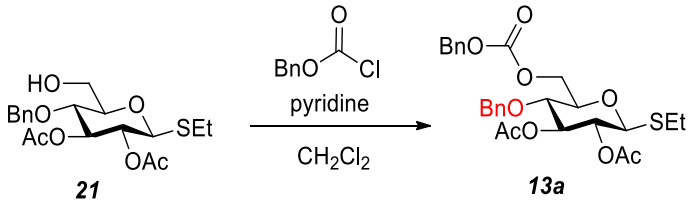

Ethyl 2,3-di-*O*-acetyl-4-*O*-benzyl-6-*O*-carboxylbenzyl-β-D-thioglucopyranose (*13a*):

Into a 100 mL round bottom flask with ***21*** (0.3 g, 0.75 mmol, 1 equiv), CH_2Cl_2 (14 mL) was added followed by benzyl chloroformate (0.19 mL, 1.3 mmol, 1.75 equiv) and pyridine (0.5 mL, 3.7 mmol, 5 equiv) at room temperature. Reaction was monitored for completion by TLC (30% ethyl acetate/hexanes) while additional portions benzyl chloroformate (0.19 mL, 1.3 mmol) were added until starting material was consumed. Reaction was then concentrated with toluene and purified by column chromatography to produce ***13a*** as a colorless solid (245 mg, 0.46 mmol, 61%).

^{1}H NMR (400 MHz, $CDCl_3$) δ 7.42 – 7.27 (m, 8H), 7.25 – 7.19 (m, 2H), 5.26 (t, J = 9.1 Hz, 1H), 5.16 (s, 2H), 4.92 (t, J = 9.6 Hz, 1H), 4.56 (q, J = 11.2, 6.7 Hz, 2H), 4.49 – 4.41 (m, 2H), 4.27 (dd, J = 11.7, 4.6 Hz, 1H), 3.71 – 3.56 (m, 2H), 2.75 – 2.57 (m, 2H), 2.04 (s, 3H), 1.96 (s, 3H), 1.23 (t, J = 7.5 Hz, 3H). ^{13}C NMR (101 MHz, $CDCl_3$) δ 170.2, 169.9, 154.9, 137.2, 135.2, 128.8, 128.7, 128.5, 128.3, 128.2, 83.4, 77.4, 77.1, 76.1, 75.6, 75.0, 70.5, 70.0, 66.3, 24.3, 21.0, 20.9, 15.0. HRMS (ESI) m/z: $[M + Na]^+$ Calcd for $C_{27}H_{32}NaO_9S$ 555.1659; Found 555.1643.

Preparation of starting material *15a*

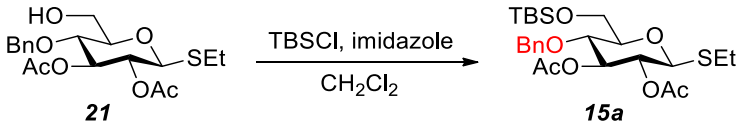

Ethyl 2,3-di-*O*-acetyl-4-*O*-benzyl-6-*O*-*tert*-butyldimethylsilyl-β-D-thioglucopyranose (*15a*):

Into a 100 mL round bottom flask with ***21*** (0.3 g, 0.75 mmol, 1 equiv), CH_2Cl_2 (5 mL) was added followed by imidazole (130 mg, 1.9 mmol, 2.5 equiv) and TBSCl (142 mg, 0.94 mmol, 1.25 equiv) at room temperature. Reaction was stirred overnight and monitored for completion by TLC (30% ethyl acetate/hexanes). Reaction was then concentrated and purified by column chromatography to produce ***15a*** as a colorless solid (321 mg, 0.62 mmol, 83%).

^{1}H NMR (400 MHz, $CDCl_3$) δ 7.37 – 7.23 (m, 5H), 5.22 (t, J = 9.4 Hz, 1H), 4.91 (t, J = 9.7 Hz, 1H), 4.67 (d, J = 11.3 Hz, 1H), 4.59 (d, J = 11.3 Hz, 1H), 4.42 (d, J = 10.0 Hz, 1H), 3.89 (s, 2H), 3.76 (t, J = 9.6 Hz, 1H), 3.37 (d, J = 9.7 Hz, 1H), 2.77 – 2.57 (m, 2H), 2.04 (s, 3H), 1.91 (s, 3H), 1.25 (t, J = 7.5 Hz, 3H), 0.92 (s, 9H), 0.09 (d, J = 6.3 Hz, 6H). ^{13}C NMR (101 MHz, $CDCl_3$) δ 170.3, 170.0, 138.1, 128.6, 128.1, 128.0, 82.7, 80.2, 76.1, 75.4, 74.8, 70.6, 61.9, 26.0, 23.5, 21.0, 21.0, 18.5, 15.1, -4.9, -5.2. HRMS (ESI) m/z: $[M + Na]^+$ Calcd for $C_{25}H_{40}NaO_7SSi$ 535.2156; Found 535.2155.

3. Experimental setups for photochemical experiments

3.1. 440 nm setup

Batch experiments using blue light were carried out using Kessil PR160-440 LED lamps (Figure S2). One or two sealed reaction vessels were placed on a stirring plate 4.5 cm away from a single lamp. Full power corresponds to 40W irradiation. To avoid heating of the reaction mixture, a fan was used for cooling. All reactions were performed with maximum stirring speed.

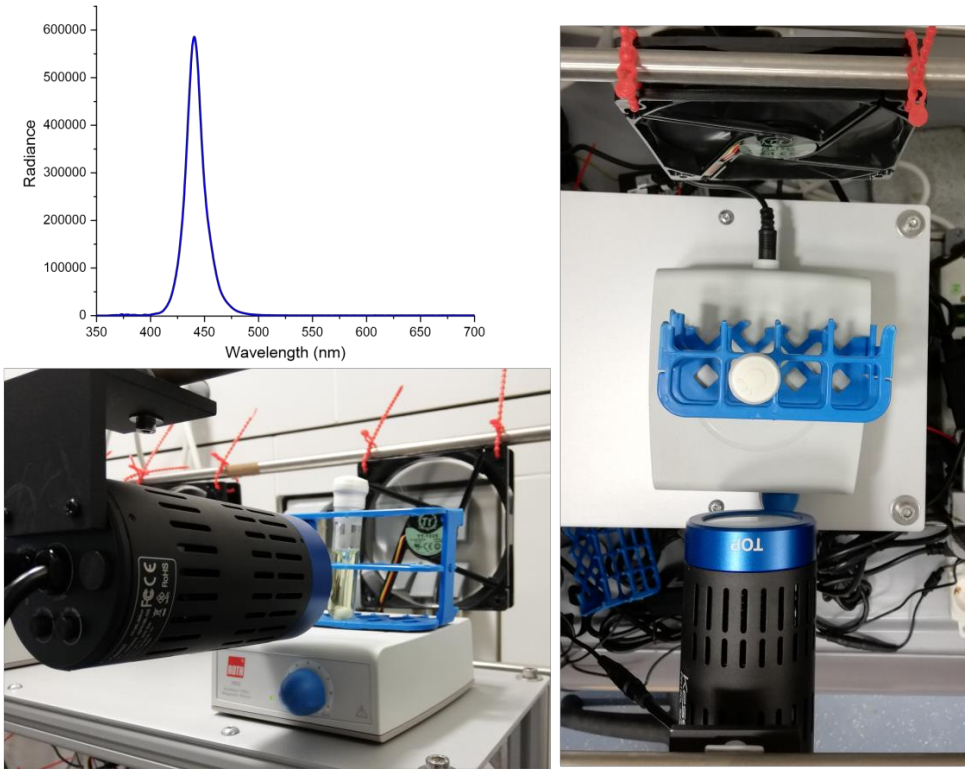

Figure S2: Emission spectrum of the Kessil PR160-440 and setup for blue light experiments.

3.2. 525 nm setup

Batch experiments using green light were carried out using Kessil PR160-525 LED (Figure S3). One sealed reaction vessel was placed on a stirring plate 4.5 cm away from one or two lamps, depending on the required light intensity. Full power corresponds to 40W irradiation. To avoid heating of the reaction mixture, fans were used for cooling. All reactions were performed with maximum stirring speed.

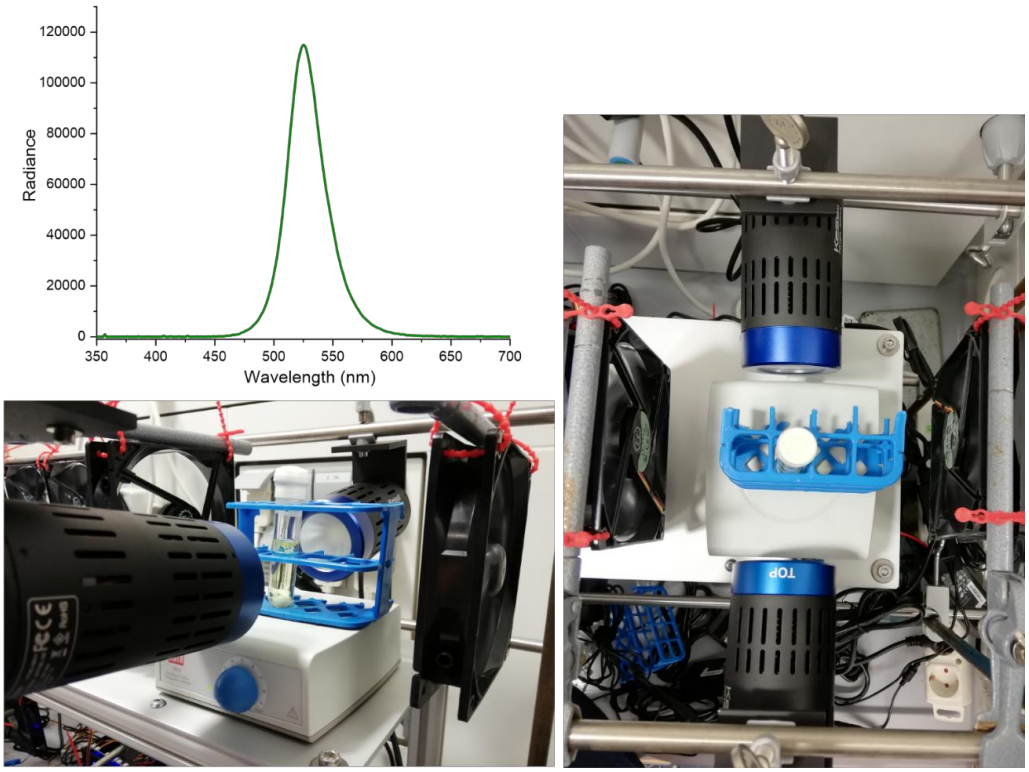

Figure S3: Emission spectrum of the Kessil PR160-525 and setup for green light experiments.

3.3. Flow-photochemical setup

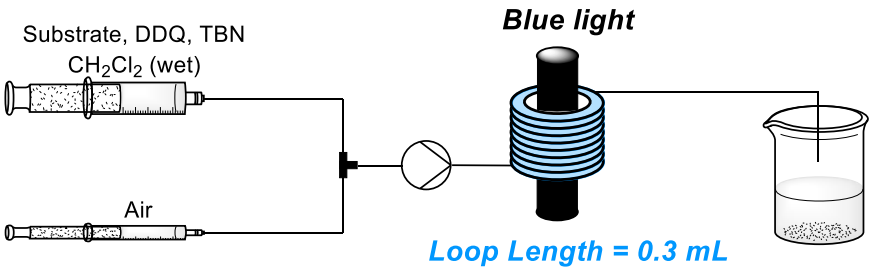

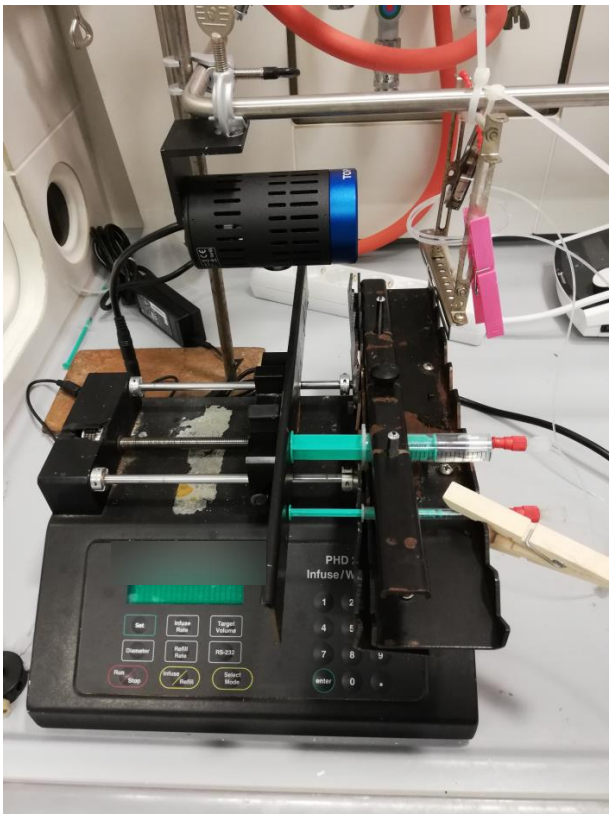

Figure S4: Experimental setup for flow experiments.

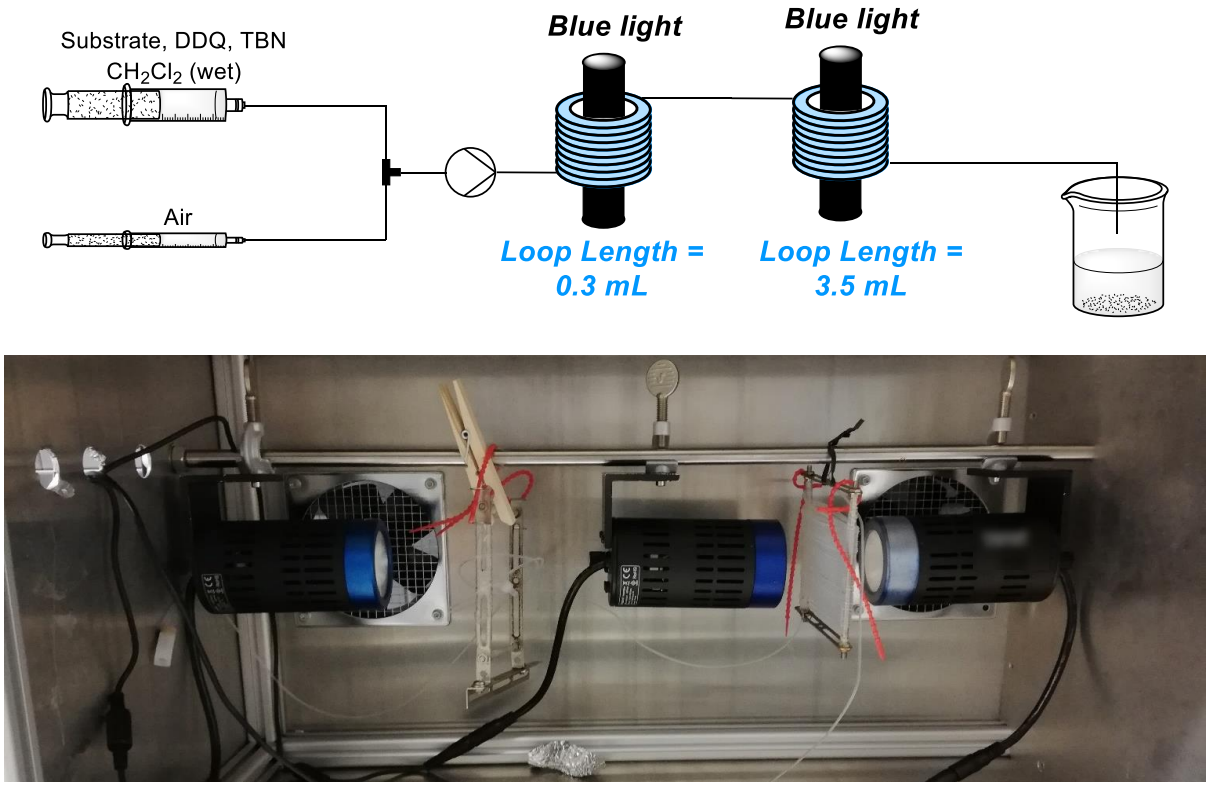

Figure S5: Experimental setup for extended retention time flow experiment.

4. Preliminary investigations using photocatalyst and stoichiometric oxidants

General procedure for screening experiments

An oven-dried, glass vial (19 x 100 mm) equipped with a stir bar was charged with ***1a***, the photocatalyst and the oxidant. Subsequently, the solvent and water were added and the vial was sealed with a septum and Parafilm. The reaction mixture was stirred for 1 minute at high speed, followed by degassing with argon for 10 minutes. The mixture was irradiated using the 440 nm setup with rapid stirring (800 rpm). After the respective reaction time, 1,3,5-trimethoxybenzene (1 equiv) or maleic acid (1 equiv) was added to the reaction mixture as internal standard. An aliquot of the resulting solution (~100 µL) was diluted in DMSO-d_6 and subjected to ^{1}H-NMR analysis.

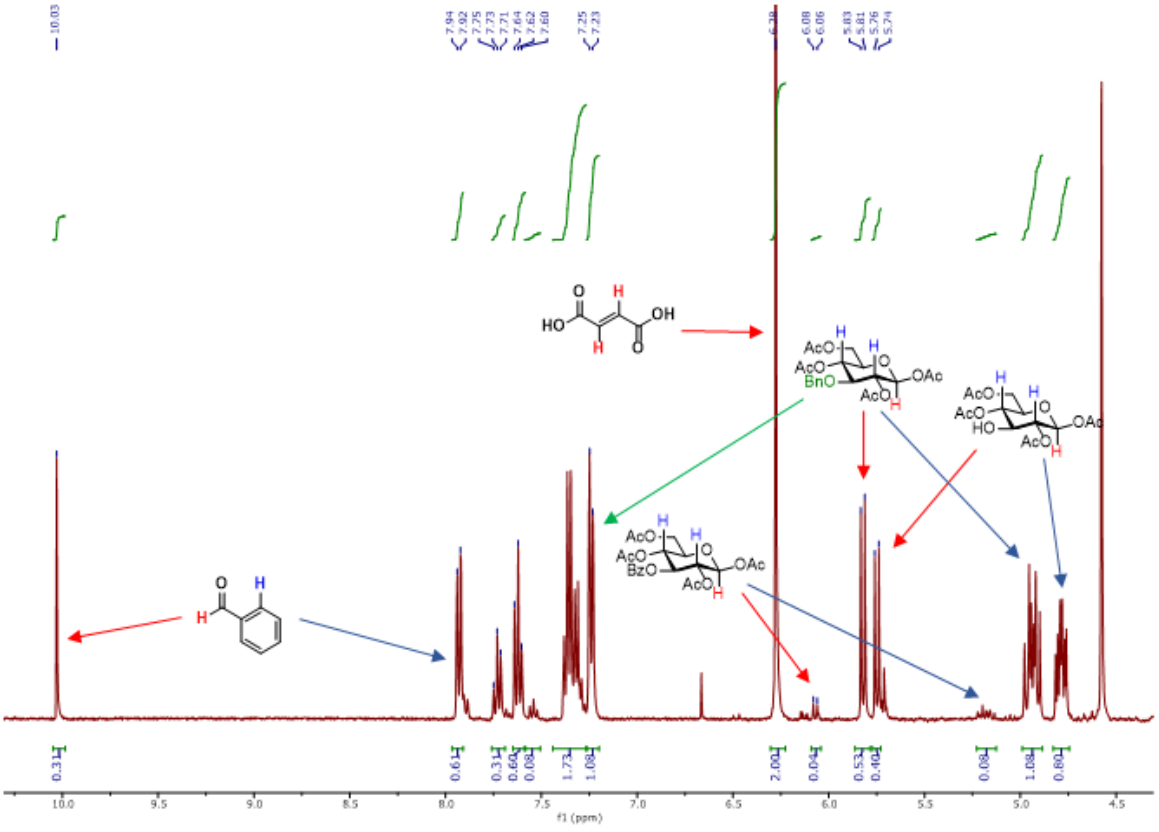

Figure S6: Example of ^{1}H NMR analysis of a crude reaction mixture.

4.1. Initial screening of photocatalysts

Table S1: Photocatalyst screening (selection).[a]

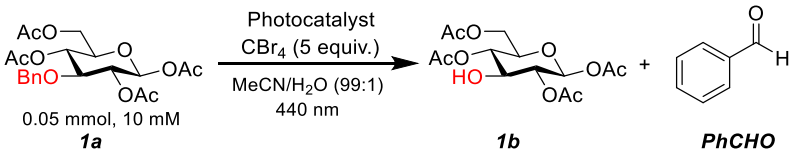

Entry	Photocatalyst	Time [h]	1a [%][b]	1b [%][b]	PhCHO [%][b]	Sum [%][b]
1	CN-OA-m (3.33mg/mL)	15	56	34	32	90
2	$Ir(ppy)_3$ (1 mol%)	15	50	25	32	75
3	TriPhPyrilium (2 mol%)	15	68	21	21	89
4	Rose Bengal (1 mol%)	15	77	14	12	91
5	Me-Mes-Acr (4 mol%)	15	43	42	41	85

[a]Reaction conditions: ***1a*** (50 µmol), Photocatalyst, CBr_4 (5 equiv), MeCN (5 mL), H_2O (50 µL), irradiation at 440 nm (20W) at rt, degassed. [b]Determined by ^{1}H-NMR using 1,3,5-trimethoxybenzene as internal standard.

Reaction conditions that were previously reported for the oxidative cleavage of PMB ethers using visible-light photoredox catalysis[6] were adapted to cleave benzyl ether ***1a*** (Table S1). The desired product ***1b*** was obtained using visible light irradiation (440 nm) of the semiconductor CN-OA-m,[7] an iridium polypyridyl complex and several organic photocatalysts in presence of stoichiometric amounts of the oxidant CBr_4. 9-Mesityl-10-methylacridinium perchlorate was selected for further investigation.

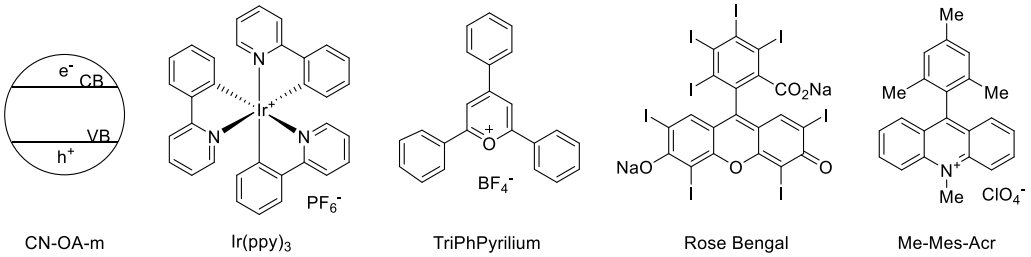

Figure S7: Set of photocatalysts used for the initial investigation of the photo-oxidative debenzylation.

4.2. Time study

Table S2: Time study.[a]

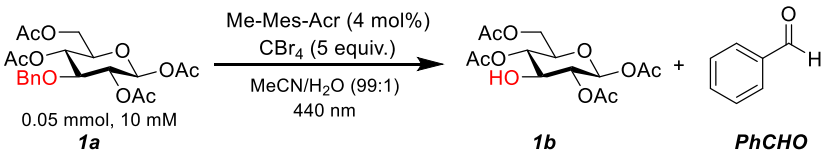

Entry	Time [h]	1a [%][b]	1b [%][b]	PhCHO [%][b]	Sum [%][b]
1	2	88	10	16	98
2	4	75	21	20	96
3	8	56	34	35	90
4	13	43	42	43	85
5	19	32	47	51	79
6	26	23	46	58	69
7	31	15	39	63	54
8	48	5	24	78	29

[a]Reaction conditions: ***1a*** (50 µmol), Me-Mes-Acr (4 mol%), CBr_4 (5 equiv), MeCN (5 mL), H_2O (50 µL), irradiation at 440 nm (20W) at rt, degassed. [b]Determined by ^{1}H- NMR using 1,3,5-trimethoxybenzene as internal standard.

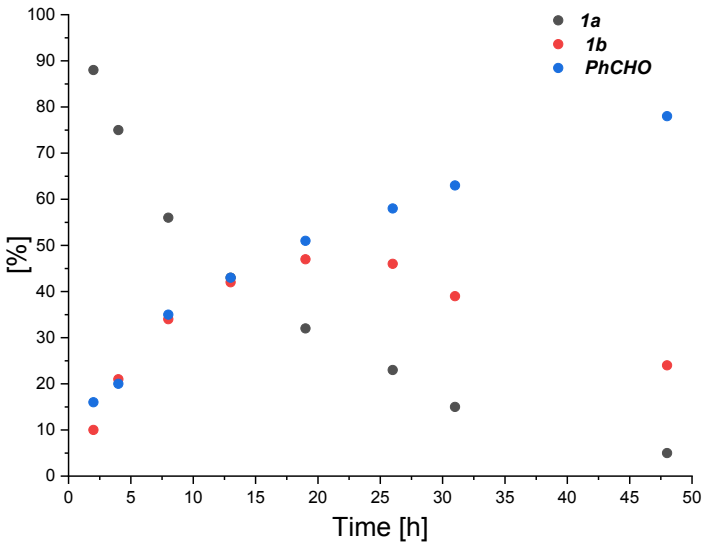

Figure S8: Time study. Data from Table S2.

4.3. Oxidant screening

Table S3: Oxidant screening.[a]

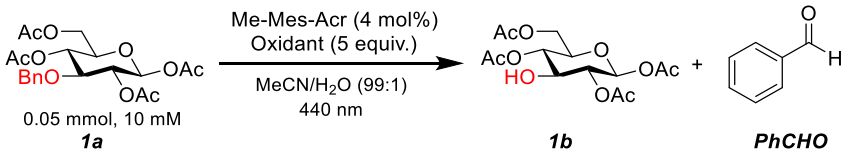

Entry	Oxidant	Time [h]	1a [%][b]	1b [%][b]	PhCHO [%][b]	Sum [%][b]
1	CBr_4	18	37	45	50	82
2	$BrCCl_3$	18	70	22	22	92
3	$Na_2S_2O_8$	18	76	23	19	99
4	*tert*-Butyl peroxide	18	94	n.d.[c]	n.d.	94
5	Oxone	18	86	7	8	93
6	$Cu(OAc)_2 \cdot H_2O$	18	92	n.d.	n.d.	92

[a]Reaction conditions: **1a** (50 µmol), Me-Mes-Acr (4 mol%), Oxidant (5 equiv), MeCN (5 mL), H_2O (50 µL), irradiation at 440 nm (20W) at rt, degassed. [b]Determined by ^{1}H-NMR using 1,3,5-trimethoxybenzene as internal standard. [c]not detected.

Table S4: Experiment with stoichiometric amounts of DDQ as photooxidant.[a]

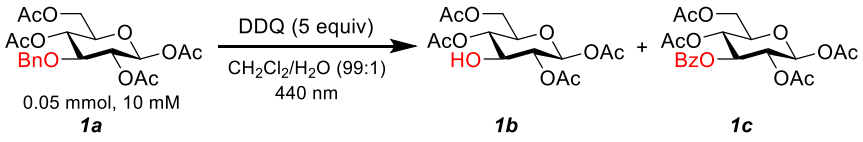

Entry	Time	1a [%][b]	1b [%][b]	1c [%][b]	PhCHO [%][b]	Sum [%][b]
1	18	n.d.[c]	83	17	47	>99

[a]Reaction conditions: ***1a*** (50 µmol), DDQ (5 equiv), MeCN (5 mL), H_2O (50 µL), irradiation at 440 nm (20W) at rt, degassed. [b]Determined by ^{1}H-NMR using maleic acid as internal standard. [c]not detected.

5. Reaction optimization for Protocol A and B

General procedure for screening experiments

An oven-dried, glass vial (19 x 100 mm) equipped with a stir bar was charged with ***1a*** and DDQ. Subsequently, the solvent and water were added and the vial was sealed with a septum and Parafilm. *tert*-Butyl nitrite was added through the septum and the resulting reaction mixture was stirred for 1 minute at high speed. The reaction vessel was degassed by bubbling argon for 10 minutes or a balloon of air was applied through the septum. The mixture was irradiated with the respective LED lamps with rapid stirring (800 rpm). After the respective reaction time, the reaction mixture was transferred into a round-bottom flask and solvents were removed under vacuum. Maleic acid (1 equiv) was added to the residue as internal standard, followed by 1.5 mL of acetonitrile. An aliquot of the resulting homogeneous solution (~100 µL) was diluted in DMSO-d_6 and subjected to ^{1}H-NMR analysis (See Figure S6).

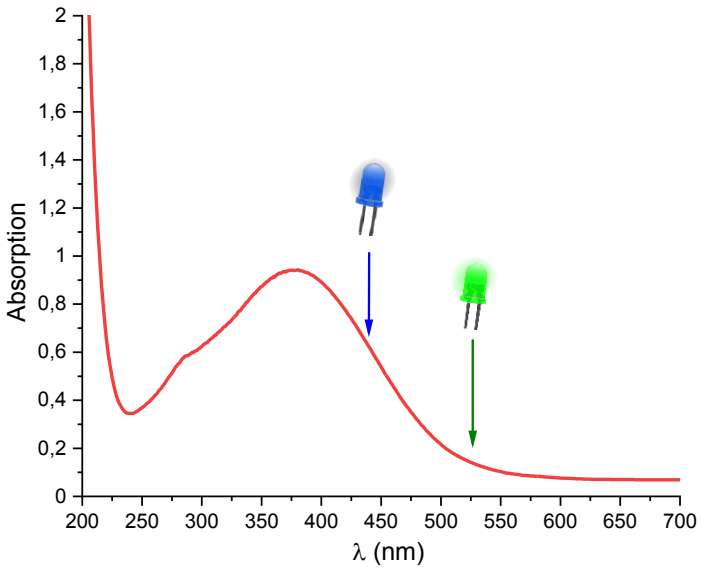

Figure S9: UV-visible absorption spectrum of DDQ (1.0 mM in CH_2Cl_2).

5.1. Selection of light source using stoichiometric DDQ

Table S5: Screening of different wavelengths.[a]

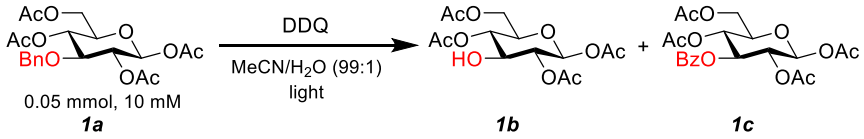

Entry	Light source	DDQ [equiv]	Time [h]	1a [%][b]	1b [%][b]	1c [%][b]	Sum [%][b]
1	None	2	24	93	n.d.[c]	n.d.	93
2	440nm, 20W	1	2	11	71	6	88
3	440nm, 20W	1	16	14	75	8	97
4	440nm, 20W	1.2	2	n.d.	88	5	93
5	440nm, 20W	1.5	2	n.d.	85	12	97
6	440nm, 20W	2	2	n.d.	87	12	99
7	440nm, 20W	5	2	n.d.	80	20	>99
8	525nm, 20W	1	17	28	66	n.d.	94
9	525nm, 20W	1.2	17	19	70	n.d.	89
10	525nm, 20W	1.5	17	14	79	n.d.	93
11	525nm, 20W	2	17	6	86	n.d.	92
12	525nm, 20W	5	8	5	87	n.d.	92
13	525nm, 20W	5	17	n.d.	95	n.d.	95
14	525nm, 40W	2	8	n.d.	94	n.d.	94
15	525nm, 80W	2	4	n.d.	89	n.d.	89

[a]Reaction conditions: **1a** (50 µmol), DDQ (1-5 equiv), MeCN (5 mL), H_2O (50 µL), light irradiation at rt. [b]Determined by ^{1}H- NMR using maleic acid as internal standard. [c]not detected.

Use of 525 nm irradiation, resulted in longer reaction times and higher selectivity (Table S5, entry 13, 95% yield) compared to 440 nm (entry 7, 80% yield). Reaction times could be reduced by using higher light intensity.

5.2. Solvent screening using stoichiometric DDQ

Table S6: Screening of different solvents.[a]

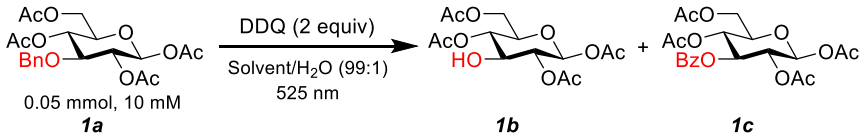

Entry	Solvent	Time [h]	1a [%][b]	1b [%][b]	1c [%][b]	Sum [%][b]
1	Acetonitrile	1	20	69	n.d.[c]	89
2	*N*,*N*-dimethylformamide	1	>99	n.d.	n.d.	>99
3	Dimethylsulfoxide	1	93	n.d.	n.d.	93
4	Acetone	1	63	27	10	>99
5	*N*,*N*-dimethylacetamide	1	95	n.d.	n.d.	95
6	Dioxane	1	92	n.d.	n.d.	92
7	Methanol	1	94	n.d.	n.d.	94
8	Tetrahydrofurane	1	94	n.d.	n.d.	94
9	Dichloromethane	1	n.d.	89	7	96
10	*N*-methyl-2-pyrrolidone	1	93	n.d.	n.d.	93
11	2-Butanone	1	54	33	n.d.	87
12	Ethyl acetate	1	39	49	n.d.	88
13	Toluene	1	97	n.d.	n.d.	97
14	Chloroform	1	0	80	5	85
15	Cyclopentanone	1	90	7	n.d.	97
16	CH_2Cl_2/MeCN (2:1)	1	18	75	n.d.	93
17	CH_2Cl_2/MeCN (4:1)	1	22	78	n.d.	>99
18	CH_2Cl_2/MeCN (4:1)	3	7	91	n.d.	98

[a]Reaction conditions: **1a** (50 µmol), DDQ (2 equiv), solvent (5 mL), H_2O (50 µL), irradiation at 525 nm (40W) at rt. [b]Determined by ^{1}H-NMR using maleic acid as internal standard. [c]not detected.

5.3. Protocol A: Optimized conditions and control experiments

Table S7: Optimized reaction conditions and control experiments for Protocol A.[a]

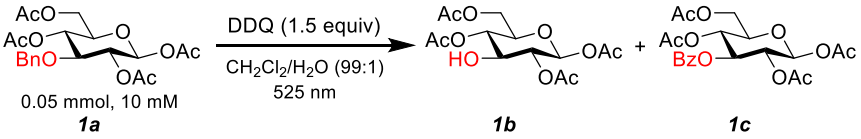

Entry	Variation	Time	1a [%][b]	1b [%][b]	1c [%][b]	Sum [%][b]
1	None	30 min	n.d.[c]	96	<2	98
2	440 nm (20W)	10 min	n.d.	78	16	94
3	No light	24 h	>99	n.d.	n.d.	>99

[a]Reaction conditions: **1a** (50 µmol), DDQ (2 equiv), CH_2Cl_2 (5 mL), H_2O (50 µL), irradiation at 525 nm (80W) at rt. [b]Determined by ^{1}H-NMR using maleic acid as internal standard. [c]not detected.

5.4. Solvent screening using dual DDQ/TBN catalysis

Table S8: Solvent screening.[a]

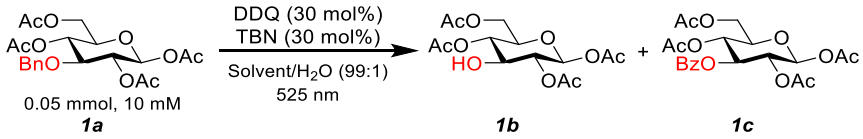

Entry	Solvent	Time [min]	1a [%][b]	1b [%][b]	1c [%][b]	Sum [%][b]
1	Acetonitrile	100	35	58	5	98
2	Dichloromethane	100	6	90	4	>99
3	Chloroform	100	3	92	4	99
4	Ethyl acetate	100	85	15	n.d.[c]	>99
5	Acetone	100	81	15	2	98
6	2-Butanone	100	90	9	n.d.	99
7	CH_2Cl_2/MeCN (3:2)	100	27	64	3	97
8	CH_2Cl_2/MeCN (7:3)	100	24	72	<2	98
9	CH_2Cl_2/MeCN (4:1)	100	33	63	4	>99
10	CH_2Cl_2/MeCN (9:1)	100	37	57	4	98

[a]Reaction conditions: **1a** (50 µmol), DDQ (30 mol%), TBN (30 mol%), solvent (5 mL), H_2O (50 µL), irradiation at 525 nm (40W) at rt, air balloon. [b]Determined by ^{1}H-NMR using maleic acid as internal standard. [c]not detected.

5.5. Screening of water content

Table S9: Screening of water contents.[a]

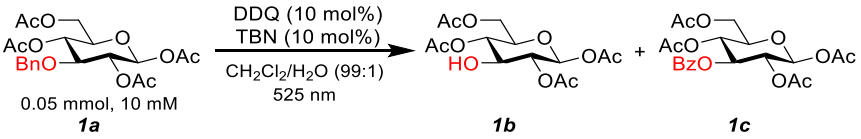

Entry	Water content	Time [min]	1a [%][b]	1b [%][b]	1c [%][b]	Sum [%][b]
1	None	100	62	33	3	98
2	0.1 %	100	65	31	n.d.[c]	96
3	1%	100	51	46	4	>99
4	2%	100	54	42	4	100
5	5%	100	71	25	3	99
6	10%	100	71	21	4	96

[a]Reaction conditions: **1a** (50 µmol), DDQ (10 mol%), TBN (10 mol%), CH_2Cl_2 (4.5-5 mL), H_2O (0-500 µL), irradiation at 525 nm (40W) at rt, air balloon. [b]Determined by ^{1}H- NMR using maleic acid as internal standard. [c]not detected.

5.6. Screening of different atmospheres

Table S10: Screening of different atmospheres.[a]

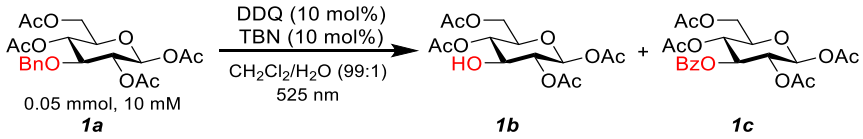

Entry	Variation	Time [min]	1a [%][b]	1b [%][b]	1c [%][b]	Sum [%][b]
1	Air balloon	100	45	51	1	97
2	Oxygen balloon	100	39	54	2	95
3	Sealed vessel	100	38	57	5	>99

[a]Reaction conditions: **1a** (50 µmol), DDQ (10 mol%), TBN (10 mol%), CH_2Cl_2 (5 mL), H_2O (50 µL), irradiation at 525 nm (40W) at rt. [b]Determined by ^{1}H-NMR using maleic acid as internal standard. [c]not detected.

Using balloons of air, oxygen or the sealed vessel gave no significant difference in formation of ***1b*** or ***1c***.

5.7. Screening of different concentrations

Table S11: Screening of different concentrations.[a]

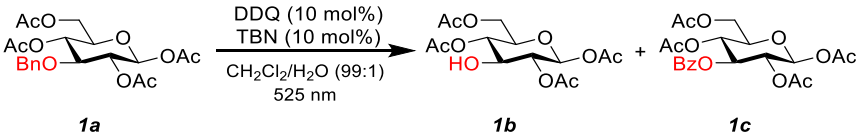

1a *1b* *1c*

Entry	Concentration, Scale	Time [min]	1a [%][b]	1b [%][b]	1c [%][b]	Sum [%][b]
1	5 mM, 25 µmol	100	77	21	2	>99
2	10 mM, 50 µmol	100	40	56	4	>99
3	25 mM, 125 µmol	100	56	42	1	99
4	50 mM, 250 µmol	100	66	33	1	>99
5	100 mM, 500 µmol	100	79	21	n.d.[c]	>99
6	200 mM, 100 µmol	100	81	19	n.d.	>99

[a]Reaction conditions: **1a** (25-500 µmol), DDQ (10 mol%), TBN (10 mol%), CH_2Cl_2 (0.5-5 mL), H_2O (50 µL), irradiation at 525 nm (40W) at rt. [b]Determined by ^{1}H-NMR using maleic acid as internal standard. [c]not detected.

5.8. Screening of catalyst loadings using dual DDQ/TBN catalysis

Table S12: Screening of catalyst loadings.[a]

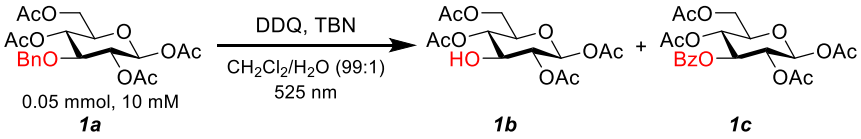

0.05 mmol, 10 mM

1a ***1b*** ***1c***

Entry	DDQ, TBN	Time [min]	1a [%][b]	1b [%][b]	1c [%][b]	Sum [%][b]
1	1 mol%	100	98	n.d.[c]	2	>99
2	5 mol%	100	70	26	4	98
3	10 mol%	100	41	56	3	>99
4	15 mol%	100	35	59	5	99
5	20 mol%	100	13	80	5	98
6	25 mol%	100	2	94	4	>99
7	30 mol%	100	7	91	2	>99
8	40 mol%	100	n.d.	90	6	96

[a]Reaction conditions: **1a** (50 µmol), DDQ (1-40 mol%), TBN (1-40 mol%), CH_2Cl_2 (5 mL), H_2O (50 µL), irradiation at 525 nm (40W) at rt. [b]Determined by ^{1}H-NMR using maleic acid as internal standard. [c]not detected.

5.9. Protocol B: Optimized conditions and control experiments

Table S13: Optimized reaction conditions and control experiments for Protocol B.[a]

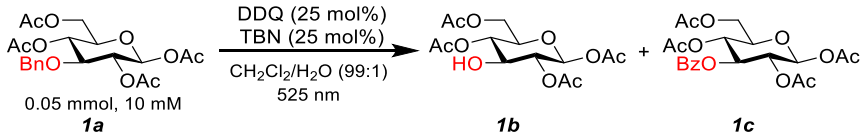

Entry	Variation	Time [min]	1a [%][b]	1b [%][b]	1c [%][b]	Sum [%][b]
1	none	120	n.d.[c]	97	2	99
2	440 nm (20W)	30 min	n.d.	88	9	97
3	440 nm (40W)	30 min	n.d.	87	11	98
4	No light	120	96	2	n.d.	98
5	No TBN	120	77	23	n.d.	>99
6	No DDQ	120	>99	n.d.	n.d.	>99
7	No TBN and no DDQ	120	>99	n.d.	n.d.	>99
8	No DDQ and no light	120	>99	n.d.	n.d.	>99
9	Degassed with argon	120	55	39	<2	96

[a]Reaction conditions: **1a** (50 µmol), DDQ (25 mol%), TBN (25 mol%), CH_2Cl_2 (5 mL), H_2O (50 µL), irradiation at 525 nm (40W) at rt. [b]Determined by ^{1}H-NMR using maleic acid as internal standard. [c]not detected.

6. *In situ* NMR studies using a LED-NMR setup

6.1. General remarks and experimental setup

^{1}H NMR spectra were obtained using a Varian 600 Spectrometer (600 MHz, Bruker) at 298 K, with the following settings: Acquisition points 30952; Acquisition time 1.3 s; Relaxation delay 1.0 s; Receiver gain (as autogain) 101; Spectral width 16.0 ppm; Number of scans 30 ; Number of dummy scans 0.

All *in situ* ^{1}H NMR spectra were obtained by a sequence of experiments of 30 sec. The reaction was carried out under blue light irradiation *via* an optic fiber connected to THORLABS M450LP1 (450nm, 1850 mW).

Figure S10: (A) Optic fiber inside a NMR tube (inner diameter 2.1 mm) embedded in a NMR tube (inner diameter 4.0 mm) sealed with a septum. (B) Varian 600 Spectrometer (600 MHz, Bruker). (C) THORLABS M450LP1 lamp with optic fiber attached.

6.2. Obtaining and processing the *in* situ NMR data

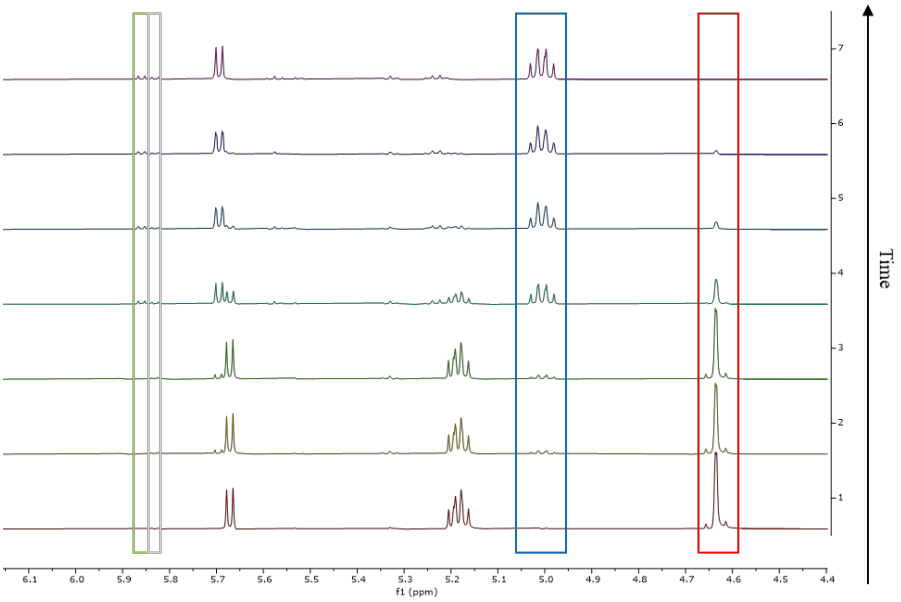

Figure S11: ^{1}H NMR reaction profile of the debenzylation of ***1a***. The highlighted peaks were used to track the reaction progress: conversion of ***1a*** (red), formation of ***1b*** (blue), unidentified side products (grey and green).

Due to the formation of side products the data were presented as substrate consumption:

$$\text{Substrate consumption} = \left(1 - \frac{substrate_{Integral}}{substrate_{Integral} + product_{Integral} + side\ product\ A_{Integral} + side\ product\ B_{Integral}}\right) \cdot 100$$

Diethyl ethylidenemalonate was used as internal standard in the NMR analysis to determine the mass balance and validate the calculation.

6.3. Photo-oxidative debenzylation of *1a* studied with *in situ* NMR spectroscopy

Experimental Procedure: An oven dried vial (19 x 100 mm) equipped with a stir bar was charged with ***1a*** (4.38 mg, 10 µmol) and DDQ (0.11 mg, 0.5 µmol, 5 mol%). Deuterated chloroform (1.0 mL) and *tert*-butyl nitrite (2.39 µL, 20 µmol, 2 equiv) were added and the vial was sealed with a septum and Parafilm. After stirring for 1 minute, the reaction solution (0.5 mL) and water (5 µL) were transferred into an oven dried NMR tube (inner diameter 4mm). A second oven-dried NMR tube (inner diameter 2.1 mm), was installed coaxially inside the first one using a rubber septum. The optic fiber was inserted into the inner NMR tube and the reaction progress was tracked over 100 min of irradiation, using ^{1}H NMR spectroscopy.

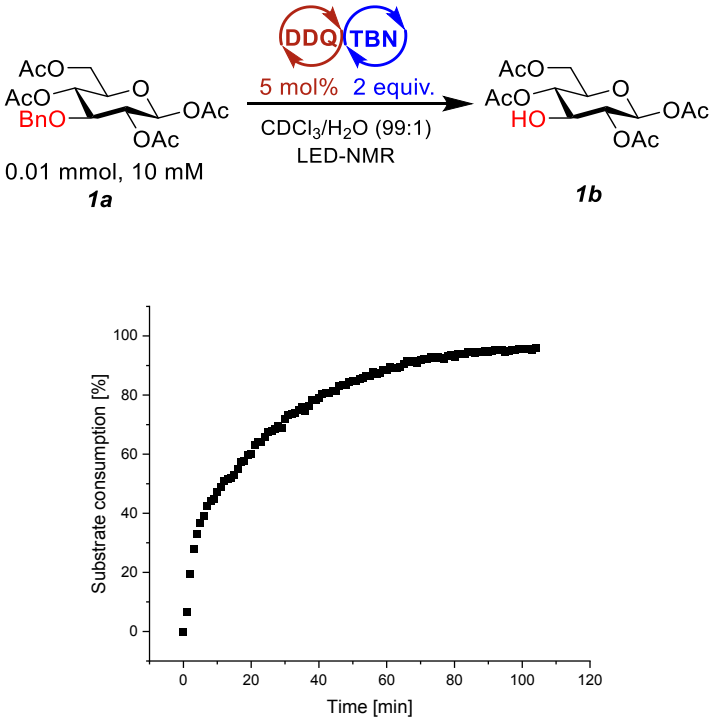

Figure S12: Debenzylation of ***1a***. Reaction conditions and concentration profile.

6.4. Delayed injection experiment studied with *in* situ NMR spectroscopy

Experimental procedure: An oven dried vial (19 x 100 mm) equipped with a stir bar was charged with ***1a*** (4.38 mg, 10 µmol) and DDQ (0.34 mg, 1.5 µmol, 15 mol%). Deuterated chloroform (1.0 mL) was added and the vial was sealed with a septum and Parafilm. After stirring for 1 minute, the reaction solution (0.5 mL) and water (5 µL) were transferred into an oven dried NMR tube (inner diameter 4mm). A second oven-dried NMR tube (inner diameter 2.mm1), was installed coaxially inside the first one using a rubber septum. The optic fiber was inserted into the inner NMR tube and the reaction progress was tracked using ^{1}H NMR spectroscopy. After 30 minutes of irradiation, *tert*-butyl nitrite (4.78 µL, 40 µmol, 4 equiv) was added to the reaction solution and the irradiation was continued for 70 min.

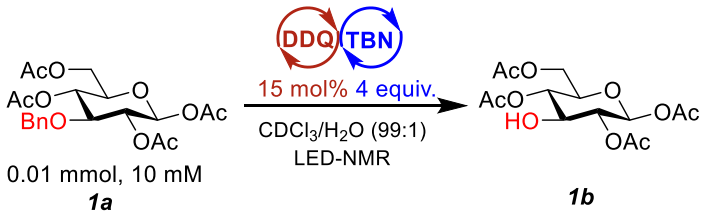

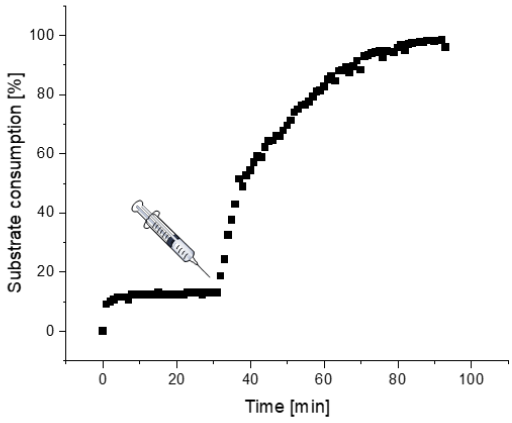

Figure S13: Delayed addition experiment for the debenzylation of ***1a***. Reaction conditions and concentration profile.

6.5. On/off experiment studied with *in* situ NMR spectroscopy

Experimental Procedure: An oven dried vial (19 x 100 mm) equipped with a stir bar was charged with ***1a*** (4.38 mg, 10 µmol) and DDQ (0.11 mg, 0.5 µmol, 5 mol%). Deuterated chloroform (1.0 mL) and *tert*-butyl nitrite (2.39 µL, 20 µmol, 2 equiv) were added and the vial was sealed with a septum and Parafilm. After stirring for 1 minute, the reaction solution (0.5 mL) and water (5 µL) were transferred into an oven dried NMR tube (inner diameter 4mm). A second oven-dried NMR tube (inner diameter 2.1 mm), was installed coaxially inside the first one using a rubber septum. The optic fiber was inserted into the inner NMR tube and the reaction progress was tracked using ^{1}H NMR spectroscopy with cycles of 15 minutes of irradiation and 20 minutes in the dark. After the end of the second cycle (70 minutes in total) reaction was tracked until completion under irradiation.

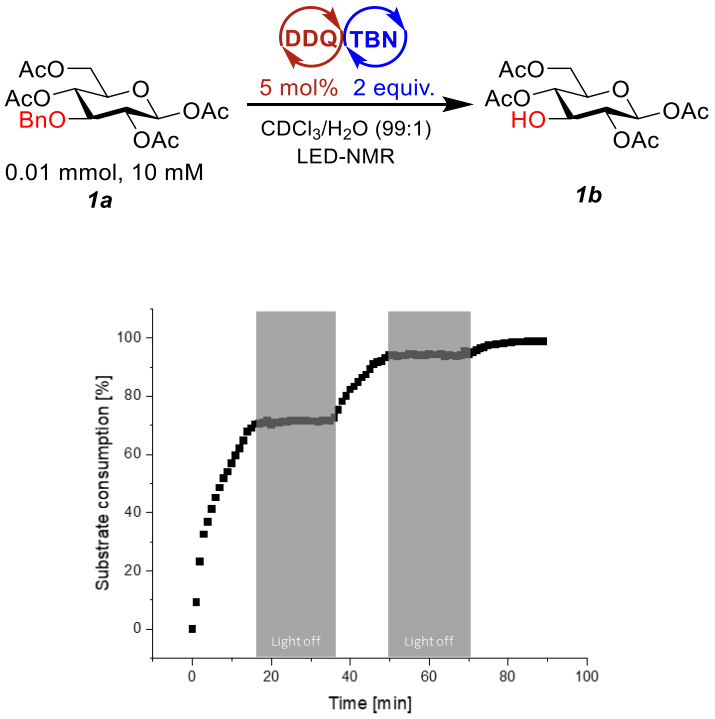

Figure S14: On/off experiment for the debenzylation of ***1a***. Reaction conditions and concentration profile.

7. Mechanistic hypothesis

Based on literature[6, 8] and on our experimental results, we suggest the following considerations about the mechanism of the dual DDQ/TBN catalyzed photo-oxidative cleavage of benzyl ethers (Scheme S1).

Photoirradiation of DDQ generates the highly oxidizing triplet state ^{3}DDQ* (E = 3.18 V vs SCE)[9] which is responsible for oxidation of ***1a***. No product formation was detected in absence of DDQ or light (Table S14, entries 6 & 4). Moreover, *in situ* monitoring of the reaction by NMR spectroscopy highlighted how interrupting irradiation inhibits product formation (Figure S14). Our evidence is too limited to discriminate whether single electron transfer (SET) or hydrogen atom transfer (HAT) is the first oxidation event happening between ^{3}DDQ* and ***1a***. However both SET/HAT and HAT/SET sequences are possible and lead to formation of the oxacarbenium intermediate ***1a***$^+$ which is hydrolyzed by water to afford the product ***1b***. Alternatively, after an SET event between ^{3}DDQ* and ***1a***, the reduced form of DDQ can abstract a hydrogen atom of CH_2Cl_2, generating a carbon centered radical that then interacts abstracts a hydrogen atom from the radical cation of ***1a***.

Photodecomposition of TBN generates nitrous oxide, which is oxidized to nitrogen dioxide by oxygen. Nitrogen dioxide is known to restore 2,3-dichloro-5,6-dicyano-1,4-dihydroquinone ($DDQH_2$) to the quinone form. The combined activity of DDQ and TBN was proved in a delayed injection experiment (Figure S13), omission of TBN resulted in the reaction remaining silent after conversion of DDQ to $DDQH_2$. Injection of TBN allowed to turn over DDQ and completion of the reaction.

Scheme S1: Possible mechanisms for the photo-oxidative benzyl cleavage using dual DDQ/TBN catalysis.

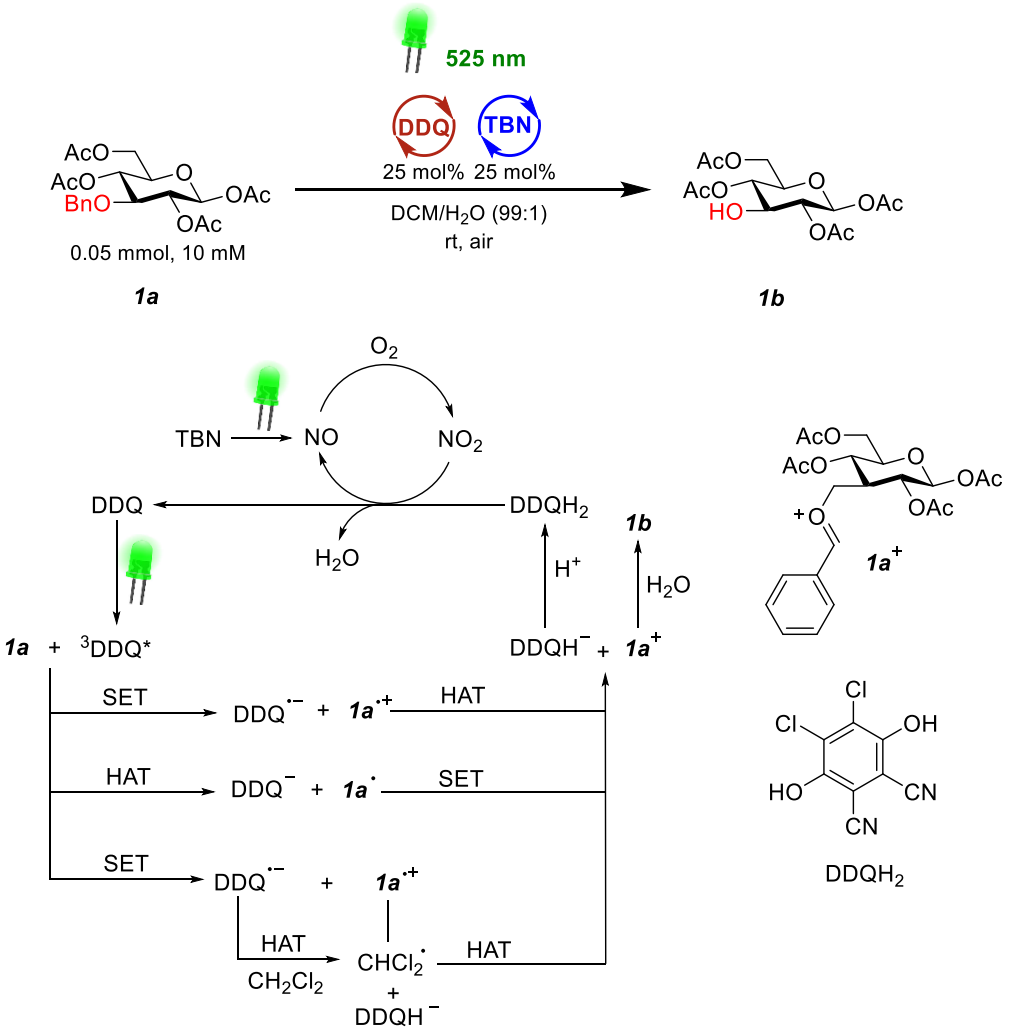

8. Scope and limitations

General procedure A

An oven-dried, glass vial (19 x 100 mm) equipped with a stir bar was charged with the starting material (100 μmol, 1 equiv) and DDQ (1.5 equiv per benzyl group), and then sealed with a septum and Parafilm. After evacuating and backfilling the vial with argon 3 times, degassed DCM (5 mL) and water (50 μL) were added through the septum and the mixture was stirred for 1 minute at high speed. The reaction mixture was irradiated in front of two green LED lamps (525 nm) at full power until consumption of the starting material was detected by TLC analysis. The reaction mixture was transferred into a round-bottom flask, solvents were removed under vacuum and the residue was loaded on a silica column and purified by flash chromatography.

In some cases chromatography afforded mixed fractions of the product and DDQ. DDQ was removed by basic washing of the fractions with aqueous saturated $NaHCO_3$, followed by drying over Na_2SO_4 and solvent evaporation.

General procedure B

An oven-dried, glass vial (19 x 100 mm) equipped with a stir bar was charged with the starting material (50 or 100 μmol, 1 equiv) and DDQ (25 mol% per benzyl group). Subsequently, the solvent (5.0 mL) and water (50 μL) were added and the vial was sealed with a septum and Parafilm. *tert*-Butyl nitrite (2 equiv) was added through the septum and the mixture was stirred for 1 minute at high speed. The reaction mixture was irradiated in front of two green LED lamps (525 nm) at full power until consumption of the starting material was detected by TLC analysis. The reaction mixture was transferred into a round-bottom flask, solvents were removed under vacuum and the residue was loaded on a silica column and purified by flash chromatography.

General procedure C (Continuous Flow)

A vial (5 mL) was charged with the starting material (1 equiv) and DDQ (25 mol% per benzyl group). Subsequently, wet CH_2Cl_2 (0.02 M) was added and the vial was sealed with a septum. *tert*-Butyl nitrite (2 or 6 equiv) was added through the septum. The reaction mixture was transferred into a 10 mL syringe and placed on a Harvard PHD 2000 syringe pump alongside a 1 mL syringe filled with air. Beginning at 1 mL the air syringe was pushed (5 mL min^{-1}) until the plunger was equal to that of the liquid syringe at which point the pump was set to the desired flow rate. The biphasic reaction mixture was pumped through a FPE loop (0.3 mL) to be irradiated by one blue LED lamp (Kessil PR160-440, 440 nm, power = 100%) at a distance of 5 cm. The reaction mixture was collected into a round-bottom flask, solvents were reduced under vacuum (0.2 mL) and then loaded directly on a silica column and purified by flash chromatography.

	Starting material	Protocol A		Protocol B		Protocol C	
		Reaction time	Isolated yield	Reaction time	Isolated yield	Retention time	Isolated yield
1a	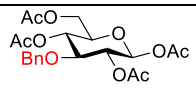	30 min	96%	1 h	95%	-	-
2a	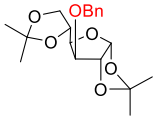	1 h	98%	3 h	90%	2.5 min	91%
3a	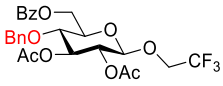	1.5 h	92%	4 h	84%	-	-
4a	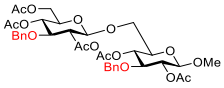	1.5 h	83%	3.5 h	80%	10 min	82%
5a	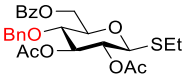	2 h	74%	6 h	65%	-	-
6a	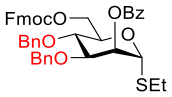	8 h	85%	24 h	85%	10 min	69%
7a	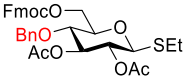	23 h	78%	52 h	89%	-	-
8a	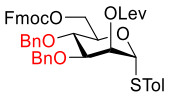	15 h	95%	43 h	79%	-	-
9a	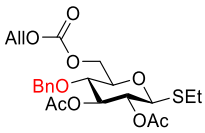	1.5 h	79%	17 h	71%	-	-
10a	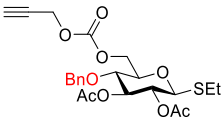	2.5 h	76%	15 h	68%	3 min	77%
11a	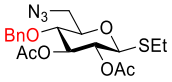	4 h	87%	6 h	75%	-	-
12a	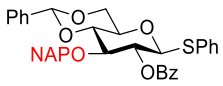	4 h	89%	15 h	86%	-	-
13a	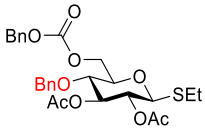	4 h	53%	-	-	-	-

8.1. Isolated compounds

Acetyl 2,4,6-tri-*O*-acetyl-β-D-glucopyranose (*1b*)

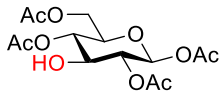

1b

Protocol A

1a (43.8 mg, 100 µmol) was treated according to general procedure A. Irradiation time was 30 minutes. Flash chromatography (gradient 40-60% ethyl acetate/hexane), followed by basic washing afforded ***1b*** (33.5 mg, 96.2 µmol, 96%) as a white solid.

Protocol B

1a (21.9 mg, 50 µmol) was treated according to general procedure B. Irradiation time was 1 hour. Flash chromatography (40% ethyl acetate/hexane) afforded ***1b*** (16.6 mg, 47.6 µmol, 95%) as a white solid.

^{1}H NMR (400 MHz, $CDCl_3$) δ 5.67 (d, J = 8.3 Hz, 1H), 5.02 – 4.94 (m, 2H), 4.30 (dd, J = 12.5, 4.6 Hz, 1H), 4.12 (dd, J = 12.5, 2.2 Hz, 1H), 3.81 – 3.74 (m, 2H), 2.13 – 2.12 (m, 6H), 2.12 (s, 3H), 2.09 (s, 3H). ^{13}C NMR (151 MHz, $CDCl_3$) δ 170.8, 170.8, 170.5, 169.3, 91.8, 73.9, 73.0, 72.9, 70.5, 61.8, 21.0, 20.9, 20.9, 20.9. HRMS (ESI) m/z: $[M + Na]^+$ Calcd for $C_{14}H_{20}NaO_{10}$ 371.0954; Found 371.0945.

These data are in full agreement with those previously published in the literature.[10]

1,2:5,6-Di-*O*-isopropylidene-α-D-glucofuranose (*2b*)

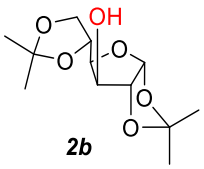

2b

Protocol A

2a (35.0 mg, 100 µmol) was treated according to general procedure A. Irradiation time was 1 hour. Flash chromatography (20% ethyl acetate/hexane) afforded ***2b*** (25.4 mg, 97.6 µmol, 98%) as a white solid.

Protocol B

2a (35.0 mg, 100 µmol) was treated according to general procedure B. Irradiation time was 3 hours. Flash chromatography (gradient 20-40% ethyl acetate/hexane) afforded ***2b*** (23.3 mg, 89.5 µmol, 90%) as a white solid.

Protocol B-large scale

An oven dried vial (19 x 100 mm) equipped with a stir bar was charged with ***2a*** (525.6 mg, 1.50 mmol, 1 equiv) and DDQ (85.1 mg, 0.375 mmol, 25 mol%). Subsequently, dichloromethane (37.5 mL) and water (375 µL) were added and the vial was sealed with a septum and Parafilm. *tert*-Butyl nitrite (357 µL, 3.00 mmol, 2 equiv) was added through the septum and the emulsion was stirred for 1 minute at high speed. The reaction mixture was irradiated at 525 nm (80W) for 4 hours. The reaction mixture was transferred into a round-bottom flask, solvents were removed under vacuum and the residue was loaded on a silica column. Flash chromatography (gradient 10-30% ethyl acetate/hexane) afforded ***2b*** (366.1 mg, 1.41 mmol, 94%) as a white solid.

Protocol C

2a (14 mg, 40 µmol) was treated according to general procedure C (TBN = 2 equiv, flow rate = 0.115 mL min^{-1}). Flash chromatography (30% ethyl acetate/hexane) afforded ***2b*** (9.5 mg, 36 µmol, 91%) as a white solid.

^{1}H NMR (600 MHz, $CDCl_3$) δ 5.94 (d, *J* = 3.6 Hz, 1H), 4.53 (d, *J* = 3.6 Hz, 1H), 4.34-4.31 (m, 2H), 4.17 (dd, *J* = 8.7, 6.2 Hz, 1H), 4.07 (dd, *J* = 7.6, 2.8 Hz, 1H), 3.98 (dd, *J* = 8.6, 5.3 Hz, 1H), 1.49 (s, 3H), 1.44 (s, 3H), 1.36 (s, 3H), 1.32 (s, 3H). ^{13}C NMR (151 MHz, $CDCl_3$) δ 112.0, 109.8, 105.4, 85.2, 81.3, 75.4, 73.6, 67.8, 27.0, 26.9, 26.3, 25.3.

These data are in full agreement with those previously published in the literature.[11]

2,2,2-Trifluoroethyl 2,3-di-*O*-acetyl-6-*O*-benzoyl-D-glucopyranose (*3b*)

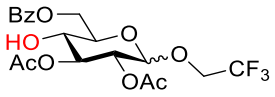

3b

Protocol A

3a (54.0 mg, 100 µmol, α/β 8:92) was treated according to general procedure A. Irradiation time was 1.5 hours. Flash chromatography (1. gradient 5-20% ethyl acetate/DCM; 2. gradient 5-50% ethyl acetate/hexane) afforded ***3b*** (α:β =1:10, 41.4 mg, 91.9 µmol, 92%) as a white solid.

Protocol B

3a (54.0 mg, 100 µmol, α/β 8:92) was treated according to general procedure B. Irradiation time was 4 hours. Flash chromatography (1. gradient 10-50% ethyl acetate/hexane; 2. gradient 10-50% ethyl acetate/hexane) afforded ***3b*** (37.7 mg, 83.7 µmol, 84%, α/β 10:90) as a yellowish solid.

Characterization for ***3b*-β**: ^{1}H NMR (600 MHz, $CDCl_3$) δ 8.07 (d, *J* = 7.6 Hz, 2H), 7.61 (t, *J* = 7.5 Hz, 1H), 7.48 (t, *J* = 6.9 Hz, 2H), 5.09 (t, *J* = 8.3 Hz, 1H), 4.97 (t, *J* = 8.7 Hz, 1H), 4.78 (d, *J* = 12.2 Hz, 1H), 4.65 (d, *J* = 7.9 Hz, 1H), 4.56 (d, *J* = 12.2 Hz, 1H), 4.17 – 4.07 (m, 1H), 4.00 – 3.91 (m, 1H), 3.71 – 3.64 (m, 2H), 2.09 (s, 3H), 2.06 (s, 3H). ^{13}C NMR (151 MHz, $CDCl_3$) δ 171.5, 169.7, 167.3, 133.7, 130.0, 129.4, 128.7, 123.5 (q, C-F, ^{1}J C-F = 278.8 Hz), 101.0, 75.0, 74.8, 70.9, 68.8, 66.0 (q, C-F, ^{2}J C-F = 34.8 Hz), 63.1, 21.0, 20.6. ^{19}F NMR (564 MHz, $CDCl_3$) δ -74.44 (t, *J* = 8.5 Hz). HRMS (ESI) m/z: $[M + Na]^+$ Calcd for $C_{19}H_{21}F_3NaO_9$ 473.1035; Found 473.1024.

Methyl 2,4,6-tri-*O*-acetyl-3-*O*-benzyl-β-D-glucopyranosyl-(1→6)-2,4,6-tri-*O*-acetyl-3-*O*-benzyl-β-D-glucopyranoside (*4b*):

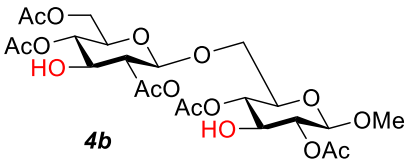

4b

Protocol A

4a (74.7 mg, 100 µmol) was treated according to general procedure A. Irradiation time was 1.5 hours. Flash chromatography (1. gradient 50-100% ethyl acetate/hexane; 2. 80% ethyl acetate/hexane) afforded ***4b*** (47.0 mg, 83.0 µmol, 83%) as a reddish solid.

Protocol B

4a (74.7 mg, 100 µmol) was treated according to general procedure B. Irradiation time was 3.5 hours. Flash chromatography (gradient 70-100% ethyl acetate/hexane) afforded ***4b*** (45.1 mg, 79.6 µmol, 80%) as a white solid.

Protocol C

4a (29 mg, 40 µmol) was treated according to general procedure C (TBN = 6 equiv, flow rate = 0.02 mL min^{-1}). Flash chromatography (gradient 30-100% ethyl acetate/hexane) afforded ***4b*** (18.5 mg, 82%) as a white solid.

^{1}H NMR (600 MHz, $CDCl_3$) δ 4.93 (t, *J* = 9.6 Hz, 1H), 4.87 – 4.83 (m, 1H), 4.83 – 4.78 (m, 2H), 4.54 (d, *J* = 7.8 Hz, 1H), 4.33 (d, *J* = 7.9 Hz, 1H), 4.25 (dd, *J* = 12.3, 4.8 Hz, 1H), 4.20 (dd, *J* = 12.3, 2.5 Hz, 1H), 3.89 (d, *J* = 9.8 Hz, 1H), 3.70 (td, *J* = 9.4, 3.6 Hz, 2H), 3.65 – 3.58 (m, 3H), 3.50 (s, 3H), 2.13 (s, 3H), 2.12 – 2.10 (m, 9H), 2.09 (s, 3H). ^{13}C NMR (151 MHz, $CDCl_3$) δ 170.9, 170.9, 170.8, 170.7, 170.7, 101.5, 100.9, 74.2, 74.1, 74.0, 73.6, 72.1, 71.7, 71.0, 68.6, 62.1, 57.1, 21.1, 21.0, 21.0, 20.9. HRMS (ESI) m/z: $[M + NH_4]^+$ Calcd for $C_{23}H_{38}NO_{16}$ 584.2191; Found 584.2192.

Ethyl 2,3-di-*O*-acetyl-6-*O*-benzoyl-β-D-thioglucopyranose (*5b*)

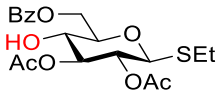

5b

Protocol A

5a (50.3 mg, 100 µmol) was treated according to general procedure A. Irradiation time was 2 hours. Flash chromatography (gradient 20-60% ethyl acetate/hexane) afforded ***5b*** (30.6 mg, 74.2 µmol, 74%) as a colorless oil.

Protocol B

5a (25.1 mg, 50 µmol) was treated according to general procedure B. Irradiation time was 6 hours. Flash chromatography (30% ethyl acetate/hexane) afforded ***5b*** (13.4 mg, 32.5 µmol, 65%) as a colorless oil.

^{1}H NMR (700 MHz, $CDCl_3$) δ 8.06 (d, *J* = 8.0 Hz, 2H), 7.60 (t, *J* = 7.4 Hz, 1H), 7.46 (t, *J* = 7.0 Hz, 2H), 5.10 (t, *J* = 8.3 Hz, 1H), 4.98 (t, *J* = 8.8 Hz, 1H), 4.75 (d, *J* = 10.0 Hz, 1H), 4.57 (d, *J* = 12.2 Hz, 1H), 4.52 (d, *J* = 10.0 Hz, 1H), 3.66 (d, *J* = 6.8 Hz, 2H), 2.77 – 2.62 (m, 2H), 2.09 (s, 3H), 2.07 (s, 3H), 1.28 – 1.24 (m, 3H). ^{13}C NMR (176 MHz, $CDCl_3$) δ 171.5, 169.8, 167.3, 133.6, 130.0, 129.6, 128.6, 83.6, 78.6, 76.6, 70.0, 69.1, 63.6, 24.3, 21.0, 20.9, 15.1. HRMS (ESI) m/z: $[M + Na]^+$ Calcd for $C_{19}H_{24}NaO_8S$ 435.1090, found 435.1081.

These data are in full agreement with those previously published in the literature.[12]

Ethyl 2-*O*-benzoyl-6-*O*-fluorenylmethoxycarbonyl-α-D-thiomannopyranose (*6b*)

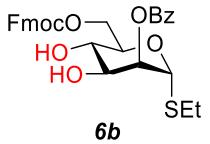

6b

Protocol A

6a (73.1 mg, 100 µmol) was treated according to general procedure A. Irradiation time was 8 hours. Flash chromatography (gradient 30-45% ethyl acetate/hexane), followed by basic washing afforded ***6b*** (46.8 mg, 85.0 µmol, 85%) as a white solid.

Protocol B

6a (36.5 mg, 50 µmol) was treated according to general procedure B. Irradiation time was 24 hours. Flash chromatography (30% ethyl acetate/hexane) afforded ***6b*** (23.5 mg, 42.7 µmol, 85%) as a yellowish solid.

Protocol C

6a (29 mg, 40 µmol) was treated according to general procedure C (TBN = 6 equiv, flow rate = 0.02 mL min^{-1}). Flash chromatography (30% ethyl acetate/hexane) afforded ***6b*** (15.2 mg, 27.6 µmol, 69%) as a colorless solid.

^{1}H NMR (600 MHz, $CDCl_3$) δ 8.06 (d, *J* = 7.8 Hz, 2H), 7.77 (d, *J* = 7.7 Hz, 2H), 7.62 (d, *J* = 6.6 Hz, 2H), 7.53 (t, *J* = 7.8 Hz, 1H), 7.40 (dt, *J* = 15.6, 7.6 Hz, 4H), 7.29 (t, *J* = 7.5 Hz, 2H), 5.49 (s, 1H), 5.45 (s, 1H), 4.66 – 4.60 (m, 1H), 4.49 (d, *J* = 12.0 Hz, 1H), 4.47 – 4.40 (m, 2H), 4.31 – 4.24 (m, 2H), 4.10 (d, *J* = 9.5 Hz, 1H), 3.96 (t, *J* = 9.7 Hz, 1H), 2.75 – 2.61 (m, 2H), 1.32 (t, *J* = 6.5 Hz, 3H). ^{13}C NMR (151 MHz, $CDCl_3$) δ 166.3, 155.9, 143.4, 141.5, 133.7, 130.0, 129.6, 128.7, 128.1, 127.4, 125.4, 125.3, 120.2, 82.7, 74.2, 71.2, 70.9, 70.4, 68.6, 67.0, 46.9, 25.9, 15.1. HRMS (ESI) m/z: $[M + Na]^+$ Calcd for $C_{30}H_{30}NaO_8S$ 573.1559; Found 573.1582.

Ethyl 2,3-di-O-acetyl-6-O-fluorenylmethoxycarbonyl-β-D-thioglucopyranose (*7b*)

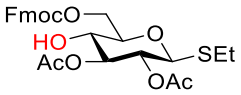

7b

Protocol A

7a (62.1 mg, 100 µmol) was treated according to general procedure A. Irradiation time was 23 hours. Flash chromatography (gradient 10-40% ethyl acetate/hexane) afforded ***7b*** (41.6 mg, 78.4 µmol, 78%) as a white solid.

Protocol B

7a (62.1 mg, 100 µmol) was treated according to general procedure B. Irradiation time was 52 hours. Flash chromatography (gradient 10-40% ethyl acetate/hexane) afforded ***7b*** (47.0 mg, 88.6 µmol, 89%) as a white solid.

^{1}H NMR (600 MHz, $CDCl_3$) δ 7.78 (d, *J* = 7.5 Hz, 2H), 7.62 (d, *J* = 7.4 Hz, 2H), 7.42 (t, *J* = 7.6 Hz, 2H), 7.36 – 7.32 (m, 2H), 5.06 (t, *J* = 9.1 Hz, 1H), 5.00 (t, *J* = 9.6 Hz, 1H), 4.54 – 4.46 (m, 3H), 4.45 (dd, *J* = 7.4, 3.4 Hz, 2H), 4.27 (t, *J* = 7.3 Hz, 1H), 3.64 (t, *J* = 9.4 Hz, 1H), 3.60 – 3.56 (m, 1H), 2.76 – 2.64 (m, 2H), 2.11 (s, 3H), 2.08 (s, 3H), 1.26 (t, *J* = 7.4 Hz, 3H). ^{13}C NMR (151 MHz, $CDCl_3$) δ 171.7, 169.7, 155.7, 143.4, 143.4, 141.5, 141.5, 128.1, 128.1, 127.4, 127.4, 125.3, 120.2, 83.6, 78.2, 77.0, 70.3, 69.9, 69.1, 66.6, 46.9, 24.3, 21.0, 20.9, 15.0. HRMS (ESI) m/z: $[M + NH_4]^+$ Calcd for $C_{27}H_{34}NO_9S$ 548.1954; Found 548.1987.

Toluyl 2-*O*-(4-oxopentanoate)-6-*O*-fluorenylmethoxycarbonyl-α-D-thiomannopyranose (*8b*)

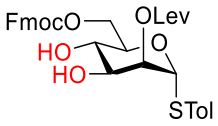

8b

Protocol A

8a (78.7 mg, 100 µmol) was treated according to general procedure A. Irradiation time was 15 hours. Flash chromatography (gradient 50-70% ethyl acetate/hexane), followed by basic washing afforded ***8b*** (57.6 mg, 94.9 µmol, 95%) as a reddish solid.

Protocol B

8a (78.7 mg, 100 µmol) was treated according to general procedure B. Irradiation time was 43 hours. Flash chromatography (gradient 30-100% ethyl acetate/hexane) afforded ***8b*** (48.0 mg, 79.1 µmol, 79%) as a pale red solid.

^{1}H NMR (400 MHz, $CDCl_3$) δ 7.77 (d, *J* = 7.5 Hz, 2H), 7.63 (d, *J* = 7.4 Hz, 2H), 7.41 (t, *J* = 7.5 Hz, 2H), 7.37 (d, *J* = 8.0 Hz, 2H), 7.31 (t, *J* = 7.5 Hz, 2H), 7.08 (d, *J* = 7.8 Hz, 2H), 5.44 (d, *J* = 2.9 Hz, 1H), 5.39 (s, 1H), 4.57 (dd, *J* = 11.9, 5.1 Hz, 1H), 4.48 – 4.36 (m, 4H), 4.26 (t, *J* = 7.2 Hz, 1H), 3.97 (dd, *J* = 9.4, 3.3 Hz, 1H), 3.75 (t, *J* = 9.6 Hz, 1H), 2.83 – 2.67 (m, 2H), 2.66 – 2.50 (m, 2H), 2.28 (s, 3H), 2.15 (s, 3H). ^{13}C NMR (101 MHz, $CDCl_3$) δ 207.9, 1723, 155.8, 143.4, 141.4, 138.4, 132.8, 130.1, 129.4, 128.1, 127.4, 127.3, 125.3, 1253, 120.2, 86.7, 73.5, 71.2, 71.1, 70.2, 68.5, 66.9, 46.9, 38.4, 29.9, 28.3, 21.3. HRMS (ESI) m/z: $[M + NH_4]^+$ Calcd for $C_{33}H_{38}NO_9S$ 624.2267; Found 624.2267.

Ethyl 2,3-di-*O*-acetyl-6-*O*-allyloxycarbonyl-β-D-thioglucopyranose (*9b*)

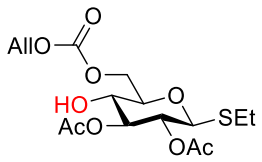

9b

Protocol A

9a (48.3 mg, 100 µmol) was treated according to general procedure A. Irradiation time was 1.5 hours. Flash chromatography (gradient 20-50% ethyl acetate/hexane) afforded ***9b*** (30.8 mg, 78.5 µmol, 79%) as a colorless oil.

Protocol B

9a (48.3 mg, 100 µmol) was treated according to general procedure B. Irradiation time was 17 hours. Flash chromatography (gradient 20-50% ethyl acetate/hexane) afforded ***9b*** (27.9 mg, 71.1 µmol, 71%) as a pale yellow oil.

^{1}H NMR (400 MHz, $CDCl_3$) δ 6.00 – 5.85 (m, 1H), 5.37 (d, *J* = 15.8 Hz, 1H), 5.28 (d, *J* = 11.6 Hz, 1H), 5.04 (t, *J* = 9.1 Hz, 1H), 4.96 (t, *J* = 9.6 Hz, 1H), 4.63 (d, *J* = 5.6 Hz, 2H), 4.51 – 4.38 (m, 3H), 3.65 (t, *J* = 8.6 Hz, 1H), 3.57 (d, *J* = 9.9 Hz, 1H), 3.00 (br s, 1H), 2.76 – 2.58 (m, 2H), 2.09 (s, 3H), 2.06 (s, 3H), 1.24 (t, *J* = 7.5 Hz, 3H). ^{13}C NMR (101 MHz, $CDCl_3$) δ 171.7, 169.8, 155.4, 131.4, 119.4, 83.4, 78.1, 76.8, 69.8, 69.0, 66.5, 24.2, 21.0, 20.9, 15.0. HRMS (ESI) m/z: $[M + Na]^+$ Calcd for $C_{16}H_{24}NaO_9S$ 415.1039; Found 415.1026.

Ethyl 2,3-di-*O*-acetyl-6-*O*-propargyloxycarbonyl-β-D-thioglucopyranose (*10b*)

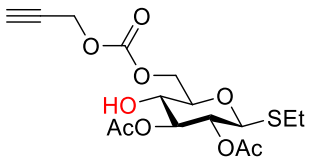

10b

Protocol A

10a (48.1 mg, 100 μmol) was treated according to general procedure A. Irradiation time was 2.5 hours. Flash chromatography (gradient 5-40% ethyl acetate/hexane) afforded ***10b*** (29.8 mg, 76.3 μmol, 76%) as a colorless oil.

Protocol B

10a (48.1 mg, 100 μmol) was treated according to general procedure B. Irradiation time was 15 hours. Flash chromatography (gradient 10-30% ethyl acetate/hexane) afforded ***10b*** (26.4 mg, 67.6 μmol, 68%) as a colorless oil.

Protocol C

10a (19.2 mg, 40 μmol) was treated according to general procedure C (TBN = 2 equiv, flow rate = 0.1 mL min^{-1}). Flash chromatography (30% ethyl acetate/hexane) afforded ***10b*** (12 mg, 31 μmol, 77%) as a colorless solid.

^{1}H NMR (600 MHz, $CDCl_3$) δ 5.03 (t, *J* = 9.1 Hz, 1H), 4.97 (t, *J* = 9.6 Hz, 1H), 4.74 (d, *J* = 2.5 Hz, 2H), 4.51 (dd, *J* = 11.9, 2.3 Hz, 1H), 4.48 (d, *J* = 9.8 Hz, 1H), 4.44 (dd, *J* = 11.9, 5.0 Hz, 1H), 3.70 – 3.64 (m, 1H), 3.60 – 3.56 (m, 1H), 2.75 – 2.63 (m, 2H), 2.54 (t, *J* = 2.5 Hz, 1H), 2.10 (s, 3H), 2.06 (s, 3H), 1.26 (t, *J* = 7.4 Hz, 3H). ^{13}C NMR (151 MHz, $CDCl_3$) δ 171.8, 169.7, 154.9, 83.5, 78.0, 77.1, 76.9, 76.1, 69.8, 69.2, 67.0, 55.7, 24.2, 21.0, 20.9, 15.0. HRMS (ESI) m/z: $[M + Na]^+$ Calcd for $C_{16}H_{22}NaO_9S$ 413.0882; Found 413.0867.

Ethyl 2,3-di-*O*-acetyl-6-deoxy-6-azido-β-D-thioglucopyranose (*11b*)

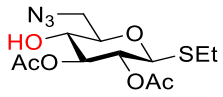

11b

Protocol A

11a (42.3 mg, 100 µmol) was treated according to general procedure A. Irradiation time was 4 hours. Flash chromatography (gradient 5-30% ethyl acetate/hexane) afforded ***11b*** (28.9 mg, 86.7 µmol, 87%) as a colorless oil.

Protocol B

11a (42.3 mg, 100 µmol) was treated according to general procedure B. Irradiation time was 6 hours. Flash chromatography (gradient 10-40% ethyl acetate/hexane) afforded ***11b*** (24.9 mg, 74.7 µmol, 75%) as a colorless oil.

^{1}H NMR (400 MHz, $CDCl_3$) δ 5.02 – 4.98 (m, 2H), 4.52 – 4.48 (m, 1H), 3.70 – 3.64 (m, 1H), 3.61 (dd, *J* = 12.9, 2.2 Hz, 1H), 3.58 – 3.52 (m, 1H), 3.47 (dd, *J* = 12.9, 5.8 Hz, 1H), 2.81 – 2.64 (m, 2H), 2.11 (s, 3H), 2.07 (s, 3H), 1.27 (t, *J* = 7.5 Hz, 3H). ^{13}C NMR (101 MHz, $CDCl_3$) δ 172.2, 169.7, 83.1, 79.5, 77.5, 70.1, 69.6, 51.4, 23.9, 21.0, 20.9, 14.8. HRMS (ESI) m/z: $[M + Na]^+$ Calcd for $C_{12}H_{19}N_3NaO_6S$ 356.0892; Found 356.0875.

Phenyl 2-*O*-benzoyl-4,6-*O*-benzylidene-β-D-thioglucopyranose (*12b*)

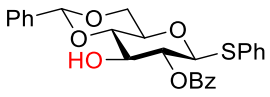

12b

Protocol A

12a (60.5 mg, 100 µmol) was treated according to general procedure A. Irradiation time was 4 hours. Flash chromatography (gradient 20-30% ethyl acetate/hexane), followed by basic washing afforded ***12b*** (41.2 mg, 88.7 µmol, 89%) as a pale red solid.

Protocol A - no irradiation

An oven dried vial (19 x 100 mm) equipped with a stir bar was charged with ***12a*** (60.5 mg, 100 µmol) and DDQ (34.1 mg, 150 µmol, 1.5 equiv), and then sealed with a septum and Parafilm. After evacuating and backfilling the vial with argon 3 times, previously degassed DCM (5 mL) and water (50 µL) were added through the septum. The reaction mixture was stirred at high speed in the dark for 5 hours, when consumption of the starting material was detected by TLC analysis. The reaction mixture was transferred into a round-bottom flask, solvents were removed under vacuum and the residue was loaded on a silica column. Flash chromatography (gradient 10-30% ethyl acetate/hexane), followed by washing with aqueous saturated $NaHCO_3$ afforded ***12b*** (45.2 mg, 97.3 µmol, 97%) as a white solid.

Protocol B

12a (60.5 mg, 100 µmol) was treated according to general procedure B. Irradiation time was 15 hours. Flash chromatography (gradient 5-25% ethyl acetate/hexane) afforded ***12b*** (40.1 mg, 86.3 µmol, 86%) as a white solid.

^{1}H NMR (600 MHz, $CDCl_3$) δ 8.10 (d, J = 7.9 Hz, 2H), 7.61 (t, J = 7.4 Hz, 1H), 7.51 – 7.44 (m, 6H), 7.40 – 7.35 (m, 3H), 7.33 – 7.28 (m, 3H), 5.57 (s, 1H), 5.17 (t, J = 9.4 Hz, 1H), 4.91 (d, J = 10.0 Hz, 1H), 4.43 (dd, J = 10.6, 4.9 Hz, 1H), 4.07 (t, J = 8.9 Hz, 1H), 3.83 (t, J = 10.2 Hz, 1H), 3.64 (t, J = 9.3 Hz, 1H), 3.59 (td, J = 9.7, 5.0 Hz, 1H). ^{13}C NMR (151 MHz, $CDCl_3$) δ 166.0, 137.0, 133.6, 133.2, 132.1, 130.2, 129.6, 129.5, 129.1, 128.6, 128.5, 128.5, 126.4, 102.1, 86.8, 80.8, 73.9, 73.4, 70.6, 68.7. HRMS (ESI) m/z: $[M + Na]^+$ Calcd for $C_{26}H_{24}NaO_6S$ 487.1191; Found 487.1188.

These data are in full agreement with those previously published in the literature.[13]

Ethyl 2,3-di-*O*-acetyl-6-*O*-benzyloxycarbonyl-β-D-thioglucopyranose (*13b*)

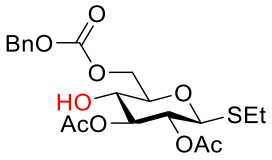

13b

Protocol A

13a (53.2 mg, 100 µmol) was treated according to general procedure A. Irradiation time was 4 hours. Flash chromatography (gradient 10-60% ethyl acetate/hexane) afforded ***13b*** (23.6 mg, 53.3 µmol, 53%) as a colorless oil.

Protocol B

13b was not obtained under these reaction conditions.

^{1}H NMR (400 MHz, $CDCl_3$) δ 7.42 – 7.31 (m, 5H), 5.17 (s, 2H), 5.04 (t, J = 9.1 Hz, 1H), 4.95 (t, J = 9.6 Hz, 1H), 4.51 – 4.38 (m, 3H), 3.67 – 3.52 (m, 2H), 2.76 – 2.59 (m, 2H), 2.08 (s, 3H), 2.06 (s, 3H), 1.23 (t, J = 7.5 Hz, 3H). ^{13}C NMR (101 MHz, $CDCl_3$) δ 171.7, 169.7, 155.5, 135.0, 128.8, 128.8, 128.5, 83.4, 78.0, 76.8, 70.2, 69.8, 69.0, 66.6, 24.2, 21.0, 20.9, 14.9. HRMS (ESI) m/z: $[M + Na]^+$ Calcd for $C_{20}H_{26}NaO_9S$ 465.1195; Found 465.1187.

8.2. Unsuccessful substrates

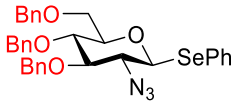

14a

Treatment of ***14a*** according to general procedure B didn't afford the desired product. After 24 hours, mass spectrometry indicated cleavage of the phenlyselenide group.

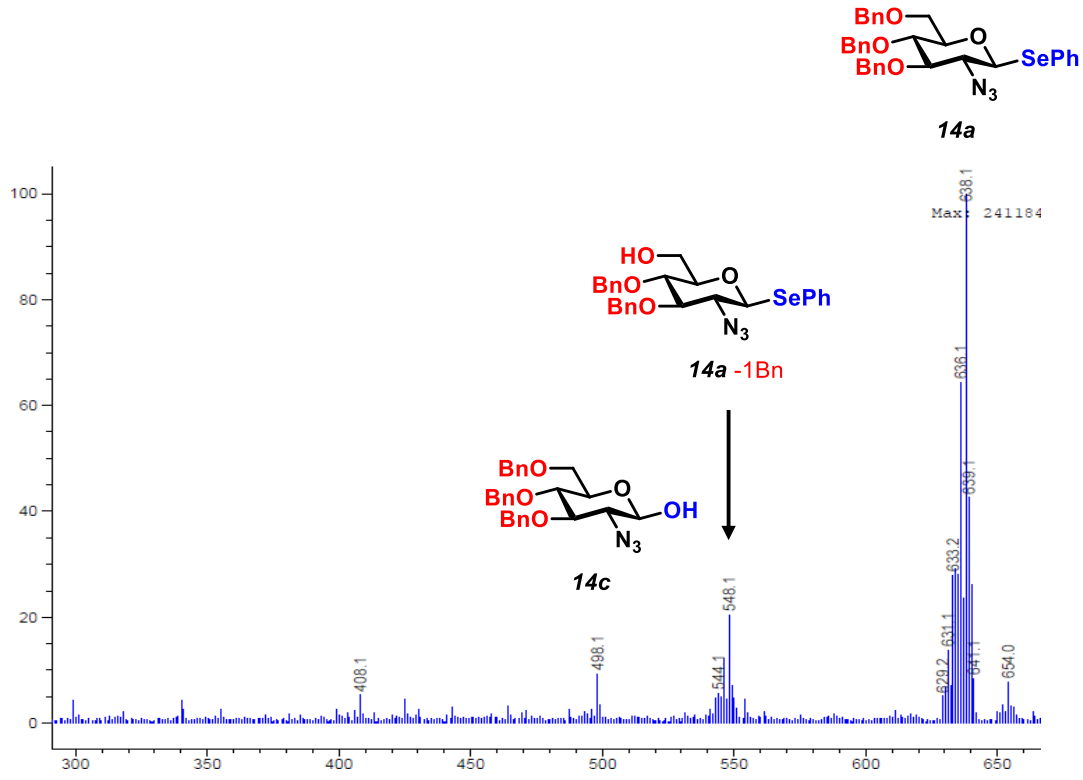

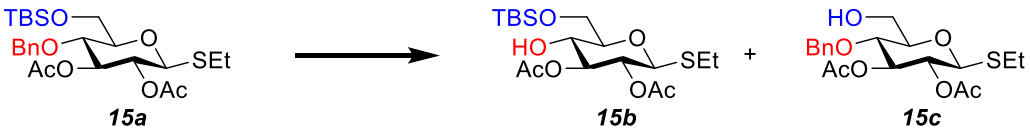

Treatment of ***15a*** according to general procedure B afforded in 24 hours a mixture of the desired product ***15b*** and the side-product ***15c***.

Mass spectrometry analysis after 6 hours:

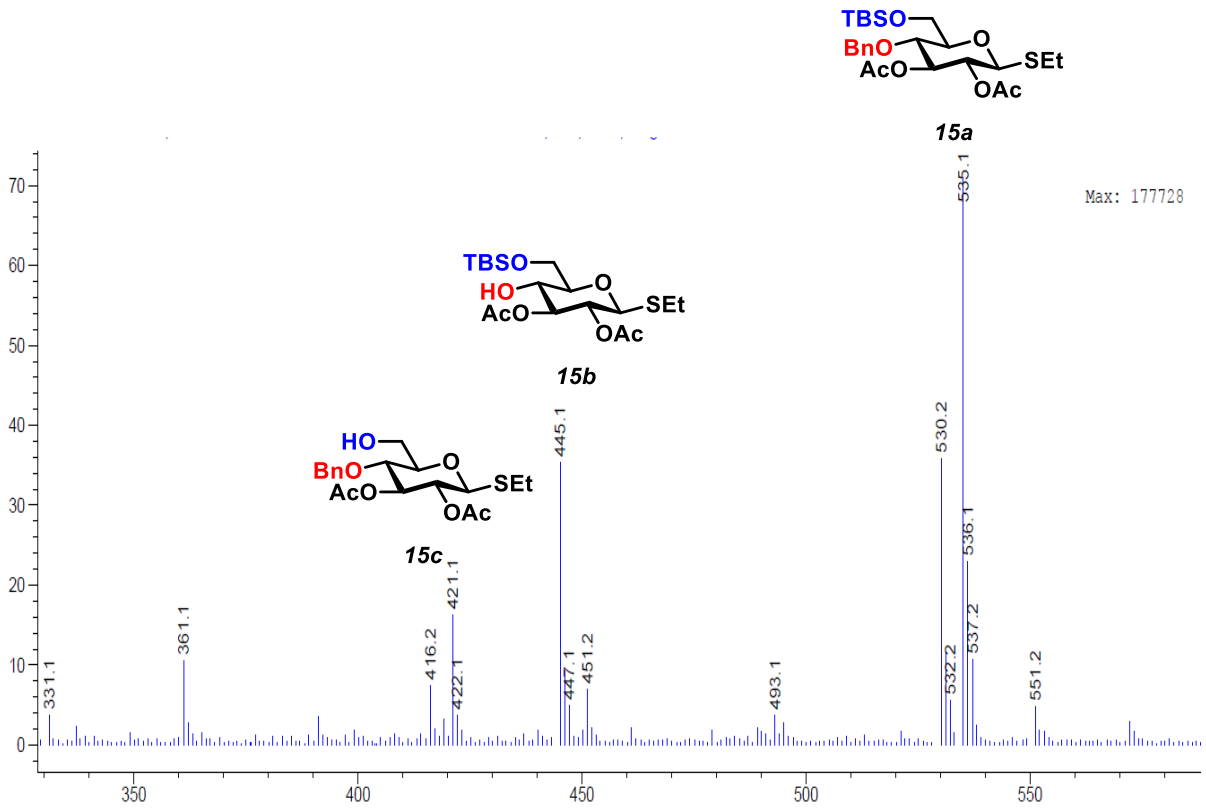

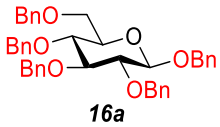

16a

Treatment of ***16a*** according to both general procedures A and B didn't afford the product. High amounts of solid precipitated during the reaction. After 24 hours, mass spectrometry indicated presence in the solution of multiple species with different levels of deprotection.

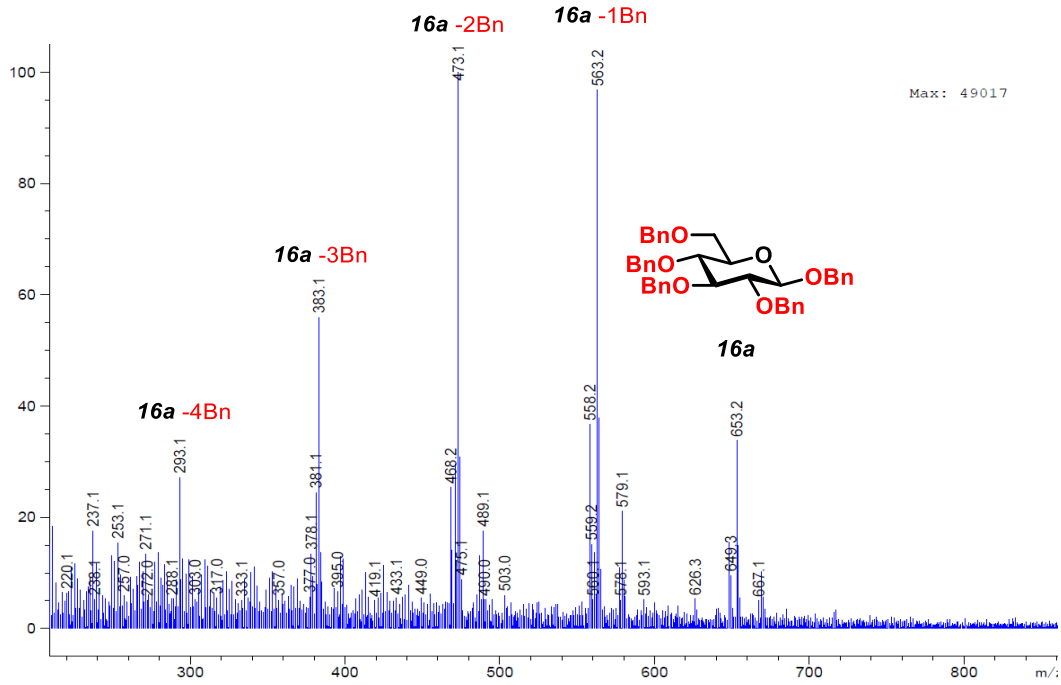

9. References

1. Kessil Photoredox products overview. https://www.kessil.com/photoreaction/PR160L.php (accessed October 2020).
2. Draskovits, M.; Kalaus, H.; Stanetty, C.; Mihovilovic, M. D. Intercepted dehomologation of aldoses by N-heterocyclic carbene catalysis – a novel transformation in carbohydrate chemistry. *Chem. Commun.* **2019,** *55*, 12144-12147.
3. Naresh, K.; Schumacher, F.; Hahm, H. S.; Seeberger, P. H. Pushing the limits of automated glycan assembly: synthesis of a 50mer polymannoside. *Chem. Commun.* **2017,** *53*, 9085-9088.
4. Lu, W.; Navidpour, L.; Taylor, S. D. An expedient synthesis of benzyl 2,3,4-tri-O-benzyl-β-d-glucopyranoside and benzyl 2,3,4-tri-O-benzyl-β-d-mannopyranoside. *Carbohydr. Res.* **2005,** *340*, 1213-1217.
5. Virlouvet, M.; Gartner, M.; Koroniak, K.; Sleeman, J. P.; Bräse, S. Multi-Gram Synthesis of a Hyaluronic Acid Subunit and Synthesis of Fully Protected Oligomers. *Adv. Synth. Catal.* **2010,** *352*, 2657-2662.
6. Tucker, J. W.; Narayanam, J. M. R.; Shah, P. S.; Stephenson, C. R. J. Oxidative photoredox catalysis: mild and selective deprotection of PMB ethers mediated by visible light. *Chem. Commun.* **2011,** *47*, 5040-5042.
7. Zhang, G.; Li, G.; Lan, Z.-A.; Lin, L.; Savateev, A.; Heil, T.; Zafeiratos, S.; Wang, X.; Antonietti, M. Optimizing Optical Absorption, Exciton Dissociation, and Charge Transfer of a Polymeric Carbon Nitride with Ultrahigh Solar Hydrogen Production Activity. *Angew. Chem. Int. Ed.* **2017,** *56*, 13445-13449.
8. Guo, X.; Zipse, H.; Mayr, H. Mechanisms of Hydride Abstractions by Quinones. *J. Am. Chem. Soc.* **2014,** *136*, 13863-13873.
9. Ohkubo, K.; Fujimoto, A.; Fukuzumi, S. Visible-Light-Induced Oxygenation of Benzene by the Triplet Excited State of 2,3-Dichloro-5,6-dicyano-p-benzoquinone. *J. Am. Chem. Soc.* **2013,** *135*, 5368-5371.
10. Utamura, T.; Kuromatsu, K.; Suwa, K.; Koizumi, K.; Shingu, T. Syntheses and 1H- and 13C-Nuclear Magnetic Resonance Spectra of All Positional Isomers of Tetra-O-acetyl-D-glucopyranoses, and Their Monobenzyl and Monotrityl Derivatives. *Chem. Pharm. Bull.* **1986,** *34*, 2341-2353.
11. Kienle, M.; Eisenring, P.; Stoessel, B.; Horlacher, O. P.; Hasler, S.; van Colen, G.; Hartkoorn, R. C.; Vocat, A.; Cole, S. T.; Altmann, K.-H. Synthesis and Structure–Activity Relationship Studies of C2-Modified Analogs of the Antimycobacterial Natural Product Pyridomycin. *J. Med. Chem.* **2020,** *63*, 1105-1131.
12. Cheng, S.; Du, Y.; Bing, F.; Zhang, G. Synthesis of flaccidoside II, a bidesmosidic triterpene saponin isolated from Chinese folk medicine Di Wu. *Carbohydr. Res.* **2008,** *343*, 462-469.
13. Lemanski, G.; Ziegler, T. Chemical Synthesis of a Tetrasaccharide Fragment Related to the Exopolysaccharide of Arthrobacter sp. CE-17. *Eur. J. Org. Chem.* **2000,** *2000*, 181-186.

Copies of NMR spectra of isolated compounds

Copies of NMR spectra of isolated compounds are available in the Supporting Information through the website of the Publisher. https://doi.org/10.1021/acs.orglett.0c04026

Abbreviations List

^{3}DDQ*	Triplet excited state of DDQ
^{3}MLCT	Triplet excited state resulting from a metal-to-ligand charge transfer transition
A	Electron acceptor
BIPA	*N*-*tert*-Butylisopropylamine
Bn	Benzyl
Boc-Pro-OH	*N*-(*tert*-Butoxycarbonyl)proline
bpy	2,2'-Bipyridine
Bz	Benzoyl
CB	Conduction band
cbz	Benzyloxycarbonyl
CN	Carbon nitride
CTC	Charge-transfer complex
D	Electron donor
d	Doublet
DABCO	1,4-Diazabicyclo[2.2. 2]octane
DBU	1,8-Diazabicyclo[5.4.0]undec-7-ene
DCM	Dichloromethane
DDQ	2,3-Dichloro-5,6-dicyano-1,4-benzoquinone
$DDQH_2$	2,3-Dichloro-5,6-dicyano-1,4-hydroquinone
$dF(CF_3)ppy$	2-(2,4-Difluorophenyl)-5-(trifluoromethyl)pyridine
diglyme	Diethylene glycol dimethyl ether
DIPEA	*N*,*N*-diisopropylethylamine
DMA or DMAc	*N*,*N*-Dimethylacetamide

DMAP	*N*,*N*-Dimethylaminopyridine
DMF	*N*,*N*-Dimethylformamide
DMPU	*N*,*N'*-Dimethylpropyleneurea
DMSO	Dimethylsulfoxide
donor*	Excited state partecipating in energy transfers
dtbbpy	4,4'-Di-tert-butyl-2,2'-bipyridine
EDA	Electron-donor acceptor (complex)
EI	Electronic ionization
EnT	Energy transfer
EPR	Electron paramagnetic resonance spectroscopy
ESI	Electrospray ionization
ET	Electron transfer
FTIR	Fourier-transform infrared spectroscopy
g-CN	Graphitic carbon nitride
GC-MS	Gas chromatography-mass spectrometry
glyme	1,2-Dimethoxyethane
HAT	Hydrogen atom transfer
HOMO	Highest occupied molecular orbital
HPLC	High-performance liquid chromatography
HR-MS	High resolution mass spectrometry
ISC	Intersystem crossing
K_m	Michaelis menten constant
LG	Leaving group
LUMO	Lowest unoccupied molecular orbital
m	Multiplet
MeCN	Acetonitrile

MeOH	Methanol
Mes-Acr+	9-Mesityl-10-methylacridinium
MLCT	Metal-to-ligand charge transfer
MS	Mass spectrometry
n.d.	Not detected
n.d.o.	Not determined due to overlapping peaks
NMR	Nuclear magnetic resonance spectroscopy
OSET	Outer-sphere single electron transfer
PC	Photocatalyst
PC*	Excited state of the photocatalyst
PC^{ox}	Photocatalyst after oxidative quenching
PC^{red}	Photocatalyst after reductive quenching
PET	Photoinduced electron tranfer
PG	Protecting group
PMB	*para*-Methoxybenzyl (ether)
ppy	2-Phenylpyridyne
PRC	Photoredox catalysis
q	Quartet
RPKA	Reaction progress kinetic analysis
s	Singlet
S_0	Singlet state
S_1	Singlet excited state
SCE	Saturated calomel electrode
SET	Single electron transfer
t	Triplet
T_1	Triplet excited state

TBN	*tert*-Butyl nitrite
$TEDA^{2+\bullet}$	(*N*-(chloromethyl)triethylenediamine)
TEMPO	2,2,6,6-Tetramethylpiperidine-1-oxyl
THF	Tetrahydrofurane
TLC	Thin layer chromatography
Tol	Toluene
V_0	Initial reaction rate
V_{max}	Maximum reaction rat
VB	Valence band
VTNA	Variable time normalization analysis